INTER-UNIVERSITY ACCELERATOR CENTRE

(An Autonomous Inter-University Centre of UGC)
Aruna Asaf Ali Marg, New Delhi-110 067

वार्षिक प्रतिवेदन 2017-18

Annual Report 2017-2018

ANNUAL REPORT
2017-2018

अन्तर–विश्वविद्यालय त्वरक केन्द्र
Inter-University Accelerator Centre

(विश्वविद्यालय अनुदान आयोग का स्वायत्त केन्द्र)

(An Autonomous Inter-University Centre of UGC)

Post Box No. 10502, Aruna Asaf Ali Marg, New Delhi - 110 067 (India)
Tel: 011-24126018, 24126022, 24126024-26, 24126029
Fax: 011-24126036, 24126041 Website : www.iuac.res.in

Published by:
Inter-University Accelerator Centre, New Delhi

Layout & Printed by:
Neelkanth Printers, New Delhi

For comments/suggestions, please write to:
editorial@iuac.res.in

Available online at:
http://www.iuac.res.in/reports/index.html

DIRECTOR'S REPORT

It gives us immense pleasure to present the Annual report of the Inter-University Accelerator Centre (IUAC) containing the research and developmental activities of the Centre during April, 2017 to March, 2018. The report comprises mainly the glimpses of the high-quality developments in the front ranking areas related to modern accelerators and associated research facilities, as well as the findings of some of the internationally competitive accelerator-based research programs in the areas of nuclear physics, materials sciences, atomic and molecular physics, radiation biology and geochronology. IUAC has become the premier ion beam-based research centre in the country providing varieties of ion beams in the energy range varying from a few keV to hundreds of MeV.

The number of research groups utilizing the research facilities at IUAC has been increasing very fast due to availability of newer facilities in the areas of low energy positive and negative ions beams, Rutherford back scattering/channelling and other sample preparation/characterization facilities along with the excellent performance and utilization of large accelerators e.g., 15UD Tandem Pelletron Accelerator and Complete Superconducting Linear Accelerator (SC-LINAC). A large number of scholars from all over India and abroad have been completing their PhD Theses using the facilities at IUAC. The SC-LINAC along with the liquid helium (LHe) plant, cryostats and cryogenic distribution systems performed excellently for about six months continuously delivering beams for experiments for about five months. A series of nuclear physics experiments related to nuclear reaction and nuclear structure have been performed using the world class experimental nuclear physics facilities e.g., NAND, HYRA and INGA.

The Centre has been following the road-map meticulously to address the future requirements and challenges by adding new accelerator facilities like high current injector (HCI), compact Free Electron Laser (partly funded by BRNS), High Resolution Secondary Ion Mass Spectrometer (HR-SIMS) and 6-8 MV Tandem (both as part of the various advanced facilities being established as national facility for Geochronology program at IUAC). The existing 500 kV Tandem Pelltron for Accelerator Mass Spectrometry (AMS) is being used extensively for Carbon, Beryllium, Aluminium dating. It is planned to develop a dedicated electron beam irradiation facility at IUAC, based on mutual discussions on its use by ISRO and users' community of IUAC, after getting the proposal sanctioned by ISRO.

I would like to congratulate my highly talented colleagues at IUAC for their hard work in taking the Centre to a new height through sustained advanced development and research activities in the spirit of cooperation, collaboration and coordination. The large number of researchers from the universities, institutes and laboratories from all over India and abroad have been carrying

out exciting and innovative experiments. The large number of publications in internationally reputed peer-reviewed journals bear the testimony of our excellence in the focused research and developmental activities at IUAC.

The Centre keeps organizing various national and international schools, conferences, workshops and outreach programs. Many of our colleagues and scholars have been awarded for their excellence in research and developmental activities nationally and internationally. An ultra-modern Auditorium powered by Solar Power is about to be ready for holding future programs. We are grateful to the members of the administrative committees, statutory and advisory committees/bodies for their help and advice.

The dedicated services provided by various sections of the administrative and support staff for efficient and smooth functioning of the Centre are highly appreciated.

We are very thankful to the University Grants Commission for its full support for the internationally competitive focussed research activities, upgradation of the existing facilities, and the development of the newer facilities and research activities as per the road-map of the Centre.

The continued supports in project-mode received from other Government agencies like Department of Science and Technology, Board of Research in Nuclear Sciences of Department of Atomic Energy, Ministry of Earth Sciences for development of advanced research facilities and activities of current interest at IUAC are gratefully acknowledged.

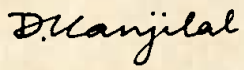

Dinakar Kanjilal
Director

CONTENTS

1. ACCELERATOR

1.1 PELLETRON

1.1.1 Operational Summary

G Raturi, J Singh, Pranav Singh, S Kumar, S Mohan, N S Panwar, M P Singh, R Kumar, J Prasad, M Archunan, V P Patel, R P Sharma, G Umapathy, Rajveer, Pankaj Kumar, K Devarani, M Sota, Abhilash, A Kothari, P Barua, S Ojha, S Gargari, R Joshi and S Chopra

The performance of 15 UD Pelletron accelerator was excellent from 15th March 2017 to 25th September 2017 with few breakdowns. There was only one scheduled tank opening maintenance, during the mentioned period. The operational summary of the accelerator from April 2017 to March 2018 is as below:

Total No. of Chain Hours	=	7150 Hours
Total Beam utilization	=	5243 Hours
Machine breakdown	=	0599 Hours
Accelerator Conditioning	=	0474 Hours
Beam Change Time	=	0011 Hours
Tank opening maintenance	=	0935 Hours
Beam tuning time	=	0339 Hours
Experimental setup time	=	0096 Hours
Accelerator set up time after maintenance	=	0046 Hours

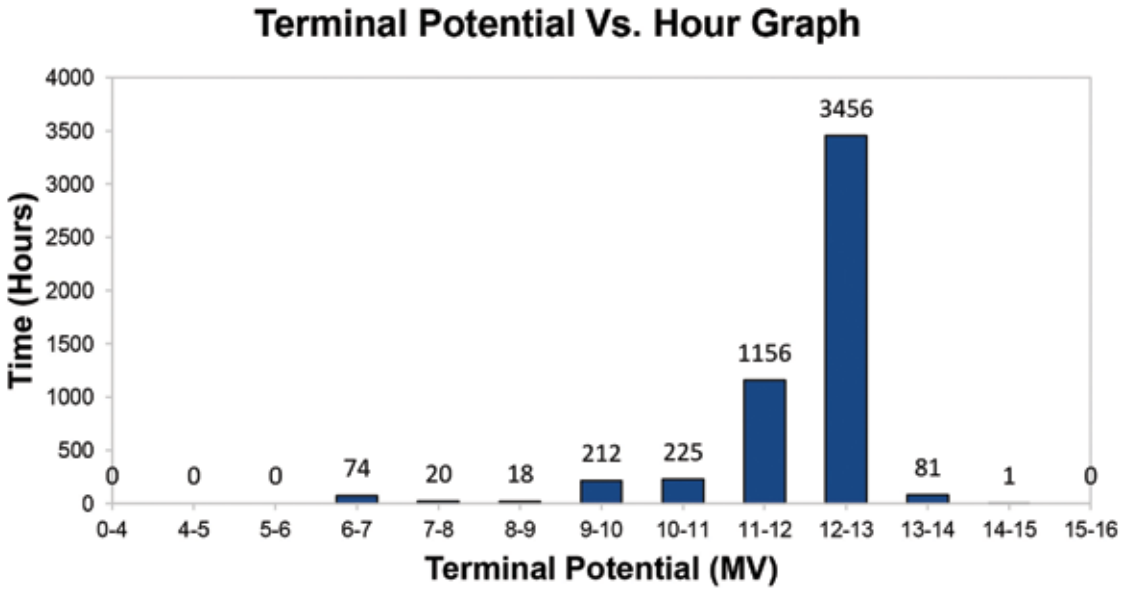

Figure 1.1.1: Terminal potential vs hour graph

A total number of 655 shifts were used for experiment during mentioned period, 495 shifts were used for pulsed beam users and 160 for DC beam users. The machine up time for this period is 91.62% and the beam time utilization is 73.33%. The voltage distribution graph of Terminal Potential used for different experiments during above mentioned period is shown in figure 1.1.1. ^{19}F, 7^{+}, 120 MeV pulsed beam at maximum terminal potential 14.95 MV and ^{6}Li, 3^{+}, 26 MeV dc beam at the minimum terminal potential of 6.45 MV were delivered to users. Maximum terminal voltage achieved during conditioning in this year was 15.3 MV.

Figure 1.1.2 shows the Chain hours utilization for mentioned period.

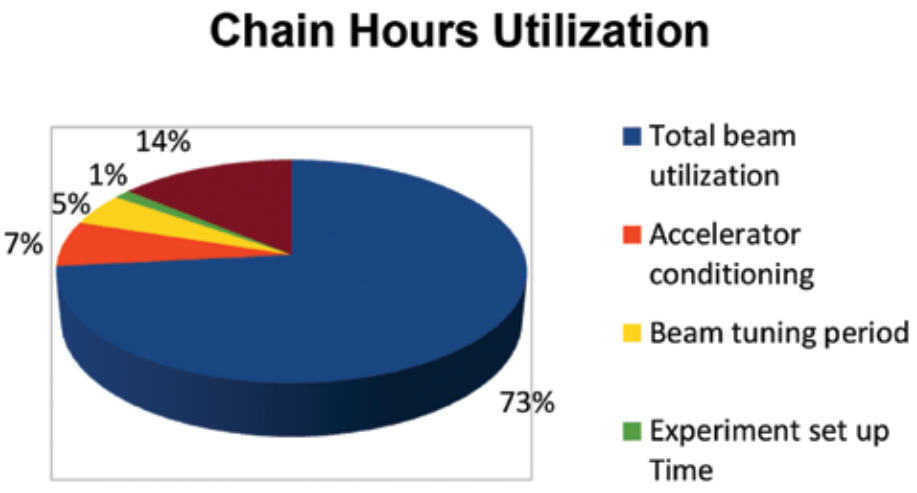

Figure 1.1.2: Chain hours utlization

Duration of beam run time in percentage, for different ions species, is shown in table 1.

Table 1

Beam Delivered	Utilization (%age of total time)	Beam Delivered	Utilization (%age of total time)
^{6}Li	1.32%	^{19} Si	10.13%
^{7}Li	1.92%	^{32} S	10.83%
^{12} C	2.70%	^{35} Cl	1.09%
^{13} C	1.72%	^{37} Cl	1.49%
^{16} O	7.75%	^{48} Ti	8.37%
^{18} O	11.12%	^{58} Ni	0.89%
^{19} F	5.42%	^{107} Ag	6.22%
^{28} Si	26.67%	^{197} Au	2.36%

Pi- chart in figure 3 shows the distribution of delivered beam species during beam run from 1st April 2016 to 31st March 2017.

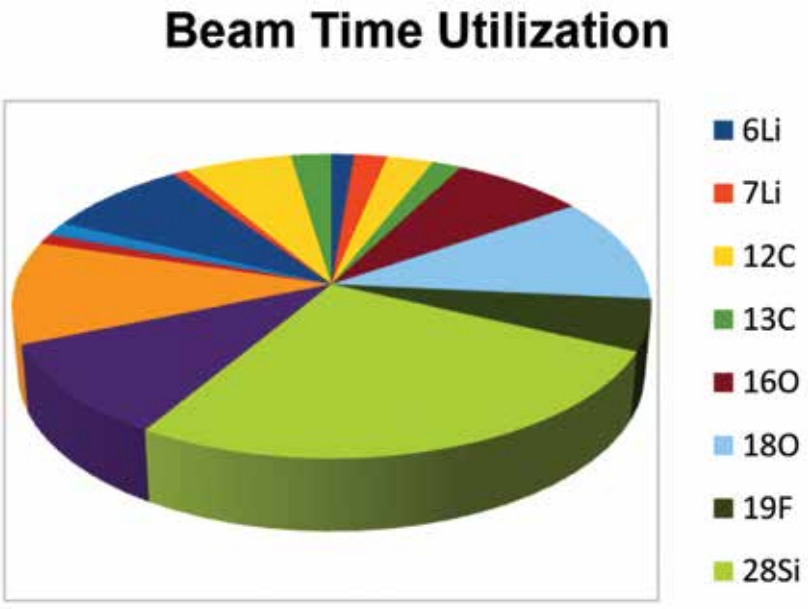

Figure 1.1.3: Beam Time utilization

1.1.2 Maintenance and development activities

There were three tank opening maintenances in the last academic year. The first and third maintenances were scheduled and second one was unscheduled. Details of the maintenances are mentioned below.

Tests performed before tank opening

The first tank opening maintenance of the academic year was scheduled maintenance. The 15 UD Pelletron was operated successfully for the users' experiment from 15th March 2017 to 25th September 2017. Thereafter the 15 UD Pelletron accelerator was taken for scheduled maintenance and this maintenance was scheduled from 25th September 2017 to 4th November 2017.

Major maintenance jobs performed during scheduled tank opening maintenance:

1. Charging system maintenance

The High voltage terminal was grounded by connecting it with tank body, so that terminal should not accumulate any charge if chains are running and condition of both the charging systems was checked. Idler wheels on up – charge side, in unit #18, 22 and 27 for charging system #1, were damaged. All those three damaged idler wheels were replaced and aligned. Both the chains ran and condition of all idler wheels for both the charging systems was checked in running condition and found to be satisfactory.

Condition of nylon links for both of the charging chains was inspected also for cracks and no crack was found. Performance of both the charging systems was checked electrically at different CPS from 2 kV to 7 kV and it was found to be satisfactory. Both the chains were cleaned and the charging systems were kept ON for four overnights to check its mechanical performance. All the nuts and bolts for both the charging systems, in terminal area and at tank bottom, were checked and tightened, if required. Semiconductor band of all the pulleys of both the charging systems were oiled with TP oil to reduce the friction between pulley and chain. Pillow blocks and chain motors of both the charging systems were properly greased. The ground connection of terminal was disconnected and completed the charging system maintenance.

2. Maintenance of Rotating parts inside accelerator tank

Thorough maintenance of all the rotating parts, such as charging chain motors, rotating shaft motors, separator box assemblies for rotating shafts and blower motor was done. Bearings of eighteen separator boxes were replaced, ten in low energy side and eight in high energy side. Bearings of these assemblies were replaced by new bearings. Rubber couplers in two of the separator box assemblies (between unit #6–7 and unit #8–9) were also replaced as those got cracked. All the repaired separator box assemblies were installed back and aligned after maintenance. All in five tank motors (2 chain motors, 2 rotating shaft motors and a blower motor) were also greased properly.

3. Stripper foil loading in terminal and High Energy Dead Section (HEDS)

During the maintenance, fresh stripper foils were loaded in the high voltage terminal and HEDS. 34 LPA Stripper foils, of Munich make, and 131 stripper foils of IUAC make, were installed in terminal. However 124 IUAC make stripper foils and 49 Munich make stripper foils were loaded in HEDS area.

4. Repairing of Column Support Post (CSP) gaps

The condition of CSP and accelerating tubes should be good for stable operation of tandem accelerator. If condition of even a single CSP gap or accelerating tube gap, is bad, machine will not be able to handle rated high voltage and this may also lead to instability in beam.

During inspection, a big vertical crack on ceramic surface across gap #8 in unit #28 was observed. The cracked gap was shorted and now the total number of 35 CSP gaps was shorted (17 in LES and 18 in HES).

5. Hoop Screws maintenance

Equi-potential rings are mounted on every accelerating unit of tandem accelerator. These hoops are responsible of proper field distribution. The hoop screws are the screws which hold the hoops at the mounting position on Column Support Posts. Resistance between hoop screw and equi-potential rings must be zero. But this resistance value varies from few ohms to Mega ohms and sometimes even open due to deposition of by-products of SF_6 gas. Resistance measurement between Hoop screws and equi-potential rings was done for full machine. The Hoop screw which shows more than 1 kilo ohm value was changed for 15 units. The remaining screws will be replaced in next scheduled maintenance.

6. Corona probe maintenance

The condition of all seven corona probe needles was good. Therefore, none of the corona needles were replaced.

Other maintenance outside Pelletron Accelerator tank

1. Maintenance of Vacuum related components

Routine maintenance of all ion pumps and sublimator pumps along with their controllers was performed and required repair work was done.

2. Maintenance related to different devices

The routine checkup and breakdown maintenance of different devices, such as Beam Line Valves (BLVs), Faraday Cup controller, a power supply, CAMAC control system etc., was also done.

1.1.3 Ion source activities

Operation

The operation and ion beam delivery of MC-SNIC ion source had been excellent from April 2017 to March 2018. Routinely, energized ion beam of various ion species in the energy range, 130 to 200 keV were delivered for the experiments conducted regularly using Pelletron accelerator system. Ion source ran in its high capacity to provide pulsed ion beam. Other than routinely delivered ion beam, various enriched isotope ion beam, ^{6}Li, ^{13}C, ^{18}O, ^{30}Si and ^{37}Cl were produced. In regular interval, varieties of cathode samples were prepared and loaded to the cathode wheel as and when required.

Maintenance

1. Preventive Maintenances

As a preventive measure, thorough cleaning of ion source system, HV deck, multiplier stack and filter stack of HV power supply, high voltage enclosure as well as the entire room were performed in regular interval as per requirements. Ion source components get dirty with time because of deposition of cesium and other chemicals used for ion beam production. As the pumping station of the injector system is located at the accelerator tubes (GP tubes) grounding end, there exists a pressure gradient from the source to this end. Thus, cesium vapor were transported and deposited on the travel path i.e. the extractor-lens (einzel lens assembly) and the accelerating tubes (GP tubes). To clean the ion source system, the preventive maintenance was performed once in the month of November, 2011. The details are as follows.

a. Ion source assembly

The ion source assembly was detached from the beam line and opened. Its entire components including ionizer assembly were sand blasted, then cleaned with alcohol. However, the cesium line of the ion source housing was first cleaned with water and then the whole body with alcohol. The cleaned components were dried with hot air blower. Ion source components, after cleaning, were assembled back and aligned with an alignment kit. The gate valve which isolates ion source from the beam line was also cleaned and ion sourcegatewas mounted back to the valve.

b. Einzel lens assembly

The gap insulations of einzel lens were measured with Megger and found them in few tens of MΩ range. Therefore, it was detached from the beam line. The spare einzel lens housing was sand blasted, cleaned thoroughly with alcohol and dried. The two stainless steel electrodes for extractor and focus were also cleaned using alcohol and dried them. Assembled back the einzel lens by carefully maintaining the gaps of extractor and focus electrodes; alignment was done with the help of alignment kit. The gap insulation of cleaned einzel lens improved in few hundred Giga Ω range. The lens was installed back to the beam line. Ion source and the lens were connected by carefully aligning them.

A new cesium ampoule was loaded after flushing out entire ion source chamber with argon. Vacuum was created approximately up to low x 10^{-6} torr range. The cathode samples were prepared and loaded. After baking the source, ion source was tested for normal operation.

General purpose accelerating tubes (GP tubes): The high voltage holding capability of GP tubes deteriorated with time. The ceramic insulations of accelerating tubes and toroids were cleaned. Burnt and defective resistors were replaced with new ones. GP tubes were conditioned for improving high voltage holding capability. Initially,

lots of X-rays were observed at HVS, 210KV. We could achieve up to 250KV with stability. Time to time, the conditionings of GP tubes were also carried out as per requirements.

2. Breakdown Maintenances

Breakdown maintenance was performed once in the month of January, 2018. The ion beam profiles of X, Y were steering in +X, +Y direction with immersion lens voltage. As the material is consumed due to sputtering, the focusing point of cesium beam onto the cathode surface needs to be changed with time. Therefore, to cater stable and intense ion beam, the operator need to tune the immersion lens parameter. This problem led to change in beam profile, hence beam transmission got affected, especially in case of pulsed beam. Therefore, ion source was opened. While dismantling ion source, it was observed that cesium spot on cathode surface displaced in -X, -Y (3rd quadrant) direction while ion beam spot on the ionizer opening was exactly opposite. The parts of the ion source were cleaned, assembled using alignment kit. The ceramic gap insulations of einzel lens were checked and found them in few Giga ohm range. To avoid misalignment of the ion source, ion source was connected to the einzel lens by aligning it with long bolts. Vacuum approximately in the range of low 10^{-6} torr range was created and subsequently, ion source was baked and tested for normal operation.

Development activities

Guide Rail Assembly for ion source

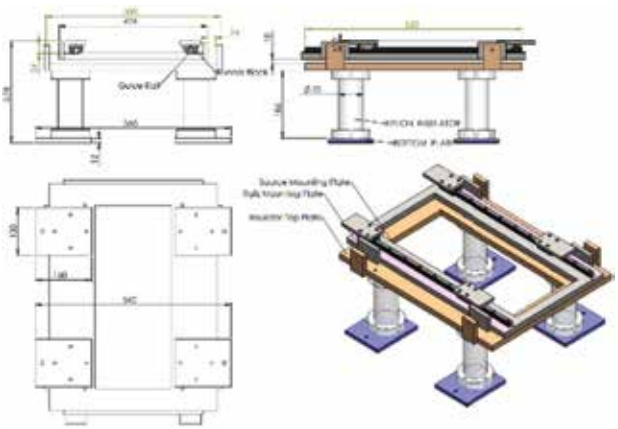

It is quite difficult to align the ion source with respect to Beam line whenever the ion source assembly is mounted back after ion source opening maintenance since it is quite bulky. A slight miss matched in the alignment caused steering of ion beam, beam loss and instability in the operation of the source. In fact, the source was opened at least twice to solve misalignment in this academic year itself. Therefore, it was felt to include a guide rail for smooth handling and alignment of the ion source during maintenance. The design was taken from the test bench guide rail of negative ion implanter facility. The dimensions had been changed to adjust the height of the beam line. The guide rail was fabricated, assembled and ready for installation on the high voltage deck in the coming tank opening maintenance.

1.1.4 Beam Pulsing system

Operation

A total of 495 shifts of beam time was used for pulsed beam runs using Multi Harmonic Buncher (MHB) along with low energy chopper. Traveling Wave Deflector (TWD) was also used whenever different repetition rates of pulsed beam, other than 250 ns, is required. All the pulsed beams were utilized by users to perform their experiments in different experimental lines. Out of 495 shifts, 186 shifts were utilized using Pelletron only and the bunched beams were ^{6}Li, ^{7}Li, ^{12}C, ^{16}O, ^{18}O, ^{19}F, ^{28}Si, ^{32}S, ^{35}Cl and ^{37}Cl. LINAC was used for remaining 309 shifts for the user experiments and the beam bunched were ^{16}O, ^{18}O, ^{28}Si, ^{30}Si and ^{48}Ti.

All the pulsed beam runs were quite stable.

Maintenance

a) Chopper maintenance

The routine maintenance of chopper was carried out after 50 Ω pure resistive dummy load was connected at the

output of amplifier and output stage of amplifier was tuned for maximum power transfer. The output of amplifier was then disconnected from dummy load and connected to tank circuit of chopper. The chopper tank circuit was then tuned for maximum power transfer from chopper amplifier. The chopper tank circuit could be tuned to get maximum forward power of ~20 W with reflected power of ~0.5 W. The chopper amplifier was kept ON for three days and its stability was satisfactory.

b) Traveling Wave Deflector (TWD) maintenance

In routine maintenance of TWD, all the control electronics and switching amplifier electronics was checked and the performance of TWD electronics was good.

Apart from routine maintenance, a breakdown maintenance was also carried out for TWD as TWD had stopped working during one of the runs. Its deflecting voltage was getting loaded due to shorting of diodes in its clipper circuit. All the diodes were replaced to solve the problem and one of the dead deflecting channel of TWD was repaired to make it active.

1.1.5 Low energy Negative Ion Implanter facility

Operation

The operational status and ion beam delivery of the implanter facility had been excellent during the academic year (2017-2018). Utilization of this facility for implantation work grew remarkably. About 24 users from different colleges, universities and institutes availed the beam time from April, 2017 to March, 2018. Together, there were 33 runs. The sanctioned beam times up to AUC 63 as well as few beam times approved by Director, IUAC, were being successfully performed. The particulars about the implantation experiment performed during this period are given below:

- Number of beam run: 33
- Total number of shifts utilized: 99
- Total number of samples implanted: 831
- Ion fluencies used: $5x10^{11}$ to $1x10^{17}$ ions/cm^2
- Ion species utilized: ^{7}Li, ^{12}C, ^{16}O, ^{27}Al, ^{28}Si, ^{31}P, ^{32}S, ^{48}Ti, ^{56}Fe, ^{58}Ni, ^{59}Co, ^{63}Cu, ^{107}Ag, ^{197}Au
- Energy range utilized : 15 to 200 KeV

Maintenance and development activities

The implanter accelerator system had a smooth run except for the monsoon season (from mid June to August, 2017). In regular interval, the operation had to stop for cathode sample loadings and regular cleanings. Ion source was performing well and no specific problem was observed and it was not opened for a regular maintenance during this period. In general, ion source gets dirty when it runs for longer duration. However, there were very few minor breakdowns such as failures in control system and vacuum components which were resolved.

A major break down occurred during the rainy season due to rise in the relative humidity to 76% of the ion source room. The accelerating tubes had difficulty in holding high voltages up to 200 KV with stability. The ceramic gaps of GP tubes were gradually building up with lots of spark marks. These spark marks covered almost whole insulation gaps of the accelerating tubes that weakened their insulation strength, which in turn made the ceramic gap to allow discharge paths. The probable reason for marks may be dust falling from the inlet AC openings just above the accelerating tubes and three other nearby AC diffuser openings. Due to high voltage, low temperature (18ºC) in addition to the high humidity of the room, dust can stick to the gaps. Therefore, to fix this trouble, AC inlet exactly above the tubes was cleaned and closed. All the three AC diffuser openings were removed, cleaned and fixed. The roof of ion source room was also cleaned. To clean the stains on the GP tubes, the rings were removed and made the ceramic gaps wetted with alcohol. Even after rigorous cleaning, the stains of the 1st tube did not go. The other two tubes were cleaned and rings were mounted back. They were dried with hot air blower. Efforts were made to improve the relative humidity of the room. The openings of the room's windows were enclosed with glass pane to isolate the room from the corridor for effective AC circulation. New hygrometer for monitoring the humidity of the room was mounted on the wall of high voltage room. The conditionings of the accelerating gaps were also done to improve voltage holding capability.

Apart from operation and helping users for their experiment, new beams were developed as per user's request. ^{62}Cr beam was attempted to develop and Cr cathodes were prepared by pressing chromium powder in the cathode capsule. A few nA of ^{62}Cr, 524nA of ^{62}CrH2 and 200 nA of ^{62}CrH was developed.

1.2 LINAC

B. K. Sahu, R. Ahuja, J. Antony, S. Babu, J. Chacko, G. K. Chaudhari, A. Chowdhary, T. S. Datta, R. N. Dutt, S. Ghosh, M. Jain, R. Joshi, S. Kar, J. Karmakar, B. Karmakar, M. Kumar, R. Kumar, N. Kumar, D. S. Mathuria, K. K. Mistry, A. Pandey, P. Patra, P. N. Prakash, A. Rai, S. Sahu, A. Sarkar, A. Sharma, K. Singh, P. Singh, S. S. K. Sonti, S. K. Suman, S. Tripathi, J. Zacharias and D. Kanjilal

1.2.1 Status of the Superconducting Linac

The superconducting (SC) linac working as the energy booster of the Pelletron accelerator consists of five cryostats containing twenty seven quarter wave resonators out of which twenty four accelerate the ion beam and the remaing three are responsible for longitudinal focussing or defocussing (only for Rebuncher) of the beam. During last academic year, energized ion beams from Pelletron and SC linac are delivered in different beam lines e.g. Hybrid Recoil Mass Analyser (HYRA) and National Array of Neutron Detectors (NAND) for scheduled experiments. During this year, this was the first time when all the three linac cryostats with 24 resonators were installed and powered in three accelerating modules. Out of 24 resonator, 22 took part in the beam acceleration along with the single and couple of resonators in super buncher and re-buncher cryostats respectively.Prior to the last linac operation, more surface treatment was applied on many resonators to improve the operational field gradient. All the resonators of 2nd/3rd accelerating module were rinsed by high pressure de-ionised water. The linac operation had been started on 10 April '17 and continued up to 16 Sept. '17 when the many ion beam viz. $^{16,18}O$, $^{28,30}Si$ and ^{48}Ti were accelerated and the beam was delivered to accomplish fourteen experiments in the field of Nuclear physics in the beam line of HYRA and NAND. During the beam acceleration, an energy gain of about 9 MeV/q had been demonstrated. However, to achieve the long term stability and trouble free operation, twenty two resonators could take part in the beam acceleration process with the reduction of accelerating fields in some resonators to a stable level and a maximum energy gain close to 8 MeV/q had been delivered for routine experiments. About $\leq$ 50% resonators were selected to change their accelerating phases from 70^0 (or 80^0) to 110^0 (or 100^0) to reduce the longitudinal emittance and to improve beam transmission. The ion beams accelerated using linac are listed in Table-1.

Table 1. Beam acceleration schedule using Linac

Experimental Area	Beam	Schedule	Shifts	Energy Delivered (MeV)	Δt measured (ps)
HYRA	$16O^{8+}$	09/05/2017 -13/05/2017	N/A	150	N/A
HYRA	$16O^{8+}$	14/05/2017 - 17/05/2017	12	125,116,108	N/A
HYRA	$18O^{8+}$	19/5/2017 - 22/5/2017	10	124, 120, 115, 111, 107, 103	N/A
NAND	$18O^{8+}$	22/05/2017-28/05/2017	18	155,144,125,115,110,105	768
HYRA	$18O^{8+}$	28/5/2017 - 01/6/2017	14	150, 138, 126, 115, 103	N/A
HYRA	$16O^{8+}$	02/06/2017-05/06/2017	12	150, 138, 115, 103	N/A
NAND	$30Si^{11+}$	08/06/2017-21/06/2017	48	193,187,180,174,167, 160,153,146,140	740
NAND	$30Si^{11+}$	22/06/2017-28/062017	21	178,172,166,160,155,149,143,138	740
NAND	$48Ti^{15+}$	30/06/2017-06/07/2017	21	251,241,233,226,219,213,207	N/A
HYRA	$48Ti^{15+}$	07/07/2017 - 09/07/2017	9	251, 249, 243, 236	N/A
NAND	$48Ti^{14+}$	11/07/2017-15/07/2017	15	236,230,224,217,211	493
NAND	$48Ti^{14+}$	16/07/2017-23/07/2017	24	236,217,209,203,198	600
NAND	$28Si^{11+}$	24/07/2017-03/08/2017	33	200,180,170,160	415
NAND	$28Si^{11+}$	07/8/2017 - 16/8/2017	28	204, 194, 184, 174, 164, 160, 157, 153, 194	N/A
NAND	$28Si^{11+}$	16/8/2017 - 19/8/2017	9	204, 194, 184, 173, 156, 145	N/A
NAND	$30Si^{11+}$	19/8/2017 - 23/8/2017	7	204, 194, 184, 174, 165, 157, 145, 136	N/A
NAND	$28Si^{11+}$	23/08/2017-31/08/2017	25	150,185,180,175,170,165, 160,155,150145,140,135	N/A
HYRA	$28Si^{11+}$	31/08/2017-11/09/2017	35	185	N/A

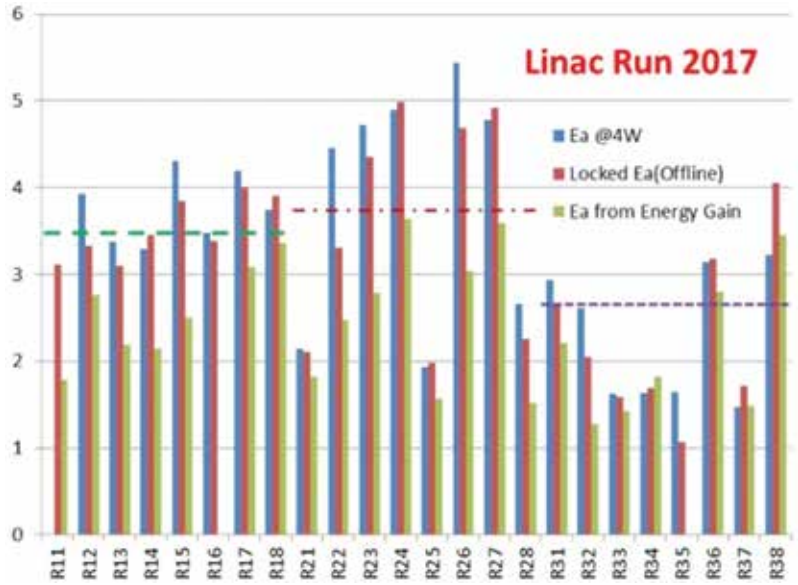

Figure 1.2.1 Accelerating gradients during linac operation

The linac operation was made to be very reliable with many automation process and only <1% beam time was lost due to linac related problem. The smoother operation of linac was made possible as the accelerating fields of the resonators were optimized for long term stability. The improved control dynamics using Pulse Width Modulator based frequency tuners in Linac-I and Piezoelectric actuator based frequency tuning system in Linac-II and Linac-III helped to avoid frequent unlocking of the resonators. The Capacitive Pickup device was used to verify the beam energy during the energy tuning and change of beam energy from linac.The accelerating field performance of all the twenty four resonators installed in the three accelerating modules during the last linac operation is shown in figure 1.2.1.

It is clear from the figure 1.2.1, the performance of most of the resonators in Linac-III cryostat is found to be much less than the desired value. The possible reason for the same may be attributed to the long time exposure of resonators in atmosphere during loading in the third cryostat. Post linac operation, steps are taken to improve the performance of resonators in Linac III. Based on the past history of the resonators, four cavities (R32, R34, R36, R37) were electropolished and all the cavities were rinsed with high pressure (~80 bar) 18 MΩ-cm deionized water along with their couplers, slow tuner bellows and pickups inside clas-100 clean room. The resonators were also assembled in same clean room before loading them in the cryostat inside class-5000 clean room. An Offline test of Linac III was done in March 2018 to evaluate the performance of the resonators post surface treatment. Significant improvement in the performance of all the resonators except R36 was observed as compared to the last linac operation. The performance improvement graph is shown in figure 1.2.2. Except one resonator (R36), the locked accelerating fields of all the resonator had improved. The reverse performance of R36 is yet to be understood.

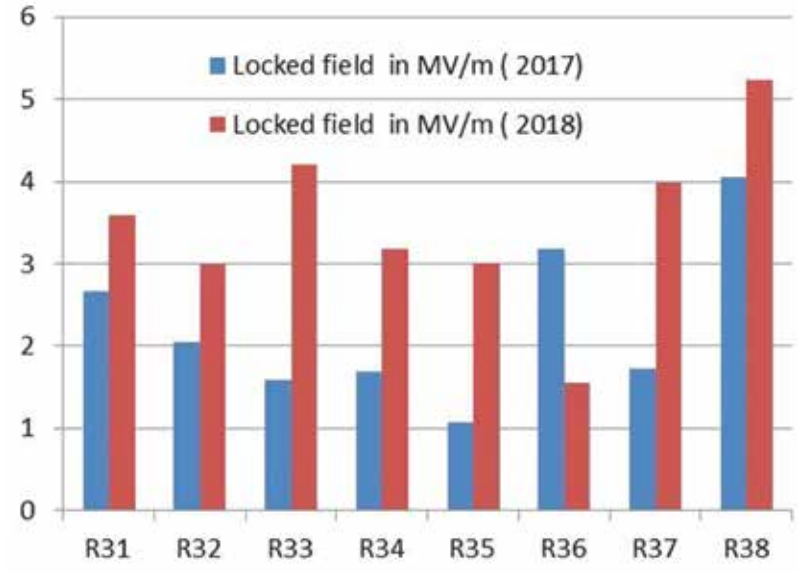

Figure 1.2.2: Accelerating gradients of linac 3 resonators during off-line test

1.2.2 Developmental activities accomplished to improve the performance and the reliability of SC linac

A. Implementation of Nitrogen purging system and Helium pulse conditioning of the resonators

As the RF surface of a superconducting resonator is very sensitive to contaminants, it is important to preserve the quality of the surface after electropolishing and HPR prior to their generation of accelerating fields in the cryostat. As the resonator vacuum is not isolated from the cryostat vacuum for our linac, during venting and evacuation, the contaminants from the cryostat can easily migrate to the RF surface of the resonator. In order to preserve the cleanliness of the resonator, a nitrogen purge line is installed on every pickup flange of every resonator of second and third linac module through which dry nitrogen flows and keeps the resonators at a positive pressure during evacuation and venting. The same purging mechanism is being used during the maintenance of these cryostats. Helium conditioning was also done for all resonators of the second linac module and four resonators of the third linac module. Boil off from liquid helium was injected in to the vacuum space of the cryostat through a motorized dosing valve. High power pulse conditioning is usually done for ~30 mins at a partial pressure of ~10^{-5} mbar of helium gas. Helium pulse conditioning has improved the performance of number of resonators in second and third linac module.

B. Improvements in the control scheme for better operational efficiency

The first accelerating module uses pneumatic helium gas operated tuners for phase locking of the resonators. The control scheme of all these gas operated tuners were improved with a pulse width modulation (PWM) based control mechanism and the same was successfully tested to phase lock all the resonators of linac 1 during the linac acceleration. As the response time of this control mechanism is hundreds of millisecond, it can correct the slow drifts in frequency at a faster rate thereby making the resonators less prone from frequency unlocking and reducing the RF power requirement. Implementation of the PWM based tuner control mechanism on the resonators of the super buncher (SB) cryostat and re-buncher cryostat is also taken up, So during the upcoming linac operation, the new PWM mechanism will control all the resonators of SB and RB cryostats in addition to the resonators of Linac-1.

An alternate tuning scheme using piezoelectric actuator based tuner, acting in the range of milliseconds were already operational in the second and third accelerating modules. Continuous improvement in this mechanism had enabled us to maintain the mean resonant frequency constant on a faster time scale at higher field gradients and also counteracting the microphonics originating due to the excitation of the mechanical modes in the resonator. This had led to a substantial reduction of the required RF power for phase locking.

Earlier the first and third accelerating module were being controlled and operated through VME based scheme whereas the second and the part of the third accelerating module were controlled using CAMAC based control scheme. In order to maintain uniformity and optimization of space, all the linac modules has been made operational through VME based control modules. can it be deleted ? For remote operation of PWM and piezoelectric based tuners, complete fabrication of 4 nos. of VME based router modules using multi-functional VME 6500 control board were carried out and tested with existing Piezoelectric/PWM Controller. The same had been made operational in linac cryostats and software interface for client operation was done. For coarse movement of the mechanical tuner attached with the piezoelectric actuator, a python based client server architecture using Rasberry- Pi microcomputer, interfaced with existing stepper motor control was made ready and proper graphical user interface was made for client operation. In order to monitor and control the frequency difference of each individual resonator from the reference frequency, earlier an 8 channel CAMAC Frequency to Digital converter (FDC) module has been developed and tested with linac control scheme. As the linac control scheme is upgraded to VME based control scheme, a 24 channel VME module for frequency read-back has been developed for remote monitoring of the frequency difference and automatic tuning of the frequency using mechanical tuner control. The module has capability to measure frequency range up to 64 kHz with 1Hz accuracy and has readout mode of 22bit or 16bit.

When the resonators produce high accelerating fields especially at the time of High Power Pulse conditioning, access is often restricted due to the presence of X-rays. To overcome this problem, a remote control system using incremental encoders for closed loop position control of the power couplers to couple power in to the superconducting resonators was developed. The system is responsible for control of the 27 RF power couplers from the control room. High Power RF conditioning of many resonators of the three accelerating modules of the superconducting linac has been done during the last linac operation using the newly built system.

C. Implementation of Optimum Phase focussing technique in Linac operation

During the ion beam acceleration, conventionally a phase angle of 70 or 80º (sine value) is chosen to accelerate the ion particle. This method is adopted to achieve the longitudinal focussing of the beam while being accelerated.

However, if the total length from the linac exit to the experimental station is substantial (> 15 m), then the extreme leading and lagging particle in a beam bunch will exchange their place due to larger energy modulation and that will finally result a larger spread in time and energy of the beam bunch which is often not accepted by the stringent requirement of the Nuclear physics experiments. In the past, the resonators in Re-buncher cryostat were used to perform the time (or energy) bunching. Since many energies of the same ion beam needed to be delivered during the scheduled experiments, so re-buncher resonators were to be adjusted at every energy change of the ion beam which was time consuming. To overcome this problem, a technique is adopted where the accelerating phases of ≤ 50% resonators will be kept at 110º/100º instead of 70º/80º. In order to select the optimum phase focussing (OPF) of the resonators, an in-house made code written in Fortran was developed. With the help of this code, during the last linac operation, the use of re-buncher could be completely avoided and that saved lot of precious beam time. In addition, this benefit, the transmission of the beam from linac exit to the experimental station also was improved up to a factor of 3 by using the OPF method.

D. Routine operation of Capacitive pickup for Energy measurement

Earlier a couple of Capacitive pickup devices were installed at the linac exit. This year both were routinely being used to measure the energy of the ion beam by Time Of Flight method using dedicated Electronics modules. This device, being a non-interceptive one, is used continuously to measure the beam energy during the beam delivery. The use of the device saved beam time during the delivery of the ion beam with many steps of reduced energies and the confirmative measurements with the surface barrier detector could be avoided.

E. Test of superconducting Quarter Wave Resonator as a Beam Phase Detector

The linac energy tuning procedure being followed at IUAC utilises gold foil scattering set up in a scattering chamber at the exit of the accelerating modules along with the suitable surface barrier (SB) detector system for energy and time measurement. In an alternate development, a new technique based on the superconducting QWR operating in a beam bunch phase detection mode was developed and tested along with the existing linac tuning technique using SB detectors. Both the techniques were used to derive a full set of phase tuning parameters for beam acceleration. Verification of the superconducting phase detector was accomplished with the measurements from surface barrier detector. The new technique was not so sensitive to the changing beam current, was independent of beam steering/focussing and had the capability to quickly tune the complete linac consisting of 24 QWRs. The developed new technique has the potential to perform the auto energy tuning of the complete linac.

1.2.3 Superconducting Niobium Resonators

P. N. Prakash, A. Rai, S. S. K. Sonti, K. K. Mistri

The construction of six spare quarter wave resonators (QWRs) and additional slow tuner bellows for the superconducting linac has progressed well. Nb-SS brazed transition rings were attached on the two SSR1 niobium Single Spoke Resonators which had come back to India for installation of the outer SS helium vessel. Under the Indian Institutions and Fermilab Collaboration (IIFC), the 2nd 650 MHz, β=0.6 single cell low beta niobium cavity jointly developed by IUAC and Variable Energy Cyclotron Centre (VECC), Kolkata, was successfully completed.

1.2.3.1 Construction of Spare QWRs and Slow Tuners for Linac

Construction of the six spare QWRs for the superconducting linac has progressed well. The QWRs and slow tuner bellows are being built both as spares for the Linac as well as for conducting other offline development works. Several parts / sub-assemblies for the resonators, e.g. loading arms, drift tube cylinders, outer niobium housings and slow tuner bellows, have either been completed or in advance state of completion. In figure 1.2.3, several parts / assemblies, are shown.

1.2.3.2 SSR1 Single Spoke Resonators

The two SSR1 niobium single spoke resonators came back to IUAC after the VTS tests at Fermilab, USA, for attaching the Nb-SS brazed transition rings. These rings are to be attached before the outer stainless steel helium vessel can be installed. Last year IUAC had helped BARC, Mumbai in getting the Nb-SS rings readied for brazing. The brazed Nb-SS rings were successfully attached on the SSR1 resonators and sent to BARC for the installation of the outer helium vessel. In figure 1.2.4, the various stages of the process, are shown.

Figure 1.2.3: Clockwise from top-left: (i) niobium housings, drift tube cylinders, loading arms, coupling ports, beam ports etc., (ii) niobium leaves for the slow tuner bellows, (iii) drift tube cylinder with copper end caps (for checking the dimensions), (iv) top: slow tuner weld rings, (bottom): drift tube beam ports, (v) niobium outer housing cylinders.

Figure 1.2.4: Clockwise from top-left: (i) SSR1 niobium single spoke resonator before attaching the Nb-SS brazed transition ring, (ii) Nb-SS brazed transition rings for the two SSR1 resonators, (iii) EBW set up for attaching the transition ring to the resonator, and (iv) SSR1 resonator after attaching the Nb-SS brazed transition ring just before sending to BARC, Mumbai, for the installation of the outer SS helium vessel.

1.2.3.3 2nd 650 MHz Single Cell Low Beta Niobium Cavity

Under the Indian Institutions and Fermi Lab Collaboration (IIFC), Variable Energy Cyclotron Centre (VECC), Kolkata and IUAC had developed a β=0.6, 650 MHz single cell niobium low beta cavity (LBC) which was successfully tested at Fermilab. However, this cavity was fabricated following a procedure that is suitable for making a single cell cavity alone but not suitable for constructing multi-cell cavities. So it was decided to construct a second single cell niobium cavity by adopting a procedure that would help in realizing a multi-cell cavity later. The 2nd single cell LBC was successfully developed following the new procedure. In figure 1.2.5, this cavity is shown.

Figure 1.2.5: The second single cell 650 MHz, β=0.6 niobium LBC developed jointly by VECC and IUAC by adopting a procedure that is suitable for realizing multi-cell cavities.

1.3 LOW ENERGY ION BEAM FACILITY

A) Operation

The performance of electron cyclotron resonance ion source (ECRIS) based new low energy ion beam facility (n-LEIBF) in terms of the development of gaseous beams of highly positive charged ions and the beam delivery for user experiments in all three beam lines (viz. 75º, 90º and 105º) has been satisfactory in the last academic year (2017-2018). We have done all the user experiments scheduled by the academic cell as part of the AUC-57, 58, 59, 60, 61 and 62. About 47 users (including 33 AUC experiments) from various universities and research institutes availed the beam time during February 2017 to February 2018. The user experiments, done in the past four years and the facility utilization in this academic year are shown in Figure 1.3.1 and 1.3.2 respectively.

Figure 1.3.1: User exp. summary for the past 4 years

Figure 1.3.2: LEIBF Utilization

Apart from assisting users, we keep on trying to enhance the intensity of highly charged ions by optimizing the source parameters and using different techniques for the feasibility of new experiments. In the past academic year 2017-18, the highest intensity of Ar^{8+} was 9 eμA at frequency 8.59GHz with the DC bias tube of length 165mm as shown in figure 1.3.3(a).

Table 1: Effect of the dc bias tube's length, frequency tuning and gas mixing effect on the beam intensity of Ar^{8+}

S.N.	Length (mm)	(Ar^{+} He) plasma pressure (torr)	DC Bias Voltage (V)	Power (W)	Dominant Frequency (GHz)	Intensity of Ar^{8+} (eμA)
1.	165	1.03E-5	-60	9	8.59	9
2.	130	1.76E-5	-141	16	9.43	12.5
3.	135	2.0E-5	-139	28	9.36	13.5
4.	140	2.11E-5	-119	20	10.108	10
5.	145	1.75E-5	-88	29	9.64	13.5
6.	150	1.23E-5	-81	26	8.567	19
7.	153	1.76E-5	-81	21	8.56	25
8.	156	1.47E5	-62	30	8.605	19

To further enhance the intensity of Ar^{8+}, we had planned to change the length of the DC bias tube. The length of the DC bias tube was varied from 130 mm to 156mm and total 8 DC bias tube were installed. For each DC bias tube, the microwave frequency was varied from 8.5 to 10.5GHz in steps of 10MHz. The frequency tuning and gas mixing techniques were simultaneously employed and acquired useful data for the feasibility of new experiment. The dominant frequency and beam intensity of Ar^{8+} for each DC bias tube are shown in table 1. The highest beam intensity of Ar^{8+} was found 25 eμA with the DC bias tube of length 153mm and at frequency 8.56GHz. A typical charge state distribution (CSD) of argon plasma mixed with helium at frequency 8.56 GHz is shown in Figure 1.3.3 (b).

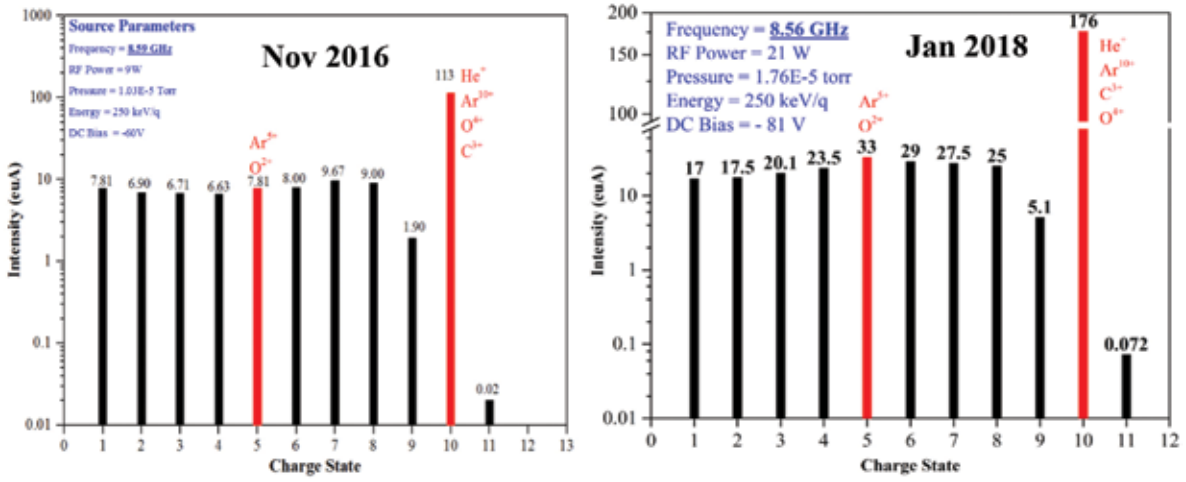

Figure 1.3.3: A typical charge state distribution of argon mixed with helium showing the influence of the dc bias tube of length 165mm (a), and 153mm (b).

Apart from the Argon beam, the source parameters were also optimized for the high charge states of other beams like Carbon, Nitrogen, Oxygen, Krypton and Xenon with the DC bias tube of length 153mm. The intensities of the highly charged ions of the beam as mentioned above were increased with this DC bias tube. The available beam intensities of different charge states with energy 250 keV/q are shown in Table 2.

B) Maintenance

In this academic year, there was no major breakdown of the facility and it ran smoothly round the year. We had only small maintenance jobs viz. ion source cleaning, replacement of few scroll pumps, gauges, and repairing of the RF amplifier.

Ions /q	1+	2+	3+	4+	5+	6+	7+	8+	9+	10+	11+	12+	13+	14+	15+	16+	17+	18+	19+	20+	21+	22+
H	130																					
He	200	20																				
C	15	7		0.5																		
N	102	64	29	13	4.8	0.3																
O	150	78	30	20	13	5.5	0.2															
Ne	59	29	16	9	7.2	3	0.6	0.2	0.01													
Ar	101	60	38	26		29	28	25	5.1		0.32	0.06										
Kr	17	14		7.5	6.3			3.3	2.5	2.1	1.8		1.0		0.33	0.14	0.04					
Xe	6.5	5		3.7	3.5		2.9	2.5	1.2	0.7		0.45	0.36	0.4	0.43		0.49	0.4	0.26	0.15	0.6	0.03

C) Development

For the improvement of the facility in terms of the beam transport, we have designed an electrostatic steerer for the main beam line. The internal assembly is shown in figure 4. The existing steerers are all magnetic in Low Energy Ion Beam Facility. We are facing the problem with the main beam line steerer. Since, this facility has an ECR ion source which gives several beams with different charge states, high values of currents are required for these steerers.

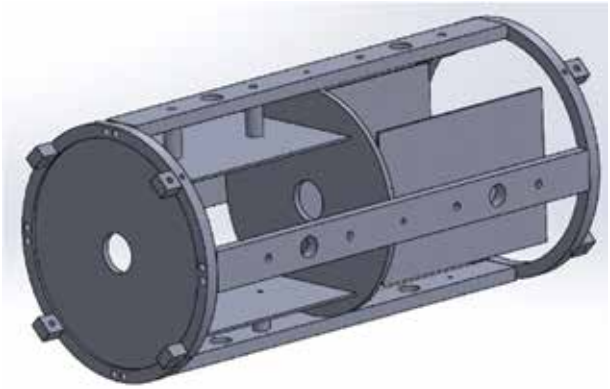

Figure 1.3.4: The inner parts of an Electrostatic Steerer power supply to get the analysed beam of high m/q ratio at the centre of the Faraday cup.

As a result, the non-analysed beam is itself dispersed in the main beam line and deteriorates the vacuum. The inner and outer parts of this steerer are ready and will be assembled very soon. The fabricated inner parts of the steerer are shown in figure 1.3.5.

Figure 1.3.5: The fabricated inner parts of an Electrostatic Streerer.

In the 105º beam line, a new chamber for the time of flight spectrometer was installed for better resolution of the detector as shown in figure 1.3.6. Very recently, the time of flight spectrometer was tested with beam and is working fine.

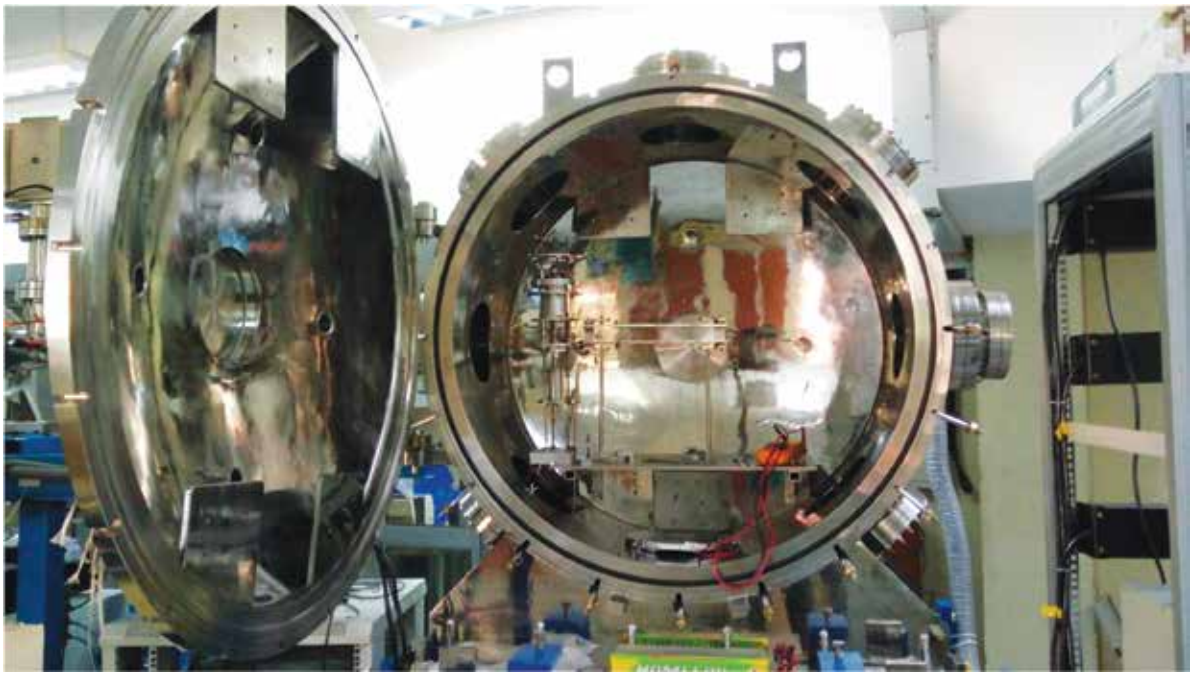

Figure 1.3.6: Time of flight spectrometer installed in the new chamber

1.4 PARAS (1.7 MV PELLETRON ACCELERATOR AND RBS ENDSTATION)

1.4.1 Operation

1.7 MV Pelletron accelerator for Rutherford backscattering facility was in regular operation all year round. Total 1811 measurements of 69 users from 30 Universities, colleges and institutes were performed. RBS, Resonance RBS for Oxygen and Nitrogen, Channeling and ERDA measurements were routinely performed. RBS, one of the popular methods of ion beam analyses performed for different types of samples including thin films on substrates, free standing, carbon supported grown by different techniques such as thermal evaporation, RF sputtering, MBE and PLD. The ion implanted and irradiated single crystals, thin films and bulk samples are also characterized using RBS and Channeling. Ion channeling is very accurate method for probing defects caused by implantation. Some examples are mentioned in table 1

Table 1: Defect type, nature and examples

Sl No	Types	Defect	Nature of defects	Detected by RBS at IUAC
1	Category I	Subthreshold damage defect	Prior to the formation of an amorphous layer	Si irradiation with dose less the 1e15 at/cm^2
2	Category II	defects beyond the amorphous/crystalline (a/c) interface	Formation of an fully amorphous layer	Si irradiation in Si(100) in any dose
3	Category III	micro twins, hairpin dislocations and segregation related defects	Residual defects in SPEG and other annealing methods	SPGE/IBIEC in Si and SiC and PLD grown films
4	Category IV	Clamshell and zipper defects	Defects which form when the two a/c interfaces meet	In all irradiated Single crystals
5	Category V	Precipitates or dislocation loops.	Solid solubility of the implanted species in the substrate at the annealing temperature	Ni Silicide formation on annealing or ion irradiation

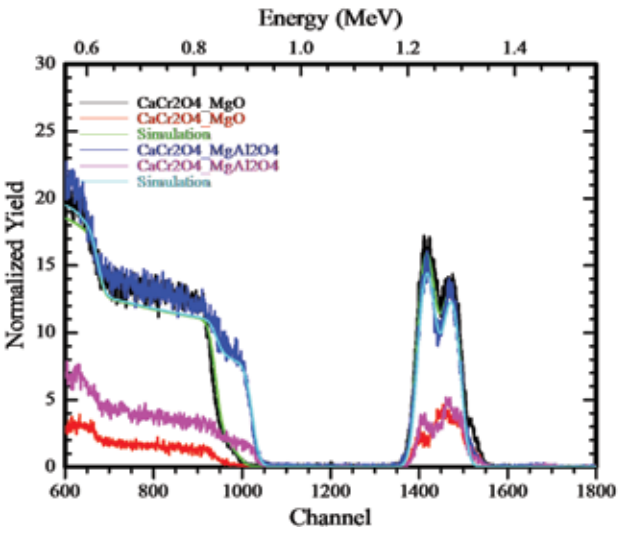

Fig 1.4.1: RBS Channeled spectra of CaCr2O4 thin film on MgO and MgAl2O4 substrate indicating good quality of epitaxial nature.

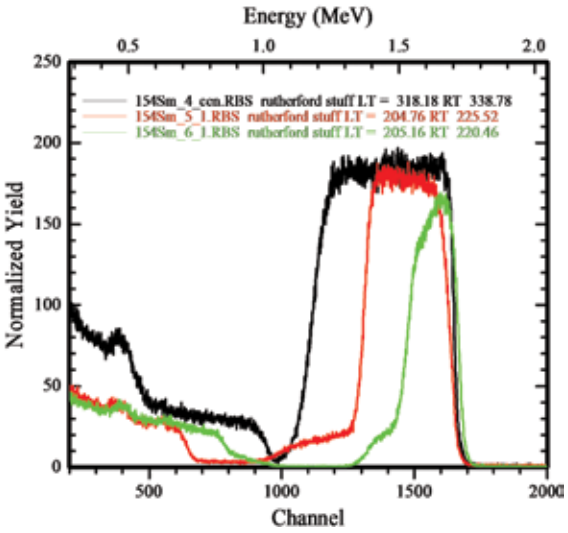

Fig 1.4.2: RBS spectra of 154Sm deposited on carbon backing by thermal evaporation showing different thickness with variation in distance.

Resonance backscattering 16O (α,α) 16O at 3.045 MeV, 14N (α,α) 14N at 3.69 Mev commonly referred as resonance RBS as has been used for oxygen and Nitrogen depth profiling in various thin oxide films, implanted and processed materials respectively.

ERDA setup at IUAC is suitable for hydrogen estimation up to depth 0.5–1μ. Measurements are performed with 2.7- 3.045 MeV alpha projectiles impinging over 75 deg to surface normal. Forward recoiled protons at round 30 degrees are detected by detector with a stopper foil to stop scattered alpha particle. Secondary electron suppressors can't be used during ERDA setup because goniometer position at 75 degree tilt hits the suppressor ring. Therefore prior to ERDA, RBS measurements are performed to calibrate backscattered counts for different incident charge. During ERDA measurement, backscattered counts are also measured. These backscattered counts provide information of incident charge on the sample.

1.4.2 Maintenance

1.4.2.1 Ion Source Maintenance

Ion source maintenance and rebuilding of RF charge exchange cell was performed in January 2018. The ion source components including charge exchange cell were opened for maintenance. Rb in charge exchange cell present as vapor medium which allows He^+ to gain electron hence extracted as He^- for injecting to tandem accelerator. The Rubidium choked on the different part of charge exchange cell and associated parts were observed. All the sections were properly cleaned and reassembled. The quartz tube was replaced. The helium extractor aperture and its canal holder were also replaced. The leak detection was done prior to fresh rubidium loading. Approximately 10 grams rubidium was filled in reservoir in Argon environment. On few hours of conditioning, continuous and stable He- beam was achieved.

1.4.2.2 The 5SDH2MV Pelletron Accelerator and Endstation Maintenance

The SF6 pressure in the tank was raised to 55 PSIG from 35 PSIG which can hold the terminal voltage 1.1210 MV during conditioning and operation. The SF6 pressure is stable indicating there is no leak from the tank. No major breakdown occurred in the Pelletron and endstation.

Terminal Potential (MV)	Charge State	Energy (MEV)	Measurement
0.86-0.987	+1	1.8-2	RBS and Channeling
1.07-1.25	+2	3.045-3.09	O resonance RBS
1.198	+2	3.61	N resonance RBS
1.32	+2	4.02	C resonance RBS
0.92	+2	2.8	ERDA

TABEL 2: The Operation details of Terminal Voltage , Charge state, Energy for different measurement technique using He beam

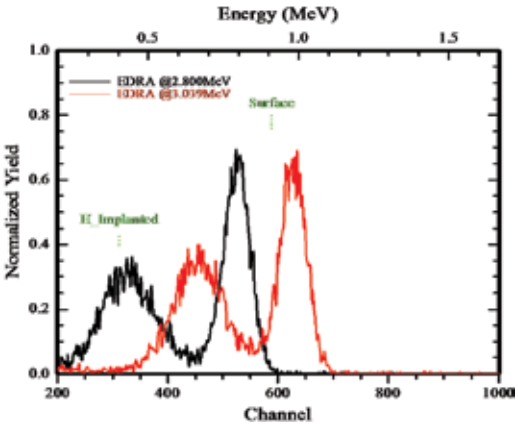

Fig 1.4.3: ERDA spectra of 30kev H implanted in Si substrate measured using He energy 2.8 Mev and 3.045 Mev

1.5 AMS AND GEOCHRONOLOGY FACILITIES

1.5.1 Accelerator Mass Spectrometry

G Raturi, J Singh, Pranav Singh, S Kumar, S Mohan, N S Panwar, M P Singh, R Kumar, J Prasad, Umapathy G R, Rajveer Sharma, Soumya Prakash Dhal, Chinmaya Maharana, Pankaj Kumar, K Devarani, M Sota, S Ojha, S Gargari, R Joshi, S Chopra and D Kanjilal

An Accelerator Mass Spectrometry facility for the measurement of ^{14}C, ^{10}Be and ^{26}Al has been established and made operational in March, 2015. This facility is equipped with a dedicated National Electrostatic Corporation (NEC) 1.5SDH tandem accelerator, a graphitization laboratory for the sample preparation of ^{14}C measurements and a clean chemistry laboratory for the sample preparation of ^{10}Be and ^{26}Al measurements.

1.5.1.1 Graphitization Laboratory

Graphitization laboratory is equipped with all the equipment required for the sample pre-treatment and graphitization. Charcoal, wood, macrofossils, plant remains, sediment and carbonate samples (shells, foraminifera) are processed routinely in this laboratory. Different pre-treatment methods, depending upon the type of samples, are followed. This laboratory is equipped with three Automated Graphitization Equipment (AGE) coupled with elemental analysers for the graphitization of organic samples. Out of these three AGE, one AGE is also coupled with carbonate handling system (CHS) for the graphitization of carbonate samples. During April 2017-March, 2018, about 1000 samples have been pre-treated and graphitized by 35 users from different universities and institutes for their research work.

1.5.1.2 Clean chemistry lab for ^{10}Be and ^{26}Al sample preparation

During last one year, this laboratory was under major renovation, in which hepa filters of the clean room as well as hepa and pre-filters of laminar flow units were replaced with new ones. A new laminar flow unit for sample digestion was procured and installed. Two new hot plates covered with Teflon sheet were also procured for heating the samples upto 250ºC. Water treatment unit was repaired and relocated to Graphitization laboratory to avoid its corrosion by acidic fumes. After renovation, laboratory was brought to operation and about 60 samples were prepared for ^{10}Be measurements.

1.5.1.3 XCAMS facility

Measurements

The AMS system at IUAC is designated as XCAMS i.e. Compact ^{14}C Accelerator Mass Spectrometer eXtended for ^{10}Be and ^{26}Al. This system is routinely utilized for the measurement of ^{14}C, ^{10}Be and ^{26}Al. Accelerator was down due to maintenance activities and therefore, out of 1000 samples graphitised, only 600 ^{14}C measurements have been performed for 23 users from various universities and institutes. The outcomes of these measurements are reported in research section. ^{10}Be measurements are performed at terminal potential of 550 kV this year and few standards and blanks have been measured.

Maintenance

Following maintenance activities were carried out in this facility.

- 134 MC SNICS source was opened for routine maintenance. Einzel lens was cleaned with high pressure rinsing facility. Ionizer was cleaned with alcohol and Cs was loaded.
- Cathode alignment was disturbed in 134 MC SNICS. Cathodes were re-aligned by adjusting the guiding rods. After each adjustment, cathode was operated for 30 minutes and then source was opened and Cs spot was observed under microscopic. Cathodes were aligned when Cs spot was in the center of cathode.
- 40 MC SNICS was opened for routine maintenance. Ionizer and other parts were cleaned. Input voltage module (D/A converter) in process control station was replaced with newer one.
- Accelerator tank was opened for the maintenance on 08/03/2018. A lot of dust was observed inside tank. Accelerating column and tank walls were cleaned with compressed air and tissue papers. Charging system was tested. Number of pellets was also counted in Pelletron chain. There are 67 pellets in this chain. Hydrocarbon trap was baked for 4 hrs using turbo molecular pump set up at base vacuum of 1.6 x 10^{-6} torr. Dessicant was also baked at 200 °C for 1 hr. Accelerator tank was closed after maintenance on 28/03/2018.

Optimization of stripper pressure in XCAMS for radiocarbon measurements

A study for the optimization of stripper pressure in XCAMS for radiocarbon measurements has been conducted. In this study, stripper pressure was varied from 20 mTorr to 30 mTorr. ^{12}C transmission and $^{14}C/^{12}C$, $^{14}C/^{13}C$ and $^{13}C/^{12}C$ ratios were observed using an alpha graphite (Graphite Powder, 100 mesh, purity 99.9995%, procured from Alpha Aesar) cathode. Results are shown in Fig. 1.5.1 and 1.5.2. At 20 mTorr, transmission was 45% but background ratio was of the order of modern carbon. As we increase the pressure up to 26 mTorr, transmission reduced to 42% and background was in the acceptable range (< 1 x 10-15). Further increase of stripper gas pressure does not change the background but deteriorate the transmission of the beam. Similar trends were also observed for $^{14}C/^{13}C$ ratio. $^{13}C/^{12}C$ ratio also decreases as stripper pressure increases but it is relatively constant between 25–27.5 mTorr (varies between 1.0807 to 1.0809). This study leads to the conclusion that stripper pressure range from 26 to 27.5 mTorr is suitable for routine radiocarbon measurement.

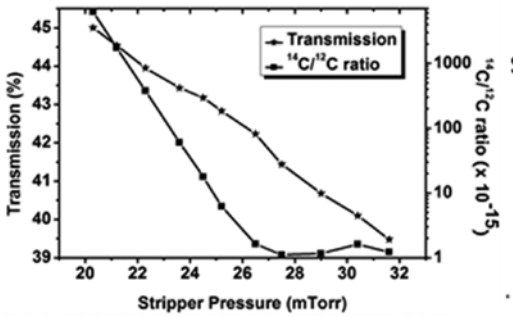

Fig. 1.5.1 Variation of ^{12}C transmission and alpha graphite blank values with stripper pressure

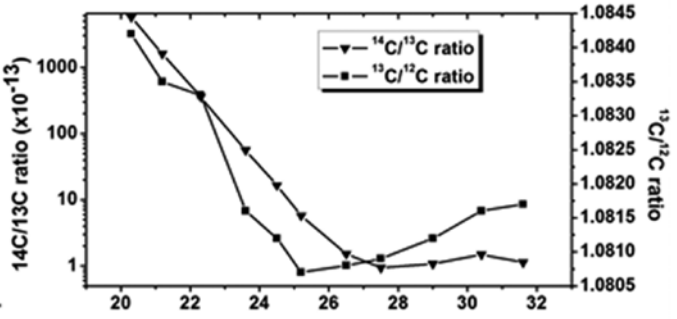

Fig. 1.5.2. Variation of $^{14}C/^{13}C$ and $^{13}C/^{12}C$ ratios of alpha graphite sample with stripper pressure

1.5.2 National Geochronology facility

Umapathi G. R, Rajveer Sharma, Soumya Prakash Dhal, Chinmaya Maharana, Pankaj Kumar, S Ojha, S Gargari, R Joshi, S Chopra and D Kanjilal

The objective of the project is to develop a comprehensive Geochronology facility at IUAC that will permit measurement of quality isotopic data for Geochronological purposes including relevant characterization at the highest international level. The dedicated geochronology facility at IUAC will enable researchers from Indian Universities and research institutes to study different aspects related to Earth Sciences. The proposed geochronology facility will enhance the research capabilities in the country with the following objectives.

- Carrying out various research studies in the field of climate change, palaeo-climate studies, global carbon cycle, oceanographic parameters, Antarctica research programs, archaeology, biomedicine and history of art etc.
- Capacity building: Initiation of new PhD programs using the facility for universities and research institutions.
- Generating geochronological data that shall be of interest to Earth Scientists, which require precise geochronology.

Following instrumentation has been commissioned under this project:

Inductively coupled plasma mass spectrometry (ICPMS)

Quadrupole (Q ICP-MS) and high resolution inductively coupled plasma mass spectrometer (HR-ICP-MS) have been installed at IUAC. A Teledyne make femto second laser will be interfaced with both of these ICP-MS. The technique is widely used for high precision trace element analysis and being utilized for U-Pb dating of different phases of minerals.

Fig. 1.5.3: Q-ICPMS and HR-ICPMS facilities at IUAC

Wave length Dispersive X-Ray fluorescence and X-Ray Diffraction

X rays fluorescence spectrometry is utilized for non-destructive elemental analysis of rocks, mineral, sediments and fluids for geological applications. A sequential wavelength dispersive X-rays fluorescence spectrometer along with necessary standards has been installed. A fuse bid machine, pellet press and vibratory cup mill have been installed for the sample preparation required for XRF measurements.

X rays diffractometry is used for studying lattice structure to determine minerology of different geological samples i.e clay, sediments etc. X rays diffractometer has been installed and utilized routinely by geologist for characterization of their samples.

Fig. 1.5.4 (a) WD XRF and (b) XRD

Field Emission Scanning Electron Microscope with Cl, EDS and EBSD

FESEM provides surface topography from few nm to microns and it is one of the best tools for surface morphological studies of geological samples. The X-ray detector coupled with FESEM can record the characteristic X- ray emitted from sample covering a range of elements (Boron to Uranium) in the periodic table. The instrument is widely used to analyze geological samples like rock, sediment, silicate, oxide, sulfates, carbonates, halides, phosphates and sulfides. The X-ray mapping provides information of elemental distribution in the sample, while electron backscatter diffraction (EBSD) can reveal the mineral phases and crystal structure of the sample, to give information about motion of tectonic plates, effect of high pressure metamorphism etc. Zircon mapping is carried out with cathodoluminescence detector installed in FESEM facility. FE-SEM facility is being utilized routinely.

Fig. 1.5.5 FE-SEM facility at IUAC

1.6 TABLETOP ACCELERATORS

1.6.1 Usage of Tabletop Accelerators

IUAC has designed, developed & installed 30 kV & 60 kV Tabletop Accelerators in house. Both of them have been in regular use during last year. The following table indicates the usage of the accelerators during last year.

	60 kV Tabletop Accelerator	30 kV Tabletop Accelerator
No. of runs	10	9
No. of users	6	8
No. of samples implanted	118	155

1.6.2 Development of Rotary cum Linear Feed Through with New Sample Holder for Tabletop Accelerators

We have been using a single sided sample holder mounted on 100 mm linear feed through which was able to accommodate a maximum of 3 samples along with Faradaycup & beam viewer mounted on the same side. A new rotary cum linear feed through having 360 deg rotary motion with 100 mm linear motion has been purchased locally. This feed through is magnetically coupled without any vacuum bellow. The newsample holder is having three sides to mount samples. We have also mounted faradaycup & beam viewer on the same holder. Now we are able to mount 10 samples at a time with this new arrangement. This new sample holder has been installed in both 60 & 30 kV tabletop accelerators. The photographs of sample holder & experimental chamber are shown below.

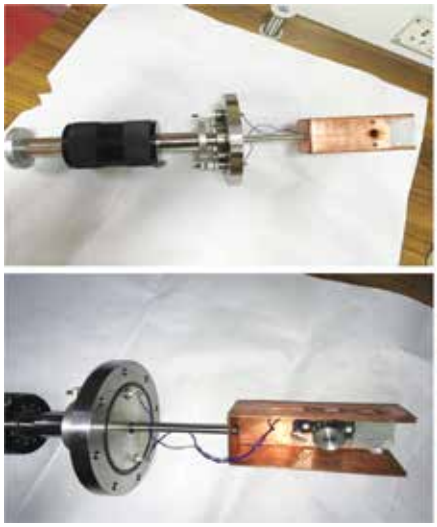

Fig. 1.6.1: Sample holder with rotary cum linear feed through.

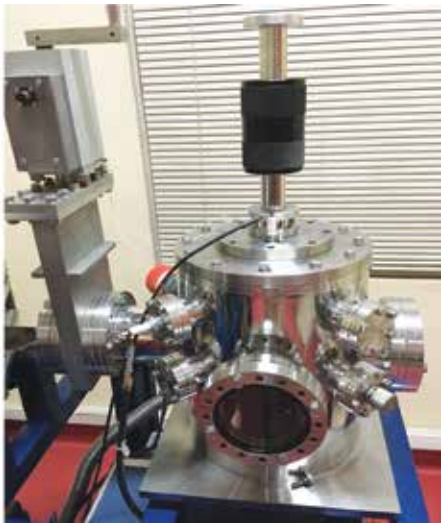

Fig. 1.6.2: Experimental chamber

2. ACCELERATOR AUGMENTATION

2.1 HIGH CURRENT INJECTOR

The High Current Injector (HCI) Project will accelerate the ion beam from ECR source using room temperature Radio-Frequency Quadrupole (RFQ), IH type Drift Tube Linac (DTL) and superconducting low beta cavity module to match the input velocity at our existing superconducting linear accelerator. This year beam was successfully accelerated (A/Q=3 & 2) through RFQ to achieve the design energy output of 180 keV/amu.

2.1.1 18 GHz HTS ECR ion source, PKDELIS and LEBT

G. Rodrigues, P. S. Lakshmy, Y. Mathur, Sarvesh Kumar, U. K. Rao, D. Kanjilal

(a) Operations

Various charge states of helium nitrogen and oxygen beams were extracted from the ECR ion source. He^{2+}, N^{4+}, O^{5+} and O^{6+} beams were injected into RFQ for low power tests to test the RFQ acceleration. In this testing, DC beam as well as bunched beams were injected into the RFQ for testing. Best bunch widths were measured up to 2.5 ns which were achieved using the 12.125 MHz multi harmonic buncher. Fig. 2.1.1 shows beam bunch width of O^{5+} measured using the fast Faraday cup. A set up consisting of magnetic quadrupoles and 45º bending magnet as shown in Fig. 2.1.2 was installed to measure the energy gain from RFQ. The optics for the system is shown in figure 2.1.3. Due to RF interferences observed on BPM's mounted close to the RFQ, a beam viewer was instead fabricated and installed. Fig. 2.1.3 and Fig. 2.1.4 depict the beam size and shape on the beam viewer and the beam profile respectively at the RFQ exit.

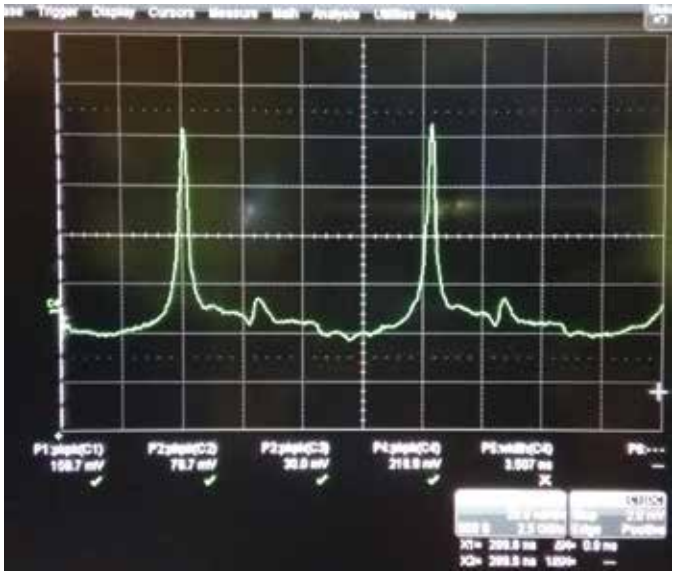

Figure 2.1.1: 8 keV/u bunched beam (O^{5+}) measured at the fast Faraday cup

Figure 2.1.2: Set-up for measuring the energy gain after RFQ acceleration

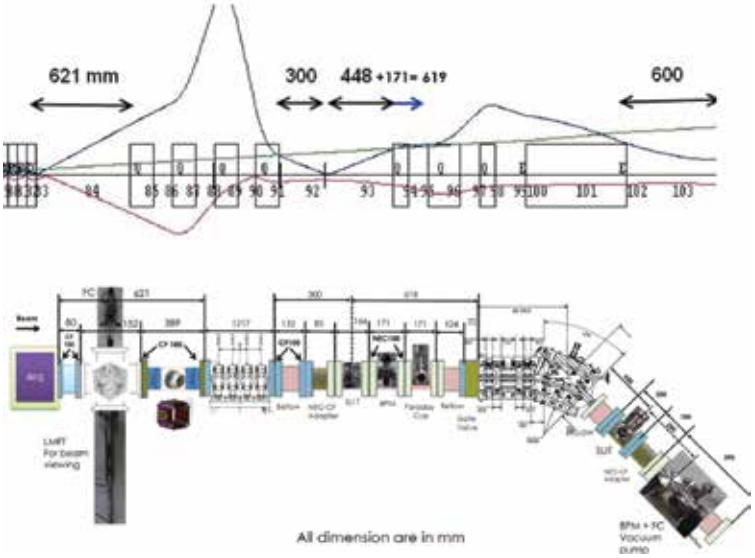

Figure 2.1.3: Optics through the system to measure the energy gain

b) Refurbishing and installation of LEBT

In the old configuration of the source and LEBT, diagnostics between the ion source and the analysing magnet took a lot of space and appreciable amount of beam loss was envitable. Additionally, the 30 kV high voltage platform which was installed physically near to ground level was prone to dusty environments and problems further evolved with power supplies not functioning and could not be finally used. The tuning effect of the negative DC bias voltage on the output of highly charged ions was difficult to realise, which is one of the most critical tuning parameter for an ECR ion source. Even during the ion source maintenance, for example, when the ion source was required to be opened up, the injection turbo-molecular pump had to be dismantled. This however caused a lot of downtime for the system. To circumvent all these issues, the source was brought closer to the analysing magnet by removing diagnostics and steerers. This also facilitated to couple the 30 kV high voltage platform close to the ion source and keep it movable for maintenance. The existing extraction system which consisted of a longer Einzel lens with 4 electrodes was removed and an alternate system was installed which was originally tested with the ion source at the test bench in France. The reason was the improper alignment of the longer electrodes, due to which beam steering was inevitable and could not be rectified. After the source was started with all the above modifications, there has been a tremendous improvement in the performance of the ion source and transmission. An off-shoot of this modification is the increased x-ray radiation levels. Necessary shielding is being worked out to get it installed as early as possible. A view of the modified LEBT is shown in figure 2.1.4.

Figure 2.1.4: View of the modified LEBT (Left: view of the 30 kV platform and Ion Source, Right: view of the extraction system, magnetic quadrupole and analysing magnet)

(c) Plasma potential Measurements

Plasma potential measurements were carried out using the 'magnetic rigidity' technique by using the 90º bending magnet which analyses the extracted beam from the ion source. Different charge states of oxygen beam were extracted at different extraction voltages and measured the magnetic field of the analyzer magnet by optimizing the beam current on a Faraday cup located close to the exit of the magnet. A 5 mm slit placed after the magnet was used to focus the beam precisely onto the Faraday cup. The measurements were carried out for charge states

3+, 5+ and 6+ of oxygen beam by varying the extraction voltage and keeping all other source parameters fixed. The beam intensities were measured using a Keithley digital electrometer and a Group 3 instruments digital Tesla meter to precisely measure the analyser magnetic field. All the measurements were carried out at constant gas pressure of $1x10^{-6}$ mbar, microwave power of 700W and 134A/112A of currents of injection/extraction superconducting coils. Plasma potentials were estimated by plotting the square of the measured magnetic field as a function of the extraction voltage and by fitting the data with a least square fit. The offset voltage at the intercept shows the mean plasma potential which is evaluated as 53.65 V and the calculated energy spread turns out to be 321.9 eV in the case of O^{6+}. Figure 2.1.5 shows V_{ext} as a function of B^2 for O^{3+}, O^{5+} and O^{6+}, a least square fit of each plot and the extrapolation. Plasma potentials were also measured as a function of microwave power and gas pressure.

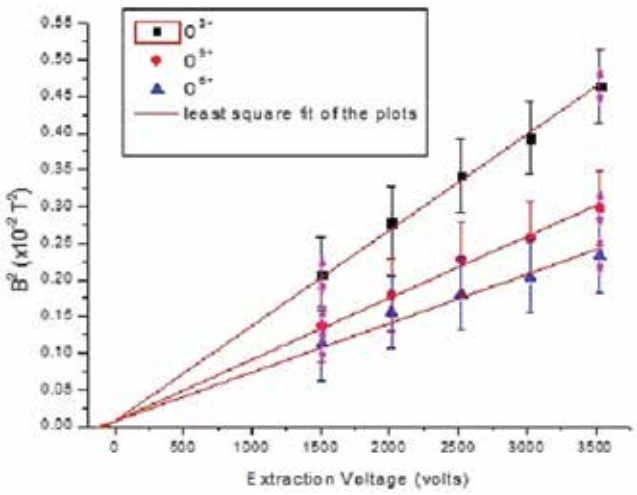

Figure 2.1.5: Mean plasma potentials measured using the 'magnetic rigidity' technique

(d) Longitudinal emittance measurements

The longitudinal emittance of the bunched beam was measured by using the 12.125 MHz multi harmonic buncher and a fast Faraday cup. The multi harmonic buncher operates at a fundamental frequency of 12.125 MHz and a saw tooth voltage is generated by the superposition of the fundamental and its harmonics at 24.25 MHz, 36.375 MHz and 48.5 MHz. In the present measurement, the fundamental and the first two harmonics at 24.25MHz and 36.375MHz are used. The bunch width was measured at a distance of 3 meters from the buncher, where the fast Faraday cup is placed. By using the thin buncher approximation, the square of the bunch width (t) measured at a distance (L) from the buncher is a quadratic function of the saw tooth voltage applied across the buncher gap.

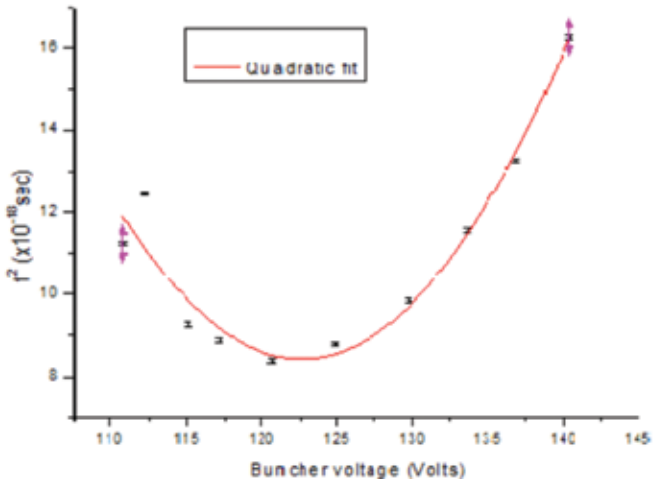

Figure 2.1.6: Measured variation of square of the beam bunch width (FWHM) as a function of the buncher voltage

The bunch width was measured for different buncher voltages (Vs) after optimizing the bunch width to 2.8 ns at the fast Faraday cup. The FWHM was measured in each case by considering the total pulse height which includes the contribution from the electrons as well and the electron current is estimated to be about 10%. The data were taken for O^{5+} by optimising the source parameters at an extraction voltage of 25.6 kV, microwave power 700W, coil currents 134.6A/112.82A and gas pressure $1.32\ x10^{-6}$ mbar. The fitting coefficients were

computed by plotting square of the FWHM of the bunch as a function of the buncher voltage and by performing a quadratic fit as shown in figure 2.1.6. The bunch width at the same source conditions were measured as a function of the buncher voltage by only changing the 4 magnetic quadrupoles and two steerers after the buncher.

(e) Electronics Work - Development and Maintenance

1) Traveling Wave Tube (TWT) Amplifier was installed on the high voltage deck of HCI. A python based control program was developed to operate the TWT amplifier remotely from the console of the HCI in beam hall-III. The amplifier was first tested on the dummy load for its full rated power (250W) by operating it remotely from the console. This microwave TWT amplifier was then coupled to the PKDELIS ECR ion source. This system has an advantage of frequency also as TWT is a broadband device. It was used successfully to generate the Argon beam from the PKDELIS ECR source.

2) 1.7kW, 18 GHz microwave power generator underwent four breakdown maintenances in this year. There was one component failure due to high voltage spark and aging effect. High voltage for the Klystron microwave tube was tripping frequently even though the generator remains in the ready state. It was diagnosed that it was due to the faulty diode D22 1N4148 across relay RE6 in CD control unit, which is responsible for starting the high voltage for the generator. We faced problem of low air pressure, which was preventing the generator achieving ready state. This problem was solved by repairing the air leaks with better sealings and also calibrating the air pressure interlock settings. There was problem with IC3 TL082 in the frequent failure of EC control unit, which was responsible for providing the control signal for microwave power of IC. On detailed inspection it was found that due to overheating restrictions in hot air exhaust from the Klystron genrator caused failure of IC. Exhaust passage was then cleared to solve this problem. In the fourth time we faced the problem that as soon as we start microwave pulsing of the klystron generator, it stopped giving any output. Its IC3 TL082 in the EC control unit went bad. We diagnosed that it was due to the fault in the functoon generator output, which was giving a more that 20 V peak voltage for TTL pulse output signal.

3) Another problem with the control electronics for the high temperature superconducting solenoid coils caused gfalse tripping of the solenoid coils power supplies signalling various faults wrongly. On detatiled checking we found that the multi-output, very compact, power supply was malfuctioning. This was responsible for providing +12 V, --12 V, 24 V and 5 V voltages for control electronics. Since the identical spare for this power supply was not available, we replaced it with four power supplies of required rating and mouted on the chasis. This system now works satisfactorily.

4) Negative high voltage power supply on the second deck for the bias electrode of the PKDELIS had failed. When it was replaced with the spare power supply, that also went bad after a short time. On detaled inspection and tetsing, it was diagnosed that one ADC (Analog to Digital Converter) channel for remote monitoring of this power supply was faulty. It was causing the defucting of the bias power supplies. That control was then shited to another ADC channed to solve this problem. High voltage power supply was also again replaced. It is now working satisfactorily.

5) Another problem was that, there was no negative bias output to the bias electrode of the PKDELIS ECR ion source as per the corresponding input even though the high voltage bias power supply was ok. On detailed checking we found that one fiber optic channel for providing control to the bias power supply on the second high voltage deck was not fucnctionng properly. IC AD650 in its link module was faulty. We replaced the IC and thus solved the problem.

6) Made bufferd interface circuit for remote operation of the HTS coils.

7) The pre- amplifier for fast Faraday cup failed due to which we were not able to tune the beam properly through MHB. From our earlier experience of repairing, we were able to repair it fast this time. We found that the input stage of the IC had gone faulty. We then repaired it successfully by replacing the faulty components. It is now being used in the system.

2.1.2 Status of the MULTI-HARMONIC BUNCHER for the HIGH CURRENT INJECTOR

A Sarkar, Sarvesh Kumar, Rajesh Kumar, R Ahuja, S K Suman, Y Mathur, P Barua, A Kothari, A J Malyadri, V V V Satyanarayana, B P Ajithkumar

A fully indigenously developed multi-harmonic buncher (MHB) has been designed, fabricated and commissioned in the beamline for the high current injector (HCI) at IUAC, New Delhi. The tank circuit to generate the four harmonics, sits on top of the vacuum chamber which contains a gridded bunching gap structure across which the approximated saw-tooth voltage is applied. The buncher is tuned for 12.125 MHz and its harmonics using vector network analyser such that reflected power is less than 2%. The entire control electronics along with an RF power amplifier is integrated with the tank circuits connected to the bunching girds. In low energy section, a multi-harmonic buncher (MHB) at 12.125 MHz fundamental frequency is chosen with its three harmonics. A saw-tooth voltage generated across a single gap formed by a closely spaced pair of Molybdenum grids, at the center of the MHB chamber, will be used for bunching the DC beam. This saw-tooth voltage is produced by adding a sinewave (12.125 MHz) with its higher harmonics in proper phase and amplitude. The higher frequencies used in the MHB are 24.25 MHz, 36.375 MHz and 48.5 MHz which are multiples of the fundamental frequency (12.125 MHz). All these frequencies are the sub-harmonics of the SC-LINAC frequency i.e. 97 MHz. The ideal saw-tooth waveform is generated by mixing different frequencies in proper phase and amplitude. By Fourier's series an ideal saw-tooth signal can be obtained overlapping an infinite number of sine harmonics but by using three harmonics across a single gap, one can obtain a close approximation to the ideal waveform. The coils for 12.125 MHz, 24.25 MHz, and 36.375 MHz are mounted in mutually perpendicular directions to minimize the cross-talk between them. The 48.5 MHz tank circuit is connected to the grids through de-coupling capacitors. The coils for 12.125 MHz, 24.25 MHz, and the grid assembly holder copper tube are cooled by a co-axial de-ionised water cooling arrangement. The 36.375 MHz coils are smaller and need no cooling. All the tuning capacitors are 3 -30 pF vacuum variable type. The 12.125 MHz tank circuit is tuned by changing the inductance of the coil. Inductive couplers for the different frequencies are used to feed in RF power to the tank circuits. The schematics of LEBT are shown in Fig. 2.1.7. The installed configuration of LEBT section is shown in Fig. 2.1.8.

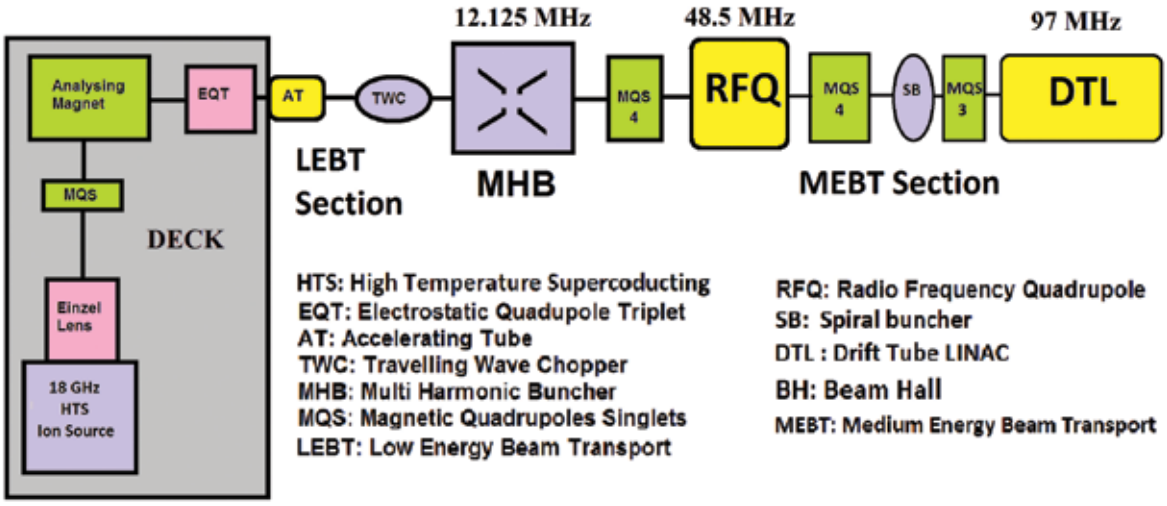

Figure 2.1.7: LEBT schematics

Nitrogen and Oxygen beam of A/q less than 6 generated by the ECR source was successfully bunched by the MHB. A fast Faraday cup installed just before the entrance of the RFQ was used to detect the beam bunching. Beam bunches of the order of few ns FWHM was seen directly on the oscilloscope from FFC via a MITEQ preamplifier of broad bandwidth with 50 dB gain. We have obtained best beam bunch with 720 nA beam current for 128 keV Oxygen ion beam around 2.5 ns as shown in Fig. 2.1,9.

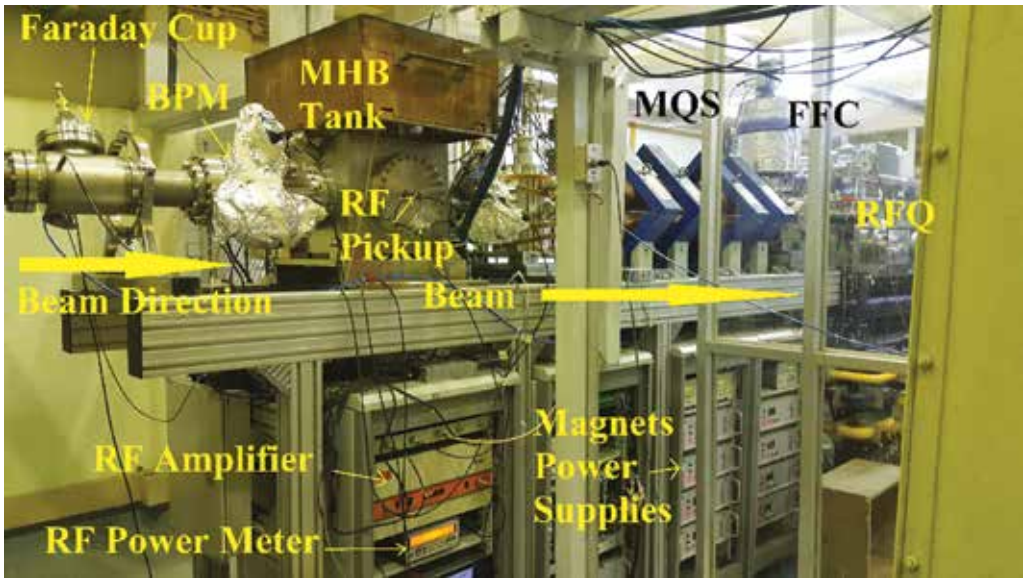

Figure 2.1.8: LEBT section with installed buncher and Fast Faraday Cup

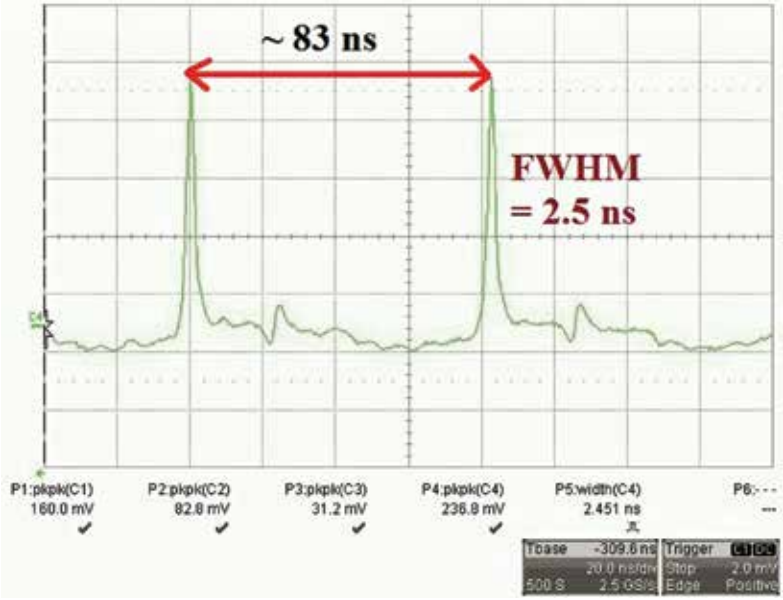

Figure 2.1.9: Beam bunch of 2.5 ns at the Fast Faraday Cup

2.1.3. High power RF TESTS and beam test on RADIO FREQUENCY QUADRUPOLE

Sugam Kumar, R. Ahuja, A. Kothari, C.P. Safvan

HIGH POWER RF TESTS

The purpose of high power RF tests were to check the RF and temperature stability of the RFQ as well as to survey both the RF and X-ray leaks from the RFQ cavity. The flow rate and temperature of the cooling water were measured using commercially available water meter at the water outlet. Forward and reflected power was monitored using BIRD electronics analog RF meter during high power run. The amplitudes of pick up signal, RF drive, and forward power were monitored on oscilloscope. The power coupler is air cooled and its temperature also monitored continuously during run. The conditioning started with an input power of 1 kW while carefully monitoring the cavity vacuum pressure and checking reflected power for signs of sparking. The RF power was increased slowly where we noticed that vacuum pressure deteriorates to $1x10^{-6}$ mbar due to sparking and consequently the power level was decreased until the vacuum improves and the sparking rate reduced. Gradually, we reached 30kW without losing any RF contact. The RFQ was conditioned at 30kW for few hours only due to rise in air temperature (>50ºC) coming out of power coupler. But at 23kW the RFQ was conditioned for almost 8 hours.

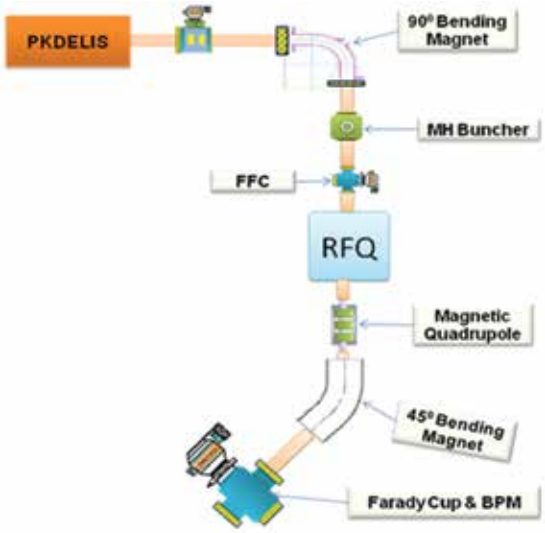

Figure 2.1.10: Beam line setup for the measurement of energy and transmission through RFQ.

We encountered no major sparking or vacuum degradation in the cavity. After 8 hours of conditioning the vacuum pressure in the cavity was 7.5×10^{-8} mbar at 23kW. We observed marginal rise in water temperature from 19ºC to 21ºC at 32kW. Very small but non-uniform local heating also observed at the bottom SS chamber. Base pressure increased from 4 x 10^{-9} mbar (no RF power) to 1.3 x 10^{-8} mbar at 30kW. The RF leak was inspected with a commercial RF survey meter. The electromagnetic radiation was undetectable even in the lowest range (full scale being 2.65 x 10^{-2} mW/cm^2) of the survey meter at 30 kW RF power level. The X-rays leak was examined with a survey meter at several points on the outer surface of the RFQ cavity. Under the same condition of rf power, the X-rays leak was less than 15 µR/h, well below the maximum exposure rate of 100 µR/h.

BEAM TEST

After successful high power tests it was decided to setup beam line elements and beam diagnostic devices for beam acceleration tests. For the energy measurement of the accelerated beam a 45º bending magnet was installed after RFQ. Two Faradays cups were installed just downstream the beam before the 45º bending magnet and another Faraday cup system along with BPM installed at the end of diagnostic chamber to measure the current and beam profile of accelerated beam. The input current were measured with Fast Faradays cups installed upstream the RFQ. Beam acceleration tests have been performed by injecting 32keV DC beam of He^{2+} and 128keV of O^{6+} ion beam into the RFQ. The output beam energy was estimated from momentum spectrum of the beam, which was taken with the 45º bending magnet. The estimated output energy of He^{2+} beam was 707keV ± 3% at 13kW RF power, which was in fairly good agreement. The input and output beam current were measured with Faraday cups. The beam transmissions of He^{2+} approaches sharply from zero to 90% at 13kW and stay constant afterward, whereas the beam transmission of O^{6+} reaches maximum at 23kW. Successful acceleration of ion beams from 8keV/u to 180keV/u validates the design of RFQ modulation. We should be able to accelerate the ions beam of A/q = 6 also to 180keV/u very soon.

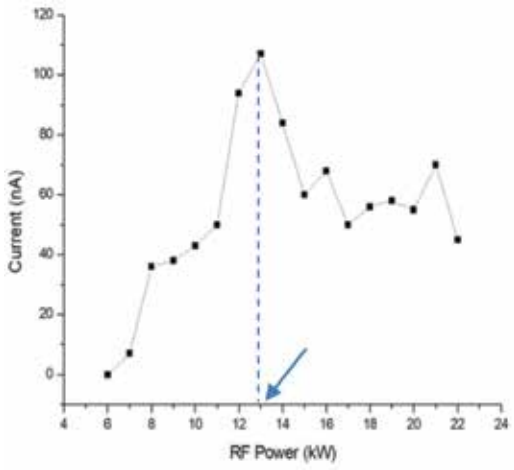

Figure 2.1.11: He^{2+} ion beam transmissions through the RFQ as a function of RF power.

2.1.4 Drift Tube LINAC Resonator

The role of the room temperature DTL is to accelerate the 180keV/u beam from the RFQ to 1.8 MeV/u. The DTL consists of 6 multiple gap IH type cavity resonators, operating at 97 MHz. The transverse focusing is done by compact quadrupole triplets, placed in between the resonator tanks. The design of the DTL incorporates bunching sections inside the cavity to take care of the longitudinal focusing. All the resonators are different with length ranging from 38 cm to 94 cm and power ranging from 5kW to 25kW.

Out of the six resonators, the first one has been tested with full power and ready to be tested with beam. The second resonator assembly is almost over, including the accelerating tubes and their support structures. The outer shells of the remaining four resonators are completed and tested for vacuum. The six resonators will be mounted on a structure made in three sections. The first two resonators and corresponding magnetic quadrupole triplets will be mounted on the first section. A photograph of Resonator #1 mounted on the structure is shown in the figure.

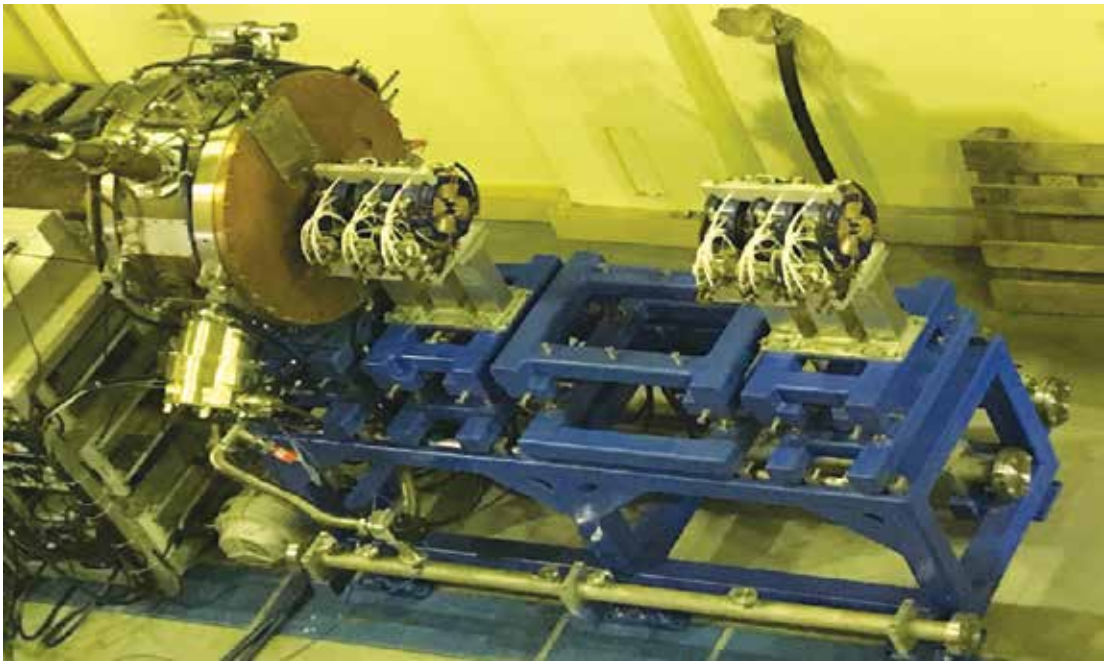

Figure 2.1.12: Resonator #1 mounted on the structure

Most of the RF power amplifiers required for the resonators have been procured. Currently we have two 20 kW units and two 28 kW units, both are solid state designs. A 30kW vacuum tube design was procured earlier.

Even though the first resonator has been tested with full power and the electric field distribution is measured by the bead-pull test, there is no measurement available on the actual voltage present across the accelerating gaps. It is planned to test one DTL structure using the beam from the Pelletron, so that from the energy gain we can calculate the total accelerating voltage for a given input RF power. For this purpose, the outer shell of the sixth resonator has been assembled with a drift tube assembly suitable for higher energy beams (2.5 MeV/u). This setup is nearly ready and will be tested on the GDA beam line.

2.1.5 Travelling wave chopper

S Kedia, Rajesh Kumar and R Mehta

The Traveling Wave Chopper (TWC) is required in the LEBT section of the High Current Injector (HCI), to provide the chopped beam with various repetition rates to the IUAC experimental facilities. The TWC will select 60 ns of beam at the different frequencies of 4, 2, 1, 0.5, 0.25 and 0.125 MHz. The complete design has been simulated in various simulation codes including CST MWS, Trace 3D, Solid Works and Python. The mechanical assembly has been divided into two parts inner assembly & outer housing. The inner assembly has been fabricated and assembled within the accuracy of 500 µm. The outer chamber has been fabricated and leak tested upto $1x10^{-10}$ mbar l/s. The inner plate assembly has been mounted on the outer chamber. The alignment of the complete assembly was carried out using the slip gauge and CMM system. Final assembly is within accuracy of 500 µm. Figure 2.1.13 shows various views of the assembly. A test has been planned in the Low Energy Ion Beam Facility to calibrate the voltage required for obtaining the design deflection.

Figure 2.1.13: The mechanical assembly of TWC, (a) Inner Assembly, (b) side view, (c) Top View

2.1.6 High Power Test of 48.5 MHz Spiral Buncher for MEBT Section of HCI

R Mehta, S Kedia, R V Hariwal and R Ahuja

A 48.5 MHz spiral buncher has been designed and developed to match the longitudinal emittance between RFQ and DTL. The RF characterization was carried out to measure the resonant frequency and quality factor, bead pull technique was used to measure the electric field profile along & off the beam axis. The cavity has been tested up to 1 kW of input power to generate gap voltage of 30 kV validating the design requirement. The X-ray measurements were carried out to verify the gap voltage.

HIGH POWER TEST During assembly of the system a vacuum leak through the brazed joint was found in the spiral section of the buncher. Repeated unsuccessful attempts to overcome the vacuum leak by doing the vacuum brazing deformed the spiral. In order to validate the power requirement and high power RF characteristics of the buncher we decided to use silicon based high vacuum sealant to overcome the vacuum leak and do the power test. Due to the deformation beam axis of spiral was shifted vertically by 20 mm. In order to use the same spiral we designed and fabricated an aluminium stem. With this new stem we corrected the beam axis shift as well as the frequency shift of the cavity due to deformation. A new air cooled high power input coupler was designed, fabricated and optimized for 50 ohm characteristic impedance with respect to the cavity. A frequency tuner was also installed to correct the frequency shift during operation. After complete installation the quality factor deteriorated to 2200, this can be attributed to the poor surface quality after rework and vacuum sealant spray. With this quality factor we reached 1 kW input power level with less than 35 dB of reflected power. The ultimate vacuum reached was $1x10^{-7}$ torr. Figure 2.1.14 shows results at 1kW input power.

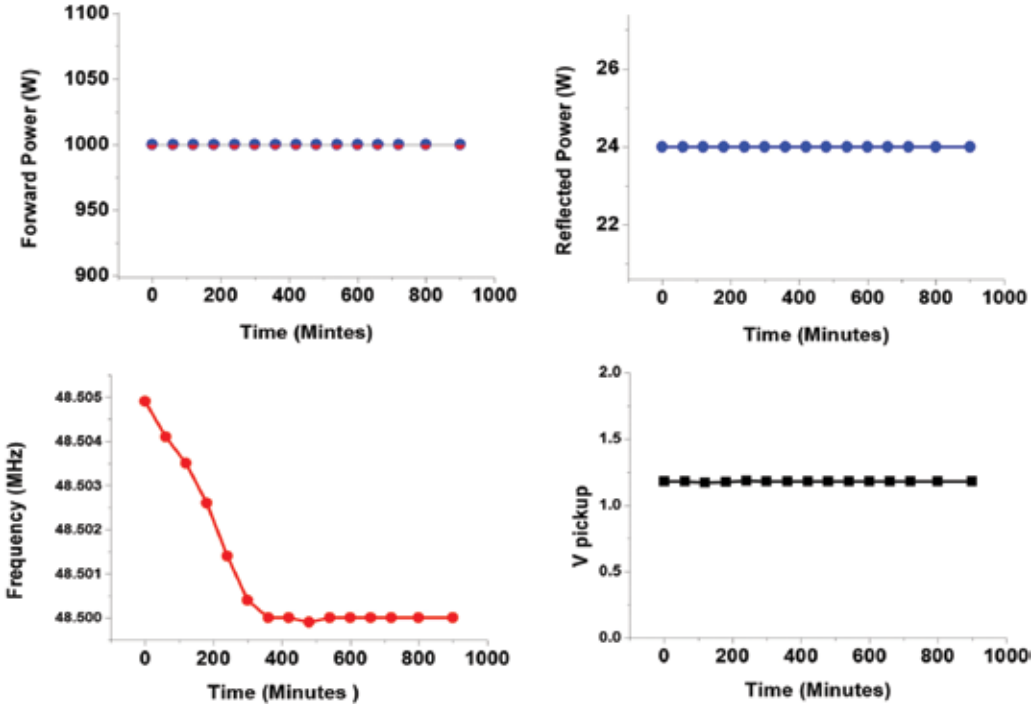

Figure 2.1.14: Variation of Reflected Power, Pickup Signal and Frequency at 1 kW Forward Power

X-Ray measurements were carried out at various forward power level to estimate the gap voltage and the results matched nicely with the simulated values of gap voltage. The X-Ray spectrum at 1000 watts of input power is as shown in figure 2.1.15.

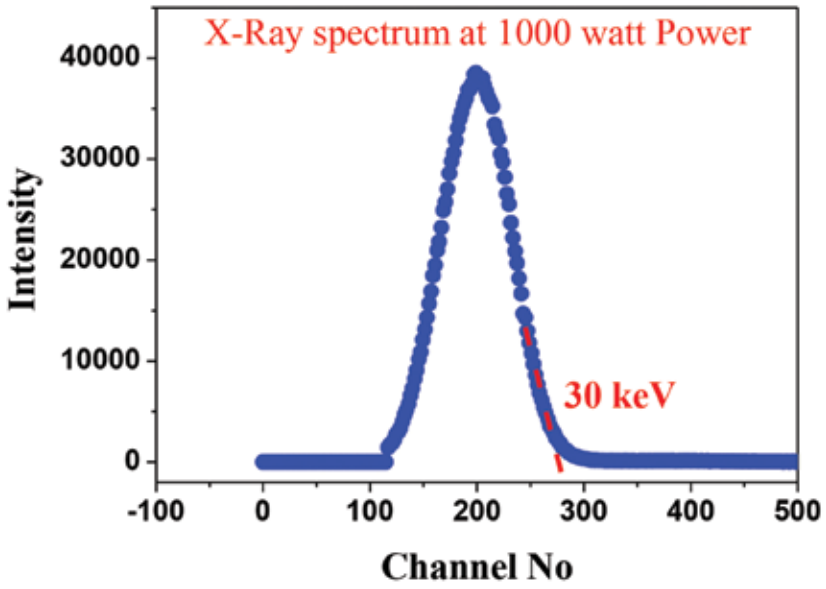

Figure 2.1.15: X-Ray Spectrum at 1 kW Input Power

The spiral buncher is ready for installation in the MEBT section. In parallel we also initiated a process to explore the possibility of using a stainless steel based spiral with copper plating of 100 micron on the outer surface as a replacement of the existing copper spiral. Thermal and RF analysis were carried out in CST MWS. After confirming the design we placed an order for the SS spiral and the fabricated spiral is ready for the copper plating.

2.1.7 Status of Compact Transverse and Longitudinal Beam Diagnostics for HCI

R. V. Hariwal, S Kedia, R. Mehta

Development of Compact Transverse Beam Diagnostic System

To preserve the transverse emittances and overcome the space limitations at the entrance of Drift Tube Linac (DTL) resonators in Medium Energy Beam Transport (MEBT) section of High Current Injector (HCI), a multipurpose beam diagnostic system, have been developed indigenously at Inter-University Accelerator Centre (IUAC). After successfully validating the working of various components of CBDS, it was decided to modify the design to have better alignment fixtures and mountability of the components. The modifications will be helpful during the installation and alignment of the system. The components can easily be replaced by similar components after the implementation of required modifications. The weight of the system was another important concern due to the direct attachment of CBDS with DTL end plate without any support and we have tried to cut down the extra material to reduce the DB's weight. The beam aperture of DB has also been modified from 20 mm to 30 mm to increase its beam acceptance. The provision of handling has been provided in the modified system with the help of two I-bolts for the safer installation. The required modifications in the 3D design of DB, FC and SSC have been carried out using Solid Works software. The machining and modifications in the CBDS are implemented as per new designs. The modified designs are shown in Fig.2.1.16. The machining was performed with the help of CNC and wire cutting to maintain the alignments of each component. All the components were cleaned with the help of ultrasonic cleaner using subsequent soap solution, acetone and alcohol. The assembly of modified CBDS is over and now we are in process to install it in the HCI again for beam test very soon. The modified structure of CBDS embedded with FC and SSC are displayed in Fig.2.1.17.

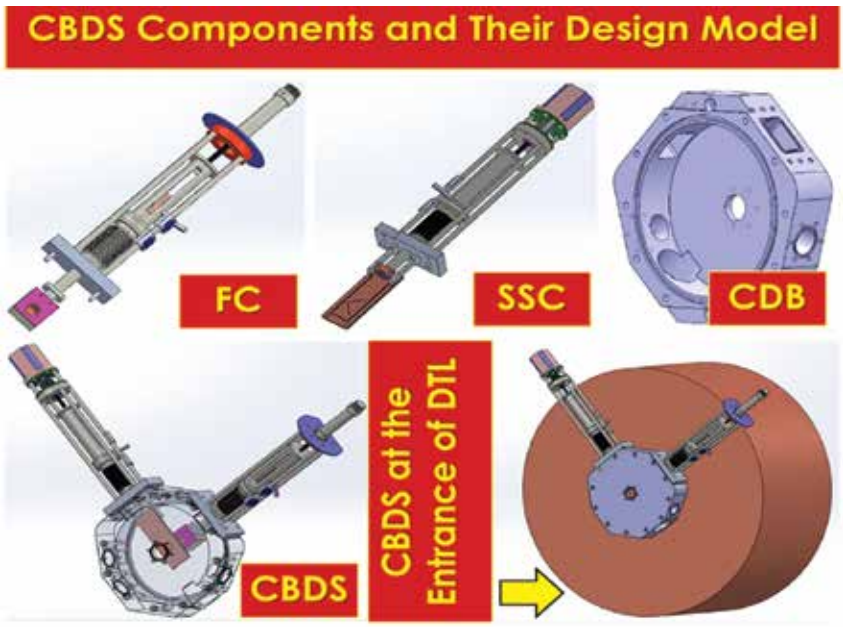

Fig.2.1.16: Modified 3D design of FC, SSC, CDB, CBDS and CBDS with DTL

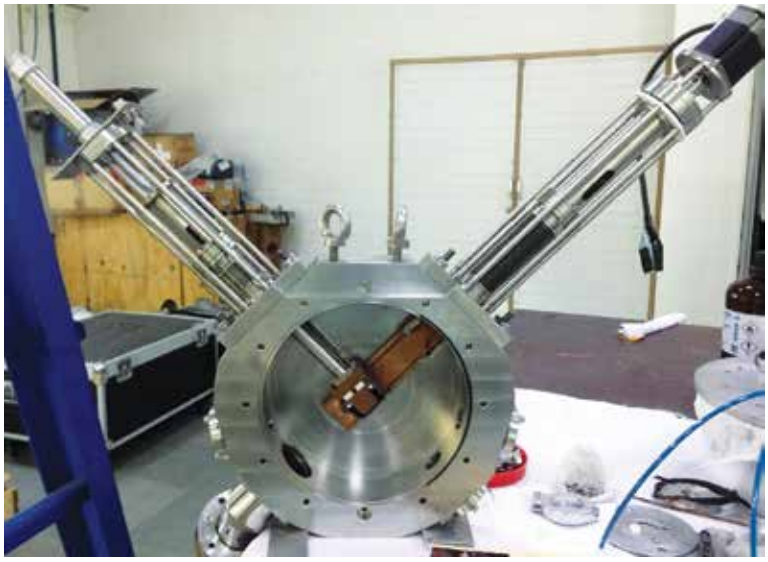

Fig.2.1.17: Modified structure of CBDS embedded with FC and SSC

Development of Beam Profile Monitor for FFC chamber

We have developed a new type of slit scanner with rotatable flange for the measurement of noise free beam profile upstream the RFQ in HCI. This can provide the beam density profile with the help of current read by Fast Faraday Cup (FFC) in the current mode. This was developed to install in the FFC chamber. The mechanical and electrical operations have been checked using a PLC based stepper motor electronic module. The fiducials for beam line centre have been calibrated and the linear motion of the system has been verified using multiple operations. A separate PLC based stepper motor control module has also been developed for its smooth operations. The module will be able to control the direction, speed, acceleration and number of steps etc. during the online operation.

Development and Testing of RF Tuner for Spiral Buncher

To tune the resonant frequency of the spiral buncher, we have developed a stepper motor based RF tuner. The tuner was assembled with the cavity, leak tested and the leak rate was found to be ~2.3 x10^{-10} mbar.l/s. The tuner has been installed in the cavity and the frequency of spiral buncher was tuned to 48.5 MHz using this tuner. The frequency shift of ~180 kHz was observed with respect to the ~55 mm motion in the linear direction towards the spiral. The direction, speed, steps and linear motion have been controlled using the PLC based stepper motor control module running by Python code. Here, Fig.2.1.21, (a) displays the RF Tuner for spiral Buncher (b) tuner installed with spiral buncher (c) RF tuning to 48.5 MHz and (d) shows the Frequency shift vs Tunner Positions.

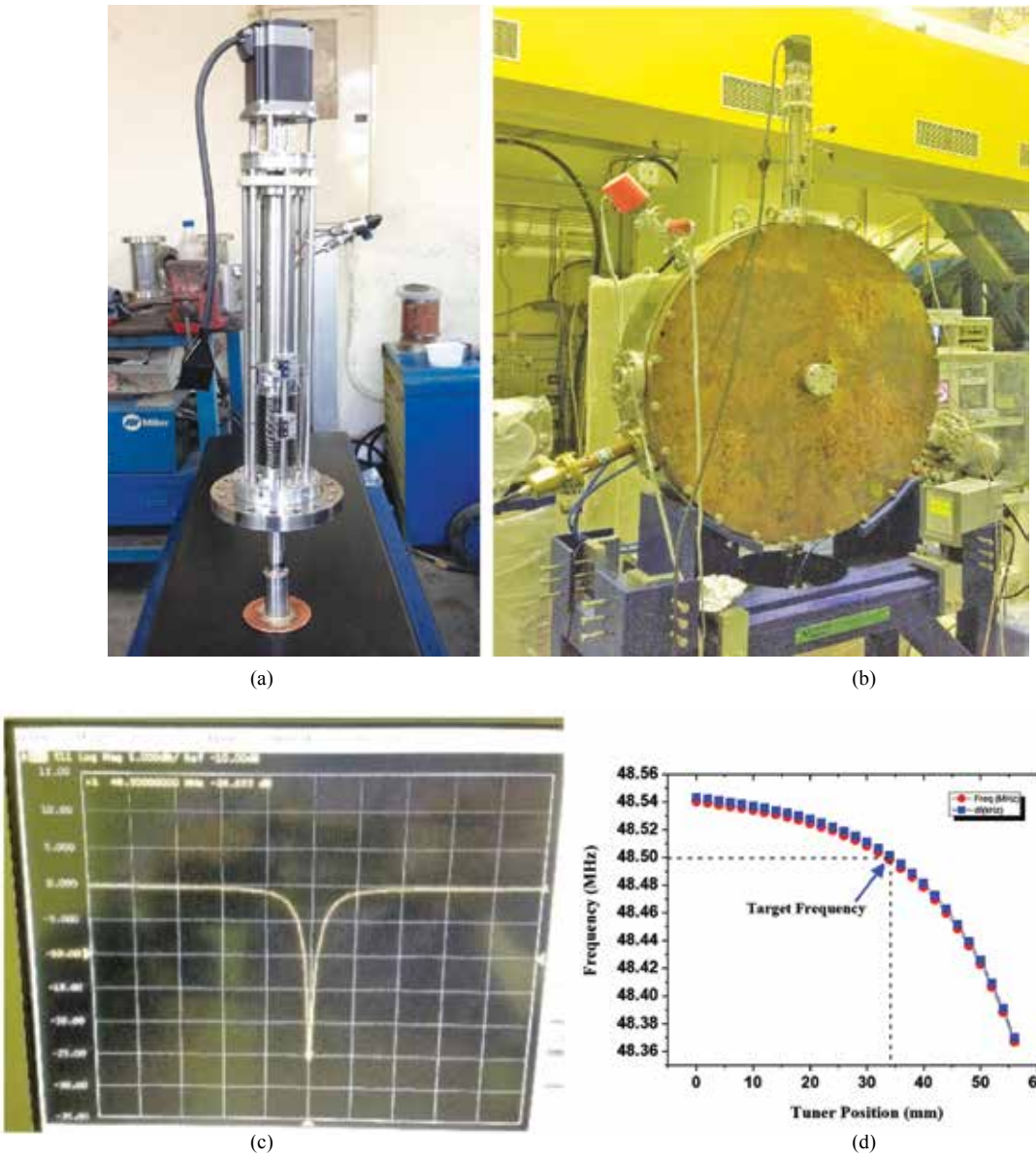

Fig.2.1.19: (a) RF Tuner for spiral Buncher (b) tuner installed with spiral buncher
(c) RF tuning to 48.5 MHz and (d) Frequency shift vs Tuner Positions.

2.1.8 Instrumentation development

2.1.8.1 Control instrumentation for Chopper cum Deflection System (CDS)

Rajesh Kumar, Sanjay Kedia, S.k. Suman, Mukesh Kumar, Rajeev Mehta

The 4-plate TWC (Fig. 2.1.22) will have variable frequency operations @ 4 MHz, 2 MHz, 1 MHz, 500 kHz, 250 kHz and 125 kHz. Because of variable frequency operations, non-resonant type 1kV square wave pulser will be used for chopping and deflecting the beam. Since 4MHz@1kV high voltage high frequency (HVHF) pulser are not off the self available commercially, hence efforts has been made to develop such pulser in-house, but failed because the cooling requirement comes out to be unworkable with the in-house available technique and within the required compact size. After thus meeting a dead-end in the development possibilities, three leading Pulser manufacturers namely BHELKE, EKSPLA and QEI were contacted to give a customised solution. Initially BEHLKE offered a customized push-pull pulser operating at 4MHz, which is completely commensurate with our requirement, but later the company backed out and stop responding. At present it has been decided that the off-the-shelf available 2MHz Pulser will be procured from BHELKE for initial commissioning of the TWC. The complete instrumentation for the TWC pulsing system will includes four main sections of instrumentation; the pulsers with required cooling system, high voltage and low voltage bias power supplies, generation and synchronisation of simultaneous pulses (trigger unit) and the operation algorithm and safety control (operation control unit). Except the operation control unit, for rest of the units/ sections commercially available options will be used. The control unit will be developed in house as per the safety, operational and control requirements of HCI facility.

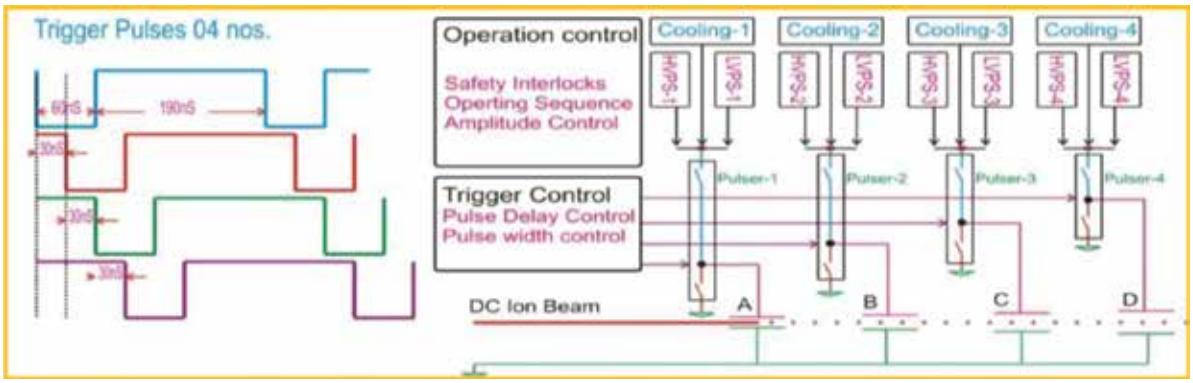

Fig. 2.1.20

A Pre-Execution Report (PER), describing the "Electronic Instrumentation" requirement for the “Travelling Wave Chopper" (TWC) of the High Current Injector (HCI) has been prepared. The report also includes the system integration and operation details to have a reliable pulsing system with high degree of performance. Hence the design is final and will be executed based on the priority.

2.1.8.2 Low level RF based controller for single gap Multi-Harmonic Buncher (MHB)

S.K.Suman, Rajesh Kumar, V.V.V.Satyanarayana

The sawtooth wave driven single gap Multi-Harmonic Buncher (MHB) was commissioned last year and in operation since then. The MHB operates at 12.125 MHz a sub-harmonic of 97MHz, resonance frequency of the SC-LINAC. A close loop controller based on analog Low Level RF (LLRF) is developed. It combines the fundamental 12.125 MHz with three consecutive harmonics in proper phase and amplitude to generate a saw-tooth wave and maintains its amplitude and phase over time. The composite output signal from the controller is amplified by a RF power amplifier and fed to the MHB grids via tank circuits. The feedback from the MHB grids is taken using two capacitively coupled probes and fed back to the controller to achieve active close loop control of phase and amplitude of the saw-tooth voltage across grids. The phase and amplitude of the MHB are stable over time and the control flexibility is proved to be very useful in optimizing the bunch width. The controller and the best optimised pickup waveform is shown in Fig. 2.1.21.

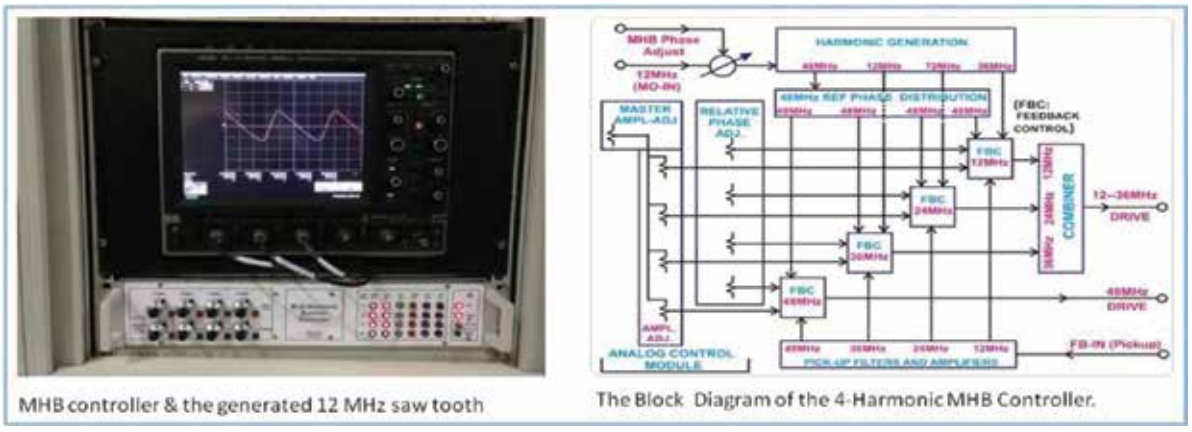

Fig. 2.1.21

This year the quiescent operating point of the controller feedback loops has been optimized twice to preserve the control dynamic range. Firstly the feedback signal reduced of its own from the MHB tank circuit and secondly the RF amplifier (100W) has been changed having a different transfer function then the previous one.

2.1.8.3 Low Level RF (LLRF) controls for HCI RF cavities (RFQ, DTL & Spiral Buncher)

S.K.Suman, Rajesh Kumar

The LLRF control system at HCI is used for the MHB & single frequency spiral buncher as well for the accelerating RF cavities RFQ and DTL. All these operate with radio frequency power amplifiers that have to be

synchronized with each other in phase and amplitude. Following decision was taken related to implementation; all the RF cavities will have independent and identical controls except TWC and MHB; common design for 48.5MHz and 97 MHz accelerating cavities.

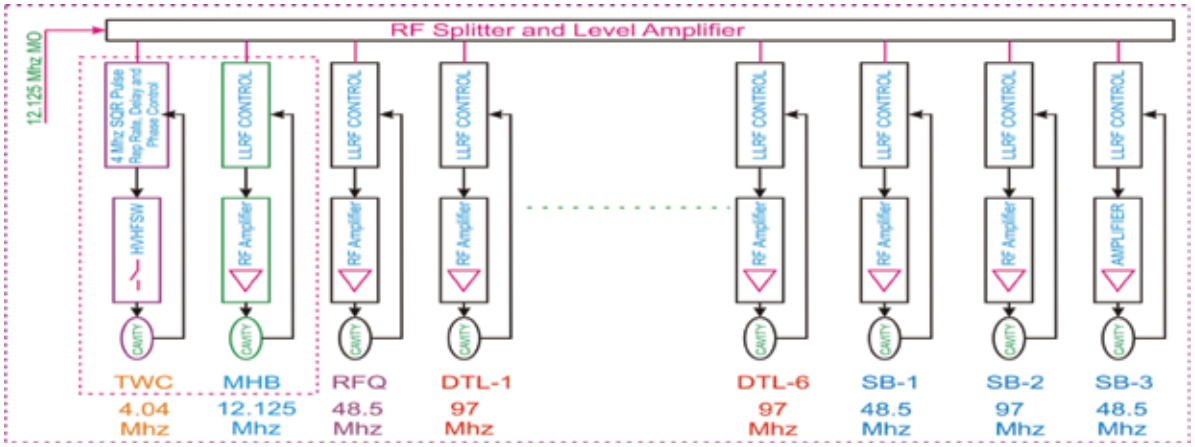

Fig. 2.1.22

For the LLRF control implementation, analog GDR scheme is chosen as it is simple to implement and does not require any special software and hardware to implement and test. All the required functions are grouped in different units considering easy and fast servicing. The amplitude, phase and frequency controls has been implemented successfully and is in operation with RFQ.

Amplitude & Phase control Loop

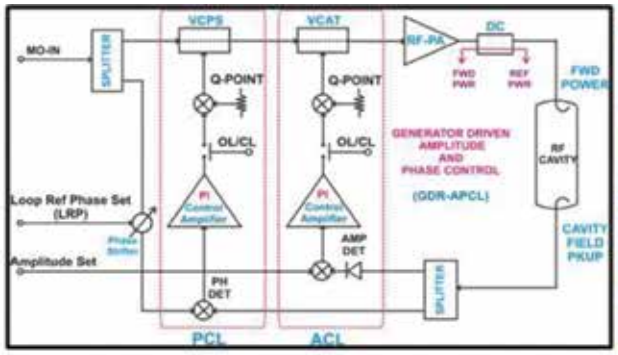

Block diagram of Amplitude & Phase Control Loop

Photograph of Amplitude & Phase Control Loop

Fig. 2.1.23

This year three units (final design) of Amplitude & phase control loop has been assembled and installed with all the three-type of HCI-RF cavities. The design of the phase and amplitude controller was modified to enable smooth transfer from open loop to close loop at high RF power. Additionally the new controller has been provided with the remote control facility. The LLRF control with the RFQ is in full operation since last one year, and for DTL & SB it is use for initial powering of these cavities. Amplitude stability of 0.002% and phase stability of 0.03º has been achieved with RFQ cavity at 25kW for 4 hours.

Frequency Control Loop

A stepper motor driven mechanical tuner is used in HCI-RF cavities to tune the cavity frequency. The controller is developed to operate the frequency tuner in closed loop for keeping the cavity tuned irrespective of temperature effects. This is an on/off type control based on bipolar window comparator with hysteresis. Whenever the phase difference between the cavity pickup and forward power exceeds the maximum phase error limit, the phase window comparator generates direction and drive signal to drive the tuner motor. The first prototype of the FCL is in operation with RFQ since last one year to acquire more operational and functional data for the final implementation. In terms of performance the controller is able to keep the frequency drifts within limits even with large thermal variations in the cavity. This year the design has been modified for the final product implementation. In the modified design the phase comparator window and hysteresis setting has been made programmable to have different settings at different power level to achieve stable operation without tripping the RF power amplifier. In the new design along with local control, remote control has been provided for all the programmable functions.

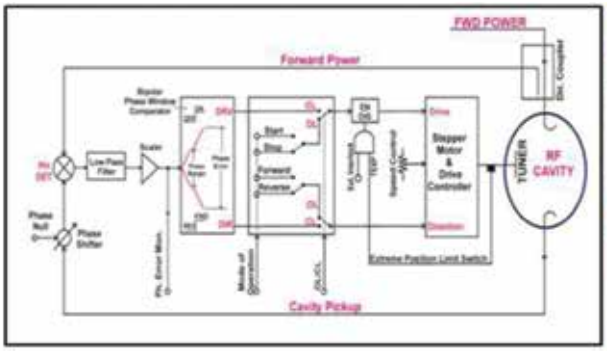

Block Diagram of the Frequency Tuner Controller

Photograph of the Frequency Tuner Controller

Fig. 2.1.24

Master Oscillator (MO) and RF Distribution Unit

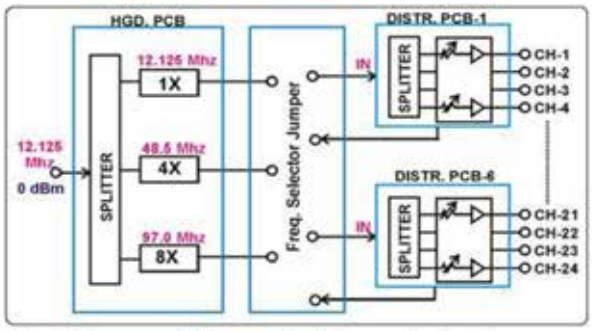

Block Diagram of Master Oscillator Distribution

Photograph of the Master Oscillator Distribution

Fig. 2.1.25

Master oscillator is the reference phase for the HCI-RF cavities. For synchronised stable operation of the accelerator the MO phase should be highly stable, low noise and jitter free. RF signals as phase reference for each cavity are derived from the MO unit. This year a modular RF distribution system has been designed and built to distribute the master oscillator (MO) signal. The MO distribution system is designed in a modular and flexible way allowing for easy reconfiguration and system extension in case of need for more channels. To overcome the losses due to signal splitting and sending it over a coaxial cable, the MO RF signal level is maintained around 0 dBm using amplifiers and attenuator combination. At present the MO is taking reference from a low phase noise signal source (Agilent make), later on the reference phase will be taken from MO of the Pelletron-Linac accelerator. The MO distribution system has been in use at HCI for nearly 3 months.

2.2 DEVELOPMENT OF A COMPACT FREE ELECTRON LASER

S. Ghosh[1], B. K. Sahu[1], P. Patra[1], S. R. Abhilash[1], J. Karmakar[1], B. Karmakar[1], D. Kabiraj[1], S. Tripathi[1], N. Kumar[1], A. Sharma[1], V. Joshi[1], G. K. Chaudhari[1], A. Pandey[1], S. Kumar[1], G. O. Rodrigues[1], J. Urakawa[2], A. Aryshev[2], V. Naik[3], T. Rao[4], R. K. Bhandari[1] and D. Kanjilal[1]

[1]Inter University Accelerator Centre (IUAC), Aruna Asaf Ali Marg, New Delhi, India
[2]High Energy Accelerator Research Organization, KEK, Tsukuba, Japan
[3]Variable Energy Cyclotron Center, Kolkata, India
[4]Brookhaven National Laboratory, USA

Introduction

Typically, in Free Electron laser (FEL), the microbunching of the electron takes place inside the undulator and spacing between the microbunches is equal to the radiation wavelength produced by the electron. In the Phase-I of the Delhi Light Source (DLS) project at IUAC [1], the microbunching will take place at the Photocathode [2,3], the location of the initial production of the electrons. Then the electron micro-bunches will be accelerated by the cavity acting as the electron gun and will be injected in to the compact undulator magnet to produce the THz radiation in the range of 0.18 to 3.0 THz. The electron beam and the THz radiation can be transported to several experimental stations to perform fundamental as well as applied research experiments in the various

interdisciplinary fields. The complete accelerator facility including the laser hut, photocathode deposition system and all the experimental stations are being accommodated inside the newly built class 10000 clean room at the basement of beam hall-3.

Development of various subsystems of phase-I of DLS

The developments in the major areas of the Phase - I are listed in the following sections:

2.2.1 Simulation of Beam Optics and THz radiation

The beam optics simulation of the Phase-I of DLS is performed with the code named as General Particle Tracer (GPT) [4]. The simulation of the Terahertz production from the electron microbunches passing through the undulator is being done with a code developed in-house.

In the beam optics simulation, electron microbunches with a number of 2, 4, 8 or 16 are produced at the photocathode and are immediately accelerated under the influence of strong accelerating fields of the electron gun. The issue of space charge effect and the merging of the electron beams among the neighbouring microbunches are controlled by optimising the various parameters e.g. (a) charge per microbunch, (b) the spot size and the temporal width of the laser pulse and (c) the magnetic field of the solenoid and the quadrupole magnet. The effort is dedicated to maximise the bunching factor of the electron macro-bunch inside the undulator. The important beam parameters of the optics calculation are shown in Table-1.

The radiation simulation from the wiggling motion of the electron microbunches is being done by using the Lienerd-Wichert Potential. First, the particle phase space at the entrance of the undulator in terms of x,y,z,p_x,p_y,p_z and t are created by using the output of GPT. Then by using Vay's particle pusher algorithm, the evolution of the phase space is found out for every small interval of distances and stored inside an array. The radiation is measured at a time 't' outside the undulator, so the retarded time co-ordinate of the electron responsible to produce the radiation will be (t-R/c) where R is the co-ordinate of the radiation measurement point from the location of the electron and c is the velocity of light. At this retarded time, the position, velocity and acceleration of the electrons at every space interval along the length of the Undulator are calculated and stored. By using these values, the electric and magnetic fields of the radiation are calculated. The total photon energy from a single 16 microbunch train for 3 THz has been calculated as ~12 μJ on a square area of 30 mm × 30 mm at a distance of 0.5 metre from the exit of undulator.

The attenuation of the THz radiation while propagating through the narrow beam pipe inside undulator is also being calculated by HFSS code. It is observed that there will be some amount of attenuation of the THz radiation while propagating through the beam pipe inside undulator.

2.2.2 Electron Gun and RF System

A 2.6 cell S-band copper cavity [1] to be used as the electron gun has already been fabricated in collaboration with KEK, Japan, tested with low power RF, and is waiting to be installed in the beam line of DLS. The resonance frequency of the cavity is 2860 MHz and the measured Q-value is ~ 15200 with low power RF. A few copper photocathode plugs are also made ready to produce the first beam from the electron gun. The RF system to power the electron gun consists of a low level RF system and high power RF system consisting of a Klystron and Modulator which have been ordered and will be delivered in the autumn of 2018. The specification of the Klystron/Modulator is shown in Table 2.

2.2.3 The photocathode deposition system

Though the initial plan to produce the electron beam with the help of copper plugs will be executed first, but substantial effort has already been dedicated to develop the deposition system to produce the semiconductor photocathodes. The design of the complete deposition process has been finalised and the system is being developed in collaboration with BNL, USA. The movements of the photocathode plugs from one chamber to the other will be performed under ultra-high vacuum with the help of multiple vacuum manipulators while maintaining the vacuum in the range of ~ 10^{-11} mbar.

Table 1: Typical beam optics parameter

Radiation frequency range (THz)	0.18	3
Accelerating field (MV/m)	59	112
Launching phase (deg)	41	30
Electron Energy (MeV)	4.0	8.2
Energy spread (%)	1.1	0.68
e-beam FWHM @ cathode (fs)	200	200
Total charge (pC)/microbunch	15	15
Number of microbunches	2	16
Av. microbunch separation at undulator's entrance (ps)	6.6	0.345
Peak Current (A) at und. entrance	20	75
$\sigma_{x,y}$ (mm) at undulator's entrance	1.75, 0.25	0.7, 0.35
Normalised emittance (x, y) π mm-mrad at undulator's entrance	3.0, 4.2,	3.2 4.8

Table 2: Main Parameters for klystron & modulator

	Parameter – RF system	Value
1	Peak output power	≥ 25 MW
2	Average output power	≥ 5 kW
3	Operating frequency	2860 MHz
4	Bandwidth (-1 dB)	± 1MHz
5	RF pulse duration	0.2 μs to 4 μs
6	Pulse repetition rate	1-50 Hz
7	Pulse top flatness	±0.3%
8	Rate of rise and fall of modulator output voltage	200-250 kV/μs
9	Long term stability	±0.05 %

2.2.4 The fiber laser system for DLS

The oscillator frequency of the laser system is chosen to be 130 MHz, however, the repetition rate of the pulses has been reduced to 5 MHz by pulse picker. The laser pulses arriving at 5 MHz is gated with the nominal duration of RF pulse period of ~ 3 μsec width which repeats at 6.25 Hz. So within an RF period, a total number of 15 laser pulses will be accommodated. Then each laser pulses can be divided in to 2,4,8 or 16 micro-pulses with an calculated energy of 0.9, 0.4, 0.19 and 0.1 μJ which will produce an estimated charge of 1.8, 0.8, 0.38, 0.2 pC and 900,400,190 and 100 pC from copper and Cs_2Te photocathode respectively. For 16 micro-pulse train within a RF period, there will be 15 × 16 × 6.25 = 1500 pulses and hence same number of electron microbunches will be produced at the photocathode.

2.2.5 The Undulator

The design of the compact hybrid undulator magnet has been finalised with the pole made by Vanadium-Permendur. With the code RADIA [5] the parameters of the undulator have been determined to produce the radiation between 0.18 to 3.0 THz and they are: (a) Undulator period - 50 mm (b) length of the undulator - 1.5 meter (c) configuration of the end field termination: 1 : ¾ : ¼ with 28 full periods and 2 magnets plus 2 poles on each side and (d) the range of opening gap are 20-45 mm with corresponding magnetic field of 0.61 and 0.11 respectively.

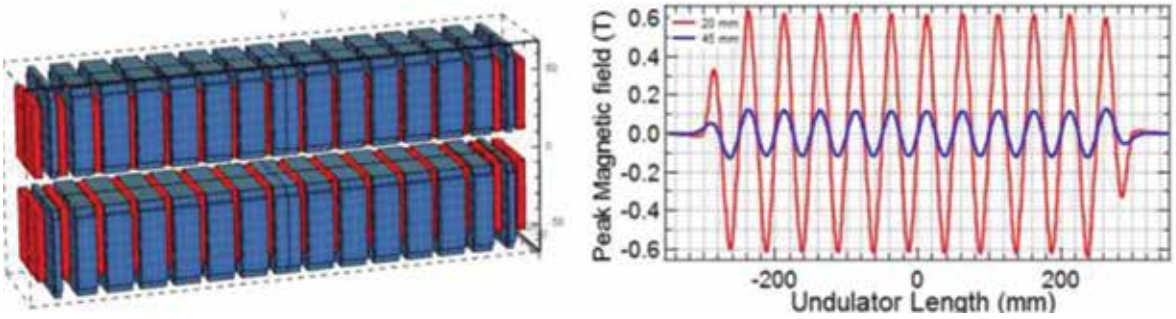

Figure 2.2.1: Undulator with 5 full periods and magnetic fields at 20 and 45 mm gap

2.2.6 The beam line design of the Phase-I of DLS

The beam line design is presently going on and the location of the various components from the RF cavity upto the undulator magnet is shown in figure 2.2.2. The solenoid magnet was designed, fabricated and tested at the factory and is placed in the beam line waiting to be aligned with the other beam line components. The design of the achromatic/non-achromatic bends with dipole and quadrupole magnets are in the final stage and soon their development / procurement process will be started. It has been decided to use strip line BPM in the beam line and three of them are being purchased. The beam view screen is being developed at IUAC and the parameter finalisation for the Integrated Current Transformer is currently going on. Effort is on to finalise the design for the laser reflector device, beam line support structure, various pumping stations, gate valves etc. It is expected that the commissioning of the beam line along with the electron gun and the solenoid magnet will be started in next few months.

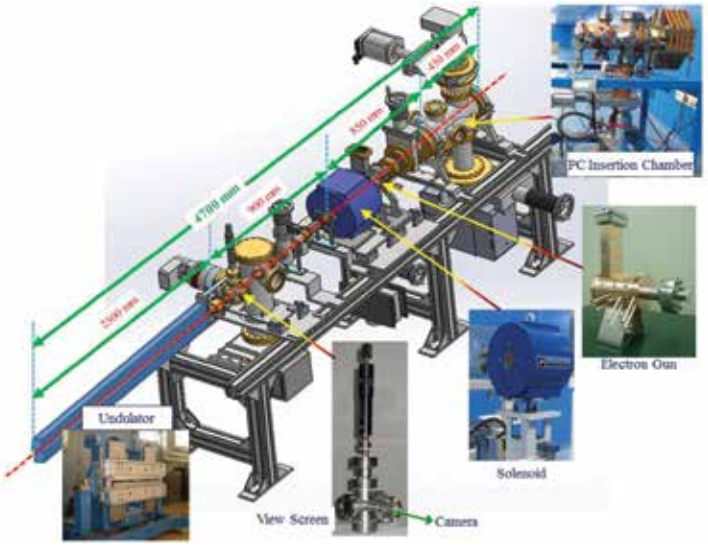

Figure 2.2.2: The proposed schematic of the beam line of the DLS

2.2.7 Beam transport after the undulator

Besides the coherent radiation being used for some dedicated experiments in the 'radiation' beamline, another dedicated experimental beamline is being set-up to utilise the electron beam exiting from the undulator. For this purpose, the electron beam needs to be diverted to the experimental station using a combination of bending magnets and quadrupoles. A tentative layout is being worked out which can have provision of measuring the energy of the electron beam and related diagnostics which will facilitate the users to perform their experiments. In-situ experiments utilising both the electron beam and the coherent radiation at the same time is also being facilitated.

Conclusion

A facility to produce low emittance electron beam and coherent THz radiation is at the commissioning stage at IUAC, New Delhi. The electron gun consisting of the copper cavity, the copper photocathode and the solenoid magnet are ready to be installed in the beam line. The high power RF system to energise the cavity will be delivered in the autumn of 2018. The necessary fiber laser system to produce the electron beam from the copper photocathode is being designed, assembled and tested. The design of the photocathode deposition system is ready and the fabrication has been started soon in collaboration with BNL, USA. The design of the undulator is finished and the procurement/development process will be started soon. The various beam line components like bending magnets for achromatic bends, quadrupole magnet, beam position monitor, Integrated Current Transformer (ICT), beam viewer, etc. are being designed, developed or procured. The class 10000 clean room (28 m × 8 m) to accommodate the complete facility is ready. It is expected that the first demonstration of the production of the electron beam and the THz radiation can be achieved by 2019.

REFERENCES

[1] S. Ghosh et al. NIMB vol. 402, p. 358-363, 2017.
[2] S. Liu and J. Urakawa, in Proc. 33th Int. Free-Electron Laser Conf. (FEL'11), China, 2011, pp. 92-95.
[3] M. Boscolo et al., NIMA vol. 577, p. 409-416, 2007. [4] General Particle Tracker,http://www.pulsar.nl/gpt/index.html
[4] General Particle Tracker,http://www.pulsar.nl/gpt/index.html
[5] RADIA, Online. Available: http://www.esrf.eu/ Accelerators/groups/Insertion Devices/Software/Radia .

2.3 2.45 GHZ MICROWAVE ION SOURCE FACILITY AND DEVELOPMENTS

G. Rodrigues, Y. Mathur, Narender Kumar, R. Ahuja, U. K. Rao, R. Ruby Shanthi, V.V.V Satyanarayana, R. N. Dutt & D. Kanjilal

A 2.45 GHz microwave ion source based high flux system is operational since the year 2017. The facility is frequently used for carrying out experiments in the field of Materials Science and Plasma Physics. In year 2017-2018, plasma characterization with the help of X-ray measurements using NaI(Tl) detector was carried out for oxygen plasma. The results have shown that X-rays in the energy range of 10 keV to 50 keV are being produced using RF power up to 100 W. This energy signature directly relates to the electron energy distribution function (EEDF) inside the plasma and is unusually high in this kind of ion sources. In these kind of over dense plasmas, the electron Bernstein wave heating phenomena is a possible explanation. In figure 2.3.1, a few of the x-ray measurement results obtained from the experiment have been shown for various source parameters.

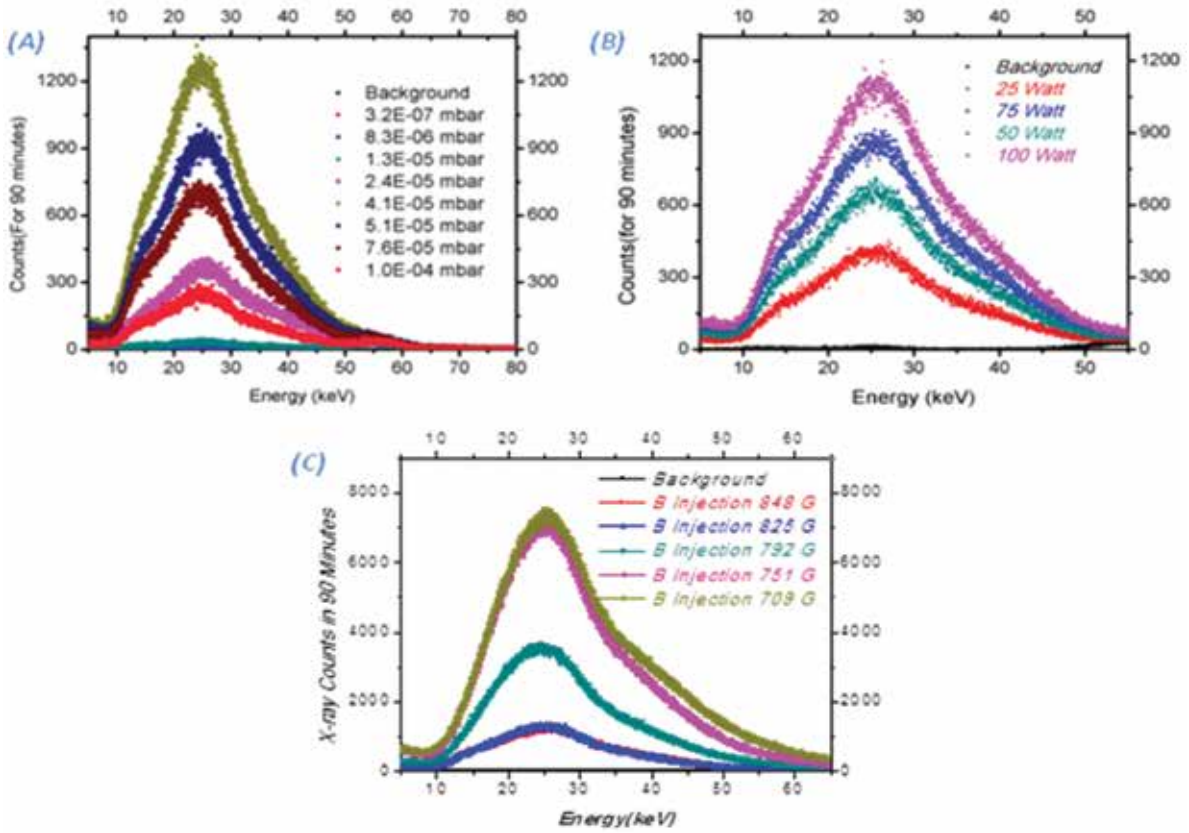

Figure 2.3.1: X-ray measurement results for (A) pressure variation, (B) microwave power variation and (C) injection magnetic field (at the location of RF window) variation.

Along with the x-ray measurements, simulation studies were performed using CST Microwave Studio to calculate the EEDF for various plasma conditions. The CST simulations were performed for various ion source parameters i.e. microwave power coupled to plasma chamber, injection magnetic field at RF launching position and for variation in time period of simulation. The simulations were carried under the assumptions that the electron-electron collisions are negligible for such short periods of time. In figure 2.3.2, one of the results obtained for the field distributions and particle distribution has been shown for an RF power of 741.7 W, injection magnetic field of 914.94 G and 18 ns time period for simulation.

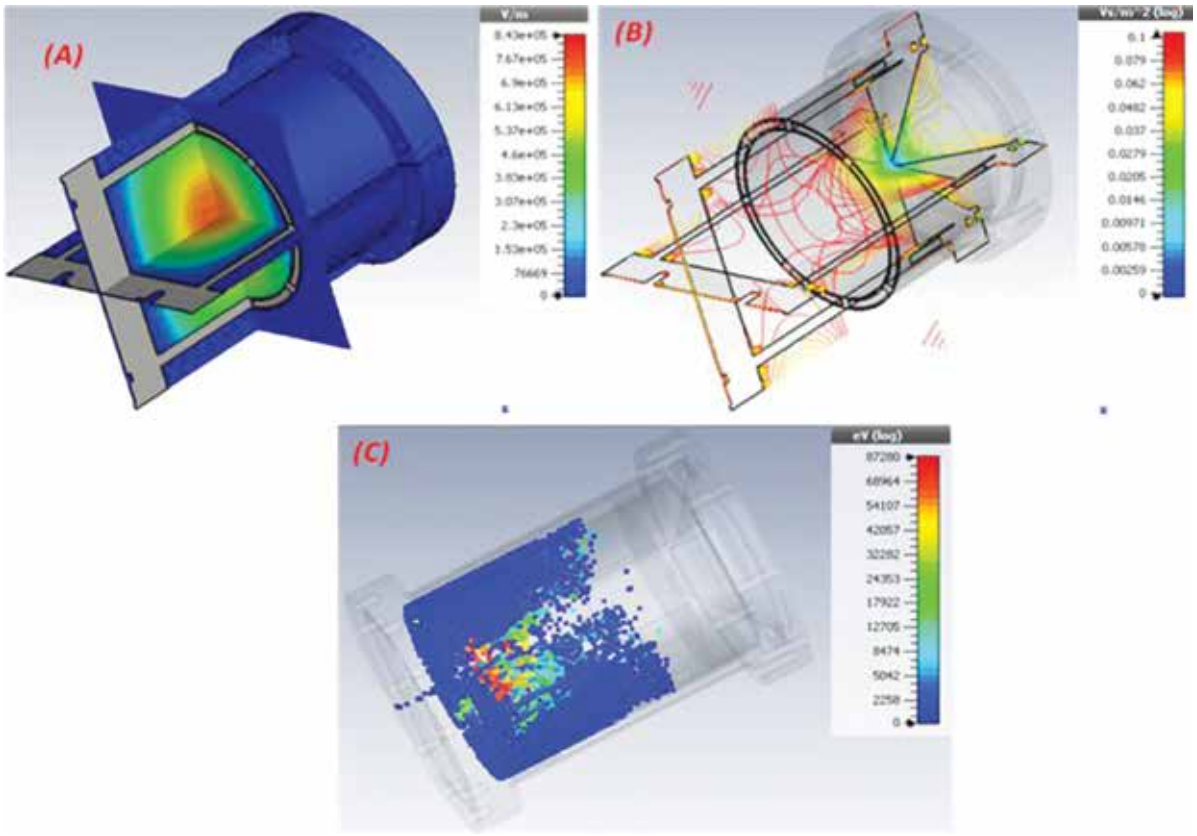

Figure 2.3.2: CST microwave studio model for (A) electric field distribution inside the plasma chamber, (B) magnetic field distribution and (C) particle distribution along with energy scale.

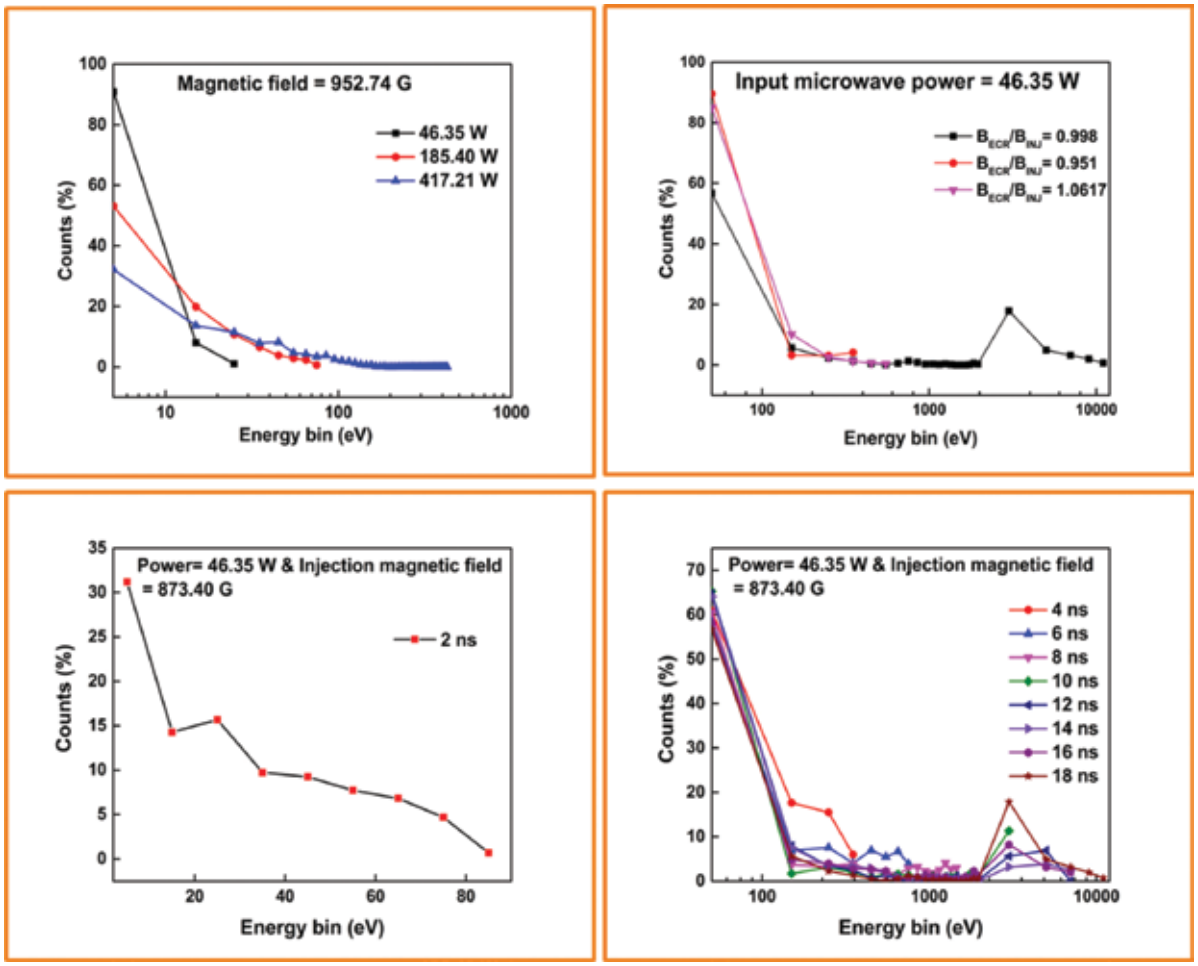

Figure 2.3.3: CST Microwave Studio results using 'Particle-in-Cell' solver for calculating the electron energy distribution function (EEDF) under various plasma conditions.

The results of the particle distribution also consist of the energy information of the particles (energy gain due to interaction with the fields). The results obtained for variation in electron energy distribution for various microwave power levels, various injection magnetic fields and various simulation time periods from the simulations are shown in figure 2.3.3.

Related diagnostics are being developed for measuring the signatures of the electron Bernstein wave heating phenomena. Additionally, a Langmuir probe based I-V characterization experiment has been planned to study the low energy distribution of the electrons and ions inside the plasma. The Langmuir probe has been tested for vacuum operation and for adjusted movement inside the plasma chamber without disturbing the vacuum. The electronic circuit for the Langmuir probe is under fabrication and is presently undergoing tests.

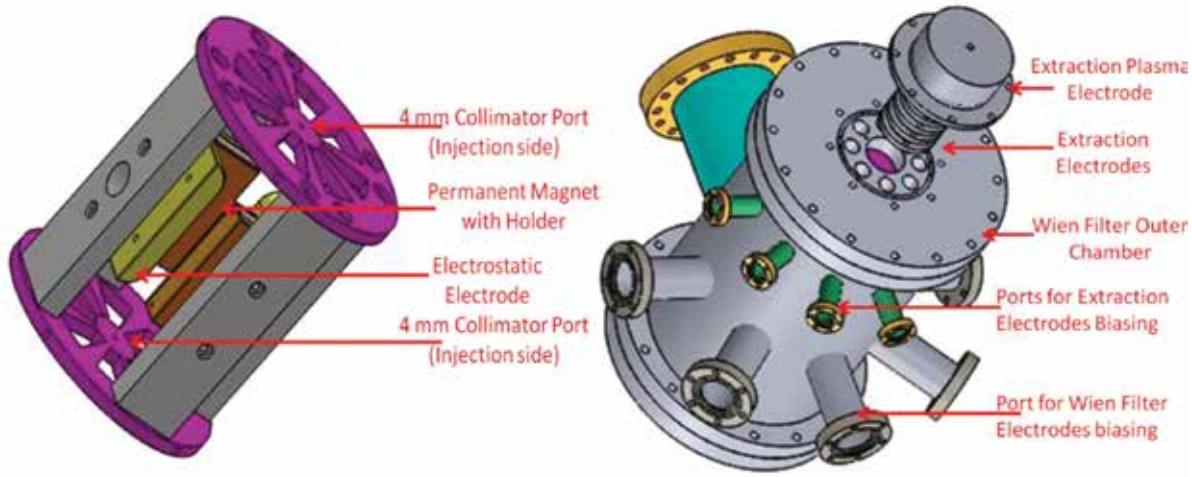

Figure 2.3.4: Mechanical design of the compact Wien Filter: (Left) Inside assembly of Wien Filter and (Right) Outer jacket of Wien filter coupled with pumping system and the extraction system.

Towards the end of the last year, Wien filter was planned to be introduced as a velocity filter for various beams. The mechanical design has been frozen and will be fabricated and coupled to the facility near future. The order for power supplies required for generating E field and permanent magnets for generating B field has been placed. The mechanical assembly of Wien filter and its outer jacket are shown in figure 2.3.4.

REFERENCES

[1] Narender Kumar, G. Rodrigues, S. Kumar, Y. Mathur, U.K. Rao, R. Ahuja and D. Kanjilal, "A Compact 2.45 GHz Microwave Ion Source and Associated Wien Filter based Analyzing System for Low Energy Ion Beam Facility", ID-80, InPAC 2018, RRCAT, Indore.

[2] R. N. Dutt, Y. Mathur, N. Kumar, U. K. Rao, G. Rodrigues and D. Kanjilal, "Control System for 2.45 GHz ECR Source based Intense Ion Beam Facility at IUAC, New Delhi", ID-103, InPAC 2018, RRCAT, Indore.

3. RESEARCH SUPPORT FACILITIES

3.1 SUPPORT LABORATORIES

3.1.1 High vacuum laboratory

Chandra Pal, A. Kothari, P. Barua, S. Chopra

High vacuum laboratory is primarily responsible for maintaining high vacuum and the vacuum systems in beamlines and experimental facilities. It provides support to different labs and users in vacuum related problems. Vacuum lab is also involved in the installation and commissioning of various beamlines, experimental and accelerator facilities at IUAC. High Current Injector [HCI] installation is in progress and installation of Energy measurement set up for RFQ accelerated beam has been completed. All the beamline devices in this experimental set up have been interfaced with VME control system and can be controlled through remote control console.

3.1.1.1 Installation of Energy Measurement set up for RFQ accelerated beam in High Current Injector

Chandra Pal, Ashok Kothari, P. Barua, DK Munda, Kundan Singh, Prem Kumar Verma, Mukesh Kumar and S K Suman

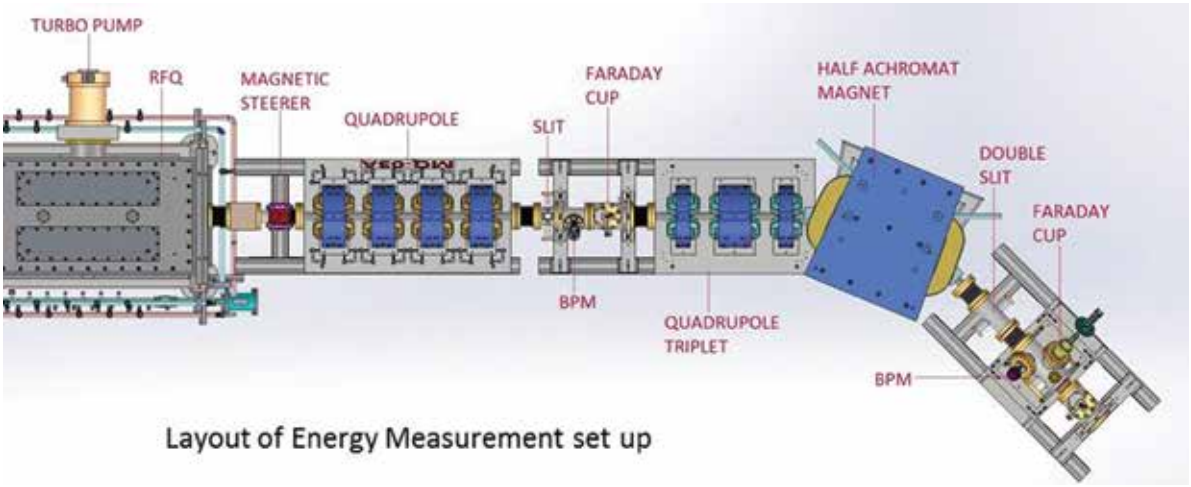

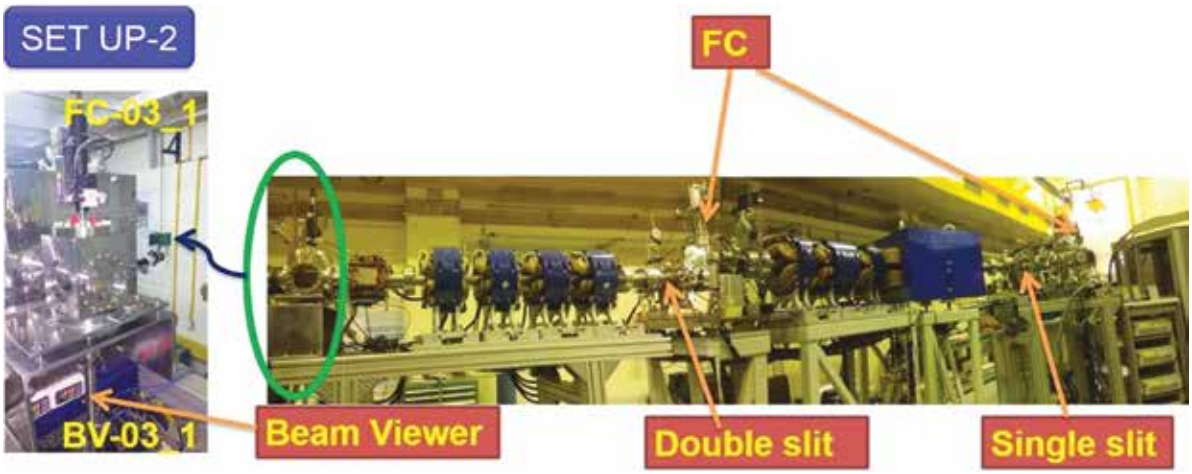

Fig. 3.1.1: Energy Measurement Set up for RFQ Accelerated beam in HCI

To measure the energy of RFQ accelerated beam an energy measurement setup was installed in the HCI beamline. The setup consists of a half achromat magnet with beam diagnostics installed before and after the magnet. A compact cuboid chamber with faraday cup, beam viewer and a turbo pump is installed at RFQ exit. Beam defining slits are also installed before and after the magnet. A compact diagnostics vacuum chamber was designed for mounting BPM, Faraday cup and Turbo pump with alignment fixtures. It was installed at the exit

of the magnet for beam diagnosis. Two turbo based pumping stations with necessary interlocks are also installed and about $5x10^{-8}$ mbar of ultimate vacuum was achieved.

All the beamline devices were interfaced through VME control crate for remote operation of devices. A control circuit for beam viewer and faraday cup assembly was designed and implemented for proper operation with necessary safety interlocks. The layout and the installed energy measurement set up are shown in figure 3.1.1.

3.1.1.2 Development, fabrication and installation of beam line device controllers and instrument crates

Chandra Pal, P. Barua

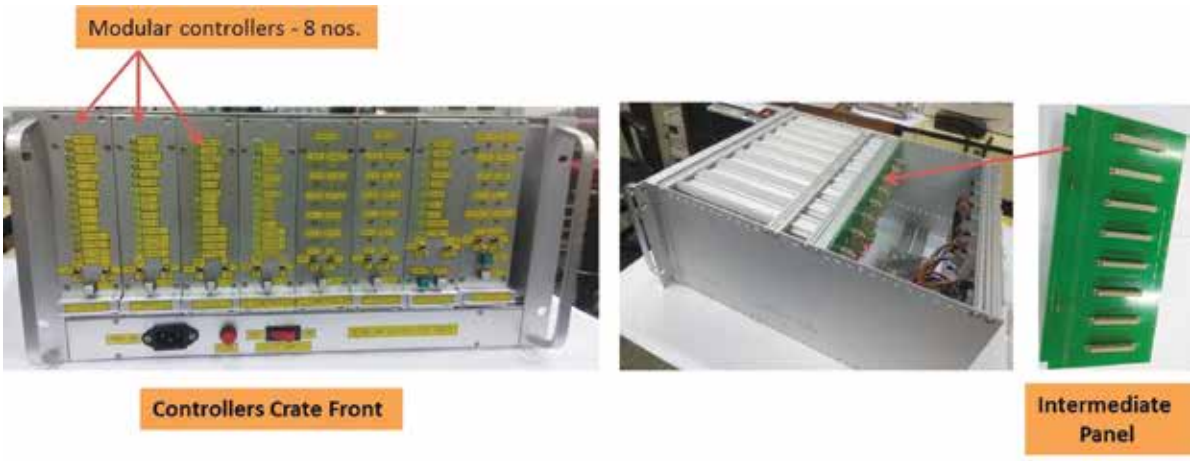

Fig. 3.1.2: Controllers crate for Beamline devices

Modular controllers for faraday cup and beam line valves: This year we fabricated 6 nos. of faraday cup modular controllers and 3 nos. of BLV modular controllers. These modular controllers are mounted in the controllers' crate, from where the signal is distributed bidirectionaly.

Controllers crate fabrication: A new controller crate for controlling beamline devices was fabricated. It can house eight modular controllers for faraday cup and beamline valves. An intermediate panel was also fabricated which is responsible for bidirectional signal distribution, as shown in figure Fig. 3.1.2.

3.1.1.3 Modification in the Position of HCI ion source (PKDELIS) on the high voltage deck

Chandra Pal, A. Kothari, P. Barua , Y. Mathur, P.S. Lakshmi, U.K. Rao and G.O. Rodrigues

Beam tests were done with the PKDELIS source in the HCI high voltage deck. Analyzed beam current measured with beam diagnostics were about 5 μA. To increase the beam current from the source it was moved towards the magnet and its distance has changed from 1282 mm to 782 mm from the magnet entry flange. The extraction system has also been replaced by old einzel lens and GP tube.

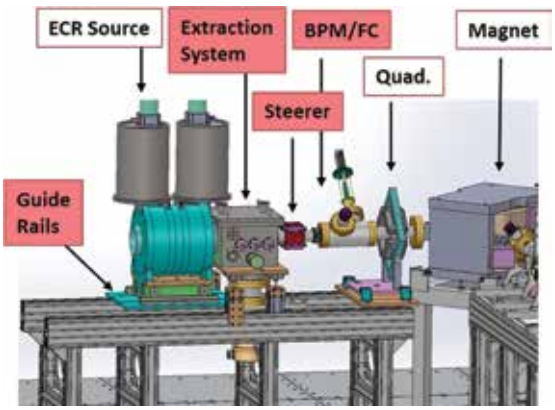

Fig. 3.1.3: ECR Source Old Position

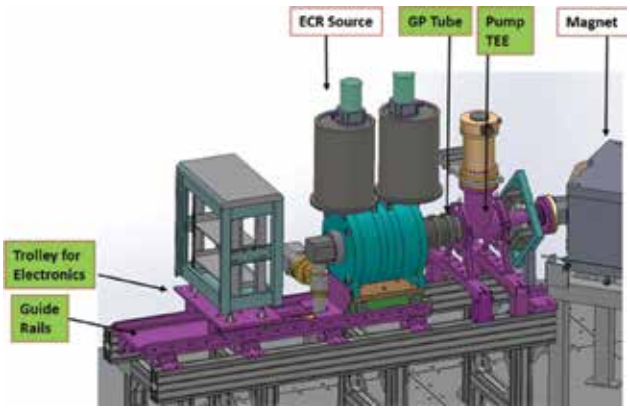

Fig. 3.1.4: ECR Source New Position

The turbo pump now is mounted on the new fabricated vacuum chamber customized as per modified layout. A new guide rail mechanism (1.62 m long and compatible with the source) was designed and fabricated for the installation of the source. A trolley for mounting electronics (for source bias) on the guide rail was also designed as shown in figure 3.1.4. The source was realigned (within 0.5 mm) with existing references available on the magnet. All the electronics for remote control and read back were also completed. The layout of the source and other components before and after modification are shown in the figure 3 and figure 4. Beam current intensity for different beams has improved significantly after the modification and further tests are going on.

3.1.1.4 Design, Fabrication and Installation of a Diagnostic chamber in NAND beamline

A new diagnostic chamber was designed, fabricated and installed in the NAND beamline area. Tap holes for mounting a pair of detectors were provided for installation of detectors at 20 degrees on either side of beam axis. A target ladder (with oblique face for beam viewer quartz) was also designed and fabricated. The existing NAND beamline was modified to install diagnostic chamber in place. A turbo pumping system with necessary interlocks was also installed and ultimate vacuum of $5x10^{-8}$ mbar was achieved.

3.1.1.5 Maintenance Activities

- Beam sweeper installed in the vault area was no longer in use so it was removed and a drift tube was installed in its place.
- BLV-04 (beam line valve in the vault area) developed a leak in the bellow. It was NEC make valve (30 years old) and was removed. It was replaced with a new all metal Vat valve (20,000 cycles).
- NEC make single slit installed in the vault area was no more required therefore it was also removed from the beamline.
- Annealing Vacuum system was not operational. Its gauge controller was very old and it had gone bad so a new gauge controller was placed and interfaced with existing system.
- Maxi gauge controller repairing: Many maxi gauge controllers had stopped working and after testing it was found that their power supply had gone bad. The spare power supply was very costly so we got the required power supply developed from a local vendor and have repaired five gauge controllers with this. It helped us save money and time. One of the controllers had bad display panel, so we changed the same with available spares and made it functional.

3.1.2 Cryogenics & Applied Superconductivity Laboratory

T S Datta, Anup Choudhury, Joby Antony, Suresh Babu, Manoj Kumar, Soumen Kar and Santosh Kumar Sahoo

In this period, cryogenic system was operated at a stretch for more than six months to have successful long Linac run. There is no major failure from Helium refrigerator, except the UPS malfunctioning during Linac operation. Efforts are on to reduce the static and dynamic heat load at 4. 2 K from beam line cryomodule and the liquid helium distribution network. Cryo- facility is also upgraded with two additional helium gas storage tanks of capacity 60 NM^3 each. The liquid Nitrogen storage capacity is upgraded from 20000 L to 40000 L. The Cryogenic Data Acquisition & Control System (CRYO- DACS) and the Complete Automation for Distribution System (CADS) performed well during Linac run. To have better redundancy, upgradation of CADS is planned in the coming year. About externally funded project, there is a significant progress on MRI project funded by Ministry of Electronics and information Technology (MeitY) through the nodal agency; SAMEER, Mumbai. Six numbers of technical design reports on Magnet Design, Bobbin Structure, Vacuum Impregnation System, Cryostat, External Interference Screen Coil, and Quench Protection System was prepared and submitted to SAMEER/ MeitY for necessary review and validation by experts. Superconducting joint techniques have been developed for the MRI magnet after a series of extensive characterization and testing at 4.2K. So far, the lowest value of joint resistance achieved is $7x10^{-13}$. A large number of cold tests have been performed on quench protection diodes, superconducting switch and detachable current lead. Regarding the project on modular Superconducting Fault Current Limiter (SFCL) funded by Central Power Research Institute, Bangalore, the indigenously developed fault current generator was integrated with main AC power supply and trial runs have been performed successfully.

3.1.2.1 Cryogenics Facility

(1) He plant Operation and Cooling of LINAC

The helium machine was operated for total time of 4700 hrs (6.5 months) this year. The most part of the run was done to keep the LINAC cavities cold for accelerating the beam. This was the longest run (5.5 months)

for carrying out LINAC experiments with beam at IUAC. Apart from the online experiments some stand alone experiments were carried out in test cryostat for the cavity characterization with quarter wave resonator after nitrogen doping and liquid helium was also used for cold test of MRI components testing and LHe level sensor development.

Two important issues need mention for the long haul LINAC run. (i) In this LINAC run average compressor discharge pressure was ~9.8 barg as compared to 10.8 barg for the 2015 LINAC run case as shown in Fig. 3.1.5. The reduction in operating pressure was a result of effort put on plucking the lossy areas of LINAC and distribution line. In the distribution line repair of the leaky pumpout ports led to improvement of the vacuum by an order from $6.4x10^{-6}$ mbar to $8x\ 10^{-7}$ mbar. On the cryostat we have tried to improve the LN_2 shield cover of the cryostat on the top side by putting additional copper sheet attached to the existing cover. Also a number of holes on the top radiation shield were covered with aluminum tapes to stop direct radiation from 300K reaching the 4.2K surface. Total additional area covered for each cryostat was around 1.1 M^3. This was done in two cryostats L2 and L3. Average cumulative power saved by these techniques was ~80 W@4.5 K which is almost 20% less than the previous run. The shield area enhancement in the remaining cryostats shall be taken up in phased manner in the coming months to improve the efficiency further. (ii) A total of 20 hrs of beam time was lost due to cryogenic failure. The small failures were due to malfunctioning of the chilled water pump supporting the turbines, problems related to indigenous level meters for LINAC and Rebuncher cryostats. The worst failure was encountered due to shut down of complete UPS power (UPS failure) which resulted in stoppage of the compressor and cold box when the full LINAC was running. All the safety precautions worked well during this crisis period. All the cryostat check valves and safety relief valves opened immediately and did not allow the pressure to go up above 7 psi (maximum pressure), and the system was restored to complete normalcy within an hour of the failure as shown in Fig. 3.1.6. During this failure a total of 140M^3 helium gas was lost to atmosphere. To avoid these big failures in future a number of steps have been initiated to improve on the services of the utilities like power water and compressed air.

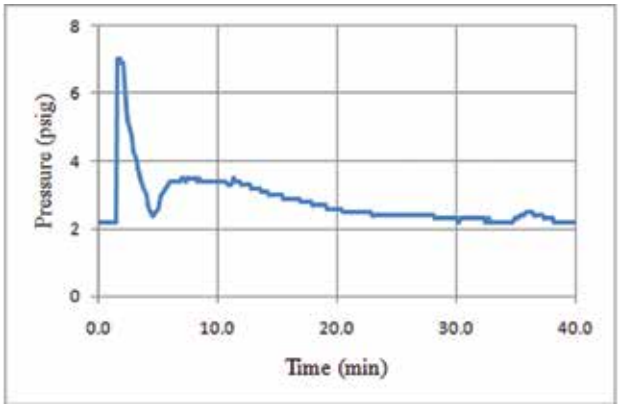

Fig. 3.1.5: Pressure rise during UPS power failure in L-1 cryostat

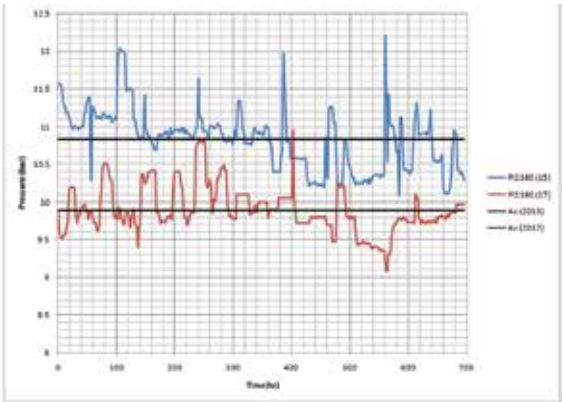

Fig. 3.1.6: Long term discharge pressure of LHe machine and its comparison for the present run vs last run

(2) Capacity upgradation of cryogenic infrastructure

With this year successful long LINAC run of 5.5 months it has been decided to make all the future LINAC runs by clubbing all experiments together. Also High Current Injector (HCI) is making rapid progress which will directly feed beams to LINAC. To cater to both these reasons we will require high uptime for cryogenics and its infrastructure. The process of upgradation for existing cryogenic infrastructure has been initiated and some are completed.

(i) **New LN_2 tank:** A 20000 lts LN_2 tank (Fig. 3.1.7) has been added to the existing LN_2 facility. This addition capacity takes the cumulative external capacity to 40000 lts. The tank has been installed and commissioned at site. The measured evaporation rate from this tank is 65 lpd (liters liquid per day). The addition of this tank will help us to mitigate the external LN_2 supply risk better and we have 15 days of buffer stock during full fledged LINAC run.

(ii) **New He gas tank:** Two numbers of 60M^3 capacity (each) helium gas tanks (Fig. 3.1.8) have been commissioned and they have also been connected to the existing helium gas tank network with pipe lines. With this addition the total helium gas holding capacity of IUAC has risen to 260M^3 and the system can hold ~3000M^3 gas at one time, which shall ensure that in case of a catastrophic failure during LINAC run we can get back to action in a short time. Both these tanks have been commissioned after getting

it evacuated to lower vacuum and then injecting with helium gas and subsequently purifying it with existing helium system.

(iii) **LN_2 transfer line:** During the previous LINAC runs when there used to have shortfall of liquid nitrogen supply from the inside plant, the supply was diverted from outside tank for smooth transition. But the supply from the outside line could not be sustained for a long time as the quality of liquid coming from that direction was very poor due to lossy line. To circumvent this problem an in house LN_2 phase separator was put in line before connecting it to the existing distribution system. With this addition the long standing problem of non delivery of liquid to the cryostat disappeared. When the gas outgo from the vapour line of the phase separator was measured it was found to be $18M^3$/hr which is equivalent to 22.5 liter per hour of liquid evaporation. The equivalent heat load in that line is 1 kW and it is 10 times higher than the evaporation rate for the standard industrial line. An effort is underway to understand the area a lossy line and take suitable corrective action.

Fig. 3.1.7: 20000 lts LN_2 tank
Total ext. capacity = 40000 lts

Fig. 3.1.8: 2x60 M^3 new helium gas tanks

(3) Other developmental activities

Anup Choudhury, Santosh Kumar Sahoo, Suresh Babu and Manoj Kumar

A few product developmental activities related to cryogenics lab were also undertaken during this year and they are:

(i) **LHe level sensor development:**

Last year a LHe level sensor was made with local superconducting wire sourced from a multi-filamentary strand of one of the magnet programs and the sensor was installed in test cryostat. The sensor was characterized with a standard Cryomagnetic make level sensor of similar length which showed linear response against the level. (i) We collected different types of wire samples including that of standard wire manufacturer of level sensors and did a characterization study of RT in a separate setup. (ii) A study setup with a 100lts helium dewar was made to conduct sample tests against standard AMI sensor with its electronics. From this characterization it was found that VECC wire had cold resistance same as that of AMI sensor wire. A 30 cm long sensor was made from VECC wire and the sensor behaved exactly

similar to a AMI sensor in cold condition (iii) The sensor was subjected to a long haul test of 2 months in LINAC-1 cryostat with the existing controller setup. Its feedback was used to control the LHe inlet valve of the cryostat. The sensor performed flawlessly in the actual setup for long run. (iv) A new sensor activation technique was found to measure the level with much lower activation compared to the conventional sensor.

Fig. 3.1.9: A few of the LHe level sensors made at IUAC, some of which have replaced the existing AMI level sensors which were damaged during handling.

(ii) ppm level moisture sensor for helium gas:

A trace level moisture detection cell (which looks at ppm level of moisture in helium gas and works on the principle of plasma spectroscopy) has been successfully tested with calibrated gases. The technique is similar to existing technology of nitrogen impurity detection which we developed 10 years back and is in use with LINDE helium plant. In the present trial run a liner signal from the detector in the range of 0-100 ppm with calibrated moisture laden helium gas was obtained. With this development it is planned to make a new setup where both nitrogen and moisture can be detected simultaneously from the same arc source which shall do away with different instruments currently used for the purpose. This process of impurity detection is a very fast technique and requires very small sample flow unlike the present method using capacitance.

3.1.2.2 Activities on Applied Superconductivity

A. Development of a whole body 1.5T Superconducting MRI magnet system

Soumen Kar, Sankar Ram Theketthil, Navneet Suman, Vijay Soni, Mukesh Kumar, Rajesh Kumar, Joby Antony, S. K Saini, R.G. Sharma and T.S. Datta

Ministry of Electronics and Information Technology (MeitY), Govt. of India has initiated a multi-institutional project to develop a 1.5T superconducting MRI scanner in India. SAMEER, Mumbai is the nodal agency of the project. IUAC is one of the partner institutes for the project on indigenous development of the 1.5T superconducting MRI scanner. IUAC-MRI team is primarily responsible for the development of 1.5T superconducting magnet and ever-cooled or zero-boil off (ZBO) cryostat for the MRI scanner.

Bobbin is one of the most critical components of the MRI magnet to provide the structural integrity of the system. The mechanical design of the bobbin has been frozen after optimization of weight considering its degree of stresses and deformation during operation of the magnet. Figure 3.1.2.10a shows the final configuration of the bobbin for the multi-coil magnet structure. Bobbin mechanics greatly influence the performance of the magnet. An extensive finite element analysis (FEA) simulation has been done on the bobbin and the superconducting coil to analyse the stresses (axial, radial and hoop) and the corresponding deformation due to winding, thermal cool-down and Lorentz forces.

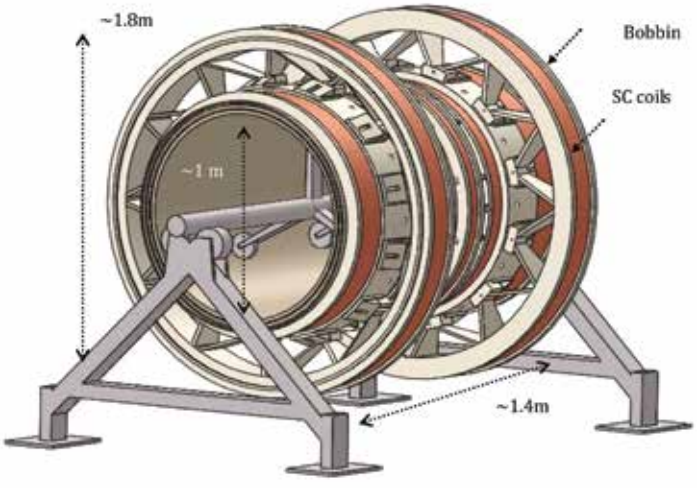

a

Figure 3.1.10a Integrated bobbin structure for 1.5T MRI magnet.

Figure 3.1.2.10(b) shows the hoop stress in the bobbin and the coils due to thermal contraction and the Figure 3.1.2.10(c) shows the overall deformation due to the thermal contraction of the bobbin and the coil during its cool-down from 300K to 4.2K.

In MRI scanner, It is also essential to have an extremely stable field which is better than 0.1ppm/hr. The gyromagnetic frequency of the hydrogen ions or the protons are proportional to the magnetic field. At 1.5T magnetic field, the gyromagnetic frequency of the hydrogen ions is 63.87 MHz. Any change in the magnetic field will lead to a change in the resonance frequency of the ions. The variation in resonance frequency has to be less than 6 Hz/hr for a 1.5T magnet of the MRI scanner. Any external magnetic disturbances may lead a change in the central magnetic field (B_0) and its homogeneity (±5ppm) in the Field of View (FOV) region of 45cm. An activley shielded magnet is relatively insensitive to the external disturbances because of its very weak coupling with any external interference. Hence the imaging volume is not perfectyly shielded against the external magnetic interference in the actively shielded MRI magnet. To achieve shielding effect against any external magnetic interference, a set of shorted superconducting coils known as 'External Interference Shielding or Screen' coil or 'EIS" coil are symmetrically positioned radially from the axis and with respect to the mid plane. It is self-activated and work passivley in the system. The spatial homogeneity of the MRI magnet needs to be preserved or even improved by the EIS coil. A set of self-shielding screening coil has been designed with a screening factor of 3.3% and mutual coupling factor of 0.265. Figure 3.1.2.10 (d) & (e) shows how the overall homogeneity is improved in the FOV region due to induction of 1 A current in the EIS coil.

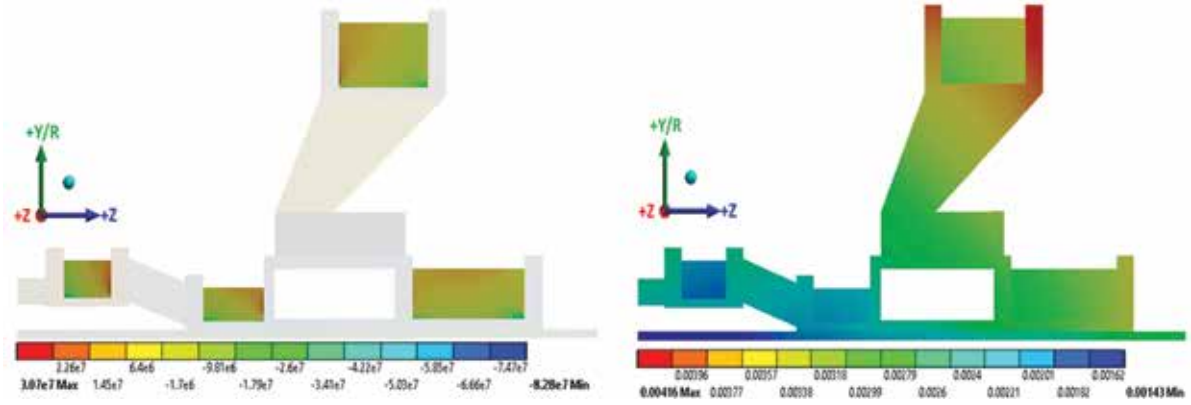

b c

Figure 3.1.10 (b) The hoop stress on the bobbin and coil due to thermal contraction (c) overall deformation of the bobbin and superconducting coils due to the thermal contraction .

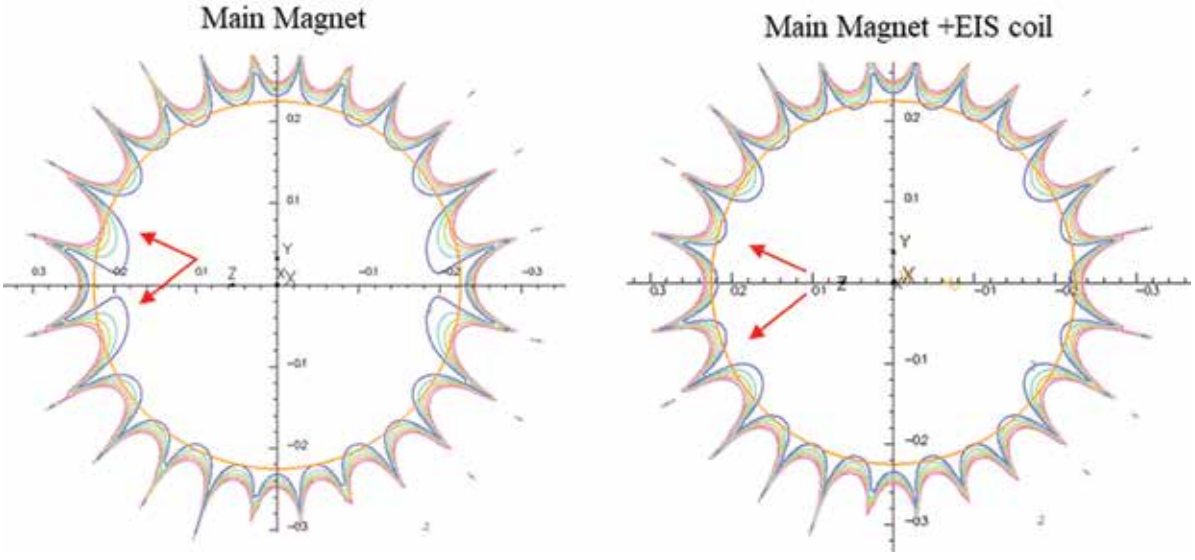

d e

Figure 3.1.2.10 (d) The overall homogeneity of the magnet at the field of view (FOV) of 45cm
(e) overall homogeneity at the FOV due to the combination of the main magnet and the superconducting EIS coil
(Innermost line represents 2ppm and outermost line represents 10ppm) .

MRI magnet needs many inter-coil electrical joints and joints between conductors of primary magnet and superconducting switch. The temporal stability (0.1ppm/hr) of the field is determined by the overall electrical resistance (< 10^{-11} Ω) of the magnet system. Hence, the superconducting joints play a crucial role in determining the stability of the magnet during operation. Superconducting joint technique has been developed using a special type soldering protocol after extensive characterization (SEM/EDX) of large number of joints between various types of superconducting wires. A 4K test rig has been developed to measure such low value of joint resistance through a current decay method. Figure 3.1.2.10(f) shows the 3D model of the 4K test rig integrated with 1.5T NbTi magnet and the superconducting primary coil to induce current into the secondary coil that is the test coil. The superconducting joint can also be tested even in presence of the magnetic field. Figure 3.1.2.10(g) shows the electrical resistance of the superconducting joints between CuNi (NbTi) conductors to be used for superconductor switch. The resistance is measured to be 7x10^{-13}Ω and 7x10^{-12}Ω respectively at 0T and 0.5T. A large number of superconducting joints have been developed for testing and characterization. A 600A/10V power supply indigenously developed by power supply lab has been used for testing the superconducting joints.

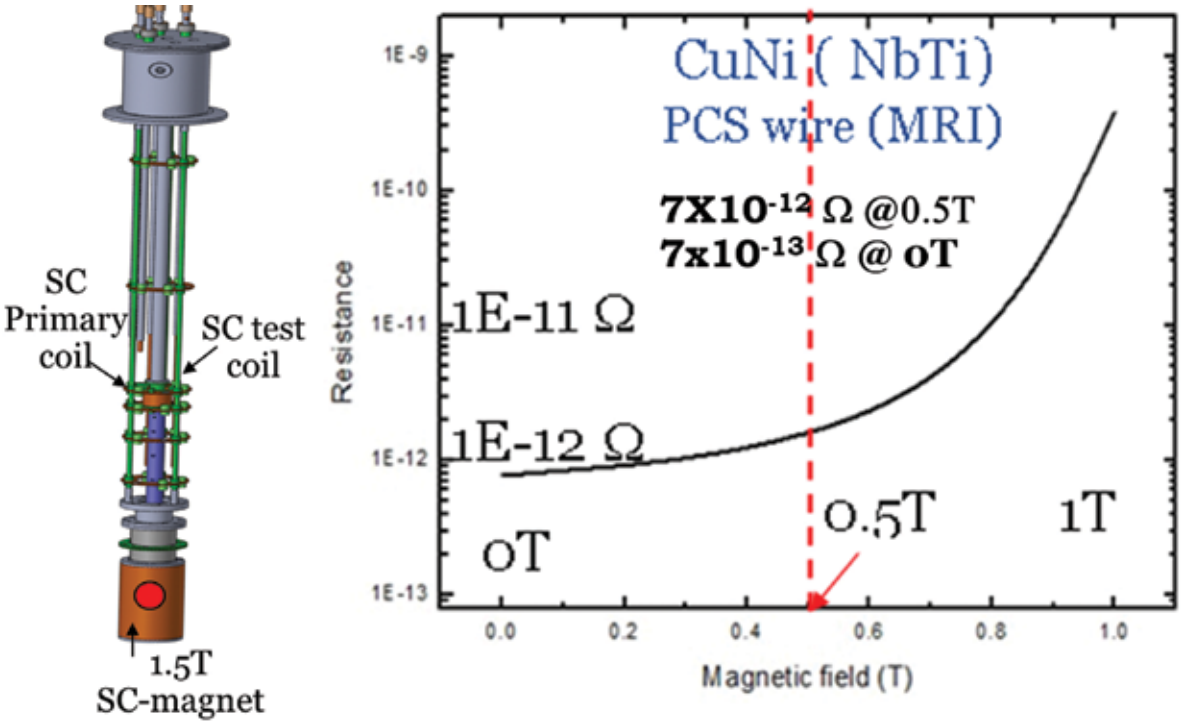

f g

Figure 3.1.2.10 (f) 3D- model of the 4K test rig for characterizing the electrical resistance of the superconducting joints using current decay principle in presence of magnet field (g) The electrical resistance of superconducting joints between CuNi(NbTi) conductor to be used for superconducting switch .

MRI cryostat, is one of the primary components for the scanner, not only houses the superconducting coils of the MRI but provides an overall structural integrity of the scanner. Cryocooler based Helium recondenser makes the present-day scanner a zero boil off (ZBO). A cryocooler based ever-cooled cryostat has been designed for the 1.5T magnet with a warm bore of 0.9m. A two stage 4K GM cryocooler has been used to maintain the intermediate temperature (~50K) on the thermal shield and recondensation for the helium bath. The iso-center of the magnet and the magnetic axis needs to be preserved even after the cool-down. A self-centring suspension system with large number of radial and axial support system has been designed to take the static and dynamic structural load. Figure 3.1.2.10(h) shows the ever-cooled MRI cryostat for 1.5T magnet.

h

Figure 3.1.2.10 (h) Cryocooler based zero-boil-off (ZBO) cryostat for 1.5T MRI magnet .

B. Characterization of 2G High temperature Superconducting tape for Modular Superconducting FCL application

Soumen Kar, Retu Bharti, Rajesh Kumar & T.S.Datta

A R&D project on "Characterization of 2G high temperature superconducting (HTS) tape for modular superconducting fault current (SFCL) application" funded by CPRI, Bengaluru is under progress at IUAC. A versatile electrical set up has been developed for characterization using a 60V/300A transformer and indigenously developed fault generator. he schematic of the experimental set up is shown in the Figure 3.1.2.10(i). The high-power thyristor based fault generator can vary number of fault cycles up to 12 cycles, fault angle, fault polarity along with repetitive fault. The maximum fault can be created up to 4kA at $60V_{rms}$. The resistive load of the circuit determines the current through the SFCL during normal operation. The perspective fault current has been measured corresponding to the voltage 20V, 40V and 60V.

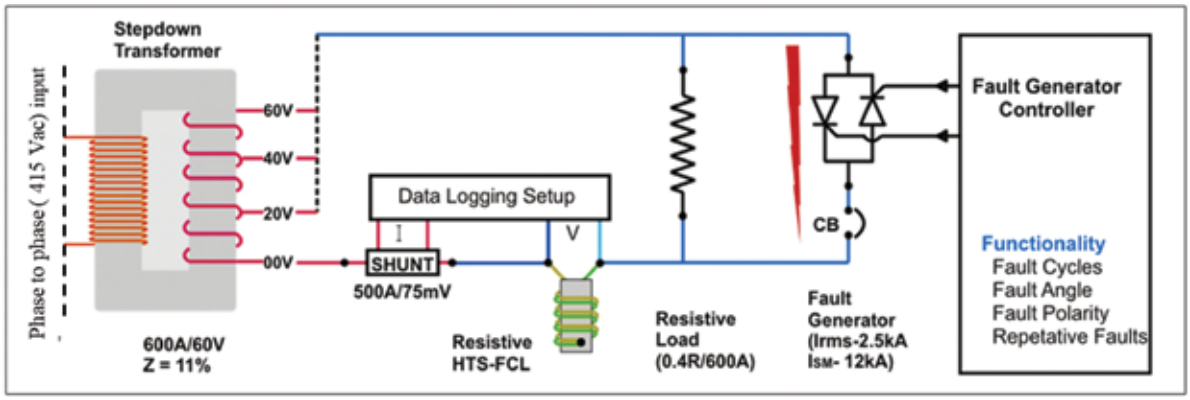

Figure 3.1.2.10(i) The schematic of the experimental test rig for AC characterization of 2G HTS tape at 77K in liquid Nitrogen.

Prior to the AC characterization on the 2G HTS tapes that has been characterized using DC power supply to study the thermal behaviour during an over-current (more than the critical current) operation. The critical current after each over-current operation has also been analysed. Figure 3.1.2.10 (j) shows the peak temperature on the HTS tapes after each cycle of over-current operation with increasing values of current exposure. Figure 3.1.2.10 (k) shows the I-V curve and corresponding critical temperature of HTS tape after each over-current operation. The critical current of the HTS tape is found to be deteriorated by 5% after exposure of 500K.

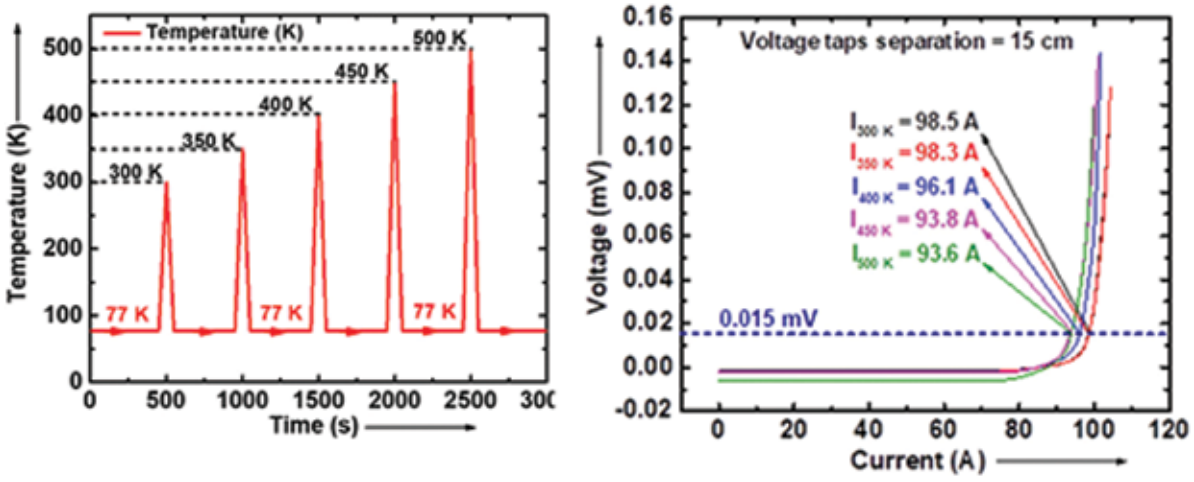

Figure 3.1.2. 10 (j) The peak temperature on the 2G-HTS tape corresponding to each over-current operation and (k) the I-V characteristics of 2G-HTS tape after each thermal spike during over-current operation.

A modular SFCL unit was developed using same HTS tape and it was characterized using the test rig at 20V. Figure 3.1.2.10(l) shows the perspective fault current at 20V without any SFCL unit. The current through the SFCL unit was $50A_{rms}$ during normal operation. Figure 3.1.2.10 (m) shows how a modular SFCL unit has brought down the fault of 1.73 KA to 0.59kA within 100ms. A series of extensive tests are under progress to define a modular SFCL unit for future application

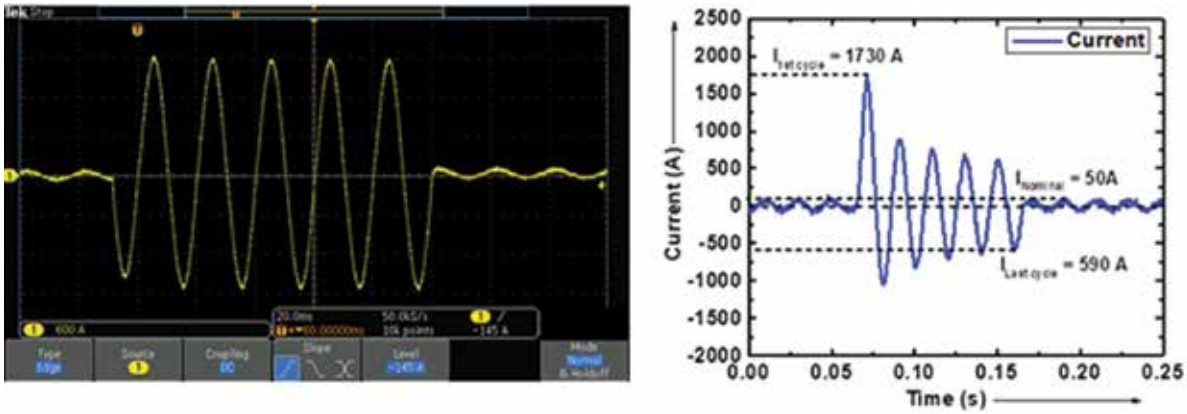

Figure 3.1.2.10 (l) The perspective fault current through the shorted terminal of the power supply at 20V_{rms} and (m) A fault of 1.73 kA has been brought down to 0.59kA within 100 ms by the modular SFCL unit.

3.1.2.3 Electronics for Cryogenics & linac: Lab activities

Joby Antony, Rajesh Nirdoshi, Anup Choudhury, Soumen Kar, T.S.Datta

(a) Cryogenic controls & Longest Linac run

The IUAC Cryogenics control room has been operational in continuous 24x7 remote mode for six months of the linac run last year. Presently the control room has the following systems installed.

CADS

CADS is the Ethernet based Crate-less model of completely indigenous Cryogenic control system for linac Cryogenic distribution systems. This system was built out of in-house designed twenty four (24) different intelligent cryogenic instruments (each has analog front-end and digital backend i.e cryogenic sensor nodes and actuator nodes) which is designed with a total of 72 embedded device-servers (on-chip http servers) inside, interconnected over Ethernet(LAN) .The networked distributed control system survived to work for the closed loop control operations of cryogenic distribution system components where in the control loops run every tens of millisecond for PID & data logging and control operations. Based on the operational experience, minor modifications are planned for next runs considering the hardware redundancy. The lesson learned is "indigenization is the only solution to rapid maintenance".

CRYO-DACS

The second system, CRYO-DACS, a VME system which was installed in the year 2002 for all the linac temperature monitoring and logging operations, has been functional.

All important signals from CADS and CRYO-DACS Cryogenic system has been now grouped and brought together to a central interface-box through analog buffers to tap 35 most important signals of cryogenics network to IUAC linac control network.

(b) Developmental activities

An AC Susceptometer development based on DSP-lockin Amplifier

Joby Antony, Prof. A.K Rastogi and Dr. K. Asokan

Developed a working prototype for High quality AC susceptometer for magnetic susceptibility measurements by designing own two phase DSP-lockin Amplifier. The entire system is computer controlled and the results appear on the PC screen as shown in Fig. 3.1.11a.

The analog front-end electronics and FPGA based digital back-end electronics are packaged into a 19 inch mountable box (as shown in Fig. 3.1.11b) and is interfaced to the PC using Ethernet.

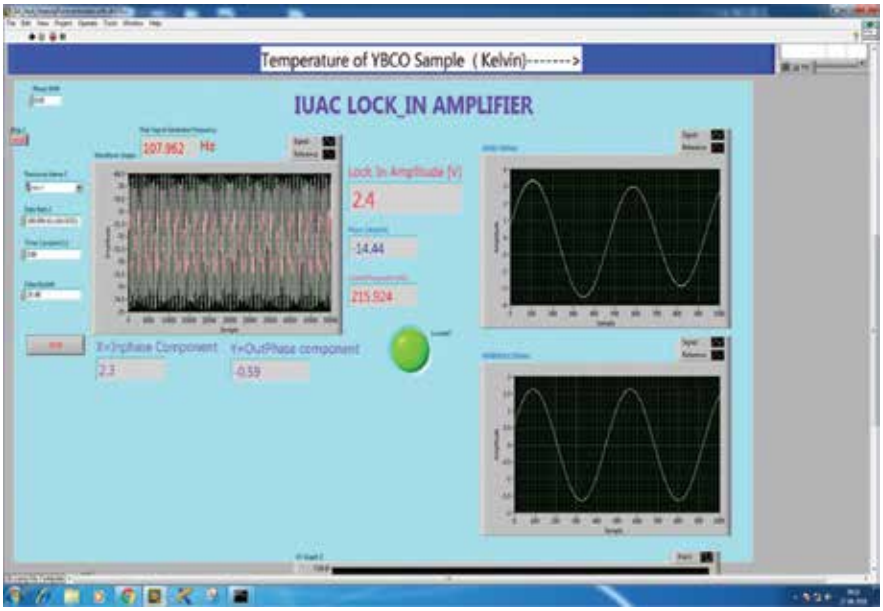

Fig. 3.1.11a

Fig. 3.1.11b: Analog front-end electronics and FPGA based digital back-end lock-in

The following is the block diagram of the indigenous susceptometer, built at IUAC

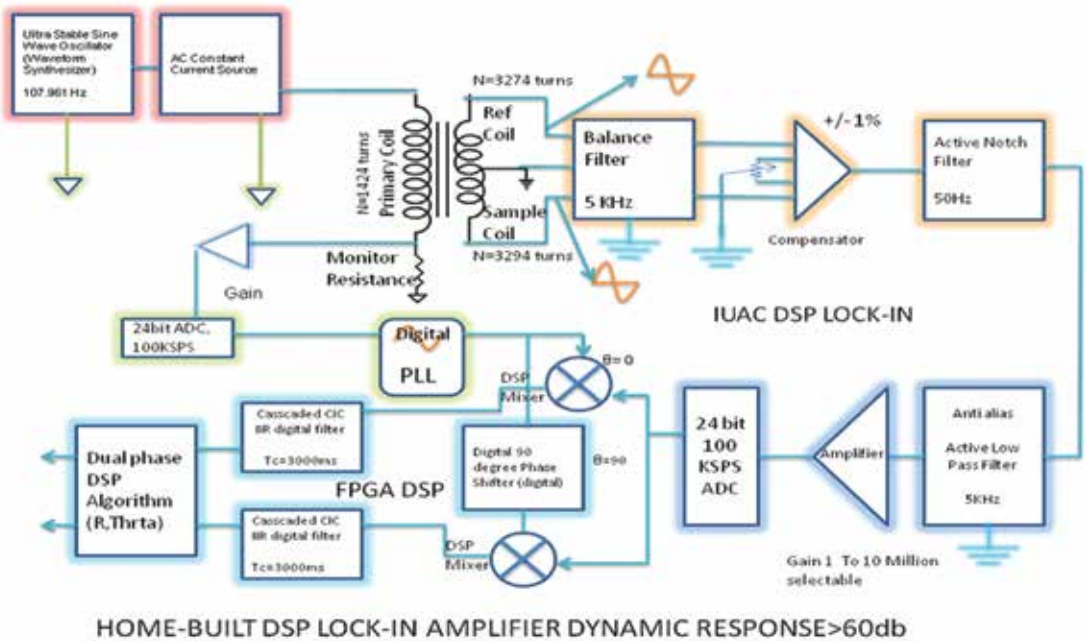

Fig. 3.1.12: Block diagram of the indigenous susceptometer

The ac susceptometer is used to study the magnetization induced in various magnetic materials in response to ac magnetic fields inside a driven solenoid which was also wound here. The indigenous list of parts for this experiment include LN_2, ac function generator, ac current source, two-phase lock-in amplifier, embedded pt100 temperature sensor, computer data acquisition system with YBCO and Gadolinium samples. The major difficulties faced in the development of such a system is the noise contained in measurement, as the noise is approx. 1000 times more than the signal because of which we used digital DSP lock-in amplifier techniques to extract the ac signal.

Results: In the first experiment, We demonstrated 294K paramagnetic to diamagnetic transition using Gallodinium (Gd) samples using this device as shown in Fig. 3.1.13.

In the second successfully tested experiment with our indigenous device, When YBCO sample is cooled to LN_2 temperature, the device gives negative diamagnetic signal and when temperature of the sample rises above 93 Kelvin diamagnetic signal becomes zero . Hence superconducting transition is demonstrated as shown in Fig. 3.1.14.

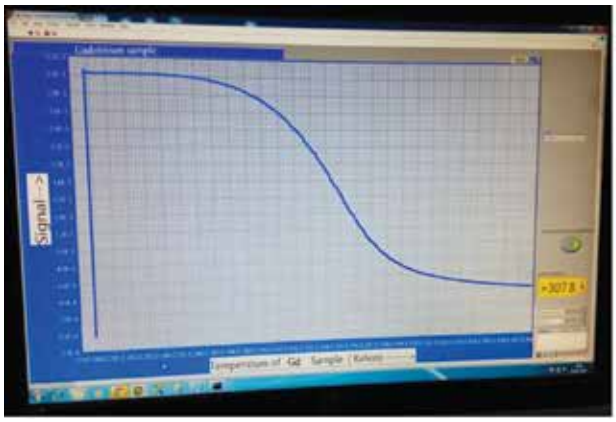

Fig. 3.1.13

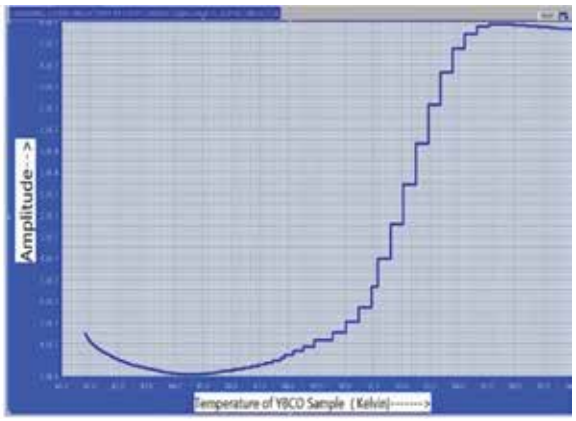

Fig. 3.1.14

MRI fast Data acquisition system: Status of development

Joby Antony, Soumen Kar and T. S. Datta

The required hardware has been bought for the development of the fast RT FPGA based data acquisition for the undergoing MRI project. This includes fast differential ADC, DAC, D I/O, RS232 modules etc.. The software development is going on. The system will use NI cRiO backplane with Labview FPGA as the base development system. The RT scanning will be at the rate of 1 millisecond per channel and the data storage will account to huge GB per day. The work involves fast data acquisition and logging for MRI monitoring and controls.

A PID based Gas Flow Processor: The GUI in linux

Joby Antony, Rajesh Nordhoshi, R. Saineesh and P. Sugathan

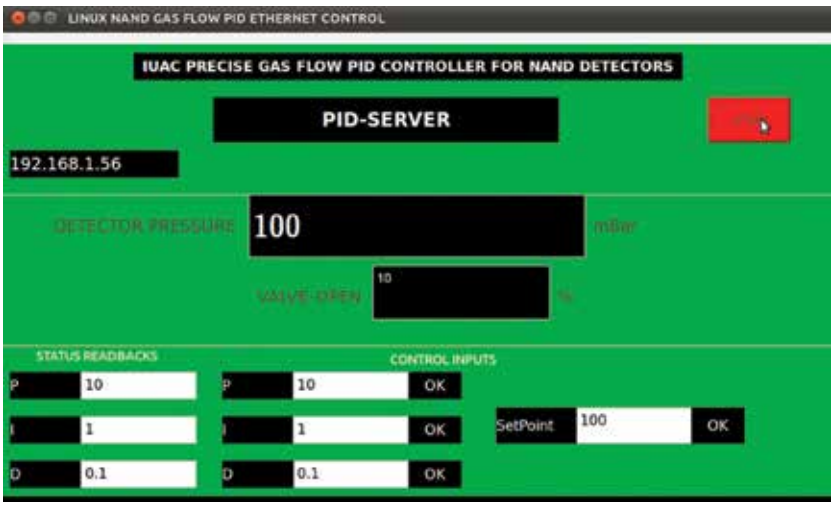

Fig. 3.1.15

Computer software GUI interface has been developed for the PID BASED GAS FLOW PROCESSOR using Qt under Linux , as shown in Figure 3.1.15 . Regulated flow through a detector system (0.0 to 99.99 Torr) with an accuracy of the order of +/- 1 milli Torr may be achieved using this indigenous device.

MULTI CAN NODES NETWORK PROTOTYPE

Rajesh Nirdoshi and J Antony

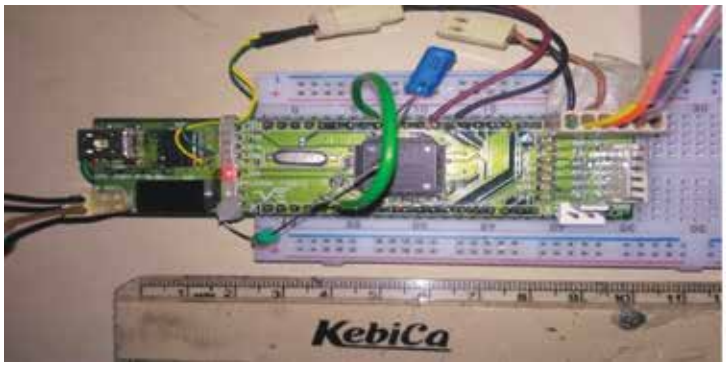

Fig. 3.1.16

Fig. 3.1.17: CAN protocol decode

A multi noded CAN sensor-network has been designed and tested using ARM processors for future use. These nodes used LPC-JOBY-DESIGN-IUAC-32bit-ARM-MCU Home made. ARM MCU boards (Figure 3.1.16) are built as 40 pin DIP which houses LPC1768 chip and are ARM MBED compatible for development. The CAN protocol was decoded to build a multimode network in future applications as shown in figure 3.1.17.

A remote Radiation unit for pelletron use

Joby Antony and Birender Singh

All gamma and neutron meters, which measure radiation during the pelleron operations, are interfaced and brought to Ethernet level. This PC based system has user friendly GUI view & to record data directly in EXCEL format. The Graphical user interface was developed using LabView® as shown in Figure 3.1.18.

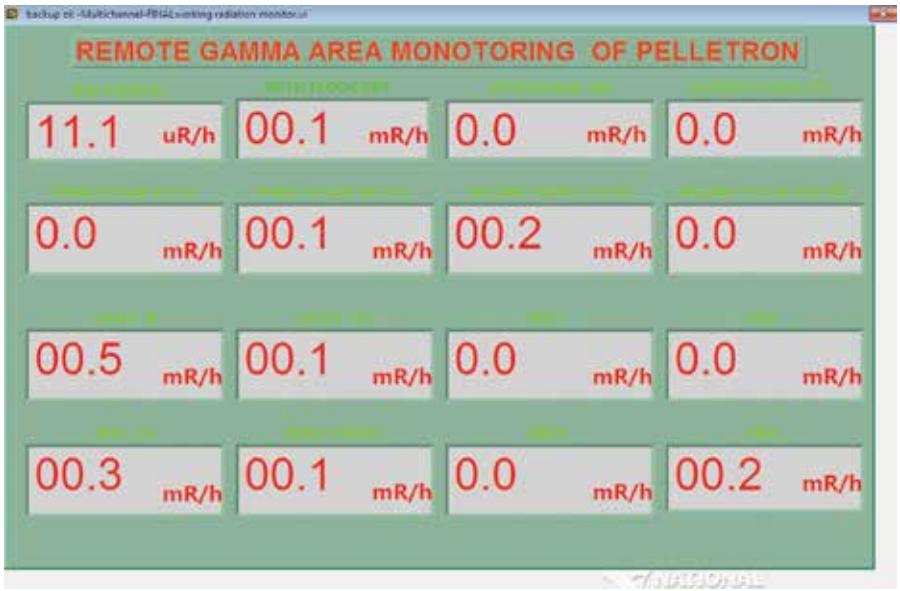

Fig. 3.1.18

Other programmes

Other activities of the lab include Electronics Apprentice management (at present 3 electronic apprentices), B.Tech/ M.Tech projects etc. Last year we had six students who did their B.Tech, Mtech, Msc internships from IIT, NIT, MIT and DU.

3.1.3 Beam Transport System Laboratory

The primary responsibility of Beam Transport System (BTS) Laboratory is to perform the preventive maintenance of the beam transport system once a year and to execute the breakdown repairs if any during normal beam time operations. The BTS Lab members investigate beam trips caused by the BTS and strive to repair it in minimum time. The Lab also designs and test new technologies for magnet power supplies and particle detector high voltage bias power supplies. Besides this the Lab is involved in design and fabrication of different type of close loop instrumentation (see section 2.1.7) for the upcoming High Current Injector (HCI) facility. The activities related to power supply development and maintenance are summarised below.

At IUAC the beam transport system of all the accelerators together with experimental facilities which includes Pelletron, LINAC, HCI, LEIBF, NIBF, HIRA and HYRA becomes very large. Large no of beam transport system associated instruments such as magnets, magnet power supplies, remote control modules, magnetic field measuring instruments, beam line selection systems etc are in round the clock operation.

3.1.3.1 Beam Transport System operation status report

During this yea the overall uptime of the beam transport magnet power supplies was recorded more than 99% and all the power supplies met the required performance in terms of stability. There was no major breakdown, except some random tripping of the power supplies due to corrosion in the power supply transistor bank fuse holders. There were occasions when power supplies failed or it was down due to the problem in the associated system such as water, electricity and remote control. The power supplies failure logs were maintained over the period to summarise the required action to be taken during scheduled preventive maintenance. The beam line selection system switchgears was out of operation since last year due to corrosion. Presently the beam line selection operation is performed manually by connecting the magnets of the selected beam line to the corresponding power supplies.

3.1.3.2 Preventive Maintenance

All the BTS instruments are regularly maintained during “scheduled maintenance period” to avoid failures during the beam time operation. The magnet power supplies which are the main part of the beam transport system instruments consists of highly-regulated (10ppm to 50 ppm) current sources with output ranging from 10A to 600A and output power ranging from a few hundred watt to almost 60kW. The regulation technologies currently in use cover several types – from linear transistor regulated to SCR rectifiers, to PWM with analog regulation control and digital remote control. Proven procedures finalized on the basis of maintenance experience to improve the performance of the equipment are followed.

Small quantities of corrosion products have created reliability issues in power supplies. The press-fit connections such as fuse holders and connectors are the worst affected. In order to minimize the corrosion effects, efforts are made to control the dust levels, which act as carriers to chemical pollutants. Beam lines and experimental facility areas rearranged, floor areas cleared to remove the accumulated dust and enable the periodic cleaning of these areas. Also it is decided to change the transistor bank silver coated fuse holders periodically and use gold or nickel coated connectors wherever possible. During this scheduled maintenance period the fuse holders of 20 power supplies have been replaced.

Preventive maintenance procedures:

Preventive maintenance was performed during November to December 2017. As the power supplies need high level of examination, monitoring and maintenance the preventive maintenance was planned and made more effective by following steps:

- Test Report Performa for each type of Power Supply
- Layout of Accelerator Beam Transport System
- Upkeep of Magnet Power supply Installation Areas to facilitate periodic cleaning.

To finalize the corrective actions during preventive maintenance, the condition of each power supply has been assessed by doing the following.

- Visual Inspection
- AC / DC Voltage measurement of different test points
- Temperature Measurement/ Thermal Analysis

The condition assessment data has been recorded in Test Report Performa. Data was analysed to assess the condition of the power supply and then to finalize the preventive maintenance actions.

Servicing Procedures -To insure output current stability

- Dust Cleaning
- Cooling water flow and temperature
- Leakage Resistance of the Cooling Water Connections due to electrolysis
- Power supply Output current ripple
- Output current stability and Calibration tests

Servicing Procedures to ensure proper functionality

- Remote control operation
- Safety interlocks
- Full power test

3.1.3.3 Power supplies development Activities

A. HCI beam transport System Magnet Power Supplies

The HCI Beam Transport System (HCI-BTS) uses approximately 84 magnets of different type which includes 8 bending magnets, 46 quadrupole and 28 steerer magnets. The power supply requirement has been categoried in two: 1) High Current Power Supply (HCPS) (100 to 200A) of single polarity for bending & quadrupole magnets and 2) low- current (± 10A) bi-polar for steerer magnets. The first category HCPS of single polarity are procured from DANFYSIK. For the Low Current Power Supply (LCPS), it was decided to design and develop these in-house. Total no of power supply requirement for HCI beam transport magnet is 140 (76 HCPS & 64 LCPS) including spare units. The LCPS units are bipolar current controlled linear power supplies, rated ±10A/±50V and provide current stability of ±100 ppm or better. In last four years approximately 45 numbers of such power supplies were assembled in house in three lots. Out of which 24 units has been installed and are in operation, performing as per the required specifications. To complete the HCI- steerer magnet power supply requirement 30 more units are needed.

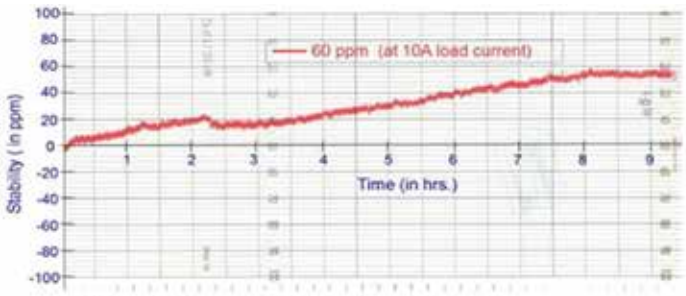

Stability of the ± 10 A bipolar LCPS ; 60ppm

Photograph of the ± 10 A bipolar LCPS

Fig. 3.1.19

B. Development of MOSFET based ±25A True Bipolar Power supply

The developent is aimed to introduce a simple technique to eliminate zero crossover distortion in the presently used bipolar current regulated power supplies. The present design of such power supplies uses BJTs in push-pull configuration to have bipolar output current. In order to eliminate the crossover distortion associated with the push-pull output stages, additional feedback loops and accurately matched shunts are used to setup a quiescent current in the push-pull stage. This technique presents a major limitation, as it depends on the current gain of the BJTs, which decreases drastically at high output current. This technique is complex and needs additional control loops, specially matched shunts and high quiescent currents, which results in high power dissipation even at zero output current. In the new technique, in place of BJTs, MOSFETs are used and the quiescent currents are set by providing an offset voltage to gates. As MOSFETs have high input impedance and constant current gain no additional feedback loops are required to control the quiescent current. The new technique is simple to implement and equally effective in low as well as high current bipolar amplifiers.

To validate the design of the new technique, a 25A bipolar power supply was assembled last year. On request for a ± 100A /50V true bipolar power supply by Thin Film Laboratory (TFL) Department of Physics, IIT –Delhi this year the same unit has been upgraded to ± 100A /50V. The unit has been installed there with a horizontal field variable Gap electromagnet for field testing. The unit is in operation, meeting the entire operational and performance requirement. They have submitted the bipolar functional and performance data as given in the figure.

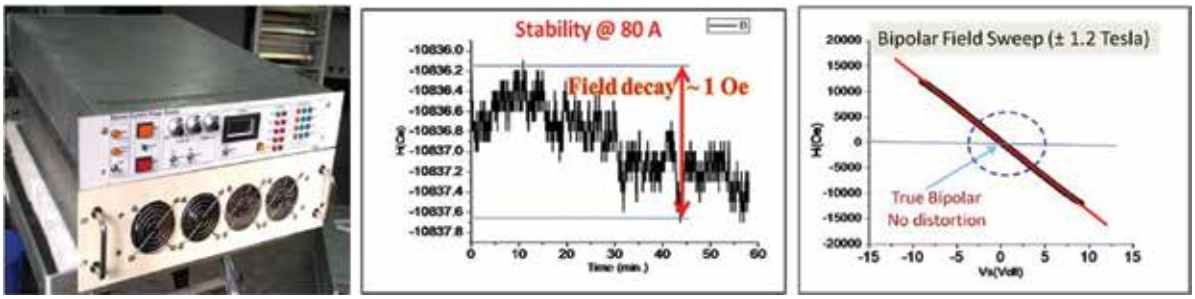

Fig. 3.1.20

C. Development of 600Adc /10 V Power supply for characterisation of MRI components:

The Applied Super Conductivity Laboratory IUAC has been awarded a project to develop MRI scanner magnet. Superconducting (SC) joint, persistent current switch (PCS) and the quench protection components are the crucial sub-technologies to be used for the MRI scanner magnet development. All these components have to be characterized at 4.2K up to 500A DC current. Special type of power supplies are needed for characterizing the SC joint because of their extremely low resistance value (~$10^{-13}\Omega$). In the year 1999, many such power supplies of 100A /10V rating were developed at IUAC primarily for the SC magnets of the LINAC and other offline setups. Instead of importing a single unit of 600A rating which would have been very costly, it was decided to use the in-house developed units in parallel to get the required current. Last year six such units were integrated to make a modular 600 A power supply. Master-slave control scheme has been adopted where the master unit performs the control and forces the remaining slave units to follow the reference current of the master. To enable the parallel operation of these power supplies, a tracking amplifier which generates a corresponding tracking signal of 0-5V for 0-100A output current have been incorporated in each module. This year the complete unit has been made operational and handed over to the MRI group. The power supply has been used extensively for characterization of MRI scanner magnet components. The photograph shows the power supply in an experimental setup.

Fig. 3.1.21

D. Development of fault current generator for AC characterization of HTS at 77K.

The Applied Super Conductivity Laboratory, IUAC, has been awarded a project from Central Power Research Institute (CPRI) Bangalore to study the behaviour of supper conductors under the influence of heavy AC fault currents. The data generated will be used to develop a high temperature superconductor (HTS) based device to be put in series with the circuit brackers to suppress the fault currents. The beam transport laboratory took–up the responsibility to develop the 4kA Fault current generator setup to facilitate the HTS characterization. A very versatile laboratory scale fault current generator has been designed, constructed and installed. The functional & electrical specifications are given below.

Functionality	Electrical specifications
• Fault duration (no of fault cycles) • The selection of fault occurrence polarity • Angle of fault incident • Repetitive Faults	Voltage (selectable): 20/40/60 Current (continuous): 600A Peak current (12 Cycles): 4000A

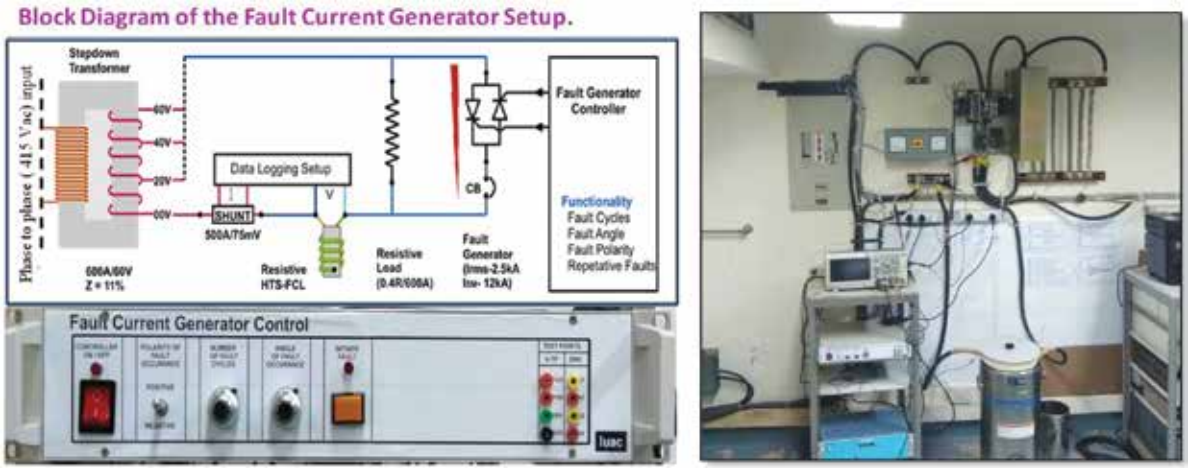

Fig. 3.1.22

The "Fault current Generator setup" is in use with full functionality and electrical capacity. The photograph shows the installed "Fault Current Generator".

3.1.4 Detector Laboratory

Mohit Kumar and Akhil Jhingan

Detector Laboratory at IUAC provides experimental support to various users in setting up charged particle detectors and readout electronics. New detectors and electronics have been designed and developed, and are used in various user experiments in HIRA, HYRA, GPSC and NAND. Detector lab provided training on experimental activities for Scientist Trainees, JRF, M.Tech, B.Sc and M.Sc students.

3.1.4.1 Integrated MWPC-SSD system

IUAC–GANIL collaboration: A large area integrated MWPC-SSD detection system has been developed for simultaneous measurement of velocity and energy of the fission fragments. The hybrid detector has a two dimensional position sensitive multi-wire proportional counter (MWPC) followed by a large area Silicon strip detector (SSD). Active area is 10 cm × 10 cm. MWPC had a 3 electrode geometry: cathode sandwiched between two position anodes. All electrodes are wire frames with cathode having a wire pitch of 300 um for master timing, and 600 um for positions. Reduced wire pitch provided higher avalanche gain as well as better timing resolutions. The position information was extracted using delay line technique, and delay line was prepared using discrete chip inductors and capacitors. The MWPC provided velocity and angle information, whereas the SSD provided energy of the fission fragments. Elimination of aluminised mylar cathode with wire frame (300 um wire pitch) reduced the energy straggling of fission fragments. The detector had a total of 26 signals (5 MWPC and 21 of SSD). Another important feature is mounting and aligning the MWPC and SSD together in the same chamber, extracting 26 signals out of the detector chamber without using bulky coaxial vacuum feedthroughs, and integrating the preamplifiers with detector. This eliminated cables between the preamp and detector, and significantly improved S/N ratio and time resolutions. The large area SSDs were provided by GANIL. The detector system was used to perform fission mass distribution measurements for the system ^{124}Xe + ^{54}Fe at VAMOS experimental facility of GANIL, France. The detector was mounted in target chamber of the VAMOS spectrometer to detect one fission fragment and the other fragment detected at the focal plane detection system of VAMOS. The preamps survived in vacuum for 10 days of beam time. A mass resolution of 2 *amu* was observed for fission fragments in combination with VAMOS. Another detector is being prepared to have a *2v-2E* measurement system at NAND facility of IUAC.

3.1.4.2 MWPC for GPSC/NAND

A new two-dimensional position sensitive MWPC has been developed with the aim of detecting low energy heavy ions at angles ranging from 2 -10 degrees. This will include low energy fusion ERs, deep inelastic events, fission fragments, projectile-like elastics etc. The idea is to perform neutron and light charged particle multiplicity measurements tagged by the events detected in MWPC. The MWPC has been prepared using a four electrode geometry, all of them wire frames. Such a design will be useful in detecting low energy ERs. Active area of the detector is 10 × 5 cm^2. Off-line measurements have been performed using ^{241}Am alpha source and ^{252}Cf fission source. In beam tests are planned in future to test the high count rate handling capability of the detector. At very forward angles, the detector is expected to be exposed to particle count rates as high as 10^6 pps. The survival and long term stability of the MWPC at such high rates needs to be established before performing actual experiments.

3.1.4.3 HYTAR in NAND

HYTAR detector system was redeployed in NAND spherical scattering chamber for performing measurements using accelerated beams from the Pelletron-LINAC accelerator combination. The detectors were placed in 3 groups of different angles. Three different gas handling systems were installed for the same so as to operate them at different pressures depending upon the energy of the reaction product to be detected. The detectors in forward hemisphere were operated at 75 mbar isobutane pressure, whereas those in back hemisphere were kept at about 65 mbar. Four detectors at 173 degree were operated at 55 mbar. A special CF100 flange along with adapter was prepared to accommodate dial gauges, precision needle and bypass valves, which was mounted on top port of the spherical scattering chamber. A common bottle of isobutane was used to feed all 3 gas handling units, and a common rotary pump was used at exit for gas circulation. System was used for the study of quasi-elastic scattering of ^{28}Si + ^{232}Th, and fission angular distribution of ^{30}Si + ^{188,192}Os.

3.1.4.4 Activities in NUSTAR collaboration, Germany

IUAC–Delhi Univ.-Panjab Univ.(Chandigarh)–GSI (Germany): The low energy branch (LEB) cave, after the Fragment Recoil Separator (FRS) requires detectors for beam diagnostics which includes an ionization chamber for the nuclear charge or Z identification of cocktail secondary beam species. The upcoming facility will have significantly increased secondary beam intensities. It is proposed to develop a new gas filled ionization chamber with tilted electrode geometry in axial field mode to handle the higher count rates. The detector will have stacked electrodes with smaller inter-electrode gaps for faster charge collection. These electrodes will be tilted at an angle of 30 degrees with respect to the normal to the beam direction. The incident beam flux and the charge carriers, liberated after ionization, move in different trajectory, thus reducing the recombination probability at higher beam intensities. The proposed design will have an active area of 20 × 8 cm^2 with 21 stacked electrodes (10 anodes and 11 cathodes). The detector is expected to provide particle identification for high energy heavy ions (~ 100-500 MeV/A), and is expected to be operated at intensities of 10^6 pps. The detector is proposed to be commissioned, in last quarter of 2018, at the exit of FRS for initial phase of NUSTAR campaigns from 2018-2022.

3.1.5 Target Development Laboratory

Abhilash S R, Ambuj Mishra and D. Kabiraj

Target development laboratory in IUAC is mainly responsible for thin film and target development for accelerator users in different streams viz; material science, atomic physics and nuclear physics. Nuclear target development, especially isotopic target development is the main activity in target laboratory where major effort is required. Many targets were fabricated in 2017 by using various techniques and instruments in target laboratory. Most of the instruments in target laboratory were well–utilized by users in the last year. Man-machine utilization in target development laboratory is shown in Figure.3.1.23 and Table.1.

It indicates that more than two facility of target laboratory has been used every day. More than 260 attempts were performed for target fabrication in different systems. In addition to IUAC pelletron users from universities, target lab had extended the service to other laboratories like VECC and GANIL. Target developments in IUAC were reported in many national symposia and inter-national journals in 2017[1-12].

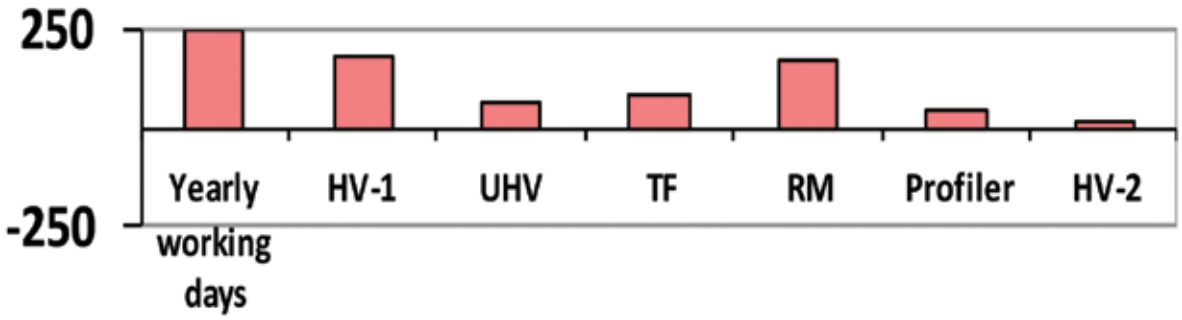

Fig. 3.1.23: Utilization of time

Facility	No of attempts
High Vacuum Evaporator-I (HV-1)	92
Ultra- High Vacuum Evaporator (UHV)	66
Tubular furnace (TF)	89
Rolling Machine (RM)	176
Profilo Meter	43
High Vacuum Evaporator-II (HV-2)	16

Table 1: Utilization of facilities

3.1.5.1 Recent updates in Isotopic Target development

In target development, 80% of the time is being utilized for the fabrication of isotopic targets. Few nuclear targets developed in the last year were the first-time-development. Table.2 shows the list of few isotopic targets developed in 2017 for nuclear physics users of IUAC. Most of the targets are fabricated by physical vapor deposition method (thermal and e-beam evaporation method).

Sl.No	Description of target	Thickness
1	^{180}W	~200µg/cm^2
2	^{166}Er	1mg/cm^2
3	^{182}W	~600µg/cm^2
4	^{184}W	~780µg/cm^2
5	^{186}W	~600µg/cm^2
6	^{130}Te	~250µg/cm^2
7	^{130}Te	~200µg/cm^2
8	^{128}Te	~200µg/cm^2
9	^{126}Te	~200µg/cm^2
10	^{156}Gd	500µg/cm^2
11	^{156}Gd	1000µg/cm^2
11	^{70}Zn	500µg/cm^2
12	^{68}Zn	500µg/cm^2
13	^{170}Yb	200µg/cm^2
14	^{61}Ni	200 µg/cm^2

Table 2: List of few isotopic targets developed in 2017

3.1.5.2 Thin target development of high melting point metals

Target development of metals having high melting point viz; Mo, W and Ta faces lots of challenges. Physical properties such as hardness, malleability and ductility play vital role in the target development by mechanical reshaping. High melting point of materials is the major constraint in the target development by evaporation technique. Target laboratory had successfully fabricated many isotopic W targets of ~150 μg/cm^2 in the past. This time the requirement was for relatively thick (> 600 μg/cm^2) W target with thin carbon backing. The W was evaporated by 6 kW e-gun on carbon film of thickness 20 μg/cm^2. The average thickness of the ^{180}W targets was 500 μg/cm^2. Degradation of parting agent $BaCl_2$ during evaporation and less quantity of available material were the main challenges during the evaporation. 150 mg material was consumed for the fabrication of 5 targets. The same procedure was used for the fabrication of targets of 182,184 W of ~800 μg/cm^2 thickness for BHU group for their experiment at NAND facility. Several trial evaporations were done to optimize the parameters with natural W powder before doing the final evaporations with isotopic material.

^{180}W targets were also prepared for an experiment using recoil mass spectrometer, HYRA. The targets prepared were in the form of $^{180}WO_3$ of 200 μg/cm^2 thickness with 30 μg/cm^2 carbon backing. The diffusion pump based coating unit was used for the fabrication of carbon backing with $BaCl_2$ as releasing agent. After annealing at 325ºC in 1 hour for stress relieving, the carbon slides were used as substrate for the deposition of WO_3. For the deposition of WO_3, a turbo pump based coating unit was used. This coating unit is equipped with a 6 kW arc suppressed electron gun. The available amount of $^{180}WO_3$ was only 126.1 mg and it was in the form powder. A 3 mm diameter pellet of $^{180}WO_3$ was made by using a hydraulic press. Pressure in the evaporator was maintained at 3.0x10^{-6} mbar during deposition with base pressure of 1x10^{-6} mbar. After the deposition, the target films were subjected to post-growth annealing at 325ºC in 1 hour and further separated from $BaCl_2$ coated glass slide by floating in hot distilled water. The fabricated targets were characterized using Rutherford Back Scattering (RBS) facility of IUAC with 2 MeV He. The presence of back scattered He peaks from carbon backing, oxygen and tungsten only in the spectra indicates the absence of heavy impurities. The analysis of RBS spectra reveals that the thickness of tungsten layer is 214 μg/cm^2 and that of the carbon backing is 25 μg/cm^2.

Many Mo targets have been developed in the past in the form of self-supporting targets of thickness order of mg/cm^2 which were prepared by cold rolling or by PVD method on thick backing. On the basis of user request fabrication of thin self-supporting $^{94, 98, 100}$Mo targets preparation was initiated. CsI, KCl and $BaCl_2$ as parting agents which are recommended in literatures have been explored. Due to repeated failure to obtain stable free-standing foils an alternative option of using thin carbon backing was tried. To start with thin carbon foils were deposited on KCl coated glass slides. These slides were annealing at 200ºC and further used as substrate for Mo deposition. After evaporation, Mo coated substrates were annealed at 250ºC for 1 hour under flowing Ar gas and then separated from substrate by floating in water and mounted the same on target holder with 10 mm diameter hole. Post growth annealing temperature turned out to be very crucial as it was observed that the annealing of slides below 200ºC was not sufficient to relieve stress in the films completely while annealing above 250ºC was degrading KCl with reduced solubility in water. The targets were analyzed by EDX and the results indicate absence of any major contamination.

3.1.5.3 Preparation of targets of oxidizing elements and its EDX Analysis

Nuclear target development of materials which get readily oxidized poses lots of challenges. Targets of oxidizing elements like Li, Ca, Pb, Nd, Gd, Sm, Ba, Ce, Pr, Bi, Er and Eu are frequently fabricated in IUAC in the form of free standing foils and foils with backing support. In some cases, foils of these elements are sandwiched between two protective foils to avoid oxidation while exposed to air. Role of sandwiching to minimize oxidation of target surface and its effect in preservation of expensive isotopic targets for longer duration were studied recently. Much effort was paid to find the ways to minimize interaction between the target material and atmospheric gases by suitable choice of capping layer element and the layer thickness. These parameters are very important because they should not affect the results of proposed experiment. It was observed that in case of highly oxidizing elements like Pr and Ca Au capping layers from both sides are essential to protect them from oxidization. But in case of Pb, carbon protecting layers are sufficient which is studied with the help of EDX analysis as shown in Figure 3.1.24. Pb foils deposited on C backing were exposed to air for few days. It is clear from the figure that the foil with a protective C layer remains unaffected whereas the uncoated film got oxidized.

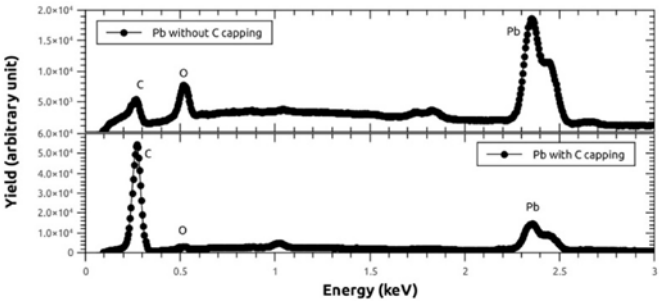

Fig. 3.1.24: EDX spectra of Pb target

3.1.5.4 Nuclear target development for collaboration experiments

^{170}Yb targets were successfully prepared for a beam time experiment of in IUAC-NAND facility. The relative abundance of ^{170}Yb is 3% and hence the cost was relatively high. As per the MoU, it was decided to develop the targets with minimum material consumption by using the expertise of target lab group in IUAC and the material was purchased by GANIL group. The experiment was proposed by GANIL group in collaboration with IUAC & BARC. The targets prepared were in the form of $^{170}Yb_2O_3$ of 200µg/cm^2 thickness with 20µg/cm^2 carbon backing. The diffusion pump based coating unit equipped with a 2Kw e-gun was used for the fabrication of carbon backing with KCl as releasing agent. After the annealing at 250ºC in 1 hour for stress relieving, the carbon slides were used as substrate for the deposition of $^{170}Yb_2O_3$. For the deposition of $^{170}Yb_2O_3$, a turbo pump based coating unit equipped with an 8kW electron was used. The available amount of $^{170}Yb_2O_3$ was only 70 mg and it was in the form powder. The isotopic material was filled and pressed in a 3mm tantalum crucible which was used as the evaporation source. Contaminations from the source and electrode material, dissimilar behaviour of isotopic and natural material were the main challenges during the fabrication. The total material consumption for making seven targets was 30mg. Many targets of 186Wwere also developed for VECC group as it was informed that they lacked the facility to prepare W target.

3.1.5.5 Fabrication, Inspection and Loading of stripper foils

More than 450 stripper foils of carbon of ~4µg/cm^2 were fabricated in this year. 14 evaporations of carbon were done in high vacuum chamber for the stripper foil. After mounting the foil on the stainless steel holder, the foils were also annealed in 200 degree for one hour. In addition to IUAC- foils, we have also prepared ~ 50 stripper foils of ~4µg/cm^2 and ~10µg/cm^2 from the carbon-coated-slides imported from Munich.

3.1.5.6 Target thickness measurement

After preparing thin films it is very important to measure their thickness. In case of free-standing thin films mostly used for experiments of Nuclear Physics the thickness are measured by Alpha particle energy loss method. Thickness of around 285 free standing nuclear targets has been measured using our facility.

For thin films deposited on thick substrates this method is not effective. For those cases a Stylus Surface Profilometer Model No.: Bruker DektakXT is used with features:

1. Stylus Force: 1 – 15 mg, 0.3 – 15 mg (N-Lite)
2. Scan Length: 55 mm.
3. Vertical Range: 1 mm
4. Vertical Resolution: 1 Å
5. Max. Sample Thickness: 50 mm

More than 121 samples of 67 users have been entertained.

3.1.5.7 New facilities

A. Commissioning of Turbo Based E-Beam Evaporator

An e-beam evaporator has been added to the list of facilities in target lab in this academic year. It is a turbo pump based coating unit and the electron gun source with the arc-suppression is the major feature of the system. The electron gun source with the arc-suppression option is ideal for many applications, such as for optical coating and for ion plating without a pressure barrier. The reduction in arcing results in improved film quality, improved yields, and fewer arc-related maintenance issues. It can be operated at pressures < 5 X 10^{-3} mbar.

This evaporator has been used by many users. Development of NiO/Fe_2O_3 bilayer is the latest work in this facility. In conventional e-beam evaporation, it is very difficult to fabricate the oxide films due to vacuum degradation by out-gassing and sparks. The bilayer of NiO/Fe_2O_3 was smoothly deposited without any spark. The vacuum in the chamber during the evaporation was varying from 5x10^{-4} to 3x10^{-5} mbar. The thickness of NiO and Fe_2O_3 deposited on the silicon substrate was 100nm and 150nm respectively.

B. Commissioning of Rolling Machine

Fig. 3.1.25: Table top rolling machine

A new table top rolling machine was recently commissioned in target lab as shown in Figure 3.1.25. The heavy load in the old machine and its frequent breakdown were the major reason for the procurement of new machine. In addition to its compactness in size, it has precise control for roller adjustment which is useful in the fine control of foil thickness and uniformity. The machine is already in regular use for the target development.

C. Compact, user friendly Alpha Energy Loss Target Thickness Measurement Setup

A compact, user friendly Alpha Energy Loss Target Thickness Measurement setup is commissioned to replace the old setup. The main problematic part was cylindrical target chamber where one had to load the foils, and mount the alpha radiation source (Am-241) and SBD detector. After completing measurement thickness of a batch of maximum of 5 foils, one had to remove whole assembly containing of alpha radiation source and SBD detector. There was high risk of damaging the SBD detector and get contaminated from alpha radiation source during this process. A new setup was built with many existing vacuum components with some items machined in IUAC Workshop. In this setup at a time 5 targets can be loaded on a target ladder, which is mounted on a linear motion feedthrough. The alpha radiation source is mounted in bottom and SBD detector is mounted in top flange. In the side flanges, vacuum pumping and a view-port are installed. A new advanced 4K MCA was purchased along with a laptop. The Linux based MCA software purchased along with the hardware was integrated with the laptop and finally a compact system housed on a 19" rack resulted as shown in Figure 3.1.26. Thickness of around 285 free standing nuclear targets has been measured using this new setup.

Fig. 3.1.26: Alpha Energy Loss Target Thickness Measurement Setup

3.1.5.8 TEM Sample Preparation Facility

TEM sample preparation facility is fully functional and up to now ~40 sample has been prepared these includes both plan view and cross sectional samples. Several samples are prepared for the performance test of the TEM during its installation process. The grinding of samples is major and most time consuming step for TEM sample preparation. To reduce time for grinding and polishing a machine is purchased. This machine has facility to adjust rotation speed, fluid flow during grinding and the ease of changing grinding and polishing paper. This will be an additional facility with the existing manual setup.

3.1.5.9 TEM Facility

The ordered TEM, JEOL Model No. is JEM F200 was delivered and TEM was unloaded form container on 21st November 2017, In the month of December 2017 the instrument was shifted to the room specially modified as per installation requirement from JEOL.

From 15th January 2018 onwards, installation was going on in many steps. The main things which have been done in hardware installation part are cabling the main TEM column to power supply console and other parts, connecting vacuum system, gate valve unit, air compressor, water chiller. Then software installation and calibration to devices part is over. JEOL main controlling software has been installed. Gatan 4k x 4k resolution camera has been installed. EDXS has been installed and software calibration has been done on 16th March 2018.

From 2nd July 2018 onwards, basic TEM training was started and over within two weeks. Many samples have been characterized using TEM for training purpose. TEM facility is now open to the users on trial basis. Up to now 4 user samples have been characterized. The Figure below shows the TEM at present form. The HR-TEM image of Ge shown in Figure (a) and the FFT of the image is shown in Figure (b). The SAED pattern is shown in Figure (c). Figure (d) shows the line scan of the Figure (a) indicating the intensity contrast of lattice fringes with peak to peak distance of 0.289 nm. The cross section sample is prepared using our facility with ion milling performed at -40ºC.

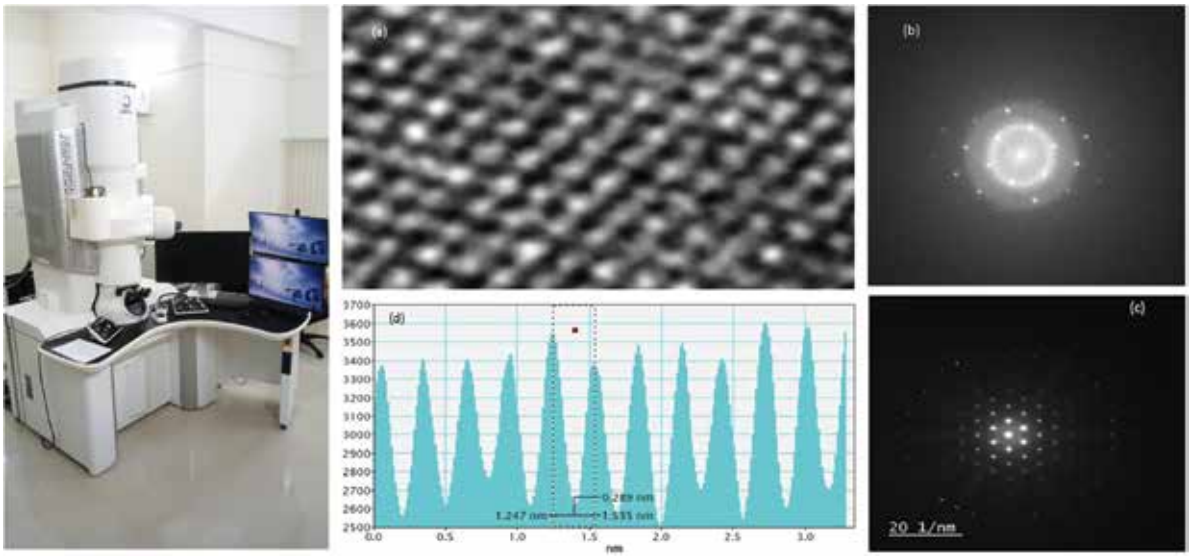

Fig. 3.1.27: (a) HR-TEM image of Ge, (b) FFT, (c) SA ED pattern and (d) line scan of the Figure 5(a)

Training on Target Fabrication

Being a very important user support laboratory, training for one month is mandatory as a part of year-long training program for newly appointed Scientist Trainees. This year training on target fabrication has been extended to five Scientist Trainees.

Target lab was successful in delivering many thin film samples and nuclear targets for IUAC users and other research groups in nuclear physics. Most of the instruments in target lab for target development are well utilized by users. The plan to run the TEM as full functional user support facility is underway.

REFERENCE

[1] Khushboo et al. Vacuum 145 (2017) 14-18
[2] A. Banerjee et al. Nuclear Inst. and Methods in Physics Research, A 887 (2018) 34–39
[3] T. Banerjee et al. Vacuum 144 (2017) 190-198
[4] Kavita et al. Vacuum 145 (2017) 11-13
[5] S. Ghosh et al. Nuclear Inst. and Methods in Physics Research, B 402 (2017) 358–363
[6] R. Mahajan et al. Vacuum 150 (2018) 203-206
[7] Abhilash S R et al., Proceedings of the DAE Symp. on Nucl. Phys. 62 (2017)
[8] S. Sanila et al., Proceedings of the DAE Symp. on Nucl. Phys. 62 (2017)
[9] Kavita Chauhan et al., Proceedings of the DAE Symp. on Nucl. Phys. 62 (2017)
[10] K. Rojeeta Devi et al., Proceedings of the DAE Symp. on Nucl. Phys. 62 (2017)
[11] Neeraj Kumar et al., Proceedings of the DAE Symp. on Nucl. Phys. 62 (2017)
[12] Neelam et al., Proceedings of the DAE Symp. on Nucl. Phys. 62 (2017)

3.1.6 RF & Electronics Laboratory

Arti Gupta, Bhuban Kumar Sahu, Deepak Kumar Munda, Kundan Singh, Mamta Jain, Parmanand Singh, Prem Kumar Verma, S.Venkataramanan and Ajith Kumar B.P

High Density Scanning 12-Bit Analog-to-Digital Converter VME board for control system applications

A new high density Versa Module Europa (VME) 6U module, SADC64, featuring 64 channels each one capable of scanning multi-range DC analog signals from beam line components, has been developed indigenously for accelerator control system applications at Inter University Accelerator centre (IUAC). Each independent channel is hardware protected from signal polarity reversal and over range voltage inputs. The complete board control logic and complexity of VMEbus slave interface logic is designed and implemented on single FPGA (Field Programmable Gate Array) device to pack the density of 64 channels on a single width VME board. Other functions like firmware revisions, board ID, control and status register are implemented on same FPGA. The firmware will be written as industrial standard HDL (hardware description language), which can be ported to the latest commercially available FPGAs. The modular design of this VME board reduces the amount of time required to develop other custom modules for control system. The VMEbus slave interface is written as a single component inside FPGA which will be used as a basic building block for any VMEbus interface project. The separate document will discuss the complete design and implementation of scanning 12-bit analog-to-digital VME module and its application in the tandem and heavy ion linear accelerator (LINAC) control system. The 4-layer PCB has been designed in-house and got it fabricated from commercial vendor. The firmware design will be implemented on Xilinx Spartan3 FPGA.

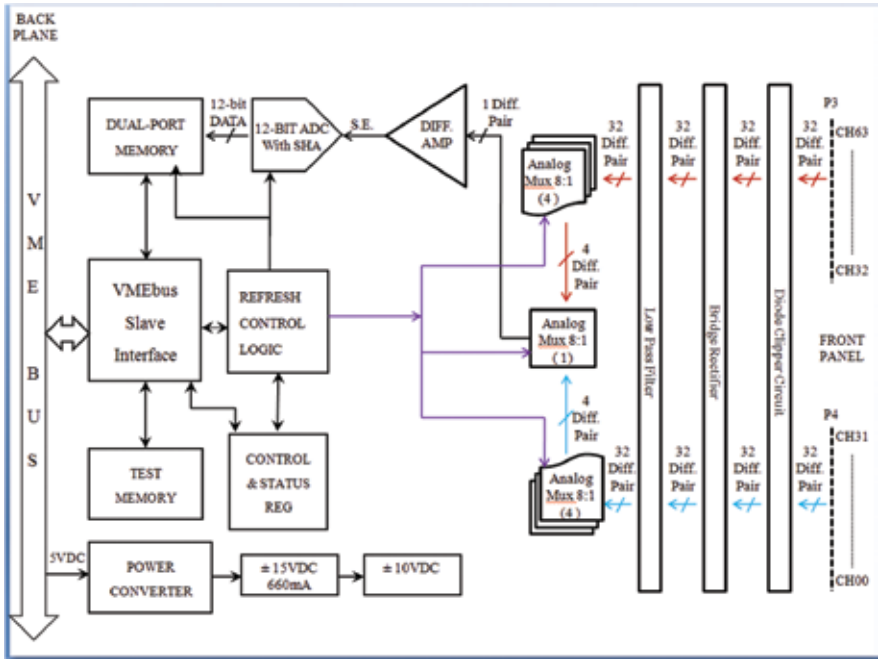

Fig. 3.1.28

Charge Sensitive Pre-amplifier for INGA type clover detector

We have continued to work this year, on various charge sensitive pre-amplifiers developed for clover type HPGe detectors of Indian National Gamma Array (INGA). The pre-amplifier type 823 which was prototyped and characterized during last year, were individually tested with a clover detector and gamma radiation source. All the in-house manufactured pre-amplifier cards were tested for long term stability (24 hours), noise contribution and manufacturing defects and documented before handing over them to the user.

Typical resolution obtained when tested with gamma radiation source Cobalt-60 are, 1.42keV (Pulser), 2.1keV (1173keV) and 2.4keV (1332keV). The pre-amplifier type 822 was redesigned and tested with a clover detector and gamma radiation source for long term stability, resolution and manufacturing defects. Typical resolution obtained when tested with gamma radiation source Eu-252 are 1.4keV (Pulser), 1.5keV (121.7keV) and 2.2keV (1408keV).

Photo multiplier tube (PMT) base for NAND array at IUAC

Spare PMT bases with built-in voltage divider network, Charge sensitive preamplifier for NAND detector array have been assembled, integrated and tested. These bases (5 numbers) will be used with spare detectors purchased for NAND array.

Spectroscopy cum discriminator module for Silicon Surface barrier (SSB) detector

General purpose, single width dual channel NIM electronics module for energy spectroscopy with SSB detector was developed earlier and reported in annual report 2011. This module is proven to be very useful for experimenters in IUAC as it outputs high quality signals and simplifies experimental setup. During this year 7 such modules were wired, assembled and tested, and they are being used with various experimental setups.

Electronics for Charge particle detector array (CPDA) at IUAC

During this year we have continued to work on front-end electronics for Charge particle detector array (CPDA) which was reported in the last annual report. We have tested the array in final configuration with limited number of available detectors (6 nos.) and front end pre-amplifiers, in vacuum to assess the long term stability of electronics. The installed CsI(Tl) detector has a thickness of 3 mm with an active area 20 mm × 20 mm and is coupled to a Si-PIN photodiode S3590-08. The array is installed in a quasi-spherical aluminium vacuum chamber wherein the signal and DC supply connections are routed through hermetically sealed 32 pin connectors. The CsI(Tl) detector array was tested with alpha source (Am-241) while maintaining the chamber vacuum around 1.1×10^{-4} Torr, for 5 days and typical resolution obtained with individual detectors were around ~6% as reported earlier.

Multichannel TAC NIM module

Three channel, single width, Time to Amplitude Converter (TAC) NIM module has been successfully developed and duplicated in limited numbers for nuclear physics experimental applications. The module also has additional block of logic Gate & Delay (GDG) generator for delaying the START/STOP signal of TAC unit. The module can be used to convert time difference of 100 ns to 5000 nS to a corresponding 0-10V linear (wagon type) analog output of varying durations. The specification of this module is given below.

Specifications of Time to Amplitude Converter module

Input Logic signals	:	Fast NIM logic (-16mA / 50 ohms) START, STOP inputs with <50nS duration
Output signal	:	Positive Linear (wagon type) output 0-10V
TAC Type	:	Hybrid micro chip BMC1522 of M/s.BEL make
Range	:	100 nS, 200 nS & 500 nS Jumper selected internal / 3 way switch- Panel selected
Multiplier	:	x1, x5 & x15 times of above range 3 way switch- Panel selected
Dead time selection	:	2.5uS or 8uS 2 way switch - Panel selected
Indicator	:	LED (5mS) blink indicates presence of STOP signal

Gate & Delay Generator

Input & Output	:	Fast NIM logic (-16mA / 50 ohms) signals with <50nS duration
Delay control	:	50nS to 2000ns in two ranges (jumper selected)
Width control	:	75ns to 500nS (PCB adjustable)

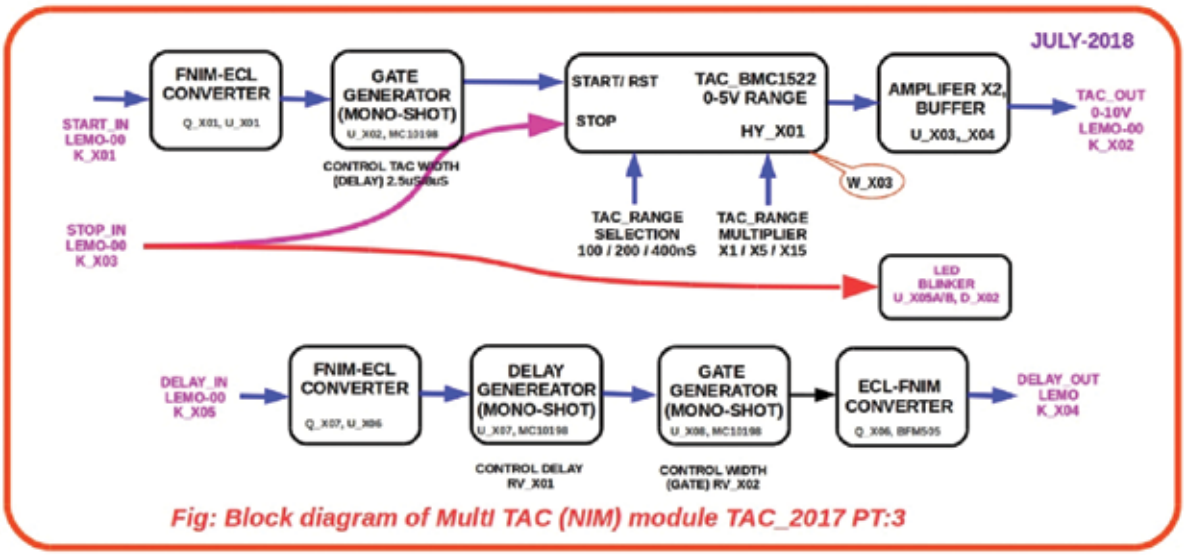

Fig. 3.1.29

Status of 400W, 97MHz Solid State RF Power Amplifier for LINAC

Superconducting LINAC cavities are being powered by in-house developed 400W, 97MHz solid state RF amplifiers. During operation of LINAC campaign between April-September 2017, 4 such amplifiers were found to be malfunctioning and replaced with spare amplifiers. After this Linac campaign, all these amplifiers were taken up for preventive maintenance. After visual inspection, the amplifiers were tested for the performances. It was found that, nearly 16 amplifiers have potential problem of complete failure due to corrosion, dust accumulation, rusting and formation of salt layer of crucial parts such as printed circuit boards, trimmer capacitors, voltage controlled attenuators due to moisture. Some of these amplifiers were partially operational due to RF MOSFET failure, damaged RF power combiner and broken RF dummy load of power splitter/combiner. All these defective parts were replaced with new components, interlock checked and recalibrated. The amplifiers were installed in the system after full power test. Sufficient spare amplifiers are available for replacement during operation failure.

RF Power Amplifier for Multi-Harmonic Buncher (MHB)

The Multi-harmonic buncher of High Current Injector (HCI) at IUAC is optimized to operate at 12.125 MHz, 25.250 MHz, 36.375 MHz and 48.5MHz. A broadband RF power amplifier has been developed with the following specifications for boosting these frequency components before supplying them to Multi-Harmonic Buncher of (HCI). The power amplifier has the capability to amplify these frequency components with minimum distortion order to realise sawtooth shape waveform before feeding it to buncher electrode. The desired power level is achieved using three stage power amplification, pre-driver, driver and power amplifier as shown in the block diagram. Off the shelf available SMPS units are used to power the amplifier blocks. A CATV module QBH2832 is used as a wide band pre-driver with high gain (+35dB) followed by a RF MOSFET MRF151 working as a driver amplifier. The main power amplifier stage consists of MRF151G, biased as class A amplifier. The input and output impedance of the amplifier are matched using wide band transmission line transformers which are loaded with ferrite cores. The RF switch at the input of the amplifier is used to divert the input power to a dummy load, in order to protect the amplifier from damaging conditions such as excess drive, over temperature and high VSWR at the output. The amplifier is assembled on a half inch thick copper heat spreader and mounted on water cooled aluminum heat sink. The amplifier has been characterized for various crucial parameters and burn in tested for a week. The amplifier has been installed and commissioned with MHB of HCI.

Specifications:

Power Output	:	100W (CW)
Power Gain	:	>65dB
Gain Flatness	:	+/- 1.5dB
Band with	:	10MHz – 50MHz (Peaking at 26 MHz)
Efficiency	:	24% (DC-RF)

Harmonics measured at 100Watts power output

for 12.125 MHz input : -14 dBc down (2^{nd}), -37 dBc down (3^{rd}), -23 dBc down (4^{th})

for 24.25 MHz input : -37 dBc down (2nd), -30 dBc down (3rd), -45 dBc down (4th)
for 36.375 MHz input : -38 dBc down (2nd), -23 dBc down (3rd), -43 dBc down (4th)
for 48.5 MHz input : -30 dBc down (2nd), -23 dBc down (3rd), -44 dBc down (4th)

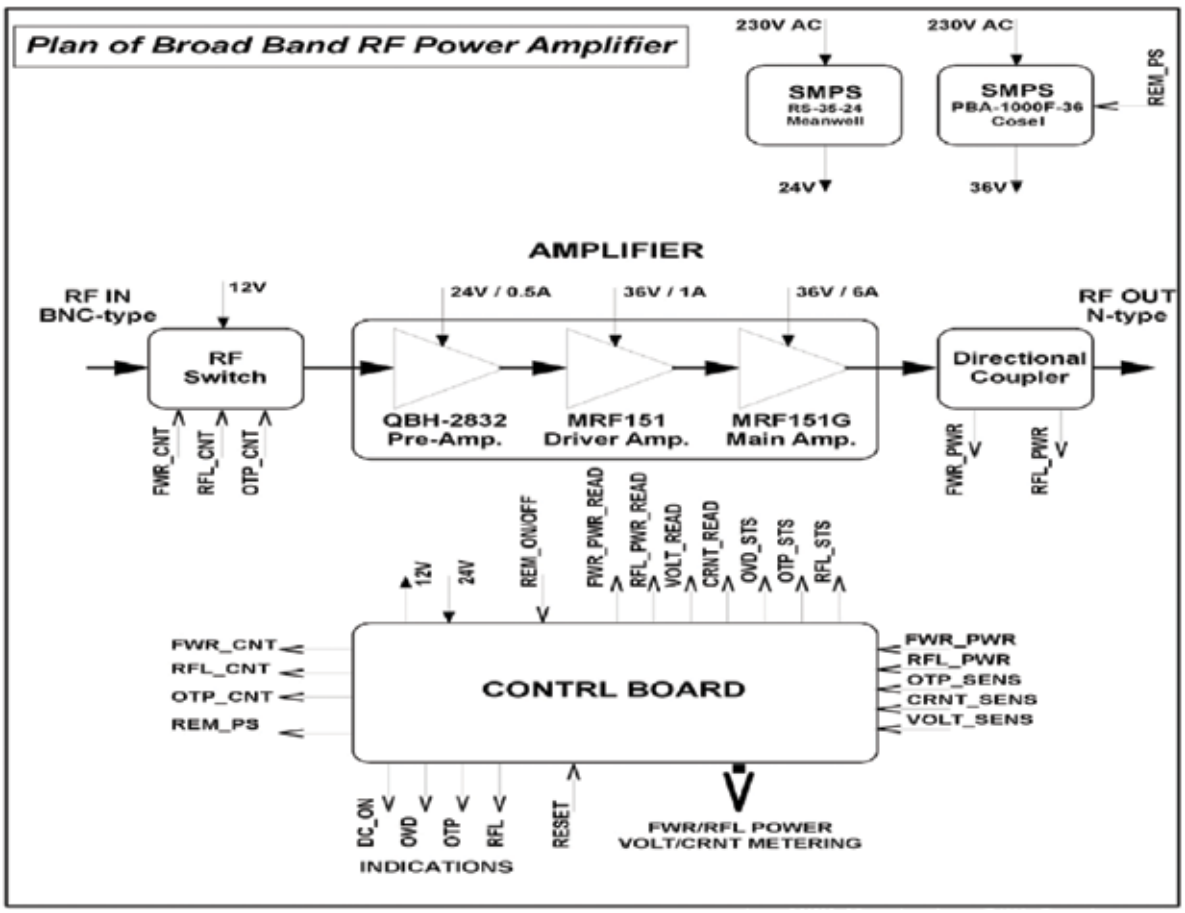

Fig. 3.1.30

3.1.7 Health Physics

Debashish Sen and Birendra Singh

Health physics group takes care of the radiation safety aspect of the Accelerator Centre. Along with this, radiation safety related research and development work is also carried out by users from different Universities & Institutes. Routine maintenance of door interlock and radiation monitors is done regularly to keep a vigil on the overall radiation safety.

Many university faculties and research scholars are using the facilities (gamma irradiation chamber, TLD reader, electrochemical work station etc.) developed and maintained by this group. A few of the research scholars have completed their Ph.D. using the facilities and a few research scholars are continuing to do so.

Facilities like Gamma irradiation chamber, TLD reader, Electrochemical work station, Furnace are open for different users from universities and Institutions. Users are from Delhi University, J N University, IIT Delhi, Shiv Nadar University, I P University, AIIMS, Amity University, NIT Jalandhar, Anna University, Nagpur University, Kolhapur University etc. The gamma chamber is working fine after being successfully relocated to a different place within the office premises. Permission for the trial run of the AMS facility has been received. It was subjected to some particular safety measures which have already been implemented. The Site approvals for the upcoming FEL (Free Electron Laser) & HCI (High Current Injector) facilities in IUAC have also been received, but the approvals for design & construction of these two facilities are yet to be received. Regular status reports for the Gamma irradiation chamber, Pelletron and RBS facility is being sent to AERB. All dose records are maintained and are also available online.

Majority of Gamma/X ray monitors/ surveymeters/ pocket dosimeters have been calibrated this year. Also the door interlock system of 255 mL underwent thorough repair.

The Health Physics Laboratory was relocated to a new location in IUAC, as the original location was utilized to set up TEM Facility.

3.1.7.1 e-LORA facility of AERB

Debashish Sen and Birendra Singh

Electronic Licensing Of Radiation Applications (eLORA) System is an e-Governance initiative by AERB. It is a basically a web-based application for automation of regulatory processes for various Radiation Facilities in India. The system is aimed at achieving paperless licensing of Radiation Facilities. The objective of the project is to enhance efficiency and transparency in the regulatory processes of AERB.
Following procedures has been carried out using this E-LORA facility:

- Submission of siting, design & construction request of a radiation facility
- Renewing license of a radiation facility
- Informing safety status of radiation facilities at regular intervals
- providing details of the radiation monitors used in the facility along with their calibration dates and other details
- providing details of radiation sources in custody of IUAC
- procurement of new radiation sources
- non compliance of any safety measures and its rectification
- Renewal of tenure of IUAC Radiation Safety Officers.

3.1.7.2 AERB Approval for different upcoming radiation facilities of IUAC (regarding radiation safety aspects)

Debashish Sen

A. Accelerator Mass Spectroscopy (AMS) facility
The design & construction, along with trial run approval has been sanctioned. Shielding aspects has been taken care of and approved by AERB. But the final approval is yet to be received.

B. Free Electron Laser (FEL) Facility (Delhi Light Source (DLS))
The Site approval has been sanctioned. The design & construction approval application has been submitted. Shielding calculations are also in the final stages.

C. High Current Injector (HCI) Facility (comprising of the high temperature superconducting electron cyclotron resonance ion source (HTS-ECRIS called PKDELIS))

The Site approval has been sanctioned. The design & construction approval application has been submitted. Shielding calculations are also in the final stages.

Beam Hall III was surveyed thoroughly, with four RF power levels 100, 400, 700 and 920 Watt. The whole area was thoroughly monitored. The staircase area (downstairs from the control/data room) and the control console area is completely safe from radiation point of view (<50 µR/hr, even with maximum power). The points A, B, C marked in the picture are the radiation-wise most hot points in the beam hall, but still they do not cross 350 µR/hr with maximum power (permissible for radiation workers is 1000 µR/hr). Point D behind the glass back door of the cage however shows non permissible radiation level, which can be brought down to safe level by using a movable lead shield covering the glass door.

Hence, with all lead shields in proper position (as per diagram), the HCI Beam Hall is completely safe for a radiation worker outside the source cage. No extra shielding is necessary. However, entry of non radiation workers should be restricted. The average radiation level even with maximum power is well below the permissible limit. But radiation workers should ensure using radiation badges as a compulsory measure.

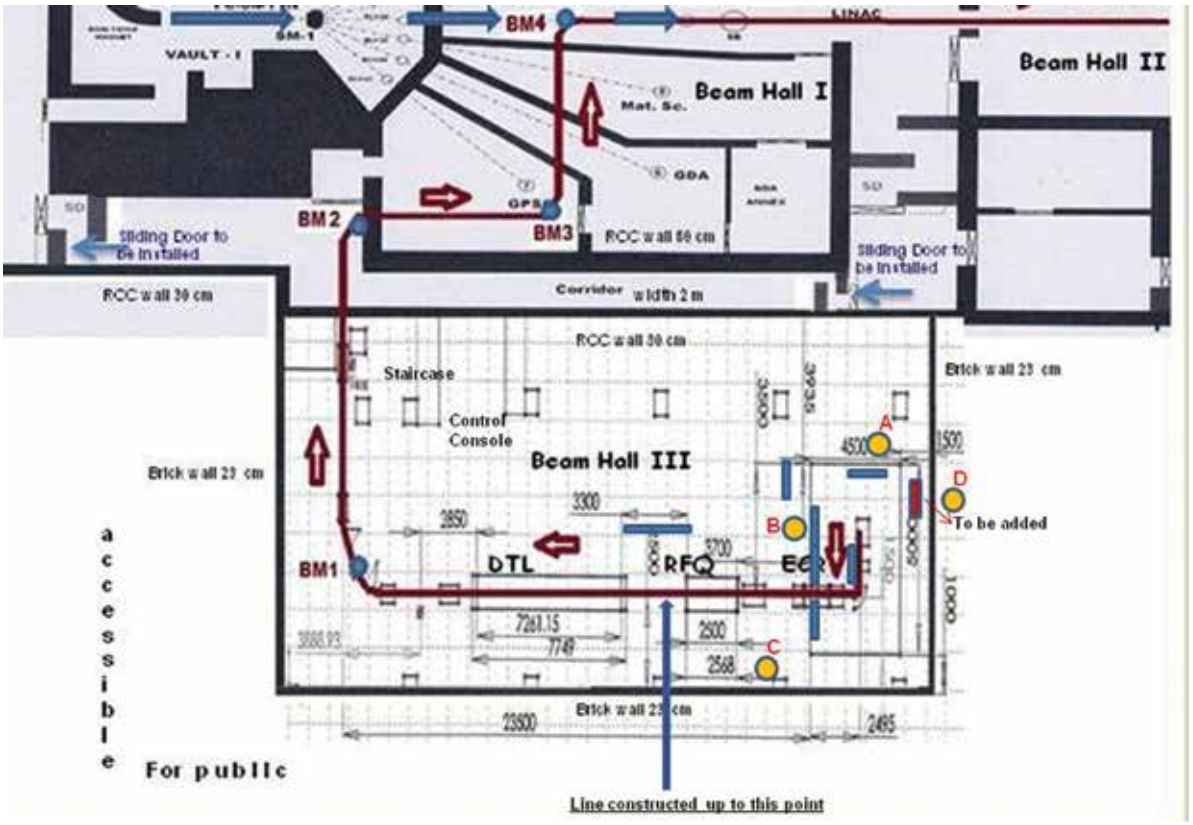

Fig. 3.1.31

Keeping the ALARA (as low as reasonable achievable) principle of radiation safety in mind, unnecessary exposures should be avoided. In future, when the total system will be operative, the control console may be moved out of the beam hall III, or may be parallelly run from a remote control console, depending upon the persisting radiation levels.

3.1.7.3 Investigating Thermoluminescent Properties of Nanocrystalline Lithium Borate Doped with Dysprosium

Kanika Sharma[1,*], A. Pandey[1], Vibha Chopra[2], Shaila Bahl[3], Pratik Kumar[3], S. P. Lochab[4] and Birendra Singh[4]

[1]Department of Physics, Sri Venkateswara College, University of Delhi, Benito Juarez Road, Dhaula Kuan, New Delhi 110021, India.
[2]P.G. Department of Physics and Electronics, DAV College, Amritsar, Punjab 143001, India.
[3]Medical Physics Unit, IRCH, AIIMS, New Delhi 110029, India.
[4]Inter-University Accelerator Centre, Aruna Asaf Ali Marg, New Delhi 110067, India.

The thermoluminescence (TL) properties of nanocrystalline $Li_2B_4O_7$:Dy was investigated. The TL properties of the said phosphor are of great interest as it has an effective atomic number close to that of a biological tissue. The phosphor is synthesized by combustion method and characterized by X-ray diffraction and transmission electron microscopy. When the nanophosphor is exposed to a range of gamma doses using cobalt-60, it exhibits a linear TL response for an extensive range of doses. Further, the reproducibility and batch homogeneity properties are also studied. In conclusion, nanocrystalline $Li_2B_4O_7$:Dy shows potential as a radiation dosimeter of gamma rays.

3.1.7.4 $BaSO_4$:Eu as an energy independent thermoluminescent radiation dosimeter for gamma rays and C^{6+} ion beam

Kanika Sharma[1,*], Shaila Bahl[2], Birendra Singh[3], Pratik Kumar[2], S. P. Lochab[3] and A. Pandey[1]

[1]Department of Physics, Sri Venkateswara College, University of Delhi, Benito Juarez Road, Dhaula Kuan, New Delhi 110021, India.
[2]Medical Physics Unit, IRCH, AIIMS, New Delhi 110029, India.
[3]Inter-University Accelerator Centre, Aruna Asaf Ali Marg, New Delhi 110067, India.

$BaSO_4$:Eu nanophosphor is delicately optimized by varying the concentration of the impurity element and compared to the commercially available thermoluminescent dosimeter (TLD) LiF:Mg,Ti (TLD-100) and by extension also to $CaSO_4$:Dy (TLD-900) so as to achieve its maximum thermoluminescence (TL) sensitivity. Further, the energy dependence property of this barite nanophosphor is also explored at length by exposing the phosphor with 1.25 MeV of Co-60, 0.662 MeV of Cs-137, 85 MeV and 65 MeV of Carbon ion beams. Various batches of the phosphor at hand (with impurity concentrations being 0.05, 0.10, 0.20, 0.50 and 1.00 mol%) are prepared by the chemical co-precipitation method out of which $BaSO_4$:Eu with 0.20 mol% Eu exhibits the maximum TL sensitivity. Further, the optimized nanophosphor exhibits a whopping 28.52 times higher TL sensitivity than the commercially available TLD-100 and 1.426 times higher sensitivity than TLD-900, a noteworthy linear response curve for an exceptionally wide range of doses i.e. 10 Gy to 2 kGy and a simple glow curve structure. Furthermore, when the newly optimized nanophosphor is exposed with two different energies of gamma radiations, namely 1.25MeV of Co-60 (dose range- 10–300 Gy) and 0.662 MeV of Cs-137 (dose range- 1–300 Gy), it is observed that the shape and structure of the glow curves remain remarkably similar for different energies of radiation while the TL response curve shows little to no variation. When exposed to different energies of carbon ion beam $BaSO_4$:Eu displays energy independence at lower doses i.e. from 6.059 to 14.497 kGy. Finally, even though energy independence is lost at higher doses, the material shows high sensitivity to higher energy (85 MeV) of carbon beam compared to the lower energy (65 MeV of C^{6+}) and saturation is apparent only after 121.199 kGy. Therefore the present nanophosphor displays potential as an energy independent TLD.

3.1.7.5 Thermoluminescence characterization of lithium based TLD materials by using swift ions and photons

Karan Kumar Gupta[1], N. S. Dhoble[2], D Sen[3] and S. J. Dhoble[1]

[1]Department of Physics, RTM Nagpur University, Nagpur 440033, India
[2]Department of Chemistry, Sevadal Mahila Mahavidyalaya, Nagpur 440009, India
[3]Inter University Accelerator Centre, Aruna Asaf Ali Marg, New Delhi 110067, India

In this work, a study on some thermoluminescence characteristics of $LiNaSO_4$ phosphor is presented. The samples in the form of powder and pellets were irradiated at room temperature with γ-rays from ^{60}Co, ^{137}Cs and C^{6+} ion beam at energy of 75 MeV for different ion fluences in the range of 2×10^{10} to 1×10^{12} ions cm^{-2}, using a 16 MV tandem van de Graaff type electrostatic accelerator (15 UD pelletron) at the Inter University Accelerator Centre, New Delhi, India. The full details of this set up are given by Kanjilal *et al.* [1]. Thermoluminescence (TL) measurements with heating rate 5 K/s were taken using Harshaw (3500) TLD reader. TL glow curve of C^{6+} ion beam irradiated phosphor at different fluences is shown in Fig. 3.1.32d. One lower temperature peak at 105ºC and other higher temperature peak at 150ºC was observed indicating that various types of defect centres are present in LNS:Eu. The LNS doped with 0.1 mol% of Eu showed 3.8 times more sensitive than commercially available $CaSO_4$:Dy^{3+} phosphor when irradiated with a carbon ion beam (Fig. 3.1.32c and 3.1.32d).

An illustration of the TSL mechanism for the $LiNaSO^4$:Eu system is constructed and shown in Fig. 3.1.33. According to the diagram, a shallow trap level (STL) and a number of deeper trap levels (DTLs) are formed in between the forbidden band gap of the host material after γ-rays and C^{6+} ion irradiation. The depth of trap levels as shown in Fig. 3.1.33 was calculated from the Kitis equations and Chen's peak shape method [2,3]. The low temperature glow peak appeared at 103 ºC in γ-ray irradiated phosphor is arises due to the transition of trapped charges from STL (0.90 eV) to the conduction band (process 1) and their recombination with counter particles at recombination centre (process 2) as the temperature increases above 50 ºC to 110 ºC. The recombination energy was then transferred (process 3) to the Eu^{2+} ion which on de-excitation gives the TL glow curve as shown by process (4). At higher temperatures, the process was quite different firstly the deeper trapped charges absorb thermal energy and some part of the trapped charges are released from the DTLs ($1.1 \leq E \geq 1.32$ eV) and re-trapped at the STL (0.90 eV) or at lower energy DTL ($1.1 \leq E \geq 1.2$ eV), shown by process (5).

The remaining trapped charges at DTL make direct transition to the conduction band as shown by process (1) and in the course of their return journey they recombine with their counter-particles at recombination center, resulting in TL emission by transferring this recombination energy to the Eu^{2+} ion (Process 3 & 4) which acts as a luminescent centre in this phosphor and give rise to other higher temperature TL peaks at 150, 211, and 278 ºC. Second-order kinetics behavior of higher temperature glow peaks also support the hypothesis of re-trapping of charge carriers which causes the trap filling of shallower traps or lower energy deeper traps which are emptied at lower and moderate temperatures. The reason behind the 106 ºC TL peak and 150 ºC TL peak is already explained in the EPR section while the appearance of higher temperature TL peaks in the C^{6+} ion irradiated phosphor is due to the formation of deep levels which takes place because of the implantation of C^{6+} ion particles.

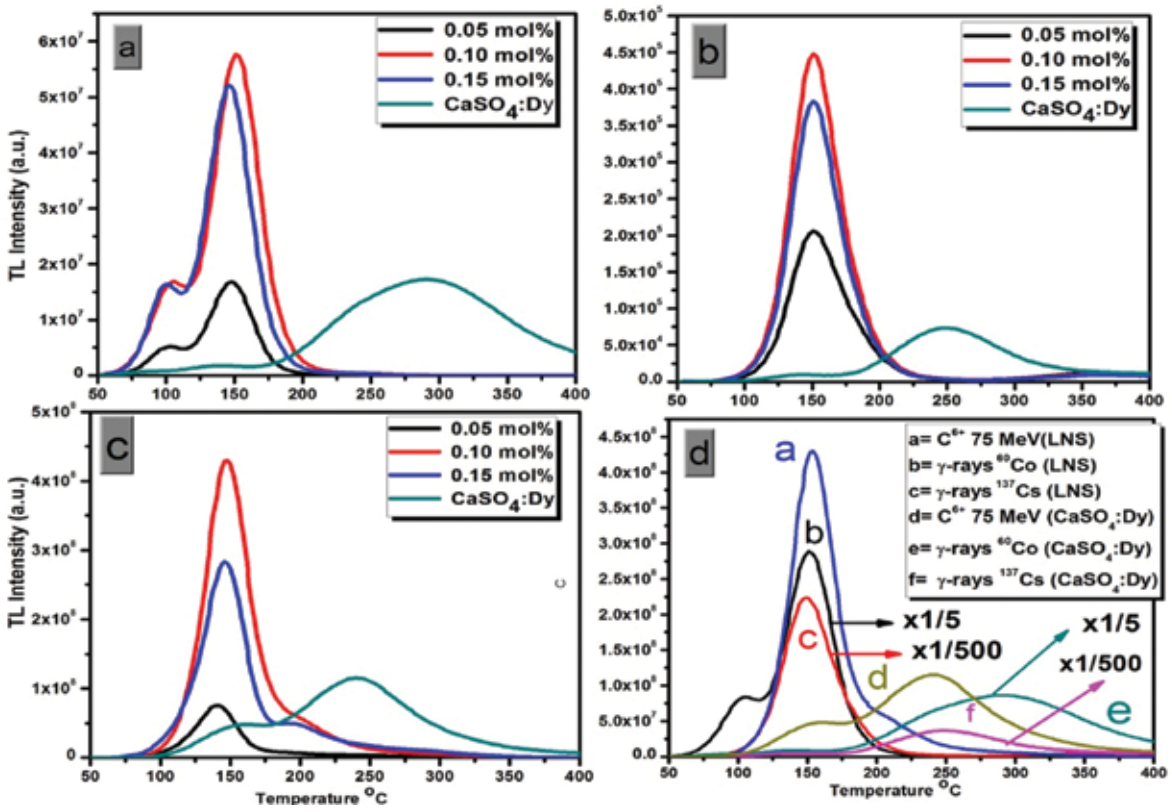

Fig. 3.1.32: TL glow curves of the LNS phosphor irradiated with (a) γ-rays from a ^{60}Co source at a 10 Gy dose, (b) γ-rays from a ^{137}Cs source at a 2200 mRad dose, (c) C^{6+} ion beam at 75 MeV with 2×10^{10} ions cm^{-2} fluence, and (d) comparison between TL glow curves of the LNS phosphor and $CaSO_4$:Dy phosphor irradiated with a C^{6+} ion beam at 75 MeV energy, and γ-rays from a ^{60}Co source at a 10 Gy dose and a ^{137}Cs source at a 2200 mRad dose. The ordinate is to be multiplied by the numbers at the curves to get the relative intensities.

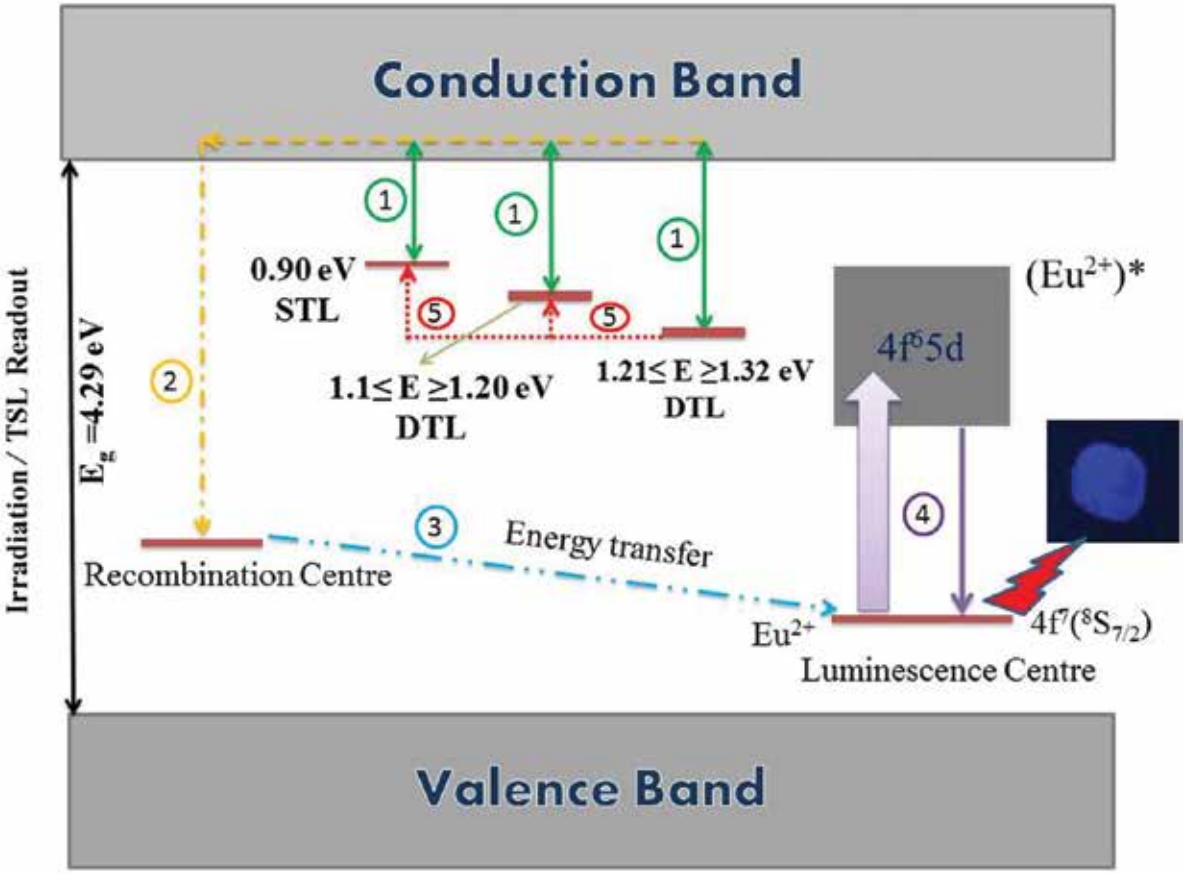

Fig. 3.1.33: The mechanism of the TSL process in $LiNaSO_4$:Eu phosphors

REFERENCES
[1] D. Kanjilal, S. Chopra, M. M. Narayanan, I.S. Iyer, J.J.R.Vandana, S.K. Datta, Nucl. Instrum. Methods A 328 (1993) 97-100.
[2] R. Chen and S. A. A. Winer, *J. Appl. Phys.,* 1970, 41, 5227–5232.
[3] G. Kitis, J. M. Gomez-Ros and J. W. N. Tuyn, *J. Phys. D. Appl. Phys.,* 1998, 31, 2636–2641

3.1.8 Data Support Laboratory

Ruby Santhi, R. Nirdoshi and P. Sugathan

Data Support Laboratory at IUAC provides (Data Acquisition) support to various users in setting up the required data acquisition & electronics setup during experiments. The lab also procures required electronic modules, co-axial connectors and cables required for user support.

In data room, two CAMAC based on-line data acquisition systems are running with LINUX based FREEDOM software using CMC 100 controllers. During the current year, many nuclear reaction experiments have been performed using CMC100 Crate Controller based DAQ in the following Beam line facilities.

- HIRA: The users studied fusion reaction studies in HIRA. Signals from the detectors were sent to the data room where data were recorded by DAQ.
- GPSC: Fission mass distribution, charged particle multiplicity, angular distribution related experiments carried out.
- ECR(2.4 GHz) ion Source: Plasma characterization.
- HCI Beam Line: Measuring X-Ray energies and off line tests.
- LEIBF Beam Line: X-ray spectroscopy experiment was performed in LEIBF.

3.1.8.1 VME based DAQ in NAND facility

Ruby Santhi, Kundan Singh

In NAND experimental facility, DAQ hardware is controlled through a VME interface and the Data Acquisition software program (Freedom and LAMPS DAQ) proceeds finally to the event building and data storage. In NAND, to accommodate more number of VME Modules, VME CRATE from M/s. w-ie-ne-r 6U VME 64 x 6023 Crate Series Model VME6023x624 procured to meet the Power requirement. V2718 (optical link bridge), CAEN V785 ADC, V775 TDC spare Modules also procured. Upgradation of Data acquisition PC: One of the rack mounted data acquisition PC OS have been replaced by Ubuntu and LAMPS with ROOT installed for data analysis. This data acquisition setup has been tested with the LAMPS and used in NAND experiments.

3.1.8.2 Data Acquisition with Wiener VM-USB crate controller

Ruby Santhi

Fig. 3.1.34

The VM-USB was chosen because of its flexibility, mesytec GUI software support and USB 2.0 computer interface. The VM-USB controller executes lists of commands (trigger stacks) upon activation of a specific trigger condition. Libusb driver compiled with Ubuntu 16.04 for VM-USB controller. Using this controller we successfully tested MADC32 VME module with Cs137 Source. MADC-32 is a fast and high quality 32 channel peak sensing ADC. It provides an 11 to 13 Bit resolution with low differential non linearity due to sliding scale method and the module has Time stamp register also. In 8 k mode it provides the high INL and resolution required for Ge detector readout. Once the command stack and readout order is defined, the VM-USB is triggered to execute the command stack (i.e. read out the data) by a NIM trigger pulse going into the front panel LEMO input "I1". Mesytec VME Software used for online and offline analysis of data and it gives Gauss fit, Rate information etc.

3.1.8.3 FPGA (Spartan -6) based Digital Emulator of radiation Sources.

Ruby Santhi, Arti Gupta

A compact prototype setup for generation of pulses emulating radiation sources events is developed. This module replaces the real presence of the dangerous source and expensive detection system and possibility to perform remote experiments independently with total health safety of experimenters. This Module generates current pulses of defined variable amplitudes (and occurrence time values that occur according to an assigned statistic distribution). The core of the system is constituted by a digital configurable device (Field Programmable Gate Array - FPGA) Xilinx Spartan 6 (XC6SLX9-TQG144) that guarantees adaptability to different simulated sources and operative conditions without hardware changes but only updating the firmware . An algorithm based on Fibonacci Linear feedback shift registers (LFSR) has been developed. It employs LFSRs to generate uniformly distributed random numbers which are then suitably processed to produce random pulses having energy characteristics of pulses generated by a neutron detector. The Random pulses from Xilinx Spartan 6 (XC6SLX9-TQG144) FPGA Xilinx Serial PROM (XCF04S) processed with NIM based board designed with 16 bit DAC and preamplifier circuits for pulse processing. The digital output of the FPGA device enters an analog front-end of classic preamplifier and the signals of different voltage levels shown in fig. 3.1.35.

Fig. 3.1.35

3.1.8.4 Servicing and Maintenance

Following modules have been serviced & made operational

- TAC/ SCA module, EG&G Ortec model 567
- 142IH preamplifier.

3.1.9 COMPUTER AND COMMUNICATIONS

S.Mookerjee, E.T Subramaniam and S. Bhatnagar

The major activities this year include a major overhaul of the Center's mail software, an incremental upgrade of the central server pool, expansion and reorganization of the Center's local network, strengthening of the internet access security mechanism to accommodate increasing numbers of mobile and wireless users, and operation and maintenance of the IUAC HPC facility.

3.1.9.1 Local area networks and servers

The local area network was extended with the addition of twenty one new wired LAN nodes, to accommodate the increasing number of desktop systems and equipment in the labs. With the wireless network also working seamlessly across all office and guest house buildings, this year saw the network traffic from the wireless LAN exceed that from the wired. Five old Extreme X350 edge switches which were more than eight years in use and had developed recurring issues were replaced with new Juniper switches. Two edge switches were added to the wired network to accommodate the new nodes, and one switch was removed from the new guest house as all network usage in this location was on the wireless network. IUAC now has a total of twenty two edge switches on the wired and twelve switches on the wireless LAN.

A major upgrade was implemented this year for the IUAC mail server. IUAC has hitherto been operating a Postfix / Dovecot / Squirrelmail mail server configured manually in-house. To add new features including shared calendars and collaboration tools, ease mail server administration and enhance security, a Linux/Zimbra based solution was evaluated last year. The solution was implemented in September 2017, and has been running successfully since then. Besides easier administration and integration of many features like calendars and group work tools, it provides a choice of modern interfaces, with one specially tailored for mobile phones. The entire mail and user database was migrated seamlessly, with practically no downtime.

With the IUAC central servers running the ERP, LTS, web, mail, firewall and DNS systems nearing end of life, four new servers were configured to replace the old servers as and when required. The new servers have 10G fiber network interfaces as against the 1G UTP interfaces in the old servers, and are expected to remove the network bottlenecks for internet and LTS access when deployed. It was also decided to switch to a configuration of fully redundant servers and core network infrastructure to ensure extremely low downtime for critical data and services; this would be implemented in the next year.

The internet traffic load went up dramatically this year with the full roll-out of the wireless LAN, as a large number of mobile devices joined the IUAC network. The number of simultaneous sessions grew from about a hundred and fifty at peak times to more than five hundred. The existing UTM system, which was capable of session-based authentication for two hundred simultaneous sessions, proved inadequate for this load, and slowed down net access significantly. As a temporary measure, the UTM was replaced by the old Linux-based software firewall, configured and updated manually in-house on a more powerful server. This is not a long-term solution, as the software firewall has performance limits and needs in-house expertise to maintain. New benchmarks for a commercial hardware firewall and UTM were finalized, and a new UTM is expected to be put in place next year.

3.1.9.2 High Performance Computing Facility

In 2008, the Department of Science and Technology sanctioned a grant of Rs. 13.54 crores to set up a high performance computing facility at the Inter University Accelerator Centre. The purpose of the grant was to provide a major computing facility for faculty and students of universities and colleges across the country. The facility has been operational since 2010, and now serves more than four hundred users from a hundred and fifty research groups in colleges, universities and institutes across the country. Fifteen new user groups started using the facility this year. Incremental software and library upgrades were made to the Intel MKL and the VASP and Quantum Espresso packages. Shell scripts for system administration were added to the pool of scripts developed in-house for monitoring and administration.

While the facility is still heavily used, with a typical load of twenty parallel and a hundred serial jobs running and as many in a wait queue, the computer servers are reaching end of life, and the cooling systems require an overhaul. The servers are maintained in-house with no software or hardware support since 2015. At the end of last year, 147 servers of the 200 compute nodes in the main production cluster k2 were live and available to users. This figure has stayed unchanged through this year. However, a major hardware problem with the Lustre parallel file system led to twenty days of downtime for the cluster; this was resolved by cannibalizing a compute node to serve as the metadata server. The cluster has since been stable. In addition to this downtime, two scheduled maintenance periods added on downtime of two weeks.

3.1.9.3 NEW GENERATION INSTRUMENTATION & ACQUISITION SYSTEM

E.T. Subramaniam, Kusum Rani and Mamta Jain

The first hand results obtained from the in situ testing stated the need for adding a hysteresis loop for the fiducial. As all the bpm's were not calibrated resulting in a dc offset, which necessitated an ac coupling for the inputs. Both were implemented as well as the software was modified to operate at the maximum update rate of 16 Hz.

Global Event-identifier Modules were developed and tested in lab in uni and multi crate configuration to be used in NIAS DAQ systems.

Simulation of Digital Time Recorder reached a level were the complexity now reached the levels of the substrate. The methodologies for compensating for the variations in die and temperature are being studied.

The 32 bit based NIAS DAQ & Control client packages were modified and / or upgraded so as is compatible with 64 / 32 bit operating systems. The existing 32 bit driver modules and server packages of bpm, aspire, ln2, candle were modified for compatibility to work with 64 bit as well as 32 bit client packages. Auto calibration module is added to CANDLE.

The multi strobed multi crate solution using in-house developed GEM modules were tested for the first in the INGA-HYRA campaign of IUAC. Probably this is the first such DAQ in India

To pursue the future NIAS DAQ systems a two pronged approach is being tried with, a) VME based high speed DAQ supporting in house development with time stamping techniques, may be add on the same for digital signal processing. In first phase, a VME controller and crate has been tested with the NiasOS (VME) via DHCP. Development of in house DAQ module is also being worked and b) develop in house development of trigger less, time stamped, universal digital signal processing modules in a tree structure. This is also envisaged with a fibre optic based event identification decision, where the query and decision traverse the the tree in a stipulated time of 3 us. This is to support decisions for future arrays, while for the time being it will be trigger less, time stamped capture and distributed storage.

Geant4 simulation of NaI, HPGe and Clover detectors were done as to get hands on with. The aim is to have a full fledged detector simulation which may be extended to run a thought experiment by adding apt modules like cascade, pace. This is being at present done with multi core SMP machines. In future it will be tried with distributed processing techniques with necessary modifications.

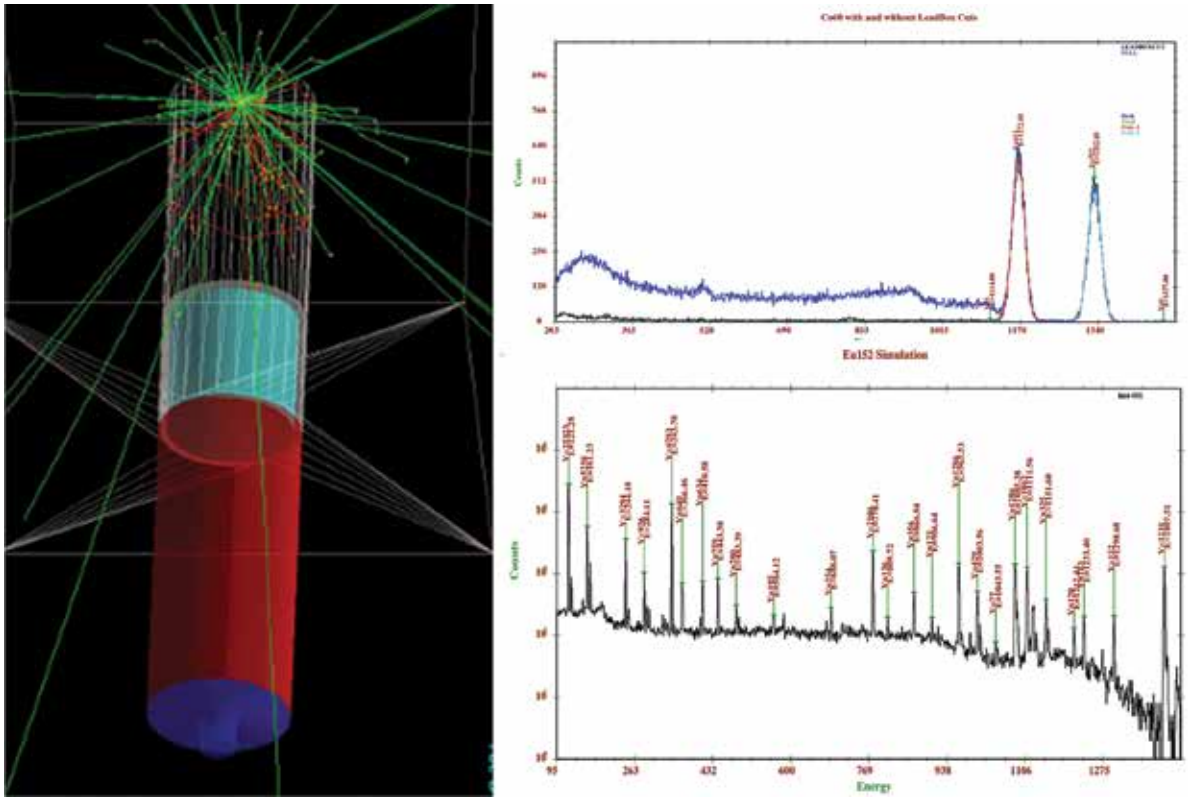

Fig. 3.1.36

3.2 UTILITY SYSTEMS

3.2.1 ELECTRICAL GROUP ACTIVITIES

U. G. Naik and Raj Kumar

This group is primarily responsible for maintaining the electrical installations of IUAC and also to develop adequate electrical infrastructure for the new scientific projects. I am happy to put on record that the uptime achieved for electrical systems was close to 100%. This was possible with judicious maintenance schedules and monitoring arrangements. This group has also successfully completed the projects and works envisaged for the year F.Y.2017-2018.

PROJECT WORKS:

ELECTRICAL WORKSFOR HIGH CURRENT INJECTOR (BH-III)

INTERNAL: Electrical group has completed the internal electrical works such as installing high current LT panels a, cables and cable trays, earthing etc. Few RFQ and DTL power supplies have been tested with new setup and testing of other power supplies is in progress.

EXTERNAL: Electrical Compact substation of capacity 1600KVA has been planned. Design has been done in-house and order has been placed for the same with completion date 2nd March 2019.

ROOF TOP SOLAR SYSTEM FOR IUAC

Roof top grid interactive 2*50 kWp solar power generation plant is fully installed and operational. Peak power generated in any particular day has reached 650 KVAH units. Average generation is 500units.

ELECTRICAL WORKS FOR XRD AND SEM FACILITIES IN LAB-2

Electrical group have created an electrical infrastructure to over all the equipments TEM facilities after close coordination with the user. Work involved internal power cabling and lighting for the lab.

SPECIAL DEDICATED GROUNDING FOR AUDIO/VIDEO INSTALLATIONS, LIGHTING CONDUCTOR

Electrical group has designed & installed dedicated grounding system for audio and video equipments as well as special dedicated earthing network for lightning protection.

AUDITORIUM WORKS

All the works related to the auditorium have been completed and the auditorium is ready for use. Handing over process is in progress. The works that were completed during the period are: internal electrical/ PA system/ Fire detection and firefighting/ LAN/surveillance system/ HVAC/ Audio-video works/ Stage lighting/ acoustic wall paneling/ false ceiling/ false flooring/ wooden stages/ fire rated exit and entry doors

MAINTENANCE ACTIVITIES:

MAINTENANCE OF ELECTRICAL INSTALLATIONS OF SUBSTATION, OFFICE BLOCKS AND RESIDENTIAL COLONY

Maintenance of electrical installations is managed through the AMC with external agency; however all the consumables required are supplied by IUAC. M/s KBS Electricals was engaged for AMC financial year 2017-18 who have carried out the maintenance in appreciable manner.

There was not even a single event occurred for the transformers or any switch gears related to transformer HT and LT.

Dehydration of transformer oil for 7 Transformers- (4500ltrs)

- Periodic maintenance of LT panels, Distribution boards and other accessories, Lighting, Fixtures, lighting and power circuits.
- Maintenance of street lighting and earthing.

CAPTIVE POWER INSTALLATIONS

Institute had a captive power base of 2500 kVA. Three DG Sets of 750 kVA are synchronized and take care of 15UD Pelletron, He Plant and HPC Data Centre. The group has shown ever readiness in running the systems round the clock O&M activities within short period if need arises. Not even a single failure has been observed during the year. Servicing of 3nos of DG sets 750KVA is being carried out through service from the manufacturer once a year. During the current year Power command card of 750kVA DG#2 has gone bad and had been replaced with new one thru authorized service of Cummins.

VOLTAGE STABILISERS

Voltage stabilizers supporting the installations having capacities from 30 kVA to 1000 kVA are working in healthy conditions with practice of periodic maintenance and have kept 100% up time. No failure occurred during the financial year.

UPS INSTALLATIONS

IUAC has 10*60 kVA UPS, 3*300 kVA, 4*200 kVA, 1*50 kVA and around 20 nos. of 2-10KVA UPS systems maintained by electrical group. These are under supervision and control of this group. Although the day to day operations is carried out by electrical group the comprehensive AMC order have been placed on the manufacturer for all the sets out of warrantee period. Capacitors in the filter sections of rectifier and invertor section of 2*300KVA UPS sets got decayed as they have exhausted their life and have been replaced during the FY 2017-18

POWER FACTOR COMPENSATION

Electrical group is very happy to declare that yet again we achieved average power factor of 0.981 lag for the year. Our system power factor without correction is about 0.85 and by raising it we saved around Rs.142 lakhs through the year from energy saving.

FIRE DETECTION AND ALARM SYSTEM

Electrical group has been maintaining fire detection & alarm system covering whole lab complex and new guesthouse. This system has been extended in Beam Hall-II stores areas. Renovation of fire detection system has been done in Beam Hall-III as this system was giving lots of troubles. All parts of the system were maintained in good health throughout the year.

3.2.2 AIR CONDITIONING, WATER SYSTEM AND COOLING EQUIPMENTS

Piyush Gupta, A. J. Malyadri and Bishamber Kumar

AC SYSTEM / Cooling Equipment

IUAC's central air conditioning / low temperature system of Phase-1 consisting of 2x200 TR + 3x100 TR Central AC plant performed with 100% uptime. Maintenance ensured that the safety record of the plant was maintained at 100% and the power consumption kept at optimum level. 2x200 TR chillers installed in 2013 have run for 21000 hours each. Other rotary equipment logged in 208,750 continuous run hours. It is relevant to note that the Indian industrial norms specify a life of ~25,000 run-hours for compressors and ~50,000 hours for other rotating equipment. Also, the Phase-II&III, screw chiller based central AC plants performed to an uptime of 100%. The highlight of the operation and maintenance of the above systems was the in-house supervision provided to the contracts. The yearly maintenance costs were 11.07% of ARV (Asset Replacement Value). The MTBF for all the equipment were within acceptable norms. The equipment entered into their twenty-eighth year of sustained operations and has far outlived their economic lives, yet has high availability.

WATER SYSTEM

IUAC's centralized water system of Phase-I feeding low temperature cooling water having a total heat removal capacity of 115 TR performed to an operational uptime of 100%. This is due to the stringent maintenance practices, which were followed over the years. The system has overshot 163,000 hours from its expected life span. IUAC's centralized water system of Phase-II&III feeding low temperature cooling water also performed to an uptime of 100%. A strict monitoring on the water quality has ensured that the flow paths of all cooling equipment are in healthy condition. 150 KLD Sewage Treatment Plant (STP) also performed satisfactorily.

Planned Works Carried Out During the Year

Extension of Process Water SS Pipes was done in SPL & Furnace rooms behind the LEIB building. Air-Conditioning of following areas was done:

- ✓ HPC porta cabin (by providing 3 nos. of 3.0 TR Cassette type Split A/C's)
- ✓ Furnace room behind LEIB (by providing 1 no. of 2.0 TR Window A/C)
- ✓ ICPMS lab and TEM room (by providing 4 nos. of 2.5 TR Split A/C's)
- ✓ Canteen VIP dining room and adjacent party room by proving 4 nos. of 1.5 TR Split A/C's

Additionally, works such as, replacement of Ph-1 A/C plant expansion tank by SS expansion tank, Painting of MS and CHW pipes at various locations, PVC sheet wrapping over the insulation foam of evaporators on 4 nos. of chillers, etc. was also carried out. The Auditorium Air-Conditioning installation works are almost over and is expected to be commissioned soon.

3.2.3 MECHANICAL WORKSHOP

D. K. Prabhakar, B. B. Choudhary, S. K. Saini, R. Ahuja and J. Zacharias

IUAC workshop is well equipped tool room type workshop with modern machining and welding facilities to support Pelletron Accelerator, various labs of IUAC and large number of users performing experiments at IUAC

The major facilities of the workshop are Machine shop and Welding shop.

Machine Shop is equipped with a five axis Vertical Machining Centre and a CNC lathe. Apart from these, there are four conventional lathe machines, two milling machines and a Radial drilling machine catering to different types of jobs. Most of these machines are of renowned brands like HMT, Batliboi, BFW. Apart from these, one cylindrical grinder, one tool and cutter grinder, one horizontal and a vertical band saw machines, etc. are also there for general requirements.

Fig. 3.2.1

Workshop has Solid Works CAD facility for the design and drafting purpose. It also has VISI CAM for with 1.8 m inspection area with 40μ accuracy is also part of workshop for highly accurate measurement and assembly.

Welding shop is having high quality TIG welding machine and equipment. Some of the TIG machines can give pulsed arc for the thin section welding. Air plasma cutter with a capacity to cut up to 40mm thickness of stainless steel is used extensively. Oxy-acetylene cutting and brazing set ups are also available. We have a

micro plasma machine from Air Liquide, France for very thin section welding. IUAC workshop is providing Apprentice training for the ITI passed students in both welding shop as well as in machine shop. Basic workshop training is also provided for the scientist trainees and Ph.D. students enrolled in IUAC.

Some of the major achievements of mechanical workshop (MG-III)

Water cooled RFQ High Power coupler

Octagonal Scattering Chamber

Acrylic Model of MRI Chamber

Current Lead Testing

Testing of DTL

Study of 1.5T imported MRI Cryostat Arrangement for MRI

RFQ installed in HCI beam line

Fig. 3.2.2

3.2.4 CIVIL WORKS

M. K. Gupta, Harshwardhan and A. J. Malyadri

Works under Civil Section:

- Major Projects
- Minor Projects
- Minor works
- Civil Maintenence
- External cleaning of Campus
- Liasion with outside agencies for statutory approvals and various civic problems

Important Civil Activities undertaken during the year 2017-18:

Following important civil works were undertaken during the year 2016-17 in addition to routine Civil maintenance and minor works:

- Completion & taking over of Civil construction work of Auditorium (including internal electricals)
- Execution of Interior works & Audio-video works of Auditorium building(ongoing)
- Appointment of M/S RITES as PMC for New Lab. complex, an MoES project
- Planning & preparation of preliminary drgs. & estimate for New Lab. Complex project
- Waterproofing and resloping of Beam Hall-I roof to avoid seepage problem in adjacent buildings
- External & internal painting of IUAC Main building
- External painting of old Guest House complex
- Civil works for establishment of ICPMS Lab. in Engineering building Gd. floor
- Civil works for TEM installation in R.N. 101, Main building
- Civil works for covering of vacant space outside Beam Hall-II & III(ongoing)
- Construction of RCC Shade for chillers of XRD & XRF facility on backside of R.N. 105, LEIB building
- Replacement of existing damaged precast drain covers with new ones in IUAC campus
- Construction of ramps near old Guest House and Canteen for elderly persons
- Making enclosure outside Beam Hall-III on S-side for protection of BH-III equipments from dust and humidity(ongoing)
- Construction of ramps near Phase I Housing for facilitating elderly persons(ongoing)
- Design consultancy work for Water fountain in IUAC(ongoing)
- Civil works for covering of open space outside Engg. Building on W & N-side(ongoing)
- Internal painting of workshop area & corridor area in Engineering Building

3.2.5 COMPRESSED AIR SYSTEM AND MATERIAL HANDLING EQUIPMENTS

K.K. Soni and Bishamber Kumar

Group is associated with the following activities:

i) **Compressed Air System:** Compressed air plant (Ph-I & II) consisting of three nos. of screw compressors each of 115M^3/Hr capacity, 4 nos of air dryers, pre/fine/oil removal filters with capacity of 3000 lpm @ 9.00 Kg/cm^2, Storage Tank of 25 cum have been maintaining uninterrupted air supply to IUAC Lab campus round the clock throughout the year. Pneumatic connections are provided to different labs/ area/ instruments as and when required.

ii) **Laboratory Gases:** Indigenous / imported various industrial / Lab purity gases / cylinders / regulators have been made available as required in different labs from time to time.

iii) **Elevator:** Proper maintenance is carried out so that elevator is operating safely without fail.

iv) **Material Handling System :** Periodic maintenance / servicing of more than 14 nos E.O.T cranes and electric hoists of various capacity varying from 1 Tonne to 7.5 Tones are being carried out periodically to ensure there smooth, uninterrupted and safe operation.

v) **Fire Safety:** Annual refilling and periodic maintenance of all the fire extinguishers are carried out. Demonstration for use of Fire extinguishers has been arranged and all the users and IUAC employees are trained to use the fire extinguishers.

Fire extinguishers have been installed in the newly built II Floor of Lab Building. For Fire safety purpose pressurised water hydrant system including underground Water tank, electric / diesel engine water pumps have been installed. With this continuous water pressure is maintained in the water hydrant line. Wet risers, down comers, hose reels, hose pipes, boxes, hydrant branches have been provided in and around different buildings i.e. Material Science building, Engineering Building, New Guest house and auditorium.

4. EXPERIMENTAL FACILITIES IN BEAM HALL

4.1 NEUTRON DETECTOR ARRAY FACILITY (NAND) & GENERAL PURPOSE SCATTERING CHAMBER (GPSC)

N. Saneesh, K.S. Golda, Mohit Kumar, A. Jhingan & P. Sugathan

4.1.1 Experiments in NAND facility

NAND facility was fully commissioned with all 100 detectors (liquid scintillators) and associated sub systems working and the DST project was closed after submitting the project completion report and audited accounts. The facility was heavily used by Indian university users performing experiments. Major achievement during the year was the completion of seven student's PhD thesis experiments in nuclear physics research using NAND facility. Some of these experiments required heavier ions and higher energy beam and Pelletron plus LINAC facility was operated for this purpose. Seven students completed their thesis experiments during this time using NAND experimental facility. Students from Panjab University, Delhi University, Andhra University and Central University of Kerala performed multiple experiments using the facility.

These experiments involved detection of neutrons in coincidence with fission fragments produced by induced fission of heavy nuclei. The fission fragments were detected in pair of large area multi wire proportional counters (MWPC) and neutrons detected by liquid scintillators. Pulsed beam of ^{48}Ti, ^{30}Si, ^{16,18}O accelerated by Pelletron plus LINAC combination were used in experiments. Fragments masses and neutron time of flight were recorded online using VME multi parameter data acquisition system. Mass gated neutron multiplicity will be extracted from these experiments to get more insights into the dynamics of fission process in these reactions. The detailed analysis of experimental data is under progress.

There were two international collaborative experiments performed in this period. In one experiment performed in NAND facility, participation of two French Physicists was involved. The experiment was proposed by Scientist from GANIL, France as part of an international collaboration project between IUAC, BARC and GANIL. 28Si beam at three beam energy (130 MeV, 122 MeV, and 119 MeV) from Pelletron was used to measure fission fragment mass distribution and neutron multiplicity. Very low cross section events were collected to identify the onset of asymmetric fission in mass region 200.

4.1.2 Experiments in GPSC

One international collaborative experiment was performed in GPSC to measure the fission fragment mass distribution in heavy ion induced fission. This was a collaborative experiment between VECC, Kolkatta, Joint Institute of Nuclear Research (JINR) Dubna, Russia and IUAC. Experiment used pulsed 19F beam of energy 80- 95 MeV from Pelletron Accelerator and a major achievement was the beam was delivered at 15MV potential for a short duration. Measurement involved mass distribution of fission fragments looking for signatures of non-compound events in fusion-fission reactions.

4.1.3 Monte Carlo simulation of a traveling source

N. Saneesh & P. Sugathan

A Monte Carlo simulation study was attempted to model the neutron emission from traveling sources such as compound nucleus and fission fragments. Mulit particle interaction and transport code, FLUKA, was used for simulation study to address the modeling of neutron sources as a function of source energy, emission angle, mass, etc. To simulate a source whose energy spectrum is continuous, we have modified the user defined source subroutine in FLUKA accordingly. The distribution function (Gaussian, Maxwellian, etc.) in energy was realized by truncated Neumann's method where we considered two independent random numbers along X axis and Y axis to fix the shape of the distribution. Though the particle emission is assumed to be isotropic in the centre of mass frame, when source moves with a given velocity, the laboratory distribution will be subjected to kinematic focusing that changes the energy angular distribution. This was taken into account using the transformation equation between laboratory and centre of mass frame.

In the simulation, the direction of velocity of neutron source was constrained by applying a coordinate transformation by rotation with respect to the vertical axis. The multiplicity and temperature of neutron emitting sources were extracted by chi-square minimization technique which depends crucially on the fitting function and coordinate transformation. A typical energy distribution of neutrons at different directions is given in the figure. Further studies are in progress.

Figure shows the energy distribution of neutrons at θnf = 4º (blue) and 86º (violet).

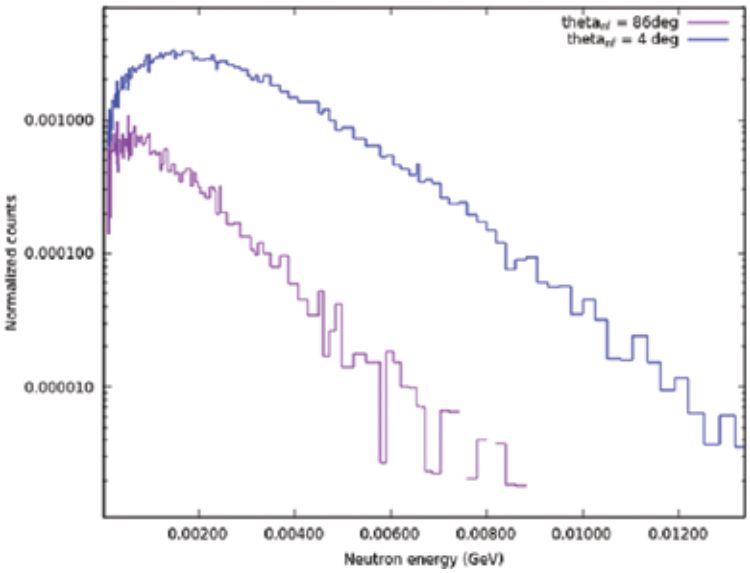

Fig. 4.1.1 the energy distribution of neutrons at θnf = 4º (blue) and 86º (violet).

4.2 GAMMA DETECTOR ARRAYS: GDA AND INGA

Yashraj, R.K. Gurjar, Indu Bala, Kusum Rani, R. Kumar, S. Muralithar and R. P. Singh

4.2.1 INDIAN NATIONAL GAMMA ARRAY (INGA)

In the last academic year two Clover and two Anti-Compton Shield (ACS) detectors were added to the INGA array at IUAC. The detectors were tested for energy resolution, peak-to-total and addback factors. The resolution of individual crystals of clover detector was about 1.9 keV for gamma ray of energy 1332 keV for amplifier shaping time of 6 microseconds. The energy resolution for each crystal at the INGA beam line was measured to be about 2.1 keV at 1408 keV (from ^{152}Eu radioactive source) at a shaping time of 3 microseconds. The addback factor was found to be about 1.5 and the resolution after addback was found to be 2.23 keV for 1332 keV peak. The timing characteristics was also measured for each crystal of the clover detectors with a BaF2 scintillator detector and the full width at half maximum of the TAC pulse was found to be about 5.6 nanosecond.

All the photo-multiplier tube outputs of the new ACS detectors were checked. The energy resolution of the ACS crystals were measured to be about 18 percent for 1332 keV gamma ray. The peak-to-total ratio for peaks of gamma lines from ^{60}Co source after Compton suppression was found to be about 40 percent after installing the detectors in the array.

Four Clover detectors from INGA array were used in GDA beam-line for experiment study of Coulomb excitation of ^{45}Sc nucleus.

Clover detector was also mounted at the HIRA target site to look for gamma rays from nuclei expected to be produced in deep sub-barrier fusion reaction.

Fig.4.2.1 Clover detector mounted at the target site in HIRA beam line to study deep-sub-barrier reaction. The detector was at a distance of about 5 cm from the target.

4.2.2 Pre-amplifiers for Clover detectors

R. K. Gurjar, Aarti Gupta, S. Venkataramanan, S. Muralithar and R. P. Singh

Pre-amplifier cards for the old and new Clover detectors were developed with electronics group. We have also performed linearity and stability tests for these cards with clover detectors in typical experimental conditions.

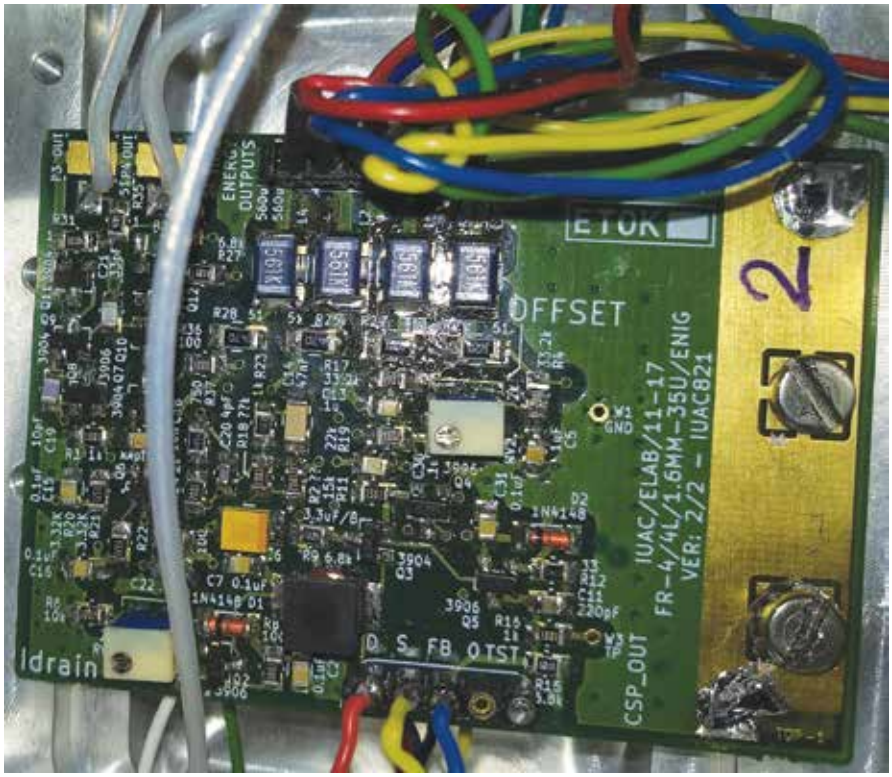

Fig. 4.2.2 Preamplifier card developed at IUAC inside the pre-amplifier housing of a clover detector.

4.2.3 LN2 filling system

R. K. Gurjar, Kusum Rani, Indu Bala, S. Muralithar and R. P. Singh

A major repair work of the INGA LN2 filling system was under taken. Apart from replacement of the faulty valves and hoses the LN2 controller card was also repaired. A new LN2 controller card is being developed.

Fig. 4.2.3

4.2.4 Gamma Detector Array (GDA)

R. K. Gurjar, Kusum Rani, Indu Bala, R. Kumar, A. Jhingan, S. Muralithar and R. P. Singh

GDA setup was used in six experiments (groups from University of Delhi, AMU, Bareily College, Central University of Jharkhand, University of Warsaw and IIT Roorkee) in the last academic year. Experiments used the HPGe detectors for study of incomplete fusion reactions with heavy ions and in one of the experiments (IIT Roorkee) one HPGe detector was used at the focal plane of HIRA spectrometer. GDA setup was also used with Clover detectors in conjunction with large annular PPAC for Coulomb excitation studies by the university of Warsaw and IUAC groups.

4.2.5 Perturbed Angular Distribution (PAD) setup

R. Kumar, P. Barua, R P Singh and S Muralithar

The cooling rings of the PAD setup in GDA beam line had developed water leaks this prevented raising the current in the coils to reach fields beyond about 5000 G. The magnet has been disassembled and process for new cooling system to be fitted in the coils is in progress.

4.2.6 New Charge Particle Detector Array

R. Kumar, Arti Gupta, T. Varughese and S. Venkataramanan

Testing of front-end electronics for the upcoming charge particle detector array (CPDA) was carried out last year with 4 CsI(Tl) detectors, supplied by the SCIONIX HOLLAND.

The CsI(Tl) detector has a thickness of 3 mm with an active area 20 mm × 20 mm, it is coupled to a Si-PIN photodiode S3590-08. Good energy resolution using the homemade pre-amplifiers and high gain electronics was achieved without vacuum as reported in last year's annual report, the next step was to perform tests in vacuum to see the stability.

The entire array is designed to be housed inside a hollow quasi-spherical aluminium chamber of thickness ~3mm. A schematic of the scattering chamber is shown in Fig 1. The chamber has an outer diameter ~ 10", so that it can be well placed inside the INGA beam-line (see Fig 4.2.4.) The thickness of wall chamber is ~3 mm which will help in reducing attenuation of low energy gamma rays. For pulse shape discrimination Ballistic deficit method was realized by comparing the output of two shaping circuits having different shaping constants (long = 3 μs and short = 1 μs).

The signals from 6 CsI(Tl) crystals were measured using electronics, developed in-house (pre-amplifier and high gain stage with differential output). A special 32 pin connector (air side plug on one side and vacuum side plug on another side: see Fig. 4.2.5) will be used to route signal and power cables from inside the vacuum chamber (preamp-detector) to outside chamber (to amplifying unit).

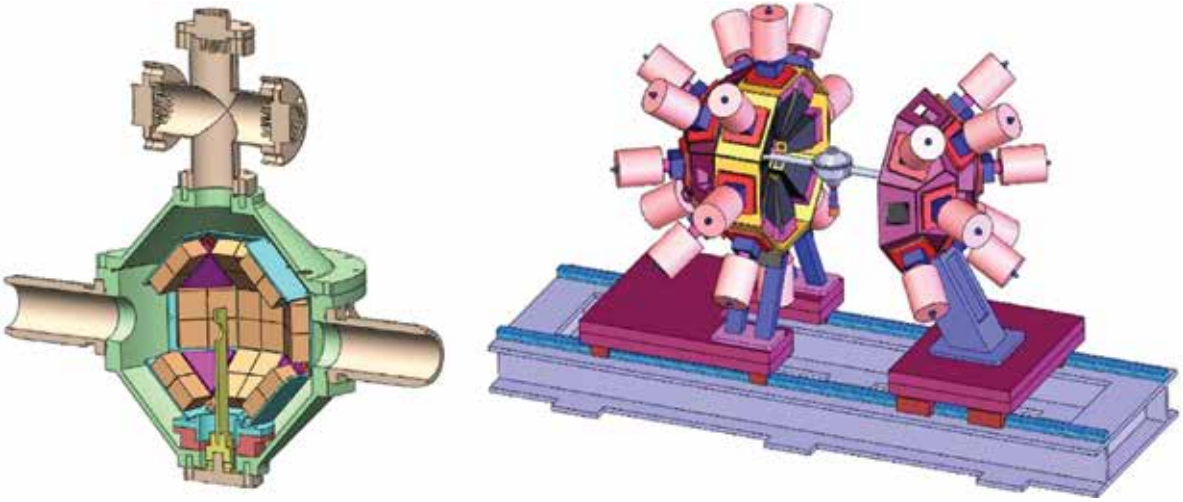

Fig. 4.2.4: Schematic of the internal view of scattering chamber (left) and inside INGA array (right)

Fig 4.2.5: Left: 32 pin connector (air side plug on one side and vacuum side plug on another side) Right: In-situ view of chamber.

Stability test was performed with 6 detectors for 5 days in Vacuum ($1.1*10^{-4}$ torr). An alpha source ^{241}Am source was used; a resolution of ~6% was achieved.

4.3 RECOIL MASS SPECTROMETERS

4.3.1 Heavy Ion Reaction Analyzer (HIRA)

S. Nath, J. Gehlot, T. Varughese and N. Madhavan

Following re-levelling of HIRA beam line last year, a series of experiments were performed to measure evaporation residue (ER) cross sections near and below the interaction barrier. A facility test was taken up to explore the capability of HIRA in measuring fusion cross sections of an asymmetric reaction deep below the barrier. Measurement could be performed down to 14% below the barrier for ^{19}F+^{181}Ta. Contamination of scattered beam-like particles in the focal plane set the limit for this measurement. No 'fusion suppression' was observed though measurements were carried out below the 'threshold' for observing hindrance in fusion, obtained from systematics. A comparative study of all the asymmetric reactions, for which deep sub-barrier fusion cross sections had been measured earlier, revealed probable roles of projectile break-up and nucleon transfer in enhancing fusion cross sections deep below the barrier. However, this observation requires further investigations.

Competition between complete and incomplete fusion and effects of low break-up threshold of the projectiles on fusion were studied in the reactions ^{6,7}Li+^{58,64}Ni. Complete fusion products were detected at the focal plane of the HIRA by a multi-wire proportional counter (MWPC) whereas an HPGe Clover detector was employed to detect the reaction products by identification of characteristic γ-rays at the target –site.

Four more user experiments were carried out to study effects of deformation, inelastic excitation and neutron transfer channels on fusion below the barrier.

4.3.2 HYbrid Recoil mass Analyzer (HYRA)

N. Madhavan, S. Nath, J. Gehlot and T. Varughese

HYRA was used in gas-filled mode in five experiments using beams from Pelletron + LINAC accelerators. While three of these experiments involved ER excitation function near and above Coulomb barrier de-exciting from heavy compound nuclei, the fourth experiment involved ER excitation function measurements combined with ER angular momentum distribution measurements at various energies using HYRA coupled to TIFR spin spectrometer. Appropriate calibration system runs were also taken to scale the transmission efficiency of HYRA for ERs according to their angular distributions.

The last experiment was to look for shape co-existence in heavy nuclei populated through alpha decay of ER and the subsequent gamma spectroscopy measurements at the focal plane of HYRA. This experiment was carried out with the participation of INGA group. For this experiment, the ERs were detected using large area MWPC detector through TOF and energy loss signals and stopped in a two-dimensional silicon detector. The subsequent alpha decay is also detected in the same silicon detector and the gamma rays emitted in coincidence were collected using a single clover germanium detector mounted closely using a re-entrant cup. The four individual crystal signals from the clover detector were collected separately from which an add-back signal (after suitable gain matching) could later be extracted.

Efforts are on to modify the focal plane detector and associated chamber which will allow use of up to 7 clover detectors for future isomer decay measurements using gas-filled mode of HYRA. The design has been finalised for the same.

Some earlier years' experimental results were published in journals and/or presented in conferences/symposia.

Ph. D. Student/Affiliation	System studied	Measurements carried out
M. M. Hosamani, Karnatak University, Dharwad	$^{16}O + ^{208}Pb$ and $^{18}O + ^{206}Pb$	ER excitation function and spin (angular momentum) distributions
P. Sandya Devi, Andhra University, Visakhapatnam	$^{16}O + ^{204,206}Pb$, $^{18}O + ^{204}$ Pb	ER excitation function
Rajesh K. K., Calicut University, Calicut	$^{48}Ti + ^{138}Ba$	ER excitation function
Laveen P. V., Calicut University	$^{28}Si + ^{188,192}Os$	ER excitation function
Akashrup Banerjee, University of Delhi, Delhi	$^{28}Si + ^{164}Er$	ER alpha decay followed by gamma spectroscopy

4.4 MATERIALS SCIENCE FACILITY

A. Tripathi, K. Asokan, V.V. Sivakumar, Fouran Singh, S.A. Khan, P. K. Kulriya, I. Sulania and R.C. Meena

The materials science facilities continue to support research programmes of a large number of users from different universities and institutions. This year there were a total of 44 user experiments spread over 125 shifts and were performed without any major beam time loss due to facility break down in materials science beamline in beamhall I. BTA experiments associated with students' Ph.D. programmes continued to get priority with 22 runs spread over 64 shifts. Though the swift heavy ion (SHI) irradiation and related experiments mostly utilize irradiation chamber in the materials science beamlines in beamhall-I, one experiment of 3 shifts utilizing in-situ XRD facility, was performed in the materials science beamline in beamhall-II and 3 other runs of 8 shifts took place in BH II. Besides this, 2 experiments of 6 shifts requiring low fluence irradiation were performed in GPSC beamline. The details of the experiments being done in areas of SHI induced materials modification and characterizations are given in Section 5.2.

Besides irradiation facilities, materials science group is also providing many materials synthesis and characterization facilities such as XRD, AFM, SEM, Raman, UV-Vis, I-V, Hall measurement etc and these are heavily utilized by users. This year more than 2100 samples were characterized.

4.4.1 Maintenance of Irradiation chambersin Beam Hall I

S. A. Khan, R. C. Meena and A. Tripathi,

The beamline with low and high temperature irradiation and in-situ measurement facilities was used by a large number of materials science users and 39 experiments of 107 shifts were performed in this chamber. There were no breakdowns this year and a faulty ion pump was replaced without any loss of user beamtime.

4.4.2 Contact angle measurement setup

I. Sulania

The contact angle measurement set-up is in regular operation (with the help of Ms Chetna Tyagi) to study hydrophobic or/and hydrophilic nature of the sample surfaces. Smooth operation requires refilling water every six months and is being followed. Nearly 150 samples from 16 users were studied using contact angle measurement.

4.4.3 Scanning Probe Microscope

Indra Sulania and A. Tripathi

The SPM facility performed satisfactorily throughout last year without any major problem. A faulty computer monitor was replaced. About 400 samples from over 60 users were characterized with SPM in different modes including 80 samples in MFM mode, 10 samples in C-AFM mode, 2 in STM mode and about 310 samples in Tapping AFM mode.

4.4.4 Field Emission Scanning Electron Microscope (FE-SEM)

S. A. Khan and A. Tripathi

TESCAN MIRA II LMH scanning electron microscope at IUAC was utilized for characterizing various types of samples from 21 users from 10 different institutes/universities. The surface morphology of a total of 81 and compositional analysis of 27 samples from 5 users were studied in energy dispersive x-ray spectroscopy mode.

Quorum Technologies Q150TS sputter coater is utilized to coat Au-Pd conductive coating to eliminate the charging effect. This year, the coater was used to deposit Au-Pd thin film on 83 such samples of 9 users.

The computer used for operation of SEM developed a non-repairable fault in its motherboard. Since the computer was quite old, its motherboard could not be replaced with a new one by the local vendors. A new replacement computer was ordered from TESCAN Brno. The computer on procurement was integrated and tested with the help from the authorized Indian engineers of the company.

4.4.5 Installation of Materials Science off-line Facilities

Ramcharan Meena, Anha Masarrat, Anuradha, Ashish Kumar, Razia Nongjai and K.Asokan

Last year, we have installed two facilities (a) Rapid thermal annealing (b) Magneto-resistance set up

(a) Rapid thermal annealing:

Rapid thermal anneal (RTA) is a subset of Rapid Thermal Processing. It is a process used in semiconductor device fabrication to modify the electrical properties. This heat treatment is designed to activate dopants, change film-to-film or film-to-wafer substrate interfaces, densify deposited films, change states of grown films, repair damage from ion implantation, move dopants, to drive dopants from one film into another or and from a film into the wafer substrate. Rapid thermal annealing is performed by equipment that heats a single wafer at a time using lamp based heating. Unlike furnace anneals they are short in duration, processing each wafer in several minutes.

The present RTA system can go up to 1000ºC, within short period of time, 10-15 sec. It is having 18 halogen lamps that heat up very sudden. The maximum sample size is 3 inch. The temperature uniformity is around ±1ºC. The annealing can be done in four mediums- (Vacuum, Ar, N_2, O_2). The pressure of gas can vary from 0 SCCM to 1000 SCCM. Vacuum is of the order ~10^{-3} mbar, which is done with the help of rotary pump.

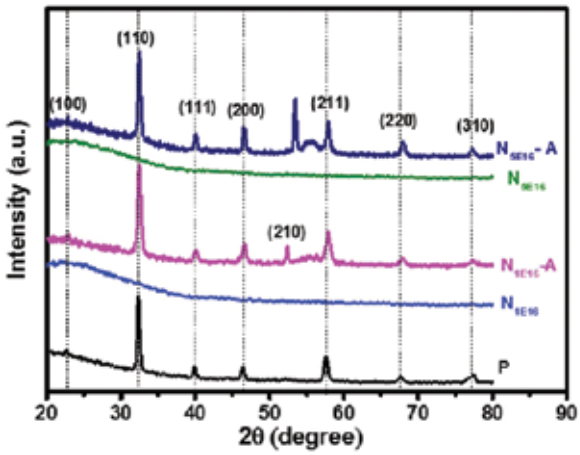

Fig. 4.4.1: X-Ray Diffraction patterns of P, Implanted and RTA implanted STO thin films.

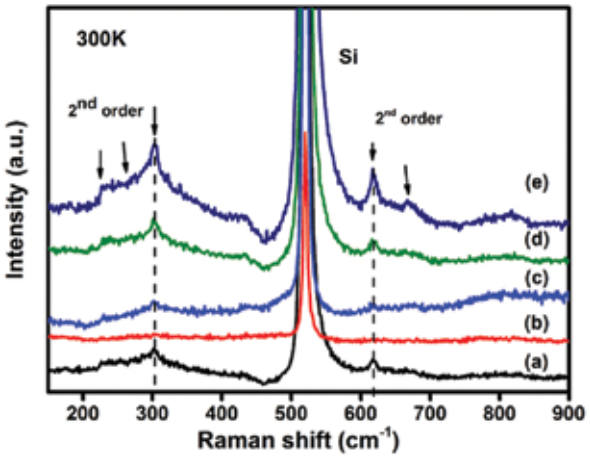

Fig. 4.4.2: Raman spectra of (a) P, (b) N_{1E16}, (c) $N_{5E1}6$, (d) N_{1E16} –A, (e) N_{5E16} –A

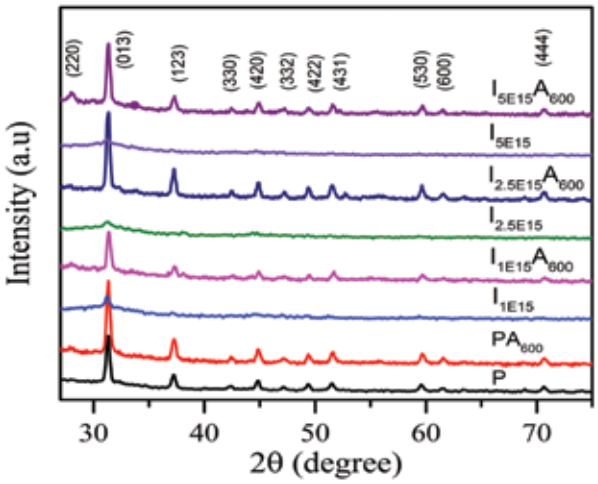

Fig. 4.4.3: XRD pattern of $CoSb_3$ thin films

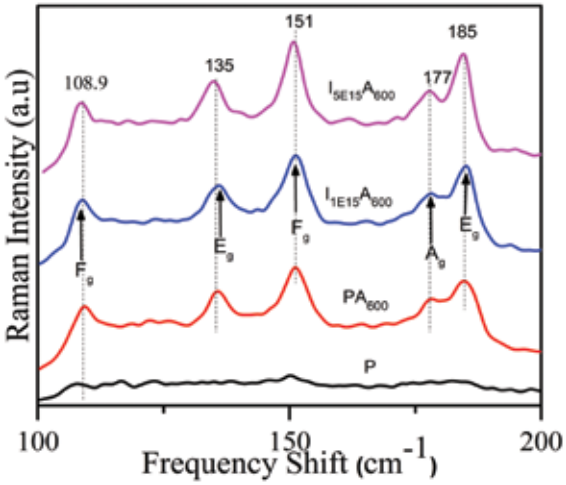

Fig. 4.4.4: Raman spectra of $CoSb_3$ thin films

(b) Magneto Resistance set up:

Fig. 4.4.5

This setup used for the magneto resistance of the sample. The magnetic field of the magnet is around 1.7 Tesla at the gap of 45 mm. The vacuum of the chamber is around $2x10^{-3}$ mbar. The temperature can be varied from 80K -450 K. All the electronics is interfaced with the LabView. This set up is suitable for the magneto resistance and magneto-dielectric measurement.

This set up was calibrated with standard Pt-100 and DT- 470 sensors and graphs are given below.

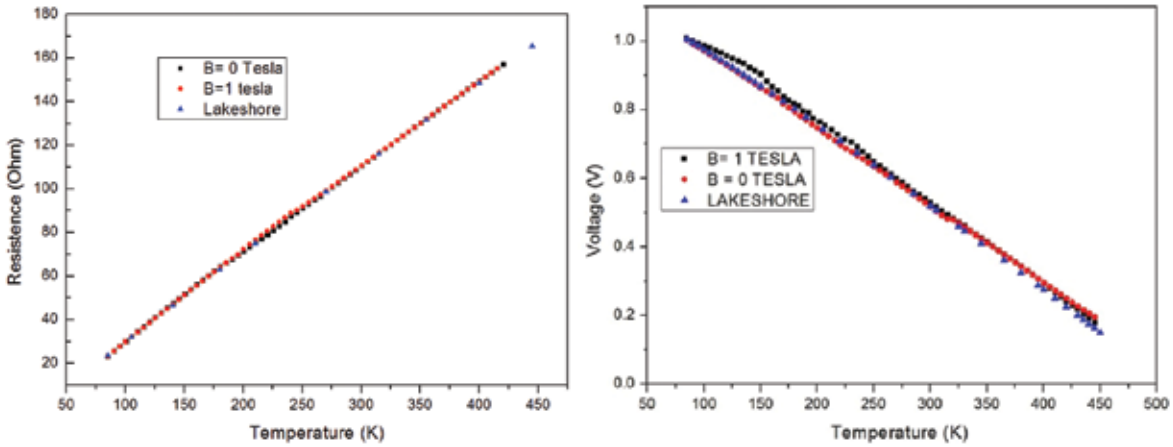

Fig. 4.4.6: (i) Pt-100 calibration curve. (ii) DT-470 calibration curve.

4.4.6 Status report on spectroscopy facilities

Pawan K. Kulriya and Fouran Singh

There have been several experiments besides regular upkeep and utilization of the structure and spectroscopy facilities for research in materials Science. There is no implementation of any new facility. However, *In-situ* X-ray diffraction (XRD) facility has been extensively used for structural characterization of materials. This year offline XRD system has been used for characterization of around 400 samples. Two *in-situ* experiments, in which structural characterization was carried out during ion irradiation, were also performed. Another facility namely high temperature irradiation setup also exists in the same beam line and two experiments were performed by keeping target at elevated temperature during swift heavy ion irradiation. QMA setup has been shifted from BH-I to BH-II for studying the evolution gases under irradiation at high temperature.

Micro-Raman facility is another heavily utilized facility for the materials characterizations. This facility operates in two modes as *ex-situ* and in-situ modes. About 670 spectra were measured for large number users across the country in *ex-situ* mode. Facility is operational and being utilized regularly. However, laser power has gone down and thus new laser may be procured in future. The other facilities such as UV-photoluminescence and ionoluminescence are also operation and being utilized for regular experiments. About 150 PL spectra were measured on various types of samples pre- and post irradiation of samples. Solar simulator facility for the characterizations of solar cells and photo diodes is also operational. RF sputtering setup has been upgraded by installing mass flow controller and thickness monitor. There are series of good publications based on the utilization of these facilities emerged during this period.

4.4.7 RF sputtering system, dc sputtering system and ball milling system

V. V. Siva Kumar.

The RF parallel plate diode sputtering system was maintained in proper working condition. A thickness monitor was installed, tested and the results were verified using RBS. It was used regularly for measurement of thickness during thin films deposition by RF sputtering. An arrangement for substrate bias was made and used to grow thin films of ZnO on substrates kept at floating potential (0 V) and negative potential upto -60 Volts. The application of negative bias to substrate holder resulted in repulsion of electrons and acceleration of Argon ions from the plasma sheath. Significant improvement in (002) orientation of wurtzite ZnO phase was obtained due to argon ion bombardment of the film. The RF sputtering system was used to grow thin films of CuO, Cu_2O, ZnO and ZnO-Ag material.

The DC sputtering system was used for deposition of copper oxide thin films by users. A copper target was used to grow copper oxide thin films with oxygen plasma. Thin films of Cu, Fe, and Al were also grown. About 100 thin films were grown by users from different universities for various studies,

The ball milling system was used to pulverize thermo-luminescent materials for using it for ion beam related studies. Users from University of Delhi used the system for their research work.

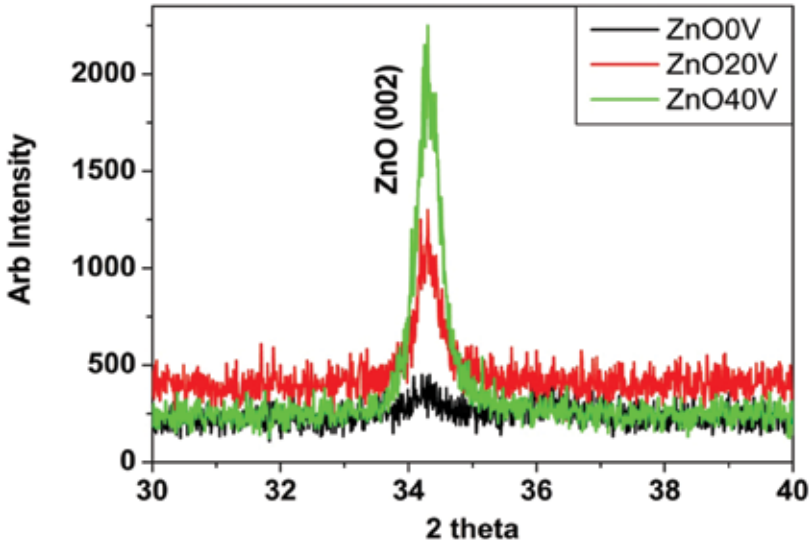

Fig.4.4.7 XRD patterns of films showing significant increase in intensity of ZnO (002) peak for films deposited with substrate bias of -20 and -40 V.

4.5 STATUS OF THE RESEARCH WORK DONE IN THE RADIATION BIOLOGY FACILITY

A. Sarma

Presently, one student from Banaras Hindu University and three students from Kalyani University are continuing with the experiments related to the approved projects using the dedicated Radiation Biology Beam line of IUAC and utilizing the ASPIRE [Automated sample positioning and irradiation system for radiation biology experiments] system. In this system the irradiation of cells by accelerated heavy ions can be done at atmospheric pressure with a set of preset doses. The system is characterized by the dose uniformity over a field of 40 mm diameter within 2 % standard deviation. The mean fluence is within 1 % of the electronically measured value at the centre of the field. The characterization of the system has also been done using irradiating SSNTD [CN 85].

The radiation biology laboratory is having following equipment to facilitate the sample preparation and post irradiation treatments.

- Two CO_2 incubators, Two biosafety cabinets, one small laminar flow bench for cell culture
- Field Inversion Gel electrophoresis, Normal gel electrophoresis, protein gel electrophoresis set up
- Image based cell counter Countess [Invitrogen] which also gives information about cell viability and Beckman-Coulter Z2 cell counter
- PCR machine, a crude gel documentation system, UV-Vis Spectrophotometer and a Fluorescence microscope.
- Perkin Elmer Multimode Plate Reader, Eppendorf and Plastocraft Refrigerated Centrifuge and a Biotek micro-plate washer.

Apart from that, LN2 Dewars, -80C ultra freezer, -20 deep freezer and other refrigerators serve as the storage facilities. The laboratory section has independent Split AC supply isolated from the central AC system. The CO_2 supply to the twin incubators is done from outside the lab area, which facilitates the replacement of empty cylinder without disturbing the laboratory environment.

Regular work is going on in the laboratory on Analytical procedures involving gene expression studies using PCR, Western Blot, Fluorescence Immuno-staining studies etc by the University Users.

5 RESEARCH ACTIVITIES

5.1 NUCLEAR PHYSICS

S. Muralithar, N. Madhavan and P. Sugathan

IUAC bought two Compton suppressed Clover Ge detectors and placed order for two more detectors to augment the Indian National Gamma Array (INGA) facility. Experiments were performed using the Gamma Detector Array (GDA) facility by user groups from University of Delhi, Aligarh Muslim University, Bareilly College, Central University of Jharkhand, University of Warsaw and IIT Roorkee. Experiments done in both GDA and INGA lead to several publications this year on the nuclear structure studies of ^{66}Ga, ^{188}Pt, ^{127}Xe and incomplete fusion (ICF) dynamics covering different aspects like entrance channel effects on yield, spin distribution of evaporation residues, feeding in ICF, effects of ICF on complete fusion above the Coulomb barrier. The users' report for this year covers nuclear structure studies of ^{124}Te, ^{129}La and ^{63}Cu. Next series of experiments in INGA is planned in the latter half of this year for which resources are being pooled in.

The Heavy Ion Reaction Analyzer (HIRA) was successfully used to measure very low evaporation residue (ER) cross sections well below the one-dimensional barrier, after its re-levelling which had been reported last year. The experiment to optimally populate ^{97}Ru nuclei (which have potential application in diagnosis) through heavy ion-induced fusion evaporation experiment in HIRA was taken to successful completion. Beams provided by Pelletron-LINAC combination were used to carry out experiments to look for entrance channel and/or shell effects through ER excitation function and ER angular momentum distributions. The set-up of the first stage of HYbrid Recoil mass Analyzer (HYRA) followed by a single Clover Ge detector at its focal plane, used couple of years back to identify a new microsecond isomer in ^{195}Bi, was again employed to study gamma transitions following the alpha decay of heavy ERs selected by HYRA. The gamma rays were gated with alpha decay to reduce the background. Two data acquisition systems were used for the first time at IUAC with time stamping. Such experiments, once perfected, will find great boost with the planned multi-Clover detector assembly at the focal plane of HYRA.

Several experiments were performed in the National Array of Neutron Detectors (NAND) facility using the Pelletron-LINAC beams completing Ph.D thesis experiments of students from Punjab University, Delhi University, Andhra University and Central University of Kerala. Mass-gated neutron multiplicity, fission fragment mass and angular distribution and barrier distribution measurements were performed in reactions forming very heavy nuclei. Two collaborative experiments exploring the influence of shell effects in fragment mass distributions were performed by groups from GANIL, France and Dubna, Russia with collaborators from BARC, Mumbai and VECC, Kolkata. In one of these experiments, Pelletron was tuned to the maximum potential of 15 MV to deliver pulsed of beam 19F in GPSC. A few incomplete fusion reactions were studied through recoil range distributions in the General Purpose Scattering Chamber (GPSC) in beam hall I.

5.1.1 Study of effect of entrance channel magicity on fusion fission dynamics

T. K. Ghosh[1], A. Sen[1], A. Chaudhuri[1], S. Bhattacharya[1], C. Bhattacharya[1], Samir Kundu[1], S. Manna[1], J. K. Meena[1], P. Sugathan[2], K. S. Golda[2], N. Saneesh[2], I. M. Harca[3], I. Pchelintsev[3] and E. M. Kozulin[3]

[1]Variable Energy Cyclotron Centre, 1/AF Bidhan Nagar, Kolkata 700064, India
[2]Inter-University Accelerator Centre, Aruna Asaf Ali Marg, New Delhi 110067, India
[3]Flerov Laboratory of Nuclear Reactions, JINR, Dubna, Russia

One of the major aspects of contemporary Nuclear Physics research is the choice of the proper projectile-target combination for the synthesis of Super Heavy Elements (SHE). SHE exist due to presence of shell effects in the fusion-fission dynamics. Hence, an experimental project has been taken up by the VECC group in collaboration with Flerov Laboratory of Nuclear Reactions, JINR, Dubna, Russia to elucidate the role of entrance channel magicity in the fusion-fission dynamics of heavy nuclei [1]. A series of experiments have been planned to be carried out for several target-projectile systems. While we study the fission of SHE (atomic number = 114) at Russian accelerator facility as they can provide heavy beams (e.g; Cr, Fe, Ni, etc) [2]; in India, we study the heavy elements as we have comparatively lighter beams.

As a part of this collaborative experimental project, one experiment was carried out at the 15UD Pelletron accelerator facility at IUAC, New Delhi in November 2017 to understand the effects of entrance channel magicity on fusion-fission dynamics. Pulsed ^{19}F beam of energy 77-120 MeV, was bombarded on an enriched target of ^{205}Tl to populate the compound nucleus ^{224}Th. It is to be noted that neither the target nor the projectile is shell

closed nucleus. The results of the experiment will be compared with other systems (*e.g.* $^{16}O+^{208}Pb$, $^{18}O+^{206}Pb$) producing the same compound nucleus. The experiment was carried out at the GPSC facility using two large area (20×6 cm^2) MWPC gas detectors, indigenously developed at VECC. Fig. 5.1.1 shows the experimental setup.

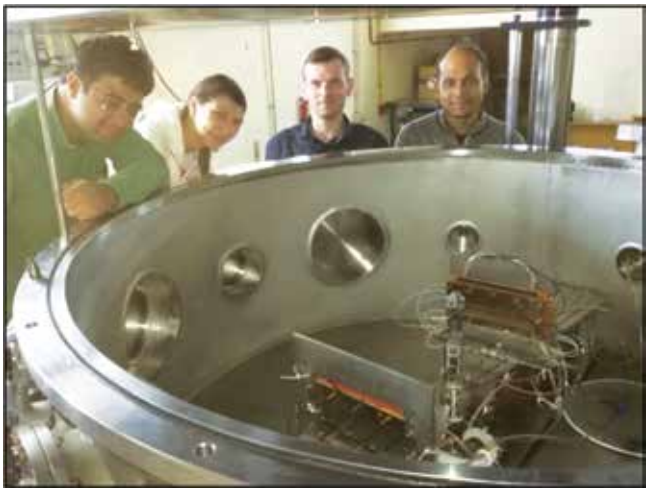

Fig. 5.1.1: Experimental setup.
Two MWPCs mounted inside the scattering chamber.

Fig. 5.1.2: Beam was delivered at 15MV terminal potential.

On 22nd November, 2017 at 11:00 am, ^{19}F pulsed beam was delivered at energy 120 MeV with 20 nA beam current on the target. This required a terminal potential of 15 MV (shown in Fig. 5.1.2), which was achieved during the experiment. Fig. 5.1.3 shows the preliminary results of the measured mass distribution at the highest energy in which fission data were collected for more than 100 thousand events.

Preliminary analysis of the data has been carried out and mass distributions are found to be symmetric in nature at energies above the Coulomb barrier. A theoretical model [3] is being used to compare and understand the measured mass distributions. The data would also be compared with another experiment where ^{16}O beam was bombarded on a ^{208}Pb target (both doubly shell closed) to populate the same compound nucleus ^{224}Th. Comparison of data from the two experiments, where one set of projectile-target are shell closed while the other set is not shell closed, shall provide conclusive information on the influence of entrance channel magicity on the dynamics of fusion-fission process.

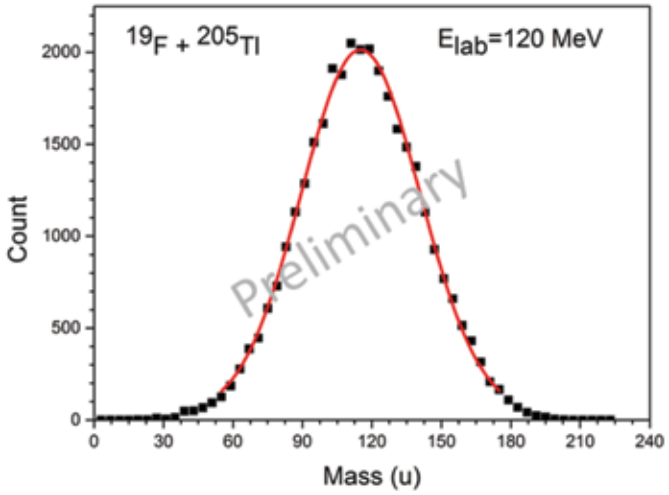

Fig. 5.1.3: Measured mass distribution for 19F+205Tl at 120 MeV beam energy.

REFERENCES

1. C. Simenel, *et al.,* Phys. Lett. B **710,** 607 (2012).
2. E. M. Kozulin *et al.,* Phys. Rev. C **94,** 054613 (2016).
3. V. I. Zagrebaev and W. Greiner, Nucl. Phys. A **944,** 257 (2015).

5.1.2 Low energy incomplete fusion reactions in $^{19}F+^{175}Lu$ system

Mohd. Shuaib[1], Vijay R. Sharma[2], Abhishek Yadav[2], Ishfaq M. Bhatt[1], Manoj Kumar Sharma[3], Pushpendra P. Singh[4], Devendra P. Singh[5], S. Muralithar[2], R. P. Singh[2], R. Kumar[2], B. P. Singh[1] and R. Prasad[1]

[1]Nuclear Physics Laboratory, Department of Physics, Aligarh Muslim University, Aligarh 202002, India
[2]Nuclear Physics Group, Inter University Accelerator Centre, New Delhi 110067, India
[3]Physics Department, S. V. College, Aligarh 202001, India
[4]Department of Physics, Indian Institute of Technology Ropar, Punjab 140001, India
[5]Department of Physics, University of Petroleum and Energy Studies, Dehradun 248007, India

Widespread experimental and theoretical efforts have been made to understand the reaction dynamics of incomplete fusion (ICF) reactions in heavy-ion (HI) collisions at energies ≈ 4-7 MeV/nucleon [1,2]. Generally, at these energies, the complete fusion (CF) process is the main contributor to the reaction cross-section and is well explained by the statistical model (PACE4) predictions [1,2]. However, the substantial enhancement in the production cross section of residues involving α-particle(s) in the exit channel as compared to the statistical model predictions indicates the contribution coming from the incomplete fusion reactions [1,2] which created a resurgent interest to study such reactions. In the present work, the excitation functions (EFs) of various evaporation residues populated in ^{19}F + ^{175}Lu system via CF and/or ICF channels are measured using off-line γ-ray spectroscopy over a wide range of energy and analyzed within the framework of statistical mode code PACE4 [1, 2]. The EFs of xn/pxn channels are found to agree well with the theoretical outcomes of PACE4 and confirmed the production of these channels solely via CF mode. However, a significant enhancement in the EFs of α-emitting channels as compared to PACE4 predictions has been observed [3]. This enhancement has been attributed due to the contribution from the ICF reactions at the studied range of energy. Further, an attempt has been made to study the effect of projectile (strongly bound α-cluster and non α-cluster nuclei) break-up on fusion cross-section, above the Coulomb barrier, within the framework of universal fusion function (UFF) [3], which does not depend on the system parameters. The experimentally measured complete fusion functions F(x) have been deduced for various projectile-target combinations (viz; $^{19}F+^{159}Tb$, $^{19}F+^{169}Tm$, $^{19}F+^{175}Lu$, $^{16}O+^{159}Tb$, $^{16}O+^{169}Tm$, and $^{13}C+^{169}Tm$) and compared with the UFF as shown in Fig. 5.1.4. It may be pertinent to mention that, at energies well above the Coulomb barrier, inelastic excitations and transfer channel coupling effects are not significant. Therefore, the difference between the experimental fusion function and UFF is mainly due to the break-up effects of the projectile. As can be seen from Fig. 5.1.4, complete fusion function F(x) is suppressed by 10 – 35% (see Ref. 3 for more details) above the barrier, indicating that it is essentially due to the prompt break-up (incomplete fusion) of the strongly bound projectiles. Fig. 5.1.5 represents an exponential relation between the suppression factor in terms of break-up threshold energy ($E_{B.U.}$) of the projectile. The deduced CF suppression factor for ^{19}F projectile is found to be lower than for weakly bound projectile ^{9}Be and higher than strongly bound projectile ^{10}B, which is related to the fact that the break-up threshold energy of ^{19}F is larger than that of ^{9}Be and smaller than that of ^{10}B. The deduced CF suppression factor for the ^{19}F projectile (present work) on different targets presented in Fig. 5.1.5 exhibits a well-established conspicuous exponential relationship between the suppression factor and break-up threshold energy of the projectile, i.e., the suppression in CF is related to the break-up threshold energy of the projectile.

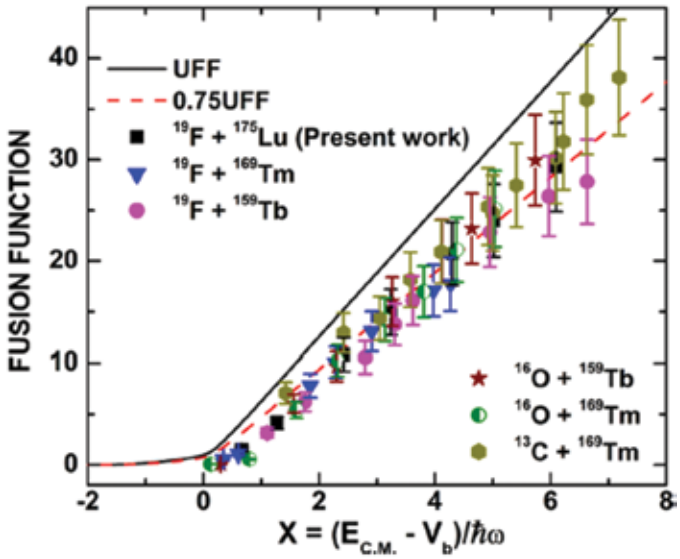

Fig. 5.1.4: The complete fusion function for strongly bound projectiles on different target nuclei. The solid black line is UFF. The dotted line is UFF multiplied by 0.75.

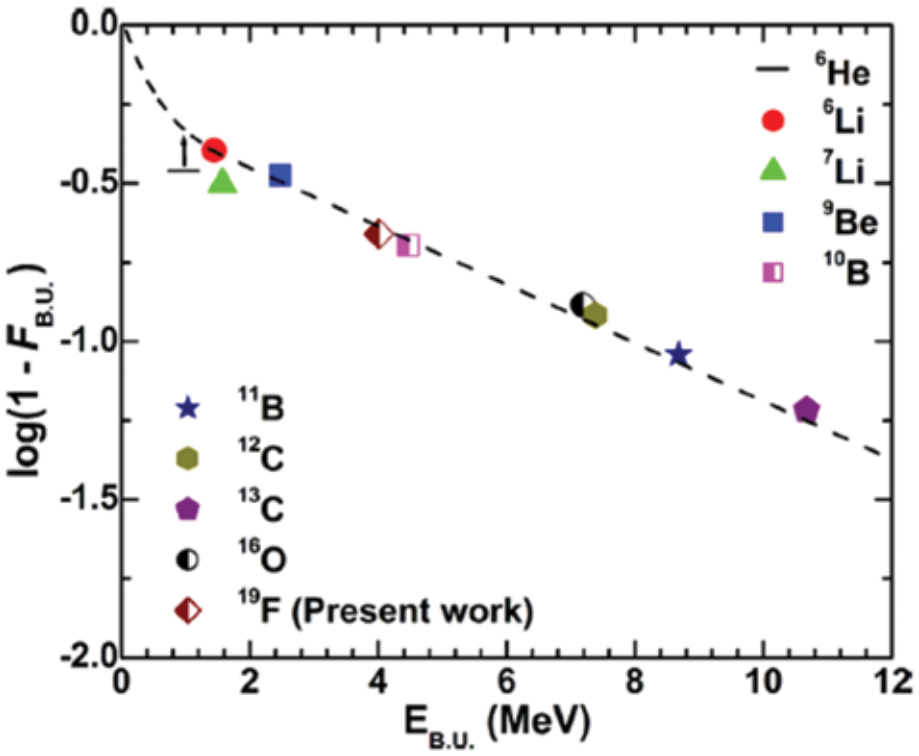

Fig. 5.1.4: The complete fusion function for strongly bound projectiles on different target nuclei. The solid black line is UFF. The dotted line is UFF multiplied by 0.75.

REFERENCES

1. Mohd. Shuaib, *et al.,* Phys. Rev. C **94,** 014613 (2016).
2. Mohd. Shuaib, *et al.,* J. Phys. G: Nucl. Part. Phys. **44,** 105108 (2017).
3. Mohd. Shuaib, *et al.,* Phys. Rev. C **98,** 014605 (2018).

5.1.3 Fission fragment angular distribution measurements

A. Shamlath[1], E. Prasad[1], A. C. Visakh[1], P. Sugathan[2], A. Jhingan[2], N. Saneesh[2], K. S. Golda[2], Mohit Kumar[2], A. M. Vinodkumar[3], S. K. Duggi[4], P. V. Laveen[1], Gurpreet Kaur[5], Md. Moin Shaikh[2], M. M. Hosamani[6], Rudra N. Sahoo[7], Arshiya Sood[7], Shruti Narang[5], V. Srivastava[2] and A. Tejaswi[4]

[1]Department of Physics, Central University of Kerala, Nileshwar 671314, India
[2]Inter-University Accelerator Centre, Aruna Asaf Ali Marg, New Delhi 110067, India
[3]Department of Physics, University of Calicut, Calicut 673635, India
[4]Department of Nuclear Physics, Andhra University, Visakhapatnam 530003, India
[5]Department of Physics, Panjab University, Chandigarh 160014, India
[6]Department of Physics, Karnatak University, Dharwad 580003, India
[7]Department of Physics, Indian Institute of Technology Ropar, Punjab 140001, India

Fission fragment angular distribution studies have been performed using the scattering chamber of the National Array of Neutron Detectors (NAND) facility [1] at IUAC. The measurements were performed for the ^{28,30}Si+^{180}Hf reactions in the beam energy range 145 to 204 MeV and 136 to 203.7 MeV, respectively. The fission fragments were detected using an array of 16 hybrid detector telescopes [2,3]. The detectors are arranged in three sets. One set has six telescopes placed on the right arm with an angular coverage of θ_{lab} = 60º to 110º and another six telescopes were mounted on the left arm that covers angles of 110º to 160º with an angular pitch of 10º. Third group of four telescope detectors, two of them in-plane and another two out-of-plane, each at an angle of 173º, were arranged in a symmetrical-cone geometry. Each telescope in the array composed of a gas ionization chamber (ΔE) in the front followed by a silicon detector (E) at the back as the stopping detector. The ionization chamber (IC) measures the energy loss of the reaction products and the silicon detector records the residual energy (E) of the same, downstream. Left panel of Fig. 5.1.6 shows the two dimensional plot of residual energy (E) versus energy loss (ΔE) of reaction products at lab angle 173º for the ^{30}Si+^{180}Hf reaction at E_{beam} = 145 MeV. It can be seen that the fission fragments are well separated from other reaction products. Two passivated implanted planar silicon (PIPS) detectors of thickness 300 µm were positioned at ±13º with respect to beam direction to monitor the beam. The Rutherford events registered in these detectors were used for the absolute normalization of fission cross sections.

The measured fission fragment angular distributions in the laboratory framewere transformed to the centre of mass frame using Viola systematics [4]. Before the centerof mass frame conversion, beam energy loss through the backing and half thickness of thetarget were taken into account. The differential fission cross section can be calculated using the equation

$$W(\theta_{c.m.}) \propto \left(\frac{d\sigma_{fiss}}{d}\right)_{c.m.} = \frac{1}{2}\frac{Y_{fiss}}{Y_{mon}}\left(\frac{d\sigma}{d}\right)_{R}\frac{mon}{fiss} \quad G,$$

where Y_{fiss} and Y_{mon} are the yields of the fission fragments and Rutherford events, respectively. $\left(\frac{d\sigma}{d}\right)_{R}$ is the differential Rutherford cross section in the laboratory frame of reference, $_{mon}$ and $_{fiss}$ are the solid angles subtended by the monitor and fission detectors, respectively. G is the Jacobian which transforms the cross section from the laboratory frame to center of mass (c.m.) frame of reference. Total fission cross section σfis is calculated by integrating the differential cross sections. The measured total fission cross sections for the ^{30}Si+^{180}Hf reaction is shown in the right panel of Fig. 5.1.6.

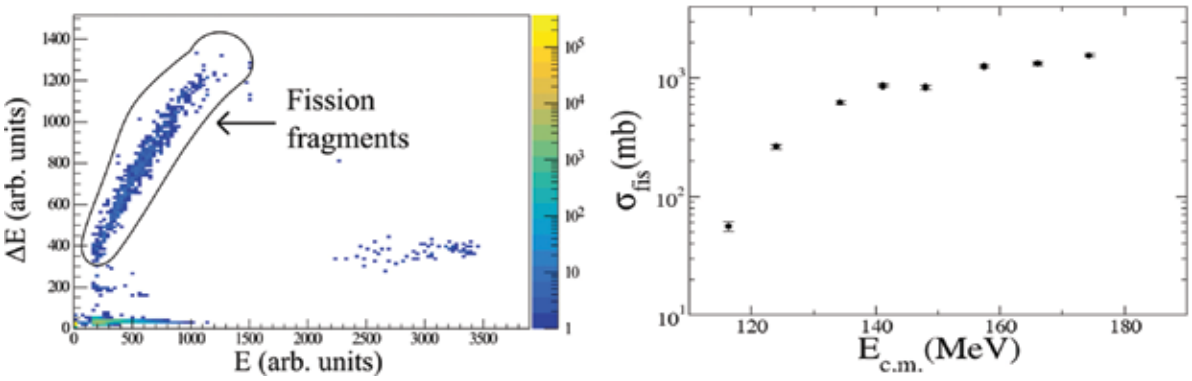

Fig. 5.1.6: Scatter plot of energy (E) versus energy loss (ΔE) of reaction products for the system ^{30}Si+^{180}Hf at E_{beam} = 145 MeV with the hybrid telescope detector kept at θ_{lab} = 173° (left panel). Total fission cross section for the ^{30}Si+^{180}Hf reaction as a function of energy available in the c.m. frame of reference (right panel).

REFERENCES

1. http://www.iuac.res.in/research/np/nand/nand main.html.
2. A. Jhingan *et al.,* Proc. DAE Symp. Nucl. Phys. **59,** 830 (2014).
3. A. Jhingan *et al.,* Proc. DAE Symp. Nucl. Phys. **60,** 936 (2015).
4. V. E. Viola *et al.,* Phys. Rev. C **31,** 1550 (1985).

5.1.4 Evaporation residue excitation function measurements for thorium compound nuclei

P. Sandya Devi[1], S. K. Duggi[1], G. Naga Jyothi[1], A. Tejaswi[1], M. Ratna Raju[1], P. V. Madhusudhana Rao[1], N. Madhavan[2], J. Gehlot[2], S. Nath[2], A. Jhingan[2], T. Varughese[2], M. M. Hosamani[3], A. Shamlath[4], M. Shareef[4], P.V. Laveen[4], P. N. Patil[3], A. Vinayak[3], Rohan Biswas[2], V. Srivasthava[2], Md. Moin. Shaikh[2], A. Parihari[2], P. Sugathan[2] and B. K. Nayak[5]

[1]Swami Jnanananda Laboratories for Nuclear Research, Andhra University, Visakhapatnam 530003, India
[2]Inter University Accelerator Centre, Aruna Asaf Ali Marg, New Delhi 110067, India
[3]Department of Physics, Karnatak University, Dharwad 580003, India
[4]Department of Physics, Central University of Kerala, Kasaragod 671314, India
[5]Nuclear Physics Division, Bhabha Atomic Research Centre, Mumbai 400085, India

Quest to elucidate the role of nuclear structure in reaction mechanism and influence of nuclear reaction mechanism on nucleosynthesis have been the basis for research in nuclear reaction studies. In fusion reactions, the compound nucleus formation and decay probabilities provide vital inputs in understanding the latter process. In the present study, heavy ion induced fusion reactions were used to produce thorium compound nuclei and their subsequent evaporation residues (ERs). In the mass region $200 \leq A \leq 240$ amu with $80 \leq Z \leq 90$, compound nucleus decays by both evaporation and fission modes that compete with each other. Understanding the evaporation and fission competition in this heavy mass region can provide insights into the production of super heavy nuclei. ER cross section is one of the sensitive tools that sheds light on formation of the compound nucleus and its fission survival

probabilities. Measurement of ER cross sections for thorium compound nuclei is of special interest as these nuclei predominantly undergo fission and very small fraction of them will form ERs. This is due to the very low fission barrier of about 5 MeV. Experimental data on ER cross sections are scarce for thorium compound nuclei due to their very low cross sections in the presence of very strong fission. Here we report measurements of ER excitation functions for O+Pb systems leading to ^{220,222,226}Th* compound nuclei at laboratory energies ranging between 85 – 150 MeV using 15UD Pelletron [1] - superconducting LINAC booster [2] and the recoil separator HYRA [3] at IUAC. Pulsed beams of ^{16,18}O with a pulse separation of 2 μs and 4 μs were bombarded on isotopically enriched ^{204,206,208}Pb targets of thickness 150−300 μg/cm^2 sandwiched between carbon layers of 30 μg/cm^2 (backing) and 10 μg/cm^2 (capping). Vacuum evaporation method was used to fabricate the targets at the target laboratory of IUAC.

HYRA in gas-filled mode is used to separate ERs from intense background of un-interacted beam component and elastically scattered particles in the zero-degree relative to beam direction. Helium gas pressure was maintained at 0.15 Torr throughout the experiment. Two silicon surface-barrier detectors were placed inside the target chamber at angles of ±26º to monitor the incident beam flux by detecting the elastically scattered particles which was used for beam flux normalisation. The ERs recoiling out of thin target were separated from the intense flux of un-interacted beam component and scattered particles close to and around 0º relative to the beam direction. ERs were detected at the focal plane by a position sensitive multi-wire proportional counter of active area 6"×2" which provided 2-D position of the ERs. Due to low background in the focal plane ERs could be identified with the help of time of flight (TOF) measurements. Typical TOF spectrum was generated between delayed anode signal of MWPC and the RF signal from the LINAC. Fig. 5.1.7(a) shows the energy loss (ΔE) vs TOF spectrum which was helpful in the identification of ERs. ER excitation functions in arbitrary units are shown in Fig. 5.1.7(b).

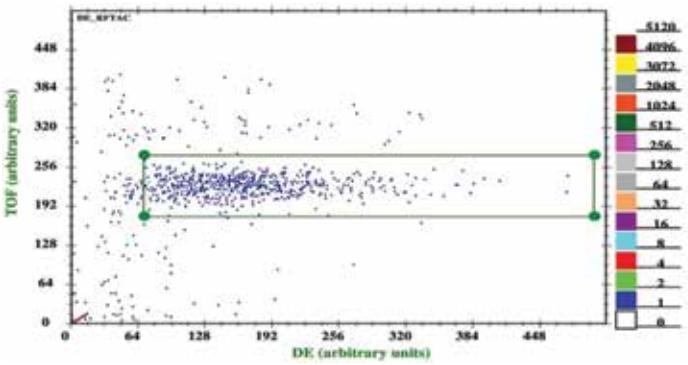

Fig. 5.1.7 (a): The ΔE versus TOF spectrum for ^{16}O+^{206}Pb at E_{beam} = 85 MeV.

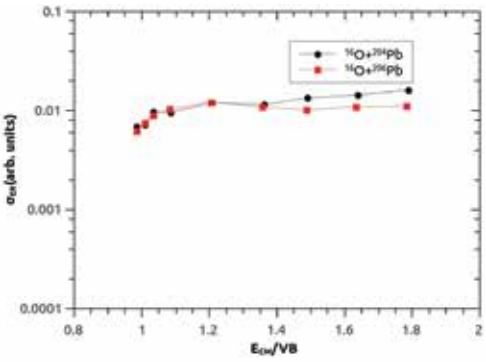

Fig. 5.1.7 (b): ER excitation function for the reactions ^{16}O+^{204,206}Pb.

REFERENCES

[1] D. Kanjilal *et al.,* Nucl. Instrum. Methods A **328,** 97 (1993).
[2] S. Ghosh *et al.,* Phys. Rev. ST. Accel. Beams **12,** 040101 (2009).
[3] N. Madhavan *et al.,* Pramana - J. Phys. **75,** 317 (2010).
[4] D. J. Hinde *et al.,* Phys. Rev. Lett. **89,** 282701 (2002).
[5] S. Nath, Comput. Phys. Commun. **180,** 2392 (2009).

5.1.5 Production of ^{97}Ru in ^{32}S-induced reaction with ^{70}Zn

D. Kumar[1], R. Prajapat[1], M. Maiti[1], A. Chauhan[1], R. Biswas[2], J. Gehlot[2], N. Madhavan[2], S. Nath[2], R. Kumar[2], G. Naga Jyothi[3], Rudra N. Sahoo[4], Md. Moin Shaikh[2] and V. Srivastava[2]

[1] Department of Physics, Indian Institute of Technology Roorkee, Roorkee, Uttarakhand 247667, India
[2] Nuclear Physics Group, Inter University Accelerator Centre,Aruna Asaf Ali Marg, New Delhi 110067, India
[3] Department of Nuclear Physics, Andhra University, Visakhapatnam 530003, India
[4] Department of Physics, Indian Institute of Technology Ropar, Rupnagar 140001, Punjab, India

^{97}Ru is one of the most versatile radionuclides because of its excellent physico-chemical properties. It may have a wide range of diagnostic or therapeutic applications¬ as several potential ^{97}Ru-labelled compounds have been tested so far [1,2]. Several possible production routes have been examined using heavy ion induced reactions till now [2,3]. As a part of our continuous effort, fusion reaction dynamics of ^{32}S-induced reaction on ^{70}Zn has been studied, which also gives an estimate of the production of ^{97}Ru radionuclide.

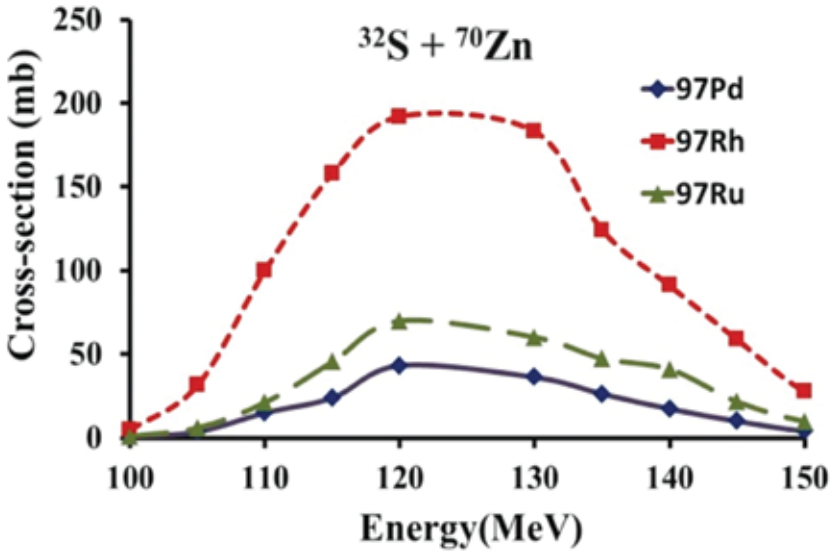

Fig. 5.1.8: Theoretical excitation functions obtained from PACE4.

The Hauser-Feshbach formalism was used to find the optimum energy window for the production of ^{97}Ru, 97Rh, ^{97}Pd radionuclides in the ^{32}S+^{70}Zn reaction within the 100-150 MeV energy range, as shown in Fig. 5.1.8. It is observed that an appreciable amount of ^{97}Ru could be produced within E_{beam} = 110 – 135 MeV; since the higher charge isobars ^{97}Rh (30.7 min), ^{97m}Rh (46.2 min) and ^{97}Pd (3.10 min) will decay to the relatively long-lived ^{97}Ru (2.83 d). The maximum direct production cross-section of ^{97}Ru is seen (~200 mb) near 125 MeV. Being inspired by the theoretical study, an experiment was performed using the 15UD Pelletron of IUAC. The 250 ns pulsed beam of 32S, in the range Ebeam = 100 – 135 MeV, was bombarded on the 350 µg/cm^{270}Zn target and the residues of mass fraction ^{97} amu were separated using the Heavy Ion Reaction Analyzer (HIRA) [4]. The HIRA was kept at zero degree with respect to beam direction with solid angle coverage of 5 msr. Evaporation residues (ERs) produced at the target during irradiation were transported to the focal plane of HIRA and detected by a 15.2×5.1 cm^2 multi-wire proportional counter (MWPC) operated at a pressure of 4 mbar of isobutane gas. Inside the target chamber, two silicon-surface barrier detectors (SSBDs) were placed symmetrically at θ_{lab} = 15º with respect to beam direction and at a distance of 9.6 cm from the target. These detectors were utilized to monitor the beam direction during the online experiment and for normalization of cross-sections during the data analysis.

A carbon reset foil (35 µg/cm^2) was mounted 10 cm downstream from the target in order to reset the charge state of the residues after probable internal conversion processes. The separation between different mass/charge $\left(\frac{m}{q}\right)$achieved during the experiment is shown inFig. 5.1.9, which describes the two-dimensional spectrum of ER energy loss (ΔE) vs *x*-position of the MWPC at E_{beam} = 130 MeV for ^{32}S+^{70}Zn. Two broad separate groups are visible here corresponding to the two different charge states of ERs, where each charge state (*q*) group shows the separation of different masses. During the experiment, production of 97Ru was also confirmed using a HPGe detector placed behind the MWPC.

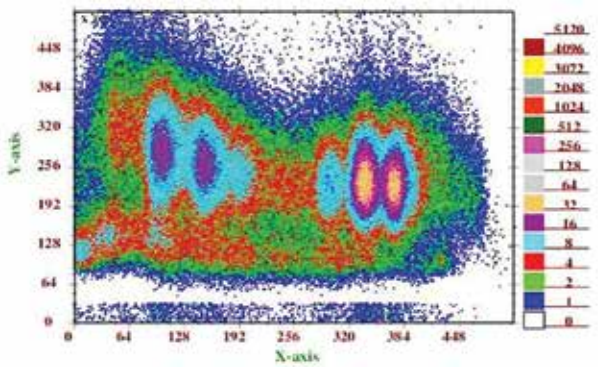

Fig. 5.1.9: A two-dimensional spectrum of the energy loss (ΔE) of the residues vs *x*-position at the MWPC corresponding to E_{beam} = 130 MeV.

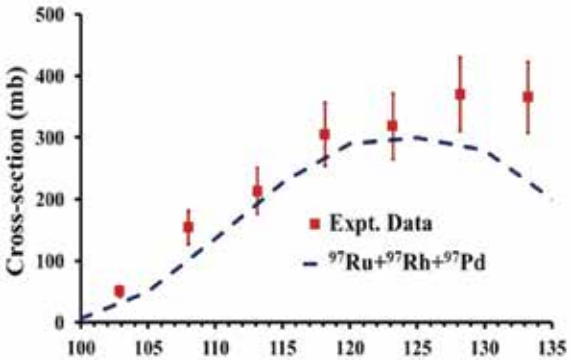

Fig. 5.1.10: Comparison of the measured cross-section with the theoretical estimation at different energies, E_{beam} = 100 – 135 MeV.

Offline data analysis was carried out using the CANDLE software. The transmission efficiency of ER through HIRA is estimated theoretically from the semi-microscopic Monte Carlo code, TERS [5]. The measured cross-sections of the mass-97 amu fraction are the sum of the counts of ^{97}Ru, ^{97}Rh, ^{97}Pd isobars populated in E_{beam} = 100 – 135 MeV energy range as shown in the Fig. 5.1.10. Theoretical estimation reproduces the measured data satisfactorily up to E_{beam} = 125 MeV indicating the evaporation channel as a major contributor. Maximum production cross-section (~363 mb) for ^{97}Ru+^{97}Rh+^{97}Pd was observed at E_{beam} ~128 MeV. The mass-97 amu residues can be collected at the back side of the MWPC for further study. Detail data analysis is in progress.

We sincerely thank Gamma Detector Array (GDA) group for providing the HPGe detector and necessary help required during the experiment.

REFERENCES

1. M. Maiti and S. Lahiri, Radiochim. Acta. **103,** 7 (2015) and references therein.
2. M. Maiti and S. Lahiri, Radiochim. Acta, **99,** 359 (2011).
3. D. Kumar, M. Maiti and S. Lahiri, Sep. Sci. Technol. **52,** 2372 (2017) and references therein.
4. A. K. Sinha, N. Madhavan, J. J. Das, P. Sugathan, D. O. Kataria, et al., Nucl. Instrum. Methods A **339,** 543 (1994).
5. S. Nath, Comput. Phys. Commun. **180,** 2392 (2009).

5.1.6 Fission fragment mass distribution studies of ^{188,190}Pt

Kavita[1], Hardev Singh[1], Rakesh Kumar[1], K. S Golda[2], Saneesh[2], Mohit[2], Abhishek Yadav[2], C. Yadav[2], Rakesh Dubey[2], Neeraj Kumar[3], Akashrup Banerjee[3], Anjali[3], S. K Duggi[4], Kavita Rani[5], Jaimin Acharya[6] and Shoaib Noor[7]

[1]Kurukshetra University, Kurukshetra, Haryana 136119, India
[2]Inter University Accelerator Centre, Aruna Asaf Ali Marg, New Delhi 110067, India
[3]Department of Physics and Astrophysics, University of Delhi, Delhi 110007, India
[4]Department of Nuclear Physics, Andhra University, Visakhapatnam 530003, India
[5]Department of Physics, Panjab University, Chandigarh 160014, India
[6]Department of Physics, Thapar University, Patiala, Punjab 147004, India
[7]Department of Physic, M. S. University of Baroda, Vadodara, Gujarat 390002, India

In recent years, observation of the presence of quasi-fission (QF) in relatively less fissile systems has been a topic of current interest for the last few years [1-3]. QF is partly responsible for the very low production cross section of the super heavy elements (SHEs). Many experimental measurements of mass distribution of fission fragments (FF) using different projectile-target combinations are conducted by different groups to explore the characteristics of quasifission (QF) process in medium mass region. Fission fragment mass distribution (FFMD) measurements provide valuable information about the potential energy landscape of fissioning nucleus [4]. In the present experiment, FFMD measurements were carried out for the reactions, ^{28}Si+^{160}Gd and ^{12}C+^{178}Hf at IUAC, using the General Purpose Scattering Chamber (GPSC) set-up and Pelletron accelerator facility. Pulsed beams of ^{28}Si and ^{12}C in the energy range of 120 – 140 MeV and 60 – 88.2 MeV, respectively, were bombarded on ^{160}Gd and ^{178}Hf targets, both having thickness ~ 200 μg/cm^2.The coincident fission fragments were detected using two Multi-Wire Proportional Counters (MWPCs) placed at folding angle for respective reactions. The target ladder was kept at 45° with respect to the beam direction in order to avoid the shadowing of either of the two gas detectors. Two silicon surface barrier detectors (SSBD) were mounted at ±10° with respect to the beam direction for monitoring the beam throughout the experiment.

The data analyses have been performed using LAMP software package [5]. The details of the analysis method have been reported in [6].Fig. 5.1.11 represents the plot of correlation of polar and azimuthal angle of all fission fragments measured at lab energy of 88.2 MeV for the ^{12}C+^{178}Hf reaction.The correlation between the measured perpendicular and parallel component of velocities of the fission fragments for the reaction ^{12}C+^{178}Hf at 88.2 MeV is shown in Fig. 5.1.12. Further analysis to extract the mass variance and folding angle variations for both the reactions is under process.

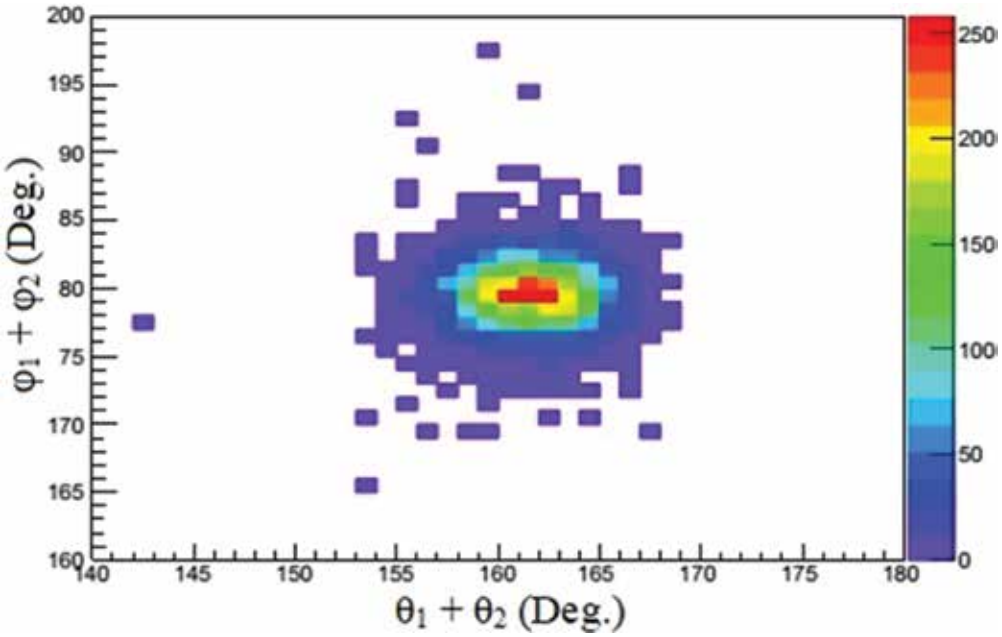

Fig. 5.1.11. The distribution of polar (θ) and azimuthal (ϕ) correlations for the $^{12}C + ^{178}Hf$ at E_{lab} = 88.2 MeV.

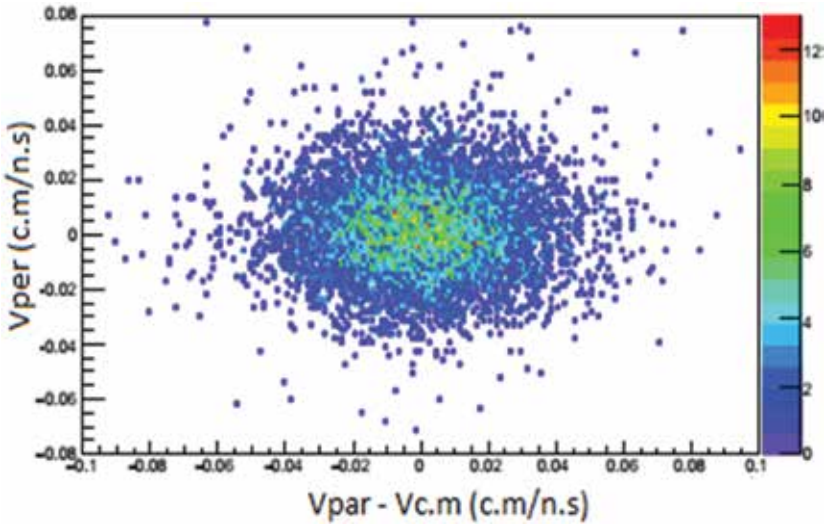

Fig. 5.1.12. Measured distribution of velocity of fissioning nuclei in the reaction $^{12}C + ^{178}Hf$ at E_{lab} = 88.2 MeV.

REFERENCES

1. D. J Hinde *et al.,* Phys. Rev. C **53,** 1290 (1996).
2. M. G. Itkis *et al.,* Nucl. Phys. A **787,** 150 (2007).
3. E. Prasad *et al.,* Phys. Rev. C **96,** 034608 (2013).
4. T. K. Ghosh *et al.,* Phys. Rev C **79,** 011604 (2004).
5. http://www.tifr.res.in/~pell//lamps_files/vme.html
6. R. G. Thomas *et al.,* Phys. Rev. C **77,** 034610 (2008).

5.1.7 Measurement of ER spin distributions using HYRA and TIFR 4π spin spectrometer

M. M. Hosamani[1], N. M. Badiger[1], N. Madhavan[2], I. Mazumdar[3], S. Nath[2], J. Gehlot[2], A. K. Sinha[4], S. M. Patel[3], P. B. Chavan[3], T. Varughese[2], V. Srivastava[2], Md. Moin Shaikh[2], P. Sandya Devi[6], P. V. Laveen[5], A. Shamlath[5], M. Shareef[5], S. K. Duggi[6], P. V. Madhusudhana Rao[6], G. Naga Jyothi[6], A. Tejaswi[6], P. N. Patil[1], A. Vinayak[1], Rajesh K. K.[7], M. Ratna Raju[6], D. P. Kaur[8], Abhishek Yadav[2], J. Joseph[9], A. Parihari[2] and Santanu Pal[10]

[1]Department of Studies in Physics, Karnatak University, Dharwad 580003, India
[2]Inter University Accelerator Centre, Aruna Asaf Ali Marg, New Delhi 110067, India

[3]Tata Institute of Fundamental Research, Mumbai 400005, India
[4]UGC-DAE Consortium for Scintific Research, Kolkata Centre, Kolkata 700098, India
[5]Department of Physics, Central University of Kerala, Kasaragod 671314, India
[6]Department of Nuclear Physics, Andhra University 530003, India
[7]Department of Physics, University of Calicut, Kerala 673635, India
[8]Department of Physics, Panjab University, Chandigarh 160014, India
[9]Kuriakose Elias College, Mannanam, Kerala 686561, India
[10]CS-6/1 Golf Green, Kolkata 700095, India

It is well known that measurements of evaporation residue (ER) cross sections and spin distributions at energies near fusion barrier would provide the information not only about the fission process but also about viscosity of nuclear fluid. In the present work we have used the IUAC facilities to study the nuclear fission hindrance in ^{224}Th compound nucleus formed by ^{16}O + ^{208}Pb and ^{18}O + ^{206}Pb systems. We have measured ER cross sections using HYbrid Recoil mass Analyzer (HYRA) [1] and spin distributions of ER using TIFR 4π spin spectrometer [2] placed in beam hall II at IUAC. Measurements were carried out for both the systems in the energy range E_{Beam} = 85 to 125 MeV. The beam with energy range 85 to 125 MeV was selected using Pelletron and Pelletron+LINAC facilities. Experimentally measured ER cross sections in arbitrary units are shown in Fig. 5.1.13. The ER cross section and the ER-gated spin distribution measurements were very challenging as the ERs survival probability is very low for these reactions. The kinetic energy of the ERs was also low at this energy range, thus making detection of the ERs at the focal plane very difficult. However, the ERs could be detected at the focal plane with careful optimization of gas pressure and bias voltages of the MWPC. The efficiency corrected absolute ER cross sections can be estimated using the following expression

$$\sigma_{ER} = \frac{Y_{ER}}{Y_{mon}} \left(\frac{d\sigma}{d\Omega}\right)_R \Omega mon \frac{1}{\eta_{HYRA}}$$

where η_{HYRA} is the transmission efficiency of HYRA and is to be estimated for the above studied systems. For the efficiency estimation the nearby system ^{16}O+^{197}Au was studied as a calibration system. For the above systems, one measurement has been done for the ERs at same lab energy, where the absolute cross section for the calibration system is available in literature. The efficiency estimation for our system is to be finalized [3].

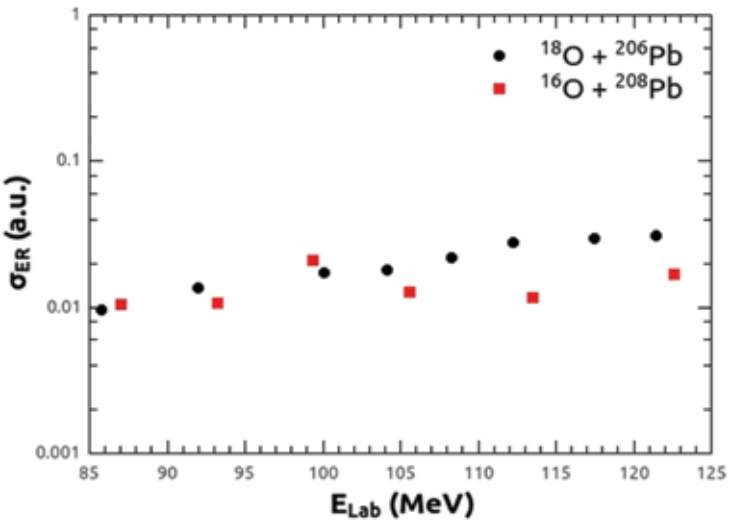

Fig. 5.1.13: ER excitation functions in arbitrary units.

Regarding spin distribution, the analysis is in progress and the convolution method has been adopted to extract the multiplicity distributions from the fold distributions [4]. To estimate the detection and the geometrical efficiencies of the 4π spin spectrometer, the computational simulation code Geant4 is used.

The authors are thankful to the Pelletron and LINAC groups for providing stable beams of requisite properties throughout the experiment and the target laboratory of IUAC for fabrication of targets.

REFERENCES

1. N. Madhavan *et al.,* Pramana - J. Phys. **75,** 317 (2010).
2. N. Madhavan *et al.,* EPJ Web Conf. **17,** 14003 (2011).
3. E. Prasad *et al.,* Phy. Rev. C **84,** 064606 (2011).
4. S. Y. Van Der Werf, Nucl. Instr. Meth. **153,** 221 (1978).

5.1.8 In-beam γ-ray spectroscopy of 124Te

S. S. Tiwary[1], H. P. Sharma[1], S. Chakraborty[1], C. Majumder[1], S. Rai2, Pragati[3], Mayank[4], S. S. Bhattacharjee[5], R. P. Singh[5], S. Muralithar[5], P. Banerjee[6], S. Ganguly[7], S. Kumar[8] and A. Kumar[9]

[1]Department of Physics, Institute of Science, Banaras Hindu University, Varanasi, India
[2]Department of Physics, Visva-Bharati, Santiniketan, India
[3]Department of Physics, Indian Institute of Technology, Roorkee, India
[4]Amity Institute of Nuclear Science and Technology, Amity University, Noida, India
[5]Nuclear Physics Group, Inter-University Accelerator Centre, New Delhi, India
[6]Nuclear Physics Division, Saha Institute of Nuclear Physics, Kolkata, India
[7]Department of Physics, Bethune College, Kolkata, India
[8]Department of Physics and Astrophysics, University of Delhi, Delhi, India
[9]Department of Physics, Panjab University, Chandigarh, India

Tellurium isotopes belong to transitional region between spherical Sn and triaxially deformed Xe−isotopes. Hence, investigation of Te-isotopes could provide a platform to study the shape and phase evolution in nuclei. The study also helps us to understand the interactions of valance nucleons with the spherical core, as the interaction is responsible for shape evolution and quantum phase transitions in nuclei. Previously, some critical point symmetries were theoretically predicted to exist in A~125 amu mass region, using IBM calculations [1]. The study also suggests 124Te could be the possible case for E(5) critical point symmetry, hence, it became important to search for the existence of such critical point symmetry in ^{124}Te. Te-isotopes are well studied up to A = 122 amu [2]. Hence, based on above arguments and in order to extend the systematics, present work is intended to study ^{124}Te, which is also needed to investigate the structural behaviour of heavier Te-isotopes. One of the major challenge in studying heavier Te−isotopes, is the unavailability of suitable target-projectile combination for fusion evaporation reaction. This is essential to get better statistics with higher angular momentum. Experimental information for these heavier isotopes is mainly available via transfer reactions [3, 5, 6], β-decay studies [3], Coulomb excitations [4] and fission spectroscopy [7, 8]. In the present work ^{124}Te has been studied via fusion evaporation reaction.

The excited states of ^{124}Te were populated via ^{122}Sn(^{9}Be, α3n)^{124}Te fusion evaporation reaction, with ^{9}Be beam of 48 MeV beam energy. The experiment was performed using INGA array [9] with 15UD tandem accelerator facility [10,11] at IUAC. The array contained 14 Compton-suppressed Clover detectors, arranged in three different angles at 148º, 123oºand 90º with respect to beam axis.

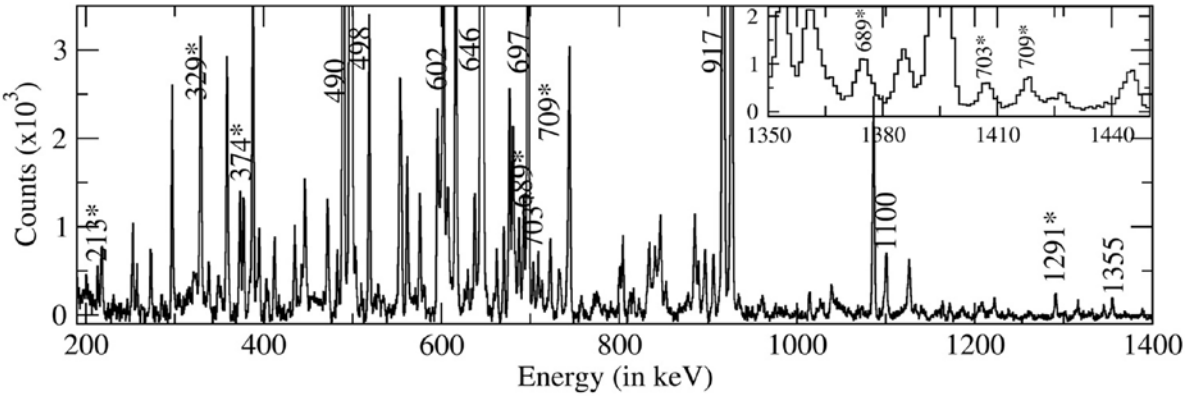

Fig. 5.1.14: 603 keV energy gated coincidence spectrum, where new transitions are marked with asterisks (*). The inset shows the γ-transitions of very close energies.

The data were recorded with two or higher fold coincidence conditions. Off-line data analysis was carried out using the INGA-sort and RadWare analysis package. Details of the experimental set up and data analysis are available in Ref. [12].

The present analysis is carried out, on the basis of γ-γ-coincidence relationship. The 603 keV γ-gated spectrum is shown in Fig. 5.1.14. Previously, several spin multiplets were found in ^{124}Te up to spin 6ħ [5]. In the present study, it is extended higher with the observation of two new spin multiplets of $I^{\pi} = 8^{+}$ at energy 2664 keV and 3038 keV and of $I^{\pi} = 10^{+}$ at energy 3154 keV and 3367 keV) (Fig. 5.1.15). The spin and parity of these states are confirmed on the basis of measuring the angular correlation between directionally oriented states and polarization

measurements of decaying γ-transitions, respectively. On the basis of systematics, nature of these excitations are predicted to be either as γ-vibrational states or as 4p-2h intruder states, as both possibilities have been systematically observed in neighboring even-even nuclei [5]. Further investigations are underway, in order to confirm the structural behavior of ^{124}Te.

Authors are thankful to the staff of target laboratory and Pelletron accelerator facility of IUAC. Authors acknowledge the INGA Collaboration supported by the University Grants Commission (UGC) and the Department of Science and Technology (DST) under INGA project (IR/S2/PF-03/2003-I). The first author is thankful to the UGC for financial support-vide contract no. 23/06/2013(I)EU-V.

REFERENCES

1. R. M. Clark *et al.,* Phys. Rev. C **69,** 064322 (2004).
2. S. Nag *et al.,* Phys. Rev. C **88,** 044335 (2013).
3. R. Georgii *et al.,* Nucl. Phys. A **592,** 307, (1995).
4. M. Saxena *et al.,* Phys. Rev. C **90,** 024316 (2014).
5. N. War *et al.,* Nucl. Phys. A **636,** 379 (1998).
6. T. von Egidy *et al.,* Phys. Rev. C **74,** 034319 (2006).
7. A. Astier *et al.,* Eur. Phys. J A **50,** 2 (2014).
8. N. Fotiades *et al.,* Phys. Rev. C **89,** 017303, (2014).
9. S. Muralithar *et al.,* Nucl. Instrum. Methods A **281,** 281 (2010).
10. G. K. Mehta *et al.,* Nucl. Instrum. Methods A **268,** 334 (1988).
11. D. Kanjilal *et al.,* Nucl. Instrum. Methods A **97,** 97 (1993).
12. S. Chakraborty *et al.,* Braz. J. Phys. **47,** 406 (2017).

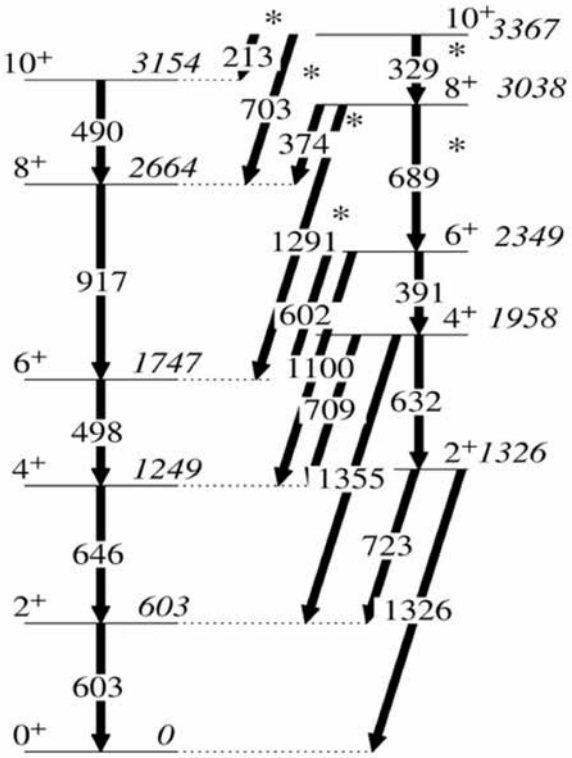

Fig. 5.1.15: Partial level scheme of 124Te, where newly placed transitions are marked with asterisks (*).

5.1.9 Probing of break-up fusion at energies above the Coulomb barrier using IUAC facilities

D. Singh[1], Sneha B. Linda[1], Pankaj K. Giri[1], Amritraj Mahato[1], Harish Kumar[2], Suhail A. Tali[2], M. Afzal Ansari[2], Asif Ali[2], Rahbar Ali[4], Nabendu Deb[3], R. Kumar[5], S. Muralithar[5] and R. P. Singh[5]

[1]Department of Physics, Central University of Jharkhand, Ranchi 835205, India
[2]Department of Physics, Aligarh Muslim University, Aligarh 202002, India
[3]Department of Physics, Gauhati University, Guwahati 781014, India
[4]Department of Physics, G.F. (P.G.), College, Shahjahanpur 242001, India
[5]Inter-University Accelerator Centre, Aruna Asaf Ali Marg, New Delhi 110067, India

The study of complete fusion (CF) and incomplete fusion (ICF) in heavy ion-induced reactions has been a subject of resurgent interest in the experimental nuclear physics. Several theoretical models have been proposed to understand the reaction mechanism of ICF. However, as such no model exists to reproduce the experimental data at projectile energy below 7 MeV/nucleon. It has been observed [1-3] that the dynamics of ICF reaction depends on many entrance channel parameters, namely, projectile energy, entrance channel mass asymmetry, α-Q value of the projectile, Coulomb Factor (Z_pZ_T) and the deformation parameter (β_2) of the target. It is important to understand how the structure of projectile and target affects ICF. An experiment has been done using ^{16}O beam on enriched ^{154}Sm target.

This experiment was performed at IUAC using recoil catcher activation technique. The targets of ^{154}Sm (enrichment ≈ 99%) of thickness ≈ 0.2-0.5 mg/cm^2 were prepared by vacuum evaporation technique in the target laboratory of IUAC. Each target was backed by an aluminium catcher of appropriate thickness to trap the recoiling products. Thickness of the target as well as Al-catchers was measured by α-transmission method. The stack was consisting of 8 targets along with Al-catchers. This stack was irradiated by the $^{16}O^{+7}$ beam at General Purpose Scattering Chamber (GPSC). The minimum laboratory energy of beams was just above the Coulomb barrier. Keeping in view the half-lives of interest, around 14-16 hrs of irradiation was carried out with beam current ≈ 2-5 pnA. The activities produced in the target and catcher foils after irradiation were recorded by a pre-calibrated High Purity Germanium Detector (HPGe) detector coupled to a CAMAC based data acquisition system. The data acquisition has been done using the software CANDLE [4]. The evaporation residues (ERs) produced and trapped in the catcher foils have been identified by their characteristic γ-rays and also by their

decay curve analysis. A γ-ray spectrum recorded in 16O+154Sm reaction at beam energy of 100 MeV has been displayed in Fig 5.1.16. The γ-rays of respective ERs have been shown by arrows. Some ERs are populated through xn-channels whereas some are populated through αxn-channels, as identified from the γ-ray spectra. These ERs can be populated through CF and / or ICF reaction dynamics.

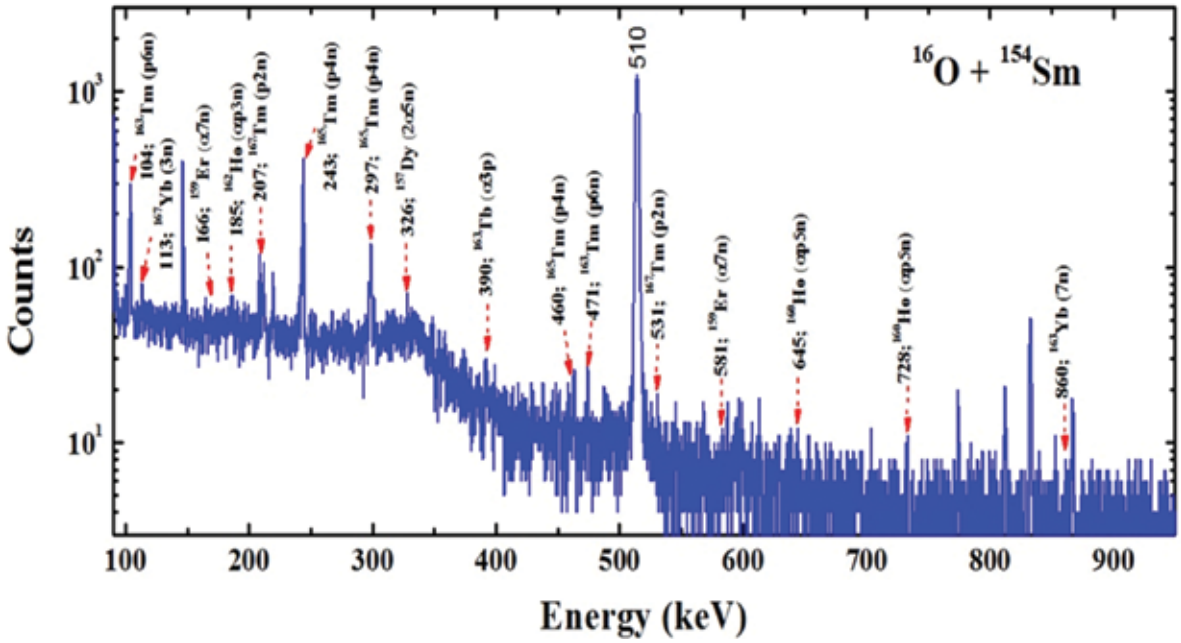

Fig. 5.1.16: Typical γ-ray spectrum showing γ-lines of different ERs populated via CF and/or ICF reaction in $^{16}O+^{154}Sm$ system at beam energy of 100 MeV.

REFERENCES

1. D. Singh, S. B. Linda, P. K. Giri, A. Mahato *et al.,* Phys. Rev. C **97,** 064604 (2018).
2. Harish Kumar, Suhail A. Tali, M. Afzal Ansari, D. Singh *et al.,* Eur. Phys. J. A **54,** 47 (2018).
3. Suhail A. Tali, H. Kumar, M. A. Ansari, A. Ali *et al.,* Nucl. Phys. A **970,** 208 (2018).
4. B. P. Ajith Kumar, E. T. Subramaniam *et al.,* DAE-BRNS Symp. Nucl. Phys, Kolkata, 2001; http://www.iuac.res.in/NIAS/

5.1.10 Fission-fragment mass distribution in neutron-deficient Po at low excitation energy

S. Gupta[1,2], C. Schmitt[3], A. Shrivastava[1,2], K. Mahata[1,2], P. Sugathan[4], A. Jhingan[4], K. S Golda[4], N. Saneesh[4], A. Chatterjee[4,5], Gurpreet Kaur[4], Divya Arora[4], Mohit Kumar[4], Louise Stuttge[3], S. K. Duggi[6], Prashant N. Patil[7], Kavita Chauhan[8], Kavita Rani[9], Honey Arora[9], Devinder Pal Kaur[9] and Vivek Mishra[10]

[1]Nuclear Physics Division, Bhabha Atomic Research Centre, Mumbai 400085, India
[2]Homi Bhabha National Institute, Anushaktinagar, Mumbai 400094, India
[3]Institut Pluridisciplinaire Hubert Curien (IPHC), CNRS/IN2P3, 23 rue du Loess, B.P. 28, F-67037 Strasbourg, France
[4]Inter University Accelerator Centre, Aruna Asaf Ali Marg, Post Box 10502, New Delhi 110067, India
[5]Department of Physics, The M.S. University of Baroda, Vadodara 390002, India
[6]Department of Nuclear Physics, Andhra University, Visakhapatnam 503003, India
[7]Department of Physics, Karnatak University, Dharwad 580003, India
[8]Department of Physics, Kurukshetra University, Kurukshetra 136119, India
[9]Departmen tof Physics, Panjab University, Chandigarh 160014, India
[10]Department of Physics, Banaras Hindu University, Varanasi 221005, India

While the importance of shell effects in the nascent fragments is well-established for low-energy fission of (trans-) actinides [1], the origin of asymmetric fission of n-deficient Hg [2], and more generally, pre-actinides in the lead region [3], remains un-explained. The possibility of a new type of asymmetric fission was raised [4].Yet, state-of-the-art models yield contradictory interpretation [4,5,6], namely about the respective role of shell effects and nuclear dynamics. Recently, the critical influence of N/Z and excitation energy of fissioning system was demonstrated [1]. A deeper insight is crucial, as it puts into question the validity of extrapolating the knowledge gained from heavy systems. Low-fissility makes the study in the region very challenging.The present measurement aimed at contributing to the worldwide intense effort in the field. We selected ^{198}Po as the fissioning system, as it is ideally situated – mid-way between Hg and actinides.Recent measurements suggest a triple-humped structurefor ^{194,196}Po [3].

The experiment was performed using the 15UD Pelletron LINAC accelerator at IUAC by bombarding a 200 μg/cm^2 thick 170Yb target (30 μg/cm^2 C backing) with a 28Si beam at three sub-barrier energies. Two large-area (16×11cm^2) multi-wire proportional counters (MWPCs) [7], were used to measure the time-of-flight (TOF) (recorded with respect to the RF signal), (x,y) position, and energy loss (ΔE) information of fragments in coincidence. The detectors were placed at 70º on each side of the beam axis at a distance of 30 cm from the target,inside the scattering chamber of the NAND facility. Fission events were selected by putting two-dimensional gate in the time of flight difference and total energy loss (ΔE_1+$\Delta\mu E_2$) spectrum, (Fig. 5.1.17(a)). The TOF and position information were used to determine the fragment velocities and emission angles.Further, the correlation plot of the folding angle and azimuthal angle along with parallel and perpendicular components of velocities of the fragments were used to clean-up the fission selection.The preliminary fragment mass distributions are shown in Fig. 5.1.17(b). Analysis of the total kinetic energy information and interpretation of the results are in progress.

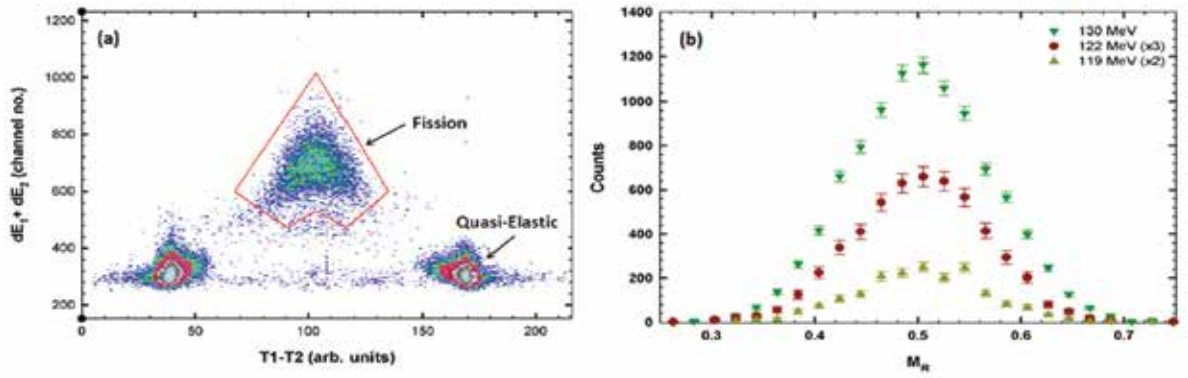

Fig. 5.1.17: (a) TOF difference vs total energy loss spectrum for particles detected in the MWPCs and (b) preliminary fragment mass distribution from ^{28}Si+^{170}Yb fusion-fission reaction at three beam energies. Yields are scaled as indicated, for legibility.

REFERENCES

1. A. N. Andreyev, K. Nishio and K.-H. Schmidt, Rep. Prog. Phys. **81,** 016301 (2018).
2. A. N. Andreyev *et al.,* Phys. Rev. Lett **105,** 252502 (2010).
3. L. Ghys, A. N. Andreyev *et al.,* Phys. Rev. C **90,** 041301(R) (2014).
4. T. Ichikawa *et al.,* Phys. Rev. C **86,** 024610 (2012).
5. S. Panebianco *et al.,* Phys. Rev. C **86,** 064601 (2012).
6. M. Warda *et al.,* Phys. Rev. C **86,** 064601 (2012).
7. A. Jhingan *et al.,* Nucl. Inst. Meth. A **745,** 106 (2014).

5.1.11 High Spin study of ^{129}La

K. Rojeeta Devi[1], Suresh Kumar[1], Naveen Kumar[1], Neelam[1], Neeraj Kumar[1], A. Banerjee[1], C. V. Ahmad[1], Anand Pandey[1], Ravi Bhushan[1], Unnati Gupta[1], S. K. Chamoli[1], S. Verma[1], Samit Kr. Mandal[1], R. Garg[2], Indu Bala[2], S. Bhatacharya[2], R. P. Singh[2], S. Muralithar[2], Pragati[3], Ajay Y. Deo[3], Sutanu Bhattacharyaa[4], T. Trivedi[4], Anupriya Sharma[5], Chandrani Majumder[6] and H. P. Sharma[6]

[1]Department of Physics and Astrophysics, University of Delhi, Delhi 110007, India
[2]Inter-University Accelerator Centre, Aruna Asaf Ali Marg, New Delhi 110067, India
[3]Department of Physics, Indian Institute of Technology Roorkee, Roorkee 247667, India
[4]Department of Pure and Applied Physics, Guru Ghasidas University, Bilaspur 495009, India
[5]Department of Physics, Banaras Hindu University, Vanarasi 221005 , India
[6]Department of Physics, Himachal Pradesh University, Shimla 171005 , India

In high spin phenomena, the shape and the structure of a nucleus is governed by the configuration of the valence nucleon and their angular momentum coupling. In mass A ~ 130 amu region, the Fermi surface is occupied by the $g_{7/2}$, $d_{5/2}$, $h_{11/2}$, $s_{1/2}$ and $d_{3/2}$ for the proton and $d_{5/2}$, $g_{7/2}$, $s_{1/2}$,$d_{3/2}$ and $h_{11/2}$ for the neutrons, single particle orbitals. The nuclei in this mass region are known as γ-soft [1] and exhibit different high spin phenomena such as magnetic rotation, anti-magnetic rotation, chiral rotation, super-deformation, identical bands. Chiral rotation and wobbling rotation, which are the signature of a triaxial nucleus were reported in ^{135}Nd [2] and ^{133}Ce [3], and ^{135}Pr [4], respectively. The ^{129}La (odd Z) nucleus come out to be an interesting candidate for the present study of nuclear high spin phenomenon as mentioned above. In the previous study of this nucleus, two strongly coupled band namely- band (1,2) and band (8,9) and many dipole bands were established having mostly tentative spin and parity assignments [5].

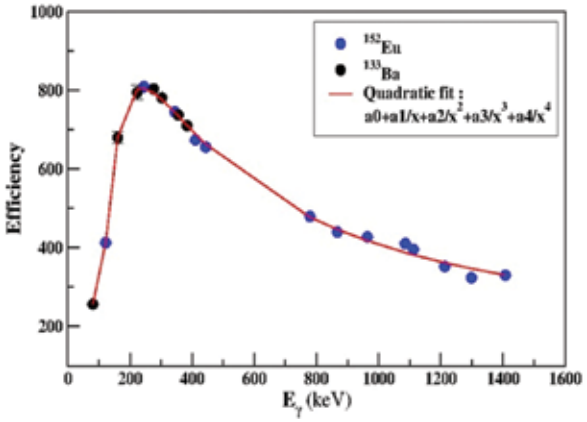

Fig. 5.1.18: Efficiency curve for Clovers at 148º.

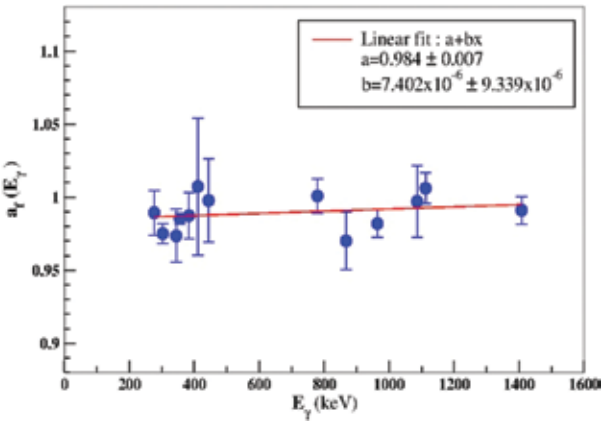

Fig. 5.1.19: Correction factor $a_I(E_\gamma)$, as a function of γ-ray energy.

The excited states of ^{129}La nucleus was populated through the reaction ^{121}Sb(^{12}C, 4*n*)^{129}La, with a beam energy of 66 MeV which was provided by the 15-UD Pelletron at IUAC. The target was ^{121}Sb of thickness 900 µg/cm^2 with a backing of 10.0 mg/cm^2 thick ^{197}Au. The γ-rays were detected by using the INGA spectrometer at IUAC [6] which consisted of 18 Compton-suppressed clover detectors with four, four, six, two and two number of detectors placed at angles 148º, 123º, 90º, 57º and 32º with respect to the beam direction, respectively. The distance between the target position and the detectors was 25 cm. The list mode data were taken in double and higher fold γ-ray coincidence using CANDLE. A total of about 13×10^7 events were recorded. The symmetric and asymmetric matrices were generated by sorting the data with CANDLE and INGASORT programs.

Table 5.1.1: Gamma energy E_γ, level energy Ei , relative intensity I_γ, R_{DCO} , polarization asymmetry Δ, multi-polarity and the initial spin J_i^π and the final spin J_f^π of the γ-decay.

E_γ(keV)	E_i (keV)	I_γ(rel.)	R_{DCO}	Δ	Multipolarity	J_i^π	J_f^π
269.7	442.1	100	1.12(5)^Q	0.06(2)	E2	15/2$^-$	11/2$^-$
445.8	2431.2	9.5(2)	0.97(9)^Q	0.16(6)	E2	23/2$^+$	19/2$^+$
474.3	916.6	82.2(16)	0.97(5)^Q	0.11(2)	E2	19/2$^-$	15/2$^-$
586.2	3017.7	12.0(2)	0.91(10)^Q	0.02(2)	E2	27/2$^+$	23/3$^+$
641.4	1558.0	63.8(13)	0.99(5)^Q	0.08(2)	E2	23/2$^-$	19/2$^-$
674.5	3017.7	1.3(4)	1.14(29)^Q	-0.06(5)	E1(ΔI=0)	27/2$^+$	27/2$^-$
714.0	3731.7	7.8(2)	0.93(9)^Q	0.09(4)	E2	31/2$^+$	27/2$^+$
785.3	2343.2	34.1(7)	0.90(6)^Q	0.06(3)	E2	27/2$^-$	23/2$^-$
823.3	4555.0	10.2(2)	1.08(20)^Q	0.11(5)	E2	35/2$^+$	31/2$^+$
873.1	2431.2	21.1(4)	1.00(17)^Q	-0.03(1)	E1(ΔI=0)	23/2$^+$	23/2$^-$
910.5	3253.5	16.1(3)	0.93(11)^Q	0.11(5)	E2	31/2$^-$	27/2$^-$
921..7	5476.7	3.2(1)	0.96(11)^Q	0.08(5)	E2	39/2$^+$	35/2$^+$
1013.2	4266.8	13.6(3)	1.04(11)^Q	0.06(2)	E2	35/2$^-$	31/2$^-$
1067.8	1985.0	6.3(2)	1.10(13)^Q	-0.07(5)	E1(ΔI=0)	19/2$^+$	19/2$^-$

In the present report, the band 3 and 4 are confirmed for gamma-ray placement and spin parity was determined using the Directional Correlation of Oriented State ratio (R_{DCO}) and polarization measurement. The intensities of the γ-rays were determined by measuring the efficiency of the array using ^{152}Eu and ^{133}Ba standard radioactive sources. The R_{DCO} were obtained by taking the events detected at 148º Clover detectors on one axis and the events detected at 90º Clover detectors on the another axis. Various gates were set on stretched Quadrupole (Q) transition of known multi-polarities to extract the R_{DCO}. The efficiency curve for 148º Clover detectors as a function of γ-ray energy is shown in Fig. 5.1.18. For the polarization measurement, the Clovers in the 90º ring of the INGA array were used as polarimeters. The correction factor, as a function of gamma-energy is plotted and is shown in Fig. 5.1.19. The calculated values are summarized in Table 5.1.1 along with the assigned multi-polarity of the γ-ray transitions. Further analysis for the other bands and the theoretical calculations are in progress.

REFERENCES

1. S. Frauendorf, J. Meng, Nucl. Phys. A **617,** 131 (1997).
2. S. Mukhopadhyay, D. Almehed, U. Garg, S. Frauendorf et al., Phys. Rev. Lett. **99,** 172501 (2007).
3. A. D. Ayangeakaa *et al.,* Phys. Rev. Lett. **110,** 172504 (2013).
4. J. T Matta *et al.,* Phys. Rev. Lett. **114,** 082501 (2015).
5. Y. He *et al.,* J. Phys. G: Nucl. Part. Phys. **18,** 99 (1992).
6. S. Muralithar *et al.,* Nucl. Instrum. Methods A **622,** 281 (2010).

5.1.12 Study of break-up fusion reactions using ^{13}C ion beam in the energy range of 4-7 MeV/nucleon

Suhail A. Tali[1], Harish Kumar[1], M. Afzal Ansari[1], Asif Ali[1], D. Singh[2], Rahbar Ali[3], Pankaj K. Giri[2], Sneha B. Linda[2], Siddharth Parashari[1], R. Kumar[4], R. P. Singh[4] and S. Muralithar[4]

[1]Department of Physics, Aligarh Muslim University, Aligarh 202002, India
[2]Centre for Applied Physics, Central University of Jharkhand, Ranchi 835205, India
[3]Department of Physics, G. F. (P. G.) College, Shahjhanpur 242001, India
[4]Inter University Accelerator Centre, Aruna Asaf Ali Marg, New Delhi 110067, India

Fusion reactions induced by heavy ions play a crucial role in nuclear physics, as they enable us to study the properties of super heavy nuclei. At projectile energies above the Coulomb barrier, complete fusion (CF) and incomplete fusion (ICF) are the two most dominant reaction modes [1, 2]. In case of CF, the incident projectile completely fuses with the target nucleus and leads to the formation of highly excited compound nucleus (CN), which de-excites via emission of light nuclear particles and gamma rays. In ICF (also known as break-up fusion or massive transfer process), the incident projectile breaks in the vicinity of target nuclear field, one of the fragment fuses with the target nucleus giving rise to a composite system of lower mass, excitation energy, charge and momentum transfer. The excited composite system also de-excites via emission of light nuclear particles and gamma rays. The unfused fragment moves as a spectator in the forward direction, with velocity nearly equal to that of the projectile, and has no impact on the way the reaction proceeds [3]. The study of CF and ICF reaction dynamics near and above the Coulomb barrier (CB) is still an enigma due to its dependence on various entrance channel parameters. Also, below 8 MeV/nucleon, there is no theoretical model available which could reproduce the experimentally measured ICF data satisfactorily [3, 4]. Furthermore, most of the studies on ICF are confined to α-cluster structure projectiles like ^{12}C, ^{16}O and ^{20}Ne. However there are a few studies available in the literature, which involve ^{13}C, ^{14}N and ^{19}F as projectiles. Thus, in order to get a proper understanding of ICF reaction dynamics and its behaviour on various entrance-channel parameters, the present work has been carried out using 13C non α-cluster projectile and ^{165}Ho as target.

The experiment was performed using 15UD-Pelletron accelerator facility of IUAC. The ^{165}Ho target foils and Al-catcher foils were fabricated at target development laboratory IUAC by using the rolling technique. In order to cover a wide energy range and to get various residues populated, stacked foil activation technique has been employed. The two stacks, each carrying four target foils backed by Al-catcher foils were irradiated separately at 88 MeV and 71 MeV in the general purpose scattering chamber (GPSC) for about seven hours. The activities induced in each target-catcher foil were recorded by using a pre-calibrated high purity germanium (HPGe) detector coupled to CAMAC based data acquisition system CANDLE.

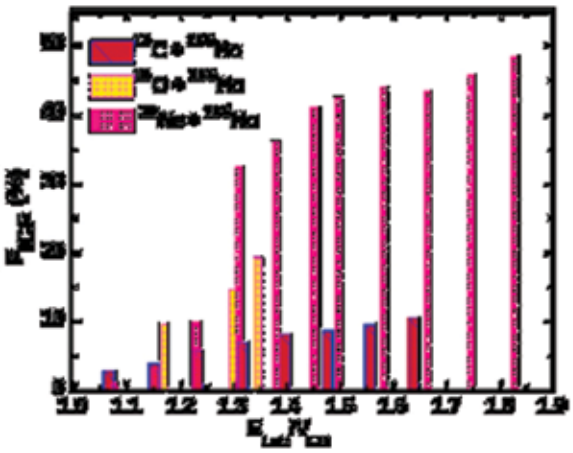

Fig. 5.1.20. The comparison of FICFvalues for different projectiles on same target ^{165}Ho. The x axis is normalized by the corresponding Coulomb barriers.

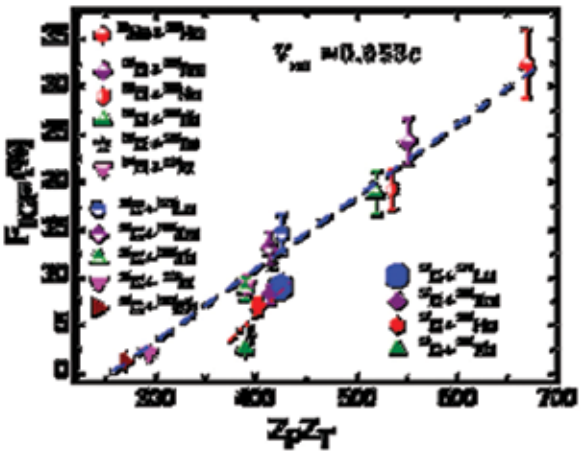

Fig. 5.1.21. Comparison of deduced FICF of ^{13}C+^{165}Ho system with systems studied earlier, as a function of entrance channel Z_PZ_T at same relative velocity (v_{rel}≈0.053c).

To understand the ICF reaction dynamics and its dependence on various entrance channel parameters, the excitation functions (EFs) of several (ERs) have been measured in the interaction of ^{13}C with ^{165}Ho at E_{lab}≈ 4–7 MeV/nucleon. The experimentally measured EFs are compared with the theoretical predictions of statistical model code PACE4, which takes into account only CF cross-sections. Hence any enhancement in the measured cross-sections from PACE4 predictions is attributed to ICF process. During the analysis it was found that experimentally measured EFs of xn and pxn channels matched well with PACE4 predictions for level density parameter value of a = A/10 MeV^{-1}. For the same level density parameter, the experimentally measured EFs of ERs populated via αxn and 2αxn show a significant enhancement from PACE4 predictions, indicating the ICF contribution. In order to understand the effect of projectile structure on ICF, the ICF fraction (FICF) for the present system has been compared with the F_{ICF} for other systems in which projectiles of different alpha separation energies interact with the same target ^{165}Ho as shown in Fig. 5.1.20. It may be observed from this figure that as the incident projectile energy increases the value of F_{ICF} also increases, but ^{13}C projectile with high break up threshold shows smaller ICF fraction than other projectile induced reactions with the same targets. It may be concluded from this observation that projectile structure strongly affects the break-up fusion process.

The influence of projectile structure on ICF is also clear from Fig. 5.1.21. In this figure the F_{ICF} has been plotted against the Coulomb factor (Z_PZ_T) at constant relative velocity ≈ 0.053c. It may be observed from this figure that due to increase in the values of Z_PZ_T, the Coulomb repulsion in the interacting system increases, which leads to the break-up of the incident projectile followed by fusion of one or more of the fragments with the target nucleus. It is important to note that for the systems with same Z_PZ_T values, the F_{ICF} is significantly different, this is again because of the strong projectile structure effect i.e., for the systems with same target, the F_{ICF} is more for those projectile induced reactions with low break-up threshold. It may be concluded from the present work that projectile structureis an important parameter which affects the ICF process.

REFERENCES

1. D. Singh *et al.,* Phys. Lett. B **774,** 7 (2017).
2. A. Yadav *et al.,* Phys. Rev. C **96,** 044614 (2017).
3. Suhail A. Tali *et al.,* Nucl. Phys. A **970,** 208 (2018).
4. Harish Kumar *et al.,* Eur. Phys. J. A **54,** 47 (2018).

5.1.13 Neutron multiplicity measurements for the near super-heavy nucleus ^{260}Rf

Meenu Thakur[1], B. R. Behera[1], Ruchi Mahajan[1], N. Saneesh[2], Gurpreet Kaur[1], M. Kumar[2], A. Yadav[2], N. Kumar[3], Kavita Rani[1], H. Arora[1], D. Kaur[1], S. Narang[1], Kavita[4], R. Kumar[4], P. Sugathan[2], A. Jhingan[2], K. S. Golda[2], A. Chatterjee[2], S. Mandal[3], A. Saxena[5], S. Kailas[5] and Santanu Pal[6]

[1]Department of Physics, Panjab University, Chandigarh 160014, India
[2]Inter University Accelerator Centre, Aruna Asaf Ali Marg, New Delhi 110067, India
[3]Department of Physics and Astrophysics, University of Delhi 110007, India
[4]Department of Physics, Kurukshetra University, Kurukshetra 136119, India
[5]Nuclear Physics Division, Bhabha Atomic Research Centre, Mumbai 400085, India
[6]CS - 6/1, Golf Green, Kolkata 700095, India

To understand the reaction mechanism of fusion-fission and quasi-fission processes, mass distribution, mass-energy distribution and mass-gated neutron multiplicity have been measured for the system ^{28}Si + ^{232}Th populating the near super-heavy compound nucleus ^{260}Rf at the beam energy ranging from 160 MeV to 200 MeV. These measurements have been carried out with ^{28}Si beam from 15UD Pelletron + LINAC booster using NAND [1] facility at IUAC, New Delhi. Both the thin (thickness of ~150 μg/cm^2 with carbon backing of thickness ~30 μg/cm^2) and thick (of thickness 1.5 mg/cm^2) ^{232}Th targets were used. The target was kept at the centre of the scattering chamber. The target ladder was tilted to an angle of 15° with respect to the beam axis in order to minimize the shadowing to position-sensitive multi-wire proportional counters (MWPC). Neutrons were detected using 50 organic liquid scintillators (BC501 A) in coincidence with either of the fission fragments detected using two large area (6.4"×4.4") MWPCs [2]. MWPCs were kept in the vertical configuration at folding angle of 159°. MWPC kept in the forward direction was at a distance of 21 cm from the target while the other detector in the backward direction was kept at a distance of 16 cm. Along with this, two silicon surface barrier detectors (SSBD) kept at ±12.5° with respect to the beam direction were used to monitor the beam flux. The detectors' signals were acquired by using VME based data acquisition system. The fission fragment detected in any of the MWPC in coincidence with RF is used as trigger for list mode data collection with LAMPS as the acquisition software.

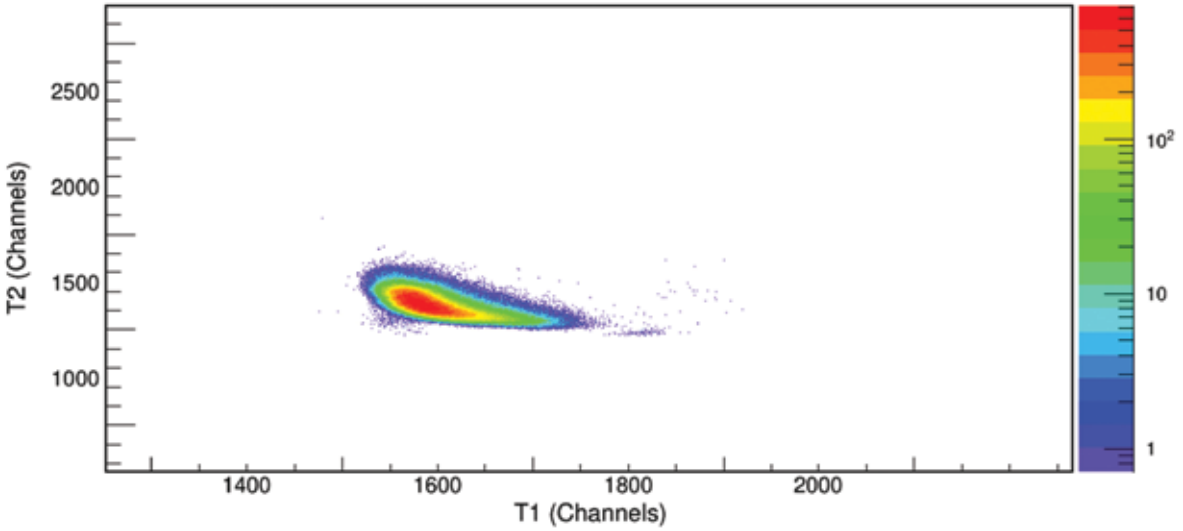

Fig. 5.1.22: Timing correlation between the two MWPCs for the ^{28}Si+^{232}Th reaction at E_{lab} = 170 MeV.

Fig. 5.1.22 shows the timing correlation between the two MWPCs for the ^{28}Si+^{232}Th reaction at E_{lab} = 200 MeV. Fig. 5.1.23 shows 2-D plots of neutron PSD vs. TOF from one of the neutron detectors. The neutron TOF is converted into neutron energy by considering the prompt gamma peak in the TOF spectrum as a time reference. Efficiency correction for the neutron detectors was performed using FLUKA [3] code. The efficiency corrected neutron energy spectrum is shown in Fig. 5.1.24, which will be next normalized with fission events.

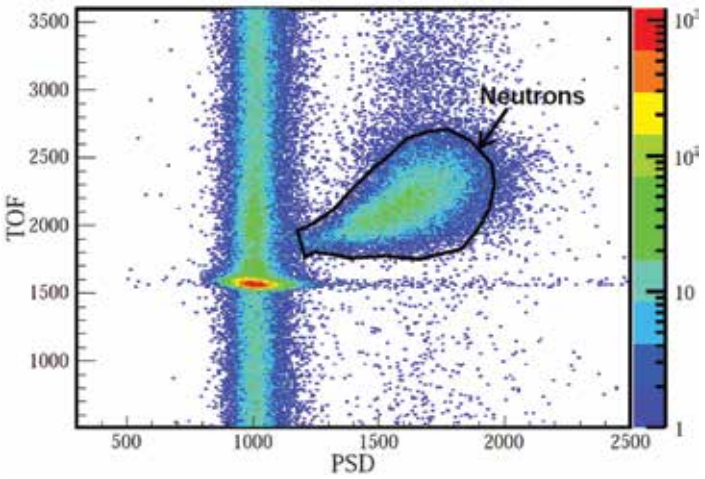

Fig. 5.1.23: 2-D plot of neutron PSD vs. TOF from neutron detector kept at zero degree with respect to fission detector. Black line indicates the neutron lobe.

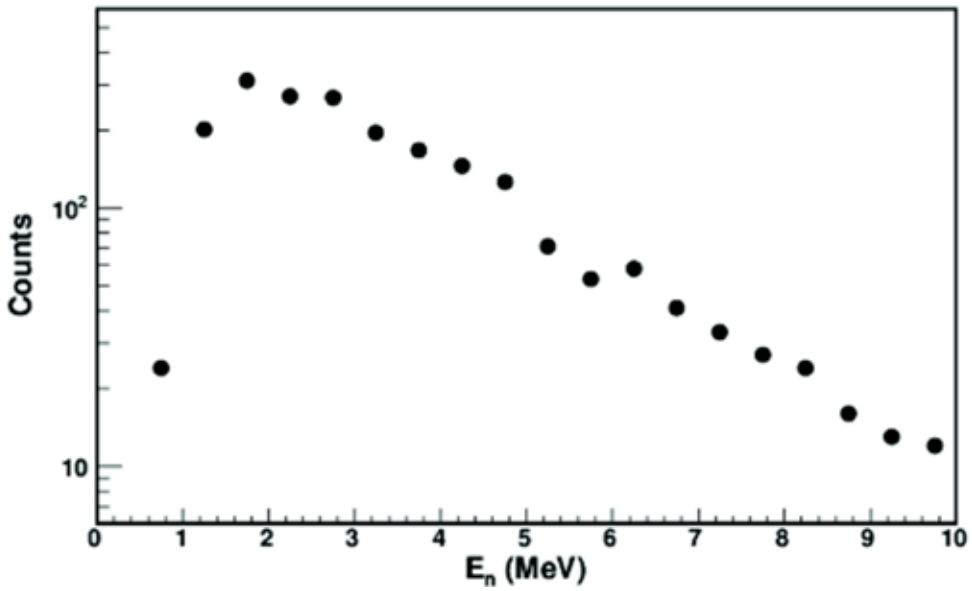

Fig. 5.1.24: Efficiency corrected neutron energy spectra from the neutron detector close to the fission detector.

The main motive of the data analysis is to extract the average neutron multiplicity, mass distribution and total kinetic energy (TKE) of the binary fragments and to correlate them with the number of emitted neutrons. The simultaneous fitting to extract neutron multiplicities is in progress.

REFERENCES

1. P. Sugathan *et al.,* Pramana **83,** 807 (2014).
2. A. Jhingan, Pramana – J. Phys. **85,** 483 (2015).
3. FLUKA, A multi-particle transport code, CERN.

5.1.14 Evaporation residue cross section measurements for the ^{28}Si + ^{188,192}Os reactions

P. V. Laveen[1], E. Prasad1, N. Madhavan[2], J. Gehlot[2], S. Nath[2], A. C. Visakh[1], M. Shareef[1], A. Shamlath[1], M. M. Hosamani[3], S. K. Duggi[4], Md. Moin. Shaikh[2], V. Srivastava[2], S. Sanila[5], R. Tripathi[6] and T. N. Nag[6]

[1]Department of Physics, SPS, Central University of Kerala, Kasaragod 671314, India
[2]Inter University Accelerator Centre, Aruna Asaf Ali Marg, New Delhi 110067, India
[3]Department of Physics, Karnatak University, Dharwad 580003, India
[4]Department of Nuclear Physics, Andhra University, Visakhapatnam 530003, India
[5]Department of Physics, University of Calicut, Calicut 673653, India
[6]Radio Chemistry Division, Bhabha Atomic Research Centre, Mumbai 400085, India

Experimental and theoretical investigations on hot fusion reactions in shell closed regions are important in the context of synthesis of super heavy elements (SHE) [1]. Efforts made to produce SHE and their isotopes provide a path to understand the basic nature of nuclei and nuclear interactions. Fusion reactions are the only established method for the SHE production till date. Evaporation residue (ER) measurements have shown a considerable difference in the cross section and a very different trend with compound nuclear excitation energies in different isotopes of thorium as compound nuclei (CN) populated through different entrance channels [2, 3]. The CN populated in these studies were differing only by two neutrons. To explore the anomaly in the reported cross sections and the difference in the trends of ER excitation functions, we started systematic studies of ER cross sections of different isotopes of thorium populated through the different entrance channels [4]. Here we report the ER cross section measurements for the ^{28}Si+ ^{188,192}Os reactions at energies above the Coulomb barrier.

Measurements were performed at the 15UD Pelletron-LINAC accelerator facilities of IUAC. The ERs were separated using the HYRA [5], operated in gas-filled mode with helium gas at 0.15 Torr. Pulsed ^{28}Si beams with a pulse separation of 2 μs were used in the measurement. The measurements were carried out at beam energies of 153, 157, 165, 174, 184, 194 and 204 MeV. Isotopically enriched osmium targets (^{188}Os and ^{192}Os), used in these measurements, were prepared by using the electro-deposition technique on thick copper backing at Radio Chemistry Division, BARC. Target chamber consisted of two monitor detectors, placed at 25° with respect to beam direction, which were used to detect the Rutherford-scattered events. A position sensitive multi-wire proportional counter (MWPC) of active area 6 inch × 2 inch was used to detect the Rs reaching the focal plane.

The MWPC was operated with isobutane gas at a pressure of 2.1 mbar throughout the experiment. A time of flight (TOF) spectrum was generated using the timing pulse from the MWPC anode signal as the start and the suitably-delayed radio frequency (RF) signal as stop. The energy loss (ΔE) versus TOF spectrum enabled an unambiguous identification of the ERs from other scattered particles reaching the focal plane. Fig. 5.1.25 shows two dimensional plot of ΔE versus TOF spectrum for the ^{28}Si + ^{192}Os reaction at 157 MeV beam energy.

In Fig. 5.1.26, we have shown the preliminary results of the trend of ER cross sections for ^{28}Si+ ^{188,192}Os reactions in arbitrary units. ER cross sections for both the systems show decreasing trend with excitation energies which could be due to the increased fission competition at higher excitation energies. Also, the heavier isotope of the CN shows larger ER cross sections which could be due to the decrease in neutron binding energy and the fissility of the CN with increasing neutron number, both favouring the neutron evaporation over fission decay in heavy isotopes. Similar observations have been made in Refs. [7, 8]. The detailed analysis of the data is in progress.

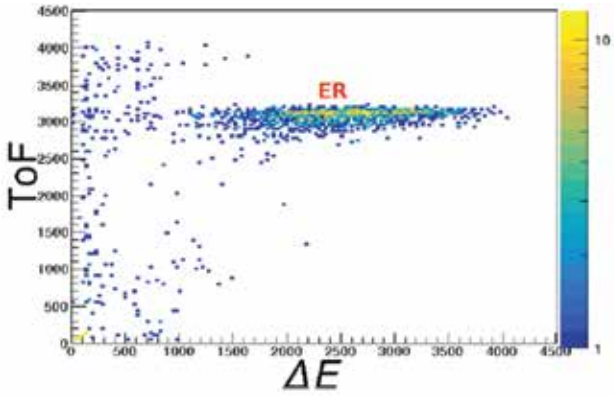

Fig. 5.1.25: Energy loss versus TOF spectrum for ^{28}Si+^{192}Os.

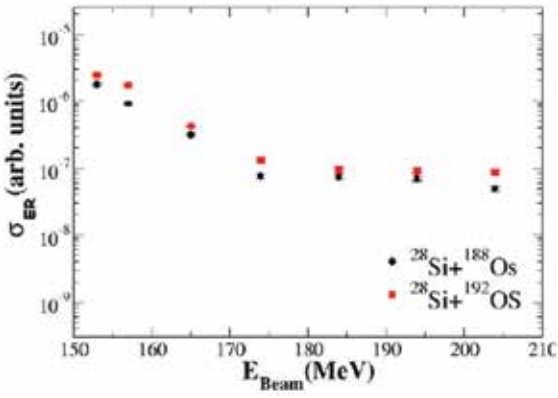

Fig. 5.1.26: ER excitation functions for the present systems in arbitrary units.

REFERENCES

[1] S. Hofmann and G. Munzenberg, Rev. Mod. Phys. **72,** 733 (2000).
[2] B. B. Back *et al.,* Phys. Rev. C **60,** 044602 (1999).
[3] S. Mitsuoka *et al.,* Phys. Rev. C **62,** 054603 (2000).
[4] P. V. Laveen *et al.,* Proc. DAE-BRNS Symp. Nucl. Phys. **60,** 558 (2015).
[5] N. Madhavan *et al.,* Pramana – J. Phys. **81,** 317 (2010).
[6] A. Shamlath *et al.,* Phys. Rev. C **95,** 034610 (2017).
[7] R. N. Sagaidak and A. N. Andreyev, Phys. Rev. C **79,** 054613 (2009).
[8] K. Satou et al., Phys. Rev. C **65,** 054602 (2002).

5.1.15 Fission fragment mass distributions from light thorium compound nuclei

S. K. Duggi[1], P. Sandya Devi[1], G. Naga Jyothi[1], A. Tejaswi[1], M. Ratna Raju[1], V. Vishnu Jyothi[1], P. V. Madhusudhana Rao[1], N. Saneesh[2], A. Jhingan[2], K. S.Golda[2], C. Yadav[2], Mohit Kumar[2], P. Sugathan[2], Meenu Thakur[3], M. Shareef [4], A. Shamlath[4], P. V. Laveen[4] and B. K. Nayak[5]

[1]Department of Nuclear Physics, Andhra University, Visakhapatnam 530003, India
[2]Inter University Accelerator Centre, Aruna Asaf Ali Marg, New Delhi 110 067, India
[3]Department of Physics, Panjab University, Chandigarh 160014, India
[4]Department of Physics, Central University of Kerala, Kasaragod 671314, India
[5]Nuclear Physics Division, Bhabha Atomic Research Centre, Mumbai 400085, India

Nuclear fission is a complex process of collective rearranging of nuclear matter. Though, it has been studied extensively, both experimentally and theoretically, since its discovery, studies are providing new insights as the new experimental tools are becoming available to explore new observables such as fission fragment mass-distribution, charge-distribution, total kinetic energy, angular-correlations and mass-energy distributions [1]. The earlier measurements of mass distributions primarily show asymmetric mass division in both spontaneous and low-energy induced fission of actinide nuclei [2]. However, in Ra-Th region, it has been observed that the mass and / or charge distributions contain two components of symmetric and asymmetric fission modes [1]. The fission dynamics can be understood by examining the individual fission modes which are suggested by Brosa et al [3]. Bimodal fission has been reported by different authors in various fissioning nuclei ranging from light actinide (thorium) to very heavy actinide nuclei. From these observations, it may be suggested that more than one scission configurations may be possible. One of them is elongated shape probably associated with

the symmetric liquid drop path while the other configuration corresponds to a compact shape which results in an asymmetric mass division due to shell stabilisation effects in the fragments. Therefore, at lower excitation energies, shell stabilisation will result in asymmetric mass division and as the excitation energy is increased the symmetric component will become the predominant mode. It is also observed that the increase in nucleon number of the fissioning heavy nucleus has shown a transition from symmetric to asymmetric fission modes in ATh nuclei (A = 222 – 226 amu). With this motivation, we have performed an experimental study of fission fragment mass distributions in ^{A}Th* nuclei (A = 222 – 226 amu) at excitation energies ranging from the lowest possible up to about 100 MeV.

Experimental measurements were performed using NAND facility [4] at IUAC. A pulsed beam of 18O with a pulse width of 1 ns and the pulse separation of 250 ns was provided by the 15UD Pelletron [5] and superconducting linac [6] combined facility. In this experiment, thin ^{204,206,207,208}Pb targets were used. Targets were prepared with thicknesses of approximately 200 μg/cm^2 deposited on 30 μg/cm^2 carbon backing. The experiment was performed at a range of beam energies from 76 MeV to 155 MeV. The fission fragment Time of Flight (TOF) was measured relative to the RF signal of the linac. Fission fragments were detected in two multi-wire proportional counters (MWPCs) in coincidence. These two detectors were placed at folding angle of 160º for the beam energies of 105 – 155 MeV and 165º for the beam energies of 76 – 95 MeV. Neutron multiplicity data were also collected at selected lower energies.

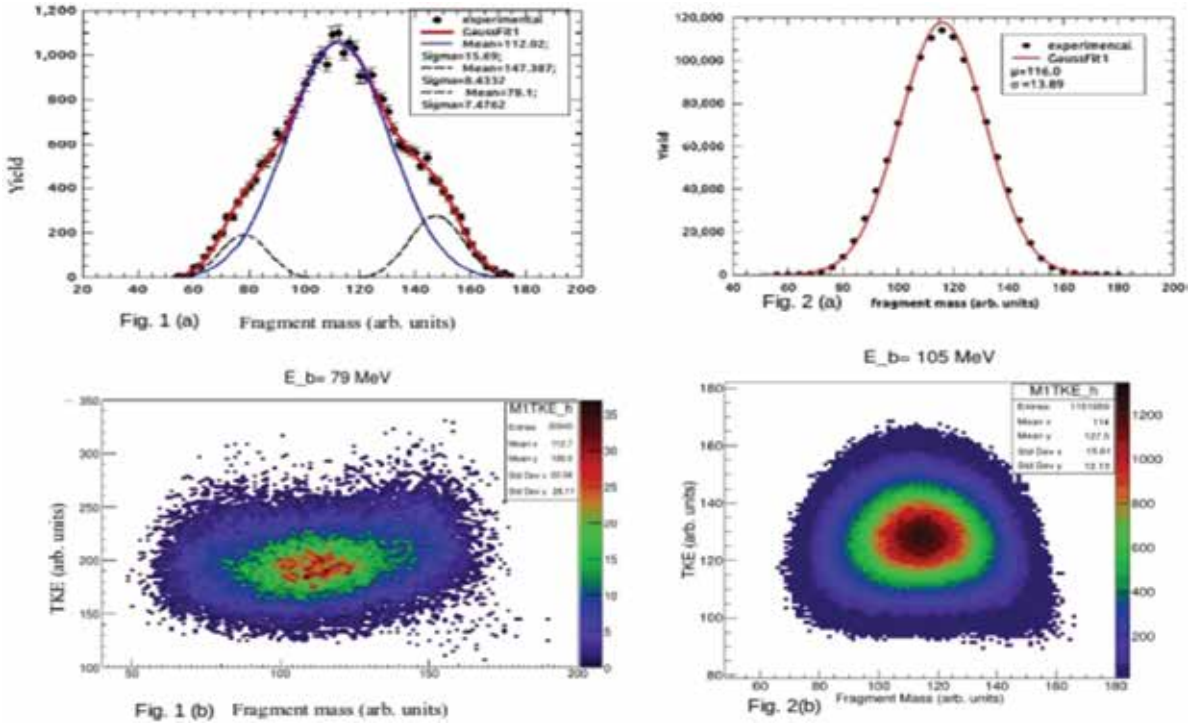

Fig. 5.1.27: Mass distribution and mass-energy distribution of fission fragments from ^{226}Th* at E* = 27 MeV (left panels). The same at E* = 50 MeV (right panels).

Here we report preliminary results of data analysis on reaction ^{18}O+^{208}Pb → ^{226}Th*. At lower most beam energies, presence of both symmetric and asymmetric components were seen to coexist. At higher energies, symmetric component was predominant and asymmetric component became very small with increasing excitation energy. The mass peaks corresponding to the asymmetric component are slowly disappearing with increasing excitation energy above 35 MeV. Fig. 5.1.27 shows the preliminary mass distribution mass-energy distribution of fission fragments from ^{226}Th*. At the lower excitation energy (27 MeV), both symmetric and asymmetric modes of fission were observed, whereas at higher excitation energy (50 MeV), only symmetric mode of fission was observed.

REFERENCES

1. M. G. Itkis *et al.,* Proc. 5th Int. Conf. on Dynamical Aspects of Nuclear Fission, pp. 177 (2001).
2. A. Chaudhuri *et al.,* Phys. Rev. C **91,** 044620 (2015).
3. U. Brosa *et al.,* Phys. Rep. **197,** 167 (1990).
4. P. Sugathan *et al.,* Pramana – J. Phys. **83,** 807 (2014).
5. D. Kanjilal *et al.,* Nucl. Instrum. Methods A **328,** 97 (1993).
6. S. Ghosh *et al.,* Phys. Rev. ST Accel. Beams **12,** 040101 (2009).

5.1.16 Investigation of nuclear structure in ^{63}Cu using ^{52}Cr(^{18}O,αp2n) reaction

S. Rai[1,2], B. Mukherjee[1], U. S. Ghosh[1], A. Biswas[1], A. Chakraborty[1], A. K. Mondal[1], S. Chakraborty[3], G. Mukherjee[4], Indu Bala[5], S. Muralithar[5] and R. P. Singh[5]

[1]Department of Physics, Siksha-Bhavana, Visva-Bharati, Santiniketan, Bolpur 731235, India
[2]Department of Physics, Salesian College, Siliguri Campus, Siliguri 734001, India
[3]Department of Physics, Institute of Science, Banaras Hindu University, Varanasi 221005, India
[4]Variable Energy Cyclotron Centre, 1/AF Bidhannagar, Kolkata 700064, India
[5]Inter-University Accelerator Centre, Aruna Asaf Ali Marg, New Delhi 110067, India

Nuclei in the vicinity of the doubly magic N = Z = 28 shell gap form an interesting region for nuclear structure studies. Due to the co-existence of both single particle and collective behavior, nuclear structure of these nuclei offers a testing ground for many theoretical predictions. In this work, we have investigated the nuclear structure of ^{63}Cu (Z = 29, N = 34)) using the fusion-evaporation reaction ^{52}Cr(^{18}O, αp2n) at a beam energy of 72.5 MeV. Fourteen Compton suppressed Clover detectors of the Indian National Gamma Array (INGA) [1] were used to collect the γ-rays emitted by the excited residual nuclei. A total of 2.12×10^9 events, in which at least two Clover detectors fired in coincidence, were collected during a beam time of around five days in a list-mode format using the data acquisition software CANDLE [2]. The raw data in the list-mode format were then sorted into several symmetric E_γ-E_γ and angle dependent matrices after gain-matching the energy of each Clover detector to 1.0 keV / channel. Further analysis of the data was performed with the help of the standard analysis packages, *viz.* Radware [3] and INGASORT [4]. Multi-polarity analysis was performed using the conventional DCO ratio analysis and using the Clover detector as Compton polarimeter, polarization asymmetry factors were also determined for many γ-rays.

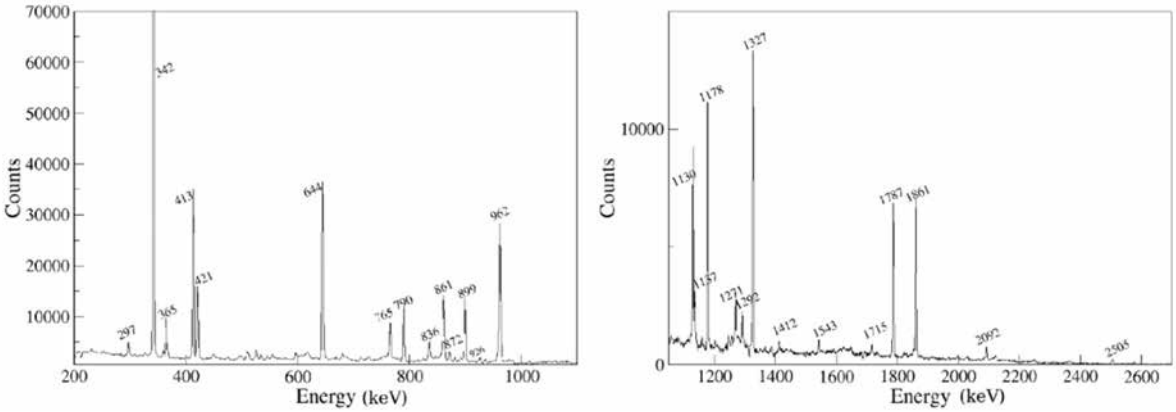

Fig. 5.1.28: Coincidence spectrum gated by 1650 keV transition of ^{63}Cu.

Based on the known ground state spin-parity, the γ-γ coincidence relationship, intensity arguments, multi-polarity and the polarization analysis, the level scheme of ^{63}Cu has been extended up to an excitation energy ~8.36 MeV and spin ~(25/2)$\hbar$ with the addition of twenty-one new gamma-ray transitions [5]. A representative coincidence spectrum gated by 1650 keV transition of ^{63}Cu is shown in Fig. 5.1.28 and the proposed level scheme is shown in Fig. 5.1.29. As far as the new level scheme is concerned, the excited levels of ^{63}Cu appear to be mainly of single particle in nature with many branchings from each excited level. Branching ratios for many transitions have also been calculated in this work. To understand the nature of the level scheme, shell model-calculations have been performed in the $f_{5/2}pg_{9/2}$ model space with ^{56}Ni core using two different effective interactions *viz.* JUN45 [6] and jj44b [7]. With a single proton and seven neutrons outside the 56Ni core, the major orbitals that affect the structure of this nucleus are the negative parity $1f_{5/2}$, $2p_{3/2}$, $2p_{1/2}$ orbitals and the positive parity $1g_{9/2}$ orbital. These calculations describe the levels fairly well in terms of level energy and transition rates. The role of the $1g_{9/2}$ orbital has been found to be of paramount importance in producing the high spin states and the excitation in the $f_{5/2}pg_{9/2}$ orbitals are more dominant in defining the observed level structure than the excitation across the magic shell gap N = Z = 28.

Authors would like to thank the staff members of the 15UD Pelletron accelerator facility and the target laboratory at IUAC for providing excellent support. We would like to thank A. Sharma (HPU), S. Nandi (VECC), S. S. Bhattacharjee (IUAC) and R. Garg (IUAC) for their help during the experiment. SR would like to acknowledge the financial assistance received from IUAC via UFR Project (UFR-49318). BM and USG acknowledge the financial support received from SERB, DST under EMR Project No. EMR/2015/000891. Constant encouragement from D. Kanjilal (IUAC) is gratefully acknowledged.

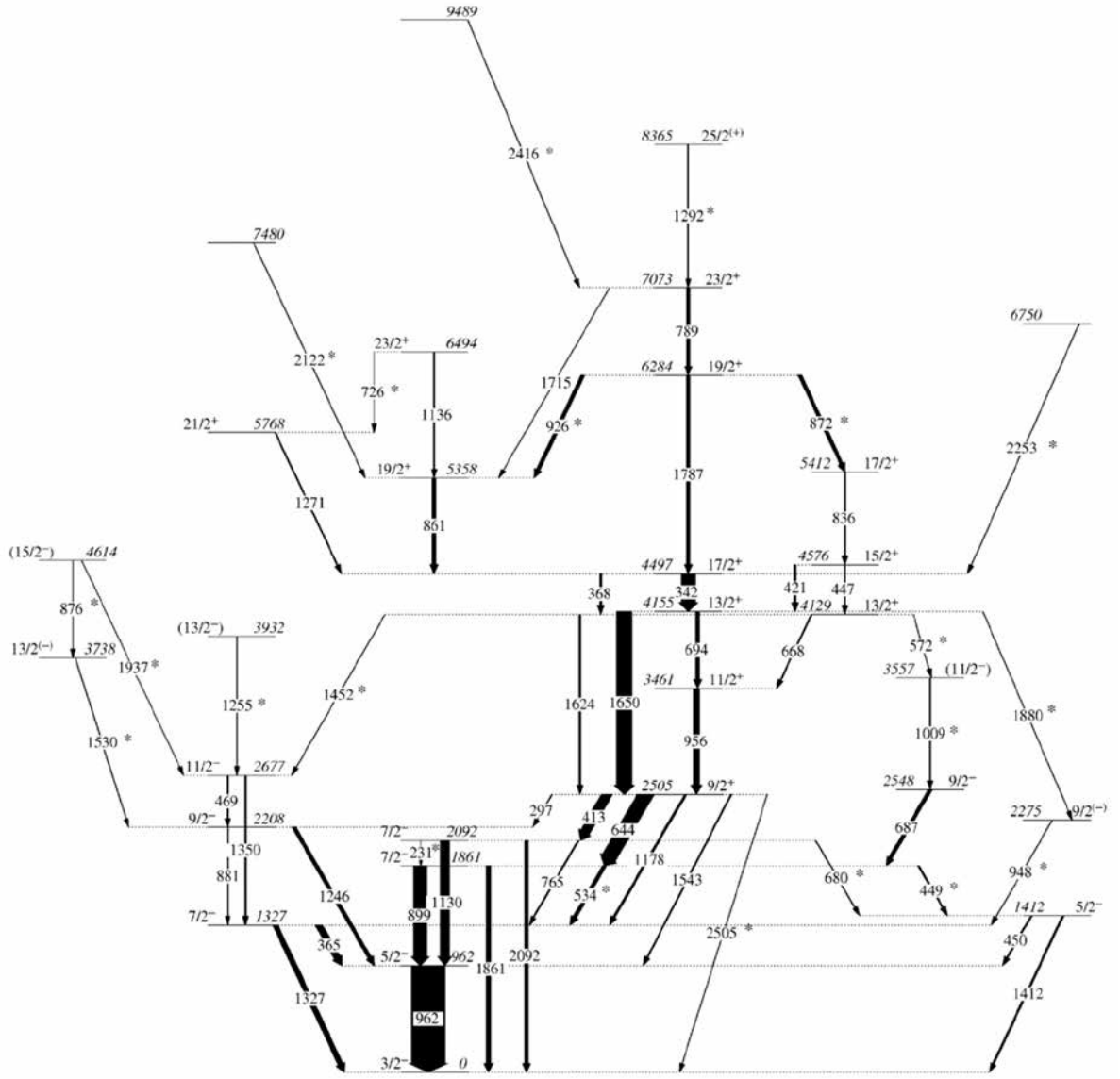

Fig 5.1.29: Proposed level scheme for ^{63}Cu. All transitions satisfy the γ-γ coincidence conditions and the widths of the arrows correspond to the relative γ-ray intensities. The level energies and the γ-ray energies are given in the units of keV.

REFERENCES

1. S. Muralithar *et al.,* Nucl. Instrum. Methods A **622,** 281 (2010).
2. B. P. Ajith Kumar *et al.,* Proc. DAE-BRNS Symp. Nucl. Phys. **44,** 390 (2001).
3. D. C. Radford, Nucl. Instrum. Methods A **361,** 290 (1995).
4. R. K. Bhowmik *et al.,* Proc. DAE-BRNS Symp. Nucl. Phys. **44,** 422 (2001).
5. S. Rai *et al.* Eur. Phys. J. A **54,** 84 (2018).
6. M. Honma *et al.,* Phys. Rev. C **80,** 064323 (2009).
7. B. A. Brown, A. F. Lisetskiy, private communication; see also endnote [28] in Cheal et al., Phys. Rev. Lett. **104,** 252502 (2010).

5.1.17 Barrier distribution measurements for ^{28}Si+^{232}Th reaction

Gurpreet Kaur[1],[2], B. R. Behera[1], A. Jhingan[2], N. Saneesh[2], Mohit Kumar[2], Meenu Thakur[1], Abhishek Yadav[2], Ruchi Mahajan[1], Kavita[1], Shruti[1] and P. Sugathan[2]

[1]Department of Physics, Panjab University, Chandigarh 160014, India
[2]Inter-University Accelerator Centre, Aruna Asaf Ali Marg, New Delhi 110067, India

The cold-fusion reactions based on lead or bismuth targets and the hot-fusion reactions based on the act in ide targets are successfully use dinthe synthesis of heavy and super-heavy elements (SHE). The set wo types of reactions significantly differ by the amount of released thermal energy and the static deformation of the associated target nuclei. It is revealed from the experimentally measured excitation functions that, in cold-fusion,

the highest cross-sections are obtained at beam energies where a contact configuration between the project ile and the spherical target nucleusis just reached. However, in hot fusion, the maximum cross-sections are obtained at beam energies which are high enough so that projectile (like ^{48}Ca) and prolate target nuclei can come into contact at minimal distance (equatorial collisions) and thus form a most compact starting configuration on the way to the compound nucleus. The cross-sections decrease rapidly with drop in energy to values where the interaction is limited to polar collisions and the probability for re-separation of there action partners is high.

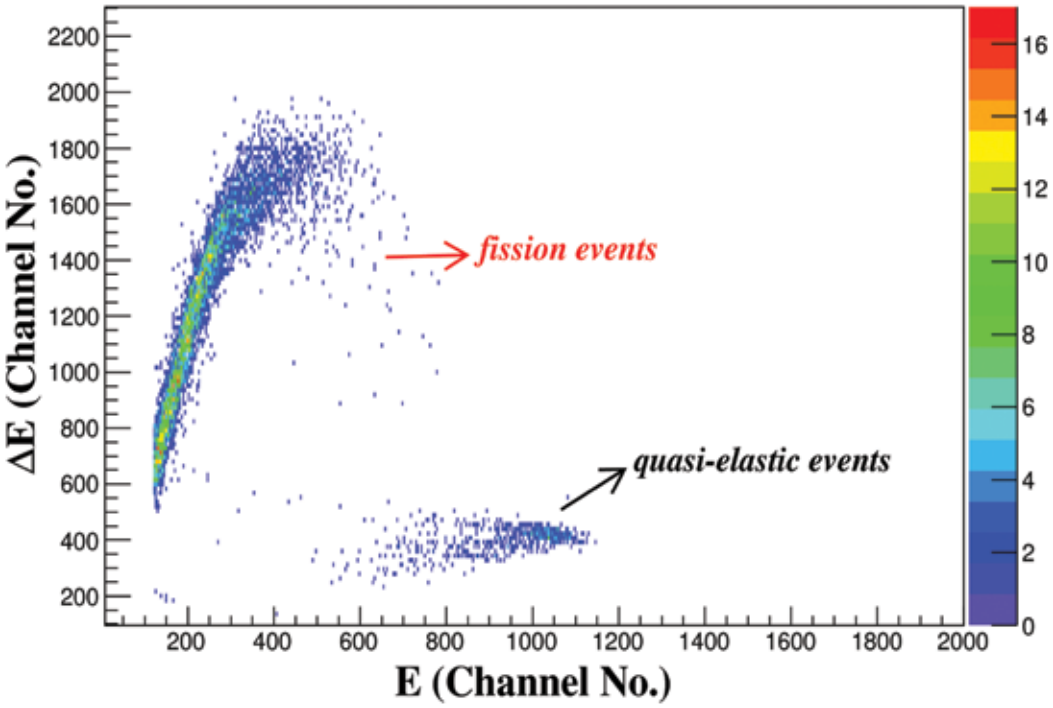

Fig.5.1.30: Two-dimensional correlation plot of E-ΔE signals from the hybrid telescope detector at 173º with respect to the beam direction in the ^{28}Si+^{232} Th reaction at E_{lab}=170MeV.

However, the results are different in the case of projectiles significantly lighter than ^{48}Ca. For example, in thereaction ^{16}O+^{238}U, the experimental data show a large enhancement of evaporation residue (ER) cross-section satsub-barrier energies, indicating fusion is independen to f the orientation of the target nucleus. Hence one may expect a transition from the orientation-independent fusion using light projectiles to the case of equatorial fusion using ^{48}Ca projectiles. In order to study the anticipated transition we had chosen the reaction ^{28}Si+^{232}Th with a projectile between ^{16}O and ^{48}Ca; the chosen target ^{232}Th has similar collective states as ^{238}U. To study the effec to f target orientation, we measured the barrier distribution (BD) for the ^{28}Si+^{232}Th system which may possibly form SHE ^{260}Rf$_{104}$*. To extract the BD, the technique of quasi-elastic (QE) scattering at large backward angles is utilized. The experiment was performed using the 15 UD Pelletron-linac accelerator facility of IUAC. To measure the QE events, the HYTAR facility [1], an array of hybrid telescope detectors comprising of ΔE and E detectors, was employed. The detectors were placed at angles from 160º to120º with an angular pitch of 10º and adome arrangement containing four detectors was placed at 173º with respect to the beam direction. The details about the detector system are available in Ref. [1]. Fig.5.1.30 shows the two-dimensional correlation plot of ΔE-E signals from the hybrid telescope detector at 173º with respect to the beam direction in the ^{28}Si+^{232}Th reactionat E_{lab}=170MeV. As each scattering angle corresponds to scattering at a certain impact parameter, the cross-sections will be scaled in energy by taking into account the centrifugal correction, i.e., $E_{eff} = \frac{2E_{c.m.}}{1+_{csc}\frac{\Delta_{c.m.}}{2}}$

Hence, combining the data from all detectors, the final QE cross-section σ_{QE} *(E)*, relative to the Rutherfords cattering cross-section σ_R *(E)*, with energy step of less than 1 MeV will be obtained [2]. Using this excitation function, the BD will be extracted by taking its first derivative, that is $\frac{\left(\frac{\sigma_{QE}{}^{(E)}}{\sigma_R{}^{(E)}}\right)}{dE}$. The analysis and the theoretical interpretation of BD are in progress.

REFERENCES

1. A. Jhingan et al., acceptedin Nucl. Instrum. Methods **903,** 326 (2018).
2. Gurpreet Kaur et al., Acta Phys. Pol. **B49,** 651(2018).

5.1.18 Sub-Barrier fusion of ^{32}S with ^{128,130}Te

G. Naga Jyothi[1], A. Tejaswi[1], P. Sandya Devi[1], S. K. Duggi[1], P. V. Madhusudhana Rao[1], S. Nath[2], N. Madhavan[2], J. Gehlot[2], A. Jhingan[2], T. Varughese[2], Md. Moin Shaikh[2], Rohan Biswas[2], Anjali Rani[3], P. Sugathan and B. K. Nayak[4]

[1]Department of Nuclear Physics, Andhra University, Visakhapatnam 530003, India
[2]Inter-University Accelerator Centre, Aruna Asaf Ali Marg, New Delhi 110067, India
[3]Department of physics and Astrophysics, University of Delhi, Delhi 110007, India
[4]Nuclear Physics Division, Bhabha Atomic Research Centre, Mumbai 400085 , India

Heavy ion fusion reactions occur when the interacting nuclei have their relative energies more than the barrier energy, and are forbidden at energies below the Coulomb barrier, classically. In sub-barrier region, fusion can occur due to the act of quantum mechanical tunnelling through the barrier. Enhancements in fusion cross sections were observed at low energies with respect to simple one dimensional barrier penetration model. These enhancements were due to coupling of internal degrees of freedom of projectile and target nuclei and also due to single-nucleon transfer process. Coupled-channels calculations (CC) have reproduced the experimental data by including the structural effects like nuclear vibration and deformation [1,2] in several reactions. In some reactions, the above channel couplings were unable to reproduce the experimental excitation functions for those systems having positive Q-value multi-neutron transfer channels [3]. Therefore, to find the effect of those channels on sub-barrier fusion, experiments were performed with two systems ^{32}S+ ^{128,130}Te. Both the systems have positive Q-value neutron transfer channels up to five and six, respectively.

In these experiments, fusion evaporation excitation functions were measured for ^{32}S+^{128,130}Te from below to above the Coulomb barrier using ^{32}S beam delivered by the 15UD Pelletron accelerator at IUAC [4]. Enriched targets of ^{128,130}Te (thickness ~300 μg/cm^2) were prepared by electron beam-based evaporation. Fusion excitation function measurements were carried out using the recoil mass spectrometer, Heavy Ion Reaction Analyzer (HIRA) [5], at lab energies from 140 to 110 MeV in steps of 2 MeV around barrier region. HIRA was positioned at 0º with respect to beam-axis with 5 mSr entrance aperture for the present measurements. A multi-wire proportional counter (MWPC) with active area of 150×50 mm^2 was used at the focal plane of HIRA to detect the fusion evaporation residues (ERs). Two silicon surface barrier detectors were placed, in the target chamber, at angles of 15º with respect to beam direction for beam monitoring and for normalization of cross-sections. A time of flight (TOF) signal was set up between the anode of MWPC and RF signal from the superconducting linac and used to separate the ER from background events. The ER excitation functions plotted in arbitrary units are shown in Fig. 5.1.31. A two-dimensional spectrum between energy loss in MWPC and TOF is shown in Fig. 5.1.32.

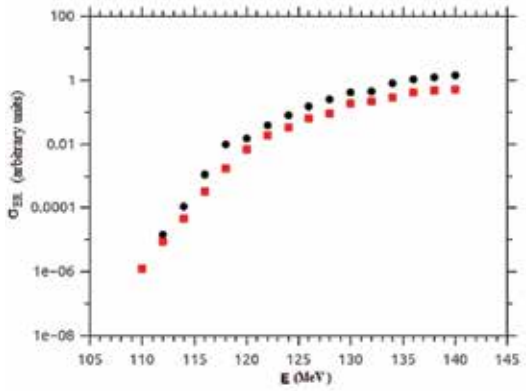

Fig. 5.1.31: Comparison of fusion excitation functions of the two reactions.

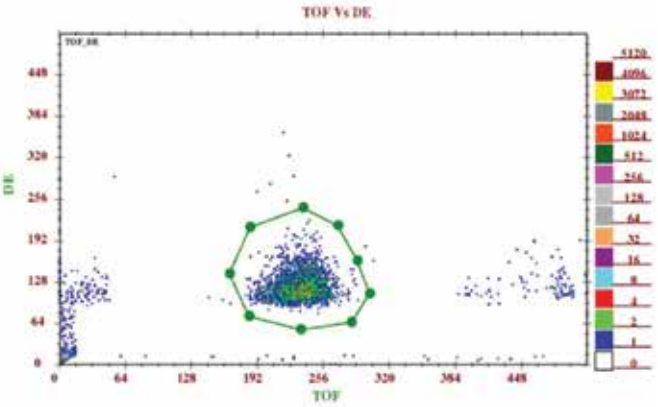

Fig. 5.1.32: 2-D projection of TOF-ΔE for ^{32}S+^{128}Te at E_{lab} = 120 MeV.

REFERENCES

1. A. M. Stefanini *et al.,* Phys. Rev. C **52,** R1727 (1995).
2. J. O. Newton *et al.,* Phys. Rev. C **64,** 064608 (2001).
3. L. S. Danu *et al.,* Phys. Rev. C **89,** 044607 (2001).
4. D. Kanjilal *et al.,* Nucl. Instrum. Methods A **328,** 97 (1993).
5. A. K. Sinha *et al.,* Nucl. Instrum. Methods A **339,** 543 (1994).

5.1.19 Multi-nucleon transfer and shape degrees of freedom in sub-barrier fusion

A. Tejaswi[1], G. Naga Jyothi[1], P. Sandya Devi[1], S. K. Duggi[1], P. V. Madhusudhana Rao[1], R. U. Amarnadh[2], S. Nath[3], J. Gehlot[3], Md. Moin Shaikh[3], Rohan Biswas[3], N. Madhavan[3], A. Jhingan[3] and B. K. Nayak[4]

[1]Department of Nuclear Physics, Andhra University, Visakhapatnam 530003, India
[2]Department of Physics, University College, University of Kerala, Thiruvananthapuram 695034, India
[3]Inter-University Accelerator Centre, Aruna Asaf Ali Marg, New Delhi 110067, India
[4] Nuclear Physics Division, Bhabha Atomic Research Centre, Mumbai 400085, India

Heavy ion fusion reactions play vital role in various branches of nuclear physics. Fusion reactions at higher incident energies relative to the nominal Coulomb barrier can be explained within the framework of statistical model of the compound nucleus. However, fusion excitation functions around the barrier are observed to have been influenced by various degrees of freedom of the interacting nuclei. Low energy surface vibrations and static deformed shapes of the fusing nuclei and also transfer of nucleons were suggested to provide doorways to the fusion process.

Fusion of heavy nuclei depends on the coupling of the internal degrees of freedom to the relative motion of the colliding nuclei in near-barrier energies. Experimentally measured enhancement of fusion cross sections may be explained by including nuclear structure effects in coupled-channels (CC) calculations. In certain reactions, CC calculations are unable to reproduce the experimental excitation functions. In such cases, the influence of positive Q-value neutron transfer channels may play a significant role and the same may have to be included in the CC calculations. Neutrons are insensitive to the Coulomb barrier and, therefore, their transfer starts at larger separations which will open doorways for fusion process.

In the present project, we performed measurements to study the influence of positive Q-value neutron transfer reaction channels on the fusion process in near and sub-barrier energies. Sub-barrier fusion excitation functions were measured down to 1 μb level for the reactions with ^{32}S beam on ^{94,98,100}Mo targets. In case of deformed ^{100}Mo target nucleus, in addition to deformation, there exist several positive Q-value neutron transfer channels (up to 6n-channel). It is interesting to investigate the interplay of deformation and neutron transfer degrees of freedom on fusion in the near- and sub-barrier regions.

The experiments were carried out using ^{32}S ion beam, with 1 μs pulse separation, from the 15UD / 16 MV Pelletron accelerator at IUAC. Isotopically enriched ^{94,98,100}Mo targets, of 100-500 μg/cm^2 thickness with 35 μg/cm^2 carbon backing, were used in the present experiment. The fusion excitation function measurements were performed at laboratory energies in the range of 85 to 130 MeV at 2 MeV steps. Two silicon surface barrier detectors were placed symmetrically at about ±15° angle with respect to the beam direction to detect the elastically-scattered particles which were used for beam flux normalization while determining the fusion cross sections. The fusion evaporation residues (ER) nuclei, produced inside the target, recoiled out of the thin target and travelled in the forward direction around 0°. The ERs were separated from the intense flux of scattered beam component and elastic recoils using the Heavy Ion Reaction Analyser (HIRA) and detected at the focal plane using a two-dimensional position sensitive multi-wire proportional counter. The yields of ERs were extracted from the two-dimensional projection spectra between x-position (X) and energy loss (ΔE) in the MWPC for above barrier energies while energy loss (ΔE) and time of flight (TOF) projections at below barrier energies. The transmission efficiency through HIRA was estimated by the Monte-Carlo simulation code TERS for each set of data. Typical two-dimensional projection spectrum between energy loss (ΔE) and TOF is shown in Fig. 5.1.33. The preliminary fusion excitation functions for ^{32}S+^{94,98,100}Mo systems are shown in Fig. 5.1.34.

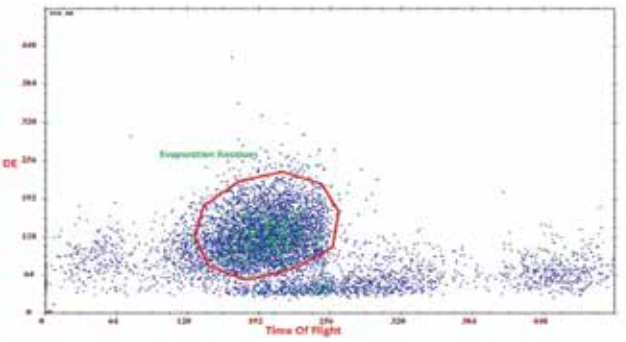

Fig. 5.1.33: Two-dimensional spectrum of TOF versus ΔE for ^{32}S+^{98}Mo at E_{lab} = 108 MeV.

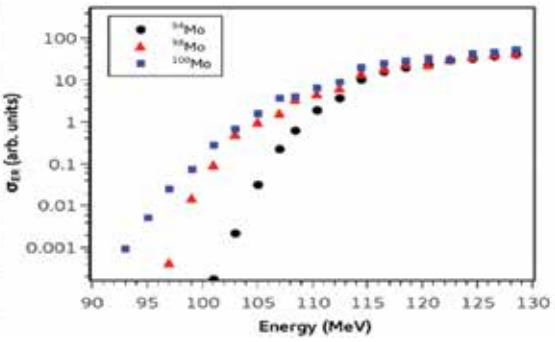

Fig. 5.1.34: Experimental fusion excitation functions for ^{32}S+^{94,98,100}Mo in arbitrary units.

REFERENCES
1. H. M. Jia *et al.,* Phys. Rev. C **89,** 064605 (2014).
2. H. Q. Zhang *et al.,* Phys. Rev. C **82,** 054609 (2010).
3. S. Nath, Comput. Phys. Commun. **180,** 2392 (2009).

5.1.20 Mass-distribution measurements for ^{48}Ti+^{144,154}Sm systems

Ruchi Mahajan[1], B. R. Behera[1], Meenu Thakur[1], Gurpreet Kaur[1], N. Saneesh[2], Mohit Kumar[2], Neeraj Kumar[3], K. Rani[1], D. Kaur[1], S. Narang[1], Kavita[4], Rakesh Kumar[4], P. Sugathan[2], A. Jhingan[2], K. S. Golda[2], A. Saxena[5], A. Chatterjee[2] and Santanu Pal[6]

[1]Department of Physics, Punjab University, Chandigarh 160014, India
[2]Inter-University Accelerator Centre, Aruna Asaf Ali Marg, New Delhi 110067, India
[3]Department of Physics and Astrophysics, University of Delhi, Delhi 110007, India
[4]Department of Physics, Kurukshetra University, Kurukshetra 136119, India
[5]Nuclear Physics Division, Bhabha Atomic Research Centre, Mumbai 400085, India
[6]CS-6/1, Golf Green, Kolkata 700095, India

For fusion-fission (FF) reactions induced between heavy ions, along with complete fusion, there are other competing channels such as quasi-fission (QF), and transfer induced fission at energies around the Coulomb barrier [1]. In the case of complete fusion, equilibration in all degrees of freedom is attained whereas QF is characterized by full energy dissipation but incomplete drift toward the energetically favoured mass-symmetric configuration [2]. For the actinide targets, transfer induced fission also plays crucial role in the fission dynamics. Measurements of fission fragment angular distribution (FFAD), mass-distribution (MD) and mass-energy correlation help in distinguishing between FF and QF processes [3]. The width of the MD is strongly influenced by the entrance channel properties, such as mass-asymmetry, deformation of interacting nuclei, collision energy and the charge product (Z_pZ_T) of the interacting partners. Any sudden change in the width of the MD would indicate departure from full equilibration. With this motivation, we have measured MD for the systems ^{48}Ti+^{144,154}Sm populating ^{192,202}Po compound nuclei (CN) with incident laboratory energy (E_{lab}) varying between 198 – 246 MeV. Knyazheva *et al.* [4] have studied the MD and FFAD for ^{48}Ca+^{144,154}Sm systems where fusion suppression and the presence of QF at energies near and below the Coulomb barrier were observed for the reactions with the deformed target ^{154}Sm. In this work, our aim is to compare the MD results of the ^{48}Ti+^{144,154}Sm systems with the one reported in ref. [4]. The experiment was performed at IUAC Pelletron-linac facility. Pulsed beam of ^{48}Ti, having pulse separation of 250 ns, was bombarded on the ^{144,154}Sm (350 μΔg/cm^2) sandwiched targets. Fission fragments were detected in coincidence by using two position-sensitive multi-wire proportional counters (MWPCs) mounted inside the scattering chamber of National Array of Neutron Detectors (NAND) kept at fission fragment folding angle (59° each). The MWPCs had an active area of 11 cm × 16 cm each and were kept at a distance of 16.5 cm from the target. Two silicon surface barrier detectors were also placed inside the chamber at ±12.5° with respect to beam direction for monitoring the beam. The trigger of the data acquisition was generated by setting up a coincidence between RF of the beam pulse and any of the fission detectors. The VME based data acquisition using LAMPS software was used to acquire and store event mode data. A plot of time of flight spectrum (TOF1 vs TOF2; 1 and 2 refer to the fragments detected in MWPC detectors 1 and 2, respectively) for ^{48}Ti+^{144}Sm at E_{lab} = 246 MeV is shown in Fig. 5.1.35 (left panel). A clear separation between the fission (fragment-fragment coincidence) and quasi-elastic scattering (projectile like-target like coincidence) events was obtained. The calibrated positions and the time of fight information from the MWPCs were used to obtain the fragment emission angles and velocities assuming two-body kinematics [5]. The fission events were selected by imposing a two-dimensional gate in the timing spectrum. The folding angle distribution is plotted by adding the emission angle for each event, that peaks around 125° at E_{lab} = 246 MeV as shown in Fig. 5.1.35 (right panel). The fission cross-section at 217 MeV relative to that at 246 MeV is smaller by a factor of 10, while at 203 MeV it is smaller by a factor of 500. At the lowest energy, the event rate corresponding to the quasielastic scattering is many orders of magnitude larger than that of fission. Further analysis to extract MD for both the systems is in progress.

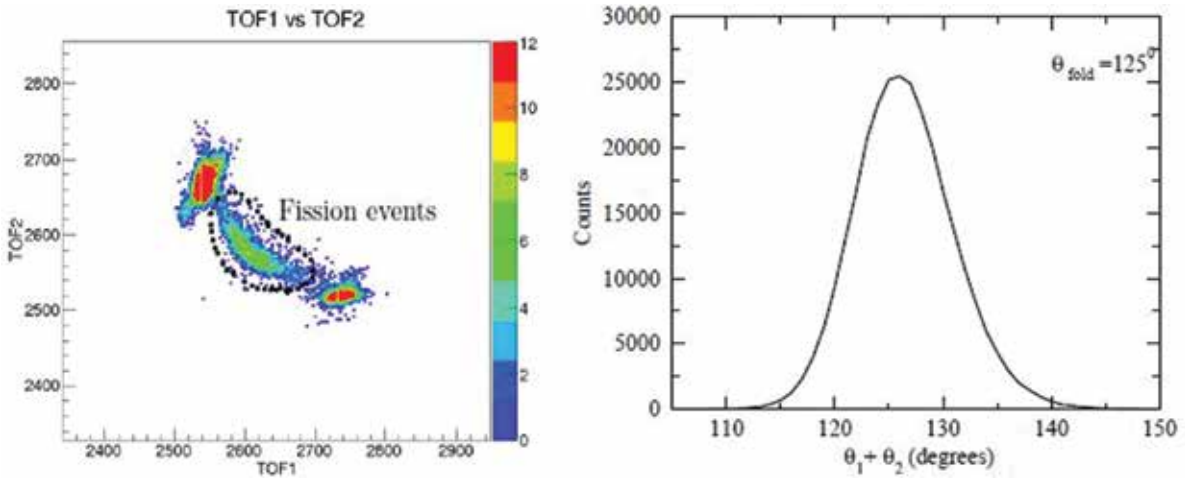

Fig. 5.1.35: (Left panel) Timing spectrum from the cathode of two MWPCs plotted against each other for ^{48}Ti+^{144}Sm at E_{lab} = 246 MeV. Events corresponding to fission are marked with a black lobe. (Right panel) Folding angle distribution of the fission fragments ($\theta_1+\theta_2$) for the same reaction at E_{lab} = 246 MeV.

REFERENCES

1. J. Toke, *et al.,* Nucl. Phys. A **440,** 327 (1985).
2. R. N. Sagaidak, *et al.,* Phys. Rev. C **79,** 054613 (2009).
3. W. J. Swiatecki, Phys. Scr. **24,** 113 (1981).
4. G. Knyazheva *et al.,* Phys.Rev. C **75,** 064602 (2007).
5. D. J. Hinde *et al.,* Phys. Rev. C **53,** 1290 (1996).

5.1.21 Fusion excitation functions and barrier distribution studies in ^{16}O+^{193}Ir,^{165}Ho systems

Amarnadh R. U.[1], K. M. Varier[1], G. Gopkumar[1], S. Nath[2], N. Madhavan[2], J. Gehlot[2], A. Jinghan[2], A. M. Vinodkumar[3], E. Prasad[4], P. V. Laveen[4], M. Shareef[4], G. Naga Jyothi[5], A. Tejaswi[5], Visakh A. C.[4], Md. Moin Shaikh[2], V. Srivastava[2] and Tathagata Banerjee[2]

[1]Department of Physics, University College, University of Kerala, Thiruvananthapuram 695034, India
[2]Inter-University Accelerator Centre, Aruna Asaf Ali Marg, New Delhi 110067, India
[3]Department of Physics, University of Calicut, Calicut 673653, India
[4]Department of Physics, Central University of Kerala, Kasaragod 671314, India
[5]Department of Nuclear Physics, Andhra University, Visakhapatnam 530003, India

Using coupled-channels Hamiltonian [1,2], a single barrier height is smeared into a distribution with weighted function of a characteristic distance (R_b). Stelson *et al.* [3] suggested that the distribution of barriers could be extracted directly from precise fusion excitation functions through a second order logarithmic derivative. In this experiment, systems populate the compound nuclei ^{209}At and ^{181}Re. Preliminary CCFULL and CCFUS [4,5] calculations are done in order to assess the theoretical cross sections for various rotational and vibrational couplings, since the targets are deformed.

The fusion studies have been carried out using the HIRA facility at compound nucleus excitation energies ranging from 36.4 – 65.1 MeV, for the heavier target and from 31.6 – 58.9 MeV, for the lighter target. Thin targets (~120 μg/cm^2 of ^{193}Ir and ~ 90 μg/cm^2 of ^{165}Ho) with thin carbon backings (20 μg/cm^2 and 15 μg/cm^2 for ^{193}Ir and ^{165}Ho, respectively) were prepared and mounted in experimental chamber where counts from two monitor detectors at angle 15.5º was used to fix beam position and normalization of cross sections. A pulsed beam with 4 μs pulse separation was used with a least possible FWHM and stable centroid. An MWPC of active cross sectional area of 6” × 2” at an isobutane pressure of 2 mbar was used in the focal plane of the spectrometer. Energy steps were chosen after applying corrections for beam energy uncertainties, and losses inside target and backing. The step size was slightly increased after E_{lab} increased to beyond 12% of PACE4-predicted [6,7] barrier. Efficiency of HIRA was estimated for the evaporation residues (ERs) using the semi-microscopic Monte Carlo code TERS [8]. Analysis of data was done with CANDLE [9]. Measured ER excitation function in arbitrary units for ^{16}O+^{165}Ho is shown in Fig. 5.1.36. Extraction of the barrier distributions is in progress.

The first author thankfully acknowledges the extensive help from S. R. Abhilash of the target laboratory, IUAC.

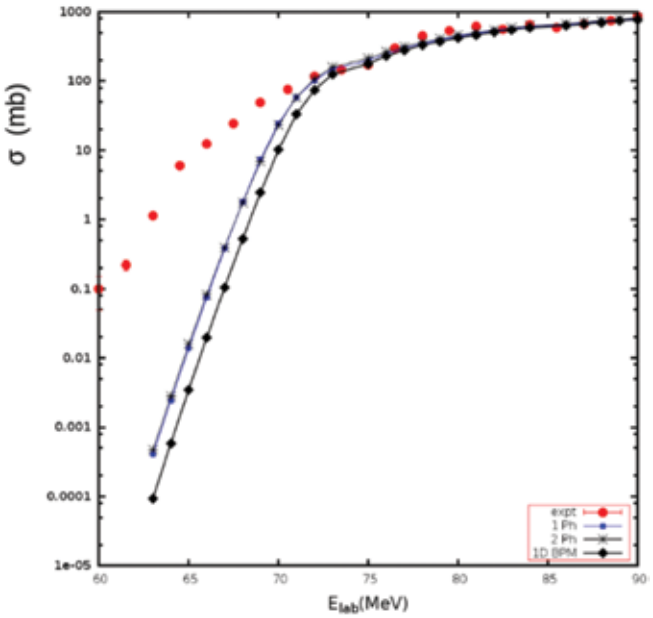

Fig. 5.1.36: Fusion excitation function with coupled-channels calculations for $^{16}O+^{165}Ho$.

REFERENCES

1. N. Rowley, Nucl. Phys. A **538,** 205c (1992).
2. C. L. Jiang *et al.,* Phys. Rev. Lett. **93,** 012701 (2004).
3. P. H. Stelson *et al.,* Phys. Rev. C **41,** 1584 (1990).
4. K. Hagino *et al.,* Comput. Phys. Commun. **123,** 143 (1999).
5. C. H. Dasso *et al.,* Comput. Phys. Commun. **46,** 187 (1987).
6. O. B. Tarasov, D. Bazin, Nucl. Instrum. Methods B **266,** 4657 (2008).
7. A. Gavron, Phys. Rev. C **21,** 230 (1980).
8. S. Nath, Comput. Phys. Commun. **180,** 2392 (2009).
9. B. P Ajithkumar *et al.,* Proc. DAE Symp. Nucl. Phys. **44B,** 390 (2001).

5.1.22 Heavy ion reaction induced alpha-gated gamma spectroscopy for structural study of nuclei around the Z = 82 shell closure

A. Banerjee[1], S. Mandal[1], G. Mukherjee[2], N. Madhavan[3], S. Nath[3], S. Bhattacharyya[2], R. Palit[4], S. S. Ghugre[5], A. Jhingan[3], Soumik Bhattacharya[2], Suresh Kumar[1], Abhishek Yadav[3], J. Gehlot[3], M. M. Hosamani[6], Mohit Kumar[3], Anjali Rani[1], Ruchika Gupta[1], Kajol Chakraborty[1], Neeraj Kumar[1], C. V. Ahmad[1], Unnati Gupta[1], G. Jnaneshwari[1], S. Muralithar[3], R. P. Singh[3], R. Kumar[3], Indu Bala[3], R. K. Gurjar[3], T. Varughese[3], Neelam[1] and K. Rojeeta Devi[1]

[1]Department of Physics and Astrophysics, University of Delhi, Delhi 110007, India
[2]Variable Energy Cyclotron Center, 1/AF Bidhan Nagar, Kolkata 700064, India
[3]Inter-University Accelerator Centre, Aruna Asaf Ali Marg, New Delhi 110067, India
[4]Department of Nuclear and Atomic Physics, Tata Institute of Fundamental Research, Mumbai 400005, India
[5]UGC-DAE-CSR Kolkata Centre, Sector III, LB-8 Bidhan Nagar, Kolkata 700098, India
[6]Department of Studies in Physics, Karnatak University, Dharwad 580003, India

Shape co-existence is a well-studied phenomenon, both theoretically and experimentally. It refers to the existence of multiple deformations, in single nuclei, generally at low spin and energy values. The nucleus ^{186}Pb has well established shape coexistence [1-3]. The motivation to conduct the reported experiment was rooted in the concept that the neighbouring nuclei (Z = 82 region), would have only a slightly varying structure, with respect to the strong presence of shape coexistence in ^{186}Pb nucleus [4-6].

Thus, using a beam of ^{28}Si, we bombarded ^{164}Er target to produce ^{192}Pb nucleus, which upon subsequent few neutron evaporation and α-decays would yield the nuclei of interest. The setup was used at the HYRA beamline, where the focal plane chamber had been slightly modified to accommodate an HPGe Clover detector in a head-on fashion with respect to the beam direction. Further, in order to identify the various heavy ions and particles, a silicon pad detector was placed inside the focal plane chamber downstream of the multi-wire proportional

counter (MWPC). A pair of HPGe Clover detectors was also placed at the target chamber location at angles of 90º and 135º, in order to assist in identification of the cocktail of nuclei produced at the target plane. HYRA was used in the momentum dispersive, gas-filled mode. Good separation for the various α-particles could be attained, using which a clear idea of correlated γ-emissions could be identified. TAC (time-to-amplitude conversion) spectra with a range of 10 μs were also collected in correlation with the Si-PAD detector as well as the MWPC and the Clover detector. These spectra would be useful in identification of isomers in the produced nuclei, with reference to their decay γ-spectroscopy at the focal plane Clover detector. Data analysis for isomer decay studies are being carried out using CANDLE software and lifetime of the isomers is being calculated by the standard method followed earlier [7].

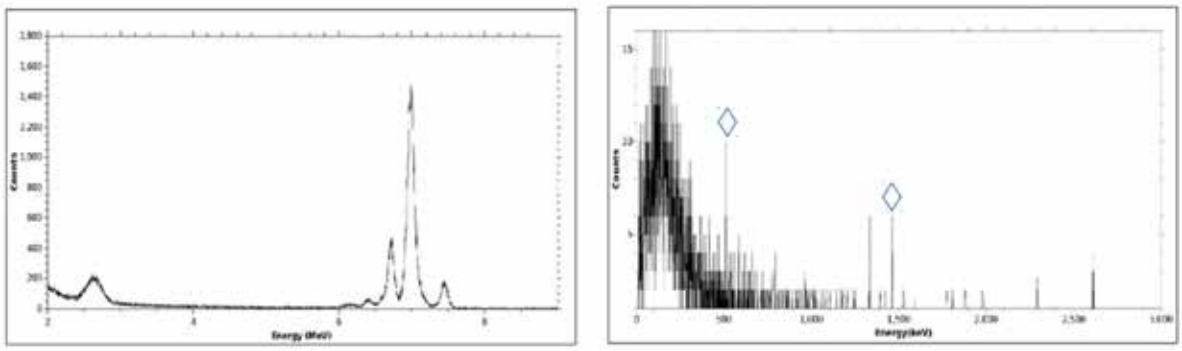

Fig. 5.1.37: (Left) Obtained alpha information from the Si-PAD detectors. (Right) Clover data gated by the Si-PAD channels from 6 – 8 MeV. Peaks marked with ◊ are background energies.

REFERENCES

1. A. N. Andreyev *et al.,* Nature (London) **405,** 430 (2000).
2. K. Van de Vel *et al.,* Phys. Rev. C **68,** 054311 (2003).
3. Bonn *et al.,* Phys. Lett. B **38,** 308 (1972).
4. Rud *et al.,* Phys. Rev. Lett. **31,** 1421 (1973).
5. Proetel et al., Phys. Lett. B **48,** 102 (1974).
6. Hamilton et al., Phys. Rev. Lett. **35,** 562 (1975).
7. T. Roy et al., Eur. Phys. J. A **51,** 153 (2015).

5.2 MATERIALS SCIENCE

AmbujTripathi

The materials science research programmes are being carried out in a wide range of energies varying from tens of keV to hundreds of MeV. This year there were many interesting results in the various areas of research including those on ion beams induced nanostructuring, synthesis of nanocomposites and applications, novel phase formations, etc. There were 44 user experiments of 125 shifts and these included 22 runs spread over 64 shifts which were students' BTA experiments associated with their Ph.D. programmes. The experiments are mostly performed in the irradiation chamber in the materials science beamlines in beamhall-I, though 1 experiment of 3 shifts utilizing in-situ XRD facility alongwith 3 other runs of 8 shifts were performed in materials science beamline in beamhall-II and 2 experiments of 6 shifts requiring low fluence irradiation were performed in GPSC. The users also utilized various synthesis techniques and offline characterization facilities such as XRD, AFM, SEM, Raman, UV-Vis, I-V, Hall measurement and this year more than 2100 samples were characterized.

Earlier studies on irradiation temperature dependence of shape elongation of vanadium nanoparticles (V NPs) in silica, were extended to exclude the possibility of, NPs having increased their sizes due to thermally enhanced diffusion with increasing the irradiation temperature. It was shown that the observed irradiation temperature dependence is not a spurious effect due to size changes of the NPs due to thermally-enhanced diffusion, but due to a true irradiation temperature dependence of the shape elongation of NPs. The development of α–Al_2O_3 was attempted by the novel approach of C^+(100keV) implantation method with application in field of an efficient medical radiation dosimeter. Electrical transport (I-V & R-T) facilities were used to understand the change in transport mechanisms under the application of electric field in $LaMnO_3/_{La0.7}Ca_{0.3}MnO_3$ and $LaMnO_3/Nd_{0.7}Sr_{0.3}MnO_3$ bilayers based devices in field effect geometry on (100) single crystalline $SrTiO_3$ substrate. Implantation of metal nanoparticles (Ag, Au) possessing surface plasmon resonance (SPR) peaks has been shown to enhance effective absorption of dye in TiO_2 matrix after low energy(80-120 keV) implantation. The interfacial stability of Nb/Cu bilayers was investigated after irradiation with 80-200 keV Si ions and it was shown that irradiation with

higher fluences produced significant changes at the interface. Engineering of electronic properties of graphene was shown and a fivefold increase in electron-hole mobilities and an increase in conductivity was demonstrated after irradiation with 100 MeV Ag ions at lower fluences. The systematic in-situ transport measurements and microstructural evolution studies in GaN Schottky diodes and GaN epitaxial layers was undertaken to study its radiation hardness using 200 MeV Ag and 100 MeV O ions at various fluences at two irradiation temperatures (80 K and 300 K). Analysis of defect assisted transport properties of GaN after Irradiation by 100 MeV oxygen and 200 MeV silver, showed an increase in the thermopower with irradiation resulting from decrease in electrical conductivity and Hall mobility. The studies on Graphene Oxide under SHI irradiation showed annealing at lower fluences after irradiation with SHI. The application of Gold –GO nanocomposites for Enzyme less glucose monitoring was also shown. Irradiation of ZnO NR arrays with 150 MeV Ag ions showed change in local surface chemistry due to formation of surface oxygen related defects resulting in superhydrophobic behaviour. The contribution of irradiation induced inplane strain on modification of the surface electronic properties of MoS_2 nanosheets was analyzed and it is observed that work function is linearly proportional to tensile strain along the basal plane. Gas sensing application of SHI irradiated epitaxial graphene on SiC was studied to determine an optimal fluence and consequently an optimal amounts of defects which maximize the gas sensing response towards NO_2 and NH_3 gases. Electromagnetic interference shielding of PMMA/NG nanocomposites and synthesis of nanostructured single phase $CoSb_3$ by low energy ion processing of Co/Sb bilayer with better thermoelectric properties were also demonstrated.

5.2.1 In-situ I-V Characterization of ZnO/NiO Heterojunction under swift heavy ion irradiation

P. K. Das[1], R. Biswal[2], R. J. Choudhary[3], S. A. Khan[4], R. C. Meena[4], N. C. Mishra[5] and P. Mallick[1],*

[1]Department of Physics, North Orissa University, Baripada 757003, India
[2]Deptartment of Applied Physics and Ballistics, Fakir Mohan University, Balasore 756019, India
[3]UGC-DAE Consortium for Scientific Research, Khandwa Road, Indore 452 017, India
[4]Inter-University Accelerator Center, Aruna Asaf Ali Marg, P.O. Box 10502, New Delhi 110 067, India
[5]Department of Physics, Utkal University, Bhubaneswar 751004, India

ZnO/NiO heterojunctions having each of layer thickness of 100nm were deposited on Si(100) substrate by PLD. The optimised samples are subjected to 200 MeV Ag ion irradiationsat IUAC, New Delhi. An in-situ IV characterisation is done after each dose of irradiation process. The sample irradiated with 200 MeV Ag ions showed an increase in leakage current as compared to pristine one (Fig. 5.2.1(a)). The ideality factor (η) first increases with increasing ion fluence from 1.57 (Pristine) to 1.65 (5.3×10^{12}ions cm^{-2}) and the same decreases to 1.63 with further increase in ion influence to 1×10^{13} ions cm^{-2}. On the other hand, the barrier height decreases exponentially with increasing ion fluence. the exponential decrease of barrier height with ion fluence could possibly due to the irradiation induced temperature rise due to thermal spike model of ion-matter interaction [1]. It can also be due to the evolution of oxygen at the surface of ZnO in the process of ion matter interaction and hence the decrease of barrier height with ion fluence [2]. The lnI~lnV (Fig. 5.2.1(b)) follows the relation $I \alpha V^m$, so the conduction mechanism follows the power law model of conduction [3]. The values of track radiuswere also calculated from various parameters like variation of barrier height, slope of the 2 regions of the lnI~lnV, increase of leakage currentetc. The calculated value of track radius was found to be ~ 2.8 nm.

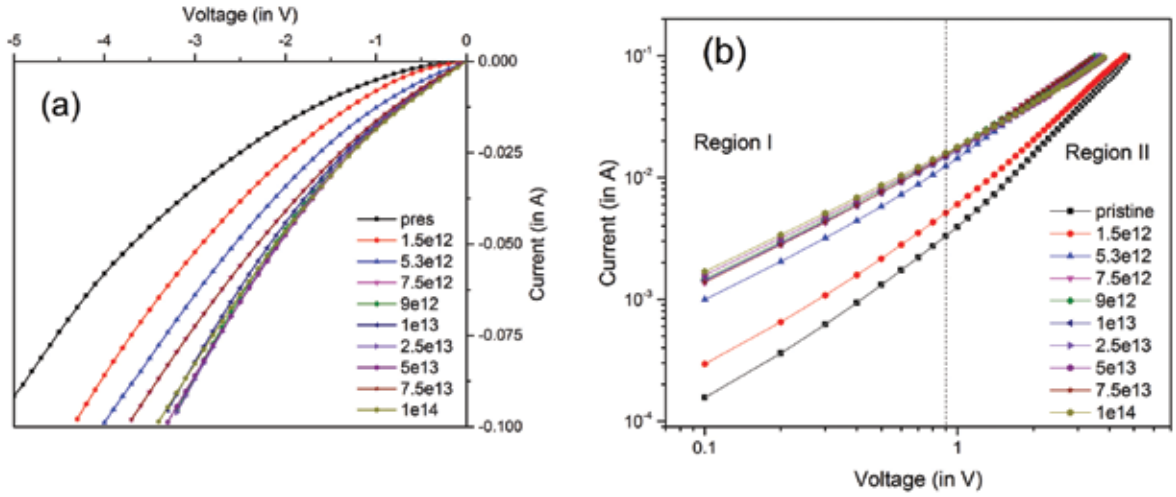

Fig.5.2.1: (a) In-situ I-V characteristics of the ZnO/NiO grown on Si(100) irradiated with 200 MeV Ag ions (Reverse bias Region), (b) Variation of lnI~lnV in the forward biased region for different ion fluences

The rectifying nature of the ZnO/NiO heterojunction got suppressed and it acquired ohmic nature at and above the fluence of 5×10^{13} ions cm^{-2}. The mechanism of electrical conduction in our case seems to follow the power law model. The variation of barrier height and ideality factor with ion fluence indicated the applicability of thermal spike model of ion-matter interaction. The cause of exponential suppression of the various parameters like barrier height, reversed biased voltage, slope of I-V curve with ion fluence is attributed to the implantation of ion track in the sample.

REFERENCES

[1] M. Toulemonde, E. Paumier, and C. Dufour, Radiat. Eff. Defects Solids 126(1-4) (1993) 201-206.
[2] Q. Xu, D. Ju, Z. Zhang, S. Yuan, J. Zhang, H. Xu and B. Cao, Sens. Actuators B Chem. 225 (2015) 16-23.
[3] M. Cavas et al.,J. Sol-gel Sci. Technol. 64(1) (2012) 219-223.

5.2.2 Irradiation temperature dependence of shape elongation of metal nanoparticles induced by swift heavy ion irradiation

Hiro Amekura[1], Saif Ahmad Khan[2], Sonu Hooda[2,3], Ramcharan Meena[2], Debdulal Kabiraj[2], Pawan K. Kulriya[2], and Devesh Kumar Avasthi[2,4]

[1]National Institute for Materials Science (NIMS), Tsukuba 305-0003, Japan.
[2]Inter-UniversityAcceleratorCentre,ArunaAsafAliMarg,NewDelhi-110067,India.
[3]NUSNNI-Nanocore, National University of Singapore, Singapore
[4]Amity University, Noida 201313, India.

In the previous beam-times, the irradiation temperature dependence of shape elongation of vanadiumnanoparticles (V NPs) in silica was evaluatedbetween 100 and 600 K under 120 MeV Ag^{9+} ion irradiation to a fluence of 1.0×10^{14} ions/cm^2. The V NPs were formed in silica (amorphous SiO_2) of KU-1 type as an embedded form by 60 keV V+ ion implantation to a fluence of 1.0×10^{17} ions/cm^2. Cross-sectional transmission electron microscopy (XTEM) showed that the most of the NPs were observed between 10 and 70 nm in depth [1], and that the mean diameter and the standard deviation was 9.0 nm and 2.9 nm, respectively [2]. The samples were then irradiated with 120 MeV Ag^{9+} ions with an incident angle of 45º, in order to detect the shape elongation as anisotropic optical absorption [3]. The irradiations were carried out at five different temperatures 100, 300, 433, 515, and 600K, using either the low-temperature chamber in the beam hall I or the high-temperature chamber in the beam hall II.

The anisotropic absorption, i.e., the difference of the optical density polarized to 0º and 90º from the elongation direction, which represents the degree of the shape elongation of V NPs, is plotted by open circles (samples without pre-annealing) in Fig. 5.2.2. The elongation slightly decreases with increasing the irradiation temperature from 100K up to 400K, and increases again from 400K to the highest temperature 600K. However, there is a criticism: With increasing the irradiation temperature, NPs could increase their sizes due to thermally-enhanced diffusion, which results in further enhanced efficiency of the elongation. To exclude this possibility, another set of the irradiations were carried out in the present beam-time. Each sample was pre-annealed at the highest temperature 600K for 5 h before the irradiation at each temperature (300, 433, 515, and 600K). The results are exhibited in Fig. 5.2.2 as closed circles. The data points with the pre-annealing were very close to those without the pre-annealing. This observation indicates that the pre-annealing at 600K for 5 h induces only negligible thermally-induced size changes on the NPs. Therefore, the observed irradiation temperature dependence is not a spurious effect due to size changes of the NPs due to thermally-enhanced diffusion, but due to a true irradiation temperature dependence of the shape elongation of NPs.

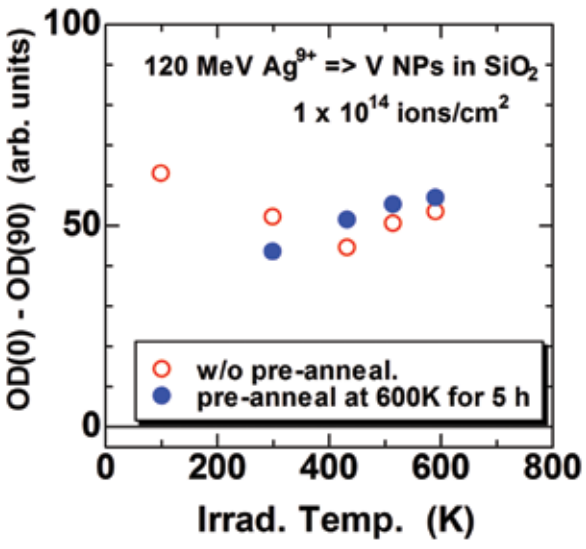

Fig. 5.2.2: Irradiation temperature dependence of the shape elongation of vanadium nanoparticles embedded in silica, detected by anisotropy of linearly polarized optical absorption. Closed and open circles indicate the data with and without a pre-annealing at 600K for 5 h before the irradiation, respectively.

REFERENCES
[1] H. Amekura, et al., Thin Solid Films520 (2012) 5528.
[2] H. Amekura, et al., Nucl. Instr. and Methods in Phys. Res. B 269 (2011) 2730.
[3] H. Amekura, et al., Phys. Rev. B 83 (2011) 205401.

5.2.3 Effect of SHI on structural, morphological, mechanical and electrical properties of ion track-etch Synthesized Cu Nanowires

Rashi Gupta and Rajesh Kumar

University School of Basic and Applied Sciences,Guru Gobind Singh Indraprastha University, New Delhi-110078, India

In the present work, Cu nanowires were grown in polycarbonate track-etched (PCTE) membrane (thickness of 10µm, pore density 3×10^8 pores/cm^2, and pore diameter 200nm) by cathodic electrodeposition two electrode setup [1]. The conducting Cu tape acted as a working electrode and a cylindrical copper rod as a counter electrode. During the electrodeposition, the electroactive species migrating into the nanochannels have to reach the barrier layer quite fast such that homogenous electrodeposition in the pores can be obtained. The SHI irradiation was carried out in high vacuum in materials science chamber using a 15 UD Pelletron accelerator at Inter University Accelerator Centre (IUAC), New Delhi, India. The copper nanowires were irradiated with 150 MeV Ti^{9+} ion beam at four different fluences of 5×10^{10}, 1×10^{11}, 5×10^{11} and 1×10^{12} ions/cm^2 keeping the current constant at 0.5pnA.

The Scanning Electron Microscopy (SEM) images of pristine and irradiated Cu nanowires are shown in Fig. 5.2.3. The SEM studies reveal that the nanowires are standing and have a uniform diameter equal to the diameter of the template in pristine as well as irradiated nanowires [2]. Few wires have aggregated together after the dissolution of the membrane due to the surface tension of the solvent drops. The template-assisted electrodeposited nanowires were found to be highly ordered, smooth, cylindrical shaped and vertically aligned. No change in the external morphology of the nanowires has been observed after irradiation.

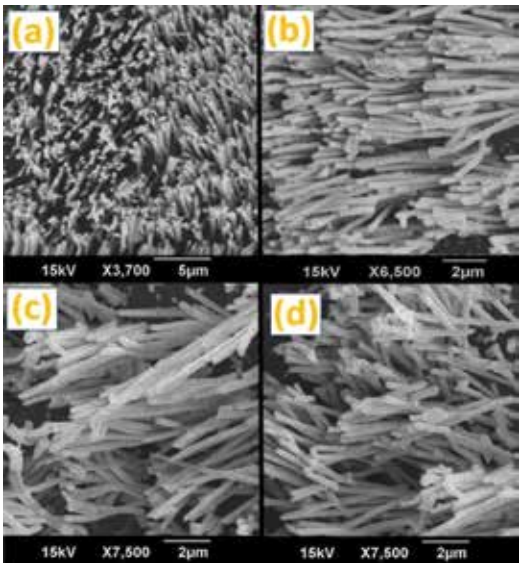

Fig. 5.2.3: SEM images of Cu nanowires (a,b) Pristine at two different magnifications, (c) Irradiated at 5×10^{10} ions/cm^2 and (d) Irradiated at 1×10^{12} ions/cm^2.

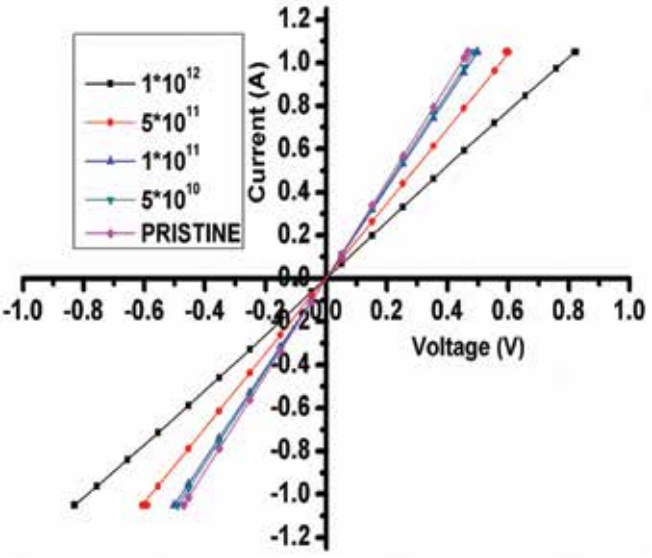

Fig. 5.2.4: I-V plot of pristine and irradiated Cu nanowires at four different fluences of 5×10^{10}, 1×10^{11}, 5×10^{11} and 1×10^{12} ions/cm^2. Fit to the data, the Resistance R is extracted from the inverse of the slope.

Fig. 5.2.4 shows the IV characteristics of pristine and irradiated nanowires. Clearly, the resistance data are typical of a good metal. All I-V curves manifest perfect linear dependence, thus exhibiting the ohmic behaviour. At room temperature, the resistance of pristine Cu nanowire was about 40.36Ω. It increases with increase in ion fluence. The resistivity of pristine nanowire was calculated to be 0.112 µΩm and resistivity increased with increase in ion fluence. The Swift Heavy Ions (SHI) deposit their energy in the incident material medium that leads to excitation and ionization in lattice atoms. The primary knock out of atom is followed by the cascade that increases the number of defects. The kinetic energy produced by the Ti^{9+} ion in a cascade is very high that the material is driven outside the thermodynamic equilibrium leading to defect formation. The defects

can be like point defects, dislocations, faults and Frenkel pairs. These defects act as trapping centres for the conduction electrons that leads to decrease in electrical conductivity. The energy of incident Ti^{9+} ion is 150 MeV, hence electronic energy loss dominates over nuclear energy loss. The electronic energy loss takes place via ionization and excitation process. This process is also accompanied by recombination of ions and atoms. This recombination and dense electronic excitation and de-excitation process lead to a generation of heat energy which causes an increase in the amplitude of lattice vibration. The increase in lattice vibration leads to increase in scattering of charge carriers, change in preferred orientation and diffusion of dislocation and cavities [3]. The scattering of charge carriers from surface interface and grain boundaries $\rho_{M\text{-}F}$ is governed by MS and FS [4]. Thus, the formation of new grains by fragmentation leads to decrease in crystallite size and increase in resistivity of Cu nanowires with increasing fluence. Thus, increase in defects and grain boundaries in Cu nanowires with increasing fluence leads to decrease in electrical conductivity of the nanowires.

REFERENCES

[1] K. Takahashi, S.J. Limmer, Y. Wang, and G. Cao, J. Phys. Chem. B 2004, 108, 9795-9800.
[2] R. Gupta, R.P. Chauhan, S.K. Chakarvarti, R. Kumar, Ionics, 24 (2018), 1-12.
[3] Itoh N, Stoneham AM, Radiat. Eff. Defects Solids. 155 (2001) 277–290.
[4] Zheng P, Gall D, J Appl Phys 122 (2017) 135301.

5.2.4 Effect of 200 MeV Ag ion irradiation on $NdMn_{1-x}ZnxO_3$ and(1-X)ZnO- (X)$BaTiO_3$ thin films

Malay Udeshi[1], Brinda Vyas[1,3], Hetal Kundalia[1], Indra Sulaniya[2], K. Asokan[2], Fouran Singh[2], Saif A. Khan[2] and D. G. Kuberkar[3]

[1]Department of Physics, Saurashtra University, Rajkot-360005, India
[2]Inter-University Accelerator Centre (IUAC), New Delhi-110067, India
[3]Department of Nanoscience and Advanced materials, Saurashtra University, Rajkot-360005, India

Swift Heavy Ion (SHI) Irradiation experiment was carried out using 200MeV Ag^{+15} ion bombarded on $NdMn_{1-x}ZnxO_3$ (x = 0.0, 0.05, 0.10)/SNTO and (1-X) ZnO - (X) $BaTiO_3/Al_2O_3$ [X=0.20 – 0.50] thin films with different ion fluencies, such as, ~ $5X10^{10}$ (5E10), $5X10^{11}$ (5E11), $1X10^{12}$ (1E12), $5X10^{12}$ (5E12) and $1X10^{13}$ (1E13) ions/cm^2. Further characterization of these samples were performed using XRD, AFM, I-V, R-T, Raman and temperature dependent dielectric measurements at IUAC, New Delhi.

Irradiated films of $NdMn_{1-x}Zn_xO_3$ (x = 0.0, 0.05, 0.10)/SNTO were characterized by XRD to know the structure and irradiation induced strain effects. Atomic Force Microscopy was carried out to determine effect of irradiation on the evolution of grains. Room temperature Raman spectroscopy measurements on pristine and irradiated films performed show shift in Raman modes with doping. Temperature dependent I-V and Dielectric studies were carried out in the temperature range 80 - 300 K. The appearance of dielectric anomaly around the magnetic ordering temperature (T_N) ~ 80 K of $NdMnO_3$ system shifts with irradiation fluence.

Dielectric behaviour of the films studied at room temperature shows that, dielectric constant decreases with increase in ion fluence due to the creation of defects which obstructs the flow of charge carriers. Fitting of Cole–Cole plots for the pristine and 5E11 NMO films show, two semi–circular arc type behaviour indicating the contribution from grains & grain boundaries, while dielectric response of 5E10 and 5E12 film has been attributed to the individual contribution from grain boundaries and grains, respectively. Temperature dependent dielectric behaviour studied for pristine and 5×10^{10} ions/cm^2 irradiated NMO film show dielectric anomalies at the onset of magnetic transition temperature (T_N) which has been understood on the basis of electronic effect or electron – lattice effect [1-3]. Since there is no structural phase transition at ~ T_N, the anomaly possibly signifies multiferroicity and can be attributed to coupling between orbital and spin order in pristine and irradiated films. Impedance spectra for the pristine and irradiated films obtained as a function of frequency at different temperatures show, relaxation behaviour which signifies the non–Debye type relaxation. In order to understand the role of grains and grain boundary evolution with irradiation at higher fluence, Nyquist plots using R–C circuit model were studied.

Temperature dependent I-V and R-T measurements were performed on $NdMn_{1-x}CuxO_3$ (x= 0.0,0.05,0.10) (NMCO)/SNTO films over a temperature range 80 - 300 K. Hereafter Cu doped composition in $NdMn_{1-x}Cu_xO_3$ films where x = 0.00, 0.05 and 0.10 will be termed as NMO, NMC5 and NMC10, respectively. I–V characteristics of NMCO/SNTO films have been understood as a function of temperature and Cu concentration. The data for the films were obtained by sweeping the dc bias voltage using Keithley 6517B Electrometer. Temperature dependent I–V measurements show p–n junction diode like behavior along with rectifying hysteresis confirming the presence of RS switching in the NMCO/SNTO heterostructure. In order to understand RS behavior as a function of Cu doping and as a function of temperature, various conduction mechanisms were employed to

understand the role of charge carriers, oxygen vacancies and Cu ions in the device performance. Detailed analysis of temperature dependent I–V behavior of all the films show that, all the films exhibit rectifying hysteresis behavior which becomes more pronounced with increase in Cu– concentration. Values of V_d and V_b increases at lower temperature for NMO film, have been explained on the basis of charge localization at the interface of film–substrate interface. Resistive switching (RS) behaviour for all the films have been studied at 80 K and 300 K. At lower temperature, the RS behaviour gets modified with Cu doping, which has been explained due to trapping of charge carriersat the interface and formation of conductive filamentarypath in case of 10 % Cu doped NMO film [4]. Study of conduction mechanisms for all the films confirmed that, SCLC mechanism is dominant at low applied voltage whereas F–N tunnelling mechanism is dominant at higher bias voltage. Resistivity data shows decrement with increase in Cu concentration due to enhancement of DE interactions. The value of E_a for NMC5 film obtained by fitting SPH model is less as compared to the NMO and NMC10 films, which can be attributed to the higher value of structural strain in NMC5 film.

REFERENCES

[1] N. Ikeda et al., Nature (London) 436 (2005) 1136.
[2] L. Paolasini, R.Caciuffo, A. Sollier, P. Ghigna and M. Altarelli, Phys. Rev. Lett. 88(2002)106403.
[3] P. Mondal, D. Bhattacharya and P. Choudhary J. Phys. Condens. Matter. 18(2006) 6869.
[4] C. Liang, K. Terabe, T. Hasegawa and M. Aono, Nanotechnology 18 (2007) 485202.

5.2.5 Swift Heavy Ion (SHI) Irradiation Studies on Manganite based Thin Film Devices

Bhargav Rajyaguru[1], K. Asokan[2], N.A. Shah[1] and P.S. Solanki[1]

[1]Department of Physics, Saurashtra University, Rajkot – 360005
[2]Inter-University Accelerator Center, New Delhi, Delhi -110067

$LaMnO_3/La_{0.7}Ca_{0.3}MnO_3$ and $LaMnO_3/Nd_{0.7}Sr_{0.3}MnO_3$ bilayers were fabricated in field effect geometry on *(100)* single crystalline SrTiO3 substrate using cost effective and easy chemical solution deposition (CSD) spin coating technique at Department of Physics, Saurashtra University, Rajkot. These devices were irradiated with different ion fluencies (5×10^{11} ions/cm^2, 5×10^{12} ions/cm^2, 5×10^{13} ions/cm^2) of 120 MeV (100MeV) Ag^{9+} (O^{7+}) ions at Materials Science Beam line of 15UD Pelletron accelerator at Inter University Accelerator Centre (IUAC) New Delhi.Electrical transport (I-V & R-T) facilities were used to understand the change in transport mechanisms under the application of electric field in field effect devices.

Customized LabVIEW program has been developed for (i) special requirement for application of electric field with polarizable gate electrode and (ii) various protocols like ZFC, FCC, FCW (usually seen in magnetic measurements) by using existing low temperature setup of transport lab at IUAC New Delhi.Below, Fig. 5.2.5, is the typical example of one of the R-T measurements of $LaMnO_3/Nd_{0.7}Sr_{0.3}MnO_3$ device irradiated with 5×10^{11} ions/cm^2 of O^{7+} characterized using customized LabVIEW program for ZFC, FCC, FCW measurements.

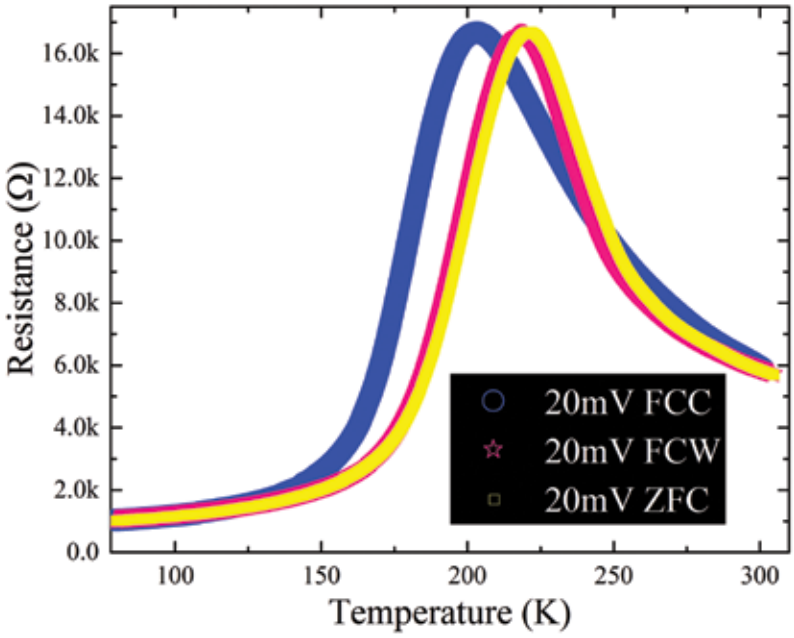

Fig. 5.2.5: R-T measurements of $LaMnO_3/Nd_{0.7}Sr_{0.3}MnO_3$ device irradiated with 5×10^{11} ions/cm^2 of 100MeV O^{7+}ions

Uses of other facilities like AFM, SEM, PL, Raman and RBS are planned, in near future, to examine the changes in the devices introduced by SHI irradiation.

5.2.6 Synthesis and testing the radiation resistance of Lanthanum Zirconate using low energy ion beam irradiation

Asha[1], P.K. Kulriya[2], Chetna Tyagi[2], F. Singh[2] and N.L. Singh[1]

[1]Department of Physics, The Maharaja Sayajirao University of Baroda, Vadodara, Gujarat, 390002
[2]Inter-University Accelerator Center, New Delhi, Delhi -110067

The main objective behind our work is safe long-term disposal of long-lived waste actinides. Pyrochlore is one such ceramic which may fulfil the requirement for long term disposal. Pyrochlore belongs to Fd3m space group with stoichiometric formula $A_2B_2O_7$. Where A and B can be cation with 8 and 6 coordination number respectively. Pyrochlore possess a super structure of Fluorite, MO_2 [1-3].Simulation for thousands of year's damage is required for safe disposal that can ensure reliability on these materials in extreme conditions [2].

Some of the previous studies have discussed about defect and their effects on stability under extreme conditions [4], still many fundamental understandings about how these effects expand and what phenomenon they follow, remains. In this present work, ion irradiation with various fluence is used to simulate the damage and study the fundamentals of these damages in the lanthanum zirconate.

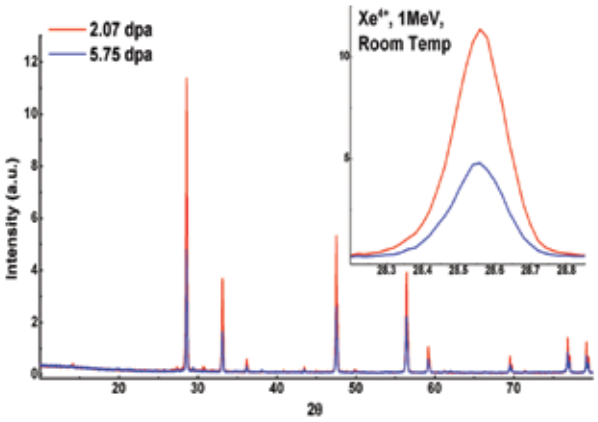

Fig.5.2.6: X-ray powder diffraction of Lanthanum Zirconate irradiated with 1 MeV Xe^{4+} ions

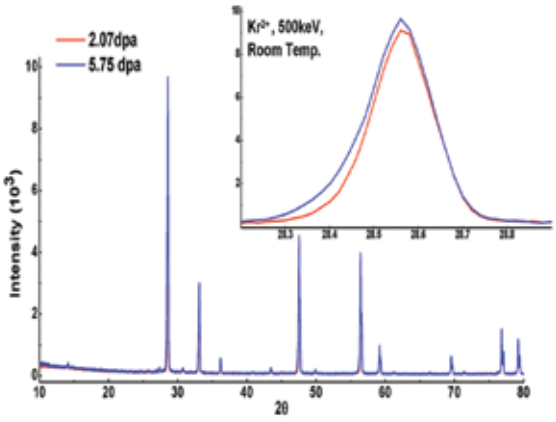

Fig.5.2.7: X-ray powder diffraction of LZ irradiated with 500 keV Kr^{2+}

It is predicted that due to low defect activation energy [4], lanthanum zirconate transforms to defect fluorite structure which is way more radiation resistant than pyrochlore. Therefore, a study for radiation resistance of LZ was conducted with 1MeV Xe^{4+} and 500keV Kr^{2+} at room temperature and Liquid nitrogen temperature with various ion fluences. The X-ray powder diffraction pattern is shown in Fig.5.2.6 and Fig.5.2.7 for irradiation with 1MeV Xe^{4+} and 500keV Kr^{2+} at room temperature. Fig.5.2.6 & 5.2.7 clearly indicate that the damage depends not only on ion fluence but also on the type of ion, charge state and energy of ion, the decreased intensity for higher dose, Fig. 5.2.6, shows that upper radiation exposed layer is being transferred amorphous phase. The results are being communicated in SCI Journal.

REFERENCES

[1] M. Langet al.,Nucl. Instr. and Methods in Phys. Res., Section B, 268(19)(2010) 2951–2959.
[2] M. K. Patelet al., Nucl. Instr. and Methods in Phys. Res., Section B 266(12–13) (2008) 2898–2901.
[3] M. Subramanianet al., Rev. Lit. And Arts Of The Amer, 15(1983) 55–143.
[4] F. X. Zhanget al., Physical Review Letters 100(4)(2008) 2–5.

5.2.7 XRD Structural Analysis of 80 MeV O^{6+} ion Irradiated Ferroelectric Ceramic/Polymer Nanocomposites

Mandakini Sharma[1], Anurag Gaur[2] and J. K. Quamara[2]

[1]School of Materials Science & Technology, National Institute of Technology, Kurukshetra
[2]Department of Physics, National Institute of Technology, Kurukshetra

The ferroelectric ceramic/polymer nanocomposites with enhanced physical and structural properties are important and relatively new class of material with variety of applications like electromagnetic shielding of electronic equipments, capacitors, sensors, switching devices etc. [1, 2]. The radiation effect investigations

on the physical and structural properties of such composites are required when such devices are being used in radiation environment. However, not much work has been reported on irradiation effect on ferroelectric ceramic / polymer composites. In present study, the structural properties of PVDF/$BaTiO_3$ nano composites irradiated by O^{6+} swift heavy ionshave been investigated. The ferroelectric $BaTiO_3$ ceramic nanoparticles were synthesized by co-precipitation method followed by the preparation of (1-x)PVDF/(x)$BaTiO_3$ nano composites (x=0.2 and 0.5) via solution mixing method [3].The samples were irradiated by 80 MeV O^{6+} ion beam(fluence 5×10^{10} ions/cm^2) using Material Science beam line at IUAC, New Delhi.

X-ray diffraction analysis of the samples was done using Rigaku Miniflex II X-ray diffractometer with Cu Kα radiation (λ = 1.54 Å) with a step size = 0.02° at 0.33° s^{-1} speed at an accelerating voltage and current of 30 kV and 15 mA, respectively.Fig.5.2.8 (a&b) illustrates the XRD patterns of un-irradiated and irradiated samples. An increase in crystallite size of PVDF can be observed after irradiation (Fig. 5.2.8(b)), which indicates the crosslinking of the PVDF matrix and implying that the polymer becomes more crystalline after irradiation. However, after irradiation, the flattening of XRD peaks for $BaTiO_3$ is observed owing toits transition from crystalline phase to amorphous phase. A complete such transition is observed for (0.5)PVDF/(0.5)$BaTiO_3$ irradiated samples.Thus, after irradiation the crystalline nature of PVDF increases while for$BaTiO_3$, its crystalline nature decreases.

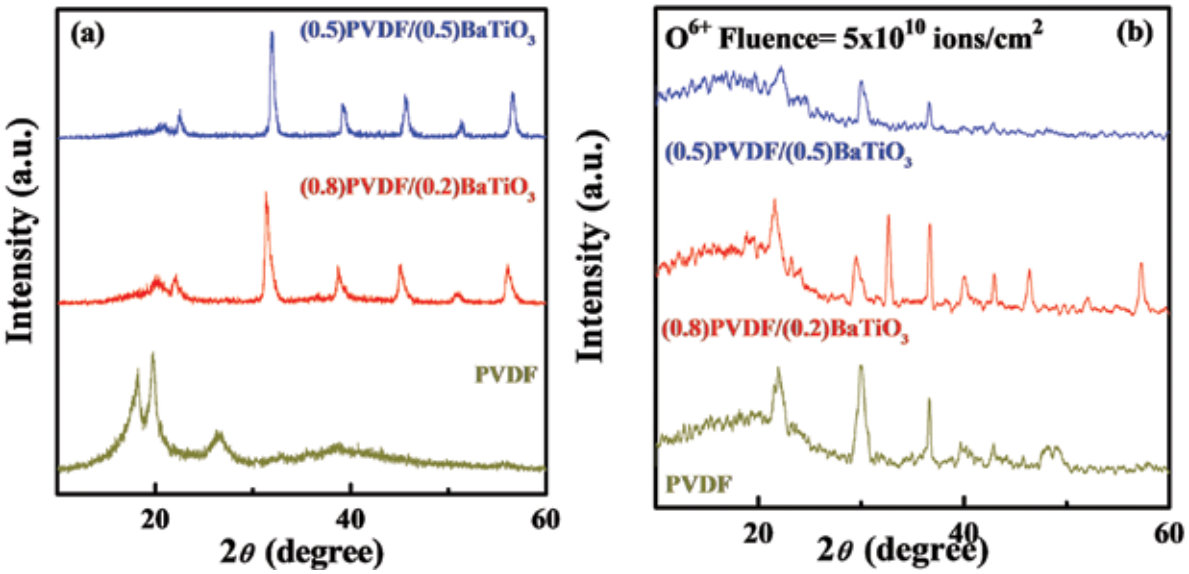

Fig.5.2.8: XRD pattern of PVDF and (1-x)PVDF/(x) $BaTiO_3$ nano composites
(a) un-irradiated and (b) irradiated by O^{6+} ion with fluence 5×10^{10} ions/cm^2.

REFERENCES

[1] D. Rana and J. K. Quamara, Optoelectronics and Advanced Materials, Rapid Communications 4(2010) 839.
[2] Sejal Shah et al., Nuclear Instruments and Methods in Physics Research B 266(2008) 1768–1774.
[3] M. Sharma,J. K. Quamara andA. Guar,J Mater Sci: Mater Electron 29(2018) 10875.

5.2.8 Effect of 100 MeV O^{7+} ions irradiation on optical properties of Polystyrene/Al_2O_3 polymer nanocomposites

Shilpa Bhavsar[1], Gnansagar B. Patel[1], N.L. Singh[1] and Fouran Singh[2]

[1]Department of Physics, Faculty of Science, The M. S. University of Baroda, Vadodara-390002 India
[2]Inter-University Accelerator Center, New Delhi, Delhi -110067

Polystyrene (PS)/Al2O_3 polymer nanocomposites are synthesized from PS:Al2O_3 (1–x):x mixture (x=3 wt%) by solution casting method. 3 wt% Al_2O_3 doped PS films (pristine) have been labelled as PSA3. The polymer nanocomposites were irradiated with 100 MeV O^{7+} ions using 15UD Pelletron accelerator at IUAC, New Delhi. Fig. 5.2.9 shows UV-Visible spectra of pristine and irradiated polymer films. The UV-Visible spectra of irradiated polymer films show shifting of absorption edge with increasing fluence. This can be attributed to creation of conjugated system of bonds. The absorption edge of irradiated sample is also observed to shift towards longer wavelength with increasing dose due to the formation of extended systems of conjugated bonds. The direct band gaps (E_g) of pure PS and PS/Al_2O_3 composite films were calculated using the Tauc relation. The band gap of PS and 3 wt% Al_2O_3 doped PS (PSA3) is observed 4.38 eV and 4.34 eV, respectively, whereas band gap of oxygen ion irradiated PSA3 polymer films is 4.15 eV and 3.95 eV at the fluence of $1x10^{11}$ ions/cm^2 and $1x10^{12}$ ions/cm^2 respectively.

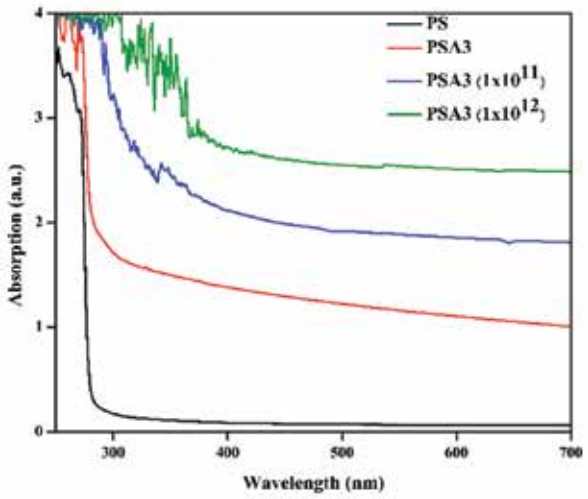

Fig.5.2.9: UV-Visible spectra of pristineand irradiated samples

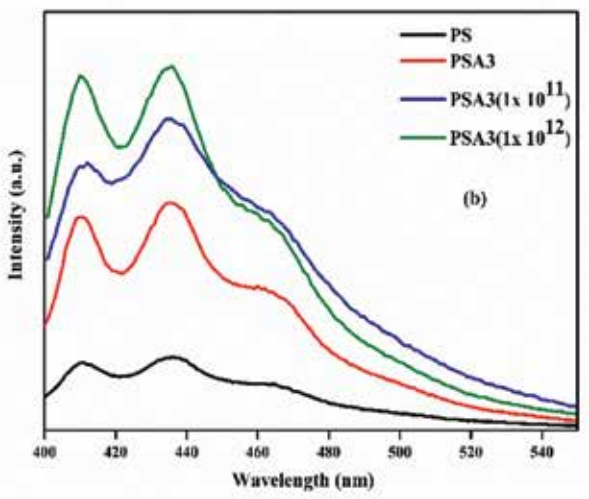

Fig. 5.2.10: PL spectra of pristine and irradiated samples

Photoluminescence (PL) emission spectra of pristine and irradiated PS and PSA3 polymer films are shown in Fig. 5.2.10. The PL emission spectra of PS show three distinct emission peaks at 410,435 and 461 nm under excitation wavelength of 380 nm in violet-blue region.The emission spectrum of PS is due to formation of luminescence substances such as benzoic acid, styrene, methyl benzoate, stilbene, etc., under the absorption of wavelength 380 nm. It was found that after irradiation the luminosity of PSA3 nanocomposite enhanced, which is attributed to the change in microstructure of PS matrix afterirradiation with swift heavy ions. This result indicates that polymeric film under the study has an application in OLED.

REFERENCES

[1] J. Tauc, R. Grigorovici, A. Vancu, Phys. Status Solidi 15 (1966) 627.
[2] K. Binnemans, Chem. Rev. 109 (2009) 4283.

5.2.9 Swift Heavy Ion irradiation effects on ternary MoS_2-rGO@PPyNTs nanocomposites for supercapacitor application

Devalina Sarmah[1], Ashok Kumar[1*] and Fouran Singh[2]

[1]Department of Physics, Tezpur University, Napaam, Assam-784028, India.
[2]Inter University Accelerator Centre, New Delhi-110067, India.

Molybdenum Disulfide (MoS_2) is a two-dimensional (2D) energy storage material in the category of Transition Metal Dichalcogenides (TMDCs). Bulk MoS_2 can be exfoliated to single or few layer nanosheets by mechanical or chemical route which exhibits unusual physical and electronic properties as well as widely used in energy storage applications because of some unexpected properties such as high catalytic activity, high available surface area, cycling stability and higher theoretical capacitance than that of graphene [1, 2]. Graphene has attracted recent attention in energy storage application due to the higher specific surface area, electrical conductivity, stability, easy access of electrolyte ions provided by exterior major surface area [3]. 1-D Polypyrrole nanotubes are ideal building blocks to fabricate supercapacitor electrode due to the availability of radially accessible surface area and open tubular networks [3, 4]. Here, MoS_2 nanosheets were prepared with positively charged CTAB were assembled around negatively charged GO nanosheets through electrostatic interaction. Vacuum dried GO-MoS_2 layered structures were mixed with pre-synthesized PPyNTs followed by hydrothermal treatment, without using any reducing agent to obtain MoS_2-rGO@PPyNTs ternary nanocomposite. Intercalation of MoS_2 nanosheets between the rGO nanosheets forms a three-dimensional conductive network, which not only minimizes the restacking of MoS_2 nanosheets but also prevents the agglomeration of rGO, providing more electro-active sites between the different layers and simultaneously offers excellent electrochemical performance. Here, the ternary nanocomposites MoS_2-rGO@PPyNTs have been irradiated with 100 MeV O^{7+} swift heavy ions. Fluence dependence modifications have been investigated for both pristine and irradiated nanocomposites.

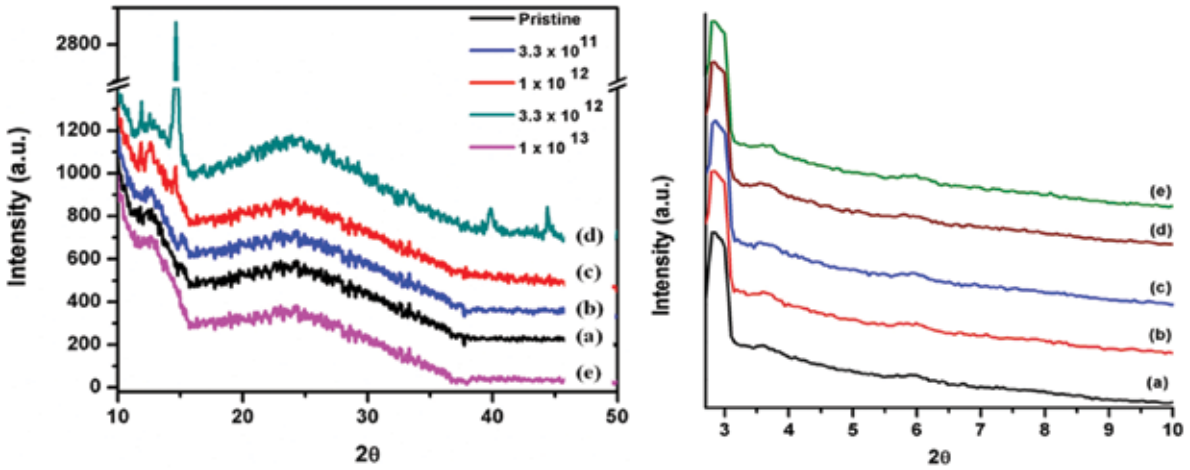

Fig. 5.2.11: XRD pattern of MoS_2-rGO@PPyNTs (i) and (ii), where (a) Pristine MoS_2-rGO@PPyNTs and irradiated MoS_2-rGO@PPyNTs with fluence of (b) $3.3x10^{11}$, (c) $1x10^{12}$, (d) $3.3x10^{12}$ and (e) $1x10^{13}$ ions cm^{-2}

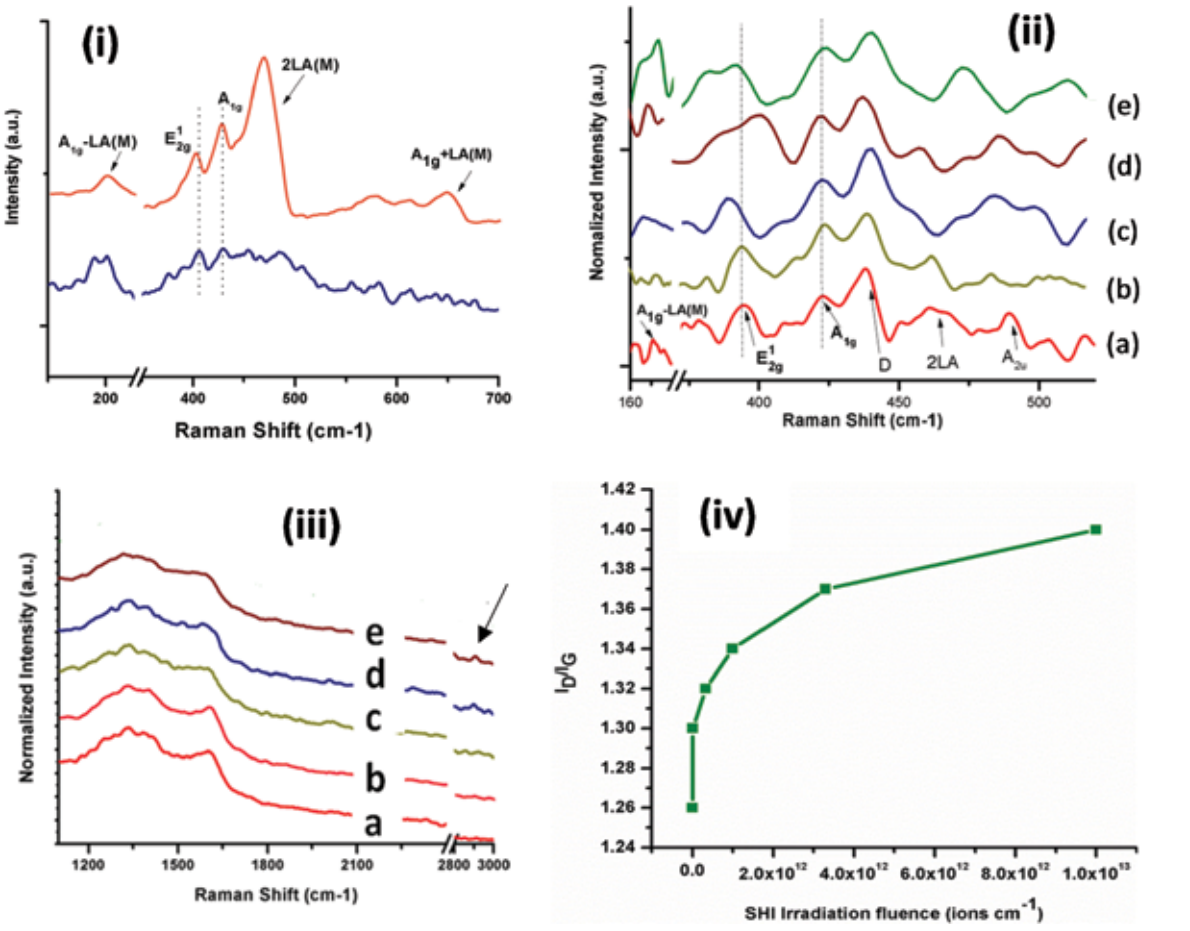

Fig. 5.2.12: RAMAN spectra of (i) bulk and single layered MoS_2 and (ii) and (iii) pristine MoS_2-rGO@PPyNTs (a) nanocomposite and irradiated MoS_2-rGO@PPyNTs with fluence of (b) $3.3x10^{11}$, (c) $1x10^{12}$, (d) $3.3x10^{12}$ and (e) $1x10^{13}$ ions cm^{-2},(iv) variation of ID/IG ratio with increasing SHI fluence

The structural modifications of MoS_2-rGO@PPyNTs nanocomposite induced by SHI irradiation have been studied with XRD. XRD patterns of pristine and 100 MeV O^{7+} SHI ion-irradiated MoS_2-rGO@PPyNTs nanocomposites are displayed in Fig. 5.2.11(i). Fig. 5.2.11 (ii) shows the XRD patterns of the ternary MoS_2-rGO@PPyNTs towards lower diffraction angles. The diffraction pattern of pristine MoS_2-rGO@PPyNTs, shows a distinct peak at $2\theta = 2.81°$ (Fig. 5.2.11(ii)) corresponding to intercalation of MoS_2 with rGO nanosheets and a broad hump is observed from $2\theta = 15°–35°$, which may be due to the overlapping of MoS_2 intercalated rGO and PPyNTs. A small broad peak is also observed at $2\theta = 14.42°$ due to the limited restacking of MoS_2 nanosheets on rGO nanosheets. The intensity of the peak around $2\theta = 15°–35°$ increases up to fluence $3.3x10^{12}$ and decreases at the

highest fluence of $1x10^{13}$ ions cm^{-2}. Crystallinity corresponding to pristine and irradiated samples is calculated to be 20%, 20.6%, 23%, 26% and 18%, respectively with increasing fluence. The decrease in crystallinity at the highest fluence may be ascribed to the chain-scission and local disordering of the polymer. On the other hand, no changes are observed in the rGO intercalated MoS2 nanosheets (Fig. 5.2.11 (ii)) as the peak appears at lower diffraction angle don't show any such distinct changes since rGO nanosheets protect the MoS2 nanosheets from SHI irradiation [5].

Raman spectra of bulk and single layered MoS_2 are displayed in Fig. 5.2.12 (i) measured with measured with E_L =1.58 eV (λ_L =785 nm). Fig.5.2.12 (ii) shows the evolution of the Raman spectrum of the pristine MoS_2-rGO@ PPyNTs nanocomposite and with increasing SHI irradiation fluence. The Raman spectrum of bulk MoS_2 contain peaks around 180, 470 and 634 cm^{-1}, besides its characteristic peaks (E^1_{2g} (403 cm^{-1}) and A1g (424 cm^{-1})) owing to the resonance Raman scattering. The peak at 470 cm^{-1} appears due to second order zone edge phonon (2LA) and first order optical phonon (A_{2u}). The peaks at 180 and 634 cm^{-1} are assigned to A_{1g}(M) − LA(M) and A_{1g}(M) + LA(M) Raman modes. A new peak observed around 190 cm^{-1} for the fluence of $1x10^{12}$ ions cm^{-1} corresponds to LA mode. LA mode is the defect induced mode. The E^1_{2g} peak becomes broad with increasing fluence due to lattice defects. The shifting to a lower frequency indicates the tensile stress in irradiated MoS_2. The Raman peak at 450 cm^{-1} (D) can be ascribed to Mo-S vibrations for oxysulfide species as oxygen may attack Mo–S–Mo bonds especially present at the edges of the flakes. Fig. 5.2.12 (iii) displays the Raman spectra of bulk and irradiated MoS^2-rGO@PPyNTs in increasing fluence. The G and D bands appear around 1605 cm^{-1} and 1331 cm^{-1}, respectively. The G peak corresponds to the E_{2g} phonon at the Brillouin zone center. The D peak is due to the breathing modes of six-atom rings and requires a defect for its activation. At higher fluence of $3.3x10^{12}$ and $1x10^{13}$ ions cm^{-2}, D+D/ band appears around 2911 cm^{-1}. The D + D/ band is the combination of phonons with different momenta (around K and Γ point in Brillouin zone), thus requires a defect for its activation for its appearance. The I_D/I_G ratio is used to measure the structural defects induced in graphene and known as disorder parameter. The change in disorder parameters with increasing fluence are shown in Fig. 5.2.12 (iv). The I_D/I_G ratio increases with increasing SHI irradiation fluence indicating the increase in structural disorder and defects densities in the ternary nanocomposite.

REFERENCES

[1] Y.X. Wang, S.L. Chou, D. Wexler, H. K. Liu, S. X. Dou, Chem. Commun. 50 (2014)10730–10733.
[2] Hong Lin et al., 2D Mater. 3 (2016) 1–22.
[3] S. Zaharaddeen, C. Iro, S.S. Subramani, Dash, Int. J. Electrochem. Sci. 11 (2016) 10628–10643.
[4] Junhong Zhao et al., Prog. Nat. Sci.: Mater. Int. 26 (2016) 237–242.
[5] Gerardo Algara-Siller et al., Applied Physics Letters 103, (2013) 203107.

5.2.10 85 MeV C^{6+} ion irradiation induced enhanced electrochemical performance of reduced graphene oxide – polypyrrole nanotubes nanocomposites

Madhabi Devi[1], A. Kumar[1], Fouran Singh[2] and P.K. Kularia[2]

[1]Department of Physics, Tezpur University, Napaam, Assam-784028, India.
[2]Inter University Accelerator Centre, New Delhi-110067, India.

Nanocomposites of reduced graphene oxide (RGO) nanosheets and polypyrrole nanotubes (PPyNTs) have been synthesized by in-situ reduction of graphene oxide in presence of PPyNTs as spacers. The nanocomposite films are irradiated with 85 MeV C^{6+} swift heavy ions at different fluences of 6×10^{10}, 3.6×10^{11}, 2.2×10^{12} and 1.3×10^{13} ions cm^{-2}. Morphological, structural and electrical properties of the pristine and irradiated nanocomposites have been investigated by FESEM, micro-Raman and conductivity measurements. The modifications in the BET specific surface area, porosity and surface wettability of the nanocomposite electrodes have been determined by N_2 adsorption-desorption and contact angle measurements. The fluence dependent electrochemical performance of the irradiated nanocomposites as electrodes has been studied by cyclic voltammetry and galvanostatic charge-discharge and impedance spectroscopy and compared with that of pristine.

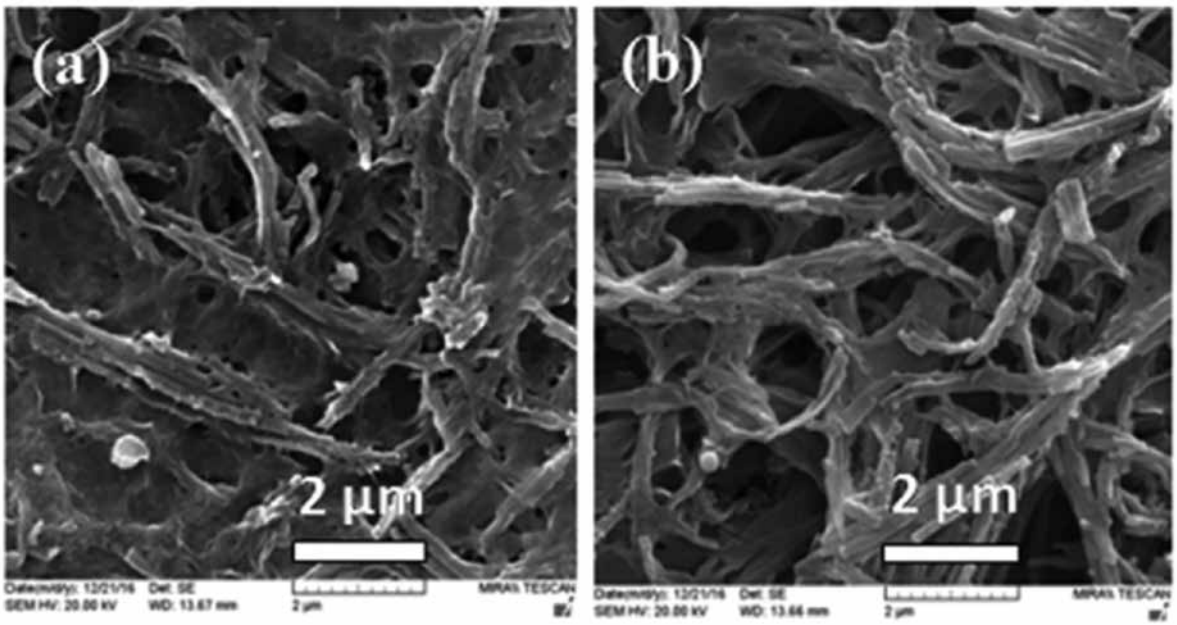

Fig. 5.2.13: FESEM images of RGO-PPyNTs nanocomposites (a) pristine, and irradiated with fluence of (b) 1.3×10^{13} ions cm^{-2} at a magnification of 25 kx.

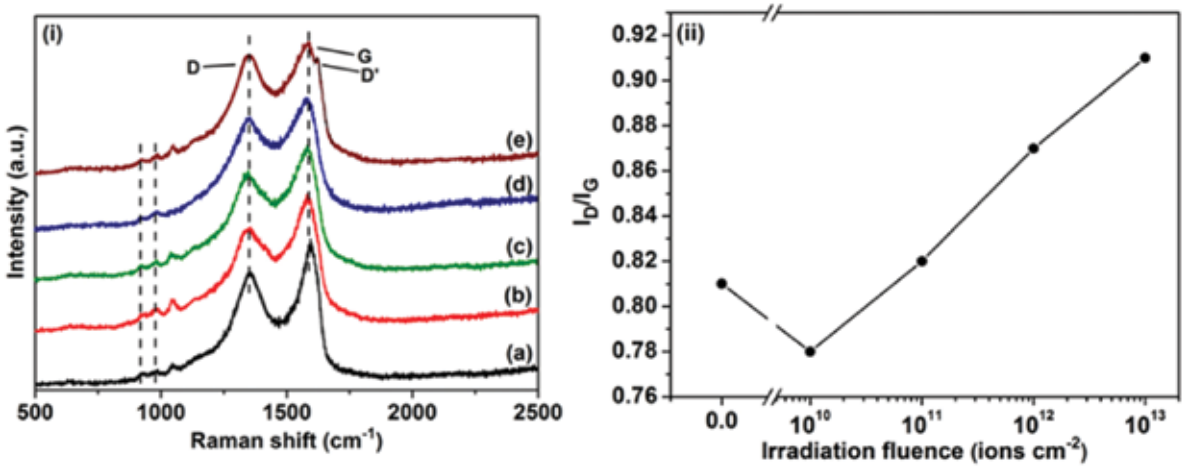

Fig. 5.2.14: (i) Micro-Raman spectra of RGO-PPyNTs nanocomposites (a) pristine, and irradiated with fluence of (b) 6×10^{10}, (c) 3.6×10^{11}, (d) 2.2×10^{12} and (e) 1.3×10^{13} ions cm^{-2}; (ii) Variation of disorder parameter (I_D/I_G) with irradiation fluence.

FESEM studies (Fig. 5.2.13) reveal the widening of pores of the nanocomposite electrode and a decrease in the diameter of PPyNTs with increasing irradiation fluence. SHI irradiation produces large electronic energy loss, which causes excitation and ionization of electrons of the target material resulting in the formation of defects and structural damage at the ion impact site, leading to the widening of the pores at higher fluence [1]. Micro-Raman spectra (Fig. 5.2.14) depict an increase in the disorder parameter (ID/IG) of the nanocomposite electrode upon irradiation at a low fluence of 6×10^{10} ions cm^{-2}, beyond which the I_D/I_G increases with increasing fluence. The initial decrease in disorder parameter may be ascribed to the annealing or ordering of RGO at moderate temperatures that occurs at a low fluence of 6×10^{10} ions cm^{-2} due to the energy dissipated by the incident energetic ions [2], above which defects are induced with increasing fluences attaining the highest density at the fluence of 1.3×10^{13} ions cm^{-2}. This occurs because defect sites increase in the nanocomposite at the fluence of 1.3×10^{13} ions cm^{-2} as the energy loss of SHI is high enough to dominate over the energy loss required for annealing. Conductivity measurements display a slight increase in conductivity with a maximum value of 7.18 S cm-1 at the fluence of 2.2×10^{12} ions cm^{-2} and a decrease is observed at higher fluence. The improvement in conductivity upto a fluence of 2.2×10^{12} ions cm^{-2} could be attributed to the breaking of bonds in the target material that generates additional free charge carriers resulting in increased conductivity with increasing ion dose [3]. N_2 adsorption-desorption isotherms reveal an increase in BET specific surface area of the nanocomposite from 208.4 to 263.8 $m^2\ g^{-1}$ and average pore size from 4 to 21 nm with increasing ion fluence, which is due to the

damage tracks created by highly energetic SHI ions along its path as observed in the FESEM micrographs. Such a porous structure is beneficial for providing shorter electrolyte ion diffusion pathways resulting in the increase in electrochemically active sites in the nanocomposite films for enhanced charge storage. The enhanced specific surface area and porosity of the nanocomposite electrode significantly increases the nanocomposite electrode wettability indicating improved electrode-electrolyte interfacial interaction upon irradiation, which is beneficial for capacitive charge storage. CV curves (Fig. 5.2.15) exhibit improved current response and increased area of the nanocomposites upon irradiation upto a fluence of 2.2×10^{12} ions cm^{-2} followed by a decreased current response at higher fluence. With increasing SHI fluence upto 2.2×10^{12} ions cm^{-2}, the CV curves change from quasi-rectangular shape to non-rectangular 'leaf-like' shape that returns back to the original quasi-rectangular shape at the highest fluence of 1.3×10^{13} ions cm^{-2}. This transition and improved current response in the CV curves till a fluence of 2.2×10^{12} ions cm^{-2} are attributed to the enhanced specific surface area and porosity of the nanocomposites upon irradiation. The enhanced porosity increases the available electrochemically active sites of PPyNTs in the electrode for faradaic charge transfer [4] giving rise to an increased pseudocapacitance resulting in a non-rectangular CV shape. At the highest fluence of 1.3×10^{13} ions cm^{-2}, PPyNTs are highly fragmented and could not contribute to the charge storage process leading to a decline in pseudocapacitance. This results in the dominant contribution of EDLC and a quasi-rectangular CV shape of the nanocomposite electrode at this fluence. GCD measurements reveal a maximum specific capacitance of 346 F g^{-1} is obtained for the nanocomposite irradiated at a fluence of 2.2×10^{12} ions cm^{-2} as compared to 299 F g^{-1} for that of pristine. The specific capacitance decreases to 268 F g-1 as the irradiation fluence increases to 1.3×10^{13} ions cm^{-2} due to increased amorphicity of the polymer matrix and enhanced defect density of RGO induced by SHI in the nanocomposite.

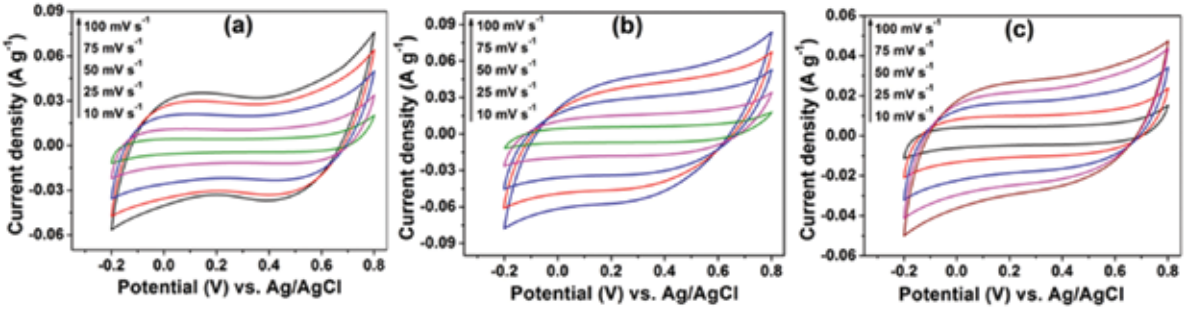

Fig.5.2.15:CV curves of RGO-PPyNTs nanocomposites
(a) pristine, and irradiated with fluence of (b) 2.2×10^{12} and (c) 1.3×10^{13} ions cm^{-2}.

REFERENCES

[1] D.K.Avasthi, S.Ghosh, S.K.Srivastava & W.Assmann,Nucl. Instr. Meth. Phys. Res. B 219 (2004) 206.
[2] S.Kumar, A.Tripathi, F.Singh, S.A. Khan, V. Baranwal& D.K. Avasthi, Nanoscale Res. Lett. 9 (2014) 126.
[3] A.Kaur, A.Dhillon & D.K. Avasthi, J. Appl. Phys. 106 (2009) 073715.
[4] E.Frackowiak et al., Chem. Phys. Lett. 361 (2002) 35.

5.2.11 Effect of Carbon ion-beam irradiation on Graphene oxide film

Chetna Tyagi[1], S.A. Khan[1], Sunil Ojha[1], DK Avasthi[2] and Ambuj Tripathi[1]

[1]Materials Science division, Inter University Accelerator Centre, Aruna Asaf Ali Marg, New Delhi, India-110067
[2]Amity Institute of Nanotechnology, Amity University, Noida, India-201313

Graphene oxide films were synthesized and irradiated using Carbon ion beam having energy 80 MeV with fluence varying from 10^{11} to 10^{13} ions/cm^2. Films were characterized using X-ray diffraction (Fig. 5.2.16), Raman and FTIR spectroscopy. Disorder parameter (obtained from Raman spectra) of GO films showed an increase attributing to the creation of defects in lattice. XRD and FTIR spectroscopy indicated that the water molecules were detached from the layers of GO with the increase in fluence. Theoretical simulations results (Fig. 5.2.17) showed that the maximum lattice temperature (i.e. 574 K) reached was lower than the annealing (873 K) and melting temperature (i.e. 3873 K) of GO which could not result in annealing effect.

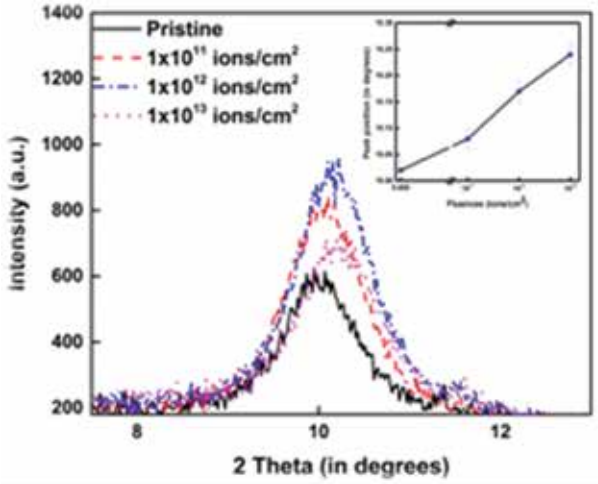

Fig. 5.2.16: XRD plots for GO samples irradiated using 80 MeV Carbon ion beam with different fluences. Inset (on top right) shows the shift in characteristic peak position towards higher angle indicating the decrease in inter-planar spacing (d) with the fluence

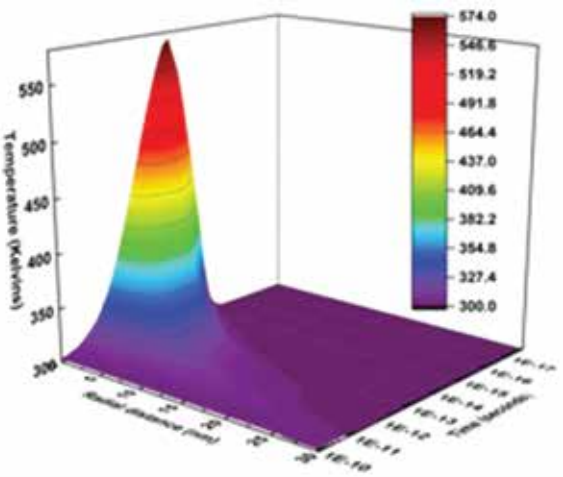

Fig. 5.2.17: 3D simulated plot (using i-TS code) for temperature evolution along the radial distance from the centre of the ion path/track formed during the ion beam irradiation.

5.2.12 Ion beam irradiation effects on the surface properties of the 3d transition metal doped Topological insulators

R. Urkude and U. Palikundwar

X-ray Research Laboratory, Department of Physics, RashtrasantTukadoji Maharaj Nagpur University, Amaravati road, Nagpur-440033.

The 3d transition metal doped Single crystals of $Bi_{2-x}A_xSe3$ (A = Mn and V) topological insulators were prepared by using evacuated (to a pressure of 10−3 Torr) quartz tube sealing method. The compounds were identified using a Bruker D8 Advance X-ray diffractometer with monochromatic nickel filtered Cu K_α radiation as the x-ray source. The powder XRD reveals the formation of rhombohedral crystal structure with space group (R-3m) with varying concentrations of Mn and V. The crystals thus grown have (003l) cleavage planes aligned parallel to the growth direction. Specimens of the as-grown crystals of dimension 12 × 5 × 0.3 mm^3 were cut along the growth direction and used for electron irradiation. The samples were irradiated with electrons of energy 200 keV for different fluences of the order 10^{14}–10^{16} cm^{-2}.

Single crystals, of thickness approximately about 0.2–0.3 mm,were used for the implantation of 1 MeV Co^{2+} and Fe^{2+} ions (implantation energy was calculated from the SRIM programme). Different fluences of the order of 10^{14}–10^{16} ions cm^{-2} were implanted into these samples by keeping it in a high vacuum chamber maintained at 10^{-8} Torr. The ion beam was focused to a spot size of 1 mm^2 and scanned over an area of 10 mm × 10 mm using a fluorescent tape to irradiate the sample uniformly. The fluence was measured by collecting the charge falling on the sample mounted on a ladder placed in a secondary electron-suppressed geometry. The ladder current was integrated with a digital current integrator and charge pulses were counted. The charge pulses produced were directly proportional to the number of Co^{2+} and Fe^{2+} ions bombarding thesample.

In this work, radiation effects of $Bi_{2-x}A_xSe_3$ (A = Mn and V) single crystals prepared by E-beam evaporation are investigated using Co^{2+} and Fe^{2+} ions irradiations at different fluences of 1 ×10^{14}, 10^{15}, 10^{16}, 3 ×10^{15} and 10^{16} ions/cm^2 with the focus on the transport and structural properties. X-ray diffraction (XRD), Scanning electron Microscopy (SEM), Energy dispersive X-ray Analysis (EDAX) and Raman spectroscopy of thesamples are obtained to assess how phase and microstructure influence the transport and structural properties. The change in the phase and microstructure was observed, under a higher fluence, 3 x 10^{15} and 10^{16} ions/cm^2. It means that, the Co and Fe ions are incorporated very well in the matrix of $Bi_{2-x}Mn_xSe_3$and $Bi_{2-x}V_xSe_3$to enhance the structural properties under intensive radiation environment. Here, the graphical representation for the Raman spectroscopy measurements have been mentioned for the Co and Fe ion implantation at different fluences. Fig.5.2.18(a) shows the Co ion implantation in Bi_2Se_3 for the fluences of 1 ×10^{14}, 10^{15}, 10^{16}, 3 ×10^{15} and 10^{16} ions/cm^2. Fig.5.2.18(b) shows the Fe ion implantation in Bi_2Se_3 for the fluences of 1 ×10^{14}, 10^{15}, 10^{16}, 3 ×10^{15} and 10^{16} ions/cm^2. Fig.5.2.18(c) shows the Fe ion implantation in $Bi_{2-x}Mn_xSe_3$ for x = 0 to 0.7 for the fluences of 1 ×10^{15} ions/cm^2 for the comparison in varying Mn contents.

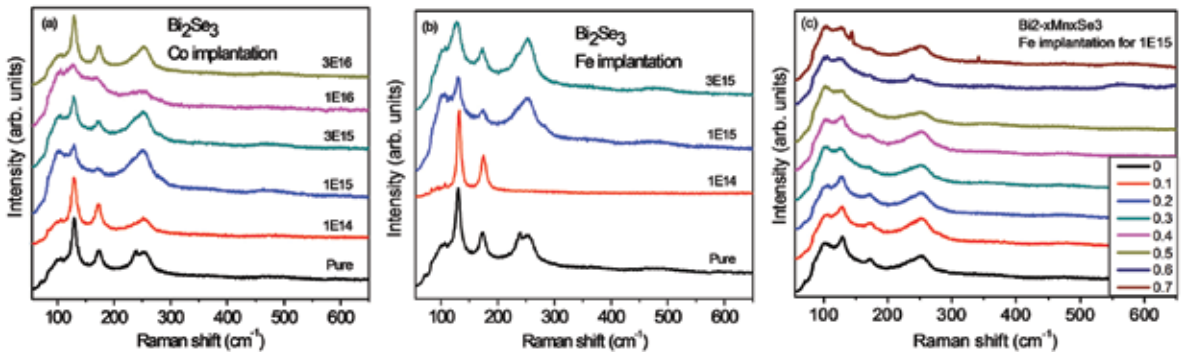

Fig.5.2.18: Raman spectra for (a) Co ion implantation in Bi_2Se_3 for different fluences (b) Fe ion implantation in Bi_2Se_3 for different fluences and (c) Fe ion implantation for 1×10^{15} in $Bi_{2-x}Mn_xSe_3$ for x = 0 to 0.7.

REFERENCES

[1] G. Fu et al., Nuclear Instruments and Methods in Physics Research B 358 (2015) 229–235.
[2] A. Saji, S. Ampili, S.-H. Yang, K. J. Ku and M. Elizabeth, J. Phys.: Condens. Matter 17 (2005) 2873–2888.

5.2.13 Effect of Ag doping on structural and electrical properties of thin films of $Ge_2Sb_2Te_5$

Neetu Kanda[1], Palwinder Singh[2,3], Anup Thakur[2], Fouran Singh[4] and A.P. Singh[1]

[1]Physics Department, Dr B R Ambedkar National Institute of Technology, Jalandhar-144011
[2]Department of Basic & Applied Sciences, Punjabi University, Patiala -147 002, Punjab, India
[3]Department of Physics, Punjabi University, Patiala, Punjab 147 002, India
[4]Inter-University Accelerator Centre, New Delhi, Delhi - 110 067

Out of the phase change memory (PCM) materials for optical storage, $Ge_2Sb_2Te_5$, GeSbTeN, GeSnSbTe, GeBiTe and GeInSbTe are most promising [1-4]. PCM material with most favourable properties is $Ge_2Sb_2Te_5$ (GST), which is the focus of the present study. The remarkable difference in their reflectivity and conductivity makes GST better material than silicon to replace for fabrication of ultrasound non-volatile memory [5]. It has been shown that the optical properties of GST can be improved by Ag doping. In this work, pure and Ag doped GST thin films are studied and the effect of Ag doping on optical, structural and transport properties of GST are also discussed using suitable characterization techniques.

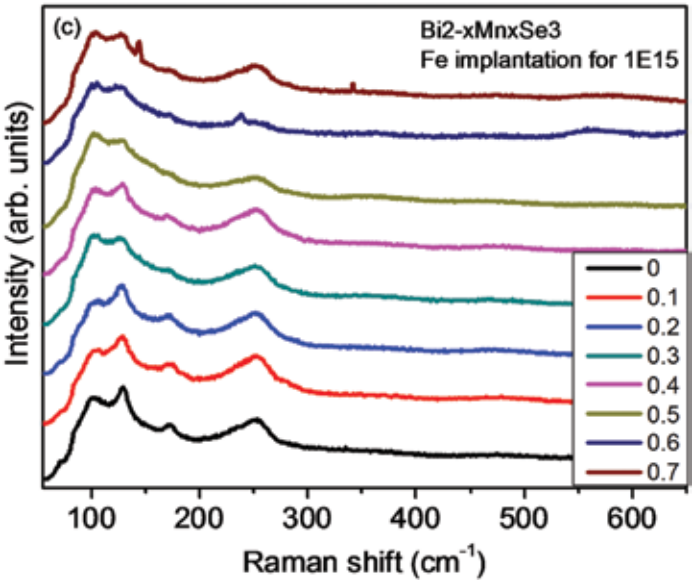

Fig.5.2.19: Change in transmission of GST films with SHI irradiation

Bulk alloy of GST and Ag doped GST were prepared by melt quenching technique. Thin films of these samples were deposited on glass substrate by thermal evaporation technique (HHV BC-300), at a deposition rate of 2-3 Å /s under the base pressure of 2.4×10^{-6} mbar. The film thickness was measured using digital thickness monitor (DTM-101) during thermal deposition. Structural and vibrational properties of the films are investigated using XRD and Raman spectroscopy, respectively. Transport characteristics of films are obtained at room temperature using I-V and Hall measurements. The films were irradiated with Ag^{9+} ions at 120 MeV energy in three shifts. $(Ge_2Sb_2Te_5)_{100-x}Ag_x$ (x = 0, 1, 3 and 5) thin films were irradiated with fluence of 5×10^{11}, 1×10^{12}, 5×10^{12} and 1×10^{13} ions/cm^2.

The XRD results show that the films are amorphous in nature with evolution of crystalline phase with irradiation. The results of the optical transmission measurements are shown in Fig. 5.2.19. The films are showing transmission greater than 80%. Overall there is a decrease in the transmittance with irradiation fluence, which can be due to the changes in the crystal structure with irradiation. Further investigations and analysis of the obtained results are being carried out to investigate the effect of irradiation on thin films.

REFERENCES

[1] M. Wuttig, H. Bhaskaran, T. Taubner, Nat. Photonics 11 (2017) 465-476.
[2] N. Bai, F.R. Liu, X.X. Han, Z. Zhu, F. Liu, X. Lin, N.X. Sun, Appl. Surf. Sci. 316 (2014) 202-206.
[3] K. Wang, D. Wamwangi, S. Ziegler, C. Steimer, M. Wuttig, J. Appl. Phys. 96 (2004) 5557.
[4] E. Rimini et al., J. Appl. Phys. 105 (2009) 123502.
[5] S. Kumar, D. Singh, R. Thangaraj, Appl. Surf. Sci. 273 (2013) 437–443.

5.2.14 Development of low cost Porous polymeric membrane for fuel cell membrane using Accelerator

Om Prakash[1], Saif A. Khan[2] and Pralay Maiti[1]

[1]School of Materials Science and Technology, Indian Institute of Technology (BHU), Varanasi 221 005, India.
[2]Inter University Accelerator Centre, Aruna Asaf Ali Marg, New Delhi 110 067, India

Nanochannels are created in poly (vinylidene fluoride) and its nanohybrid using swift heavy ions (SHI) (Ag^{+11} 120 MeV) followed by chemical etching and subsequent functionalization. The latent tracks in pure polymer and nanohybrid are generated by irradiating *SHI*. Through channels are generated by selective chemical etching of the amorphous latent track created during irradiation of *SHI*. Pore dimension and other properties of the membrane are characterized by using *SEM, AFM* and *optical microscope, XRD* and *DSC* to determine the nanostructure, morphology and crystalline structure of the sample. The comparison of the pore dimension in pure PVDF and its nanohybrid has been made. The nanochannels are suitably grafted with styrene and 3-HT (3-hexylthiophene) monomer on the pore walls of the membranes. Spectroscopic experiments have been performed for grafted polymers. Doping and functionalization on the grafted polystyrene and poly (3-hexylthiophene) has been done which increase the conductivity of the membrane. The conductivity of the modified membrane increases up to semi-conducting range (10^{-3} s/cm) from a perfect insulating *PVDF* matrix (around 12 orders of magnitude higher than pure PVDF). The morphology of Nanochannel is shown in Fig.5.2.20.

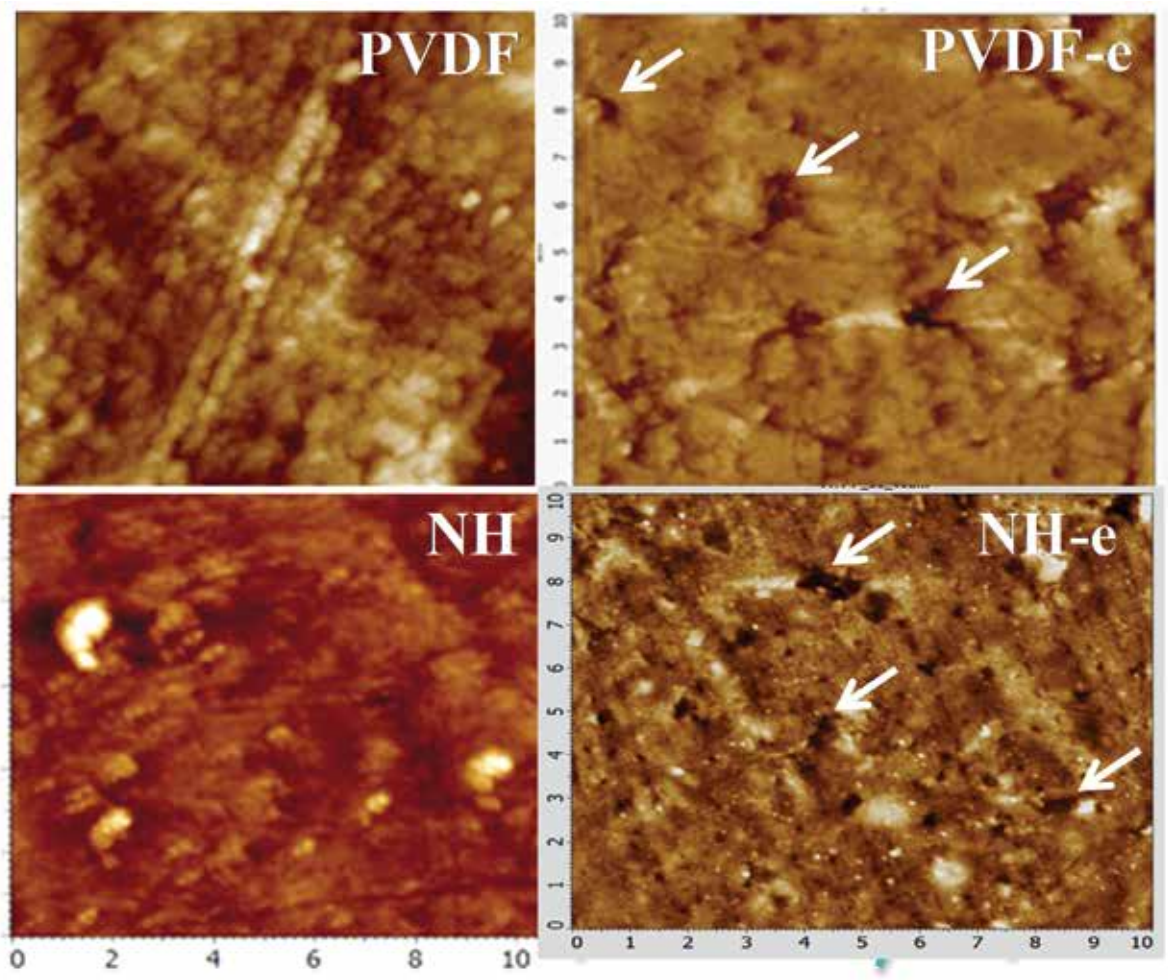

Fig. 5.2.20: *AFM* images of *PVDF* and *NH* (left images) before and (right images) after irradiation

Proton exchange membrane (PEM) is one of the most important parts of fuel cell and for conversion of chemical energy to electrical energy. In fuel cell PEM is key factor, which is used as electrolyte cum separator in fuel cell. For proton exchange properties of membrane commonly developed by the functionalization of polymer chain by different ionomers which facilitate the chemical reaction and separate electrons. Accelerator is one of the most promising technologies to generate reactive site as well as porosity in polymer membrane. Functionalized reactive site has enhanced capability of transporting ions necessary for the fuel cell efficiency.

REFERENCES

[1] K. K. Jana, O. Prakash, V. K. Shahi, D. K. Avasthi, andP. Maiti, ACS Omega 3(1)(2018) 917-928.
[2] K. K. Jana, V. K. Tiwari, D. K. Avasthi, T. Paine, and P. Maiti,ChemistrySelect2 (2017) 6413 – 6437.

5.2.15 SHI irradiation induced electrochemical enhancement in NiBTC-metal-organic framework based composite polymer electrolytes incorporated with ionic liquid

Rituraj Dutta[1], Ashok Kumar[1]*,Fouran Singh[2] and P. K. Kularia[2]

[1]Department of Physics, Tezpur University, Napaam, Assam-784028, India.
[2]Inter University Accelerator Centre, New Delhi-110067, India.

Metal-organic frameworks (MOFs) are hybrid microporous nanomaterials composed of inorganic unsaturated metal centers coordinated with organic ligands [1]. Ionic liquids (ILs) can be treated as efficient guest materials to incorporate within the pores of MOFs to maintain the phase behavior of the composite system [2]. In the present work, NiBTC-MOF has been synthesized and used as nanofiller in PVdF-HFP polymer electrolyte matrix. The composite polymer electrolyte membranes were irradiated by 100 MeV O^{7+} swift heavy ions at different fluences. IL $BMIMBF_4$ has been incorporated to the SHI irradiated membranes to investigate the electrochemical performances of the NiBTC-MOF based polymer electrolyte nanocomposite membranes upon IL incorporation.

XRD patterns of fluence dependent SHI irradiated NiBTC-MOF based PVdF-HFP nanocomposite membranes upon IL incorporation have been presented in Fig. 5.2.21. At 2θ = 8º and 2θ = 12º peaks correspond to (110) planes and (300) planes of NiBTC-MOF respectively. The characteristic peak at 2θ = 19.7o reveals (020) planes of PVdF-HFP.

As pore volume of NiBTC-MOF gets enlarged upon SHI irradiation because of extended linker defects in the BTC linker molecules so uptake of IL also increases with increasing fluence leading to increase the amorphicityof the nanocomposite membranes.The $BMIM^+$ ions may interact with the anions of the PVdF-HFP network that also contribute to minimize the degree of crystallinity of the composite polymer electrolyte membranes [3]. It is observed from Fig. 5.2.21 that the % degree of crystallinity decreases upto 20.9 with increasing ion fluence upto 3.3×10^{12} ions cm^{-2}. On further increase in fluence, at 10×10^{12} ions cm^{-2}, crystallinity again increases due to less uptake of IL. During irradiation, each ion creates a cylindrical molten zone of a few nanometers, transiently along its path, during which the temperature of the sample increases and the polymer chains get broken down resulting in decreased % degree of crystallinity. With further increase in fluence beyond 3.3×10^{12} ions cm^{-2}, the polymer nanocomposite electrolyte membranes become unstable to SHI irradiation and the uptake of IL becomes lesser due to deformation of molecular structure.

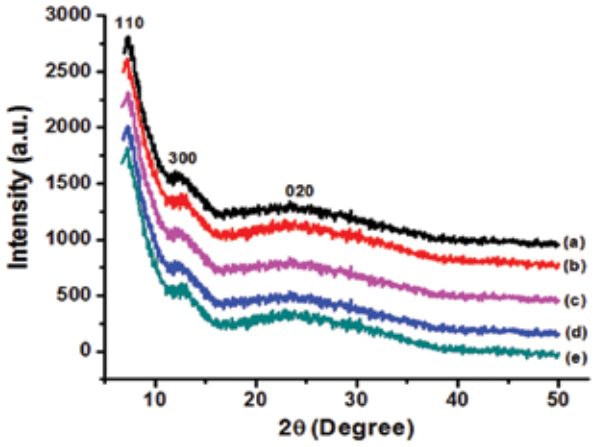

Fig. 5.2.21: XRD patterns of MOF-NiBTC based PVdF-HFP nanocomposite at different fluences upon IL incorporation, where (a) Pristine, (b) 3.3×10^{11}, (c) 10×10^{11}, (d) 3.3×10^{12}, (e) 10×10^{12} ions/cm^2 .

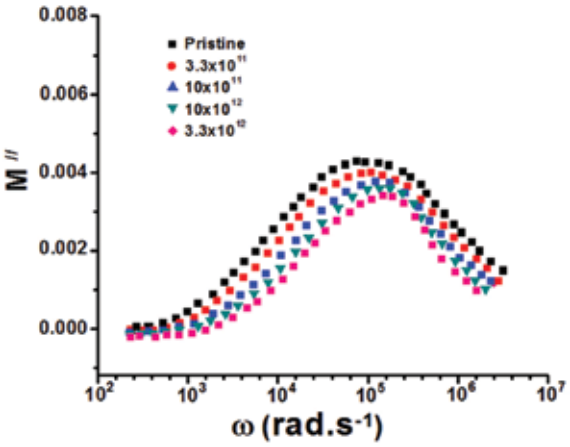

Fig. 5.2.22: Room Temperature variation of imaginary part of dielectric modulus with frequency f or MOF-NiBTC based PVdF-HFP nanocomposite at different fluences upon IL incorporation.

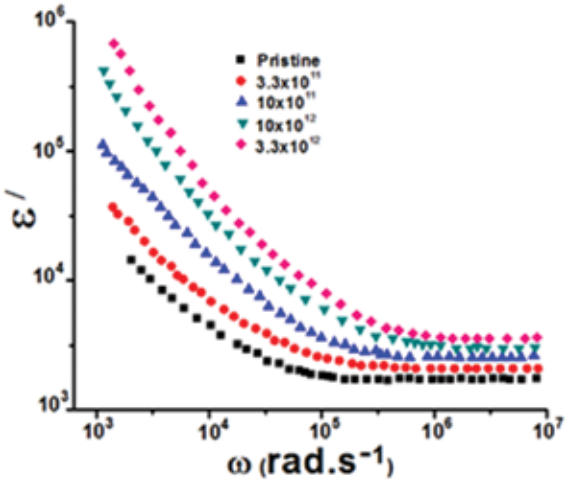

Fig. 5.2.23: Room Temperature variation of real part of permittivity with frequency for MOF-NiBTC based PVdF-HFP nanocomposite at different fluences upon IL incorporation.

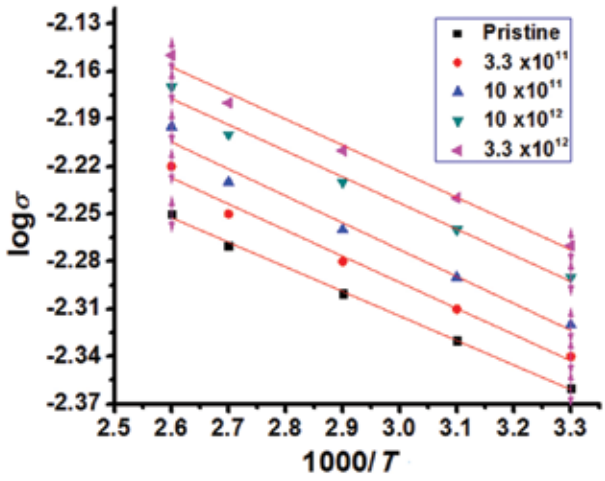

Fig. 5.2.24: Temperature dependent variation of ionic conductivity for MOF-NiBTC based PVdF-HFP nanocomposite at different fluences upon IL incorporation

The frequency dependence of dielectric permittivity (Fig. 5.2.22 and Fig. 5.2.23) and modulus spectra for the IL incorporated MOF-NiBTC based PVdF-HFP nanocomposites at different fluences can be attributed to non-Debye type behavior by the accumulation of space charge at the interface of the electrolyte [4]. Segmental motion of the polymer chain increases with increasing fluence upto 3.3 $\times 10^{12}$ ions cm^{-2} due to chain scission and that can lead to enhance in asymmetry in relaxation process.

The relaxation time (τ) decreases upto 1.53 $\times$ 10^{-8} S with increasing log ω_{max} upto 7.823 rad s^{-1} at the fluence of 3.3 $\times 10^{12}$ ions cm^{-2}. At the fluence of 10×10^{12} ions cm^{-2} segmental motion of the charge carriers disruptedowing to thecross linking of polymer chain as well as the reduction in density distribution of ions of IL within the micropores of MOF nanostructure.

The ionic conductivity of SHI irradiated NiBTC-MOF based PVdF-HFP nanocomposite membranes upon IL incorporation (Fig. 5.2.24) attains 9.9×10^{-3} Scm-1 at 380 K at the fluence of 3.3×10^{12} ions cm^{-2} due to increased segmental dynamics of polymer network. The increasing trend of ionic conductivity with increasing fluence upto 3.3×10^{12} ions cm^{-2} can be attributed to the fact that polymer chains are broken on irradiation due to heat generated in thermal spike and chain scission. Also, large interconnected pores can facilitate easier ionic movements leading to increased ionic conductivity, as the ions can easily move through the interconnected pathways. On further increase in fluence upto 10×10^{12} ions cm^{-2} the composite polymer electrolyte membranes get damaged and ionic conductivity decreases due to lesser contribution of IL ions as well as cross linking of polymer chains.

REFERENCES

[1] S. J. Dalgarno, P. K. Thallapally, L. J. Barbour and J. L. Atwood, Chem. Soc. Rev. 36(2) (2007) 236.
[2] Kazuyuki Fujie et al., Chem. Sci. 6 (2015) 4306.
[3] A. R. Polu and H.W. Rhee, International Journal of Hydrogen Energy 42(10) (2017) 7212.
[4] Anthony N Papathanassiou et al., Journal of Physics D: Applied Physics. 49 (2016) 2853.

5.2.16 Studies on the Low Temperature Lithium Ion Irradiation Effects on SiGe HBTs

Vinayakprasanna N. Hegde[1], T. M. Pradeep[1], John D. Cressler[2], Ambuj Tripathi[3], K. Asokan[3] and A. P. Gnana Prakash[1]

[1]Department of Studies in Physics, University of Mysore, Manasagangotri, Mysore -570006
[2]School of Electrical and Computer Engineering, Georgia Institute of Technology, Atlanta, GA -30332
[3]Inter-University Accelerator Center, New Delhi, Delhi -110067

Bandgap engineered silicon-germanium heterojunction bipolar transistor (SiGe HBT) is an attractive candidate for operation in extreme environments, including: at very low temperatures (~ 77 K), at elevated temperatures (~300 ºC), and in radiation intense surroundings [1]. For such applications, one clearly must also demonstrate that SiGe HBTs can simultaneously withstand exposure to radiations, while operating across a very wide temperature range. In the present work, the effects of 50 MeV Li^{3+} ion irradiation on SiGe HBTs at 150 K studied in order to understand the temperature dependence of damage production. The SiGe HBTs were irradiated with 50 MeV Li^{3+} ions at 150 K in the total dose range from 1 Mrad to 30 Mrad at 16 MV Pelletron accelerator at IUAC, New Delhi, India. The dc electrical characteristics were studied before and after irradiation at room temperature i.e., 300 K. The SiGe HBTs were also irradiated at 300 Kin the same dose range in order to comparelow temperature irradiation results with the room temperature results.The forward Gummel characteristics of SiGe HBTs subjected to 50 MeV Li^{3+} ions at 150 K and 300 K is shown in the Fig. 5.2.25 (left). The increase in forward mode base current (I_B) at lower V_{BE} was observed after irradiation at both 150 K and 300 K. The degradation in I_B is the result of increased recombination current in the emitter-base (E-B) depletion region due to radiation induced generation-recombination (G/R) traps near the EB spacer oxide. From the figure it is also evident that increase in I_B for HBTs irradiated at 150 K is very less when compared to 300 K. This is due to the fact that the Li^{3+} ions induce more G/R traps in the EB spacer oxide at 300 K than 150 K. TCAD simulations show that the peak electric field at the vicinity of the EB spacer oxide is smaller at 150 K than at 300 K, due to the increase in the EB junction built-in voltage with cooling [1]. Fig. 5.2.25 (centre) shows the variation of current gain (h_{FE}) for the HBTs irradiated at 150 K and measured at 300 K. From the Fig. 5.2.25 it is clear that the h_{FE} is found to decreases after irradiation at 150 K. Fig. 3 shows the variation of normalized peak h_{FE} after irradiation at both 150 K and 300 K. From the Fig. 5.2.25 (right), it is clear that the decrease in peak h_{FE} is more at 300 K than 150 K. The degradation of peak h_{FE} is around 13% and 35% at 150 K and 300 K respectively. The formation of trap charges at 150 K is less because the positively charged holes are immobile at such temperatures due to the absence of thermal energy in the lattice [1]. The parameters of ion irradiated SiGe HBTs is acceptable even after 30 Mrad of total dose at both the temperatures and thus SiGe HBTs are potentially useful for electronics applications requiring both low temperature operation and significant total dose radiation exposure.

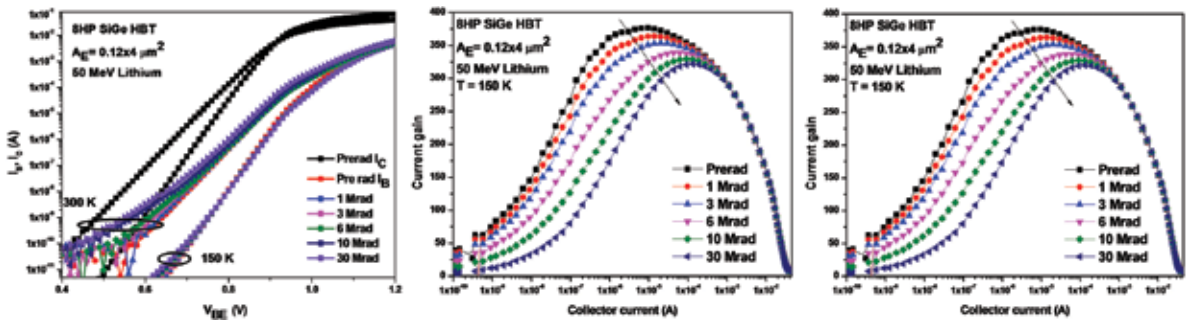

Fig. 5.2.25: Left) Forward Gummel characteristics, centre) Variation of h_{FE}, right) Normalized peak hFE versus total dose

REFERENCES

[1] A. P. Gnana Prakash et al., IEEE Transactions on Nuclear Science. 53 (2006) 3175.

5.2.17 Effect of ion irradiation on enhancement of electroactive β-phase in PDVF composites

Hari Sankar Mohanty[1], Pawan K. Kulriya[2], Ashok Kumar[3] and Dillip K. Pradhan[1*]

[1]Department of Physics and Astronomy, National Institute of Technology, Rourkela, Odisha 769008, India
[2]Materials Science Group, Inter-University Accelerator Centre, New Delhi 110 067, India
[3]CSIR- National Physical Laboratory, Dr. K.S. Krishnan Marg, New Delhi 110012, India

In this report, 50 MeV $^{7}Li^{+3}$ ion beam irradiation using 15 UD Pelletron at Inter University Accelerator Centre (IUAC), New Delhi was performed on PVDF based polymer composites (i.e., PVDF - ϕ*wt.* %of $0.94Na_{0.5}Bi_{0.5}TiO_3$-$0.06BaTiO_3$ (BNBT) withϕ =0, 35) with sample size 1 × 1 cm^2 and thickness 20 µm.

Solution casting technique has been adapted to prepare PVDF- ϕ *wt.*% of BNBT (ϕ =0, 5, 10, 15, 20, 25, 30, 35,40 & 50) composite filmsusing solution casting technique. BNBT was used as ferroelectric ceramics filler whereas PVDF was used as polymer matrix for the preparation of the composites. Single-phase polycrystalline BNBT solid solution was prepared by Sol-gel auto combustion method and sintered using microwave sintering technique. Sintered pellets were ball milled to be used as filler for preparation of polymer composite film. The main motivation of ion irradiation is to increase the electroactive β-phase fraction. In PVDF, the polar β-phase shows highest ferroelectric and dielectric properties as compared to other phases, which is necessary for device applications. Literature survey suggests that ion irradiation has the capability to transform structural changes from α to β-form in pristine PVDF [1, 2].

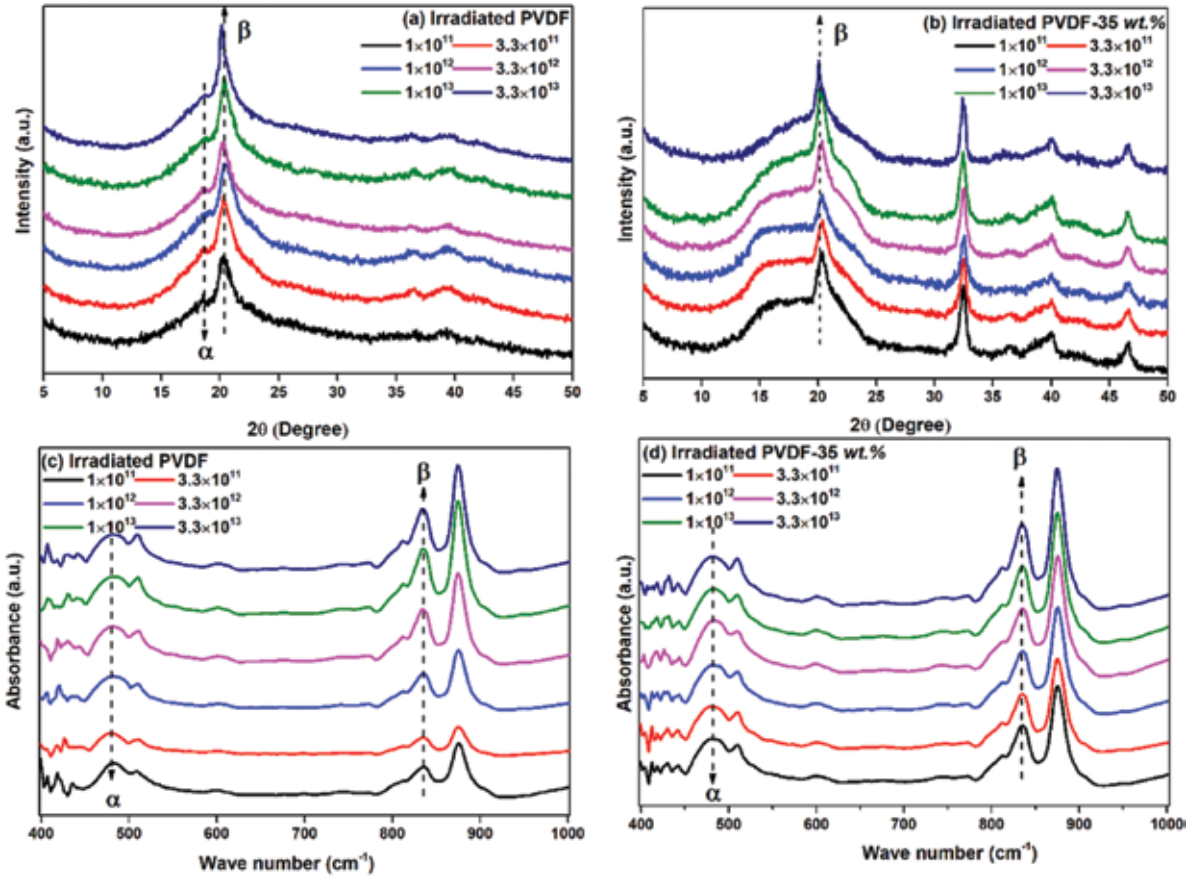

Fig. 5.2.26: XRD patterns and FTIR spectra of PVDF and ϕ = 35 wt.% BNBT composites for different ion fluence.

The X-Ray diffraction (XRD) and Fourier Transform Infrared (FTIR) spectroscopic technique are useful to quantify the presence of β-phase in PVDF based composites. In our experiment, the fluence range is varied form 1×10^{11} to 3.3×10^{13} ions cm^{-2} and the ion beam current is fixed to 1pnA. Fig.5.2.26(a) and (b) show the room temperature XRD patterns of ion irradiated pristine PVDF and for ϕ = 35*wt.*% BNBT composites respectively. The intensity of β-phase observed at an angle 20.12° increases and α-phase observed at 18.2° decreases with the irradiation fluence as observed from XRD data. The highest β-phase fraction for both the films has been observed for the fluence of 3.3×10^{13} ions cm^{-2}. FTIR spectrum has been shown in the Fig.5.2.26 (c) and (d) for the irradiated PVDF and ϕ = 35*wt.*% BNBT composites respectively. The effect of irradiation increases the fraction of β-phase and decreases the α-phase for both PVDF and ϕ = 35 *wt.*% composite. For the highest irradiation, the PVDF and 35 *wt.*% composite shows fraction of β-phase to be ~40% and ~82% respectively as calculated from FTIR data.

REFERENCES

[1] V. K. Tiwari, D. K. Avasthi,and P.Maiti, ACS Appl. Mater. Interfaces 3 (2011) 1398.
[2] S. Chandra et al.,J Appl.Polym. Sci. 115 (2010) 2502.

5.2.18 Investigating the Thermoluminescent Properties of $BaSO_4$:Eu and Li_2B4O_7:Dy as Radiation Dosimeters

Anant Pandey[1], Kanika Sharma[1], Pratik Kumar[2], S. P. Lochab[3] and Birendra Singh[3]

[1]Department of Physics, Sri Venkateswara College, University of Delhi, Benito Juarez Road, DhaulaKuan, New Delhi 110021, India.
[2]Medical Physics Unit, IRCH, AIIMS, New Delhi 110029, India.
[3]Inter-University Accelerator Centre, Aruna Asaf Ali Marg, New Delhi 110067, India.

$BaSO_4$:Eu nanophosphor is delicately optimized by varying the concentration of the impurity element and compared to the commercially available thermoluminescent dosimeter (TLD) LiF:Mg,Ti (TLD-100) and by extension also to $CaSO_4$:Dy (TLD-900) so as to achieve its maximum thermoluminescence (TL) sensitivity. Further, the energy dependence property of this barite nanophosphor is also explored at length by exposing the phosphor with 1.25 MeV of Co-60, 0.662 MeV of Cs-137, 85 MeV and 65 MeV of Carbon ion beams. Various batches of the phosphor at hand (with impurity concentrations being 0.05, 0.10, 0.20, 0.50 and 1.00 mol%) are prepared by the chemical co-precipitation method out of which $BaSO_4$:Eu with 0.20 mol% Eu exhibits the maximum TL sensitivity. Further, the optimized nanophosphor exhibits a whopping 28.52 times higher TL sensitivity than the commercially available TLD-100 and 1.426 times higher sensitivity than TLD-900, a noteworthy linear response curve for an exceptionally wide range of doses i.e. 10 Gy to 2 kGy and a simple glow curve structure. Furthermore, when the newly optimized nanophosphor is exposed with two different energies of gamma radiations, namely 1.25MeV of Co-60 (dose range- 10–300 Gy) and 0.662 MeV of Cs-137 (dose range- 1–300 Gy), it is observed that the shape and structure of the glow curves remain remarkably similar for different energies of radiation while the TL response curve shows little to no variation. When exposed to different energies of carbon ion beam BaSO4:Eu displays energy independence at lower doses i.e. from 6.059 to 14.497 kGy. Finally, even though energy independence is lost at higher doses, the material shows high sensitivity to higher energy (85 MeV) of carbon beam compared to the lower energy (65 MeV of C^{6+}) and saturation is apparent only after 121.199 kGy. Therefore, the present nanophosphor displays potential as an energy independent TLD.

This work has beenpublished in Radiation Physics and Chemistry, Volume 145 (2018) Pages 64-73 as a full length paper [1].

Further, the thermoluminescence (TL) properties of nanocrystalline $Li_2B_4O_7$:Dy were investigated. The TL properties of the said phosphor are of great interest as it has an effective atomic number close to that of a biological tissue. The phosphor is synthesized by combustion method and characterized by X-ray diffraction and transmission electron microscopy [2]. When the nanophosphor is exposed to a range of gamma doses using cobalt-60, it exhibits a linear TL response for an extensive range of doses. Further, the reproducibility and batch homogeneity properties are also studied. In conclusion, nanocrystalline $Li_2B_4O_7$:Dy shows potential as a radiation dosimeter of gamma rays.

REFERENCES

[1] K. Sharma et al.,Radiation Phys. and Chem. 145 (2018) 64-73.
[2] L. Singh, V. Chopra,S. P.Lochab, J. Lumin. 131(6) (2011) 1177-1183.

5.2.19 Interface modification in bilayers of immiscible Cu-Nb system through low energy ion beam irradiation

Debarati Bhattacharya[1,4], Priya Maheshwari[2], K. Devarani Devi[3] and P. K. Pujari[2,4]

[1]Solid State Physics Division, Bhabha Atomic Research Centre, Trombay, Mumbai 400085.
[2]Radiochemistry Division, Bhabha Atomic Research Centre, Trombay, Mumbai 400085.
[3]Pelletron Group, Inter-University Accelerator Center, Aruna Asaf Ali Marg, New Delhi, Delhi -110067
[4]Homi Bhabha National Institute, Anushaktinagar, Mumbai 400094.

The Nb-Cu system is characterized by positive heat of formation of 4kJ/mol and exhibits limited mutual solid solubility. Layered structures of this system are very interesting, since the Nb/Cu interfaces are compositionally constrained against migration. Low energy ion beam irradiation has the potential to produce defects at the interfaces of such immiscible components. Subsequently, the property of immiscibility of the Nb-Cu system can be exploited to form nanocomposites in the interfacial region; which possess high thermal stability, superior mechanical strength and enhanced radiation resistance. The Nb/Cu interfaces act as sinks for the radiation induced defects; accelerating the recombination of vacancies and interstitials, thereby producing improved radiation damage tolerance. Analysis of the depth distribution of defects in these layers and interfaces can provide valuable insight towards the radiation resistant property of these materials; which make them very useful in nuclear reactor applications.

In this work, the interfacial stability of magnetron sputter deposited Nb/Cu bilayers on Si substrates with respect to low energy ion beam radiation, was investigated using depth sensitive analytical techniques of X-Ray Reflectivity (XRR) and Positron Annihilation Spectroscopy (PAS). The sensitivity of specular XRR to the variation of electron density as a function of depth was effectively used to provide structural information about the layered system before and after irradiation. The presence of an interface width between the Nb and Cu layers aided the reflectivity analyses of this otherwise low electron density contrast system. Defect depth profiling of the interfacial structure as well as individual layers was carried out using beam-based PAS, by adjusting the energy of slow positrons between a few eV and several tens of keV. Grazing incidence X-ray diffraction was also used to measure changes in grain sizes of the irradiated layers. Nb/Cu interfaces were irradiated using 80 keV and 200 keV singly charged Siion beam from the low energy negative ion implanter facility at IUAC, New Delhi. Defect depth distribution was studied as a function of fluence, which was varied from 10^{14} to 10^{16} ions/cm^2. Depth profiling study revealed interesting modifications produced in irradiated bilayers when compared with unirradiated ones. It was observed that the lower values of fluence did not affect the interfacial region to a large extent. However, irradiation at the highest fluence produced the most significant changes at the interface of Nb and Cu layers as well as the individual layers, with respect to changes in thickness and density.

5.2.20 80 keV Xe^+ ion irradiation effects on rGO/PEDOT:PSS nanocomposite as anode catalyst for methanol oxidation

Bhagyalakhi Baruah[1], Ashok Kumar[1*], Fouran Singh[2], and P. K. Kularia[2]

[1]Department of Physics, Tezpur University, Napaam, Assam-784028, India.
[2]Inter University Accelerator Centre, New Delhi-110067, India.

Growing demand of renewable and clean energy resources increases the quest of the researchers for advancement of sustainable energy storage and conversion systems. Among the advanced energy conversion devices, direct methanol fuel cells (DMFC) are drawing great attention of the scientists due to large energy density (5.04 kWh L^{-1}), easy handling, light weight, low operating temperature and low pollutant emission over hydrogen fuel cell [1]. PEDOT: PSS (Poly(3,4-ethylenedioxythiophene): polystyrene sulfonate) is a conjugate polymer, where PSS is a polyelectrolyte which makes PEDOT soluble in water and carries a negative charge and PEDOT, the conjugate polymer carries a positive charge. Among the carbon compounds, two dimensional sp^2 hybridized monolayer graphene sheets have attained tremendous attention due to large surface area (2630 m^2/g), excellent electrical conductivity (6000 S/cm) and high tensile strength. In present work, the synthesis of rGO/PEDOT:PSS nanocomposite by *in-situ* polymerization technique for methanol oxidation in alkaline media is reported. The synthesized rGO/PEDOT:PSS nanocomposites are irradiated with 80 keV Xe^+ ion at different fluences.

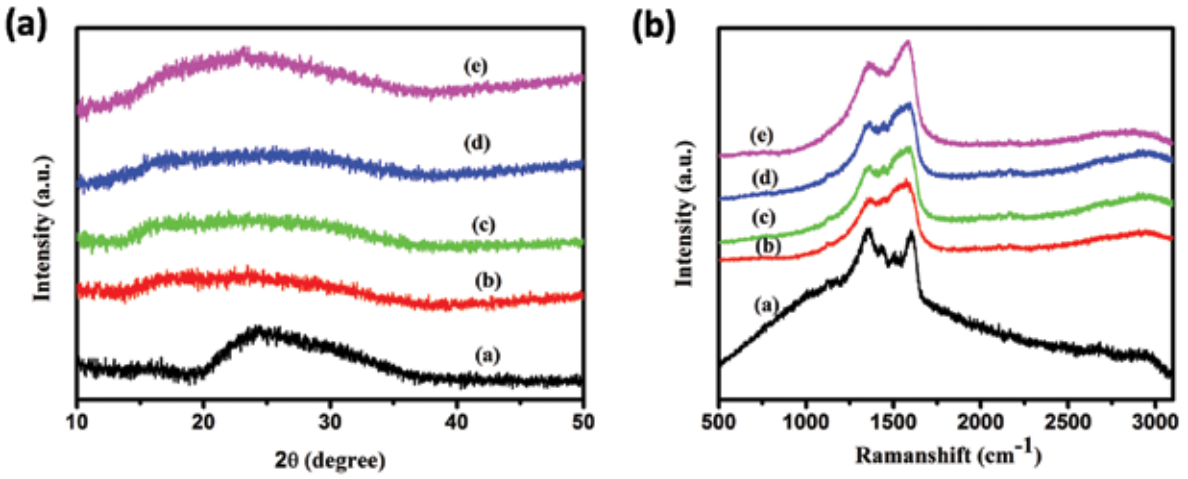

Fig. 5.2.27: (a) XRD patterns (b) and Raman spectra of rGO/PEDOT:PSS nanocomposites (a) pristine and irradiated with fluence of (b) 3.3×10^{14} , (c) 1×10^{15}, (d) 3.3×10^{15} and (e) 1×10^{16} ions cm^{-2}

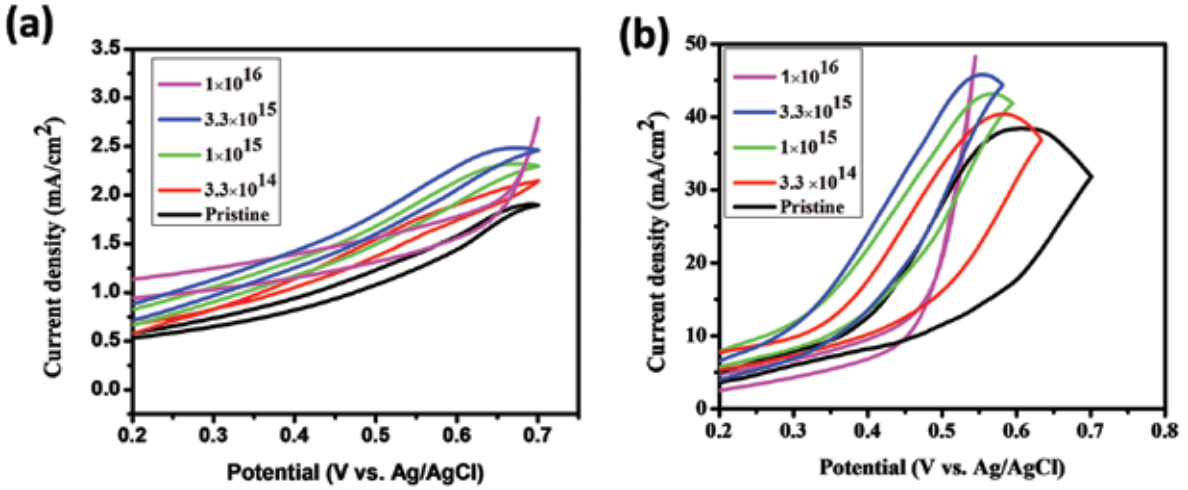

Fig. 5.2.28: CV curves of pristine and irradiated rGO/PEDOT:PSS nanocomposites with fluence of 3.3×10^{14} , 1×10^{15}, 3.3×10^{15} and 1×10^{16} ions cm^{-2} (a) in absence and (b) in presence of 0.5 M methanol containing 0.5 M NaOH solution.

Fig.5.2.27(a) and 5.2.27(b) presents the XRD pattern and Raman spectra of the pristine and Xe^{+} irradiated rGO/PEDOT:PSS nanocomposites. Pure PEDOT:PSS is semi-crystalline showing its characteristics peaks around 12º and 26º. rGO/PEDOT:PSS nanocomposite exhibits its characteristic broad peak around 23º, which indicates successful *in situ* polymerization of the polymer on rGO nanosheets. It is observed that crystallinity decreases with increasing ion fluence. In Raman Spectrum characteristic peaks of rGO appear around 1353 cm^{-1} (D band), 1604 cm-1 (G band) and 2768 cm^{-1} (2D band). The G band in rGO appears due to in plane vibration of sp^2 hybridized C-C stretching mode, which is referred to as E_{2g} mode [2]. Thiophene ring of PEDOT resonates between benzoid and quinoid structure within the range of 1400-1500 cm^{-1}. The low energy ion implantation causes graphitization of the nanocomposite due to which G peak becomes prominent on increase in ion fluence.

Fig.5.2.28(a) and (b) show the CV curves of pristine and irradiated rGO/PEDOT:PSS nanocomposites in absence and in presence of methanol, respectively. The pristine sample exhibits methanol oxidation peak at 0.59V whereas the oxidation potential of irradiated samples shifts to negative side and finally the nanocomposites irradiated with fluence 1×10^{16} ions/cm^2 exhibit oxidation peak at 0.54 V. The oxidation current increases upto 48 mA/cm^2 with fluence upto 1×10^{16} ions/cm^2. Unlike the broad CV pattern of pristine samples, the irradiated rGO/PEDOT:PSS nanocomposite with fluence 1×10^{16} ions/cm^2 exhibits sharp rise of current at 0.54 V. The gradual change in CV pattern can be ascribed to the gradual structural changes with increase in fluence as described here: (i) degassing, where the functional groups present in the nanocomposites transform to 'pre-carbon' structures, (ii) growth of carbon-rich clusters, (iii) the carbon clusters aggregate to form quasi-continuous carbonaceous layer and (iv) at the highest fluence i.e. 10^{16} ions cm^{-2}, the carbonaceous layer transforms to graphite like material [3].

REFERENCES
[1] J.C. Park and C.H Choi,Journal of Power Sources. 358 (2017) 76.
[2] R. Beams, L. G. Cançado and L. Novotny, Journal of Physics: Condensed Matter 27 (2015)083002.
[3] V.N.Popok,Rev. Adv. Mater. Sci30 (2012)1-26.

5.2.21 Effect of 80 keV Xe^+ irradiation on layered nano-systems

Saurabh Jyoti Hazarika[1], Hemanga Jyoti Sarmah[1], Pawan Kulriya[2], D. Kanjilal and D. Mohanta[1]

[1]Nanoscience and Soft Matter Laboratory, Department of Physics, Tezpur University, Tezpur,-784 028, India
[2]Inter University Accelerator Centre, Aruna Asaf Ali Marg, New Delhi -110 067, India.

Layered systems, like graphite and transition metal dichalcogenides (TMDCs) have attracted the researchers across the globe because of exhibition of not only exciting properties but also versatile applications in diverse fields of research [1,2]. Tungsten disulfide (WS_2), an active member of TMDC family has not been explored much as regards irradiation induced effects. Herein, the structural and morphological features of 80 keV Xe^+ ion irradiation effect on the commercially available pencil graphite and as-synthesized WS_2 nanosystems is reported.

Graphite samples were collected from the writing pencil (10B, Camlin) and cut into small pieces (diameter: 6 mm, thickness: 5 mm), followed by mechanical polishing. Again, WS_2 nanoparticles were synthesized using a cost-effective hydrothermal process. For irradiation experiment, the as-prepared nanoparticles were dispersed in a low molecular weight polyvinyl alcohol (PVA) matrix. The samples were then casted on laboratory glass slides of size 1 × 1 cm^2. Both of graphite and WS_2 systems were irradiated by 80 keV Xe^+ ions using the low-energy ion beam facility (LEIBF) available at IUAC, New Delhi. The irradiation was done with a constant beam current (~2 μA). In the case of graphitic specimen, the angle of irradiation was varied from 0o to 70º, keeping the fluence fixed at 1×10^{15} ions/cm^2; whereas, the fluence was varied as, 5×10^{15}, 1×10^{16} and 5×10^{16} ions/cm^2 in case of WS_2 considering normal incidence of ions.

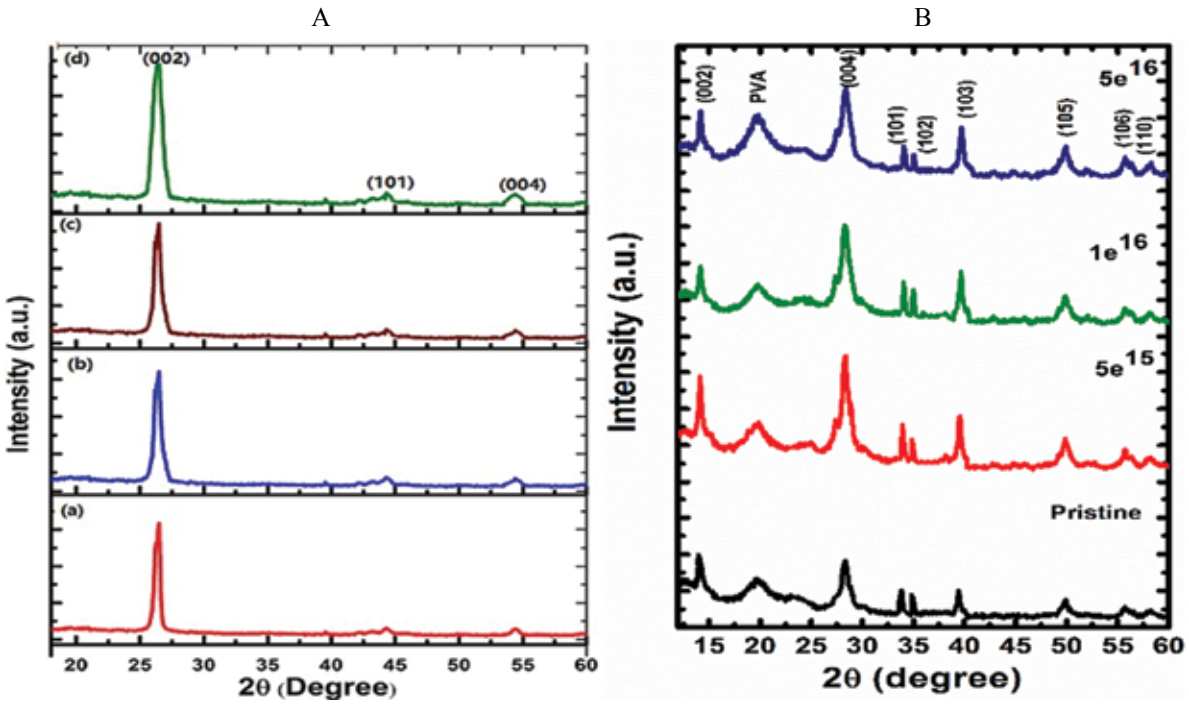

Fig.5.2.29: XRD patterns of (A) graphite and (B) nano-WS_2 systems. In (A), while (a) depicts for pristine graphite, others characterize graphitic systems irradiated ($1x10^{15}$ ions/cm^2) with different angle of incidence such as, (b) 0º (normal incidence), c) 50º and d) 70º. Meant for nano-WS_2, in (B), only normal incidence was considered with different fluences.

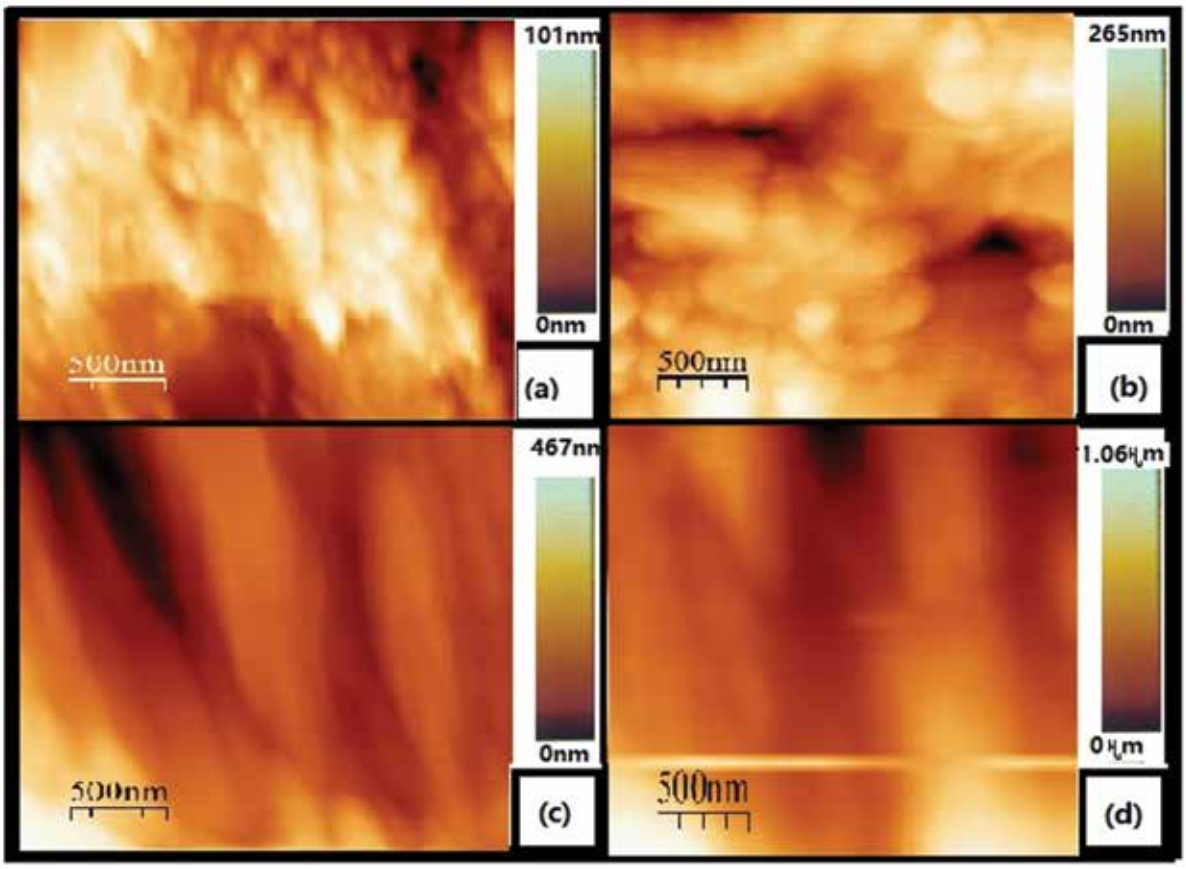

Fig.5.2.30: AFM images of graphitic samples: (a) pristine, and irradiated with a fluence of $1x10^{15}$ ions/cm^2 and with respective angle of incidences of(b) 0º (normal incidence), (c) 50º and (d) 70º.

Fig. 5.2.29(A) shows the XRD patterns of the pristine and irradiated graphite samples. The XRD data were analyzed using JANA-2006 software package [3]. The graphitic samples, before and after irradiation exhibits hexagonal phase (space group: 194). The crystallite size of the samples was found to decrease with increasing angle of incidence of ions. Fig. 5.2.29(B) shows the XRD patterns of the pristine and irradiated nano-WS_2 samples. Apparently, the district diffraction peaks corresponded to the hexagonal phase of WS_2 (JCPDF file no 41-1487). Moreover, there is no indication of extra peak after the irradiation process. However, the peak intensity of the diffraction peaks was found to vary with ion fluence variation. The average crystallite size of the samples was also found to alter as a result of irradiation. The crystallite size increases from 20.4 nm (for pristine) to 25.2 nm on irradiation with a fluence of 5×10^{15} ion/cm^2. However, on further irradiation, the crystallite size decreases to 22.3 nm and 23.5 nm as for irradiation with fluences of 1×10^{16} ion/cm^2 and 5×10^{16} ion/cm^2; respectively. This change in the crystallite size could be attributed to the localized amorphization/disorder in the WS_2 samples as a result of ion irradiation [4].

Again, morphological analyses of the graphite samples were carried out employing atomic force microscope operating in non-contact mode. In general, hillocks and ripple formation have been encountered with increasing angle of incidence (Fig. 5.2.30). The RMS roughness was found to increase from a value of 21 nm (pristine) to 193 nm (angle of incidence 70º). Moreover, evidence of micron to nanoscale defects have been witnessed. Further analysis in this regard is in progress.

REFERENCES

[1] Q.H. Wang, K.K. Zadeh, A. Kis, J.N. Coleman, M.S. Strano, Nat. Nanotechnol. 7 (2012) 699–712.
[2] S. Manzeli, D Ovchinnikov, D Pasquier, O.V. Yazyev, A Kis, Nat. Rev. Mater, 2(8) (2017) 7033.
[3] V. Petricek et al., *Zeitschrift fur Kristallographie*-Crystalline Materials, 231(5) (2016)301-312.
[4] V. Surbhi, S. Sharma, P. Singh, K. Garg, K. Asokanand K. Sachdev, Mater. Res. Express 5 (2018) 025037.

5.2.22 Surface Modification of Titania Nanotube Arrays using Low Energy Ion Beam in Nitrogen Environment for Photocatalytic and Sensing Applications

S. Wadhwa[1], D. Singh[2], A. Tripathi[3] and D. Devi[3]

[1]Amity Institute of Nanotechnology, Amity University, Sec-125, Noida 201313, UP

[2]Department of Applied Physics, Amity School of Engineering and Technology (GGSIP University, Delhi), Noida-201313, Uttar Pradesh, India
[3]Inter University Accelerator Centre, Delhi, India

Vertically aligned titania nanotubes (TiNT) have been extensively investigated owing to its absorbance in the UV region, excellent uniformity, conformability and facile preparation method. To expand light absorption in visible range, doping or co-doping with metals [1, 2] or non-metals [3], surface treatments e.g. exposure to acid or alkali chemicals, laser radiation, ion implantation and cold plasmas [4] and anodization have been widely exploited. Ion implantation serves a better technique for surface modification as it improves electronic properties of the material and has been found to induce co-catalytic activity for photocatalytic H_2-evolution in TiO_2 nanotubes [5]. In addition, nontoxicity, biocompatibility, high specific area, and environmental safety are some of the desirable properties of TiO_2 [6]which can be exploited in biological applications. TiNTs are able to form well-defined nanostructured platforms with high surface area available to interact with biomolecules and allowing their use as an electrode [7], as matrices for immobilization of proteins and enzymes for use in biosensors [8]. Herein, our primary aim is to modify TiNT surface with low energy ion beam (LEIB) in nitrogen (N), gold (Au) and silver (Ag) ions for sensing and photocatalytic properties.

LEIB facility at IUAC, Delhi was used to modify TiNT surface with 80 keV N ions, 80 keV Ag ions and 80 keV Au ions with fluences of 10^{14}, 10^{15}, 10^{16} ions/cm^2.

Investigation involved the detection of L-tyrosine using ion beam modified TiNT thin film to understand the electronic and sensing properties of modified TiNT thin films. Following are the glimpse of the results obtained with Au modified TiNT electrode as indicated by the Fig. 5.2.31.

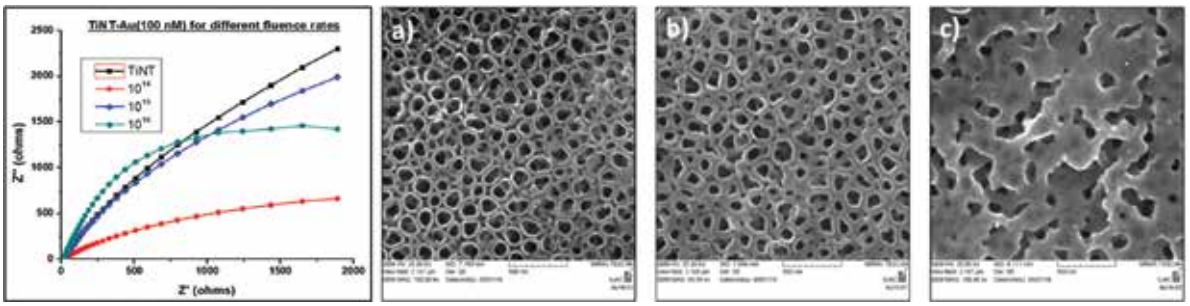

Fig. 5.2.31:Nyquist plots and SEM micrographs of TiNT modified with Au at fluences a) 10^{14} b) 10^{15} c) 10^{16} ions/cm^2

REFERENCES

[1] C. N. R. Rao and A.K. Cheetham. J. Mat. Chem. 11 (2001) 2887-2894.
[2] K. M. Prabu and P. M. Anbarasan. Int. J. Sci. Res. 3 (2014) 132-137.
[3] K.A. Vijayalakshmi. N. Karthikeyan and K. Vignesh. UGC Sponsored National Seminar on Emerging Trends in Plasma Technology and its Applications (ETPTA-2014), 20-21 August 2014, India.
[4] C. Yao and T.J. Webster. J. Nanosci. Nanotechnol., 6 (2006) 2682-2692.
[5] X. Zhou, V. Hublein, E M. Zolnhoferand P. SchmukiAngew, Chem. Int. Ed. 55 (2016) 3763– 3767.
[6] S. Sagadevan. Nanosci. Nanotechnol., 3 (2013) 62-74.
[7] H.C. Lee. L.F. Zhang. J.L. Lin. Y.L. Chin & T.P. Sun. Sensors, 13 (2013) 14161-14174.
[8] J. Wang. G. Xu. X. Zhang. J. Lv. X. Zhang. Z. Zheng & Y. Wu. Dalt. Trans., 44 (2015) 7662-7672.

5.2.23 Modification of structural and electrical properties of semi-insulating GaAs by silicon negative ion implantation

S. K. Dubey[1], Ajay Yaday[1], R. L. Dubey[1], S.Vishwakarma[1], Indra Sulania[2] and D. Kanjilal[2]

[1]Department of Physics, University of Mumbai, Mumbai- 400 098
[2]Inter-University Accelerator Centre, New Delhi, 110 067

The process of ion implantation requires an alternative technique for a solution to a semiconductor wafer sample charging problem in Integrated circuit/device, LSI and ULSI device fabrication at room temperature with high reliability. Negative ion implantation is one of the promising techniques to solve this problem, since the incoming negative charge of implanted negative ions is easily balanced by the outgoing negative charge as a part of secondary electron [1-3]. Silicon ion implantation in GaAs finds applications in optoelectronic devices, junction devices, Field effect devices and MOSFET devices.

In the present work, semi-insulating un doped GaAs wafers were implanted with 100 keV silicon negative ions (Si^{-1}) with fluences varying between 1 x 10^{15} and 4 x 10^{17} ions cm^{-2} at room temperature using MC-SNICS ion source at Low energy ion beam accelerator facility in IUAC, New Delhi. Implanted samples were characterized using AFM, Raman spectroscopy, RBS measurement, Hall measurement and I-V measurement techniques.The 3 Dimensional AFM image of un -implanted GaAs sample showed a smooth micrograph with root mean square surface roughness of 0.987 nm, whereas for all the implanted samples, the r.m.s surface roughness was found to increase with ion fluence upto 2×10^{17} ion cm^{-2} and it decreased for sample implanted with fluence of 4×10^{17} ion cm^{-2}. Fig.5.2.32 shows the representative 2D AFM image (2µm × 2µm) of GaAs sample surface implanted with silicon negative ion at 100 keV with fluence of 4×10^{17} ions cm^{-2} with various parameters extracted from section analysis.

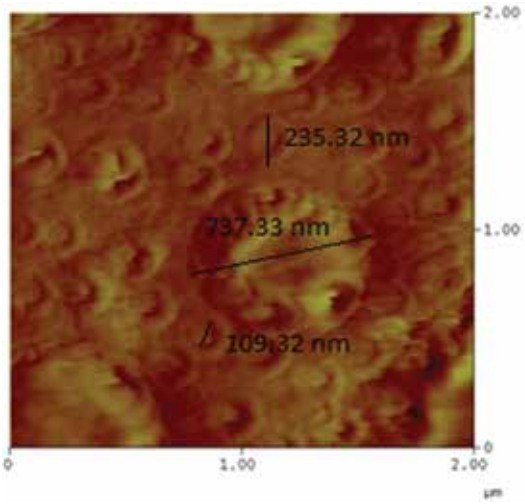

Fig.5.2.32:2 D AFM image (2µm x 2µm) for GaAs implanted with 4×10^{17} ions cm^{-2}

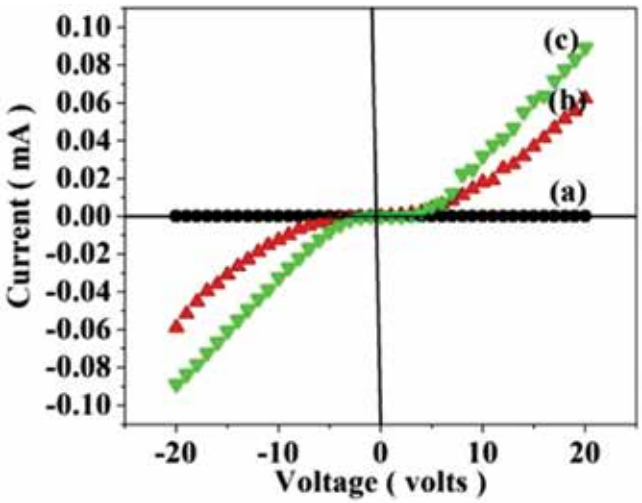

Fig.5.2.33: I-V characteristics for GaAs samples (a) un-implanted and implanted with 100 keV silicon negative ions with fluences of (b) 5×10^{16} and (c) 1×10^{17} ions cm^{-2}.

Fig.5.2.33 shows the electrical characteristics for un-implanted GaAs sample and GaAs samples implanted with 100 keV silicon negative ions with fluence of 5 x 10^{16} and 1 x 10^{17} ions cm^{-2}. For un-implanted GaAs sample, the current was in nA range whereas for implanted samples the current was in mA range. Improvement of I-V characteristic for the implanted GaAs samples had been observed with respect to un-implanted GaAs sample may be due to spontaneous recovery of lattice damage. Raman spectroscopy measurements and RBS measurements have also been carried out and the analysis of the same is under process.

REFERENCES

[1] Junzo Ishikawa et al., Nuclear Instruments and Methods in Physics ResearchB 96 (1995) 7.
[2] Junzo Ishikawa, H. Tsuji and YasuhitohGotoh, Surface & Coating Technology, 203 (2009) 2351.
[3] Junzo Ishikawa, Surface and Coating Technology, 65 (1994) 64.

5.2.24 Studies on the effect of Al and N implantation in ZnO thin films

Amaresh Das[1], Debdulal Kabiraj[2] and Durga Basak[1]

[1]Indian Association for the Cultivation of Science, Jadavpur, Kolkata-70032, India
[2]Inter-University Accelerator Centre, Aruna Asaf Ali Marg, New Delhi - 110 067, India

Using the beam time facility at IUAC, the structural properties of Al implanted ZnO thin films have been reported using X-ray diffractometry (XRD). At first, ZnO thin films of thickness 500 nm were deposited on pre-cleaned glass substrate using RF magnetron sputtering system using ZnO target with RF power of 150 W. The as-prepared ZnO thin films were subjected to Al ion implantation with an energy of 100 keV in vacuum at RT using LIBR beam line at IUAC, New Delhi. The nominal doses of Al implantation were 1×10^{14}, 2.5×10^{14}, 5×10^{14}, 7.5×10^{14} and 1×10^{15} ions/cm^2, respectively. After implantation, the Al-implanted ZnO films were annealed in Ar ambient at 450 °C for 60 min with a ramping rate of 5 °C/min.

The XRD patterns of all the films show a sharp single peak which corresponds to the (002) peak of the hexagonal wurtzite structure of ZnO. Presence of a highly intense (002) peak and absence of other intense peak of wurtzite structure of ZnO in the XRD patterns indicate that the films have been grown preferentially along the c-axis. Fig. 5.2.34 shows the enlarged view of (002) XRD peakof the annealed Al implanted ZnO films.A small shift in the (002) peak position towards lower angle is observed in theimplanted samples compared to that of the pristine

sample (shown inFig. 5.2.34), indicating the incorporation of Al in the lattice. Fig. 5.2.35shows thevariation of(002) peak intensity and the Values of FHHM with doses. The intensity of the XRD (002) peak is observed to increase with dose in the range from 1×10^{14} to 7.5×10^{14} ions/cm^2. Further increase in the dose results in a decrease in the intensity of (002) peak. On the other hand, the FWHM decreases with increasing dose in the range from 1×10^{14} to 5×10^{14} ions/cm^2 and then, it starts to increase with the increase of dose. The crystallite size of all the samples estimated using the well-known Scherrer's formula has been summarized in Table 1. The crystallite size increases with the increase of dose and at 5×10^{14} ions/cm^2, it becomes maximum.

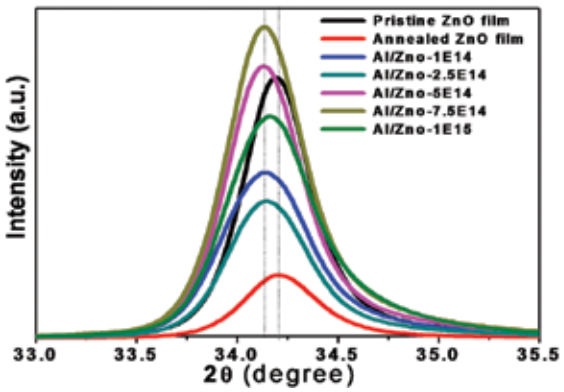

Fig.5.2.34: (002) peak in the XRD patterns of the samples

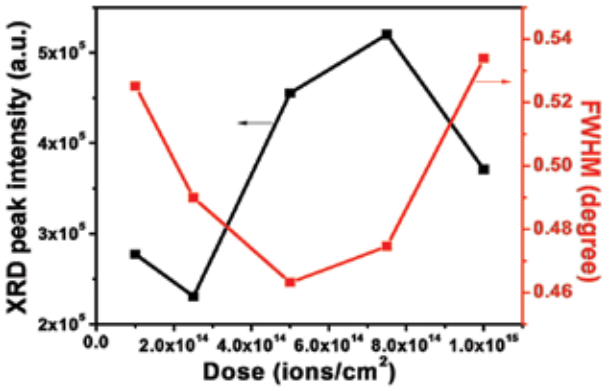

Fig.5.2.35: Variation of peak intensity and FWHM of (002) peak

Table. 1 Crystallite size of pristine, annealed and Al implanted ZnO thin films

Dose(ions/cm^2)	Pristine	Annealed	1×10^{14}	2.5×10^{14}	5×10^{14}	7.5×10^{14}	1×10^{15}
Crystallite size (nm)	20.68	18.95	16.53	17.718	18.74	18.29	16.26

Electrical conductivity and optical measurements of all the samples are under progress. Characterizations of the N implanted films are also being done. After completion of allthe measurements, all the data will be analyzed to understand the effects of Al and N ion irradiation on the structural, optical and electrical properties of ZnO thin films.

5.2.25 Raman spectroscopic analysis on Li, N and (Li, N) implanted ZnO

Apu Mondal[1], S. Pal[1,2], A. Sarkar[3], T. S. Bhattacharya[4], Avishek Das[5], N. Gogurla[6], S.K. Ray[7], Pravin Kumar[8], D. Kanjilal[8], K.D. Devi[8], A. Singha[4], S. Chattopadhyay[5] and D. Jana[1]

[1]Department of Physics, University of Calcutta, 92, A. P. C. Road, Kolkata 700009, India.
[2]Department of Physics, School of Natural Sciences, Shiv Nadar University, NH 91, Gautam Buddha Nagar, U. P.- 201314, India.
[3]Department of Physics, Bangabasi Morning College, 19 Rajkumar Chakraborty Sarani, Kolkata 700009, India.
[4]Department of Physics, Bose Institute, 93/1, A. P. C. Road, Kolkata 700009, India.
[5]Department of Electronic Science, University of Calcutta, 92, A. P. C. Road, Kolkata 700009, India.
[6]Department of Physics, Indian Institute of Technology, Kharagpur 721302, India.
[7]S. N. Bose National Centre for Basic Sciences, JD Block, Sector-III, Salt Lake City, Kolkata 700106, India.
[8]Inter University Accelerator Centre, Post Box 10502, Aruna Asaf Ali Marg, New Delhi 110067, India.

In this report, we have investigated the effect of 50 keV Li, N and (Li,N) co-implantation on the Raman modes for the polycrystalline ZnO. It has been observed that 275 cm^{-1} Raman mode does not appear in pristine or any Li-implanted ZnO (Fig. 1)which indicates that this particular mode is neither a characteristic one of ZnO nor due to the activation of any silent mode with disorder. Monotonic increase of peak intensity with fluence in N ion implantation has been noted significantly. However, the rate of increment of its intensity is reduced in presence of Li. Hence, one can unambiguously assign the 275 cm^{-1} Raman mode as N related defect complex. Some researchers have assigned this mode as NO-IZn complex defect [1]. Another debated Raman mode is 510 cm^{-1}, quite a few researchers assign it as N related mode. However, our observation reveals that although N implantation causes rise in intensity of this mode but this mode is also, observed in Li implantation (Fig. 2). The appearance of this mode in both type (Li and N ions) of implantation and its generic weak nature lead us to believe that its origin must be related to any complex type of defect, related to interstitials. Theoretical prediction

claims I_{Zn}-VO type of defects responsible for activation of 510 cm^{-1} Raman mode [1]. Signature of N-related 645 cm−1 Raman modes has been also noticed in N implanted samples. Besides, 680 and 856 cm^{-1} Raman modes are found to be disorder activated. Another distinguishable broad Raman signature has been seen at 475 cm^{-1} only for co-implanted sample (with fluence 10^{16} ions/cm^2) which has been assigned as an indication Zn clusters in ZnO [2]. In high fluence implanted samples, interstitial dislocation loops and larger open volumes may dynamically be separated [3]. Due to high formation energy of I_{Zn}s in ZnO [4], either they form complex (such as, I_{Zn}–V_O or I_{Zn}–N_O) or segregate as Zn clusters in the region with higher I_{Zn} concentration. Therefore 475 cm^{-1} mode is highly probable in the high fluence co-implanted samples. Further, an unknown highly intense 1562 cm^{-1} Raman mode is found (Fig. 3) in all implanted samples but with specific high intensity in co-implanted ZnO samples (with fluence 5×10^{15} and 10^{16} ions/cm^2). Our results show that 1562 cm^{-1} Raman mode is not at all carbon related as claimed by Kerr et al. [5]. Both the Raman modes 475 and1562 cm^{-1} need more careful extensive research for their identification. The origin of 1562 cm^{-1} Raman mode is not clear at the moment but it might be due to a defect (admixture of native defects along with N and Li) which has a resonating effect in presence of N and Li ion.

At low temperature DLE, I_{Zn} and VO related defect induced emission has been observed and a correlation between the fitted area of 555 and 579 cm^{-1} Raman mode with the above-mentioned PL emission has been established (not shown). At NBE (at 10 K), appearance of new peak at 3.368eV and 3.363 eV has been noted in N implantation and Li implantation (at high fluence). Both of them are donor in nature confirmed by thermal evolution of the peaks. An implicit presence of deep acceptors can be understood by the slow fall of 3eV peak with temperature and it is more vivid in Li implantation case. At room temperature PL, the most noticeable change is the broad emission ranging from 2.8-3.1 eV for co-implanted ZnO samples. This emission might be due to simultaneous presence of two emissions one is the electronic transition from conduction band to a deep Li_{Zn} acceptor level located nearly 300meV above the valence band (correspond to emission ~2.8eV) and another one is extended states of I_{Zn} to V_{Zn} related shallow acceptor level localized near the GB region. Overall, the signature of acceptor states has been observed in the low temperature PL spectra but they are certainly not the shallow ones.

REFERENCE

[1] F. Friedrich, M.A. Gluba and N.H. Nickel, Appl. Phys. Lett. 95 (2009) 141903.
[2] S. Khachadorian et al., Phys. Status Solidi (b) 252 (2015) 2620.
[3] S. Pal et al., J. Phys. D: Appl. Phys. 51 (2018)105107.
[4] A. Janotti and C.G. van de Walle, Native point defects in ZnO, Phys. Rev. B 76 (2007)165202.
[5] L.L. Kerr, X. Li, M. Canepa and A.J. Sommer, Thin Solid Films 515 (2007) 5282.

5.2.26 Metal ion implantation in TiO_2

N. Kaur[1], O. Prakash[1], A. Mahajan[1*], D. P. Singh[1], F. Singh[2], D. D. Kshetri[2] and S. Chopra[2]

[1]Department of Physics, Guru Nanak Dev University, Amritsar-143005, India
[2]Inter University Accelerator Center, New Delhi-110067, India

Recently, plasmonic nanoparticles have been incorporated into photoanodes of dye sensitized solar cells (DSSCs) to utilize their surface plasmon (SP) property for significant boosting of dye absorption and hence their photo conversion efficiency [1-3]. The various research studies [4-5] reveal that the nanoparticle size, composition, shape, crystallinity and dielectric environment further affect the position and strength of SPR band.The major limitation of these systems is that these bare nanoparticles, without any protective shell or linkages with TiO_2, cannot be used as such in DSSC due to their chemical instability with iodide/triiodide couple-based electrolyte. In addition to this, it can act as charge recombination centers. In recent days, ion beam has emerged as an effective approach to overcome these issues. Here, first metal nanoparticles are implanted in dielectric matrix with low energy (KeV) metallic ions and then this implanted matrix is irradiated with highly energetic metallic ions in order to modify various properties viz. corrosion resistant, morphology, crystallography, optical and electronic band structure of the embedded nanoparticles [6-8]. On the basis of literature survey and preliminary [9,10] investigations on DSSC, irradiations were done with objectives of: 1) Implantation of metal nanoparticles (Ag, Au, Cu and Al) possessing surface plasmon resonance (SPR) peaks for enhancing effective absorption cross-section of dye in TiO_2 matrix using low energy beam (few keV), 2) Implantation of metal alloy nanostructures in TiO_2 matrix to further enhance and broaden the SPR

For the commencement of the work, photo-anodes for fabrication of DSSCs were prepared. For that, FTO's have been thoroughly cleaned and buffer layers of TiO_2 are spin coated onto FTO substrates, followed by formation of 6 µm thick TiO_2 porous layer through doctor blading technique. The Ag and Au ions are implanted onto the prepared photoanodes with energy 80 and 120 KeV, respectively by varying fluence from 10^{12} to

10^{16} ions/cm^2. The Ag/Au alloys are formed by the implantation of Au ions onto the Ag ions implanted photo anodes. The implanted samples have been characterized through XRD, XPS, FESEM, EDS, UV-Vis and Raman spectroscopic techniques. XPS and EDS shows maximum 5 wt.% of Ag and Au nps in implanted samples. The UV-Vis studies depicts an increase in the absorption with increase in the fluence upto 10^9 ions/cm^2 and the same variation is observed in efficiency of DSSCs with a 20% increment at fluence of 10^{15} ions/cm^2 incomparison to reference DSSCs.

REFERENCES

[1] Y. Lou, S. Yuan, Y. Zhao, P. Hu, Z. Wang, M. Zhang, L. Shi, and D. Li, Dalton Trans. 42 (2013) 5330.
[2] C. Andrei, E.Lestini, S. Crosbie, C. Frein, T.O'Reilly, D. Zerulla, PLOS ONE 9 (2014) e109836.
[3] Z. Tian, L. Wang, L.Jia, Q. Li, Q. Song, S. Su and H. Yang, RSC Advances 3 (2013)6369.
[4] A. Tanvi et al., Journal of Applied Physics 117 (2015) 083111.
[5] E. Almeida et al., Appl. Phys. B 108(2012) 9.
[6] Y. K. Mishra et al., Applied Physics Letters 91 (2007) 063103.
[7] F. Singh et al., in The Seventh International Symposium on Swift Heavy Ions in Matter (Lyon, France, 2008).
[8] Avesh Kumar et al., App. Phy. Lett. 99(1) (2011) 013109.
[9] A.L.Stepanov, Rev. Adv. Mater. Sci 26 (2010)1.
[10] A.L.Stepanov, Reviews on Advanced Materials Science 30 (2012) 150.

5.2.27 Low energy ion irradiation of α–Al_2O_3

Mini Agarwal[1], B. S.K. Garg[2], K. Asokan[3], D. S. Thulkar[4], S. Chander[5], M.K. Dalai[6], A. Pratik Kumar[1]

[1]Medical Physics Unit, IRCH, AIIMS, New Delhi 110 029
[2]University Department of Physics, Patna University, Patna, Bihar 800 005
[3]Inter-University Accelerator Centre, Aruna Asaf Ali Marg, New Delhi 110 067
[4]Radiology Unit, IRCH, AIIMS, New Delhi 110 029
[5]Dept. of Radiotherapy, IRCH, AIIMS, New Delhi 110 029
[6]CSIR - National Physical Laboratory, Dr. K. S. Krishnan Marg, New Delhi - 110012

The present work reports the fabrication and characterization of α–Al_2O_3:C, a highly sensitive low effective atomic number (Z_{eff}=10.7) OSL material for medical dosimetry, through a new approach of doping via implantation. In this study, a Single Crystallineα–Al_2O_3 (SCALO) and a Sapphire α–Al_2O_3 (SALO) are used and implanted with 100 keV of C+ at various fluences (mol%) from 2.5 × 10^{14} ions cm^{-2} (~0.04%) to 6.25× 10^{15} ions cm^{-2} (~1%) and are pre-heated up to 220 °C. The structural, optical, morphological and luminescent studies of the Carbon doped α–Al_2O_3 (α–Al_2O_3:C) were carried out using X-ray diffraction, Ultraviolet-visible spectroscopy (UV–Vis), Photo-luminescence (PL), Time of Flight Secondary Ion Mass Spectrometry (TOF-SIMS), Optically Stimulated Luminescence (OSL), and Thermo-Luminescence (TL). The doping of ~1 mol% of C^+ is found at an optimized doping level due to its high intensity of luminescence. This phenomenon is studied for heavy charged particle (HCP) dosimetry, which might prove effective for cancer treatment. It is found that α –ALO:C (both the single crystalline and the sapphire alumina) has the capability to measure large radiation doses (~kGy). This is attributed to the generation of stable defects after the incorporation of Carbon that results in a linear response with the dose and in extraordinary efficiency. Thus, this study confirms the development of α–Al_2O_3 by the novel approach of C_+ implantation method and the findings result in an efficient medical radiation dosimeter.

5.2.28 Effect of 200 keV ion irradiation on structural and morphological properties of SnO_2-TiO_2 nano composite thin films

Vikas Kumar and Rajesh Kumar

University School of Basic and Applied Sciences,Guru Gobind Singh Indraprastha University, New Delhi-110078, India

In the present study, study the modifications in SnO_2-TiO_2 nanocomposite thin films caused by 200 keV Ar^+ ion irradiation with varying fluence 5×10^{13} ions/cm^2, 5×10^{14} ions/cm^2, 5×10^{15} ions/cm^2 and 5×10^{16} ions/cm^2 by low energy ion accelerator at IUAC, Delhi, India has been carried out. ITO coated glass and silicon (100) substrate have been used to synthesize SnO_2-TiO_2 nano composite thin films by RF magnetron sputtering technique [1]. A pellet with diameter of 5 cm and thickness of 4 mm was prepared for thin film deposition. The target has been prepared by mixed SnO_2-TiO_2 powder after crushed in pastel mortar for 12 hours at successive intervals and then sintered at 1200 ºC for 24 hours. As prepared target used in RF deposition technique. All samples were deposited in single run and at same environmental condition so that there is not any variation in the deposited thin films. The surface morphology and sectional analysis wereobtained by Atomic Force Microscope (AFM) measurement [2]. Crystallite size and crystallinity were characterized by Glancing Angle X-ray Diffraction (GAXRD)[3].

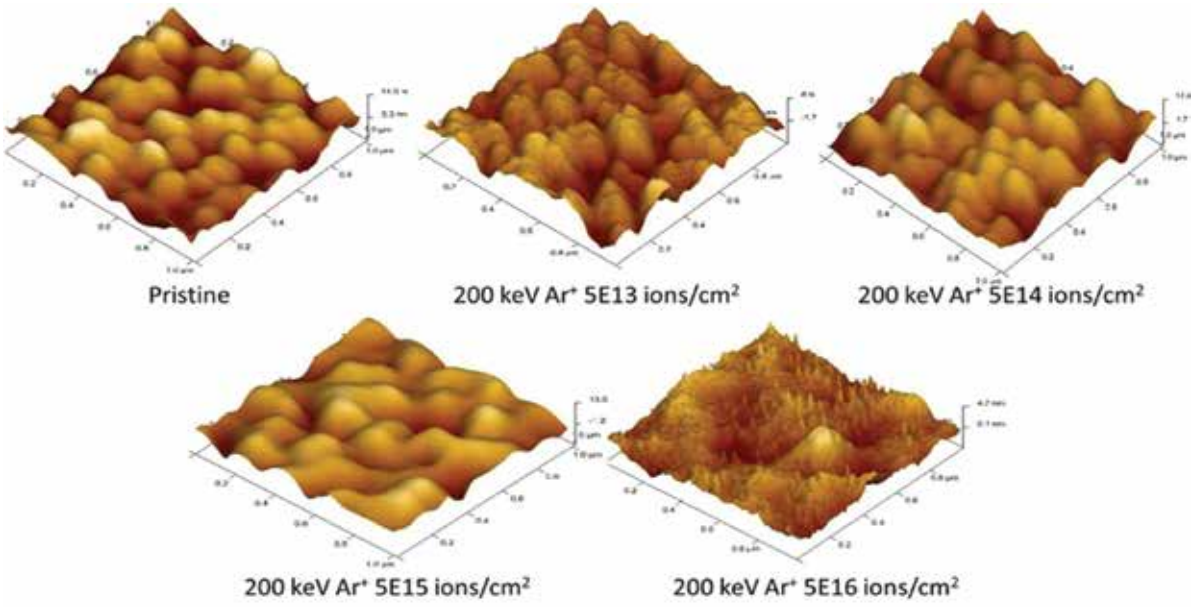

Fig. 5.2.36: AFM images of SnO_2-TiO_2 nanocomposite thin film of pristine and 200 keV Ar^+ ions irradiated films with varying fluence of 5×10^{13} ions/cm^2, 5×10^{14} ions/cm^2, 5×10^{15} ions/cm^2 and 5×10^{16} ions/cm^2

The surface morphology of Three-dimensional AFM images for the pristine and irradiated thin films is shown in Fig. 5.2.36.The average roughness R_a and Root-Mean-Square (RMS) R_q value was found to vary with varying ion fluence. For the pristine sample, the average roughness was measured 3.43 nm and for the irradiated sample with a varying fluence of 5×10^{13} ions/cm^2, 5×10^{14} ions/cm^2, 5×10^{15} ions/cm^2 and 5×10^{16} ions/cm^2 were measured 3.44nm, 3.53nm, 9.34nm and 2.21nm respectively. The average grain size was measured 176.1nm for pristine and for the irradiated sample with a varying fluence of 5×10^{13} ions/cm^2, 5×10^{14} ions/cm^2, 5×10^{15} ions/cm^2 and 5×10^{16} ions/cm^2 were measured 187.5nm, 187.5nm, 212.5nm and 183.7nm respectively. The X-Ray Diffraction (XRD) was used to investigate the crystal structure, and crystallite size of SnO_2-TiO_2 nanocomposite thin films as shown in Fig. 5.2.37.The significant peaks observed in the GAXRD pattern are at 26.95, 34.27, 37.60, 50.88 and 52.46. The pristine and irradiated thin films show the lattice planes of (110), (101), (200) (211), and (220) that corresponded to the standard rutile phase of the polycrystalline structure of SnO_2 as compared with JCPDS card No.41-1445 [4]. The monoclinic phase of g-Ti_3O_5 crystalline has been obtained from its diffraction pattern with peaks (011), ($\bar{1}$12), (020) and ($\bar{3}$21) at diffracting angle 21.67º, 30.48º, 35.35º and 45.40º respectively as compared with JCPDS card No. 76-1066. The formation of gamma phase in the thin film also verified that material composition exists in the form of molecular formula $Ti_nO_{(2n-1)}$ where n=3. The g-Ti_3O_5 structure identifies that, all the reflexions indices *hkl* satisfied the relation $h+k+l=2n$, and the value of n in between the range $1\leq n\leq 3$. [5]

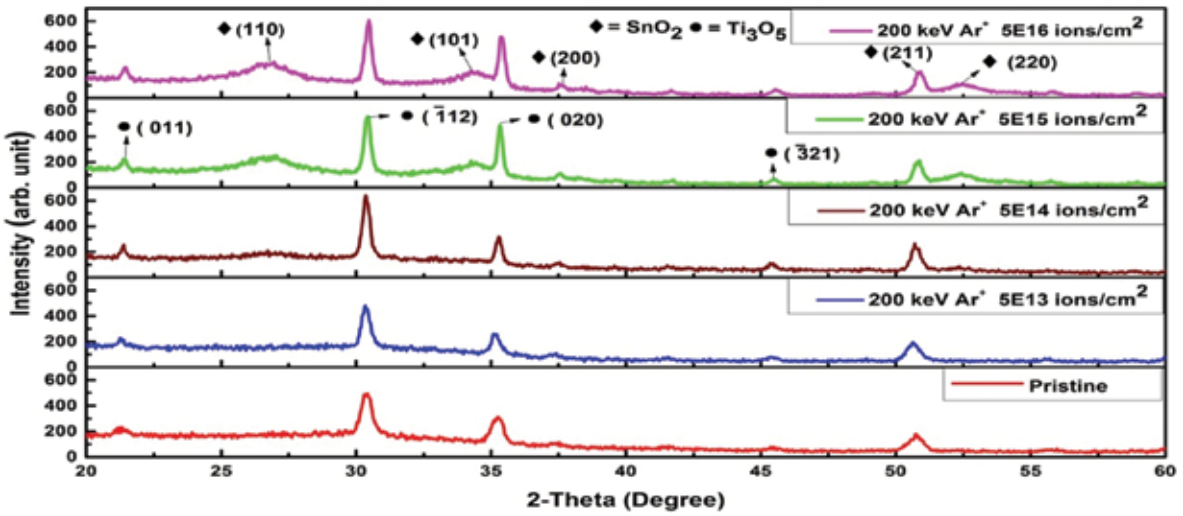

Fig. 5.2.37: GAXRD plot of Pristine and 200 keV Ar^+ ions irradiated SnO_2-TiO_2 nanocomposite thin films with varying fluence of 5×10^{13} ions/cm2, 5×10^{14} ions/cm^2, 5×10^{15} ions/cm^2 and 5×10^{16} ions/cm^2.

REFERENCES

[1] M. Toulemonde, C. Dufour, and E. Paumier, Phys. Rev. B. 46 (1992) 14362.
[2] R. Sivakumar et al., J. Appl. Phys. 101 (2007) 034913.
[3] M. K. Jaiswal et al.,Appl. Surf. Sci. 332 (2015) 726.
[4] S. Rani et al.,Nucl. Instrum. Methods Phys. Res., Sect. B. 266 (2008) 1987.
[5] S.-H. Hong and S. Äsbrink, Acta Crystallogr., Sect. B: Struct. Sci.38 (1982) 2570.

5.3 RADIATION BIOLOGY

5.3.1 Radiosensitization of Human Cancer Cells Using G-Quadruplex Ligands

S. Ghosh[1], A. Sarma[2] and U.Ghosh[1]

[1]University of Kalyani, Kalyani, Nadia, West Bengal,
[2]Inter-University Accelerator Center, New Delhi.

DNA G-quadruplexes are tertiary DNA structures that are formed by Hoogsteen base pairing between four Guanine residues[1]. They are prevalent in G rich region of human DNA like telomere and promoter region of some oncogenes[2] [3]. G- quadruplex ligands are small molecules that can bind and stabilises this G-quartret structure[4] [5]. So they can produce DNA damages and can inhibit synthesis of some oncoproteins. Now a day's DNA G- quadruplexes become potential target for cancer drugs and many G- quadruplex ligands are now under clinical trial[6]. On the other hand Carbon ion beam has several advantages over conventional ionising radiation in cancer treatmen[7]. Here we tried to radio sensitise human lung cancer cell A549 with a well known G-quadruplex ligand Pyridostatin (PDS).

Methods and Materials:

- **Cell culture:** A549 cells were obtained from NCCS, Pune. They were cultured in DMEM supplemented with 10% FBS in presence of 5% CO_2 under humified condition. Pyridostatin was procured from Sigma. The main stock was prepared in DMSO and sub stocks were made in DMEM. We used 2µM concentration of PDS.
- **Irradiation:** Carbon ion irradiation was given at IUAC, New Delhi, in 15UD Pelletron using 85 MeV energy C^{12} ion. The dose in Gray was calculated from the particle fluence using the following relation: Dose [Gray] = 1.6 x 10^{-9} x LET [keV/µm] x Fluence [particles/cm^2][8].
- **Cell Survival:** About 105 A549 cells were seeded in 35 mm petri plate for overnight. Then cells were treated with pyridostatin (G-quadruplex ligand) 2 h before C12 ion exposure and allowed to grow further 24 h in presence of pyridostatin after C^{12} ion exposure. Then cells were trypsinised and seeded in triplicate in 60 mm petri plate and allowed to grow till discrete colony is formed. Then the cells were washed with PBS and then stained with crystal violate. Survival curve was drawn after colony count as per our earlier report[9].

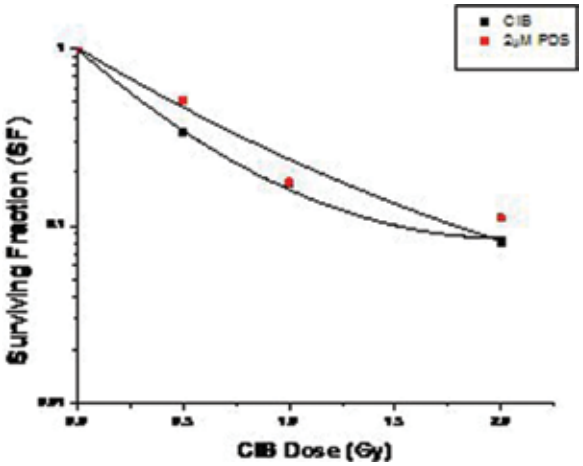

Fig. 5.3.1: Cell survival assay of A549 cells exposed with C^{12} ion with and without PDS

- **DNA breaks measurement by γH2AX using immunofluorescence:** γH2AX is a potential DNA Double strand Break (DSB) marker. We detected γH2AX foci by immunofluorescence method followig standard protocol[10].

We checked the cell survival of A549 cells in presence and absence of 2µM PDS. We found PDS alone can kill A549 cells (almost 55%). When PDS treatment was combined with CIB dose we observed a dose dependent decrease in cell survivality (Fig.5.3.1).

- **Measurement of DNA breaks by immunofluorescence:**

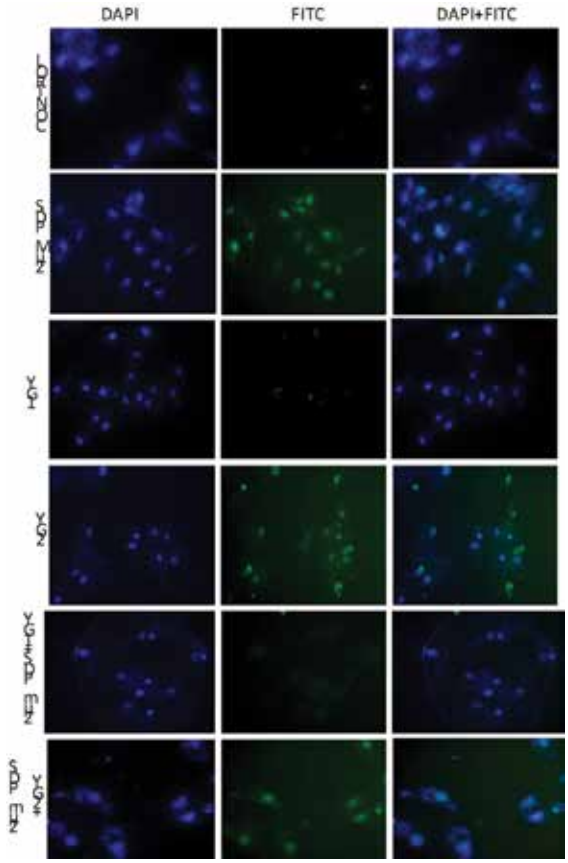

Fig. 5.3.2: Immunofluorescence of γH2AX foci in A549 cells treated with PDS and C^{12} ion

We observed DNA breaks after treatment with PDS and CIB alone or in combination by immunofluorescence and a typical picture was shown in Fig 2. The left column showed nucleus of the cells stained with DAPI (Blue) and the γH2AX foci were detected by FITC (Green) in the middle column. The right column showed the merged pictures of left and middle column. We counted number of γH2AX foci positive cells (at least one foci per cell) and then plotted as shown in Fig 3. We observed more number of γH2AX foci positive cells in CIB exposed cells than PDS treated cell. Also we found 1Gy CIB with PDS treatment can produce as much as DNA double strand breaks as 2Gy CIB dose. So we can predict that CIB in combination with DNA damaging drug can reduce the risk of high dose of CIB. However this is a preliminary result. We need to do further experiments to establish the hypothesis.

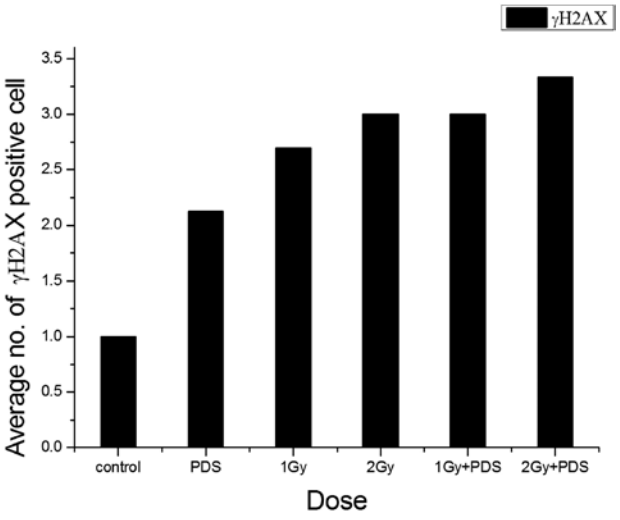

Fig. 5.3.3: Plot of average number of γH2AX foci positive cells with respect to C^{12} in presence or absence of PDS.

REFERENCES:

[1] D. Rhodes and H. J. Lipps, "SURVEY AND SUMMARY G-quadruplexes and their regulatory roles in biology," *Nucleic Acids Res.,* 2015.

[2] D. J. Patel, A. T. Phan, and V. Kuryavyi, "Human telomere, oncogenic promoter and 5'-UTR G-quadruplexes: diverse higher order DNA and RNA targets for cancer therapeutics.," *Nucleic Acids Res.*, vol. 35, no. 22, pp. 7429–55, Nov. 2007.

[3] J. L. Huppert and S. Balasubramanian, "G-quadruplexes in promoters throughout the human genome," *Nucleic Acids Res.*, vol. 35, no. 2, pp. 406–413, Jan. 2007.

[4] J. Cuesta, M. A. Read, and S. Neidle, "The design of G-quadruplex ligands as telomerase inhibitors.," *Mini Rev. Med. Chem.,* vol. 3, no. 1, pp. 11–21, Feb. 2003.

[5] S. L. Cree and M. A. Kennedy, "Relevance of G-quadruplex structures to pharmacogenetics.," *Front. Pharmacol.,* vol. 5, p. 160, 2014.

[6] S. L. Cree, M. A. Kennedy, M. R. Luizon, and C. Ross, "Relevance of G-quadruplex structures to pharmacogenetics," 2014.

[7] C. D. Schlaff, A. Krauze, A. Belard, J. J. O'Connell, and K. A. Camphausen, "Bringing the heavy: carbon ion therapy in the radiobiological and clinical context," *Radiat. Oncol.,* vol. 9, no. 1, p. 88, 2014.

[8] A. Ghorai, A. Sarma, N. P. Bhattacharyya, and U. Ghosh, "Carbon ion beam triggers both caspase-dependent and caspase-independent pathway of apoptosis in HeLa and status of PARP-1 controls intensity of apoptosis," *Apoptosis,* vol. 20, no. 4, pp. 562–580, Apr. 2015.

[9] A. Ghorai, N. P. Bhattacharyya, A. Sarma, and U. Ghosh, "Radiosensitivity and Induction of Apoptosis by High LET Carbon Ion Beam and Low LET Gamma Radiation: A Comparative Study," *Scientifica (Cairo)*., vol. 2014, pp. 1–10, 2014.

[10] R. Sadhukhan, P. Chowdhury, S. Ghosh, and U. Ghosh, "Expression of Telomere-Associated Proteins is Interdependent to Stabilize Native Telomere Structure and Telomere Dysfunction by G-Quadruplex Ligand Causes TERRA Upregulation," *Cell Biochem. Biophys.*

5.3.2 High Let Radiation Induced Effects on Signaling Pathways in Human Prostate Cancer Cell Line

Pallavi Srivastava[*], Chandra Mohini Chaturvedi[*] and Asitikantha Sarma[#]

[*]Department of Zoology, Banaras Hindu University, Varanasi
[#]Radiation Biology Lab, Inter-University Accelerator Centre, New Delhi

Radiotherapy is one of the most important modality for the treatment of cancer. High LET ^{12}C-ion beam offers advantageous activity over the conventional radiotherapy because it has different spatial pattern of energy depositionratio [1,2]. Use of radiomodulator may help to avoid recurrence of cancer and high cost for high LET ^{12}C-ion beam radiotherapy.

On the basis of our previous study[3], we want to assure the effect of PNKPi (PNKP inhibitor) on prostate cancer PC-3 cells after 48 hrs. of irradiation.

1) After 48 hrs. of carbon ion radiation combined with PNKPi the apperance of PC-3 cells has changed (Figure 5.3.4). Cell proliferation data showed that viabilty of cells in 2Gy, 2Gy+PNKPi, 4Gy and 4Gy+PNKPi group as compared to control. Further reduction was noted in the 2Gy+PNKPi and 4Gy+PNKPi groups when compared to irradiated cell groups i.e. 2Gy and 4Gy respectively (Figure 5.3.5).

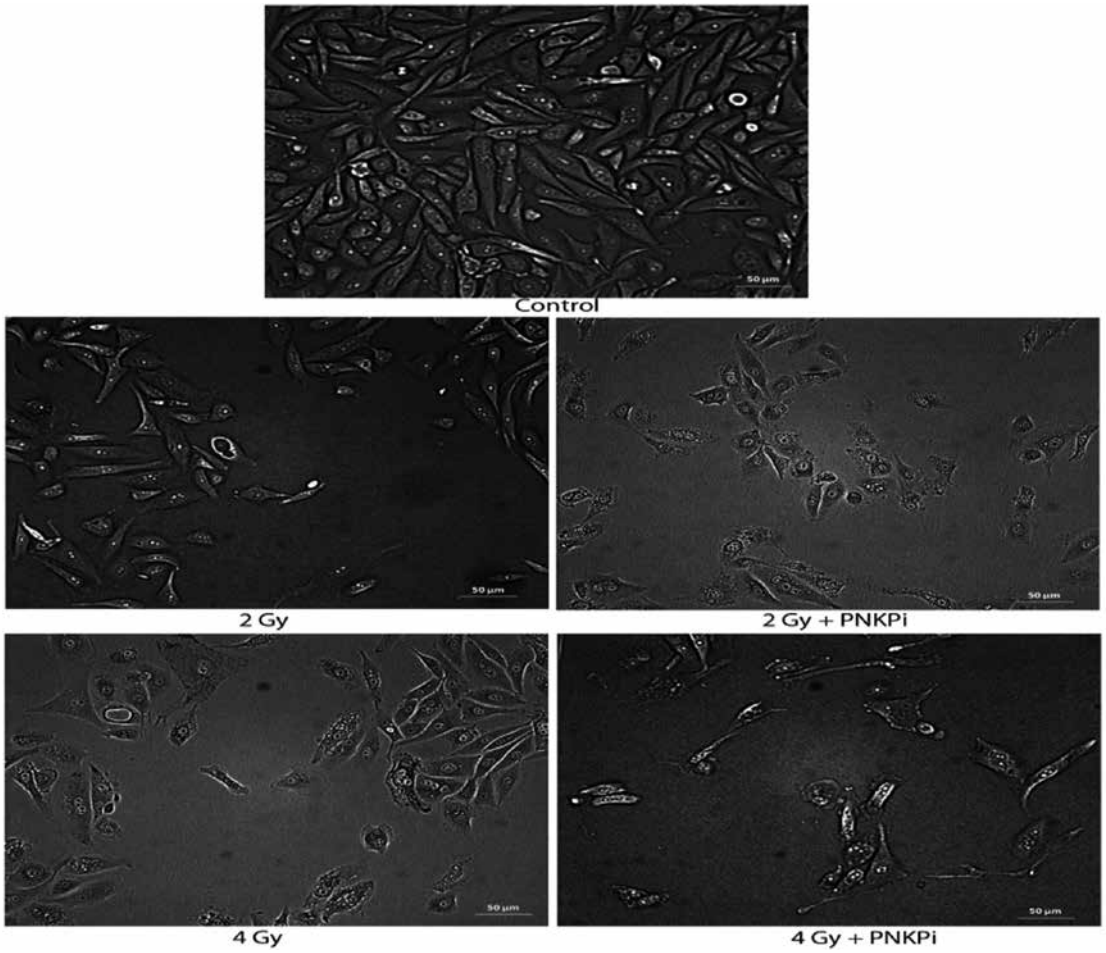

Fig.5.3.4: Morphologicalchanges of PC-3 cells with and without PNKPi (A12B4C3) treatment after 48 hrs. of 2 Gy and 4 Gy ^{12}C-ion beam exposure.

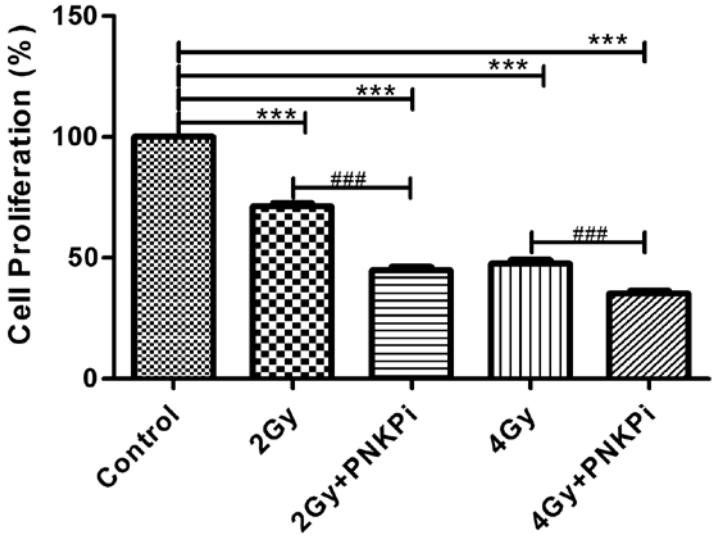

Fig. 5.3.5: Cell proliferation (%) of PC-3 cells after 48 hrs. of radiation when ^{12}C beam is combined with PNKPi. $^{***}p<0.001$, significance of difference from control and $^{###}p<0.001$, significance of difference from respective irradiated group.

2) After 48 hrs. of irradiation we found enhancement in number of apoptotic bodies in 2Gy, 2Gy+PNKPi, 4Gy and 4Gy+PNKPi groups as compared to control. Further, there was significantly higher numbers of apoptotic bodies in 2Gy+PNKPi, 4Gy+PNKPi compared to only irridiated cells (Figure 5.3.6).

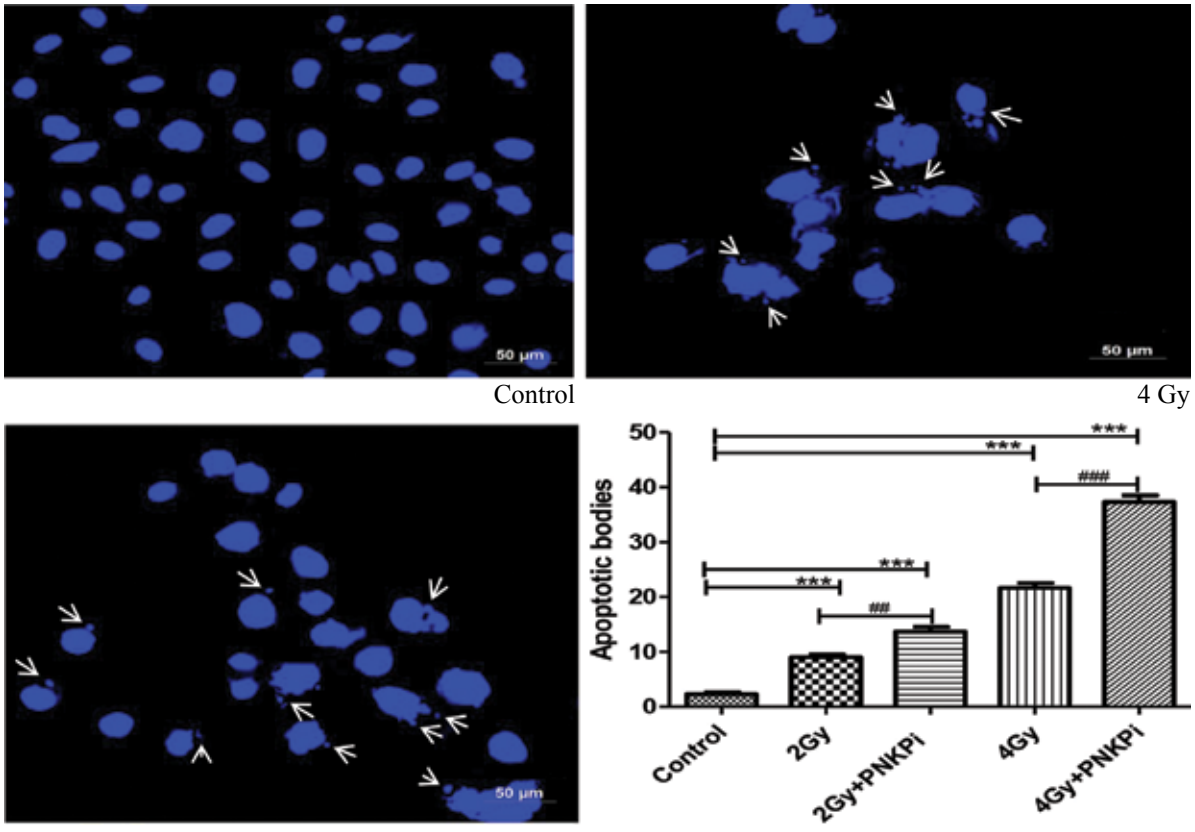

Fig. 5.3.6: Apoptotic body formation in PC-3 cells (shown by arrow) after 48 hrs. of ^{12}C beam in the absence and presence of PNKPi. Bar diagram illustrating number of apoptotic bodies.$^{***}p<0.001$, significance of difference from control and $^{##}p<0.01$, $^{###}p<0.001$, significance of difference compare to the respected irradiated group.

3) Prostate cancer cells (PC-3) showed a significant cell cycle at S phase after 48 hrs. of carbon ion irradiation in the presence of PNKPi compared to control cells while compare to only irradiated group (2Gy and 4Gy) 2Gy+PNKPi and 4Gy+PNKPi showed enhancement at S phase arrest.

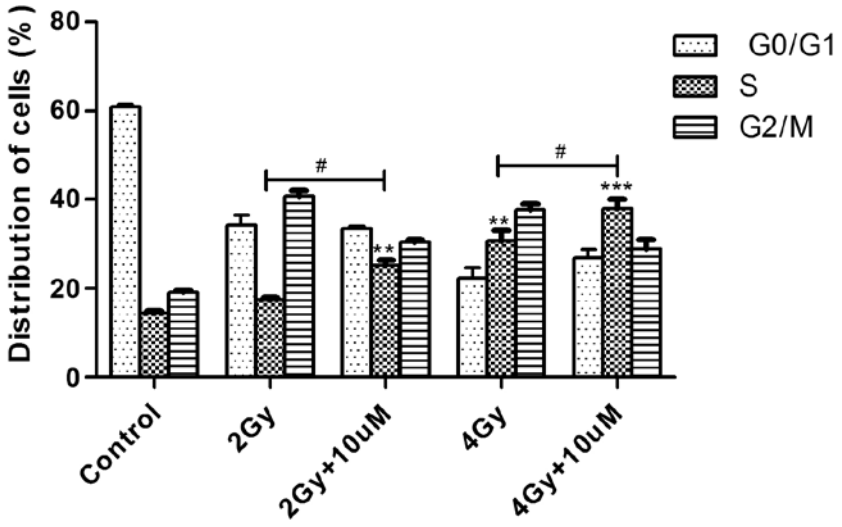

Fig. 5.3.7: FACS analysis showing distribution of cells % (cell cycle arrest at different phases) after 48 hrs. of radiation. $^{**}p<0.01$; $^{***}p<0.001$, significance of difference from S phase of control and $^{\#}p<0.05$ significance of difference from S phase of respective irradiated group.

From the above results we can conclude that PNKPi (A12B4C3) is effective after 48 hrs. of irradiation and can be used for preclinical studies.However, further time dependent studies are required to confirm the combined role of ^{12}C ion beam and PNKPi (A12B4C3) to understand the extent of radiosensitivity with the advent of time.

REFERENCES:

[1] Fukumura. A. Tsujii. H. Kamada. T.et al. Carbon-ion radiotherapy: clinical aspects and related dosimetry, Radiat. Prot Dosimetry(2009) 137
[2] Siegel. R. Naishadham. D and Jemal. A. Cancer statistics. CA Cancer J Clin. (2012) 62
[3] Srivastava. P. Sarma. A and Chaturvedi CM. Targeting DNA repair with PNKP inhibition sensitizes radioresistant prostate cancer cells to high LET radiation. Plos One (2018) 13
[4] Kramer. M.andScholz, M. Rapid calculation of biological effects in ion radiotherapy,Phys Med Biol.(2006) 51

5.3.3 Investigation of DNA Repair Pathways and Cross Talk Between Parp-1 and P53 after Carbon Ion Beam Irradiation in Cultured Human Cells

Priyanka Chowdhury[1], Asitikantha Sarma[2] and Utpal Ghosh[1]

[1]Department of Biochemistry & Biophysics, University of Kalyani, Kalyani 741235, WB, India
[2]Inter-University Accelerator Center (IUAC), Aruna Asaf Ali Marg, New Delhi 110067, India

High linear energy transfer (LET) carbon ion beam (CIB) is becoming one of the promising tool for killing tumors, especially radio-resistant tumors or deep seated tumors. It has been found to be more effective than gamma or X rays, because charged particles especially carbon ion beam deposits its maximum energy near the end of Bragg's peak, thereby keeping normal healthy cells at the entry point of the beam less affected. CIB has been found to be more effective than gamma radiation in producing DNA break and consequently cell death by apoptosis (Takahashi et. al. 1998, scientifica & apoptpsis). DNA double stranded breaks (DSBs) are produced when cells are irradiated by high LET CIB. These DSBs are more deleterious than single strand breaks (SSBs) if they remain unrepaired. Basically, there are two double stranded break repair pathways in mammalian system namely classical non-homologous end-joining (C-NHEJ) and homologous recombination (HR) (Grabarz et. al. 2012, Lieber et. al. 2006). In C-NHEJ pathway, Ku70/80 heterodimer plays a crucial role by binding to the site of DSBs and thereby initiating repair process. There are several others essential proteins involved in C-NHEJ pathway which are activated and recruited to the breaking ends such as DNA-dependent protein kinase catalytic subunit (DNA-PKcs), XRCC4, XLF and ligase IV (Hefferin et. al. 2005). HR pathway is recruited by MRN (comprised of MRE11, Rad50 & NBS1) complex, along with the help of other essential proteins like CtIP, Exonuclease 1 (EXO1), nuclease/helicase DNA2, Rad51, Rad52, BRCA1 (Mimitou et. al. 2009, Czornak et. al. 2008). There is another DSBs repair pathway, known as called back-up NHEJ (B-NHEJ) or alternative end-joining (Alt-EJ) where ligase III, ligase I, XRCC1 and PARP-1 are involved (Audebert et. al. 2004).

In addition, carbon ion beam has been also used to effectively suppress the metastatic potential of cancer cells. Ogata et. al. 2005, have shown that CIB suppresses the potential of invasion, migration and adhesion to ECM in Fibrosarcoma cells. However, how this metastatic potential is being inhibited, what are the genes and proteins

involved whose functions are altered in this suppression is still not clear. Here, we are taking an approach to study the mechanism underlying this metastatic suppression by treating cells with CIB in combination with PARP1 inhibitor.

Methods:

1. **RNA extraction and Q RT-PCR:** Total RNA was isolated from cells irradiated with CIB with or without PARP-1 inhibitor using TRIzol Reagent (Invitrogen; life technologies) following standard protocol. The RNA was treated with RNase free DNase (Sigma) for 1hr at 37°C to avoid the DNA contamination. cDNA was prepared from 1µg of RNA from all samples using M-MLV reverse transcriptase (NEB) and random hexamer (NEB). The quantitative PCR analysis was done on StepOnePlus™ Real-Time PCR System (Applied Biosystem; Life Technologies). Expression of MMP2 and MMP9 were done using SYBR green (Invitrogen).

2. **Western blot:** Western blot was done following the protocol of Ghorai et. al. 2016 (23). Expression of, Akt Antibody (9272S, 1:1500), Phospho-Akt (Ser473) (12694S, 1:1500), NF-κB p65 (8242T, 1:1500), Phospho-NF-κB p65 (Ser536) (3033T, 1:1500), p44/42 MAPK (Erk1/2) (4695T, 1:1500), Phospho-p44/42 MAPK (Erk1/2) (Thr202/Tyr204) (9106S, 1:1500), EGF Receptor (4267T, 1:1500), Phospho-EGF Receptor (Tyr1068) (2236S, 1:1500), p38 MAPK (8690T, 1:1500), Phospho-p38 MAPK (Thr180/Tyr182) (9216S, 1:1500) were studied. The secondary antibodies used are - goat anti-rabbit (sc-2004, 1:7000) and goat anti-mouse (sc-2060, 1:5000) was HRP conjugated.

Results:

1. **Expression of MMP-2 and MMP-9 genes:**

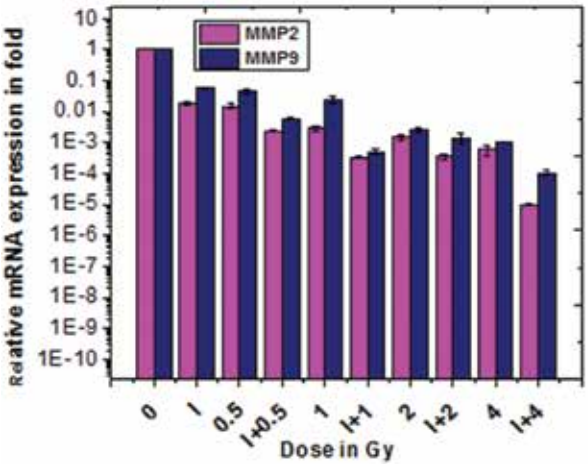

Fig. 5.3.8: Expression of the MMP2 and MMP9 genes were studied after cells were irradiated with or without PARP-1 inhibitor.

2. **Expression and phosphorylation status of the proteins involved in the upstream signaling pathway in the transcriptional regulation of MMP-2,-9:**

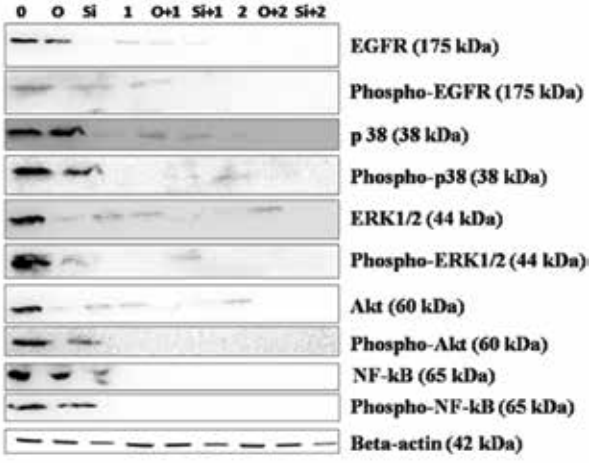

Fig. 5.3.9: Expression and phosphorylation status of the proteins involved in the upstream signaling pathway in the transcriptional regulation of MMP-2,-9. The expression of EGFR, p38, ERK1/2, Akt, NF-kB and their phosphorylated form were studied by western blot 24 h post C^{12} exposure with and without olaparib (O) or siRNA against PARP-1. Lane '0' means control; 'O' means 1 µM of olaparib; 'si' means PARP-1 knockdown cells; 1, 2 represents dose of C^{12} in Gy; C^{12} combined with olaparib or siRNA are denoted here as O+1 or si+1 respectively.

5.4 ACCELERATOR MASS SPECTROMETRY

5.4.1 Understanding the chronology of events associated with the Saraswati river system in Haryana

A. R. Chaudhri[1], Sundeep Chopra[2], Pankaj Kumar[2] and Rajveer Sharma[2]

[1]Centre of Excellence for Research on the Saraswati River, Kurukshetra University, Kurukshetra 136119, India
[2]Inter-University Accelerator Centre, Aruna Asaf Ali Marg, New Delhi 110067, India

The Saraswati river has attracted the attention of a multitude of people working on the history, geography, geology, anthropology, archaeology, indology and culture of the oriental world. The credentials of this river system are debated and both the believers and the non-believers have apparently strong beliefs and notions about this river system. The primal source of information about Saraswati River is the *Rig Veda.* The Centre of Excellence for Research on the Saraswati River set up in Kurukshetra University, funded by the Haryana Govt., endeavors to generate geo-scientific information about this river system in the Himalayan foothills in Himachal Pradesh and in the alluvial plains in Haryana, Punjab and Rajasthan. The results obtained would be examined in conjunction with fresh geological interpretation of the available indological literature and spatial location and characteristics of archaeological findings, which supports the presence of a mega paleo-river system in northern India.

Thirteen samples from different districts in Haryana were analyzed for AMS based C 14 dating in IUAC, New Delhi. The sample preparation methodology involved transferring each sample into a centrifuge tube for pretreatment using an ABA (acid-base-acid) protocol. Sediment samples were treated with 1 N HCl and placed over a shaker for about 3 hrs at 60 °C and 750 rpm to remove carbonates. The acid treated samples were neutralized by repeatedly washing these with 18.2 MΩ ultrapure water. Subsequently, the same sample treatment procedure was repeated with 0.5 N NaOH and 1 N HCl to remove humic acids and absorbed CO_2. These samples were then freeze-dried overnight to remove water. Each treated sample was packed in a tin capsule for graphitization using the Ion Plus automated graphitization equipment (AGE). For graphitization, samples were placed in an auto-sampler of the elemental analyzer (EA) and combusted at 900 °C in the presence of O_2. The purified CO_2 from this combustion was then transferred to a glass tube, where it reacted with H_2 gas and was reduced into graphite powder in the presence of Fe as a catalyst. Subsequently, graphite from each specimen was pressed into cathode capsules of the ion source of AMS for radiocarbon measurements.

The C 14 dates reveal the Quaternary constraints for this river system which are being analysed in conjunction with other dating methodologies for arenaceous carbon free sediments from the river bed and archaeological as well as indological information.

5.4.2 Paleoclimatic reconstruction from lake sediments along Odisha coast

Chinmay Dash[1], Pitambar Pati[1], Pankaj Kumar[2], S. Chopra[2] and S. P. Dhal[2]

[1]Indian Institute of Technology Roorkee, Roorkee, Uttarakhand 247667, India
[2]Inter-University Accelerator Center, Aruna Asaf Ali Marg, New Delhi 110067, India

Two sediment cores were collected from Odisha coast to study late Quaternary paleoclimatic changes (Fig. 5.4.1). The Chilka Lake core was of 2.3 m and the Anshupa Lake core was of 1.3 m. The core sediments were sub-sampled and AMS ^{14}C dated at IUAC for chronological data. The samples were pretreated with Acid-Base-Acid method, graphitized and measured for obtaining isotopic ratios of carbon ($^{14}C/^{12}C$ and $^{14}C/^{13}C$) to calculate the age. The upper age of the Chilka Lake core sample was around 9 Ka and that of the Anshupa Lake was 1400 AD. The climatic proxies like sediment geochemistry, mineral magnetism and stable isotope studies have been applied to infer the past climatic records. The Chilka Lake receives its sediments from the Eastern Ghat metamorphic rocks, whereas the Anshupa Lake receives its sediments from the sandstones of Athgarh formation. Hence, a comparison of weathering rates from catchments of two lakes will provide a comparative analysis of weathering rates between metamorphic and sedimentary rocks in a same climatic region. The study will provide wider scope for high resolution paleoclimatic study from medieval times to Early Holocene period. Since the interpretation part is in progress only an outline of the research work has been documented here.

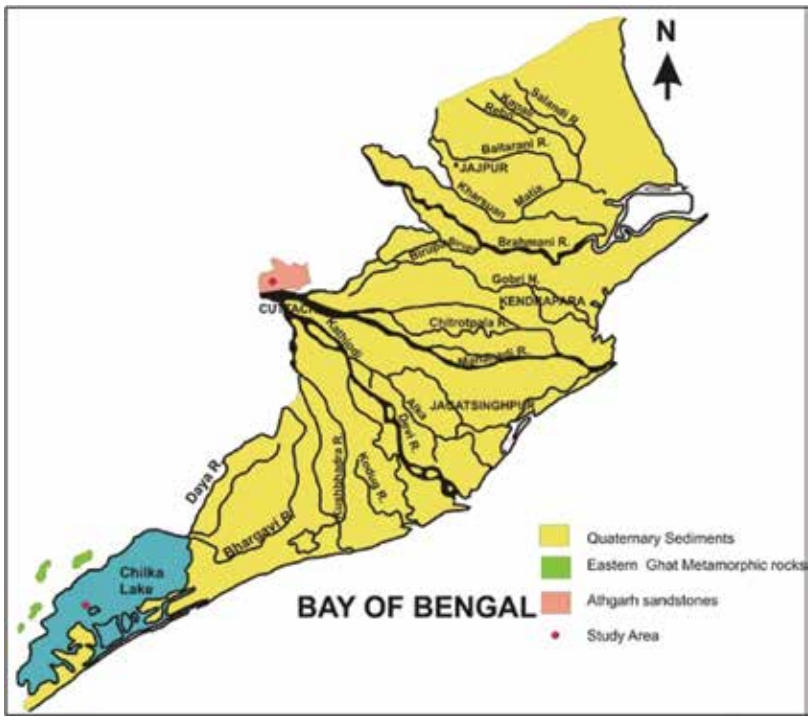

Fig. 5.4.1: Map showing study area and sample locations.

5.4.3 Carbon dynamics in the Ganga basin: implications to the sources, processes and carbon reservoirs

Chinmaya Maharana[1], Pankaj Kumar[1], Rajveer Sharma[1], Sunil Ojha[1], S. Gargari[1], Sundeep Chopra[1], S. Balakrishnan[2] and J. K. Tripathi[3]

[1]Inter-University Accelerator Center, Aruna Asaf Ali Marg, New Delhi 110067, India
[2]Department of Earth Sciences, Pondicherry University, Kalapet, Puducherry 605014, India
[3]School of Environmental Sciences, Jawaharlal Nehru University, New Delhi 110067

The objectives of the present study are (i) to elucidate the sources and processes controlling occurrence, distribution and fate of carbon in the Ganga basin and (ii) to determine the $\Delta^{14}C$ value and ^{14}C age (C-14 dating) of particulate organic carbon (POC) to elucidate the sources and age of the organic carbon reservoirs in the Ganga basin.

Field work was carried out to collect sediment samples from the Ganga River including its tributaries from the Himalaya and Peninsula. Collected sediments were then dried in oven followed by grinding in agate mortar and homogenization. Total particulate carbon (TPC) in the unleached and POC in the leached (with 0.5 M HCl) fractions were measured for the suspended sediment samples by taking few milligrams of sediments in tin capsule and their subsequent analysis by an Elementar carbon analyser at IUAC. Particulate inorganic carbon (PIC) was calculated by the subtraction of POC from TPC. Thereafter, the particulate organic fraction was subjected to graphitization using Automated Graphitisation Equipment (AGE) followed by their measurement for ^{14}C by AMS.

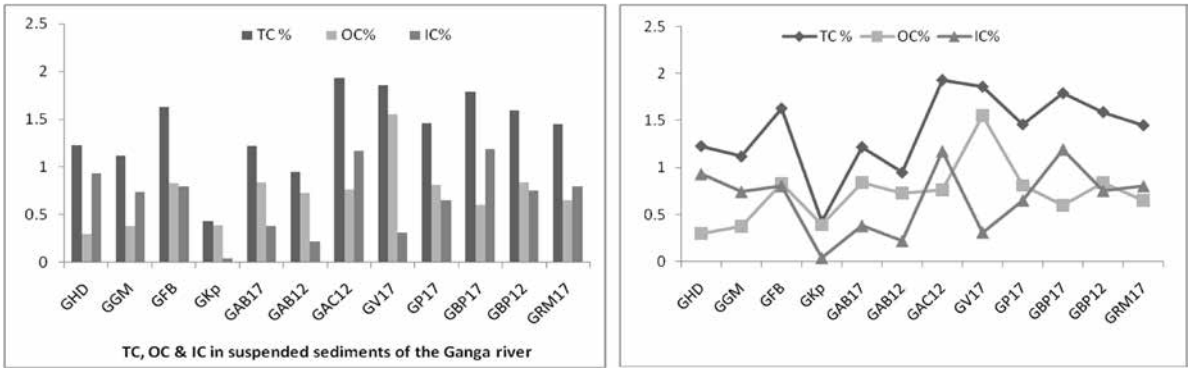

Fig. 5.4.2: Abundance and distribution of Total carbon (TC), Organic carbon (OC) and Inorganic carbon (IC) in the suspended sediments of the Ganga river.

Table 5.4.1. pMC(percent modern carbon) and Libby age for the measured river sediments.

River	pMC value	Libby age
Ganga river	44.965± 0.365 to 80.802± 0.383	6420± 65 to 1712± 38
Himalayan rivers	64.746± 0.367 to 85.119± 0.416	3491± 45 to 1294 ± 39
Peninsular rivers	50.939± 0.248 to 85.939± 0.415	5418 ± 9 to 1217 ± 38

5.4.4 Sedimentology and climatic events of the Gangotri Glacier area, Garhwal Himalaya, India

Dhruv Sen Singh[1], Chetan Anand Dubey[1], Dhirendra Kumar[1], Pankaj Kumar[2] and Rasik Ravindra[3]

[1]Department of Geology, University of Lucknow, Lucknow 226007, India
[2]Inter-University Accelerator Center, Aruna Asaf Ali Marg, New Delhi 110067, India
[3]National Centre for Polar and Ocean Research, Headland Sada, Vasco-da-Gama, Goa 403804, India

Himalaya, one of the most important regions outside the Polar Regions, also known as third pole of the earth, has witnessed several expansion and recession of glaciers during Quaternary period. Such fluctuations in glacier have given rise to diversified geomorphic landforms. Sediments coded in these landforms provide valuable tool in understanding the climate and environment. The human culture and civilization are directly governed mainly by the prevailing environmental climatic conditions. Therefore, understanding of the Quaternary climate is of great significance for sustainable development of the society.

To understand past climate changes it is important to evolve a geochronology of the dateable sequences. In the Gangotri Glacier area, various geomorphic surfaces such as Bhagirathi river valley, kame terraces and outwash plain were selected for analysis. 1 – 2 m deep trenches were made in these surfaces and 20 – 40 samples from each trench were collected at regular intervals. The sediment samples collected from different geomorphic surfaces were dated using AMS facilities at IUAC.

The samples were prepared for analysis by different processes. First of all, samples have been treated through acid-base-acid protocol. In this method the samples were treated with 0.5 M HCl for dissolving the carbonate present in the samples. After this the samples were treated with 0.1 M NaOH for removing the humic acid. This process was repeated several times for cleaning the samples completely. The samples were next put into the freezer and drier overnight for drying. The dry samples were packed in tin boats as per required weight (after ABA treatment) depending upon the percentage of carbon in every sample. The samples were then put in the eliminator for removing carbon dioxide. These samples were further analyzed for the percentage of carbon present in every sample and the dates were obtained. Twenty samples were analyzed at IUAC by two research scholars / project staff in about 20 days. These dates are being used in our upcoming publications [1,2].

REFERENCES

1. Dhruv Sen Singh *et al.,* accepted in Polar Science (https://doi.org/10.1016/j.polar.2018.05.003).
2. Dhruv Sen Singh *et al.,* communicated to Quaternary International.

5.4.5 Late Quaternary paleoclimate reconstruction of monsoonal India using lake sediment cores

Hema Achyuthan[1], Rayees A. Shah[1], Asif Mohmad Lone[1], Pankaj Kumar[2] and S. Chopra[2]

[1]Institute for Ocean Management, Anna University, Chennai 600025, India
[2]Inter-University Accelerator Centre, Aruna Asaf Ali Marg, New Delhi 110067, India

The Indian subcontinent is one of the largest monsoon-dominated regions of the world, and the climate is controlled primarily by the southwest monsoon (SWM). The term 'monsoon' refers to seasonal moisture-rich winds, and it is a unique climatic factor that differentiates south Asian countries – particularly India and parts of Asia, Australia and Africa – from the rest of the world. The Indian subcontinent is predominantly affected by the changes in these winds, which have a southerly and a westerly component. Combined together, they constitute the SWM. However, the amount and intensity of the monsoonal rains have fluctuated since the late Quaternary period. During the last two decades, scientific interest in the reconstruction of the Asian monsoon variations, particularly the SWM, since the late Quaternary to Holocene period has increased significantly. In particular, in the Indian subcontinent, many types of natural archives such as lake and marine sediment cores, palynology, tree rings and corals have been used to restructure late Quaternary–Holocene palaeoclimatic.

Sediment deposited in a closed system acts as major sinks for organic carbon. Therefore, sediment cores from such sites in the area affected by the SWM can provide a continuous, high resolution of paleoenvironmental record of the evolution of the SWM. In the Asian region, palaeoclimate records based on lake sediments indicate that both southwest summer and northeast winter rains were stronger in the early-Holocene period (10,000–7000 yr BP) than today, resulting in a wetter and cooler climate over the Asian continent. Warming started around 8000 yr BP, and the Holocene Megathermal Maximum (HMM) that occurred between 7200 and 6000 yr BP observed change particularly in vegetation zones, increase in temperatures, precipitation and sea-level fluctuations.

The main objectives of this study are to reconstruct the Holocene palaeomonsoon and palaeoenvironmental shifts using the Lake sediments throughout India. ^{14}C dating on sixty charcoal and samples of sediment cores, retrieved from various lakes throughout India, was performed at IUAC. The data generated by analysis yielded promising results and are being published in journals.

5.4.6 Paleoseismic and paleotsunami investigations in Andaman and Nicobar Islands and Himalaya

Javed N. Malik[1], Frango C. Johnson[1], Afzal Khan[1], Santiswarup Sahoo[1], Shreya Arora[1], Pankaj Kumar[2], Sundeep Chopra[2] and Debajyoti Paul[1]

[1]Department of Earth Sciences, Indian Institute of Technology Kanpur, Uttar Pradesh 208016, India
[2]Inter-University Accelerator Centre, Aruna Asaf Ali Marg, New Delhi 110067, India

Andaman and Nicobar Islands: In order to develop the chronology of the paleotsunamis and earthquakes, we have dated 20 samples (charcoal, peat, buried wood) by using ^{14}C-AMS at IUAC. The results were used to decipher eight paleotsunami events including 2004 Indian Ocean Tsunami. The Event I (Unit-b) occurred during AD 1996-2007 correlated to 2004 Sumatra-Andaman earthquake (Mw9.3) and tsunami (4 m run-up) with a land subsidence (~1 m) in the south Andaman (Fig. 5.4.3). Event II (Unit-d) occurred during AD 1847-1981 correlated with the Car Nicobar earthquake of 1881 (Mw 7.9). This was a local event that took place along Andaman segment. Event III (Unit-g) occurred during AD 1743-1884 correlated with Arakan earthquake of AD 1762 (Mw7.5). Event IV (Unit-j) occurred after AD 1287-1427 and before AD 1743-1884 was a subsidence event corroborated with the reported land subsidence near Port Blair during AD 1679 [6], with a tsunami event around AD 1640-1950 [8]. This event was felt around Arakan (Burma), Bangladesh and Chennai, and adjoining Indian Ocean [4,6]. Event V (Unit-l) that occurred after AD 420-600 and before AD 1280-1450, corresponds to the geological evidence of tsunami reported from Aceh region between AD 1290-1400 [8] and the event reported by Jankaew *et al.,* [5] and Fujino *et al.,* [3] during AD 1300-1450 from Phra Thong, Thailand. This event can also be correlated with the tsunami event reported from the west coast of Andaman Island that occurred around AD 1120–1300 [6]. It has been suggested that this event had a near source along Andaman segment and resulted in a transoceanic tsunami [6]. Event VI (Unit-n) that occurred after BC 325-1780 and before AD 420-600 probably represents an event reported from Thailand that took place during BC 800 [1,5]. Event VII (Unit-p) that occurred after BC 1370-2120 and before BC 350-1780, and the Event VIII (Unit-r) occurred before BC 1376-2123 correlated with historical texts of Sri Lanka [2] and cave deposit of Aceh, Indonesia [9].

Himalaya, India: The key to unravel future seismic activity lies in the better understanding of the fault behavior and how the associated earthquakes have repeated in space and time. Various seismic cycle models have been proposed to understand how stress on the fault plane accumulates, stores for a certain amount of time until the threshold is breached triggering slip on the fault. Of the several models, characteristic slip model which explains the slip-predictable behavior of the fault and the time predictable model which describes the time based repeatability of the earthquakes are widely known [10,11].

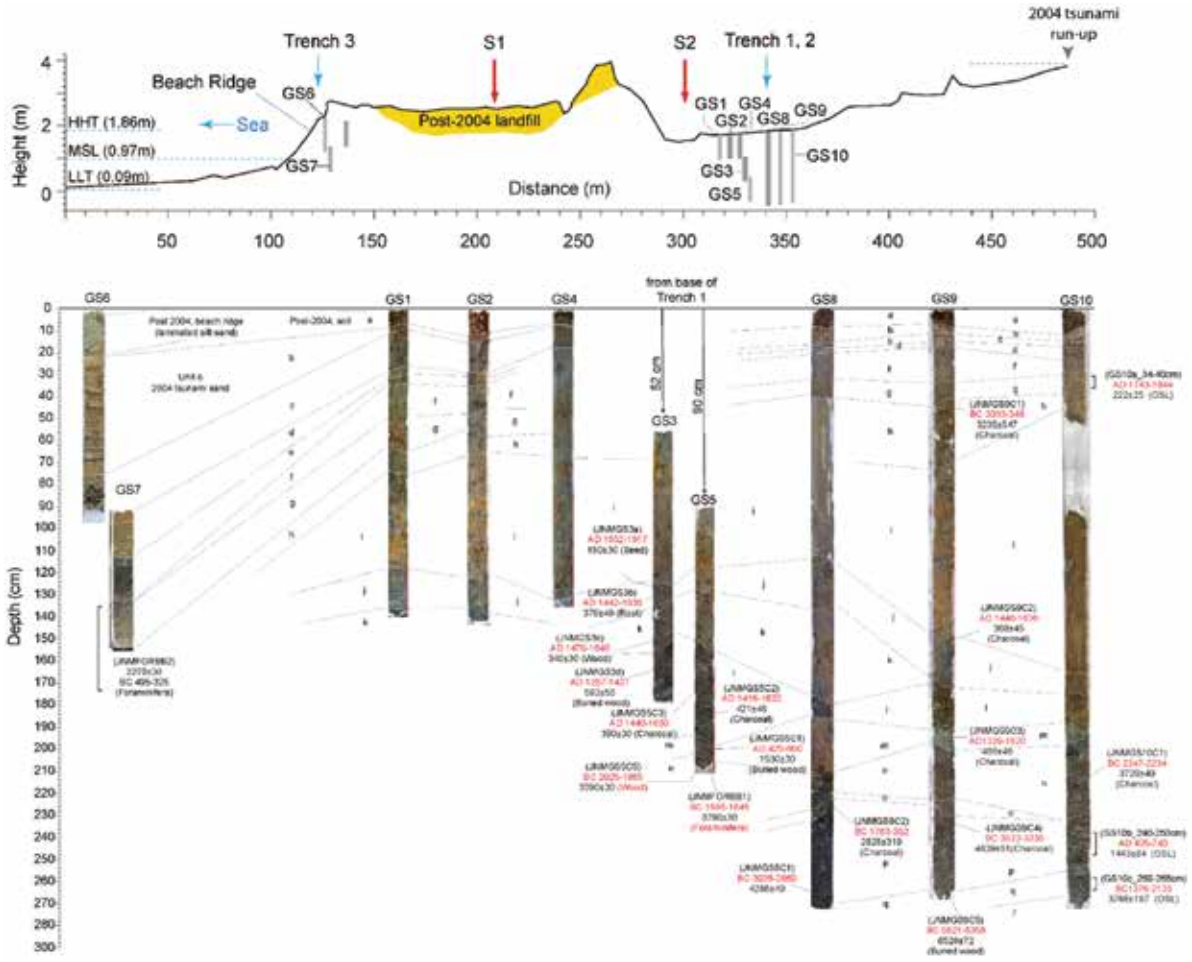

Fig. 5.4.3: A topographic profile along NWW-SSE transect across south coast of Andaman Island at Site-1: Badabalu. Location of trenches excavated and geoslice section collected are shown along the profile. The area is marked by beach-ridge swale beach- ridge topography. Stratigraphic data is based on the exposed sediment succession from 10 geoslices (GS1-GS10). GS3 and GS5 were collected from the base of the T1-trench and GS7 from T3-trench. Geoslices shows total 18 litho-units (Unit a - youngest and Unit r - oldest). The sections are placed with respect to horizontal scale. Vertical scale represents depth from the surface.

However, it has been difficult to verify both the models due to the long repeat times of the large magnitude earthquake and incompleteness of the past earthquake data especially for the Himalaya. Therefore, the reconstruction of the past earthquakes, determination of the slip rate and the expected magnitude becomes an essential criterion for the assessment of seismic hazard. The paleoseismic investigation is the only technique through which the seismic history along the faults can be determined [7] and it has been applied to the several seismically active faults around the world. Despite surrounded by the seismically active mighty Himalaya in the north, transform boundary to the west and subduction zone in the south not much attention is paid towards the proper seismic hazard assessment of India. The recent Gorkha (Mw 7.8) and Kodari (Mw 7.3) from Nepal was the testament of the awareness of the people and the preparedness of the government towards the seismic hazard. The Himalaya has been assigned under Zone V in the seismic zonation map of India in terms of the severity of ground shaking and the magnitude of the earthquakes. To our surprise, the most of the destructive recent earthquakes i.e., 1905 Kangra earthquake (Mw 7.8), Gorkha earthquake (Mw 7.8) and Muzaffarabad earthquake (Mw 7.6) produced surface deformation along the hinterland faults instead of the HFT.

Barring few paleoseismological investigations most of the work is confined to the Himalayan Frontal Thrust (HFT) and the potential of an earthquake-generation along the hinterland faults has not been realized in the Himalaya. Therefore, we decided to focus our research work along the hinterland faults in the Pinjore Dun which is an intermontane valley between the Siwalik ranges and mark the transition between the changing strike of the Himalaya. We have carried out paleoseismological surveys along the three hinterland active faults in Pinjore Dun i.e., Pinjore Garden Fault (PGF), Jhajra Fault (JF) and Khetpurali Taksal Fault (KTF) with an aim to establish the seismic event chronology, determine coseismic slip and the expected magnitude. To achieve this goal, we have carried out trenching along the identified active faults and extracted the samples either for OSL or AMS dating from the deformed and the un-deformed layers to bracket the seismic event. For our research

work, 20 detrital charcoal samples have been processed and ages have been obtained at IUAC.From the cross-cutting stratigraphy in the trench and the ages obtained, we suggest that northwest Himalaya has hosted at least two-three large magnitude earthquakes between AD 200-1600. But the absence of large magnitude earthquake from this section of Himalaya raises an alarm to the society as well as to the government for the earthquake preparedness. The data generated form our work has direct relevance to the well-being of the society.

REFERENCES

1. E. Alam, D. Dominey-Howes, C. Chagué-Goff and J. Goff, Earth Science Reviews **114,** 175 (2012).
2. K. Dahanayake and N. Kulasena, Marine Geology **254,** 180 (2008)
3. S. Fujino, H. Naruse, D. Matsumoto, T. Jarupongsakul *et al.,* Marine Geology **262,** 25 (2009).
4. R. N. Iyengar, D. Sharma and J. M. Siddiqui, Indian Journal of Historical Sciences **34,** 181 (1999).
5. K. Jankaew, B. F. Atwater, Y. Sawai, M. Choowong *et al.,* Nature **455,** 1228 (2008).
6. J. N. Malik, M. Shishikura, T. Echigo, Y. Ikeda *et al.,* Geology **39,** 559 (2011).
7. J. P. McCalpin (Ed.) Paleoseismology Vol. 95, 2nd Edition (Academic Press, New York, 2012).
8. K. Monecke, W. Finger, D. Klarer, W. Kongko *et al.,* Nature **455,** 1232 (2008).
9. C. M. Rubin, B. P. Horton, K. Sieh, J. E. Pilarczyk *et al.,* Nature Communications **8,** 16019 (2017).
10. D. P. Schwartz and K. J. Coppersmith, J. Geophys. Res. **89,** 5681 (1984).
11. P. Tapponnier *et al.,* Comptes Rendus de l'Academiedes Sciences, Serie IIA **333,** 483 (2001).

5.4.7 ^{14}C dating of organic matter associated with the sediments of the Dilpur Formation, Karewa Group, Kashmir and Lonar Lake

Meenakshi[1], J. P. Shrivastava[1], Pankaj Kumar[2], Rajveer Sharma[2] and Sundeep Chopra[2]

[1]Department of Geology, University of Delhi, Delhi 110007, India
[2]Inter University Accelerator Centre, Aruna Asaf Ali Marg, New Delhi 110067, India

The ^{14}C ages were determined for the samples collected from Shankerpora and Burzahama sections, Dilpur Formation of Karewa Group, Kashmir (Fig. 5.4.4). The samples with higher carbon percentage were selected from Burzahama, while samples from younger profiles were selected from the Shankerpora sections (Fig. 5.4.5).

Conclusions drawn from the ^{14}C dating of Karewa sediments: For refined precision and accuracy, the younger ages from 45-50 ka for Burzahama and Shankerpora loess-palaeosol successions were determined using high resolution AMS radiocarbon dating allied with the Bayesian age-depth modeling. Beyond the radiocarbon age limit, we extrapolated the ages based on sedimentation rate based time estimates. The study revealed the LGM at 18.4 - 22.5 ka. The two glacial periods spanning 67-71 ka and 124-127 ka that alternate with intervening major inter-stadials recognized in the loess-palaeosol succession. The results also revealed that the Bu-S1 to Bu-L1 and SP-S5 to SP-L1 palaeosol layers of Burzahama and Shankerpora sections are coeval, respectively.

Lonar Lake: The ^{14}C dating was carried out for sediment samples from Lonar Lake outer rim.

Pre-treatment, graphitization and AMS measurements of samples from the Lonar: Each sample was powdered, homogenized and examined under the microscope for the presence of roots. Each sample was added with 1N HCl in a 50 ml tarson centrifuge tube and placed over the thermo-shaker for ~3 hours at 60°C and 650 rpm to remove the carbonates. The acid treated sample was neutralized by repeated washing with 18.2 MΩ ultrapure water till the pH approached 7. Then it was freeze dried for 8-10 hours at a temperature of -80 °C. After the sample was completely dried, the sample was weighted and packed in the tin boats for graphitization. The exactly weighted sample was placed in the auto-sampler of the Elementar Analyzer (EA) of automated graphitization equipment (AGE). EA combusted the sample and purified CO_2 was reduced to graphite in the sealed glass tube by reacting with H_2 gas in the presence of catalyst Fe. Each graphitized sample was then pressed in the Al cathode, using a hand-press and placed in the cathode wheel of the Ion source of the AMS system for radiocarbon measurement.

AMS measurements were performed at IUAC using 500 kV Pelletron accelerator. Negative ions were generated in the ion source. As these negative ions enter the accelerator, they are attracted by positive potential at the terminal. The charges for these ions undergo change while moving through a thin carbon foil situated at the terminal. In this stripping stage, molecules also break apart and this step enhances sensitivity of the AMS by removing isobars (molecular isobar for ^{14}C is ^{13}CH and $^{12}CH_2$). These positively charged ions were repelled by positively charged electrostatic accelerator. Finally, after filtering by various electric and magnetic devices, ^{14}C is detected at the end of the system using gas detector while ^{12}C and ^{13}C ions are counted by Faraday cups. The ratio of $^{14}C/^{12}C$ is used for calculating the age of the sample. Interpretation and conclusion are yet to be completed for Lonar Lake samples.

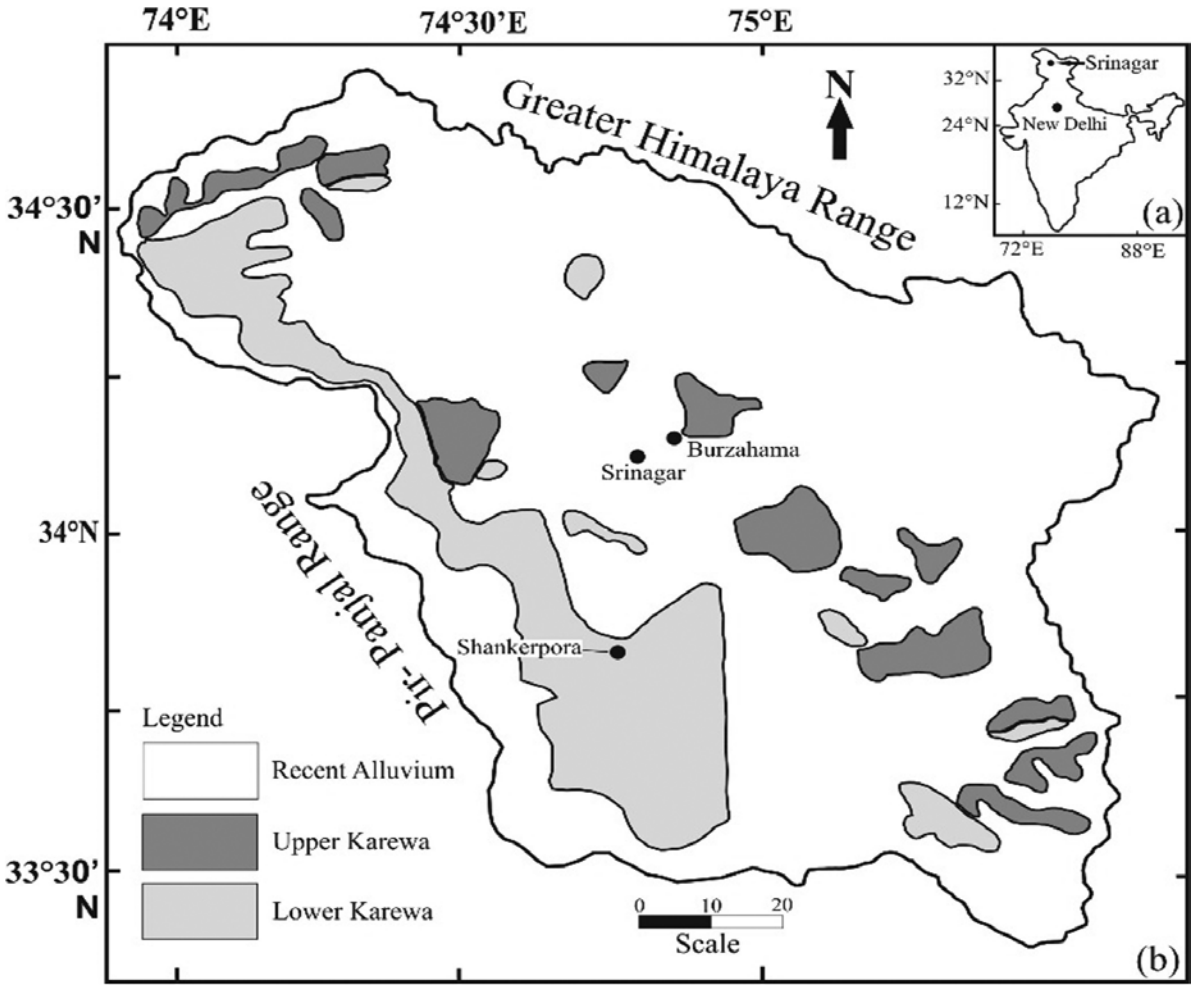

Fig. 5.4.4: Shows (a) location of the study area and (b) geological map of the Kashmir area with sampling sites (as solid circles).

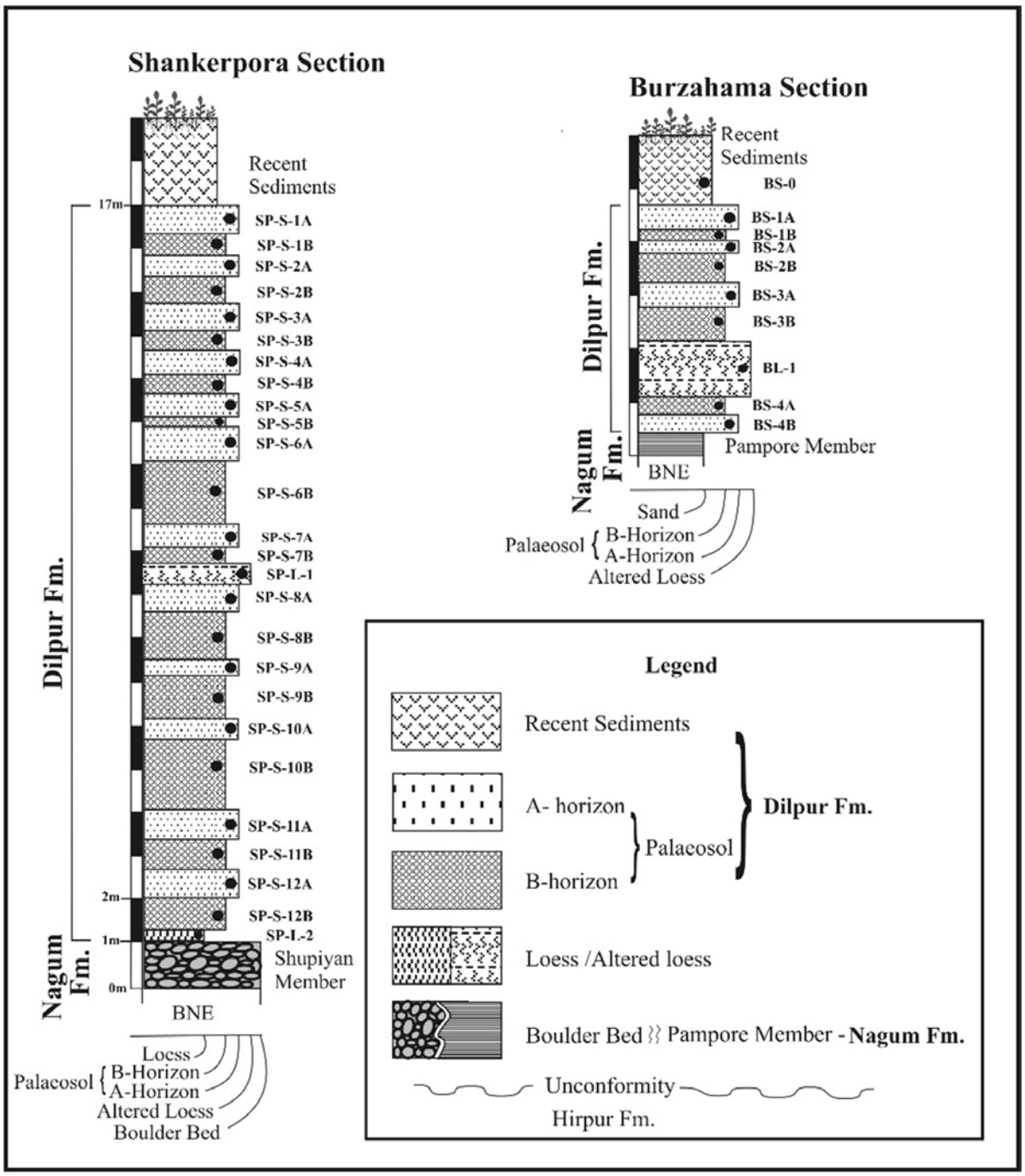

Fig. 5.4.5: Stratigraphic log of Shankerpora and Burzahama sections showing sample locations.

5.4.8 Validation of liquid scintillation spectrometry based Carbon-14 (^{14}C) measurement techniques by AMS and development of reference materials for application in environmental monitoring programmes around nuclear power plants

N. Karunakara[1], Renita Shiny D'Souza[1], S. Rashmi Nayak[1], Bhrath[1], S. Chopra[2], Pankaj Kumar[2] and Rajveer Sharma[2]

[1]Centre for Advanced Research in Environmental Radioactivity, Mangalore University, Mangalagangothri 574199, India
[2]Inter-University Accelerator Center, Aruna Asaf Ali Marg, New Delhi 110067, India

Introduction: Terrestrial plants are the primary indicators of increased ^{14}C levels in the environmental due to airborne release from nuclear power plants (NPPs). Knowledge on the release rates of ^{14}C from nuclear facilities

is essential because of its long half-life, environmental mobility, and ease of assimilation into living matter. ^{14}C is the most significant radionuclide released from a NPP that will contribute significantly to the collective radiation dose to exposed population [1]. The ^{14}C can be easily concentrated in the food chain and studies in aquatic pathways have shown that concentration factors can be as high as upto 5000 for fish and mollusks and upto 2000 for sediments [2]. Although monitoring of ^{14}C releases from NPP is mandatory in developed countries, it is not considered under the routine monitoring programmes of Environmental Survey Laboratories around the NPPs in India. Therefore data on ^{14}C release and its concentration in environmental matrices are not available.

The measurement technique employed by all the radioecology laboratories in India is based on oxidation of the samples using sample oxidizer, collection of evolved $^{14}CO_2$ ina suitable trap and subsequent analysis using a Liquid Scintillation Counter. Although, this method has been adopted by advanced countries for monitoring ^{14}C levels in the environmental matrices around the NPPs, the results obtained from this method is known to have large variability because (i) the method is sample specific (standardization such as oxidation temperature, flow rates of gases, types of traps required etc.), (ii) non- availability of reference materials for validation of the method. The reference materials for ^{14}C, made available by IAEA (matrices such as, oxalic acid, wood, sucrose, etc.), cannot be used with these instruments as the certified values of ^{14}C activity in these reference materials is below the minimum detection levels of the instrument used / method adopted, rendering them un-useful for such applications. Hence, there is a need to develop ^{14}C reference materials, which are specific and representative of environment of NPPs of India, for standardization / validation checks of the methods followed by radio-ecological laboratories in India. Accelerator mass spectrometry (AMS) is considered as the bench mark method for ^{14}C determination in environmental matrices, since this method is capable of providing results with great accuracy [3,4]. In brief, aims and objectives of the present study are:

A. Validation of sample oxidation and Liquid Scintillation Spectrometry (LSC) based measurements through intercomparison with AMS technique and

B. Development of reference materials for ^{14}C using AMS technique.

As mentioned earlier, ^{14}C may be released from a NPP and it can be easily concentrated in the food chain. Extensive studies have been reported on measurements of ^{14}C around the NPP in developed countries. All these studies have a common objective of evaluating the annual release of ^{14}C from the power plant, estimation of excess ^{14}C in the surrounding environmental matrices and resulting radiation dose to the population. While many of these studies are published as annual reports of the NPP others have been published in international journals.

Materials and methods: Vegetation and air samples were collected from the vicinity of Kaiga NPP and also from Mangalore region. The collected samples were processed and combusted in Pyrolyser. The $^{12,14}CO_2$ generated from the sample combustion was trapped in the bubbler containing 10 ml of Carbon trap. The bubbled Carbon trap was mixed with 10 ml of Carbon count scintillator and stored in dark overnight so that the chemi-luminescence was removed. The samples were then counted for ^{14}C activity in LSS. Air samples were collected through bubbling in NaOH solution, processed and counted for ^{14}C activity in LSS. For intercomparison exercise, some of the air and biota samples were analysed by AMS at IUAC.

Results and discussion: A total of 10 vegetation samples and 11 air samples were analyzed using AMS facility of IUAC. These samples were also analysed at CARER, Mangalore University by liquid scintillation method. The sample analysis in AMS was done to validate the results analyzed in Liquid Scintillation Spectrometry (LSC) and also to develop a reference material which is specific and representative of environment of NPPs of India, for standardization / validation checks of the methods followed by radio-ecological laboratories in India. Initial results have indicated that there is scope for improvement / optimization of the oxidation process followed during LSC measurements. These studies are now progressing. This requires analyses of about 25 more samples by AMS.

REFERENCES

1. W. Sohn, D. -W. Kang and W. -S. Kim, J. Nucl. Sci. Technol. **40,** 604 (2003).
2. Management of waste containing tritium and carbon-14, Report IAEA **421,** Vienna (2004).
3. W. Kutschera, Int. J. Mass Spectrom. **349-350,** 203 (2013).
4. T. J. Ognibene, G. Bench and T. A. Brown, Nucl. Instrum. Methods. B **223-224,** 12 (2004).

5.4.9 14C dating of samples from archaeological site at Binjor (4 MSR)

Sanjay Manjul[1], Arvin Manjul[1] and Pankaj Kumar[2]

[1]Institiue of Archaeology, Archaeological Survey of India, Delhi 110006, India
[2]Inter-University Accelerator Centre, Aruna Asaf Ali Marg, New Delhi 110067, India

4 MSR (Binjor) (29°12′872″N; 73°9421″E) is located on the left bank of dried River Ghaggar, about 7 km west of Anupgarh in Sri Ganganagar district of Rajasthan. This site is located around 120 km away from Kalibangan, a Harappan metropolis, and 15 km away from Baror, another Harappan site. The mound is spread over approximately 200m × 200 m with the cultural deposit of more than seven meters (159 m to 151.47 m MSL) above the natural soil. Excavation was carried out in the three field seasons from 2014 to 2017, which brought to light three fold cultural deposits:

I. Pre / early Harappan

II. Transitional phase of early to mature Harappan

III. Mature to late mature Harappan

The site is established as a craftsman's village after the discovery of 250 fireplaces such as hearths and furnaces. As part of post-excavation research twenty-one samples were brought to IUAC for ^{14}C AMS dating as part of a collaborative work. The aim of this collaboration was to establish a chronology of the site; to know the period when the focus of the habitants shifted from hunting gathering to industrial center; to know the gradual changes in the socio-economic lives of the people and to know the time when the site was abandoned.

Twenty-one samples were dated at IUAC and that provided a chronology that fits well with the archaeological data from the excavation. The result of the samples clearly proves that the site was in continuous habitation from 4500 BCE to 1900 BCE. It also suggests that the shift from agriculture to industry happened between 2700 BCE to 2600 BCE and the industrialization reached the zenith at 2400 BCE.

The outcome of the collaboration provided a detailed and clear framework about the activities at the site. This in turn helped us to understand the changes in the society and economy during third millennium BCE.

5.4.10 Radiocarbon dating of historical bricks from Nalanda

Sonia Das[1,3], Pankaj Kumar[2], M. B. Rajani[3] and Sundeep Chopra[2]

[1]The University of Trans-Disciplinary Health Sciences and Technology, Bengaluru 560064, India
[2]Inter-University Accelerator Centre, Aruna Asaf Ali Marg, New Delhi 110067, India
[3]National Institute of Advanced Studies, Bengaluru 560012, India

The study of materials associated with a site forms an important part of archaeology. Conventionally archaeologists analyse stratification of buried material or stylistic nature of architecture to suggest date for the site. Nalanda in Bihar is one such site which has been active for more than 800 years. The site has been inscribed in UNESCO's World Heritage (WH) list in 2016. Remote sensing based studies have pointed out a larger extent than what is protected under core (0.23 sq. km.) and buffer zone (0.58 sq. km.). Radiocarbon dating using Accelerator Mass Spectrometry (AMS) is a scientific method which had made possible to date even few mg archaeological samples containing atmosphere derived organic / inorganic material. The IUAC– AMS facility was thus used for the following objective:

A. To explore the possibility of dating bricks from archaeological site.

B. To use the dates obtained from AMS to study historicity of bricks collected from unprotected spatial extent of the site.

Conventionally bricks are not used for dating but recent studies have shown that it is possible to date building materials. Five brick samples from Nalanda (collected non-invasively from unprotected mound) were tested. The samples were divided in IN and OUT, where IN stands for sample collected from core of the brick and OUT is for the outer surface. The results obtained can be seen in table given below. The most important point that emerged from this study was that we were able to date bricks. This opens up a possibility to date samples from other sites, mainly sites that have brick mounds. These dates have been compared to the dates given by archaeologists and art historians. The results obtained (Table 5.4.2) have been discussed in detail in a research paper submitted to Proceedings of the Indian National Science Academy.

Table 5.4.2: Summary of the results.

Sl. No.	Sample Name	Sample ID	pMC value	Libby Age	**Calendar age Probability range (2sigma-95.4%) (Median Prob.)**
1.	51B OUT	IUACD#17C1327	97.272± 0.567	222± 46	1521 AD - 1950 AD (1751 AD)
2.	51A IN	IUACD#17C1328	86.763± 0.773	1140± 71	695 AD – 1021 AD (886 AD)
3.	51A OUT	IUACD#17C1329	86.152± 0.519	1197± 48	689 AD - 965 AD (825 AD)
4.	51B IN	IUACD#17C1326	82.307± 0.591	1564± 57	385 AD – 614 AD (489 AD)
5.	46 IN	IUACD#17C1330	71.599± 0.446	2683 ± 50	967 BC – 791 BC (848 BC)
6.	46 OUT	IUACD#17C1331	77.753± 0.475	2021± 49	166 BC – 71 AD (27 BC)
7.	47 OUT	IUACD#17C1333	92.325± 0.523	641± 45	1280 AD - 1401 AD (1346 AD)
8.	39 IN	IUACD#17C1334	76.151± 0.461	2188± 48	384 BC – 112 BC (266 BC)
9.	39 OUT	IUACD#17C1335	96.737± 0.561	266± 46	1480 AD – 1950 AD (1624 AD)

5.4.11 Signature of human settlement in the Miyar basin, Lahaul Himalaya

Milap Chand Sharma[1], Rakesh Saini[2], Pawan Kumar Kadian[1] and Pankaj Kumar[2]

[1]CSRD, Jawaharlal Nehru University New Delhi 110067, India
[2]Inter-University Accelerator Centre, Aruna Asaf Ali Marg, New Delhi 110067, India

The basic objective of the AMS experiments was to ascertain the chronology of the human settlement remains found in the Miyar basin, Lahaul Himalaya. Five samples, in all, of pine wood (THMCS02, THMCS03, THMCS04, THMCS05, and THMCS06), were excavated from the piles of shattered walls and roofs within the ruins. The first two, juniper pine samples belong to Patam site, and the other three to Tharang archaeological site. The calibration of these obtained ages indicate that during the Medieval Warm Period, the samples thrived within the Tharang end moraine complex at 95% confidence level, where the median age of these samples range from 980 AD to 1556 AD. Chronologically, the sample THMCS06 yielded the oldest radiocarbon age (1058±44) followed by THMCS04 (892±42), THMCS03 (860±42), THMCS05 (826±42), THMCS02 (393±41). The individual calibration indicates a lower age range of 885, 1032, 1044, 1052, 1462 AD and a higher range of 1040, 1080, 1101, 1212, 1642 AD.

5.4.12 Investigation of Saraswati paleochannels and associated Indus Valley Civilization in context of drainage evolution and paleoclimate

Naresh Chandra Pant[1], Apurva Alok[1], Pankaj Kumar[2] and S. Chopra[2]

[1]Department of Geology, University of Delhi, Delhi 110007, India
[2]Inter-University Accelerator Centre, Aruna Asaf Ali Marg, New Delhi 110067, India

Introduction and background: Geographical spread of the Indus Valley civilization from NE Afganistan to Pakistan and NW India from 5000-1300 BC [1], its evolution and demise have interesting geological implications as the archaeological remains of the settlements are spatially associated with the past and present basins of the Indus river. It being a dominantly agriculture based civilization, the twin resources of water and soil are of significance in settlements and their evolution. The third major factor is that of the influence of change in the climate during Holocene epoch (last 11,700 years).

Our earlier work [2,3] has described the architecture of palaeochannels in the plains of Haryana and adjacent Rajasthan and had also constrained the three fluvial events starting from >30000years. A climate change in Holocene was also described leading to a reduction in precipitation in Holocene and it coincided with certain changes in the Indus valley civilizations. The ages of these events was mainly constrained by Optically Stimulated Luminescence chronology.

A study was mounted in collaboration with IUAC nearly a year ago to establish the climate change-civilization context with greater precision for Harappan settlements in the main paleochannel as well as newly described tributaries arrived at after a remote sensing and field based hydrological-geological study [4]. In the course of this work we had also collected evidence to demonstrate the higher Himalayan (glacier water) sourcing of the paleo-river commonly referred as river Saraswati.

In the present work, samples were collected from existing palaeochannel as well as from a well-known Harappan site at Rakhigarhi (Fig. 5.4.6) to understand the evolution of the mature Harappan phase and to link it to the geological processes operative at that time. The work carried out so far includes two field campaigns, logging of the geological and cultural mounds, sampling in Rakhigarhi (three archaeological mounds), a geological flood plain succession overlain by archeological mound at Dhir village and aeolian samples (to characterize aridity), generation of ~20 AMS radiocarbon ages, XRD analysis of ~30 samples (mainly for clay mineral content to characterize soil), SEM and sedimentological analysis.

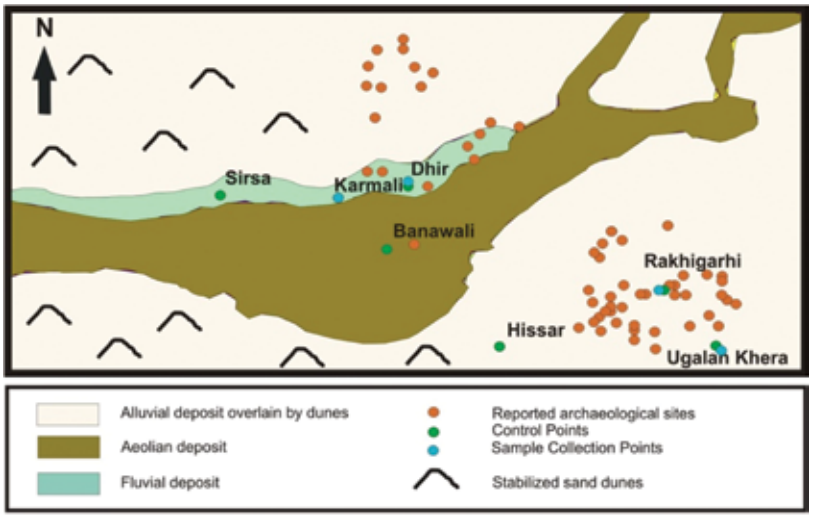

Fig. 5.4.6: Map depicting the sites from where samples were collected.

Work carried out and some results: Initial results indicate that

A. A river (Saraswati?) flowed during Holocene in the now defunct paleochannel and it had at least two major additional tributaries [4].

B. The sourcing of sediments in this continued to be from Higher Himalayas during Holocene.

C. A reworking is indicated after 4100 before present (BP) and it is likely to coincide with the 4200-3800 BP rapid global climate change event.

D. The soil generally lacked the high cation exchange capacity clay minerals (CEC) thus leading to shifting cultivation and therefore, continued relocation of settlements.

Future work: These are the preliminary inferences drawn. Work is in progress with at least one more field campaign and sampling to be carried out in near future. Though not originally requested ~10 samples from Ladakh for exposure dating (^{10}Be as well as ^{26}Al) have also been collected from the "cold" desert of Ladakh for regional correlation which will be analyzed.

REFERENCES

1. J. M. Kenoyer, Wisconsin Academy Review **33,** 22 (1987).
2. H. S. Saini *et al.,* Current Science **88,** 1994 (2005).
3. H. S. Saini *et al.,* Current Science **97,** 1634 (2009).
4. Syed Muntazir Mehdi *et al.,* Episodes **39,** 29 (2016).

5.4.13 Absolute age determination of archaeological samples collected from the palaeo-tidal region of West Bengal coast

Kaushik Gangopadhyay[1], Susanta Lahiri[2], Nabanita Naskar[2,3], Rajveer Sharma[4], Pankaj Kumar[4],Sunil Ojha[4] and Sundeep Chopra[4]

[1]Department of Archaeology, University of Calcutta, Kolkata 700027, India
[2]Department of Environmental Science, University of Calcutta, Kolkata 700019, India
[3]Saha Institute of Nuclear Physics, 1/AF Bidhannagar, Kolkata 700064, India
[4]Inter-University Accelerator Centre, Aruna Asaf Ali Marg, New Delhi 110067, India

The project was envisaged keeping in mind the possibility of dating archaeological sites in the palaeo-tidal region of coastal West Bengal. The samples were collected during archaeological excavations at the site of Erenda, by the first author on behalf of the department of Archaeology, University of Calcutta. The excavations were carried out for two field seasons 2015-16 and 2016-17. The excavations revealed that the site belonged to the Chalcolithic and Iron ages and also the historical period [1]. The Chalcolithic cultures in West Bengal are the earliest settlements in West Bengal. There are published conventional dates of these formative cultures from the upland region of West Bengal and the earliest dates available belong to the third millennium BCE. However, the dating of the Chalcolithic / Iron bearing cultures using conventional methods gives an age bracket of c.1400-600 BCE. However, the use of conventional method of age dating means that there is always a possibility of error and this may be also due to lack of proper calibration. Not a single site was dated using AMS from the coastal region of West Bengal. Therefore, this project had both methodological challenges and was expected to contribute significantly to the development of human culture in coastal region of West Bengal.

The samples were collected following the standard protocol in the field. The organic materials composed of mainly Charcoal, charred bones as well as shells. The Charcoals were collected from the floors indicated burning activities in the past as a result of cooking or firing. All the materials were collected after noting down the stratigraphic position and the depth of the samples from the present ground level was taken from a single 'datum' point. It is assumed that the dates derived from the layer indicate the date of formation of that layer, either natural or anthropogenic. The samples were prepared at the sample preparation laboratory of IUAC. Charcoal samples were chosen from different layers from bottom to the top. Laboratory protocol was followed in preparing the samples. Table 5.4.3 shows the result, where Libby age was calibrated to calendar age by Calib7.1 software [2].

Table 5.4.3: Summary of the results obtained from AMS measurements at IUAC.

Trench	Lab Code	Depth	LAYER	Dig	Calendar age, 2sigma, (Probability%)
ZA1	IUACD#17C1305	26 cm	2	Dig-3	1799- 1941 AD (62.6% Median Probability = 1824 AD
ZA1	IUACD#17C1304	122.5 cm	4	Dig-19	796 BC- 518 BC (100%) Median Probability = 644 BC
ZA1	IUACD#17C1303	130.5 cm	4	Dig-20	1059BC– 827 BC (97.4%) Median Probability = 950 BC
A1	IUACD#17C1317	45 cm	2	Dig-2	541BC- 1262AD (99.7%) Median Probability = 370 AD
A1	IUACD#17C1316	160 cm	3	Dig-17	789 BC 477 BC (98.2%) Median Probability: 632 BC
A1	IUACD#17C1315	160 cm	3	Dig-17	2065 BC- 1881 BC (88.3 %) Median Probability: 1980 BC

It is clear that in case of Trench A1 the calendar age matches with the general stratigraphy of the site. The probable age of 950 BCE is also validated by the finds of pottery. In case of Trench A1, there are two dates of 1980 BCE and 632 BCE from Dig 17 also belonging to the Chalcolithic phase. However, this contradiction needs to be addressed in future. If the age of 1980 BCE is accepted, then it will be one of the earliest settlements in West Bengal. However, the AMS date tallies well with the cultural or relative dating as the objects found from these levels are generally placed in the Chalcolithic / Iron age cultures of West Bengal (1980 BCE-640 BCE). The date of 370 AD (historical phase) and 1824 AD (coming from the top level) is also validated by the archaeological materials and general stratigraphy.

In future more samples, from the layers below the last sample (Dig 17) and the intervening layers, need to be dated. This will be significant contribution to our understanding of the development of coastal landform and human habitation during the late Meghalayan (< 5000 yrs BP) phase in the Bengal delta.

REFERENCES

1. K. Gangopadhyay, Pratnasamiksha **8,** 126 (2017).
2. N. Nabanita, K. Gangopadhyay, S. Lahiri, A. Ghosh *et al.* (forthcoming).

5.4.14 Multi-proxy paleoclimatic study in two North-western Himalayan lakes

Narendra Meena[1], Pranaya Diwate[1] and Pankaj Kumar[2]

[1]Wadia Institute of Himalayan Geology, 33 General Mahadev Singh Road, Dehradun, Uttarakhand 248001, India
[2]Inter-University Accelerator Center, Aruna Asaf Ali Marg, New Delhi 110067, India

The present study aims to understand the paleoclimatic changes in the region by quantifying the response of proxy to climatic changes. Chronology is very important to reconstruct climatic changes and given time frame to these changes. In paleoclimatic studies, AMS radiocarbon dating is a very useful technique as it provides reliable dates and require a very small quantity of sample for analysis. In the present study, 14 samples used for AMS radiocarbon dating comprise 12 bulk sediment samples and 2 wood samples, collected from two north-western Himalayan lakes (Renuka Lake and Rewalsar Lake) by employing piston coring technique. The sample was pre-treated for Carbon-14 dating in graphitization lab of IUAC. First of all, the sample was analyzed under the microscope to remove all rootles and other unwanted materials as they may influence the result. Two pre-treatment processes acid-base-acid (ABA) and base-acid–base-acid-base (BABAB) were used for analysis for bulk sediment and wood, respectively (acid - Hydrochloric Acid, base - Sodium Hydroxide). Centrifuging was done on the sample repeatedly to remove all acid and the same was check by pH meter. Further the sample was freeze-dried overnight to remove any moisture remaining in the sample. The dried sample was then graphitized in the automated Graphitization Equipment (AGE). After completion of all pre-treatment procedures, the sample was inserted into the cathode wheel to further measure for carbon isotopes (14, 13, 12) in the Accelerator Mass Spectrometer of IUAC.

The data from the analysis (14 AMS radiocarbon age) provide the chronological control on multi-proxy data (Magnetic susceptibility, Grain size, Clay mineralogy, Geochemistry, Diatoms). The chronology allows us to understand climatic changes occurred in western Himalaya during the given time frame.

5.4.15 A reliable chronology across the active faults to develop a paleoearthquake catalogue of Himalaya

R. J. Perumal[1], R. L. Mishra[1], Atul Kumar[1], S. P. Dash[1], Pankaj Kumar[2] and S. Chopra[2]

[1]Structure and Tectonics Group, Wadia Institute of Himalayan Geology, Dehradun 248001, India
[2]Inter-University Accelerator Centre, Aruna Asaf Ali Marg, New Delhi 110067, India

Objective: A reliable chronology is an important concern in the study of earthquake geology in trench exposure across active faults to develop a paleoearthquake catalogue of Himalaya.

Work done: We have processed 20 samples of Charcoal for AMS radiocarbon dating and obtained results for 19 samples (1 sample was not dated due to insufficient carbon content; Lab code: IUAC#17C 984-998: IUAC#17C 1358-1361) for the MoES-sponsored research projects.

Chenga village site: Active fault scarp was identified along the front of Siwalik Hills around Chenga village, which is adjacent to the eastern border of Nepal and Bihar (Fig. 5.4.7). The mapped fault scarp extends along its strike toward with variable height (12-17 m). A trench (17 m long × 6 m deep × 2 m width) was placed normal to the fault scarp strike and detailed paleo seismological investigation was done.

60 charcoal samples from the trench exposure and 5 samples from the pit on the hanging wall were collected to constraint the earthquake timing. Out of these samples 15 samples were processed (at IUAC) which gave age range between 12679 B.C and 91 B.C. Our results suggest that the site has recorded late Holocene earthquake, but does not show any younger event reported in eastern Nepal (For example 1255 A.D. and 1934 Bihar-Nepal earthquake). We may need to study some critical samples for radiocarbon dating for the same site.

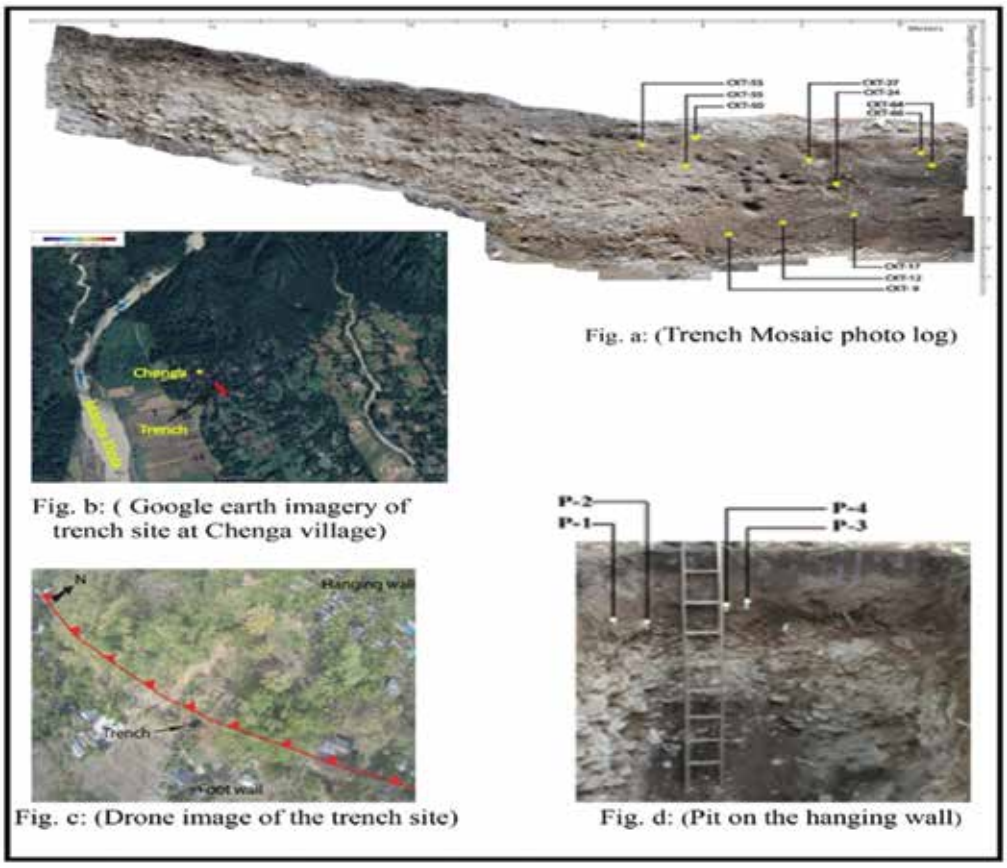

Fig. 5.4.7: Showing (a) Trench Mosaic photo log, (b) location of Trench site in google earth imagery, (c) drone image of the site and (d) photograph of the Hanging wall pit.

Kanya sot site, Kumaun sub-Himalayan region: The Central Himalayan region has experienced some great and large earthquakes in 1255, 1344, 1505, 1803, 1833, 1934, and in 2015 which have devastated this region. Kanya sot cliff section, Kumaun Himalaya falls in the Central Seismic Gap of Central Himalayan region. During geo-scientific investigation of this section, we found Siwalik rocks are juxtaposed over recent sediments containing charcoals and potteries. The vertical separation of the scarp is around 27 m, suggesting multiple earthquake events along this fault (Fig. 5.4.8).

Fig. 5.4.8: Google Earth imagery of the study region showing the exact location of the site.

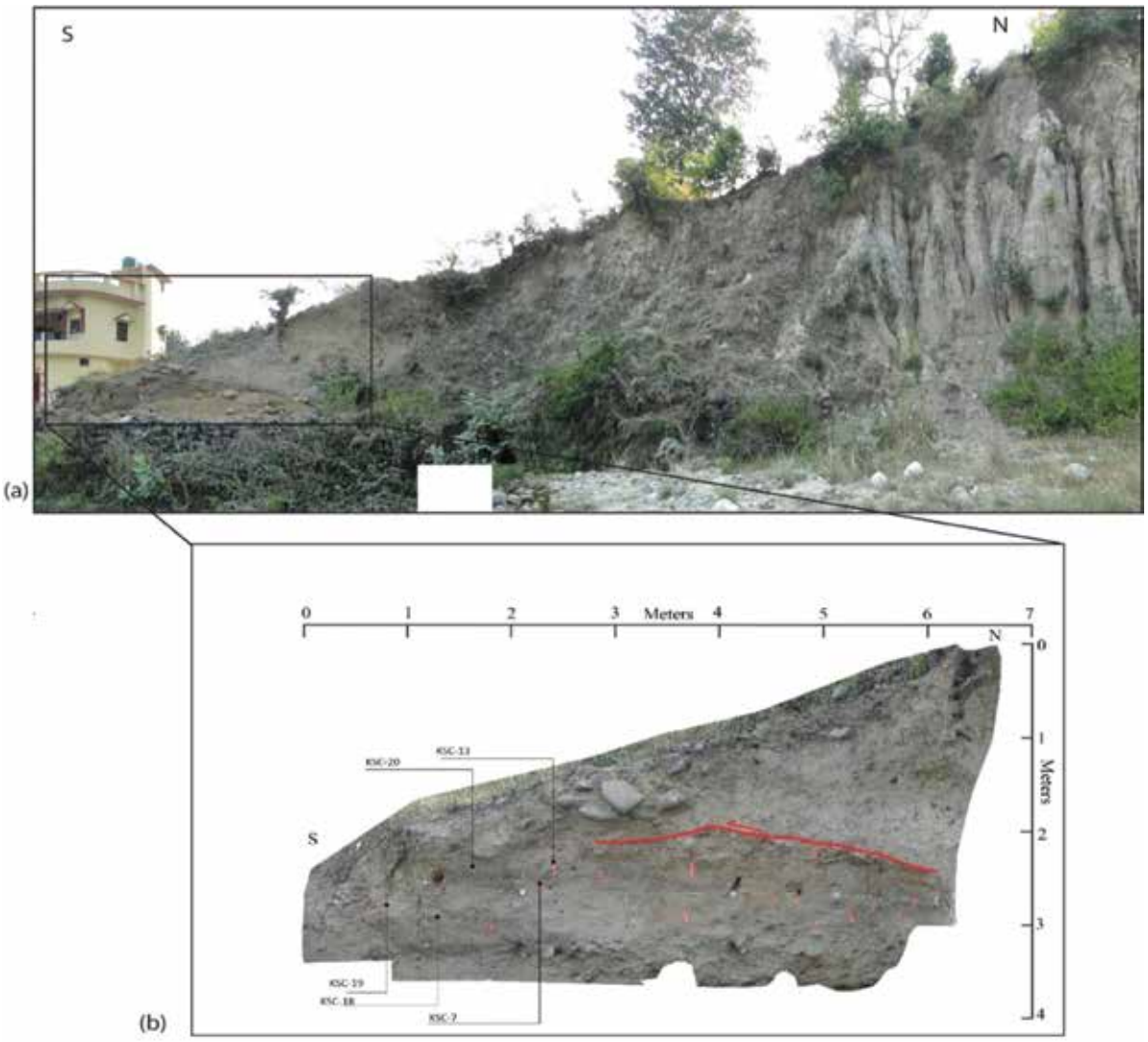

Fig. 5.4.9: (a) Panoramic view of the Kaniya sot terrace which have been faulted due to co-seismic movement and (b) Cliff section showing Siwalik rocks overriding on recent sediments; radiocarbon ages suggesting the earthquake event in last millennium.

To date the displacement event, we dated five (4) charcoal samples at IUAC. These dates have confirmed an earthquake event around 1300-1500 AD (Fig. 5.4.9).

5.4.16 Radiocarbon dating of core sediment and wood samples collected from Indian Sundarbans

Punarbasu Chaudhuri[1], Nabanita Naskar[1,2], Susanta Lahiri[2], Rajveer Sharma[3], Pankaj Kumar[3], S. Ojha[3] and S. Chopra[3]

[1]Department of Environmental Science, University of Calcutta, 35 Ballygunge Circular Road, Kol 700019, India
[2]Saha Institute of Nuclear Physics, 1/AF, Bidhannagar, Kolkata 700064, India
[3]Inter-Unversity Accelerator Centre, Aruna Asaf Ali Marg, New Delhi 110067, India

Objective: Radiocarbon dating of fossilized wood samples and core sediment samples to understand the geo-chronology in Indian Sundarbans.

Introduction: Sundarbans, the world's largest contiguous mangrove ecosystem stretches across the two nations of India and Bangladesh. UNESCO has attributed it as a natural heritage site for its bio-diversity. Rivers, creeks, inter-tidal and estuarine zones interconnect this vast archipelago of more than hundreds of islands. In 2000, Stanley and Hait [1] carried out an extensive radiometric study using Accelerator Mass Spectrometry (AMS) to understand the paleo-environmental conditions. The materials used for ^{14}C dating included peat, mud, wood, shell, plants, etc.

Experimental: For the present study, core sediment and few wood samples were collected from Indian Sundarbans and ^{14}C dating was carried out at IUAC. Sample pre-treatment was done in the chemistry laboratory of IUAC prior to AMS measurements. Sediment and wood samples were subjected to acid-base-acid (ABA) and BABAB treatment, respectively, before combustion in O_2 environment. The last step of bleaching for wood samples was carried out to extract the cellulose. CO_2, thus produced, undergoes purification and reduction to graphite in Automated Graphitization Equipment (AGE). Graphite powder, thus formed, was filled in capsule and loaded in ion source of AMS machine based on 500kV Tandem ion accelerator. NIST Standard OXII (Oxalic acid) and IAEA-C9 (Kauri wood) was considered as standard reference materials. Also a secondary standard sample (IAEA-C8) was measured for data quality assurance. Data collection was done in 10 runs (30 minutes) for each sample. Calib7.1 software was used to convert Libby age to calendar age [2].

Result and discussion: Radiocarbon dating of the wood samples provided their median calendar age (BP) in between 300 – 500 years (Table 5.4.4). The data for the core sediment sample were chronological with the oldest date (11902 cal BP) for the depth of 60-80 cm.

Table 5.4.4: Data obtained for sediment and wood samples.

Sample	Lab ID	Depth (cm)	Median Calendar age (Cal BP), 2 sigma
Wood 1	IUACD#17C1307	_	346 cal BP
Wood 2	IUACD#17C1308	_	497 cal BP
Wood 3	IUACD#17C1309	_	392 cal BP
Wood 4	IUACD#17C1310	_	386 cal BP
Gadkhali-S1	IUACD#17C1311	0-20	4176 cal BP
Gadkhali-S2	IUACD#17C1312	20-40	10339 cal BP
Gadkhali-S3	IUACD#17C1313	40-60	11211 cal BP
Gadkhali-S4	IUACD#17C1314	60-80	11902 cal BP

Conclusion: These data corroborate with those of Stanley and Hait [2000], but more sample analysis is required to validate the present dates.

REFERENCES

1. D. J. Stanley and A. K. Hait, Journal of Coastal Research **16,** 26 (2000).
2. M. Stuiver and P. J. Reimer, Radiocarbon **35,** 215 (1993).

5.4.17 Reconstruction of the past climatic and sea level changes during the Late-Quaternary

Rajeev Saraswat[1], T. Suokhrie[1], R. Dubey[1], S.M. Saalim[1] and Pankaj Kumar[2]

[1]CSIR-National Institute of Oceanography, Dona Paula, Goa 403004, India
[2]Inter-University university Accelerator Centre, Aruna Asaf Ali Marg, New Delhi 110067, India

The increase in sea level is one of the consequences of global warming. The rate of increase in sea level during the instrumental era can be assessed by using tide-gauge and remote sensing data. Long-term past records of sea level can, however, help in assessing the factors responsible for sea-level changes, prior to human intervention. The signatures of sea-stand higher than present are exposed on land. We have observed a few such exposures and those were dated to understand the timing of the high sea-stand.
A total of 20 foraminifera samples from these exposures were analysed for radiocarbon dating using the AMS facility of IUAC. The radiocarbon data were used to establish chronology of the sediments. The proxy data was then used to reconstruct past climatic changes during different time intervals.

The radiocarbon based chronology helped in inferring the followings:

- Increased terrestrial runoff in the western Bay of Bengal during the last glacial interval.
- Evidence of high sea-stand / extreme event ~800 year ago, from the raised marine terraces along the shoreline of Goa.

- The sea level off the coast of Goa was lower by 54.5 m at 7000 year BP.

Further data generation is in progress.

5.4.18 Application of multi-proxy approach to understand the past Glaciations and climatic variations of Western Himalayas

Om Kumar[1], A. L. Ramanathan[1], Jostein Bakke[2], J. P. Shrivastava[3], Pankaj Kumar[4], Rajveer Sharma[4], Kannan Deenadayalan[1] and S. Chopra[4]

[1]School of Environmental Sciences, Jawaharlal Nehru University, New Delhi 110067, India
[2]Department of Earth Science, University of Bergen, Post Box 7803, N-5020 Bergen, Norway
[3]Department of Geology, Delhi University, Delhi 110007, India
[4]Inter-University Accelerator Centre, Aruna Asaf Ali Marg, New Delhi 110067, India

To track palaeoclimatic changes, 235 and 135 cm lake sediment cores were recovered from Chandratal lake (4300 m a.s.l.), Western Himalayas (Fig. 5.4.10). The lake sediment samples were analyzed for multi-proxies. The details of sampling methods are discussed in ref. [1]. Lake sediment is widely used archives in palaeoclimatic studies and in this context a climatic history of about 50 ka is reviewed by Om et al. [2]. We present new, well-dated, multi-proxy (grain size, magnetic susceptibility, s-ratio, $\delta^{18}O$) records of past climate variation spanning early to late-Holocene. The samples were analyzed for ^{14}C dating using radiocarbon with AMS facility of IUAC. Our result reveals a significant variation in monsoon/westerlies strength over a period of 10 ka.

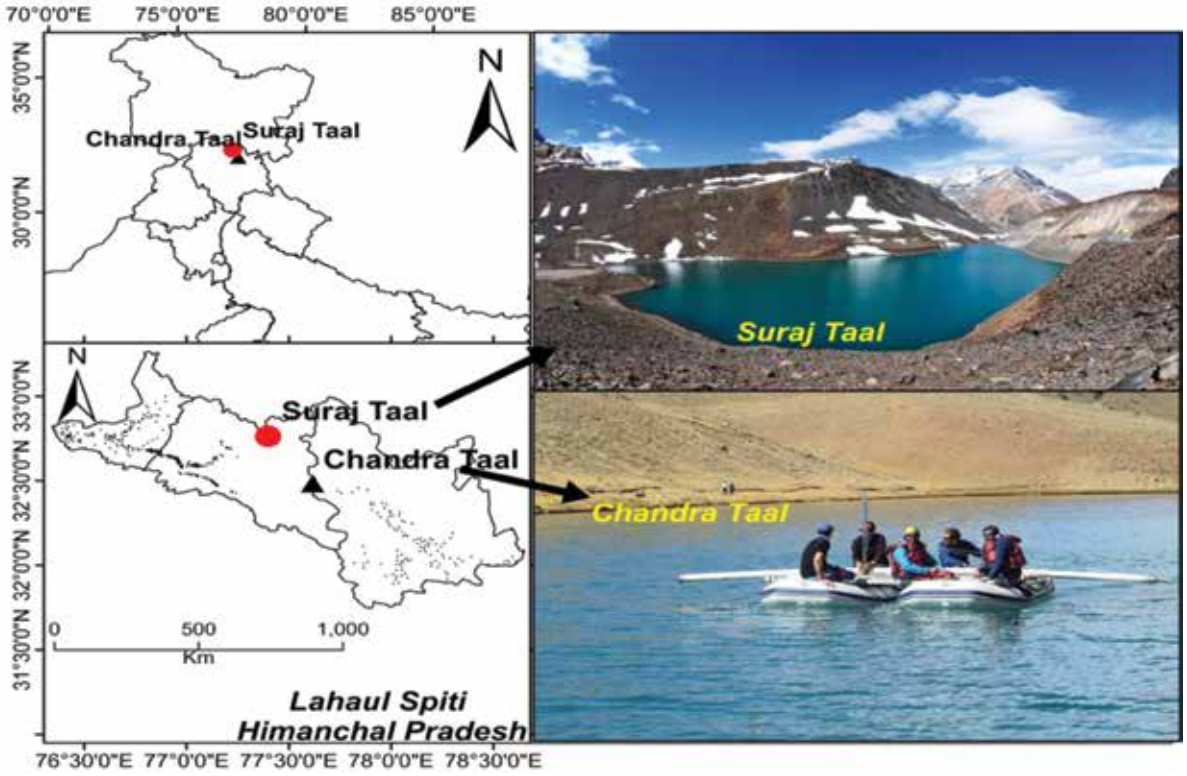

Fig.5.4.10: Map of Chandratal Lake, Western Himalaya.

Sample Analysis:

1. Twenty-five (25) sediment samples were selected for AMS ^{14}C dating and these were analyzed at IUAC AMS facility.
2. Mineral magnetics analysis was performed at Indian Institute of Geomagnetism (IIG), Mumbai.
3. Grain size analysis of sediments was performed using Lase Particle Analyzer at Jawaharlal Nehru University (JNU), New Delhi.
4. Some representative samples for XRD, XRF and SEM are needed to be analyzed for further interpretation of results.

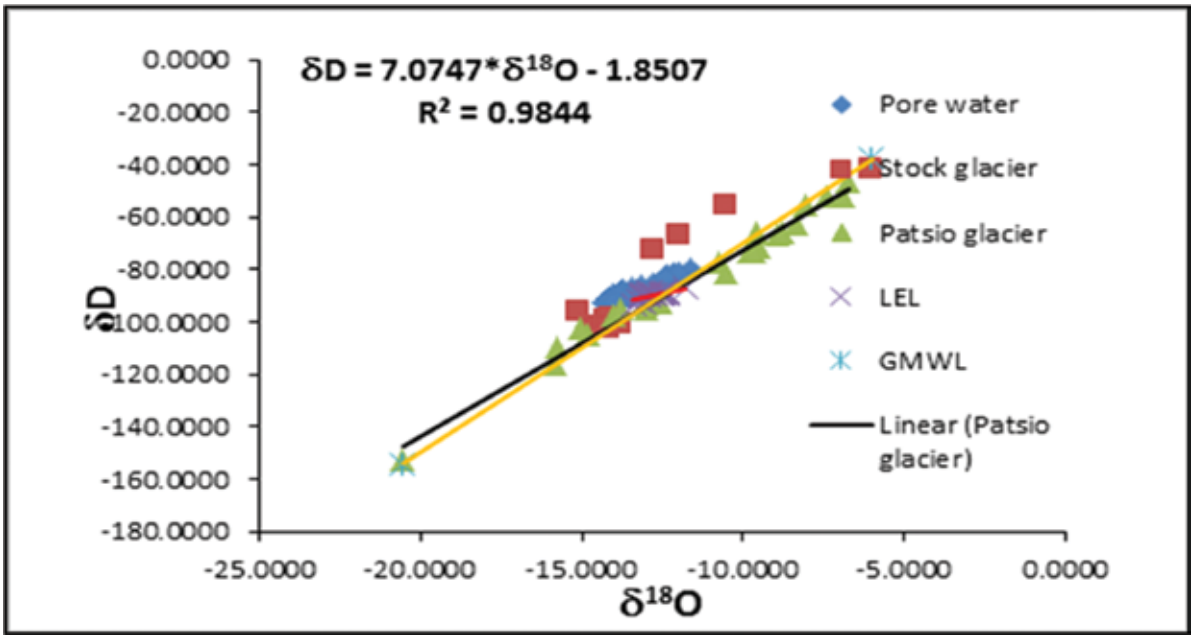

Fig.5.4.11: $\delta^{18}O$ (‰) versus δD (‰) for Patsio, stock glacier and lake pore water samples. The Local meteoric water line (LMWL) has slope 7.07 and intercept of 1.8.

Lakes have the potential of retaining many different aspects of water isotope composition in their sediments which can be used for palaeoclimate reconstruction.The water samples were collected from the 2 glaciers (Patsio and Stock) and Chandratal Lake and samples were analyzed using PICCARO ISOTOPE ANALYZER at JNU, New Delhi. The water samples for all the sites including Chandratal Lake were collected from different locations. The graph were plotted between $\delta^{18}O$ and δD and the Local Meteoric Water Line value is $\delta D = 7.0747 * \delta^{18}O - 1.0857$ (Fig.5.4.11).The global meteoric water line is expressed by the equation $\delta D = 8.17\delta^{18}O + 11.27‰$. Hydrogen and oxygen isotopes of water are widely used in ice core studies by paleo-climatologist. Now we have also extracted pore water from sediment core to get the past climatic signal.

Distribution of sand, silt and clay in Chandratal Lake: Grain size analysis provides important clues to the sediment provenance, transport history and depositional conditions [3-5]. Grain size analyses were performed by the Laser Particle Size Analyzer at JNU. Grain size are widely used as proxy to reconstruct the past rainfall intensity. Therefore we have chosen these proxies to understand the past rainfall patterns of Lahul Spitti valley, Western Himalayas.

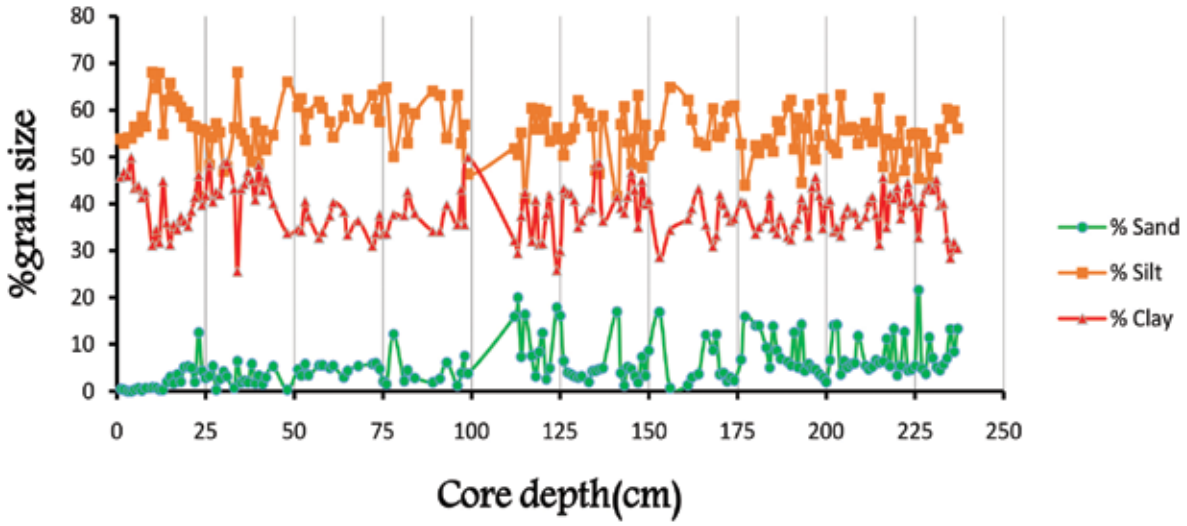

Fig.5.4.12: Percentage distribution of grain size with depth.

Magnetic proxy: Magnetic susceptibility is a proxy employed in paleoclimate reconstruction of terrestrial, marine, and lacustrine environments [6-10]. The samples were analyzed for magnetic proxies at 1 cm interval to get a high resolution picture of magnetic susceptibility variation at Indian Institute of Geomagnetism, Mumbai (Fig.5.4.13). We have also analyzed some representative samples for Scanning Electron Microscope to identify the Fe bearing magnetic minerals (Fig. 5.4.14).

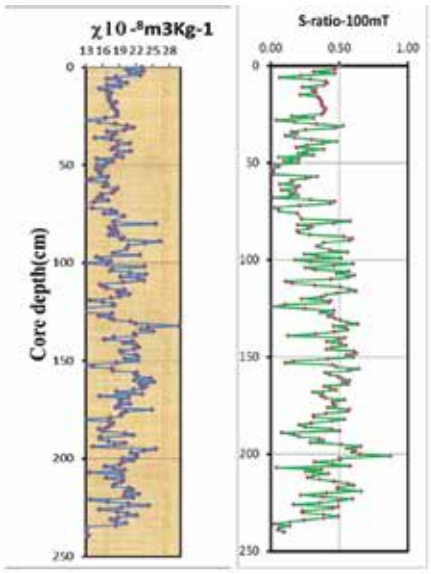

Fig.5.4.13: Magnetic susceptibility and s-ratio for Chandratal sediment core (235 cm).

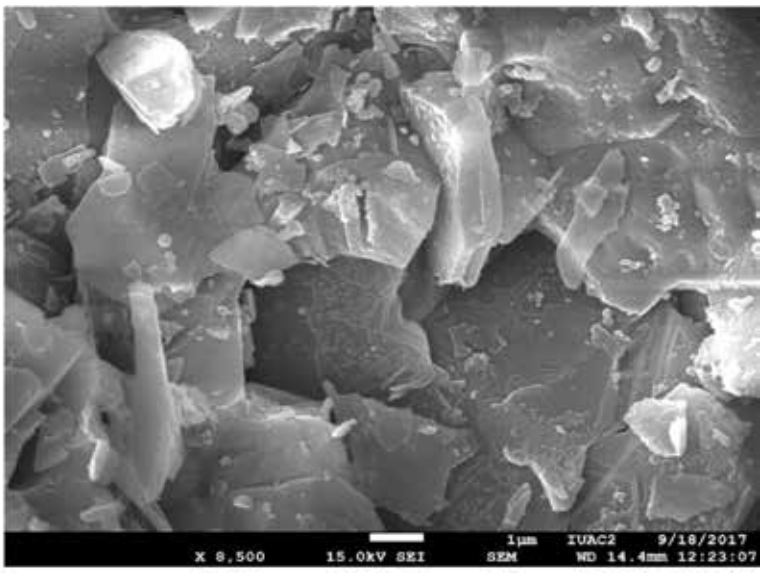

Fig. 5.4.14: Scanning electron micrograph of Chandratal Lake Sediment core of 60 cm depth.

Cosmogenic dating of moraines: Cosmogenic-exposure dating has emerged over the last two decades as the premier chronological tool to date glacial landforms such as moraines, erratic boulders, and glacially eroded bedrock. We have collected the moraines sample from Chandratal and Chhota Shigri regions (Fig. 5.4.15). The samples were crushed and treated with acetone which is now ready for further measurement.

Fig. 5.4.15: Rock sampling for cosmogenic exposure dating (^{10}Be and ^{26}Al).

REFERENCES

1. Jostein Bakke *et al.,* Journal of Climate Change **2,** 103 (2016).
2. Om Kumar *et al.,* Journal of Climate Change **3,** 11 (2017).
3. R. L. Folk and W. C. Ward, Journal of Sedimentary Research **27,** 3 (1957).
4. G. M. Friedman, Sedimentology **26,** 3 (1979).
5. E. N. Bui *et al.,* Earth Surface Processes and Landforms **14,** 157 (1990).
6. J. Chlachula *et al.,* Geophysical Journal International **132,** 128 (1998).
7. M. Evans and F. Heller, Environmental magnetism: principles and applications of enviromagnetics (Elsevier 2003).
8. B. A. Maher and R. Thompson, Quaternary Research **37,** 155 (1992).
9. B. A. Maher, Aeolian Res. **3,** 87 (2011).
10. J. Nawrocki *et al.,* Boreas **25,** 161 (1996).

5.4.19 Reconstructing fire history at Sandynullah, Nilgiris, using macrocharcoal analysis

P. K. Sarath[1], P. Ramya Bala[1], Pankaj Kumar[2] and R. Sukumar[1]

[1]Indian Institute of Science, C. V. Raman Rd, Bengaluru, Karnataka 560012, India
[2]Inter-University Accelerator Centre, Aruna Asaf Ali Marg, New Delhi 110067, India

The evidence of fire on Earth goes back over 400 Myr and has been a significant part of Earth's system for 350 Myr. The subsequent history of fire on the planet coincides with the development of terrestrial life and also the evolution of the atmosphere. The effects of fire on the terrestrial world can be devastating, leading to destruction of habitat and increased erosion, but equally may be necessary for the re-growth of specialized vegetation type. Throughout, fire has been a cause, consequence, and catalyst.

Our understanding about the occurrence of fire and the role it plays in shaping the earth developed rapidly over the past 30 years from the study of charcoal. The co-occurrence of grassland and stunted evergreen forest, the shola grassland mosaic, in Sandynallah valley and in other southern Indian mountain ranges is a matter of debate. One hypothesis is that fire plays a major role in shaping the grassland ecosystem. We also tried integrating microcharcoal data which showed similar trend as that of the macrocharcoal. Other non-pollen palynomorphs were also counted and their ecological relevance was studied. Macrocharcoal analysis showed a peak component corresponding to an average depth of 53 cm and 149 cm, whose approximate age from the ^{14}C AMS dating is 3400 and 21000 yrs BP, respectively. This can represent factors such as regional fire history and also secondary charcoal delivery to the study site.

The age-depth model for the profile from age-depth modelling software Clam that uses linear interpolation is provided below (Fig. 5.4.16).

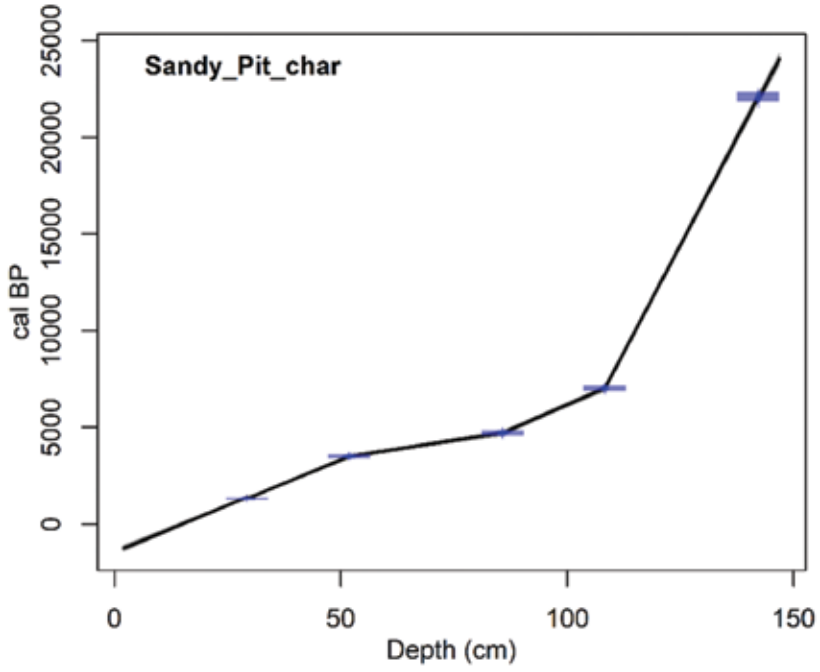

Fig. 5.4.16: Clam Age-depth model for Sandynallah profile (linear interpolation between dated layers).

Our results also point towards a local fire, but the origin of the fire whether anthropogenic or natural is not clear. Very few evidences have been collected relating to the fire history of Nilgiris so far. This area was long occupied by the indigenous tribal peoples of the Toda, Kota, Kurumba and Irula. The recent fire around 3400 yrs BP can be attributed to Toda pastoralist burning the landscape for the buffalo grazing. The method of extraction, counting and analysis are prone to various kinds of errors. Further research and evidences are required for accurate reconstruction of the fire record of the past.

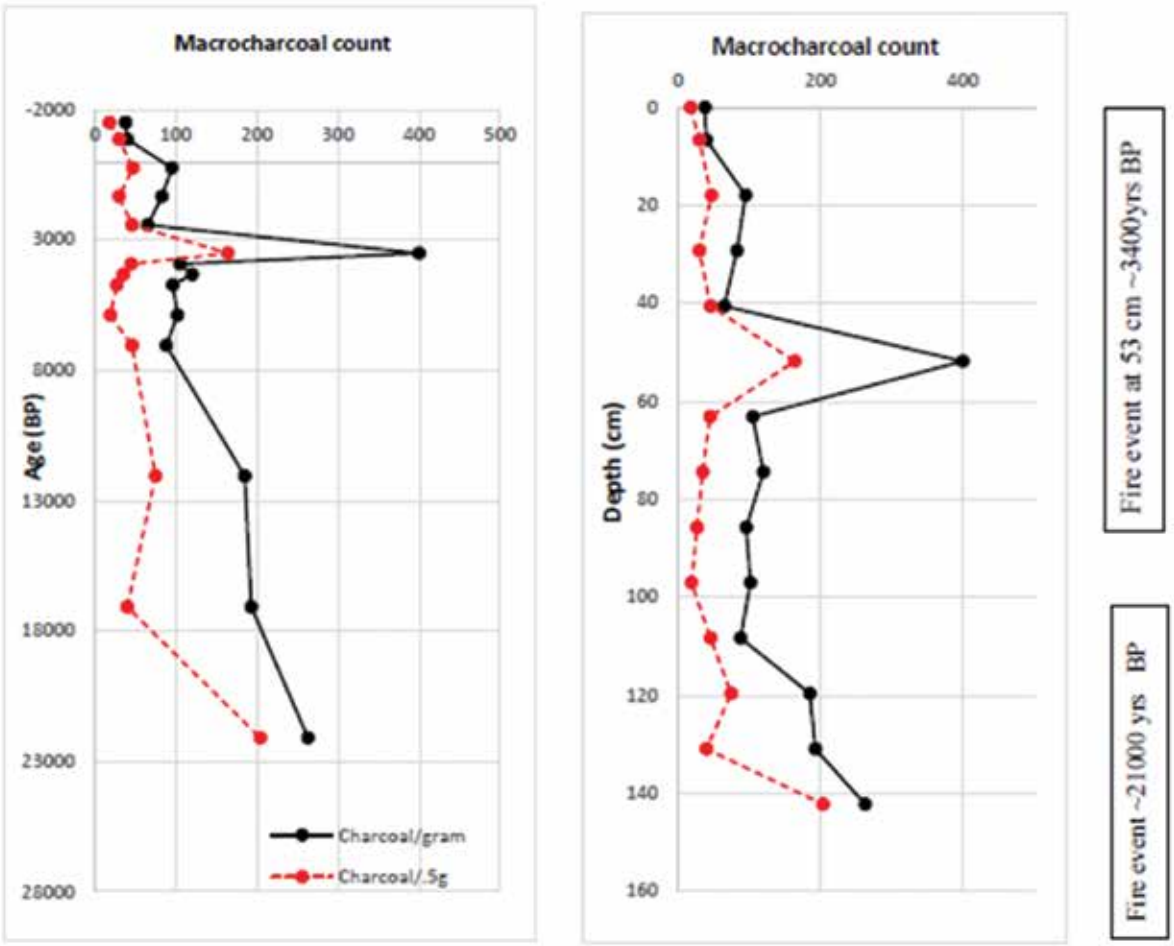

Fig. 5.4.17: Depth and age profiles of charcoal from the Sandynallah profile.

5.4.20 Analysis of plants and human relationship since Late Pleistocene from Dzuko Valley- Nagaland, Northeast India

Sandhya Misra[1] and Pankaj Kumar[2]

[1]Birbal Sahni Institute of Palaeosciences, 53 University Road, Lucknow, Uttar Pradesh 226007, India
[2]Inter-University Accelerator Centre, Aruna Asaf Ali Marg, New Delhi 110067, India

In the said project, multiproxy data have been generated from Dzukou valley towards the achievement of the objective to understand the changing landscape dynamics of Dzuku valley and adjoining regions under varied natural and human-induced conditions. Fourteen AMS dates from Direct AMS, USA and IUAC, New Delhi put a time bracket from early Holocene to present. Multi-proxy data generated in the project show that Dzukou is predominantly under the influence of C3 vegetation indicating towards the cool and dry climatic conditions prevailing at the study site with decrease in the rainfall during past 10000 years. Charcoal analysis from the study site gives a signal of both wild and human generated fire episodes in the area. In the said project eight AMS dates from IUAC have been obtained. These dates will be useful to provide the time brackets to the different events recorded from the Khonoma and Viswema sites of Nagaland. Other data required to conclude the study are being generated.

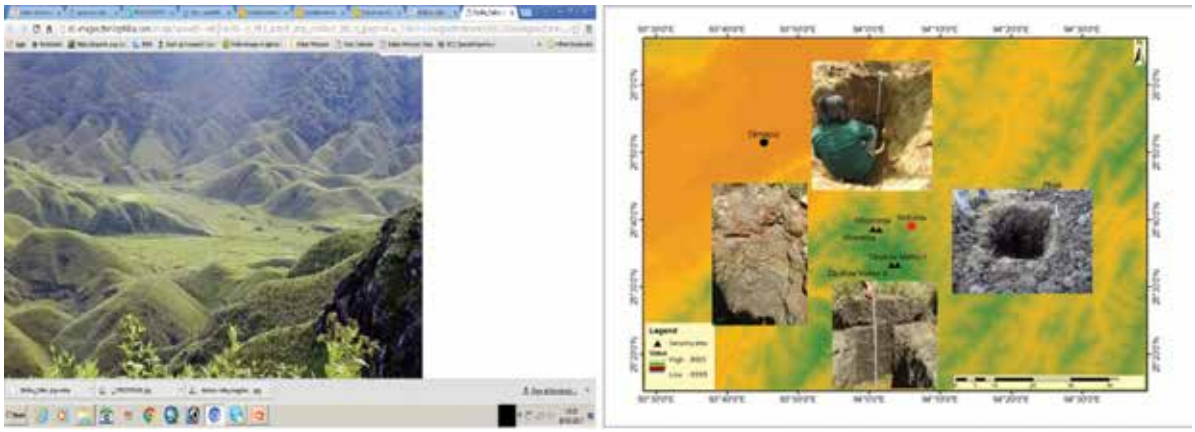

Fig. 5.4.18: Field photographs and sample collection in Dzukou Valley.

5.4.21 Signature of earliest human habitation in high altitude Ladakh, J&K, India

S. B. Ota[1] and Pankaj Kumar[2]

[1]Archaeological Survey of India, New Delhi 110 001, India
[2]Inter-University Accelerator Centre, Aruna Asaf Ali Marg, New Delhi 110067, India

As part of ongoing archaeological investigations by the Archaeological Survey of India to look into the prehistoric past of Ladakh Himalayas, Jammu & Kashmir, Ota undertook intensive exploration in Nubra Valley and located an ancient camping site on Sasoma-Saserla road at an elevation of 4300 m MSL. It was excavated in September, 2016 with a view to find out the cultural matrix at the site within a chronological framework. This investigation has in fact revealed certain cultural evidence that is characterised by microliths with blades, bone tools and a large number of faunal remains that was not known earlier from Ladakh. Further, the occurrence of bone tools that are unique to Ladakh have not been reported so far from the neighbouring areas of China and Tibet in the Karakoram area. The importance of this site lies with the fact that the dating of this site would establish the date of early human occupation with distinct cultural materials in Ladakh.

Keeping this in view, altogether 22wood charcoal samples from two different localities at this site spreading over all the strata of both the localities were subjected to AMS C14 dating in a collaborative mode with IUAC. Since emphasis was given to answer certain questions like cultural change through time, how frequently the repeated occupation took place and correlation between the two localities at the site.

All the AMS dates show consistency as sample contamination is negligible as the area forms part of snow desert. The series of AMS dates that have been done is very encouraging as it has pushed back the antiquity of the human occupation at this site to circa 9,000 BCE which is considered as the earliest dated site associated with human cultural remains in Ladakh. The AMS dates have further confirmed that this site remained occupied till circa 7200 BCE. This site with definite human cultural remains has been considered as the highest located human occupation site in the country. With this, it is now getting established that Ladakh, Tibet and adjoining areas of China in the Karakoram area was forming a single cultural zone in the past with certain regional variations.

Further, the analysis of the faunal remains recovered from the site is under study. The preliminary morphological study of bones, DNA analysis and isotopic study indicates the use of domesticated yaks at this site in the past. If this interpretation gets established, then the AMS chronology for this site becomes more interesting as it would establish the antiquity of domestication of yak in future.

5.4.22 Radiocarbon dating of soil from Kaziranga National Park, India

Pramit Kumar Deb Burman[1], Supriyo Chakraborty[1], Dipankar Sarma[2], Pankaj Kumar[3] and Rajveer Sharma[3]

[1]Centre for Climate Change Research, Indian Institute of Tropical Meteorology, Pune 411008, India
[2]Department of Environmental Sciences, Tezpur University, Tezpur 784028, India
[3]Inter-University Accelerator Center, Aruna Asaf Ali Marg, New Delhi, Delhi 110067, India

The terrestrial ecosystems are the largest sink of atmospheric CO_2 with a global sinking strength of 3.1 ± 0.9 GtC y^{-1} [1]. The soil organic matter (SOM) turnover time is an important parameter for inferring about the soil mixing and nutrient dynamics of any ecosystem that is used as an input parameter for calculating its productivity using the terrestrial biosphere models [2]. In the present proposal, we aim to estimate the land carbon pools at the Kazirana National Park (KNP), Tezpur, Assam as part of the research objectives of the MetFlux-India project by the Ministry of Earth Sciences (MoES), Government of India [3].

The Accelerator Mass Spectrometry (AMS) is a widely used technique for estimating the radiocarbon (C^{14}) age of different archaeological, geological, and biological samples and known for its precision [4]. The C^{14} dating of the soil samples from three different locations in KNP was carried out using the AMS facility at IUAC. These samples were collected in April, 2017 and preserved carefully from possible degradation / contaminations. The samples were pre-processed at the wet chemistry laboratory following the standard acid-base-acid protocol [5] in March 2018 and subsequently analyzed for ^{14}C at the IUAC AMS facility. According to the preliminary results the top soil at KNP, up to a depth of a few tens of centimeters is well mixed and has a higher percentage of modern carbon (pMC). Additionally the radiocarbon age of the soil increases with depth suggesting that the top soil is probably better-mixed than the deeply buried layers.

However, these findings are yet to be cross-checked against the supporting measurements. The carbon isotopic fractionation is an important parameter that affects the accuracy of the AMS C^{14} dating technique [6]. As recommended, we are presently in the process of measuring C^{13}/C^{12} ratio using the Isotopic Ratio Mass Spectrometer (IRMS) at IITM, Pune that can be used for an independent recalibration and recalculation of the radiocarbon dates. Additionally, various other soil parameters such as the nutrients, micronutrients, texture, bulk density etc. are being analysed for more information on the soil formation process. We plan to supplement our study with the similar measurements being done for the other ecosystems in the MetFlux-India network.

REFERENCES

1. C. Le Quéré, R. M. Andrew, J. G. Candell, S. Sitch *et al.,* Earth Syst. Sci. Data **8,** 605 (2016).
2. D. B. Clark, L. M. Mercado, S. Sitch, C. D. Jones *et al.,* Geosci. Model Dev. **4,** 701 (2011).
3. P. K. Deb Burman, D. Sarma, M. Williams, A. Karipot and S. Chakraborty, J. Earth Syst. Sci. **126,** 99 (2017).
4. L. K. Fifield, Rep. Prog. Phys. **62,** 1223 (1999).
5. R. Sharma, G. R. Umapathy, P. Kumar, S. Ojha *et al.,* Nucl. Instrum. Methods B (2018); https://doi.org/10.1016/j.nimb.2018.07.002
6. L. Calcagnile, G. Quarta and M. D'Elia, App. Radiat. Isot. **62,** 623 (2005).

5.4.23 AMS dating of the excavated Chacolithic Ste of Deltihuda Mounds, Talagh village, Cuttack District

Umakanta Mishra[1] and Pankaj Kumar[2]

[1]Department of History, Ravenshaw University, Cuttack, Odisha 753003, India
[2]Inter-University Accelerator Centre, Aruna Asaf Ali Marg, New Delhi 110067, India

Statement of Objectives: Expansion of early farming communities in the eastern state of Odisha and nature of their material cultures have not been worked out with certain degree of certitude. As late as 1990s, scholars claimed that food producing material cultures were absent in Odisha. Last two decades saw a number of explorations and excavations of archaeological sites of early farming communities. However, firm dates of these sites are not available with the exception of the site of Golabai and Khameswarpalli [1,2].

The excavations of the Deltihuda mounds in Talagarh village of Cuttack district over three seasons from 2015-17 were undertaken by the Department of History, Ravenshaw University with the objective of understanding the material culture of early farming settlers' site as well as to firmly establish the time frame of the early farming communities of Odisha. For obtaining the AMS dates of the charcoal samples collected during excavation, a collaborative work with IUAC was initiated to establish a firm date for the site so as to understand along with other evidence the chronology and the nature of the material culture of the early farming communities of Odisha.

Procedure followed: Firstly, selected charcoal samples were collected in the centrifuge tubes for cleaning by using MQ water and several chemicals like HCL and NaOH. After cleaning, the sample tubes were kept in the Thermo shaker for mixing the chemicals properly. After the chemical process, the samples were again cleaned with MQ water and Elex water to make them chemical free. Then samples were left for drying in the machine for 12 hours. In the second step several boats, which are made of aluminum foils with 2-4 g of carbon samples were prepared. After the preparation of samples, they were combusted in an elemental analyzer (EA) and the produced CO2 was absorbed onto a zeolite trap in the AGE system.

Calibrated dates obtained and its significance: The AMS dates of 14 charcoal samples were communicated by the AMS unit on June 8 2018. The calibrated AMS dates of 12 samples closely correspond with relative dating of associated materials. IUAC dating has confirmed and reinforced the chalcolithic cultural horizon of the Deltihuda site. The dates of various layers as obtained establish the fact that early farming communities of Deltihuda developed considerably later than the farming communities of north-west India and central India. This date largely corresponds with the dates from Golabai.

Other scientific analyses being done: The project report is not yet finalized as a number of other analyses are underway. The excavation has revealed a bead manufacturing workshop. XRD and FTIR analyses are being done to ascertain the rock mineral and understand manufacturing method. Paleobotanical analysis is being done to understand archaeobotanical remains. Similarly, faunal remains are being analysed with other collaborators. The preliminary report of the excavation has been published [3].

REFERENCES

1. B. K. Sinha, Puratattva **23,** 48 (1992-93).
2. P. K. Behera *et al.,* Man and Environment **XXXII,** 41 (2007).
3. S. K. Acharya *et al.,* Man and Environment **XLII,** 90 (2017).

5.4.24 Investigations into the chronology of the Harappan site of Dholavira, district Kachchh, Gujarat

V. N. Prabhakar[1,2], R. S. Bisht[2] and Pankaj Kumar[3]

[1]Indian Institute of Technology Gandhinagar, Palaj, Gandhinagar 382355, India
[2]Exploration and Excavation branch, Archaeological Survey of India, New Delhi 110003
[3]Inter-University Accelerator Centre, Aruna Asaf Ali Marg, New Delhi 110067, India

Objectives: The excavations at Dholavira for thirteen field seasons between 1989-90 to 2004-05 by Bisht of Archaeological Survey of India brought to light the origin, gradual growth and transformation of a Harappan city, documenting nearly 1500 years of its occupation. The city was dated based on the related cultural materials from other Harappan city and a few TL dates. However, radiometric dates from different occupational areas like Citadel, Bailey, Middle and Lower Towns were absent, which prevented the understanding of the expansion of the city during various periods of its occupation. The city is located at a crucial geographical location connecting mainland Gujarat (India) and Sindh (Pakistan) Harappan sites and played a much important role in the exploitation and distribution of raw materials as well as finished products. In order to understand these interactions, this project was a first attempt to understand the chronology of this prominent Harappan site.

Outcome: For the first time it has been understood that the Lower Town of Dholavira, the last occupation area to be developed by the Harappans was founded around 2500 BCE and could have continued up to 1900 BCE, which corroborated with the traditional chronology. The chronology from the other areas like Citadel, indicate its occupation around 2800 BCE. The dates were obtained using IUAC radiocarbon AMS dating facility with the charcoal samples collected from the Dholavira. More numbers of samples need to be dated to fully understand the entire chronological horizon of the city.

5.4.25 Further understanding of the protohistoric chronology of Lower Drishadvati Valley (northern Rajasthan)

V.N. Prabhakar[1, 2] and Pankaj Kumar[3]

[1]Indian Institute of Technology Gandhinagar, Palaj, Gandhinagar 382355, India
[2]Exploration and Excavation branch, Archaeological Survey of India, New Delhi 110003
[3]Inter-University Accelerator Centre, Aruna Asaf Ali Marg, New Delhi 110067, India

Objectives: The excavation of Karanpura, district Hanumangarh, Rajasthan during the field seasons 2012–13 and 2013–14 brought to light early Harappan and Harappan periods. The location of Karanpura on the presently dried up River Drishadvati between Sothi (downstream) and Siswal (upstream) at a crucial juncture facilitated the exploitation of resources, probably the copper sources of northern Rajasthan and grinding stones from Kaliana, Haryana. The excavation also brought to light a habitation deposit of around 2.5 m of early Harappan period, which was subsequently followed by the Harappan phase.

The chronology of lower Drishadvati valley is less understood due to the lack of radiometric dates, in particular AMS dates. Even though the excavations at Sothi and Siswal brought to light a cultural phase known as Sothi-Siswal culture (early Harappan), its proper chronological context was so far least understood. The primary objective of the investigations was to further correlate and understand the chronology of 3000 – 2100 BCE time

bracket obtained from the first attempt of dating 20 samples at IUAC. The other objectives include to properly place the cultural levels of early and Harappan phase, its origin in this part of Drishadvati valley and its ultimate demise.

Outcome: The investigations helped in understanding the occupation of Karanpura in the lower Drishadvati valley around 2900 BCE, indicating a contemporary chalcolithic culture corresponding with the other regional cultures. Further, the transformation of early Harappan culture into Harappan culture is datable to around 2500 BCE here, which is nearly 100 years later than the core region. The occupation at Karanpura is not as earlier when compared to sites like Kalibangan, Bhirrana (both on River Ghaggar or Sarasvati), Farmana, Girawad (both on River Drishadvati system). However, the occupation of this site around 2900 BCE and its continuous occupation up to 2100 BCE, demonstrates a long continuous occupation of lower Drishadvati valley, facilitating trade and interactions between the Harappan sites of eastern region with western region.

5.4.26 Diatom assemblages in sediment cores of the deltaic island of the Indian Sundarbans and their palaeoecological significance

Manjushree Mandal[1], Rajveer Sharma[2] and Neera Sen Sarkar[1]

[1]Phycology Section,Department of Botany, University of Kalyani, West Bengal 741235, India
[2]Inter-University Accelerator Centre, Aruna Asaf Ali Marg, New Delhi 110067, India

Sundarbans represents a mangrove ecosystem of tremendous value in terms of its rich biodiversity and strategic position. It is also an extremely vulnerable region owing to changing climatic patterns and ever increasing anthropogenic pressures. It is well established that the effects of such changes remain preserved in sediments as biological proxies. Several works exist on mangrove pollens recovered from sediments of the area to serve as indicators of past ecological history. For the present study diatom frustules, which also deposit well in sediments and are excellent palaeo-ecological indicators [1-4] were used as tools for analysing environmental changes and unravelling ecological history of the Indian Sundarbans. Many researchers have contributed to the increased value of fossil diatoms as indicators, making possible the reconstruction of a past ecological situation in detail [5-11]. These studies use multivariate techniques to reconstruct palaeoecological condition, such as surface-water temperature [12-14,], air temperature [15], salinity [16-18] and pH [19,20]. All such studies have proven diatom fossils to be immensely efficient ecological indicators.

The present study involved analysis of diatom species assemblages in sediment cores from two characteristically different study sites with emphasis on variation in species composition between the different depths anlaysed. Site-1 at Jharkhali, Sundarbans, has a mature landmass, is under the jurisdiction of the Forest Department, and occasionally gets inundated by river water of the adjoining estuarine river Choto Herobhanga. Site - 2 at Bally, Sundarbans, is a mature landmass inhabited by human population since long, about 100 m away from the influence of the adjoining estuarine river Bidya and, as such, does not get inundated under normal circumstances. Taxonomic enumeration of diatoms from the sediment cores, followed by comparison with diatom species assemblages of present times and use of the sediment core diatoms as indicators of geological periods and the environment were important aspects for the fulfilment of the objectives of this study.

Two sediment cores of 170 cm were collected and segregated into 10 cm interval samples (total 17×2 = 34 samples). Minimum 400 frustules were counted from each depth of the sediment core of each site. Qualitative (identification and taxonomic enumeration using light microscope and SEM) and quantitative (estimation of community and population dynamics indices) analyses were performed. Some important physical (pH, salinity, soil texture analysis) and chemical (Si, Organic-C, NO_2, Available-P) parameters were analysed. ^{14}C dating was performed on sediment samples at selected depths.

A total of 176 diatoms (from Site-1 and Site-2) were identified from the two sediment cores. Total 7 samples (2 samples from Site-1 and 5 samples from Site-2) were selected for ^{14}C dating at IUAC with sample codes: 17C1342, 17C1343, 17C1337, 17C1338, 17C1339, 17C1340 & 17C1341. Also ^{14}C dating of 4 samples (2 depths each from Site-1 and Site-2) were performed earlier at Birbal Sahni Institute of Palaeosciences, Lucknow with sample codes: BS-3934, BS-3935, BS-4017 & BS-4022. ^{14}C age of the depths from Site-1 were 1800±110 yrs BP (of 10-30cm), 3305±36 yrs BP (of 70-80cm), 2258±36 yrs BP (of 110-120cm) and 1800±90 yrs BP (of 140-170cm). In case of Site-2, ^{14}C age of different depths were1370±90 yrs BP (of 10-20cm), 6312±54 yrs BP (of 40-50cm), 5158±48 yrs BP (of 60-70cm), 5704±47 yrs BP (of 90-100cm), 4936±45 yrs BP (of 120-130cm), 4283±43 yrs BP (of 140-150cm) and 1500±120 yrs BP (of 140-170cm).

The chronology of both the cores suggests age reversals and sediment disturbance primarily owing to anthropogenic interference and also consequence of natural attributes of the system. Thus the sediment core collected from Site-1 yielded an age reversal on depth gradient with the oldest layer at 70 – 80 cm 3305±36 yrs BP) and the near-modern sample at depth 140 – 170 cm 1800±90 yrs BP). Even though in a disturbed state, the chronology of the depth layers could be used for mid to late Holocene scale analysis. The depth layer 70 – 80 cm was found to be interesting in terms of its diatom species assemblage as well. The species *Coscinodiscus argus,* abundant in all the other depths, was not found in this layer. The absence of *Coscinodiscus argus,* a very common planktonic form, is attributed to eutrophication. Instead *Rhopalodia musculus* was found to be dominant in this layer, which is usually known to be indicative of oligotrophic conditions. The sediment core collected from Site-2 was again a highly disturbed core in terms of its age with age reversal owing to sediment disturbance. Nevertheless, the entirety of this core, from 6312±54 yrs BP to modern times, appears chronologically robust for paleoenvironmental analysis. The layer at depth 40 – 50 cm, dated as the oldest layer was interesting in terms of its diatom frustule yield since the maximum number of frustules were encountered in this particular layer were of *Staurosira venter,* a species not reported in any of the other layers of the entire sediment core. The presence of *Eunotia pectinalis* in layers 110 – 140 cm (dated ~4283 to 4936 cal. BP) indicates lowered pH during the period, similarly, the slow reduction of *Eunotia pectinalis* from more recent sediments suggest increased deforestation leading to elevated pH in the region. A decline in Eunotia pectinalis in all the layers was found to be associated with increase in *Gomphonema parvulum,* which turns competitive in raised nutrient environments.

This work is the first attempt to study the past diatom flora of the Indian Sundarbans. Future study in the same line will be helpful to find information regarding the genesis of the Indian Sundarbans area and its probable future trend under the influence of climate change. We are thankful to IUAC for providing us this opportunity to initiate this work.

REFERENCES

1. C. G. Ehrenberg, Leiipzig **1,** 374 (1854).
2. P. S. Conger, American Journal of Science **237,** 324 (1939).
3. E. F. Stoermer and J. J. Yang, Proc. 11th Conf. Great Lakes Res., pp. **253** (1968).
4. Battarbee R.W. et al., Diatoms. In: Smol J.P., Birks H.J.B., Last W.M., Bradley R.S., Alverson K. (eds) Tracking Environmental Change Using Lake Sediments. Developments in Paleoenvironmental Research, vol 3. Springer, Dordrecht (2002).
5. F. Hustedt, Arch. Hydrobiol. Suppl. **15,** 131 (1937).
6. J. Petersen, K. danske Vid. Selsk, Biol. Medd. Kobenhavn. **17,** 1 (1943).
7. N. Foged, Folia Limnologica Scandinavica **6,** 7 (1954).
8. B. Douglas, The Journal of Ecology **46,** 295 (1958).
9. L. H. Crosby and E. F. Wood, Trans. R. Soc. NZ **86,** 1 (1959).
10. E. Fjerdingstad, International Review of Hydrobiology **50,** 475 (1965).
11. D. J. Mohan, Current Science **58,** 294 (1989).
12. W. Vyverman and K. Sabbe, Journal of Paleolimnology **13,** 65 (1995).
13. P. Rosén. U. Segerström. L. Eriksson. I. Renberg and H. Birks, The Holocene **11,** 551 (2001).
14. C. Bigler and R. I. Hall, Journal of Paleolimnology **27,** 97 (2002).
15. K. A. Koinig, C. Kamenik, R. Schmidt, A. Agustí-Panareda et al., Journal of Paleolimnology **28,** 147 (2002).
16. S. C. Fritz, S. Juggins, R. W. Battarbee and D. R. Engstrom, Nature **352,** 706 (1991).
17. K. R. Laird, S. C. Fritz, E. C. Grimm and P. G. Mueller, Limnology and Oceanography **41,** 890 (1996).
18. F. Gasse, P. Barker, P. A. Gell, S. C. Fritz and F. Chalie, Quaternary Science Review **16,** 547 (1997).
19. R. Psenner and R. Schmidt, Nature **356,** 781 (1992).
20. K. A. Koinig, R. Schmidt and S. Wokgrath, Water, Air, and Soil Pollution **104,** 167 (1998).

6. ACADEMIC ACTIVITIES

6.1 BEAM UTILIZATION BY USERS

6.1.1 LEIBF (Positive & Negative Ion) Beam Time Utilization and Experiments performed (April, 2017 to March, 2018)

Users	No. of Shifts used (1 Shift =8Hrs.)	Project in	
		Materials Science	Atomic Physics
A. Universities/Colleges			
Amity University, Noida	12	2	
Central University of Haryana, Mahendragarh	6	1	
Chaudhary Charan Singh University, Meerut	12	1	
Gautam Buddha University, Greater Noida	2	1	
Guru Nanak Dev University, Amritsar	8	3	
Jamia Millia Islamia University, New Delhi	18	2	1
Jawaharlal Nehru University, Delhi	9	3	
National University of Singapur, Singapur	4	1	
Panjab University, Chandigarh	12	1	
Rashtrasant Tukadoji Maharaj Nagpur University, Nagpur	3	1	
Shiv Nadar University, Uttar Pradash	6	1	
Shivaji University, Kolhapur	2	1	
Tezpur University, Tezpur	15	2	
The Maharaja Sayajirao University of Baroda, Vadodara	4	1	
University and Petroleum & Energy Studies, Dehradun	1	1	
University of Calcutta, Kolkata	12	1	
University of Delhi, Delhi	3	1	
University of Mumbai, Mumbai	6	1	
B. Institutions			
All India Institute of Medical Sciences, New Delhi	3	1	
Bhabha Atomic Research Centre, Mumbai	11	2	
Dayalbagh Educational Institute, Agra	6	1	
Deen Dayal Upadhyaya College, Delhi	3	1	
Defence Research & Development Organ., Delhi	3	1	
Indian Association for the Cultivation of Science	4	1	
Indian Institute of Technology, Hyderabad	3	1	
Indian Institute of Technology, Roorkee	3	1	
Institute of Physics, Bhubaneswar	12	2	
Inter-University Accelerator Centre, New Delhi	24	4	2
IUC-DAEF, Indore Centre, Indore	2	1	
Malaviya National Institute of Technology, Jaipur	9	3	
UGC-DAE-CSR, Kolkata	3	1	
C. Facility Tests	**3**		**1**
TOTAL	**224**	**45**	**4**

6.1.2 Pelletron Beam Time Utilization and Experiments performed (April, 2017 to March, 2018)

Users	No. of Shifts Used (1 Shift= 8 Hrs.)	Project in				
		Nuclear Physics	Materials Science	Radiation Biology	Atomic Physics	AMS
A. Universities/Colleges						
Andhra University, Waltair	81	4				
Anna University, Chennai	28					1
Archaeological Survey of India, Delhi	41					2
Banaras Hindu University (BHU), Varanasi	1			1		
Calicut University, Calicut	15	1				
Central University of Jharkhand, Ranchi	15	1				
Central University of Kerala, Kerala	72	3				
Central University of Rajasthan, Rajasthan	3		1			
Devi Ahilya University (DAU), Indore	3		1			
Guru Gobind Singh Indraprastha University, New Delhi	4		1			
HIL, University of Warsaw, Poland	24	1				
Jawaharlal Nehru University, New Delhi	39		2			2
Karnataka University, Dharwad	17	1				
Kurukshetra University, Kurukshetra	41	1	1			1
Mahatma Jyotiba Phule Rohilkhand University, Bareilly	15	1				
Manav Rachna International University, Faridabad	1		1			
Mangalore University, Mangalore	21					1
Nanyang Technological University, Singapore	40					1
North Orissa University, Odisha	4		1			
Panjab University, Chandigarh	72	6	1			
Punjabi University, Patiala	3		1			
Ravenshaw University, Cuttack	14					1
Saurashtra University, Rajkot	7		3			
Tezpur University, Tezpur	6		2			
The Maharaja Sayajirao University of Baroda, Vadodara	30					1
University of Calcutta, Kolkata	26					2
University of Delhi, Delhi	99	4	2			2
University of Kalyani, Kalyani	10			1		1
University at Lucknow, Lucknow	20					1
University of Madras, Chennai	6					1

Users	No. of Shifts Used (1 Shift= 8 Hrs.)	Project in				
		Nuclear Physics	Materials Science	Radiation Biology	Atomic Physics	AMS
University of Mysore, Mysore	3		1			
Utkal University, Bhubaneswar	3		1			
B. Institutions						
Birbal Sahni Institute of Palaeobotany, Lucknow	8					1
GANLC, France	21	1				
Indian Institute of Technology-BHU, Varanasi	3		1			
Indian Institute of Technology Delhi, New Delhi	4		1			
Indian Institute of Technology Gandhinagar, Palaj	45					2
Indian Institute of Technology, Kanpur	20					1
Indian Institute of Technology, Roorkee	46	1				1
Indian Institute of Technology, Ropar	27	1				
Indian Institute of Tropical Meteorology, Pune	28					1
Indian Space Research Organisation, Bangalore	3	1				
Inter-University Accelerator Centre, New Delhi	73	1	3			1
JNCASR, Bangalore	15					1
Malaviya National Institute of Technology, Jaipur	3		1			
National Institute for Material Sciences, Japan	3		1			
National Institute of Oceanography, Goa	20					1
National Institute of Technology, Kurukshetra	3		1			
National Institute of Technology, Rourkela	3		1			
Saha Institute of Nuclear Physics, Kolkata	14	1				
U.N.(Auto)College of Science and Technology Adaspur, Cuttack	3		1			
Variable Energy Cyclotron Centre, Kolkata	12	1				
Wadia Institute of Himalayan Geology, Dehradun	31					2
C. Facility Tests	**2**	**1**				
TOTAL	**1151**	**31**	**29**	**2**	**0**	**28**

6.1.3 List of Users Family

The following list includes Universities/Colleges/Institutions that have used the IUAC Pelletron facility (once or more) since 1991.

(A) UNIVERSITIES - (126)

1.	Acharya Nagarjuna University	Andhra Pradesh
2.	Alagappa University	Karaikudi
3.	Aligarh Muslim University	Aligarh
4.	Amity University	Noida
5.	Andhra University	Waltair
6.	Anna University	Chennai
7.	Assam University	Silchar
8.	Babasaheb Bhimrao Ambedkar University	Lucknow
9.	Banaras Hindu University	Varanasi
10.	Bangalore University	Bangalore
11.	Berhampur University	Berhampur
12.	Bharathiar University	Coimbatore
13.	Bharathidasan University	Tiruchirappalli
14.	Bhavnagar University	Bhavnagar
15.	Calicut University	Calicut
16.	Central University of Haryana	Mahendragarh
17.	Central University of Jharkhand	Ranchi
18.	Central University of Kerala	Kerala
19.	Central University of Rajasthan	Rajasthan
20.	Central University of South Bihar	Bihar
21.	Chaudhary Charan Singh University	Meerut
22.	Chaudhary Devi Lal University	Sirsa
23.	Cochin University of Science & Technology	Cochin
24.	Darmstadt University of Technology	Darmstadt, Germany
25.	Deenbandhu Chhotu Ram Univ. of Science and Technology	Sonipat
26.	Delhi Technological University	Delhi
27.	Devi Ahilya University	Indore
28.	Dr. Babasaheb Ambedkar Marathwada University	Aurangabad
29.	Dr. Bhim Rao Ambedkar University (Agra University)	Agra
30.	Doon University	Dehradun
31.	Gauhati University	Guwahati

32.	Gautam Buddha University	Greater Noida
33.	Goa University	Goa
34.	Govind Ballabh Pant Univ. of Agriculture and Technology	Pantnagar
35.	Gujarat Technological University	Gujarat
36.	Gujarat University	Ahmedabad
37.	Gulbarga University	Gulbarga
38.	Guru Ghasidas Vishwavidyalaya	Bilaspur
39.	Guru Gobind Singh Indraprastha University	New Delhi
40.	Guru Jambheshwar University of Science & Technology	Hisar
41.	Guru Nanak Dev University	Amritsar
42.	Hemwati Nandan Bahuguna Garhwal University	Srinagar, Garhwal
43.	Himachal Pradesh University	Simla
44.	Indira Gandhi National Open University	New Delhi
45.	Indira Gandhi University Meerpur	Haryana
46.	I.K. Gujral Punjab Technical University	Punjab
47.	Jai Prakash Vishwavidyalaya	Chapra
48.	Jamia Millia Islamia University	New Delhi
49.	Jawaharlal Nehru University	Delhi
50.	Karnataka University	Dharwad
51.	Kiel University	Germany
52.	Kolhan University	Chaibasa
53.	Kurukshetra University	Kurukshetra
54.	Kuvempu University	Shankaraghatta, Shimoga
55.	K.R. Mangalam University	Gurgaon
56.	Ludwig-Maximilians-Universität München	Germany
57.	Madurai Kamaraj University	Madurai
58.	Maharshi Dayanand University	Rohtak
59.	Maharishi Markandeshwar University	Ambala
60.	Mahatma Gandhi University	Kottayam
61.	Mahatma Jyotiba Phule Rohilkhand University	Bareilly
62.	Manav Rachna International University	Faridabad
63.	Mangalore University	Mangalore
64.	Manipur University	Imphal
65.	Manonmaniam Sundaranar University	Tirunelveli
66.	Marwadi University	Gujarat
67.	Mohanlal Sukhadia University	Udaipur

68.	Nirma University	Gujarat
69.	North Carolina State University	Raleigh, USA
70.	North-Eastern Hill University	Shillong
71.	North Maharashtra University	Jalgaon
72.	North Orissa University	Baripada
73.	Osaka University	Japan
74.	Osmania University	Hyderabad
75.	Panjab University	Chandigarh
76.	Patna University	Patna
77.	Periyar University	Chennai
78.	Pondicherry University	Pondicherry
79.	Punjab Agricultural University	Ludhiana
80.	Punjabi University	Patiala
81.	P.E.S. Institute of Technology	Bangalore
82.	Rani Durgavati Vishwavidyalaya	Jabalpur
83.	Rashtrasant Tukadoji Maharaj Nagpur University	Nagpur
84.	Ravenshaw University	Cuttack
85.	Sabanci University	Turkey
86.	Saint Petersburg Polytechnic University	Russia
87.	Saurashtra University	Rajkot
88.	Savitribai Phule Pune University	Pune
89.	Sharda University	Noida
90.	Sheffield Hallam University	Sheffield, UK
91.	Shiv Nadar University	Uttar Pradash
92.	Shivaji University	Kolhapur
93.	Shri Mata Vaishno Devi University	Katra
94.	Sikkim University	Sikkim
95.	Sri Krishnadevaraya University	Anantapur
96.	Tamil University	Thanjavur
97.	Tezpur University	Tezpur
98.	The Maharaja Sayajirao University of Baroda	Vadodara
99.	The University of Burdwan	Burdwan
100.	The University of Sheffield	Sheffield
101.	Tilka Manjhi Bhagalpur University	Bhagalpur
102.	Tumkur University	Tumkur
103.	University and Petroleum & Energy Studies	Dehradun

104.	University of Allahabad	Allahabad
105.	University of Calcutta	Kolkata
106.	University of Delhi	Delhi
107.	University of Hyderabad	Hyderabad
108.	University of Jammu	Jammu
109.	University of Kalyani	Kalyani
110.	University of Kashmir	Srinagar
111.	University at Lucknow	Lucknow
112.	University of Madras	Chennai
113.	University of Maryland	Maryland, USA
114.	University of Mumbai	Mumbai
115.	University of Mysore	Mysuru
116.	University of Notre Dame	Notre Dame, USA
117.	University of Padova	Italy
118.	University of Pune	Pune
119.	University of Rajasthan	Jaipur
120.	University of Stuttgart	Germany
121.	University of Surrey	Guildford, UK
122.	University of Warsaw	Poland
123.	Utkal University	Bhubaneswar
124.	Vikram University	Ujjain
125.	Vishwa Bharti University	Bolpur
126.	West Bengal University of Technology	Kolkata

(B) COLLEGES - (72)

1.	Anand International College of Engineering	Rajasthan
2.	Ananda Mohan College	Kolkata
3.	Armed Forces Medical College	Pune
4.	Bareilly College	Bareilly
5.	Beant College of Engineering & Technology	Gurdaspur
6.	Bharatiya Jain Sanghatana College	Pune
7.	Bhiwandi College	Mumbai
8.	B.N.N. College	Bhiwandi
9.	College of Engineering and Technology	Aligarh

10.	Doodhsakhar Mahavidyalaya	Bidri, Maharashtra
11.	Dum Dum Motijheel College	Kolkata
12.	D.A.V. College	Amritsar
13.	D.A.V. College	Jalandhar
14.	D.A.V. College	Kanpur
15.	D.A.V. College	Mumbai
16.	D.B.S. College	Dehradun
17.	Ewing Christian College	Allahabad
18.	Gandhi Faiz-E-Aam (Post Graduate) College	Shahjahanpur
19.	Goalpara College	Goalpara, Assam
20.	Government Art College	Rajahmundry, AP
21.	Government College	Ajmer
22.	Government College	Kota
23.	Government College	Mahendragarh, Haryana
24.	Guru Nanak Girls College	Ludhiana (PNJ)
25.	Gurudas College	Kolkata
26.	Iswar Chandra Vidyasagar College (formerly Belonia College)	Belonia, Tripura
27.	Jai Hind College	Mumbai
28.	Kalindi College	New Delhi
29.	Kalinga Institute of Industrial Technology	Bhubaneswar
30.	Kandi Raj College	Murshidabad, (WB)
31.	Kishinchand Chellaram College	Mumbai
32.	Kongunadu Arts & Science College	Coimbatore
33.	Koshi College	Khagaria, Bihar
34.	Krishnath College	West Bengal
35.	K.J. Somaiya College of Science & Commerce	Mumbai
36.	Lalbaba College	Kolkata
37.	Maharajah's Post Graduate College	Vizianagaram
38.	Maharani Shri Jaya College	Bharatpur
39.	Mahila Degree College	Lucknow
40.	Marwari College	Ranchi
41.	M.M.H. College	Ghaziabad
42.	Nayagarh College	Nayagarh
43.	Nizam College	Hyderabad
44.	N.S.A.M. College	Mangaluru
45.	Orissa University of Agriculture and Technology	Bhubaneswar

46.	Poorna Prajna College	Karnataka
47.	Punjab Engineering College	Chandigarh
48.	Raja Balwant Singh College	Agra
49.	R.D. & D.J. College	Bihar
50.	R.P.G. College	Ratnagiri
51.	Sanatan Dharma College	Ambala Cantt
52.	School of Physical Sciences	Nanded, Maharashtra
53.	School of Technology & Applied Sciences	Kottayam, Kerala
54.	Sharanabasaveshwar College of Science	Gulbarga
55.	Shri Varshney College	Aligarh
56.	Shri Venkateswara College	Delhi
57.	Smt. Chandibai Himathmal Mansukhani College	Ulhasnagar, Maharashtra
58.	Sree Narayana College	Kollam
59.	Sri Bhuvanendra College	Karkala
60.	Sri S. Ramasamy Naidu Memorial College	Madurai
61.	St. Edmunds College	Shillong
62.	St. Xavier's College	Kolkata
63.	St. Xavier's College	Mumbai
64.	Swami Shraddhanand College	New Delhi
65.	S.D.M. College	Ujire, Mysore
66.	S.S. Jain Subodh (PG) College	Jaipur
67.	University College	Kurukshetra
68.	University College of Science & Technology	Kolkata
69.	Vaish College	Rohtak
70.	Vardhman College	Bijnor
72.	Zakir Husain College	Delhi

(C) OTHER INSTITUTIONS – (111)

1.	All India Institute of Medical Sciences	New Delhi
2.	Amity Institute of Nanotechnology	Noida
3.	Amity School of Engineering	New Delhi
4.	Amrita School of Engineering	Bangalore
5.	Amrita Vishwa Vidyapeetham	Bangaluru
6.	Archaeological Survey of India	Agra

7.	Archaeological Survey of India,	Janpath, Delhi
8.	Archaeological Survey of India	Red Fort Complex, Delhi
9.	Archaeological Survey of India	Vadodara
10.	Atal Bihari Vajpayee Indian Inst. of Info. Tech. & Management	Gwalior
11.	AFM/XPS Laboratory	Bhubaneswar
12.	AICTE	New Delhi
13.	Bangabasi Morning College	Kolkata
14.	Bhabha Atomic Research Centre	Mumbai
15.	Birbal Sahni Institute of Palaeobotany	Lucknow
16.	Birla Institute of Technology	Jharkhand
17.	Bose Institute	Kolkata
18.	Calcutta Institute of Engineering and Management	Kolkatta
19.	Central Electronics Engineering Research Institute	Pilani
20.	Centre for Cellular and Molecular Biology	Hyderabad
21.	Centre for Superconductivity research	USA
22.	CAT	Indore
23.	CSNSM, Orsay Cedex	France
24.	Dayalbagh Educational Institute	Agra
25.	Deccan College Post-Graduate & Research Institute	Pune
26.	Defence Laboratory	Jodhpur
27.	Defence Metallurgical Research Laboratory	Hyderabad
28.	Defence Research & Development Organ.	Dehradun
29.	Dr. B.R. Ambedkar National Institutes of Technology	Jalandhar
30.	Flerov Laboratory of Nuclear Reactions	Russia
31.	Genetic Institute of Manufacturing Technology	Singapore
32.	GSI	Germany
33.	Harcourt Butler Technological Institute	Kanpur
34.	Homi Bhabha National Institute	Kolkata
35.	Indian Association for the Cultivation of Science	Kolkata
36.	Indian Institute of Engineering Science and Technology, Shibpur	West Bengal
37.	Indian Institute of Information Technology	Allahabad
38.	Indian Institute of Science	Bangalore
39.	Indian Institute of Science Education and Research	Kolkata
40.	Indian Institute of Space Science and Technology	Trivandrum
41.	Indian Institute of Technology	Kanpur
42.	Indian Institute of Technology	Kharagpur

43.	Indian Institute of Technology	Madras
44.	Indian Institute of Technology	Rajasthan
45.	Indian Institute of Technology	Roorkee
46.	Indian Institute of Technology-BHU	Varanasi
47.	Indian Institute of Technology Bhubaneswar	Odisha
48.	Indian Institute of Technology Bombay	Mumbai
49.	Indian Institute of Technology Delhi	New Delhi
50.	Indian Institute of Tropical Meteorology	Pune
51.	Indian School of Mines	Dhanbad
52.	Indian Space Research Organisation	Bangalore
53.	Indira Gandhi Centre for Atomic Research	Kalpakkam
54.	Institute for Plasma Research	Gandhinagar
55.	Institute of Basic Sciences	Agra
56.	Institute of Energy and Climate Research	Germany
57.	Institute of Materials Science	Bhubaneswar
58.	Institute of Minerals and Materials Technology	Bhubaneswar
59.	Institute of Nuclear Medicine & Allied Sciences	New Delhi
60.	Institute of Physics	Bhubaneswar
61.	Institute of Science	Mumbai
62.	International Centre for Genetic Engineering and Biotechnology	New Delhi
63.	INFN-LEGNARO	Italy
64.	INMAS	New Delhi
65.	IUC-DAEF, Calcutta Centre	Kolkata
66.	IUC-DAEF, Indore Centre	Indore
67.	Jaypee Institute of Information Technology	Noida
68.	Jawaharlal Nehru Centre for Advanced Scientific Research	Bengaluru
69.	Joint Institute of Nuclear Research	Dubna, Russia
70.	Malaviya National Institute of Technology	Jaipur
71.	Massachusetts Inst. of Technology	USA
72.	Maulana Azad National Institute of Technology	Bhopal
73.	Ministry of Defence (R & D Orgn)	Delhi
74.	Motilal Nehru National Institute of Technology	Allahabad
75.	Nanocrystals Technology	USA
76.	National Academy of Science	Allahabad
77.	National Centre for Antarctic and Ocean Research	Goa
78.	National Institute of Material Sciences	Japan

79.	National Institute of Oceanography	Goa
80.	National Institute of Science Education and Research	Bhubaneswar
81.	Indian Institute of Science Education and Research	Pune
82.	National Institute of Technology	Hamirpur, HP
83.	National Institute of Technology	Jalandhar
84.	National Institute of Technology	Kurukshetra
85.	National Institute of Technology	Rourkela
86.	National Institute of Technology	Silchar
87.	National Institute of Technology	Srinagar
88.	National Institute of Technology	Tiruchirapalli
89.	National Museum	New Delhi
90.	National Physical Laboratory	New Delhi
91.	NCCCM/BARC	Hyderabad
92.	NCSR	France
93.	Oak Ridge National Laboratory	USA
94	Physical Research Laboratory	Ahmedabad
95.	PDPM Indian Inst of Info. Tech. Design & Manufacturing	Jabalpur
96.	Research Centre Imarat (RCI), DRDO	Hyderabad
97.	Saha Institute of Nuclear Physics	Kolkata
98.	Sant Longowal Institute of Engineering & Technology	Sangrur (Punjab)
99.	Semi-Conductor Laboratory	Mohali
100.	Shree Devi Institute of Technology	Mangaluru
101.	Solid State Physics Laboratory, DRDO	Delhi
102.	SUNAG Laboratory	Odisha
103.	Tata Institute of Fundamental Research	Mumbai
104.	Thapar Institute of Engineering & Technology (Thapar University)	Patiala
105.	UM-DAC Centre for Excellence in Basic Sciences	Mumbai
106.	Variable Energy Cyclotron Centre	Kolkata
107.	Vidya Prasarak Mandal's Polytechnic	Maharashtra
108.	Visva-Bharati	Santiniketan
109.	Wadia Institute of Himalayan Geology	Dehradun

6.2 STUDENT PROGRAMMES

6.2.1 IUAC Summer Programme 2017 for B.Sc. (Physics) Students

Subir Nath

The Summer Programme 2017 for B. Sc. (Physics) students was held at IUAC from June 05 – 30, 2017. The aim of the programme was to expose young students to research opportunities in experimental physics and impart hands-on training to them by scientists of IUAC. Online applications were invited from students studying in second / third year of B.Sc. or integrated M.Sc. courses with specialization in physics. Thirteen students were selected for participation in the Summer Programme who was provided with travel support, boarding and lodging. Each student was assigned an experimental project under the supervision of a scientist of IUAC. In the last week of the Programme, upon completion of the assigned project, each participant submitted a report on the work carried out and made a presentation. Ms. C. Namitha from Sardar Vallabhbhai National Institute of Technology, Surat, Gujarat won the award for the best project presentation. Ten special lectures were arranged to make the participants familiar with research opportunities in the fields of accelerator-based basic sciences at IUAC and elsewhere. Guided tours of accelerators and experimental facilities of IUAC were also arranged for the students.

Summer Students, 2017

6.2.2 M. Sc. Orientation Programme

R Mehta

Inter-University Accelerator Centre (IUAC) conducts M. Sc. Orientation Programme to encourage interested students to supplement their knowledge and to motivate them to continue their career in science. This programme has been envisaged to provide hands-on training in fields associated with accelerator / ion beam based research to selected M. Sc. students by way of short projects. The duration of M. Sc. Orientation programme is three weeks. It is open throughout the year. Student can apply for this programme based on their convenient time. Applications can be submitted online only. This flexibility allows the students to choose the project period without hampering their main study course. Following students participated in this programe.

S.No.	Name	Affiliation
1	Ayushi Tyagi	JMI, New Delhi
2	Anand Babu	M J P Rohilkhnd University, Bareilly
3	Manasa G B	University of Mysore
4	Ms Rashmi Choudhary	Banasthali University
5	Ms Eram Khan	Andhra University
6	Ms Madhuri Padole	DAVV Indore
7	Ms Avani Sharma	DAVV Indore
8	Ms Jyoti Sheoran	IIT(ISM) Dhanbad

S.No.	Name	Affiliation
9	Ashwani Yadav	DU
10	Siddharth Ghosh	NIT, Meghalaya
11	Ms Gaba Meenal	Panjab University
13	Ms Deep Shikha	JMI, New Delhi
14	Mr Abhishek Darmora	Govt. P G College , Uttarakhand
15	Ms Seema Pant	HNBG University
16	Mr Hemant Arora	Panjab University
17	Arjun Batra	Guru Nanak Dev University
18	Ms Vrinda Garg	Delhi University
19	Mr Ashwini Udgata	Pondicherry University

Details of this programme can be accessed at: http://www.iuac.res.in/sc/msc/index.html

Online Application Portal: http://www.iuac.res.in/indico/event/mscop

6.2.3 PhD Teaching Programme

P. N. Prakash and P. Sugathan

The two semester Ph.D teaching programme for the research students of IUAC, research students from other universities and new trainee scientists of IUAC, continued during the past academic year. The programme has been receiving excellent response from students belonging to different universities. The programme consists of two semesters – the first semester, held during August-December, offers courses in Advanced Physics, Computational Techniques, and Experimental Physics, while the second semester, held during January-May, offers courses in Advanced Condensed Matter Physics, Advanced Nuclear Physics, Accelerator Physics, and Research Methodology.

The courses on Advanced Classical & Quantum Mechanics, Experimental Physics, Advanced Condensed Matter Physics, Advanced Nuclear Physics and Accelerator Physics are each 3 credit point courses. The course on Research Methodology, which includes the course on Computational Techniques, is 4 credit points course, while the course on Statistical Physics is 2 credit points course.

About a month before the semester commences, a poster containing details of the course modules, schedule etc. is uploaded on the IUAC website. The printed version of the poster is sent to the physics departments of various universities and colleges for inviting applications from research scholars and interested faculty members who are pursuing their PhD degree in physics. Accommodation and TA/DA is provided to the selected participants.

6.2.4 Teaching Laboratory Activities

Ajith Kumar B P. & V V V Satyanarayana

As a part of IUAC's outreach program, we develop computer interfaced laboratory equipment and train teachers in modern experimental data acquisition and analysis methods. An open source design of a general purpose computer interface was absorbed and released in 2017; it is named as ExpEYES-17. The details of the device are at http://www.iuac.res.in/~elab/phoenix/expeyes/index.html. A photograph of the new device is shown below.

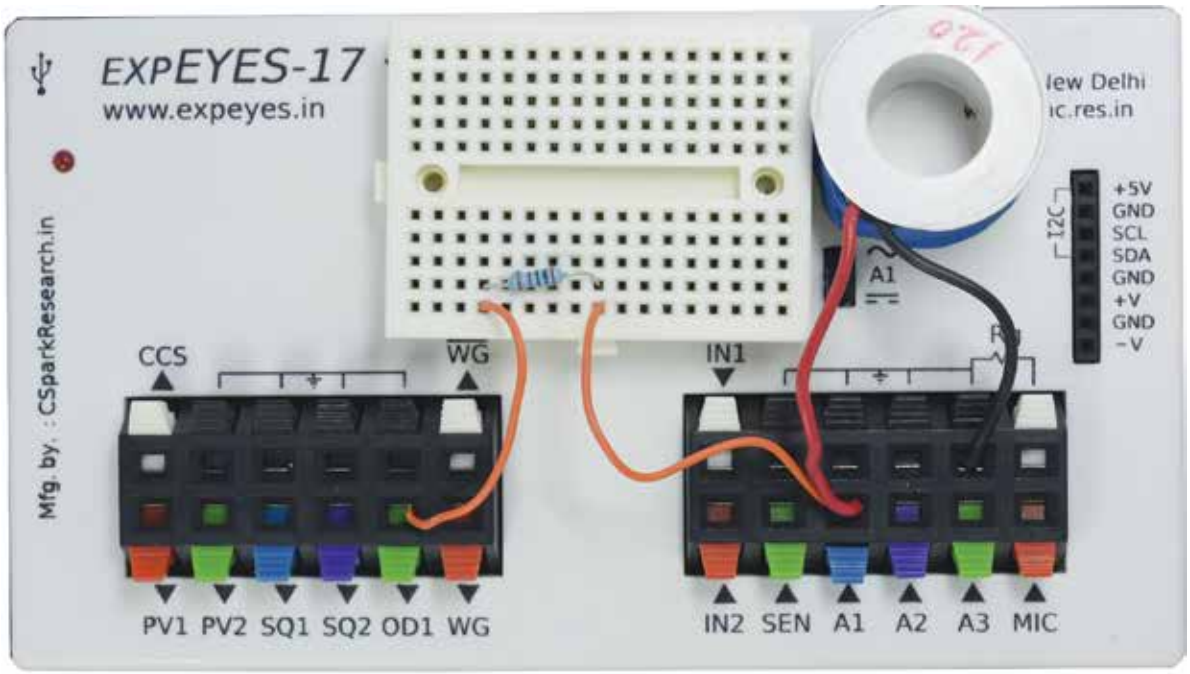

Every six months, IUAC conduct a "One week training program on computer interfaced science experiments", for college teachers, nearly ten programs were conducted last year at different places. This project has attracted the attention of the academic community in India and abroad. The device was presented in a meeting of International Union of Pure and Applied Physics, as a tool for improving the quality of science education in developing countries, with some positive outcome.

6.3 LIBRARY ACTIVITIES

Priyambada Nayak

Salient features

Working hours:	Round the clock, all days of the week
Total Books:	~2898 (broadly covering the subjects Nuclear Physics, Materials Science,Nanotechnology, Electronics, Computer Science, Radio-biology, Radiation Physics, Vacuum Instrumentation, Cryogenics, Atomic Physics, Mathematical Physics, Quantum Mechanics, Astrophysics etc.
Current E-Journals:	> 2500
Bound Journals:	~8500
Laboratory Reports:	~900 (from nearly 50 labs)
Reprints/Photocopies:	~700
Newsletters, House magazines etc.	50
Databooks, Manuals etc.:	~550
Ph.D. Thesis:	168
Clientele:	Apart from IUAC staff and students, the library is consulted by students, teaching and research staff from over 100 academic and research institutions in different parts of the country.

The technical reports and technicals memos of various projects carried out at IUAC are also compiled and kept in the library for reference purpose. Web-based OPAC and library cataloging software package "KOHA" has been used for the computerization of library documents. Apart from the current online journals, Journal archives (AIP, IOP, APS, ACS, Science Direct, Springer, Science, Nature) are also being subscribed by the library. **"Turn-it-in",** the originality check software is being used to prevent plagiarism. **"Web of Science"** is being subscribed by the library and used by the scholars for citation analysis and other purposes. The library is a member of UGC-INFONET Consortium and more than 2500 journals are being accessed on-line through these facilities. The library is open round the clock. Hence, automatic monitoring system has been installed.

6.4 ACADEMIC ACTIVITIES HELD IN 2017-18

7 April, 2017	**Acquaintance Programme at Visva Bharati, Santiniketan** (Contact Person : S. Muralithar)
10 April, 2017	**Acquaintance Programme at Central University of Himachal Pradesh, Dharamshala** (Contact Person : P. Sugathan)
1-6 May, 2017	**Training Program on Computer Interfaced Science Experiments** (Contact Persons : Ajith Kumar B.P./V.V.V.Satyanarayana)
5-30 June, 2017	**Summer Programme for B.Sc. (Physics) Students** (Contact Person : Subir Nath)
5-7 July, 2017	**Users Workshop**
8 July, 2017	**62nd AUC Meeting**
7-11 August, 2017	**Workshop on Instrumentation & Control using Open Technologies** (Contact Person : Ajith Kumar B.P.)
16-18 August, 2017	**IUAC Academic Workshop** (Contact Person : P. Sugathan)
21 August, 2017	**Ph.D Programme : Fall Semester starts** (Contact Person : P.N. Prakash)
4-9 September, 2017	**School on Characterization of Materials** (Contact Persons : K. Asokan / Fouran Singh)
11 September, 2017	**Acquaintance Programme at Karnatak University, Dharwad** (Contact Person : N. Madhavan)
14-15 September, 2017	**Workshop on INGA Experiments** (Contact Person : S. Muralithar)

20-22 September, 2017	**Workshop on Superconducting Radio Frequency Science & Technology** (Contact Person : P.N. Prakash)
4-7 October, 2017	**International Conference on Nanostructuring with Ion Beams** (Contact Person : A. Tripathi)
9-14 October, 2017	**Training Program on Computer Interfaced Science Experiments** (Contact Persons : Ajith Kumar B.P. /V.V.V.Satyanarayana)
October 30- November 4, 2017	**School on Nuclear Reactions** (Contact Persons : Akhil Jhingan /Subir Nath)
16-17 November, 2017	**Workshop on Geochronology** (Contact Person : S. Chopra)
16-18 December, 2017	**Users Workshop**
19 December, 2017	**Foundation Day Programme & 63rd AUC Meeting**
22 January, 2018	**PhD Programme : Spring Semester starts** (Contact Person : P.N. Prakash)
22-23 February, 2018	**IUAC Academic Workshop** (Contact Person : P. Sugathan)
28 February, 2018	**National Science Day** (Contact Person : Saif A. Khan)
6-9 March, 2018	**International School on Electron Accelerators, Free Electron Laser & Applications of Electron Beams/THz Radiation** (Contact Person : Subhendu Ghosh)
26 March, 2018	**Acquaintance Programme at Central University of Jammu, Jammu** (Contact Person : A. Tripathi)

6.5 FORTHCOMING EVENTS: 2018

30-May 5, 2018	**Training Programme on Computer interfaced Science Experiments** (Contact Person : Ajith Kumar B.P./V.V.V. Satyanarayana)

7-18 May, 2018	**School on Accelerator Science & Technology** (Contact Person : Rajeev Mehta)
4-29 June, 2018	**Summer Programme for B.Sc. (Physics) Students** (Contact Person : G.O. Rodrigues)
5-7 July, 2018	**Users Workshop**
8 July, 2018	**64th AUC Meeting**
12-18 July, 2018	**International School on Ion Beams in Energy Materials** (Contact Person : P.K. Kulriya/Fouran Singh)
13-14, 16 August, 2018	**IUAC Academic Workshop** (Contact Person : P. Sugathan)
20 August, 2018	**PhD Programme : Fall Semeser starts** (Contact Person : P.N. Prakash)
7 September, 2018	**Acquaintance Programme at Lucknow University, Lucknow** (Contact Person : R.P. Singh)
24-29 September, 2018	**Training Programme on Computer Interfaced Science Experiments** (Contact Person : Ajith Kumar B.P./V.V.V. Satyanarayana)
3-7 October, 2018	**International School on Ion Beams in Materials Science** (Contact Person : I. Sulania/A. Tripathi)
9-12 October, 2018	**International Conference on Ion Beams in Materials Engineering and Characterization** (Contact Person : S.A. Khan/A. Tripathi)
29 October, 2018	**Acquaintance Programme at Central University of Kerala, Kasaragod** (Contact Person : Subir Nath)
12-16 November, 2018	**School on Modern Techniques in Nuclear Structure Studies** (Contact Person : R.P. Singh/.S. Muralithar)
16-18 December, 2018	**Users Workshop**
19 December, 2018	**Foundation Day Programme & 65th AUC Meeting**

6.6 LIST OF PH.D AWARDEES

The following scholars have completed the Ph.D thesis work during 2017-18

- **Rakesh Kumar Dubey,** Thesis title: " Study of fission dynamics in heavy mass regions"
- **T Sairam,** Thesis title: " Ion induced Molecular Dynamics"
- **Tathagata Banerjee,** Thesis title: " Systematic Study of PCN in Pre-actinides"
- **B. K. Sahu,** Thesis title: "New Developments in the control scheme of superconducting niobium Quarter Wave Resonators"
- **V.V. Siva Kumar,** Thesis Title: " Controlled development of nanostructured ZnO and doped ZnO"

6.7 LIST OF PUBLICATIONS IN THE YEAR 2017-18

A. NUCLEAR PHYSICS

1. **Quest for consistent modelling of statistical decay of the compound nucleus,** Tathagata Banerjee, S. Nath and Santanu Pal, *Phys. Lett. B* ***776,*** *163 (2018).*

2. **Study of incomplete fusion reaction dynamics in $^{13}C+^{165}Ho$ system and its dependence on various entrance channel parameters,** S. A. Tali, H. Kumar, M. Afzal Ansari, A. Ali, D. Singh, R. Ali, P. K. Giri, S. B. Linda, S. Parashari, R. Kumar, R. P. Singh and S. Muralithar, *Nucl. Phys. A* ***970,*** *208 (2018).*

3. **Sensitivity of low-energy incomplete fusion to various entrance-channel parameters,** H. Kumar, S. A. Tali, M. Afzal Ansari, D. Singh, R. Ali, K. Kumar, N. P. M. Sathik, A. Ali, S. Parashari, R. Dubey, I. Bala, R. Kumar, R. P. Singh, S. Muralithar, *Eur. Phys. J. A* ***54,*** *47 (2018).*

4. **Spin distribution of evaporation residues formed in complete and incomplete fusion in $^{16}O+^{154}Sm$ system,** D. Singh, S. B. Linda, P. K. Giri, A. Mahato, R. Tripathi, H. Kumar, M. Afzal Ansari, N. P. M. Sathik, R. Ali, R. Kumar, S. Muralithar and R. P. Singh, *Phys. Lett. B* ***774,*** *7 (2017).*

5. **Fission time scale from pre-scission neutron and α multiplicities in the $^{16}O+^{194}Pt$ reaction,** K. Kapoor, S. Verma, P. Sharma, R. Mahajan, N. Kaur, G. Kaur, B. R. Behera, K. P. Singh, A. Kumar, H. Singh, R. Dubey, N. Saneesh, A. Jhingan, P. Sugathan, G. Mohanto, B. K. Nayak, A. Saxena, H. P. Sharma, S. K. Chamoli, I. Mukul and V. Singh, *Phys. Rev. C* ***96,*** *054605 (2017).*

6. **Experimental study of the transfer-induced fission fragment angular distribution in the 6Li+238U reaction,** A. Parihari, G. Mohanto, Gurpreet Kaur, A. Jhingan, K. Mahata, R. G. Thomas, P. C. Rout, E. T. Mirgule, V. V. Desai, B. Srinivasan, C. Joshi, V. Mishra, M. Kushwaha, Shilpi Gupta, D. Sarkar, S. V. Suryanarayana, A. Shrivastava, N. L. Singh, A. Misra, B. K. Nayak and A. Saxena, *Phys. Rev. C* ***96,*** *054613 (2017).*

7. **No evidence of reduced collectivity in Coulomb-excited Sn isotopes,** R. Kumar, M. Saxena, P. Doornenbal, A. Jhingan, A. Banerjee, R. K. Bhowmik, S. Dutt, R. Garg, C. Joshi, V. Mishra, P. J. Napiorkowski, S. Prajapati, P.-A. Söderström, N. Kumar, and H.-J. Wollersheim, *Phys. Rev. C* ***96,*** *054318 (2017).*

8. **Systematic study of low-energy incomplete fusion: Role of entrance channel parameters,** Abhishek Yadav, Pushpendra P. Singh, Mohd. Shuaib, Vijay R. Sharma, Indu Bala, Unnati, Sunita Gupta, D. P. Singh, M. K. Sharma, R. Kumar, S. Murlithar, R. P. Singh, B. P. Singh and R. Prasad, *Phys. Rev. C* ***96,*** *044614 (2017).*

9. **Evaporation residue cross-section measurements for ^{48}Ti-induced reactions,** P. Sharma, B. R. Behera, R. Mahajan, M. Thakur, G. Kaur, K. Kapoor, K. Rani, N. Madhavan, S. Nath, J. Gehlot, R. Dubey, I. Mazumdar, S. M. Patel, M. Dhibar, M. M. Hosamani, Khushboo, N. Kumar, A. Shamlath, G. Mohanto and S. Pal, *Phys. Rev. C* ***96,*** *034613 (2017).*

10. **Relationship between and effect of inelastic excitations and transfer channels on sub-barrier fusion enhancement,** Khushboo, S. Mandal, S. Nath, N. Madhavan, J. Gehlot, A. Jhingan, N. Kumar, T. Banerjee, G. Kaur, K. R. Devi, A. Banerjee, Neelam, T. Varughese, D. Siwal, R. Garg, I. Mukul, M. Saxena, S. Verma, S. Kumar, B. R. Behera and P. Verma, *Phys. Rev. C* ***96,*** *014614 (2017).*

11. **Effect of collective enhancement in level density in the fission of pre-actinides,** Tathagata Banerjee, S. Nath, A. Jhingan, N. Saneesh, M. Kumar, A. Yadav, G. Kaur, R. Dubey, M. Shareef, P. V. Laveen, A. Shamlath, Md. Moin Shaikh, S. Biswas, J. Gehlot, K. S. Golda, P. Sugathan and Santanu Pal, *Phys. Rev. C* ***96,*** *014618 (2017).*

12. **Shape evolution with increasing angular momentum in the ^{66}Ga nucleus,** S. S. Bhattacharjee, R. P. Singh, S. Muralithar, I. Bala, R. Garg, S. Rajbanshi, D. Singh, A. Dhal, M. Kumar Raju, S. Saha, J. Sethi and R. Palit, *Phys. Rev. C* ***95,*** *054330 (2017).*

13. **Fabrication of thin targets for nuclear reaction studies at IUAC,** Tathagata Banerjee, S. R. Abhilash, D. Kabiraj, S. Ojha, G. R. Umapathy, M. Shareef, P. V. Laveen, H. Duggal, R. U. Amarnadh, J. Gehlot, S. Nath and D. Mehta, *Vacuum* ***144,*** *190 (2017).*

14. **Influence of incomplete fusion on complete fusion at energies above the Coulomb barrier,** Mohammad Shuaib, Vijay Raj Sharma, Abhishek Yadav, Manoj Kumar Sharma, Pushpendra P. Singh, Devendra P. Singh, Rakesh Kumar, R. P. Singh, S. Muralithar, B. P. Singh and R. Prasad, *J. Phys. G: Nucl. Part. Phys.* ***44,*** *105108 (2017).*

15. **Observed side feeding in incomplete fusion dynamics in ^{16}O+^{160}Gd reaction at energy ~5.6 MeV/A: Spin distribution measurements,** R. Ali, M. Afzal Ansari, D. Singh, R. Kumar, D. P. Singh, M. K. Sharma, U. Gupta, B. P. Singh, P. D. Shidling, D. Negi, S. Muralithar, R. P. Singh, R. K. Bhowmik, *Nucl. Phys. A* ***968,*** *403 (2017).*

16. **Investigation of incomplete fusion dynamics at energy 4-8 MeV/nucleon,** H. Kumar, S. A. Tali, M. Afzal Ansari, D. Singh, R. Ali, K. Kumar, N. P. M. Sathik, S. Parashari, A. Ali, R. Dubey, I. Bala, R. Kumar, R. P. Singh and S. Muralithar, *Nucl. Phys. A* ***960,*** *53 (2017).*

17. **Lifetime measurements in shape transition nucleus ^{188}Pt,** A. Rohilla, C. K. Gupta, R. P. Singh, S. Muralithar, S. Chakraborty, H. P. Sharma, A. Kumar, I. M. Govil, D. C. Biswas and S. K. Chamoli, *Eur. Phys. J. A* ***53,*** *64 (2017).*

18. **Binary fragmentation based studies for the near super-heavy compound nucleus ^{256}Rf,** M. Thakur, B. R. Behera, R. Mahajan, N. Saneesh, G. Kaur, P. Sharma, R. Dubey, K. Kapoor, A. Yadav, N. Kumar, S. Kumar, K. Rani, P. Sugathan, A. Jhingan, A. Chatterjee, M. B. Chatterjee, S. Mandal, A. Saxena, S. Pal, S. Kailas, A. K. Nasirov and B. Kayumov, *Eur. Phys. J. A* ***53,*** *133 (2017).*

19. **Two-Neutron Alignment in ^{127}Xe,** S. Chakraborty, H. P. Sharma, S. S. Tiwary, C. Majumder, P. K. Prajapati, S. Rai, P. Popli, M. Singh, S. S. Bhattacharjee, R. P. Singh, S. Muralithar, P. Banerjee, S. Ganguly, S. Kumar, A. Kumar and R. Palit, *Braz. J. Phys.* ***47,*** *406 (2017).*

20. **Study of nuclear fusion-fission dynamics in ^{16}O+^{194}Pt reaction,** K. Kapoor, S. Verma, P. Sharma, R. Mahajan, N. Kaur, G. Kaur, B. R. Behera, K. P. Singh, H. Singh, R. Dubey, N. Saneesh, A. Jhingan, P. Sugathan, G. Mohanto, B. K. Nayak, A. Saxena, H. P. Sharma, S. K. Chamoli, I. Mukul and A. Kumar, *AIP Conf. Proc.* ***1852,*** *080005 (2017).*

B. MATERIALS SCIENCE

1. **Facile synthesis of KCl: Sm^{3+} nanophosphor as a new OSL dosimetric material achieved through charge transfer between the defect states,** M. Agarwal, S. K. Garg, K. Asokan, D. Kanjilal, and P. Kumar, *Rsc Advances* ***7,*** *13836 (2017).*

2. **Effect of gamma irradiation on resistive switching of Al/TiO_2/n^+ Si ReRAM,** K. Agashe, N. Sarwade, S. Joshi, M. Thakurdesai, S. Surwase, P. Tirmali, and K. Asokan, *Nuclear Instruments & Methods in Physics Research Section B-Beam Interactions with Materials and Atoms* ***403,*** *38 (2017).*

3. **Enhancement of thermoelectrical performance in Au-ion implanted V_2O_5 thin films,** B. Ahmad, R. Meena, P. Kumar, R. Ahmed, M. Hussain, S. M. Tantary, and K. Asokan, *Rsc Advances* ***7,*** *50648 (2017).*

4. **Voltammetric determination of epinephrine and xanthine based on sodium dodecyl sulphate assisted tungsten trioxide nanoparticles,** A. C. Anithaa, K. Asokan, and C. Sekar, *Electrochimica Acta* ***237,*** *44 (2017).*

5. **Swift heavy nickel ion irradiated ethylene diamine tetra acetic acid-assisted tungsten trioxide thin film for the electrocatalytic detection of guanine,** A. C. Anithaa, K. Asokan, and C. Sekar, *Sensors and Actuators B-Chemical* ***247,*** *814 (2017).*

6. **Highly sensitive and selective serotonin sensor based on gamma ray irradiated tungsten trioxide nanoparticles,** A. C. Anithaa, K. Asokan, and C. Sekar, *Sensors and Actuators B-Chemical* ***238,*** *667 (2017).*

7. **Improvement of opto-electro-structural properties of nanocrystalline CdS thin films induced by Au^{9+} ion irradiation,** G. Bakiyaraj, B. Gunasekaran, J. Prakash, M. Kalidasan, K. Asokan, R. Dhanasekaran, and K. Ramamurthi, *Thin Solid Films* ***626,*** *117 (2017).*

8. **Enhancement of thermoelectric power of PbTe thin films by Ag ion implantation,** M. Bala, A. Bhogra, S. A. Khan, T. S. Tripathi, S. K. Tripathi, D. K. Avasthi, and K. Asokan, *Journal of Applied Physics* ***121,*** *215301 (2017).*

9. **Evolution of nanostructured single-phase $CoSb_3$ thin films by low-energy ion beam induced mixing and their thermoelectric performance,** M. Bala, S. Gupta, S. K. Srivastava, S. Amrithapandian, T. S. Tripathi, S. K. Tripathi, C. L. Dong, C. L. Chen, D. K. Avasthi, and K. Asokan, *Physical Chemistry Chemical Physics* ***19,*** *24886 (2017).*

10. **Nanoscale self-recovery of resistive switching in Ar^+ irradiated TiO_{2-x} films,** A. Barman, C. P. Saini, P. K. Sarkar, D. Das, S. Dhar, M. Singh, A. K. Sinha, D. Kanjilal, M. Gupta, D. M. Phase, and A. Kanjilal, *Journal of Physics D-Applied Physics* ***50,*** *475304 (2017).*

11. **Photoluminescence and reflectivity studies of high energy light ions irradiated polymethyl methacrylate films,** M. L. Bharti, F. Singh, R. C. Ramola, and V. Joshi, *Optical Materials* ***73,*** *550 (2017).*

12. **Correlations of charge neutrality level with electronic structure and p-d hybridization,** A. Das, S. K. Gautam, D. K. Shukla, and F. Singh, *Scientific Reports **7,** 40843 (2017).*

13. **Virtual gap states induced modifications in charge neutrality level in cadmium oxide thin films,** A. Das, S. K. Gautam, G. R. Umapathy, S. Ojha, and F. Singh, *Materials Research Express **4,** 045901 (2017).*

14. **Electronic excitation induced anomalous band gap enhancement in $Ni_xCd_{1-x}O$ thin films,** A. Das and F. Singh, *Vacuum **146,** 287 (2017).*

15. **Studies on improved hole injection into N,N '-Bis(3-methylphenyl)-N,N '-diphenylbenzidine hole transport layer in the device by thermal annealing of indium tin oxide anode,** G. Dasi, K. Asokan, and K. Thangaraju, *Applied Physics a-Materials Science & Processing **123,** 179 (2017).*

16. **Photoluminescent Au-Ge composite nanodots formation on SiO_2 surface by ion induced dewetting,** D. P. Datta, V. Siva, A. Singh, D. Kanjilal, and P. K. Sahoo, N*uclear Instruments & Methods in Physics Research Section B-Beam Interactions with Materials and Atoms **407,** 141 (2017).*

17. **Ion induced crystallization and grain growth of hafnium oxide nano-particles in thin-films deposited by radio frequency magnetron sputtering,** M. Dhanunjaya, S. A. Khan, A. P. Pathak, D. K. Avasthi, and S. Rao, *Journal of Physics D-Applied Physics **50,** 505301 (2017).*

18. **Transport properties of $Y_{0.95}Ca_{0.05}MnO_3$/Si thin film junction,** D. Dhruv, Z. Joshi, K. Gadani, S. Solanki, J. H. Markna, A. D. Joshi, K. Asokan, P. S. Solanki, and N. A. Shah, *Physica B-Condensed Matter **518,** 33 (2017).*

19. **Investigations of structural and transport properties of Ca doped yttrium manganites,** G. Dixit, P. Kumar, P. Negi, and K. Asokan, *Ferroelectrics **516,** 74 (2017).*

20. **Current-voltage characteristics and electroresistance in $LaMnO_{3-delta}/La_{0.7}Ca_{0.3}MnO_3/LaAlO_3$ thin film composites,** K. Gadani, M. J. Keshvani, B. Rajyaguru, D. Dhruv, B. R. Kataria, A. D. Joshi, K. Asokan, N. A. Shah, and P. S. Solanki, *Physical Chemistry Chemical Physics **19,** 29294 (2017).*

21. **Aspects of ions induced texture evolution on Ge surface: A statistical assessment,** S. K. Garg, D. P. Datta, D. Kanjilal, and T. Som, *Nuclear Instruments & Methods in Physics Research Section B-Beam Interactions with Materials and Atoms **409,** 181 (2017).*

22. **A comparative investigation of Ce^{3+}/Dy^{3+} and Eu^{2+} doped $LiAlO_2$ phosphors for high dose radiation dosimetry: Explanation of defect recombination mechanism using PL, TL and EPR study,** K. K. Gupta, R. M. Kadam, N. S. Dhoble, S. P. Lochab, and S. J. Dhoble, *Journal of Luminescence **188,** 81 (2017).*

23. **Role of carrier concentration in swift heavy ion irradiation induced surface modifications,** S. Gupta, V. Ganesan, I. Sulania, and B. Das, *Surface Science **664,** 137 (2017).*

24. **Swift heavy ion irradiation induced modifications in structural, microstructural, electrical and magnetic properties of Mn doped SnO_2 thin films,** S. Gupta, F. Singh, N. P. Lalla, and B. Das, *Nuclear Instruments & Methods in Physics Research Section B-Beam Interactions with Materials and Atoms **400,** 37 (2017).*

25. **Electronic excitation-induced structural, optical, and magnetic properties of Ni-doped $HoFeO_3$ thin films,** Z. Habib, M. Ikram, K. Sultan, Abida, S. A. Mir, K. Majid, and K. Asokan, *Applied Physics a-Materials Science & Processing **123,** 442 (2017).*

26. **Enhanced supercapacitance behaviour of low energy ion beam reduced graphene oxide,** K. Hareesh, B. Shateesh, J. F. Williams, K. Asokan, D. M. Phase, K. P. Madhuri, S. K. Haram, and S. D. Dhole, *Materials Research Express* ***4,*** *065018 (2017).*

27. **Tuning ferromagnetism by varying ion beam profiles,** R. V. Hariwal, H. K. Malik, and K. Asokan, *Materials Research Express* ***4,*** *025901 (2017).*

28. **Mechanistic details of the formation and growth of nanoscale voids in Ge under extreme conditions within an ion track,** S. Hooda, K. Avchachov, S. A. Khan, F. Djurabekova, K. Nordlund, B. Satpati, S. Bernstorff, S. Ahlawat, D. Kanjilal, and D. Kabiraj, *Journal of Physics D-Applied Physics* ***50,*** *225302 (2017).*

29. **Electronic excitation induced modifications of structural, electrical and optical properties of Cu-C_{60} nanocomposite thin films,** H. Inani, R. Singhal, P. Sharma, R. Vishnoi, S. Ojha, S. Chand, and G. D. Sharma, Nuclear Instruments & Methods in Physics Research Section B-Beam Interactions with Materials and Atoms **407,** 73 (2017).

30. **Structure and electron field emission properties of ion beam reduced graphene oxide sheets,** G. Jayalakshmi, K. Saravanan, T. Arun, K. Suresh, B. Sundaravel, B. K. Panigrahi, and D. Kanjilal, *Carbon* ***119,*** *172 (2017).*

31. **Studies on the structure and dielectric properties of Ca-doped $BiFeO_3$ multiferroics,** S. Jethva, S. Katba, M. Udeshi, B. Vyas, H. Kundalia, P. Trivedi, M. Vagadia, and D. G. Kuberkar, *Ferroelectrics 516, 106 (2017).*

32. **Atomistic modeling and experimental studies of radiation damage in monazite-type $LaPO_4$ ceramics,** Y. Q. Ji, P. M. Kowalski, S. Neumeier, G. Deissmann, P. K. Kulriya, and J. D. Gale, *Nuclear Instruments & Methods in Physics Research Section B-Beam Interactions with Materials and Atoms* ***393,*** *54 (2017).*

33. **Scaling studies of self-affine nanopatterned TiO_2 surfaces created via ion implantation,** S. R. Joshi, A. Chanda, D. Kanjilal, and S. Varma, *Thin Solid Films* ***639,*** *145 (2017).*

34. **Complex damage distribution behaviour in cobalt implanted rutile TiO_2 (110) lattice, S. R. Joshi, B. Padmanabhan,** A. Chanda, S. Ojha, D. Kanjilal, and S. Varma, *Nuclear Instruments & Methods in Physics Research Section B-Beam Interactions with Materials and Atoms* ***410,*** *114 (2017).*

35. **Thermoluminescence and kinetic study of low z $LiAlO_2$:Dy/Eu phosphors,** M. R. Kadukar, P. W. Yawalkar, S. P. Lochab, S. J. Dhoble, and B. S. Reddy, Ferroelectrics Letters Section **44,** 8 (2017).

36. **Role of temperature in the radiation stability of yttria stabilized zirconia under swift heavy ion irradiation: A study from the perspective of nuclear reactor applications,** P. Kalita, S. Ghosh, G. Sattonnay, U. B. Singh, V. Grover, R. Shukla, S. Amirthapandian, R. Meena, A. K. Tyagi, and D. K. Avasthi, *Journal of Applied Physics* ***122,*** *025902 (2017).*

37. **Doping induced modifications in the electronic structure and magnetism of ZnO films: Valence band and conduction band studies,** S. Katba, S. Jethva, M. Udeshi, P. Trivedi, M. Vagadia, D. K. Shukla, R. J. Choudhary, D. M. Phase, and D. G. Kuberkar, *Applied Surface Science* ***423,*** *100 (2017).*

38. **Surface functionalization of epitaxial graphene on SiC by ion irradiation for gas sensing application,** P. D. Kaushik, I. G. Ivanov, P. C. Lin, G. Kaur, J. Eriksson, G. Lakshmi, D. K. Avasthi, V. Gupta, A. Aziz, A. M. Siddiqui, M. Syvajarvi, and G. R. Yazdi, *Applied Surface Science* ***403,*** *707 (2017).*

39. **Room temperature tunability of Mo-doped VO_2 nanofilms across semiconductor to metal phase transition,** G. R. Khan, K. Asokan, and B. Ahmad, *Thin Solid Films* ***625,*** *155 (2017).*

40. **Controlled morphological modifications of ZnO thin films by ion irradiation,** V. Kondkar, D. Rukade, D. Kanjilal, and V. Bhattacharyya, *Materials Research Express **4,** 116402 (2017).*

41. **Hydrogen pressure dependent in-situ electrical studies on Pd/C nano-composite,** P. K. Kulriya, M. Kumar, J. Singh, and D. K. Auasthi, *International Journal of Hydrogen Energy **42,** 3399 (2017).*

42. **Enhancement of thermopower in GaN by ion irradiation and possible mechanisms,** A. Kumar, J. Dhillon, R. C. Meena, P. Kumar, K. Asokan, R. Singh, and D. Kanjilal, *Applied Physics Letters **111,** 222102 (2017).*

43. **Impedance analysis and dielectric response of anatase TiO_2 nanoparticles codoped with Mn and Co ions,** A. Kumar, M. K. Kashyap, N. Sabharwal, S. Kumar, A. Kumar, P. Kumar, and K. Asokan, *Materials Research Express **4,** 115035 (2017).*

44. Structural, optical and weak magnetic properties of Co and Mn codoped TiO2 nanoparticles, A. Kumar, M. K. Kashyap, N. Sabharwal, S. Kumar, A. Kumar, P. Kumar, and K. Asokan, Solid State Sciences 73, 19 (2017).

45. **Swift heavy ions induced nano-grain fragmentation in fluoride thin films,** M. Kumar, R. K. Pandey, P. Rajput, S. A. Khan, F. Singh, D. K. Avasthi, and A. C. Pandey, *Journal of Alloys and Compounds **695,** 83 (2017).*

46. **SHI induced surface re-organization of non-amorphisable nanodimensional fluoride thin films,** M. Kumar, R. K. Pandey, P. Rajput, S. A. Khan, U. B. Singh, D. K. Avasthi, and A. C. Pandey, *Physical Chemistry Chemical Physics **19,** 23229 (2017).*

47. **Influence of High Dose Gamma Irradiation on Electrical Characteristics of Si Photo Detectors,** M. V. Kumar, S. Kumar, C. Cheng, K. Asokan, A. Kumar, V. Shobha, S. P. Karanth, and S. Krishnaveni, *Ecs Journal of Solid State Science and Technology **6,** Q132 (2017).*

48. **Influence of High Dose Gamma Irradiation on Electrical Characteristics of Si Photo Detectors,** M. V. Kumar, S. Kumar, C. Cheng, K. Asokan, A. Kumar, V. Shobha, S. P. Karanth, and S. Krishnaveni, *Ecs Journal of Solid State Science and Technology **6,** Q132 (2017).*

49. **Enhancement of ferromagnetism in C ion implanted CeO_2 thin films,** P. Kumar, F. Chand, and K. Asokan, *Materials Research Express **4,** 036403 (2017).*

50. **Structural, optical and magnetic properties of N ion implanted CeO_2 thin films,** P. Kumar, P. Kumar, A. Kumar, I. Sulania, F. Chand, and K. Asokan, *Rsc Advances **7,** 9160 (2017).*

51. **Modifications in room temperature ferromagnetism by dense electronic excitations in $Zn_{0.9}Mg_{0.1}O$ thin films,** P. Kumar, H. K. Malik, S. Gautam, K. H. Chae, K. Asokan, and D. Kanjilal, *Journal of Alloys and Compounds **710,** 831 (2017).*

52. **Evolution of relaxor properties in lanthanum (La) doped barium zirconate titanate,** R. Kumar, K. Asokan, S. Patnaik, and B. Birajdar, *Ferroelectrics **517,** 8 (2017).*

53. **HRTEM morphological features on grain boundary diffusion and particulate necking, photoluminescence and thermoluminescence investigations of nano Ce^{3+}:LuAG,** S. A. Kumar, K. Asokan, and J. Senthilselvan, *Materials Characterization **127,** 77 (2017).*

54. **Ag implantation-induced modification of Ni-Ti shape memory alloy thin films,** V. Kumar, R. Singhal, R. Vishnoi, M. K. Banerjee, M. C. Sharma, K. Asokan, and M. Kumar, *Radiation Effects and Defects in Solids **172,** 629 (2017).*

55. **Structural, optical and transport studies of nanocomposite SnO_x thin films grown by DC sputter deposition and post-annealing,** V. V. S. Kumar and D. Kanjilal, *Materials Research Express* ***4,*** *026403 (2017).*

56. **Phase-dependent radiation-resistant behavior of $BaTiO_3$: An insitu X-ray diffraction study,** R. Kumari, P. K. Kulriya, S. Mishra, V. Kotari, S. N. Achary, A. K. Tyagi, and D. K. Avasthi, *Journal of the American Ceramic Society* ***100,*** *4263 (2017).*

57. **Ion irradiation-induced, localized sp2 to sp3 hybridized carbon transformation in walls of multiwalled carbon nanotubes,** R. Kumari, F. Singh, B. S. Yadav, R. K. Kotnala, K. R. Peta, P. K. Tyagi, S. Kumar, and N. K. Puri, *Nuclear Instruments & Methods in Physics Research Section B-Beam Interactions with Materials and Atoms* ***412,*** *115 (2017).*

58. **Facile synthesis of Au-ZnO plasmonic nanohybrids for highly efficient photocatalytic degradation of methylene blue,** S. Kuriakose, K. Sahu, S. A. Khan, A. Tripathi, D. K. Avasthi, and S. Mohapatra, *Optical Materials* ***64,*** *47 (2017).*

59. **Effect of gamma irradiation on structural, electrical and gas sensing properties of tungsten oxide nanoparticles,** N. Lavanya, A. C. Anithaa, C. Sekar, K. Asokan, A. Bonavita, N. Donato, S. G. Leonardi, and G. Neri, *Journal of Alloys and Compounds* ***693,*** *366 (2017).*

60. **Enhancement of the critical current density in YBCO/Ag composites,** B. A. Malik, M. A. Malik, and K. Asokan, *Chinese Journal of Physics* ***55,*** *170 (2017).*

61. **Correlation between magnetic and micro-structural properties of low energy ion irradiated and un-irradiated $Zn_{0.95}Mn_{0.05}O$ films,** N. Midya, S. K. Neogi, M. A. Ahmed, A. Banerjee, P. Kumar, D. Kanjilal, and S. Bandyopadhyay, *Rsc Advances* ***7,*** *771 (2017).*

62. **Interaction of plasma proteins with ZnSe and ZnSe@ZnS core-shell quantum dots,** I. A. Mir, K. Rawat, and H. B. Bohidar, *Colloids and Surfaces a-Physicochemical and Engineering Aspects* ***520,*** *131 (2017).*

63. **ZnSe core and ZnSe@ZnS core-shell quantum dots as platform for folic acid sensing,** I. A. Mir, K. Rawat, P. R. Solanki, and H. B. Bohidar, *Journal of Nanoparticle Research* ***19,*** *260 (2017).*

64. **Signature of Magnetization in Xe Ions Implanted ZnO: Correlation with Oxygen Defects as Probed by Photoelectron Spectroscopy,** D. K. Mishra, S. Pattanaik, S. Dash, M. K. Sharma, P. Kumar, S. C. Ray, R. Chatterjee, and D. Kanjilal, *Journal of Nanoscience and Nanotechnology* ***17,*** *8494 (2017).*

65. **Electrocatalytic biofuel cell based on highly efficient metal-polymer nano-architectured bioelectrodes,** P. Mishra, G. Lakshmi, S. Mishra, D. K. Avasthi, H. C. Swart, A. P. F. Turner, Y. K. Mishra, and A. Tiwari, *Nano Energy* ***39,*** *601 (2017).*

66. **Magnetic Behaviour of Granular $GdMnO_3$ Film,** P. Negi, H. M. Agrawal, J. P. Singh, H. Kumar, R. C. Srivastava, K. Asokan, and K. H. Chae, *Journal of Superconductivity and Novel Magnetism* ***30,*** *1419 (2017).*

67. **Tuning of structural and optical properties by sintering of multiferroic $GdMnO_3$ precursor,** P. Negi, G. Dixit, H. M. Agrawal, H. Kumar, R. C. Srivastava, P. C. Sati, V. Gupta, and K. Asokan, *Ferroelectrics* ***519,*** *200 (2017).*

68. **Shallow acceptor state in ZnO realized by ion irradiation and annealing route,** S. Pal, T. Rakshit, S. S. Singha, K. Asokan, S. Dutta, D. Jana, and A. Sarkar, *Journal of Alloys and Compounds* ***703,*** *26 (2017).*

69. **Solvent hydrophobicity induced complex coacervation of dsDNA and in situ formed zein nanoparticles,** P. K. Pandey, P. Kaushik, K. Rawat, V. K. Aswal, and H. B. Bohidar, *Soft Matter **13,** 6784 (2017).*

70. **DNA ionogel: Structure and self-assembly,** P. K. Pandey, K. Rawat, V. K. Aswal, J. Kohlbrechere, and H. B. Bohidar, *Physical Chemistry Chemical Physics **19,** 804 (2017).*

71. **Modification of chitosan-based biodegradable polymer by irradiation with MeV ions for electrolyte applications,** G. B. Patel, N. L. Singh, and F. Singh, *Materials Science and Engineering B-Advanced Functional Solid-State Materials **225,** 150 (2017).*

72. **Complex coacervation in charge complementary biopolymers: Electrostatic versus surface patch binding,** J. Pathak, E. Priyadarshini, K. Rawat, and H. B. Bohidar, *Advances in Colloid and Interface Science **250,** 40 (2017).*

73. **Influence of Oxygen ions irradiation on Polyaniline/Single Walled Carbon Nanotubes nanocomposite,** H. K. Patil, M. A. Deshmukh, S. D. Gaikwad, G. A. Bodkhe, K. Asokan, M. Yasuzawa, P. Koinkar, and M. D. Shirsat, *Radiation Physics and Chemistry **130,** 47 (2017).*

74. **Electronic excitation induced structural and optical modifications in InGaN/GaN quantum well structures grown by MOCVD,** K. Prabakaran, R. Ramesh, M. Jayasakthi, S. Surender, S. Pradeep, M. Balaji, K. Asokan, and K. Baskar, *Nuclear Instruments & Methods in Physics Research Section B-Beam Interactions with Materials and Atoms **394,** 81 (2017).*

75. **Au@carbon dot nanoconjugates as a dual mode enzyme-free sensing platform for cholesterol,** E. Priyadarshini and K. Rawat, *Journal of Materials Chemistry B **5,** 5425 (2017).*

76. **Defect induced modification of structural, topographical and magnetic properties of zinc ferrite thin films by swift heavy ion irradiation,** L. Raghavan, P. A. Joy, B. V. Vijaykumar, R. V. Ramanujan, and M. R. Anantharaman, *Nuclear Instruments & Methods in Physics Research Section B-Beam Interactions with Materials and Atoms **396,** 68 (2017).*

77. **Study of phase transformation induced by electronic excitation in pure and yttrium doped ZrO2 thin films,** R. C. Ramola, M. Rawat, K. Joshi, A. Das, S. K. Gautam, and F. Singh, *Materials Research Express **4,** 096401 (2017).*

78. **Self-assembly and gelation of TX-100 in water,** R. Ranjan, P. Das, K. Rawat, V. K. Aswal, J. Kohlbrecher, and H. B. Bohidar, *Colloid and Polymer Science **295,** 903 (2017).*

79. **Folic acid supramolecular ionogels,** R. Ranjan, K. Rawat, and H. B. Bohidar, *Physical Chemistry Chemical Physics **19,** 22934 (2017).*

80. **Robust water repellent ZnO nanorod array by Swift Heavy Ion Irradiation: Effect of Electronic Excitation Induced Local Chemical State Modification,** K. S. Ranjith, L. R. Nivedita, K. Asokan, S. Krishnamurthy, R. Pandian, M. Kamruddin, D. K. Avasthi, and R. T. R. Kumar, *Scientific Reports **7,** 3251 (2017).*

81. **Comparison of charge transport studies of chemical solution and pulsed laser deposited manganite-based thin film devices,** K. N. Rathod, D. Dhruv, K. Gadani, H. Boricha, S. Solanki, A. D. Joshi, D. D. Pandya, K. Asokan, P. S. Solanki, and N. A. Shah, *Applied Physics a-Materials Science & Processing **123,** 558 (2017).*

82. **Structural, microstructural and dielectric behavior of sol-gel grown nanostructured $Y_{0.95}Zr_{0.05}MnO_3$,** K. N. Rathod, K. Thakrar, K. Gadani, Z. Joshi, D. Dhruv, H. Boricha, S. Kansara, D. D. Pandya, K. Asokan, P. S. Solanki, and N. A. Shah, *Materials Chemistry and Physics **198,** 200 (2017).*

83. **Ion beam modification of structural and optical properties of GeO_2 thin films deposited at various substrate temperatures using pulsed laser deposition,** M. S. Rathore, A. Vinod, R. Angalakurthi, A. P. Pathak, F. Singh, S. K. Thatikonda, and S. R. Nelamarri, *Applied Physics a-Materials Science & Processing* ***123,*** *708 (2017).*

84. **Phase evolution and magnetic properties of DC sputtered Fe-Ga (Galfenol) thin films with growth temperatures,** N. L. Raveendran, R. Pandian, S. Murugesan, K. Asokan, and R. T. R. Kumar, *Journal of Alloys and Compounds* ***704,*** *420 (2017).*

85. **Story of Superconductivity A Serendipitous Discovery,** A. Roy, *Resonance-Journal of Science Education* ***22,*** *461 (2017).*

86. **Effect of low energy proton beam irradiation on structural and electrical properties of ZnO:Al thin films,** S. K. Sahoo, S. Mangal, D. K. Mishra, P. Kumar, and U. P. Singh, *Materials Science in Semiconductor Processing* ***63,*** *76 (2017).*

87. **50keV H^+ ion beam irradiation of Al doped ZnO thin films: Studies of radiation stability for device applications,** S. K. Sahoo, S. Mangal, D. K. Mishra, U. P. Singh, and P. Kumar, *Surface and Interface Analysis* ***49,*** *1279 (2017).*

88. **Impact of Self-Trapped Excitons on Blue Photoluminescence in TiO_2 Nanorods on Chemically Etched Si Pyramids,** C. P. Saini, A. Barman, D. Banerjee, O. Grynko, S. Prucnal, M. Gupta, D. M. Phase, A. K. Sinha, D. Kanjilal, W. Skorupa, and A. Kanjilal, *Journal of Physical Chemistry C* ***121,*** *11448 (2017).*

89. **Role of Oxygen Vacancy on the Hydrophobic Behavior of TiO_2 Nanorods on Chemically Etched Si Pyramids,** C. P. Saini, A. Barman, D. Das, B. Satpati, S. R. Bhattacharyya, D. Kanjilal, A. Ponomaryov, S. Zvyagin, and A. Kanjilal, *Journal of Physical Chemistry C* ***121,*** *278 (2017).*

90. **The influence of carbon concentration on the electronic structure and magnetic properties of carbon implanted ZnO thin films,** K. Saravanan, G. Jayalakshmi, S. Chandra, B. K. Panigrahi, R. Krishnan, B. Sundaravel, S. Annapoorani, D. K. Shukla, P. Rajput, and D. Kanjilal, *Physical Chemistry Chemical Physics* ***19,*** *13316 (2017).*

91. **Hydrophilic, fluorescent and superparamagnetic iron oxide-carbon composite nanoparticles,** T. Sarkar, S. Tiwari, K. Rawat, P. R. Solanki, and H. B. Bohidar, *Colloids and Surfaces a-Physicochemical and Engineering Aspects* ***514,*** *218 (2017).*

92. **Ion induced controlled modifications in structural and optical properties of indium oxide thin films - studies with 25-keV Co- and N^+ beam implantations,** R. Sethi, P. D. Kaushik, A. Aziz, A. M. Siddiqui, and P. Kumar, *Surface and Interface Analysis* ***49,*** *910 (2017).*

93. **Work Function Modulation of Molybdenum Disulfide Nanosheets by Introducing Systematic Lattice Strain,** J. Shakya, S. Kumar, D. Kanjilal, and T. Mohanty, *Scientific Reports* ***7,*** *9576 (2017).*

94. **A Differential Temperature-Dependent Dielectric Relaxation Study of Organoclay Cloisite (TM),** A. Sharma, R. Kumar, K. Asokan, K. Rawat, and D. Kanjilal, *International Journal of Thermophysics* ***38,*** *6 (2017).*

95. **Self-healing gelatin ionogels, A. Sharma,** K. Rawat, P. R. Solanki, and H. B. Bohidar, *International Journal of Biological Macromolecules* ***95,*** *603 (2017).*

96. **Surface patch binding-induced exfoliation of nanoclays and enhancement of physical properties of gelatin organogels,** A. Sharma, K. Rawat, P. R. Solanki, and H. B. Bohidar, *Polymer International* ***66,*** *327 (2017).*

97. **Analysis of electrical conduction phenomena in highly photosensitive amorphous $In_xSb_{20-x}Ag_{10}Se_{70}$ (0 <= x <= 20) chalcogenide films,** R. Sharma, S. Sharma, P. Kumar, K. Asokan, R. Thangaraj, and M. Mian, *Journal of Non-Crystalline Solids* ***472,*** *70 (2017).*

98. **Effect of composition on steady state and transient photoconductivity in isocoordinated $In_xSb_{30-x}Se_{70}$ (0 <= x <= 25) chalcogenide films,** S. Sharma, R. Sharma, P. Kumar, R. Thangaraj, K. Asokan, and M. Mian, *Journal of Materials Science-Materials in Electronics* ***28,*** *14202 (2017).*

99. **Influence of 100 MeV Au^{+8} ion on photovoltaic response of $BiFeO_3/BaTiO_3$ multilayer structures,** S. Sharma, M. Tomar, A. Kumar, F. Singh, N. K. Puri, and V. Gupta, *Materials & Design* ***114,*** *345 (2017).*

100. **Annealing Temperature Dependent Structural and Optical Properties of RF Sputtered ZnO Thin Films,** S. Sharma, T. Varma, K. Asokan, C. Periasamy, and D. Boolchandani, *Journal of Nanoscience and Nanotechnology* ***17,*** *300 (2017).*

101. **Influence of high energy ion irradiation on fullerene derivative (PCBM) thin films,** T. Sharma, R. Singhal, R. Vishnoi, G. Lakshmi, and S. K. Biswas, *Nuclear Instruments & Methods in Physics Research Section B-Beam Interactions with Materials and Atoms* ***396,*** *5 (2017).*

102. **Ion irradiation induced modifications of P3HT: A donor material for organic photovoltaic devices,** T. Sharma, R. Singhal, R. Vishnoi, G. Lakshmi, S. Chand, D. K. Avasthi, A. Kanjilal, and S. K. Biswas, Vacuum 135, 73 (2017).

103. **High-performance radiation stable ZnO/Ag/ZnO multilayer transparent conductive electrode,** V. Sharma, P. Kumar, A. Kumar, Surbhi, K. Asokan, and K. Sachdev, *Solar Energy Materials and Solar Cells* ***169,*** *122 (2017).*

104. **Transport properties of Gallium Phosphide based Schottky contact with thin insulating layer,** N. Shiwakoti, A. Bobby, K. Asokan, and B. Antony, *Materials Science in Semiconductor Processing* ***61,*** *145 (2017).*

105. **The role of electronic energy loss in SHI irradiated Ni/oxide/n-GaP Schottky diode,** N. Shiwakoti, A. Bobby, K. Asokan, and B. Antony, *Microelectronics Reliability* ***69,*** *40 (2017).*

106. **Effect of Au^{8+} irradiation on Ni/n-GaP Schottky diode: Its influence on interface state density and relaxation time,** N. Shiwakoti, A. Bobby, K. Asokan, and B. Antony, *Physica B-Condensed Matter* ***504,*** *133 (2017).*

107. **Gamma (gamma)-ray irradiated multi-walled carbon nanotubes (MWCNTs) for hydrogen storage,** D. Silambarasan, V. J. Surya, K. Iyakutti, K. Asokan, V. Vasu, and Y. Kawazoe, *Applied Surface Science* ***418,*** *49 (2017).*

108. **Synthesis of p-n junctions in ZnO nanorods by O^+ ion implantation,** A. Singh, K. Senapati, D. P. Datta, R. Singh, T. Som, S. Bhunia, D. Kanjilal, and P. K. Sahoo, *Nuclear Instruments & Methods in Physics Research Section B-Beam Interactions with Materials and Atoms* ***409,*** *143 (2017).*

109. **Nanostructured TiO_2 thin films prepared by RF magnetron sputtering for photocatalytic applications,** J. Singh, S. A. Khan, J. Shah, R. K. Kotnala, and S. Mohapatra, *Applied Surface Science* ***422,*** *953 (2017).*

110. **Synthesis and thermoluminescence studies of gamma-irradiated Dy^{3+} doped $SrGd_2O_4$ phosphor,** J. Singh, J. Manam, and F. Singh, *Materials Research Bulletin* ***94,*** *113 (2017).*

111. **Thermoluminescence studies of solid-state reaction derived and gamma-irradiated $SrGd_2O_4$: Eu^{3+} phosphor,** J. Singh, J. Manam, and F. Singh, *Materials Research Bulletin* ***93,*** *318 (2017).*

112. **Electronic structure of magnetic Fe/MgO/Fe/Co multilayer structure by NEXAFS spectroscopy,** J. P. Singh, S. Gautam, W. C. Lim, K. Asokan, B. B. Singh, M. Raju, S. Chaudhary, D. Kabiraj, D. Kanjilal, J. M. Lee, J. M. Chen, and K. H. Chae, *Vacuum* ***138,*** *48 (2017).*

113. **Tuning of mechanical and structural properties of 20 MC 5 steel using N ion implantation and subsequent annealing,** O. Singh, H. K. Malik, R. P. Dahiya, and P. K. Kulriya, *Journal of Alloys and Compounds* ***710,*** *253 (2017).*

114. **Investigations on mechanical and electrical properties of N^+ ions implanted TiN thin films,** O. Singh, H. K. Malik, R. P. Dahiya, and P. Kumar, *Materials Research Express* ***4,*** *046403 (2017).*

115. **Fabrication of highly efficient TiO_2/Ag/TiO_2 multilayer transparent conducting electrode with N ion implantation for optoelectronic applications,** S. Singh, V. Sharma, Surbhi, D. Saini, K. Asokan, and K. Sachdev, *Ceramics International* ***43,*** *9759 (2017).*

116. **Study on swift heavy ions induced modifications of Ag-ZnO nanocomposite thin film,** S. K. Singh, R. Singhal, and V. V. S. Kumar, *Superlattices and Microstructures* ***103,*** *195 (2017).*

117. **Ag-ZnO Nanocomposite Thin Film by RF-Sputtering: An Electrical and Structural Study,** S. K. Singh, R. Singhal, and V. V. Siva Kumar, *Macromolecular Symposia* ***376,*** *1600197 (2017).*

118. **Swift heavy ion induced optical and structural modifications in RF sputtered nanocrystalline ZnO thin film,** S. K. Singh, R. Singhal, R. Vishnoi, V. V. S. Kumar, and P. K. Kulariya, *Indian Journal of Physics* ***91,*** *547 (2017).*

119. **The role of ion irradiation in activating silent Raman modes via tuning in plasmonic behaviour and surface disorder of Au/ZnO/Pt NFG system,** U. B. Singh, S. K. Gautam, S. Kumar, S. Ojha, S. Ghosh, and F. Singh, *Epl* ***119,*** *66002 (2017).*

120. **Large electronic sputtering yield of nanodimensional Au thin films: Dominant role of thermal conductivity and electron phonon coupling factor,** U. B. Singh, C. Pannu, D. C. Agarwal, S. Ojha, S. A. Khan, S. Ghosh, and D. K. Avasthi, *Journal of Applied Physics* ***121,*** *095308 (2017).*

121. **Nanostructuring and wettability of ion treated Au thin films,** U. B. Singh, R. P. Yadav, R. Kumar, S. Ojha, A. K. Mittal, S. Ghosh, and F. Singh, *Journal of Applied Physics* ***122,*** *185303 (2017).*

122. **Synthesis, characterization and thermally induced structural transformation of Au-C-70 nanocomposite thin films,** R. Singhal, R. Vishnoi, P. Sharma, G. D. Sharma, S. Chand, D. Kanjilal, and J. C. Pivin, *Vacuum* ***142,*** *146 (2017).*

123. **Interface mediated enhanced mixing of multilayered Ni-Bi thin films by swift heavy ion irradiation,** V. Siva, A. Chettah, S. Ojha, A. Tripathi, D. Kanjilal, and P. K. Sahoo, *Nuclear Instruments & Methods in Physics Research Section B-Beam Interactions with Materials and Atoms* ***409,*** *314 (2017).*

124. **Synthesis of sponge-like hydrophobic $NiBi_3$ surface by 200 keV Ar ion implantation,** V. Siva, D. P. Datta, S. Chatterjee, S. Varma, D. Kanjilal, and P. K. Sahoo, *Applied Surface Science* ***410,*** *519 (2017).*

125. **Swift Heavy Ion irradiation induced nanocrystallisation in Te/Cd/Te trilayer thin films,** S. Survase, M. Thakurdesai, I. Sulania, and D. Kanjilal, *Thin Solid Films* ***636,*** *403 (2017).*

126. **Investigations on structural and magnetic properties of Mn doped Er_2O_3,** R. Tomar, P. Kumar, A. Kumar, A. Kumar, P. Kumar, R. P. Pant, and K. Asokan, *Solid State Sciences* ***67, 8*** *(2017).*

127. **Generation and application of LET calibration curve for neutron dosimetry using CR-39 detector and microwave induced chemical etching,** S. P. Tripathy, G. S. Sahoo, S. Paul, P. Kumar, S. D. Sharma, S. Santra, A. Pal, A. Kundu, T. Bandyopadhyay, and D. K. Avasthi, *Review of Scientific Instruments* ***88,*** *063301 (2017).*

128. **Charge transport mechanisms in sol-gel grown $La_{0.7}Pb_{0.3}MnO_3/LaAlO_3$ manganite films,** E. Vaghela, M. J. Keshvani, K. Gadani, Z. Joshi, H. Boricha, K. Asokan, D. Venkateshwarlu, V. Ganesan, N. A. Shah, and P. S. Solanki, *Physical Chemistry Chemical Physics* ***19,*** *5163 (2017).*

129. **Energetic ion induced desorption of hydrogen from porous silicon studied by on-line elastic recoil detection analysis,** V. S. Vendamani, S. A. Khan, M. Dhanunjaya, A. P. Pathak, and S. Rao, *Microporous and Mesoporous Materials* ***246,*** *81 (2017).*

130. **Enhanced photoelectrochemical response of plasmonic Au embedded $BiVO_4/Fe2O_3$ heterojunction,** A. Verma, A. Srivastav, S. A. Khan, V. R. Satsangi, R. Shrivastav, D. K. Avasthi, and S. Dass, *Physical Chemistry Chemical Physics* ***19,*** *15039 (2017).*

131. **Structure and magnetic behavior of Zn doped $NdMnO_3$ manganite: Neutron diffraction study,** B. Vyas, H. Kundalia, M. Udeshi, P. Trivedi, M. Vagadia, S. Rayaprol, and D. G. Kuberkar, *Ceramics International* ***43,*** *14962 (2017).*

132. **Cost efficient PMMA/NG nanocomposites for electromagnetic interference shielding applications,** P. Yadav, S. Rattan, A. Tripathi, and S. Kumar, *Materials Research Express* ***4,*** *065601 (2017).*

C. OTHERS

1. **Pallavi Srivastava,** Asitikantha Sarma, Chandra Mohini Chaturvedi.Carbon ion radiation in combined with PNKP inhibitor radiosensitizes cultured lung cancer cells, Trends in biochemical and biomedical research: Advances and challenges (TBBR-2018), February 13-15th 2018, Department of Biochemistry, Banaras Hindu University, Varanasi, India.

2. **Pallavi Srivastava,** Asitikantha Sarma, Chandra Mohini Chaturvedi. Radiosensitization effect of Polynucleotide kinase/phosphatase inhibition in lung cancer cells A549 exposed to carbon ion radiation,International conference on cell biology, January 27-31st January, 2018, CCMB, Hyderabad, India.

3. **Pallavi Srivastava,** Asitikantha Sarma, Chandra Mohini Chaturvedi. Targeting DNA Double Strand Break Repair with PNKP Inhibition to enhance the effect of Carbon Ion Radiation in Radioresistant Prostate Cancer Cell Line (PC3). Emerging Trends in Drug Discovery and Development-2018 (ETDDD-2018), January 18-20th, 2018, Department of Pharmaceutical Engineering & Technology, Indian Institute of Technology (Banaras Hindu University) Varanasi, India.

4. Targeting DNA repair with PNKP inhibition sensitizes radioresistant prostate cancer cells to high LET radiation, Srivastava P, Sarma A, Chaturvedi CM, PLoS One. 2018 Jan 10;13(1):e0190516. doi: 10.1371/journal.pone.0190516. eCollection 2018.

5. $A1_2B4C_3$, an inhibitor of polynucleotide kinase/phosphatase enhances radio-sensitivity in PC-3cells exposed to carbon ion beam, Pallavi Srivastava , Asitikantha Sarma, Chandra Mohini Chaturvedi, Journal of Innovations in Pharmaceutical and Biological Sciences (JIPBS), Vol 5(2), 27-31, 2018

6.8 LIST OF SEMINARS CONDUCTED IN THE YEAR 2017-18

S.No.	Date	Title	Name & Affiliation
1.	25/07/2017	Free Electron Laser	Prof. Vivek Asgekar, University of Pune
2.	28/07/2017	New Concept in Synchrotron Source for Advance Materials Research	Prof. Milan K. Sanyal, Saha Institute of Nuclear Physics, Kolkata
3.	12/10/2017	Pulse shape Discrimination with Newly Developed Scintillator EJ 299 - 33	Prof. M.B. Chatterjee SINP, Kolkata
4.	16/10/2017	High Power Terahertz Pulse Generation and it Application: Spectroscopy and Imaging	Dr. Mukesh Jewariya, National Physical Laboratory, New Delhi
5.	06/10/2017	Sturdy on Thz Cherenkov Radiation by Electron Bunch Tilting at Waseeda University	Prof. M. Washio, Waseeda University, Japan
6.	08/12/2017	A Novel Experiment in the search of Physics buyond the Standard Model	Dr. Ish Mukul, Weizmann Institute of Science, Israel
7.	12/01/2018	Stored Ion Beam Experiments in AMO Physics – from Highly Charged Ions to Molecules	Prof. Andreas Wolf, Max Planck Institute for Nuclear Physics, Heidelberg, Germany
8.	15/01/2018	Trapped charge dosimetryand its application to Earth and Planetary Sciences.	Dr. Rabiul Haque Biswas, SNF Senior Researcher, Institute of Lausanne Geopolis, Switzerland
9.	22/01/2018	Neutron scattering with pulsed neutrons: modern developments and opportunities	Dr. J Ross Stewart, Excitations and Polarized Neutron Group ISIS Pulsed Neutron and Muon Facility Rutherford Appleton Laboratory, Didcot, UK
10.	24/01/2018	The GANIL trump card for fission studies: Recent campaigns and results	Dr. C, Schmitt, Institute Pluri-disciplinaire Hubert Curien (IPHC), Rue du Loess, 67000 Strasbourg, France
11.	06/02/2018	Search for ferromagnetic behaviour in TM implanted oxides	Prof. Krish Bharuth Ram, Durban University of Technology. South Africa (Material Research Division)
12.	23/02/2018	Dynamics of Fusion and Fission Process in Hot, Rotating Nuclei	Dr. Avazbek Nasirov, FLNR, Dubna, Russia
13.	26/02/2018	Einstein vs Bohr via Heisenberg	Prof. Yeshwant Waghmare, Former Prof. & Dean, IIT Kanpur
14.	28/02/2018	Exciting Aspects of Nuclear Physics	Prof. Yeshwant Waghmare, Former Prof. & Dean, IIT Kanpur
15.	23/03/2018	From Fluorescent quantum clusters (Superatoms) to nanoparticles and their applications in sensing, therapy and imaging – observing the birth of a new phase with atom level control	Dr. Pankaj Poddar, Principal Scientist, Physical & Materials Chemistry Division, CSIR – National Chemical Laboratory, Dr. Homi Bhabha Road, Pune
16.	24/03/2018	Nuclear Internal Pair Creation and Search for a Light Neutral Boson	Prof. Indranil Mazumdar, Dept. Of Nuclear & Atomic Physics, TIFR, Mumbai

6.9 SCHOOLS, WORKSHOPS, ACQUAINTANCE PROGRAMMMES, FOUNDATION DAY & NATIONAL SCIENCE DAY CELEBRATIONS

School on Accelerator Science and Technology- 2018 (SAST-2018)

Rajeev Mehta

Inter-University Accelerator Centre (IUAC) hosted a School on Accelerator Science & Technology during May 7-18, 2018 under the sponsorship of Department of Science & Technology (DST). This school was third in the series of DST sponsored accelerator school. The aim of the school was to provide educational opportunities for young scientists, engineers, faculty members, post-doctoral fellows and research scholars in this important and advanced field of research and development (R&D) and to encourage them to contribute effectively in this challenging area of R&D.

This school gave an overview and status of the existing accelerator system and also explored the possibilities of the upcoming facilities. The school covered basic physics and technologies related to the accelerators. Series of lectures were delivered by experts from various prestigious accelerator based research institutes in India. There were interactive classroom tutorials sessions, special review talks by eminent scientists and engineers on some of the advance topics related to the accelerators. During hands-on experiments session participants were exposed to some of the technologies and equipment related to accelerators.

The school was offered to graduate, postgraduate students, junior researchers and young scientists etc. from all over the India who are highly motivated to pursue their carrier in accelerator science and technology.

Programme Schedule:

The school duration was two weeks starting from 7 May 2018. The program had intensive lectures, tutorials and hands on experiments on the wide range of technologies that form the base of the particle accelerator technology. School covered the areas like Beam Dynamics, RF Accelerator (Linear & Circular), Operational Aspect of Accelerator, Ion Sources, Vacuum, Instrumentations, High Power Devices, Radiation Safety etc. The overall program had 62 sessions.

- 38 Lectures
- 10 Special Review Talks and talks on major Indian projects
- 6 Tutorials
- 4 Hands on Experiments of 2 hours each (total 8 sessions)

“Hands on Experiments” was another feature that gave the participants an exposure to some of the technologies of accelerator physics. Following experiments were performed:

- Leak Detection Techniques
- Operational Aspects of Turbo Pump
- Low level RF Measurement Techniques: Bead Pull & Q Measurement
- High Power RF Test of Cavity

Interactive tutorial sessions were held, where participants were divided into four groups and were asked to solve the problem on the board. Marking system was introduced and the winner group was facilitated in the concluding session.

Participants Detail:

All major accelerator based laboratory, Institutes & Universities in India were asked to nominate upto three participants for this school. The applications were invited online through website of the school. We received overwhelming response to the school. 20 participants were selected to attend the school. Total 38 participants attended the school.

Financial Aid:

The school was fully funded by Department of Science & Technology (DST). All the participants, speakers were provided with local hospitality and accommodation by the school Organizers. Selected participants were provided with travel assistance by 3rd AC train fare.

Excursion Trip & Special Dinners:

An excursion trip was organized for the participants. The excursion trip was free for all the participants. During this trip participants visited Akshardham Temple

IUAC School on Nuclear Reactions 2017

S. Nath and A. Jhingan

IUAC School on Nuclear Reactions 2017 was held at IUAC from October 30 to November 04, 2017. Fifty research scholars and young faculty members from different universities and national institutes, working in the field of nuclear reactions, attended the school. Eminent speakers from all over the country were invited to teach the subject of their expertise. The curricula of the school included all major types of nuclear reactions. All energy domains i.e. astrophysical, low, intermediate and relativistic were covered with proper balance of theoretical and experimental aspects of the subjects. Tutorial sessions were conducted in the evening to make the participants familiar with the computational tools frequently used in the field. Soft copies of the study material were shared with the participants at the end of the school.

4th International Conference on Nanostructuring with Ion Beams (ICNIB 2017), DAVV Indore, Oct 11-13, 2017

A. Tripathi

The 4th International Conference on Nanostructuring with Ion Beams (ICNIB 2017) was organized by Devi Ahilya Vishwavidyalaya (University) (DAVV), Indore, India, in cooperation with the and Inter-University Accelerator Centre (IUAC), New Delhi and Ion Beam Society of India (IBSI). The conference was held at DAVV Auditorium, Indore, India during October 11th to 13th, 2017.

IUAC has been organising conferences on the topic of Nanostructuring with Ion Beams (NIB) and the last three conferences in this series were held in Allahabad, Jaipur and Agra in 2011, 2013 and 2015. The topics on Synthesis of buried nanostructures by energetic ions, Nano dots and nano ripples by ion induced sputtering and surface diffusion, Synthesis of nanostructures by ion or atom assisted deposition techniques, Ion beam induced modifications of materials, thin films, polymer micro/nanostructures and related simulations were covered in the conference. The conference was accompanied by a visit to national Synchrotron Radiation Facility (INDUS). The keynote address was given by Dr Ashok Ganguly, Institute of Nanoscience and Nanotechnology, Mohali and was co-chaired by Prof Ratnesh Gupta. The conference had more than twenty invited and oral talks each and more than 100 poster contributions. The IBSI gave the prizes for best oral presentation and best poster presentation by research scholars. The best oral presentation award was bestowed to Mr M Tripathi (University of Vienna) and best poster presentation awards were given to Ms Anuradha Bhogra (IUAC, New Delhi) and Mr Jaspal Singh (IP University, New Delhi).

Invited talk by Prof. R. Cuerno

Group photograph at DAVV Auditorium

One day IUAC Acquaintance programme, CU, Jammu, March 26, 2018

A. Tripathi

Department of Physics and Astronomical Sciences, Central University of Jammu (CU Jammu) in collaboration with the Inter-University Accelerator Centre (IUAC), New Delhi organized a one day acquaintance program on 'Accelerator Based Research' at Central University, Jammu on March 26, 2018. The inaugural function of the program was graced by Hon'ble Vice-chancellor, CUJ, Prof Ashok Aima as Chief Guest and the programme was organized by Dr. Vinay Kumar as convener of the program. After the presidential remarks by Prof. Aima, the accelerator based facilities available at IUAC, the research programmes in materials science, nuclear physics etc, as well as various modules and short term courses for PG and Ph.D. students offered by the Centre were introduced. The talks were given by Prof. Arun Bharti, Prof. S. K. Khosa, Dr Tanuj Kumar from Jammu, whereas IUAC programmes were discussed by Mr Rajeev Mehta and Dr Ambuj Tripathi from IUAC. Dr. Avinash Chand Yadav, coordinator of the event presented the vote of thanks.

Prof. Aima, VC , CUJ, Jammu and others at Inaugural ceremony and technical sessions

One day IUAC Acquaintance programme, Central University of Himachal Pradesh (HP) on April 10, 2017

P. Sugathan , Pawan Kulriya

Physics Department of Central University of Himachal Pradesh (CUHP), Kangra and IUAC New Delhi jointly conducted one day acquaintance program on April 10, 2017. One day program was arranged for physics teachers and young researchers from local colleges to acquaint themselves with IUAC accelerator facilities and the research opportunities in the field of Nuclear Physics, Materials Science, Accelerator Mass Spectrometry (AMS) etc. The acquaintance program proposal was submitted by Prof. O.S.K.S Sastri and subsequently the proposal was approved and funded by IUAC.

The program was attended by teachers and students from university and nearby colleges. The program commenced with the introduction by Prof O.S.K.S Sastri who was the local convener of the program. IUAC resource persons, Dr P. Sugathan and Dr Pawan Kulriya presented the overview of research facilities and opportunities for experimental research in nuclear physics, materials science, and accelerator mass spectromery. It was followed

by discussion where possibilities of doing projects and procedures for beam time application were discussed. Some of the users described their experience using the facilities at IUAC. The program concluded with summary note and vote of thanks by Prof Sastri.

National Science Day programme

The **National Science Day programme** was organized on 28th February 2018 at IUAC to celebrate the discovery of Raman Effect in 1928. For this programme, invitations were sent to various colleges and Universities in Delhi which conduct B. Sc. In Physics programmes. Fourteen such institutions sent their respective group comprising of four students and an accompanying faculty member to participate in the programme.

Prof. Waghmare delivering his National Science Day programme lecture

A group photograph of the National Science Day programme at IUAC

The programmes started with opening remarks by Dr. D. Kanjilal, Director, IUAC. Dr. P. N. Prakash introduced the invited speaker, Prof. Yeshwant R. Waghmare (Former Prof. and Dean, IIT Kanpur), to the gathering. Prof. Waghmare delivered his lecture titled "Exciting Aspects of Nuclear Physics". During his lecture, he referred to various exciting concepts of Nuclear Physics and shared anecdotes from his experiences. This lecture was followed by the talk titled "Introduction to Accelerators at IUAC" delivered by Dr. Pankaj Kumar (IUAC). The last pre-lunch talk titled "Materials Science Research Activities at IUAC using ion beams" was given by Dr. Ambuj Tripathi (IUAC).

Post-lunch session started with the science quiz conducted by Dr. Indra Sulania (IUAC). Prizes to the winners of the quiz were distributed by Dr. Kanjilal. Thereafter, the convenor of the programme, Dr. S. A. Khan thanked the participants and the organizing team, and divided the participants in four groups for visiting various research facilities of the centre. The programme concluded with the distribution of travelling allowance and certificates to the participants.

International Yoga Day Celebration

Yoga awareness camp on 21st June, 2017 at IUAC.

The Sports and Cultural Committee of IUAC organized a Yoga awareness camp to celebrate the International Yoga Day on June 21, 2017.

Independence Day and Republic Day Celebrations

Dr. D. Kanjilal, Director IUAC hoisting the National Flag on 26th January 2018

The Independence day was celebrated at IUAC by organizing competition among children on various topics like "on the spot painting", elocution, acting and debate. Similarly, The Republic Day was also celebrated by organizing sports competitions among the children and residents of the campus.

Community Lighting on Diwali

Community lighting on Diwali at IUAC campus.

In order to celebrate a cracker-free Diwali at the IUAC campus, the Sports and Cultural committee organized a Community Lighting Ceremony at the football ground of IUAC campus. Almost 200 residents participated in the celebration by lighting the Diyas and candles.

Annual Cultural Program "Spandan"

Cultural program of SPANDAN-2017 at IUAC campus.

The annual cultural festival "SPANDAN" of IUAC for the year 2017 was organized by the Sports & Cultural Committee on 4th November, 2017. About 70-80 children supported by the elders, participated in the event adorned by various regional dances, songs, instrumental music, mime show and drama.

APPENDIX – I

COMMITTEES

A. THE COUNCIL

The Chairman
University Grants Commission
Bahadur Shah Zafar Marg
New Delhi – 110 002

The Vice Chairman
University Grants Commission
Bahadur Shah Zafar Marg
New Delhi – 110 002

Prof. M. Jagadesh Kumar
Vice Chancellor
Jawaharlal Nehru University
New Delhi – 110 067

Prof. Vir Singh
Department of Physics
Indian Institute of Technology
Roorkee
Roorkee – 247 667

Prof. A.K. Grover
Vice Chancellor
Panjab University
Sector – 14
Chandigarh – 160 014

Prof. Mihir K. Chaudhary
Vice Chancellor
Tezpur University
Napaam, Tezpur Sonitpur
Assam – 784 028

Dr. K.S. Rangappa
Distinguished Professor
Institution of Excellence
Vijnana Bhavan
University of Mysore
Manasgangotri, Mysore – 570 006

Prof. Ashutosh Sharma
Secretary
Dept. of Science & Technology
New Mehrauli Road
New Delhi – 110 016

Dr. Srikumar Banerjee
DAE Homi Bhabha Chair Professor
Bhabha Atomic Research Centre
Central Complex, Trombay
Mumbai 400 085, Maharashtra

The Secretary
University Grants Commission
Bahadur Shah Zafar Marg
New Delhi – 110 002

Prof. V.S. Chauhan
International Center for Genetic Engineering & Biotechnology (ICGEB)
Aruna Asaf Ali Marg
New Delhi – 110 067

Dr. D.K. Aswal
Director
National Physical Laboraory
Dr KS Krishnan Marg, South Patel Nagar, Pusa, New Delhi, Delhi 110012

Prof. D.G. Kuberkar
Department of Physics
Saurashtra University
Rajkot – 360 005

Prof. Sanjay V. Deshmukh
Department of Life Sciences
University of Mumbai
M.G. Road, Fort
Mumbai – 400 032

Prof. V. Ramgopal Rao
Director
Indian Institute of Technology-Delhi
Hauz Khas
New Delhi – 110 016

Dr. Shekhar Basu
Secretary
Department of Atomic Energy
Anushakti Bhawan
Chhatrapati Shivaji Mahraj Marg
Mumbai – 400 039

Dr. Girish Sahni
Director General
Council of Scientific & Industrial Research
Anusandhan Bhavan, 2, Rafi Marg
New Delhi – 110 001

Prof. A. Damodaram
Vice Chancellor
Sri Venkateswara University
Sri Padmavati Mahila Visvavidyalayam Tirupati
Andhra Pradesh - 517502

Prof. Yogesh Singh
Director
Netaji Subhas Institute of Technology
New Delhi – 110 078

Dr. Ajit K.Sinha
Director
UGC-DAE Consortium for Scientific Research
University Campus, Khandwa Road,
Indore - 452017

Prof. Shyam Sundar Patnaik
Vice Chancellor
Biju Patnaik University of Technology
Chhend Colony, Rourkela
Odisha - 769015

Dr. Sundeep Chopra
Scientist-H
Inter-University Accelerator Centre
New Delhi – 110 067

Prof. R.C. Kuhad
Vice Chancellor
Central University of Haryana
Mahendragarh (Haryana)

Prof. Gautam Bhattacharya
Fellow, Indian Academy of Sciences & National Academy of Science
Saha Institute of Nuclear Physics
Kolkata – 700 064

Prof. Alok Chakrabarti
Accelerator Physics Group
Variable Energy Cyclotron Centre
Department of Atomic Energy
Kolkata – 700 064

Dr. Dinakar Kanjilal
Director
Inter-University Accelerator Centre
New Delhi – 110 067

B. GOVERNING BOARD

Dr. Srikumar Banerjee (Chairman)
DAE Homi Bhabha Chair Professor
Bhabha Atomic Research Centre
Central Complex, Trombay
Mumbai – 400 085

Vice Chairman
University Grants Commission
Bahadur Shah Zafar Marg
New Delhi – 110 002

Dr. D.K. Aswal
Director
National Physical Laboraory
Dr KS Krishnan Marg, South Patel Nagar, Pusa,
New Delhi, Delhi 110012

Prof. Mihir K. Chaudhary
Vice Chancellor
Tezpur University
Napaam, Tezpur Sonitpur
Assam – 784 028

Prof. Rajnish Jain
Secretary
University Grants Commission
Bahadur Shah Zafar Marg, New Delhi – 110 002

Prof. M. Jagadesh Kumar
Vice Chancellor
Jawaharlal Nehru University
New Delhi – 110 067

Prof. D.G. Kuberkar
Department of Physics
Saurashtra University
Rajkot – 360 005

Prof. V.S. Chauhan
International Center for Genetic Engineering & Biotechnology (ICGEB)
Aruna Asaf Ali Marg, New Delhi – 110 067

Prof. V. Ramgopal Rao
Director
Indian Institute of Technology-Delhi
Hauz Khas, New Delhi – 110 016

Dr. Dinakar Kanjilal
Director
Inter-University Accelerator Centre
New Delhi – 110 067

Prof. Sanjay V. Deshmukh
Department of Life Science
University of Mumbai
M.G. Road, Fort, Mumbai – 400 032

Prof. Vir Singh
Department of Physics
Indian Institute of Technology
Roorkee – 247 667

Dr. K.S. Rangappa
Distinguished Professor
Institution of Excellence, Vijnana Bhavan
University of Mysore, Manasgangotri
Mysore – 570 006

Dr. Sundeep Chopra
Scientist – H
Inter-University Accelerator Centre
New Delhi – 110 067

C. FINANCE COMMITTEE

Dr. Srikumar Banerjee
DAE Homi Bhabha Chair Professor
Bhabha Atomic Research Centre
Central Complex, Trombay
Mumbai – 400 085

Prof. Rajnish Jain
Secretary
University Grants Commission
Bahadurshah Zafar Marg, New Delhi-110002

Dr. P.K. Thakur
Financial Advisor
University Grants Commission
Bahadurshah Zafar Marg, New Delhi-110002

Prof. D.G. Kuberkar
Department of Physics
Saurashtra University
Rajkot – 360 005

Dr. N. Madhavan
Scientist – H
Inter-University Accelerator Centre
New Delhi – 110 067

Mr. Jose N.J.
Administrative Officer (F&A)
(Non Member Secretary)
Inter-University Accelerator Centre, New Delhi-110067

Dr. Manju Singh
Joint Secretary & Head-IUC Bureau
University Grants Commission
Bahadurshah Zafar Marg
New Delhi-110002

Dr. B. Hari Gopal
Science & Engineering Research Board
5 & 5A Lower Ground Floor
Vasant Square Mall
Plot -A Community Centre
Vasant Kunj, New Delhi – 110 070

Dr. Fouran Singh
Inter-University Accelerator Centre
New Delhi – 110 067

Dr. Dinakar Kanjilal
Director
Inter-University Accelerator Centre
New Delhi – 110 067

D. ACCELERATOR USERS COMMITTEE

Prof. B.P. Singh (Chairman)
Department of Physics
Aligarh Muslim University
Aligarh – 202 002 (U.P.)

Dr. A.K. Mohanty
Bhabha Atomic Research Centre
Trombay, Mumbai – 400 085

Prof. Vinay Gupta
Department of Physics & Astrophysics
North Campus
University of Delhi, Delhi – 110 007

Prof. D.Mohanta
Department of Physics
Tezpur University, Napaaam, Tezpur
Sonitpur, Assam – 784 025

Prof. J. Kumar
Crystal Growth Centre
Anna University
Chennai – 600 025

Prof. N.C. Mishra
Department of Physics, Utkal University
Sachivalaya Marg, Vani Vihar
Bhubaneswar – 751 009

Prof. Surjit Mookerjee
Department of Physics, The M.S. University of Baroda
Faculty of Science, University Campus
Sayajiganj, Baroda – 390 002

Prof. J.P. Singh
Department of Physics, IIT Delhi
Hauz Khas, New Delhi – 110 016

Prof. Shirsat Mahendra
Dr. Babasaheb Bhimrao Ambedkar Marathwada University
University Campus, Samrath Nagar
Maharashtra – 431 001

Prof. H.P. Sharma
Associate Professor, Faculty of Science
Department of Applied Physics
Banaras Hindu University, Varanasi – 221 005

Dr. Dinakar Kanjilal
Director
Inter-University Accelerator Centre
New Delhi – 110 067

Dr. S. Chopra
Scientist – H
Inter-University Accelerator Centre
New Delhi – 110 067

E. SCIENTIFIC ADVISORY COMMITTEE

Members

Dr. Dinakar Kanjilal
Director
Inter-University Accelerator Centre
New Delhi – 110 067

Dr. Javed Sheikh
Department of Physics
University of Kashmir
Hazratbal
Srinagar – 190 006

Dr. D.C. Kothari
Department of Physics
University of Mumbai
Vidyanagari, Kalina
Santacruz (E)
Mumbai – 400 098

Prof. D.G. Kuberkar
Department of Physics
Saurashtra University
Saurashtra University Campus
Rajkot – 360 005

Prof. Vinay Gupta
Department of Physics
University of Delhi
Delhi – 110 007

Prof. Raghava Varma
Department of Physics
Indian Institute of Technology-Bombay
Powai
Mumbai – 400 076

Dr. Alok Chakrabarty
Department of Physics
Variable Energy Crystal Centre
1AF, Bidhannagar
Kolkata – 700 004

Dr. B.P. Ajith Kumar
Scientist
Inter-University Accelerator Centre
New Delhi – 110 067

Associated Members

Dr. P.D. Gupta
Raja Ramanna Centre for Advance Technology
P.O. CAT
Indore – 452 013

Dr. A.K. Grover
Vice Chancellor
Punjab University
Sector – 14
Chandigarh – 160 014

Prof. Hans-Arno-Synal
ETH Zurich
Labor f. Ionestrahiphysik (LIP)
HPK H 33
Otto - Stern – weg 5
8093 Zurich

Prof. T.Venky Venkatesan
Director - NUSNNI
Non Core Engineering
Block A, EA, Level 4, Room No. 27
Faculty of Engineering
National University of Singapore
Singapore 117581

Prof. Alahari Navin
Grand Accelerateur National d'Jons Lourds
Bd Henri Bacqueral
BP 55 027 – 14076
CAEN Cedex 05, France

Dr. Robert Laxdal
TRIUMF
4004, Wesbrook Mall
Vancouver, BC V6T 2A3
Canada

APPENDIX-II

April 2017 March 2018

IUAC PERSONNEL

DIRECTOR

Dr. D. Kanjilal

SCIENTISTS

Dr. T.S. Datta	Dr. Tapan K. Nandi	Dr.(Mrs.) Indra Sulania
Dr. Sundeep Chopra	Dr. Akhil Jhingan	Dr. Rajesh V. Hariwal
Dr. P.N. Prakash	Mr. Sunil Ojha	Dr. Sarvesh Kumar
Dr. S. Murlithar	Dr. Soumen Kar	Ms. Indu Bala
Dr. Ajith Kumar B.P.	Dr. Fouran Singh	Mr. Joydeep Karmakar
Dr. N. Madhavan	Dr. Rakesh Kumar	Mr. Rajveer Sharma
Dr. P. Sugathan	Dr. Subir Nath	Mr. Kedarmal
Dr. Subhendu Ghosh	Mr. Ashutosh Pandey	Mr. Saneesh N
Dr. Ambuj Tripathi	Dr. Praveen Kumar	Mr. Sanjay Kumar Kedia
Dr. G.O. Rodrigues	Mrs. K. Devrani Devi	Mr. Ram Charan Meena
Mr. Abhijit Sarkar	Dr. C.P. Safvan	Mr. Deepak Kumar Swamy
Mr. Rajeev Mehta	Dr. Saif Ahmad Khan	Mr. Bappa Karmakar
Dr. Asiti Sarma	Mrs. K.S. Golda	Mr. Mohit Kumar
Dr. D. Kabiraj	Mr. Abhishek Rai	Mr. G.R. Umapathy
Dr. R.P. Singh	Mr. Sugam Kumar	Mr. Ambuj Mishra
Mr. Debashish Sen	Dr. Pankaj Kumar	Mr. Abhishek Kumar
Dr. K. Asokan	Dr. Pawan Kumar Kulriya	Ms. Gonika
Dr. V.V.V. Siva Kumar	Mrs. P.S. Lakshmy	Ms. Deeksha Khandelwal
Dr. Bhuban Kumar Sahu	Mr. Jagdish Gehlot	Ms. Madhuri
Mr. Anup Choudhary	Mr. Padmanava Patra	Mr. Yashraj

ENGINEERS & TECHNICAL PERSONNEL

Mr. M.K. Gupta
Dr. Piyush Gupta
Mr. K.K. Soni
Dr. Sumit Mookherjee
Mr. Kundan Singh
Mrs. Ruby Shanthi
Mr. Jimson Zacharias
Mr. Rajan Joshi
Mr. U.G. Naik
Mr. S. Venkataramanan
Mr. Satinath Gargari
Mr. Joby Antony
Mr. Bishamber Kumar
Mr. A.J. Malyadri
Mr. Raj Kumar
Mr. E.T. Subramaniam
Mr. Rajeev Ahuja
Mr. Pradeep Barua
Mr. Rajesh Kumar
Mr. Santosh Kumar Sahu
Mr. Rajesh Nirdoshi
Mr. Ashish Sharma
Mr. S. Bhatnagar
Mr. U. Koteshwara Rao
Mr. Rajpal Sharma
Mr. Mukesh Sota
Mr. R.N. Dutt
Mr. S.S.K. Sonti
Mr. G.K. Choudhary
Mr. Manoj Kumar
Mr. S.K. Saini
Mr. Suresh Babu M.V.
Mr. Thomas Varughese
Mrs. Arti Gupta
Mr. Ashok Kothari
Mr. V.P. Patel
Mrs. P. Nayak
Mrs. Kusum Rani
Mr. S.K. Suman
Mr. D.K. Mathuria
Ms. Mamta Jain
Mr. Kishore Kumar Mistri
Mr. V.V.V Satyanarayana
Mr. Abhilash S.R.
Mr. Birendra Singh
Mr. M. Archunan
Mr. Yaduvansh Mathur
Mr. B.B. Choudhary
Mr. Mukesh Kumar
Mr. Parmanand Singh
Mr. Radhakishan Gurjar
Mr. Deepak Kumar Munda
Mr. Chandrapal
Mr. Harshwardhan
Mr. Davinder K. Prabhakar
Mr. Prem Kumar Verma

TECHNICIANS

Mr. Jagdish Prasad
Mr. Rakesh Kumar
Mr. Pranav Singh
Mr. M.P. Singh
Mr. Mohan Nishal
Mr. Jaswant Singh
Mr. Suraj Kumar
Mr. N.S. Panwar
Mr. Gaurav Rathuri

ADMINISTRATIVE STAFF

Mr. Bishwambhar Datt
Mr. K. Murali
Mr. M.B. Joseph
Mrs. Ranju Rishi
Mr. N.J. Jose
Mrs. Usha Kataria
Mr. Satyavan
Mr. M.R. Ramasubramaniam
Mrs. Manvinder Kaur
Mr. Sohan Singh
Mr. N.P. Ponnappan
Mr. Sudershan Sharma
Mr. Prakash S. Kumbhare
Mr. Swaroop Kr. Maurya
Mrs. Bindu Xaxa
Mr. Pethan Shanmugam
Mr. R.N. Dhyani
Mr. Rajendra Prasad
Mr. Rahul Sahni
Ms. Manisha Rani
Mr. Paras Nath
Ms. Nishtha Saxena
Mr. Bharat Sharma
Mr. Jay Prakash
Mr. Subhash Chandra
Mr. Shubham Kumar
Mr. Harish Diwakar
Mr. Raj Kumar Verma
Mrs. Chanderkala
Mr. Piyush Verma

DRIVERS

Mr. Kehar Singh
Mr. Madan Lal
Mr. Kailash Kumar
Mr. M. Samantra

RESEARCH SCHOLARS

Mr. Tathagata Banerjee
Mr. Prashant Sharma
Mr. Arkaprava Das
Ms. Chetna Tyagi
Ms. Anuradha
Ms. Himanshi Gupta
Mr. Jitendra Singh
Mr. Vipul Joshi
Mr. Rohan Biswas
Mr. Saurabh Kumar Sharma
Mr. Divya Arora
Mr. Ishtiaq Ahmed
Mr. Kasuhik Katre
Mr. Sushil Kumar
Ms. Anusmita Chakravorty

RESEARCH ASSOCIATE

Dr. Chandrabhan Yadav
Dr. Vijay Raj Sharma
Dr. Vishal Srivastava
Dr. Md. Moin Shaikh
Dr. Narender Kumar
Dr. Soumya Prakash Dal
Dr. Soumendu S. Bhattacharjee
Dr. Trivedi Priyankaben
Dr. Gurpreet Kaur
Dr. Chetan Prakash Saini
Dr. Anamika Parihari

NATIONAL POST DOCTORAL FELLOW (N - PDF) - DST PROJECT (YOUNG SCIENTISTS)

Dr. Abhishek Yadav
Dr. Chinmaya Maharana
Dr. V.S. Vendamani

DST-INSPIRE FACULTY

Dr. Kamla Rawat
Dr. Ashish Kumar
Dr. Pragya Bhatt
Dr. Budhi Singh
Dr. Pramod Kumar

DS KOTHARI POST DOCTORAL FELLOW

Dr. Himani Khanduri

Dr. Rakesh Kumar

Dr. Lisha Raghavan

UGC POST DOCTORAL FELLOW FOR WOMEN

Dr. Razia Nongial

IMRI-SAMEER-MEITY PROJECT

Dr. R.G. Sharma

Mr. Sankar Ram T

Mr. Navneet Kumar Suman

GITA-DST PROJECT

Ms. Anha Masarrat

APPENDIX - III

LIST OF USERS 2017-18

HEAVY ION RADIATION BIOLOGY

Agrawala Paban K
INMAS, DRDO
Brig. S.K. Mazumdar Road, Timarpur
Delhi, Pin Code-110 054

Alok Amit
Division of Radiation Biodosimetry
Inst. of Nuclear Medicine & Allied Sciences
Brig. S.K. Mazumdar Marg, Timarpur
Delhi, Pin Code-110 054

Bhatt Anant Narayan
Inst. of Nuclear Medicine and Allied Sciences
Delhi, Pin Code-110 054

Sharma Jai Gopal
Department of Biotechnology
Delhi Technological University
Shahbad Daulatpur
Main Bawana Road, Delhi-110 042

Utpal Ghosh
Deptt. of Biochemistry & Biophysics
University of Kalyani, Kalyani
Nadia, West Bengal-741 235

NUCLEAR PHYSICS

Agarwal Avinash
Department of Physics
Bareilly College, Bareilly
(M.J.P. Rohilkhand University Bareilly)
Pin Code-243 005

Badiger N.M.
Department of Physics
Karnatak University
Pavate Nagar
Dharwad-580 003 (Karnataka)

Behera Bivash Ranjan
Department of Physics
Panjab University
Chandigarh, Sector-14
Chandigarh-160 014

Das Mili
Ananda Mohan College
102/1 Raja Rammohan
Sarani, Kolkata-700 009

Deo Ajay Y.
Department of Physics
Indian Inst. of Technology Roorkee
Roorkee, Uttarakhand
Pin Code-247 667

Devi Sunil
School of Physics and Materials Science
Thapar University, Patiala-147 004

Bhati A.K.
Department of Physics
Punjab University
Chandigarh-160 014

Bisoi Abhijit
Indian Inst. of Engg.Science and Tech., Shibpur
Department of Physics
IIEST Shibpur, Shibpur, Howrah-711 103

Chamoli Sanjay Kumar
Deptt. of Physics Astrophysics
University of Delhi
Delhi-110 007
Kumar Ashok
Department of Physics
Panjab University
Sector-14, Chandigarh-160 014

Kumar Suresh
Deptt. of Physics and Astrophysics
University of Delhi (North Campus)
Delhi-110 007

Maiti Moumita
Department of Physics
Indian Institute of Technology Roorkee
Roorkee-247 667 (Uttarakhand)

Mandal Samit Kr.
Deptt. of Physics & Astrophysics
University of Delhi
Delhi-110 007

Mukherjee Gopal
Variable Energy Cyclotron Centre
1/AF Bidhan Nagar, Kolkata
Pin Code-700 064

Rajbanshi Subhendu
Dum Dum Motijheel College
1, Motijheel Avenue, Dum Dum
Kolkata, West Bengal, Pin Code: 700 074

Dhiman Shashi K.
Department of Physics
Himachal Pradesh University
Gyan-Path, Summer-Hill, Shimla
Himachal Pradesh-171 005

Doherty Daniel
Department of Physics
University of Surrey
Guildford- GU2 7XH, UK

Kaur Navneet
S.D. College Ambala Cantt
(Kurukshetra University)
#7678/4, Nadi Mohalla
Ambala City-134 003
Sihotra Samarjit
Department of Physics
Panjab University
Sector-14, Chandigarh-160 014

Singh B.P.
Department of Physics
Aligarh Muslim University
Aligarh-202 002

Singh Dharmendra
Centre for Applied Physics
Central University of Jharkhand
Ratu-Lohardaga Road
Brambe, Ranchi-835 205 (Jharkhand)

Singh Hardev
Department of Physics
Kurukshetra University
Kurukshetra-136 119 (Haryana)

Singh Varinderjit
Department of Physical Sciences
IKG Punjab Technical University
Jalandhar-Kapurthala Highway
Near Pushpa Gujral Science City
Ibban, Kapurthala, Punjab-144 603

Tandel Sujit
University of Mumbai
Kalina, Santacruz (East)
Mumbai, Pin Code-400 098

Rizvi Isar Ahmad
Department of Physics
Aligarh Muslim University
Aligarh-202 002 (U.P.)

Saxena Mansi
Heavy Ion Laboratory
University of Warsaw
Pasteura 5A
Warsaw, Poland-02-093

Sharma H.P.
Department of Physics
Banaras Hindu University
Varanasi-221 005

Trivedi Tarkeshwar
Deptt.of Pure & Applied Physics
Guru Ghasidas Vishwavidyalaya
Koni, Bilaspur, Pin Code-495 009

Vinodkumar A.M.
Department of Physics
Calicut University,
Malappuram, Kerala
Pin Code-673 635

MATERIALS SCIENCE

Arora Sunil Kumar
Centre for Nano Sci. & Nano Tech.
Block-II, South Campus
Panjab University, Chandigarh
Pin Code-160 014

Bala Manju
Deptt. of Physics and Astrophysics
University of Delhi
Delhi-110 007

Behera D.
Deptt. of Physics and Astronomy
National Institute of Technology Rourkela
Rourkela, Orissa-769 008

Bhasker Hari Pratap
Department of Physics
Motilal Nehru National Inst. of Tech.
Teliarganj, Allahabad-211 004

Bingham Paul A.
Materials and Engineering Research Inst.
Sheffield Hallam University
City Campus, Howard Street
Sheffield, S1 1WB, UK

Awasthi Kamlendra
Department of Physic
Malaviya National Inst. of Tech. Jaipur
Jawahar Lal Nehru Marg, Jaipur-302 017

Das Pradip
Department of Pure and Applied Physics
Guru Ghasidas University, Koni
Bilaspur, Pin Code-495 009

Das Susanta
Department of Physics
School of Physical & Chemical Sciences
Central University of South Bihar
Gaya, Bihar, Pin Code-823 001

Dhoble Sanjay J.
Department of Physics
Rashtrasant Tukadoji Maharaj Nagpur Univ.
Amravati Road, Ram Nagar
Nagpur, Maharashtra-440 033

Dhole S.D.
Department of Physics
Microtron Accelerator Lab
Savitribai Phule Pune University
Pune- 411 007

Chand Fakir
Department of Physics
Kurukshetra University
Kurukshetra-136 119 (Haryana)

Chauhan R.P.
Department of Physics
National Institute of Technology, Kurukshetra
Kurukshetra-136 119

Chopra Vibha
P.G. Deptt. of Physics & Electronics
DAV College, Katra Sher Singh
Amritsar, Punjab, Pin Code-143 001

Dahiwale Shailendra S.
Department of Physics
Savitribai Phule Pune University
Pune, Pin Code-411 007

Dar Ghulam Nabi
Department of Physics
University of Kashmir
Hazratbal, Srinagar-190 006 (J&K)

Goyal D.P.
Department of Physics
Indira Gandhi University Meerpur
Rewari-Lokri Road
Rewari, Meerpur, Haryana-123 401

H. Devendrappa
Mangalore University
Mangalagangotri-574 199 (Karnataka)

Ikram M.
Department of Physics
National Institute of Technology, Srinagar
Hazratbal, Kashmir-190 006 (J&K)

Joshi Uptal Shashikant
Department of Physics
Gujarat University
Ahmedabad, Pin Code-380 009

Dhruv Davit B.
Department of Nanotechnology
V.V.P. Engineering College
Gujarat Technological University
Rajkot, Gujarat, Pin Code-360 005

Diwan Pawan K.
Department of Applied Science
Univ. Institute of Engineering and Technology
Kurukshetra University
Kurukshetra-136 119, Haryana

Dolui Swapan Kumar
Deptt. of Chemical Sciences
Tezpur University
Napam, Tezpur, Assam-784 028

Gautam Sanjeev
Department of Physics
Panjab University, Chandigarh
Dr. S.S. Bhatnagar Univ. Inst. of Chemical Engg.& Tech.
Pin Code-160 014

Ghuman S.S.
Department of Physics
Sant Longowal Inst. of Engg. & Tech.
Campus Road, Sangrur
Longowal, Punjab-148 106

Kumar Ashok
Department of Physics
Tezpur University
Napaam, Tezpur
Sonitpur, Assam-784 028

Kumar Manoj
Department of Physics
Malaviya National Institute of Technology Jaipur
Jawahar Lal Nehru Marg, Jaipur-302 017

Kumar Rajesh
Univ. School of Basic and Applied Sciences
Guru Gobind Singh Indraprastha University
Dwarka Sector-16-C, New Delhi-110 078

Kumar Sandeep
Department of Physics
Central University of Rajasthan
Bandarsindri, Distt. Ajmer-305 817

Katharria Yashpal Singh
PDPM IIITDM Jabalpur
Dumna Airport Road
Khamaria, Jabalpur-482 005 MP

Kaushal Gaurav
D Block -115, ABV-IIITM
Morena Link Road, Gwalior-(M.P.)
Pin Code-474 015

Keshvani M.J.
Department of Physics
Marwadi University
Rajkot-Morbi Highway Road
Gauridad, Rajkot, Gujarat-360 003

Khan M. Wasi
Department of Physics
Aligarh Muslim University
Aligarh-202 002 (U.P.)

Krishnan Sheeja
Department of Physics
SDIT, Kenjar
Mangaluru-574 142

Krishnaveni S.
DOS in Physics
University of Mysore
Manasagangotri
Mysuru-570 006

Mohanty Tanuja
School of Physical Sciences
Jawaharlal Nehru University
New Delhi-110 067

Mohapatra Satyabrata
Univ. School of Basic & Applied Sciences
Guru Gobind Singh Indraprastha University
Sec-16 C, Dwarka, New Delhi-110 078

Mahajan Aman
Guru Nanak Dev University
Amritsar, Punjab-143 005

Manikanthababu N.
Indira Gandhi Centre for Atomic Research
Room No.194 A/B, 17th Avenue JRF Enclave
DAE Township Kalpakkam-603 102

Mehta Priti J.
Institute of Pharmacy
Nirma University
Sarkhej-Gandhinagar Highway
Chandlodia, Gota
Ahmedabad, Gujarat-382 481

Mittal Jagjiwan
Amity Inst. of Nanotechnology
Amity University
UP Sector-125
Noida (UP)-201301

Modi Kunal B.
Department of Physics
Saurashtra University
Rajkot, Pin Code-360 005

Mohanta Dambarudhar
Department of Physics
Tezpur University
Napaam, Tezpur
Sonitpur, Assam-784 028

Patnaik Satyabrata
Condense Matter Physics Lab-119
School of Physical Sciences
Jawaharlal Nehru University
New Delhi-110 067.

Rajendrakumar R.T.
Department of Nanoscience and Tech.
Bharathiar University
Marudhamalai Road
Coimbatore-641 046 (Tamil Nadu)

Nair Lekha
Department of Physics
Jamia Millia Islamia University
Mohammad Ali Johar Marg
Jamia Nagar, Okhla
New Delhi-110 025

Niazi Asad
Department of Physics
Jamia Millia Islamia University
Mohammad Ali Johar Marg
Jamia Nagar, Okhla
New Delhi-110 025

Palikundwar U.A.
Department of Physics
R.T.M.N. University
Nagpur, Pin Code-440 033

Pandey Anant
Department of Physics
Sri Venkateswara College
University of Delhi, Delhi
Pin Code-110 021

Pannu Compesh
C/o Prof. Santanu Ghosh
Department of Physics
Indian Institute of Technology Delhi
Hauz Khas, New Delhi-110 016

Panwar Neeraj
Department of Physics
Central University of Rajasthan
NH-8, Bandar Sindri
Dist-Ajmer-305817, Rajasthan

Patel Shiv Poojan
Deptt. of Pure and Applied Physics
Guru Ghasidas Vishwavidyalaya
(A Central University), Koni
Bilaspur-495 009 (C.G.)

Shirsat Mahendra D.
RUSA-Center for Advanced Sensor Technology
Dr. Babasaheb Ambedkar Marathwada University
University Campus, Near Soneri Mahal
Jaisingpura, Aurangabad, Maharashtra-431 004

Rana J.M.S.
Department of Physics
Hemwati Nandan Bahuguna Garhwal University
Srinagar-Dist. Pauri Garhwal
(Uttarakhand) India-246 174

Rao S.V.S. Nageswara
School of Physics
University of Hyderabad
Central University P.O.
Hyderabad-500 046 (Andhra Pradesh)

Roy Somnath C.
Department of Physics
Indian Institute of Technology Madras
I.I.T. Post Office, Chennai-600 036

Sachdev Kanupriya
Materials Research Centre
Malaviya National Inst. of Tech. Jaipur
Jawahar Lal Nehru Marg, Jaipur-302 017

Samad Rubiya
Solid State Research Lab
Department of Physics
University of Kashmir
Srinagar, Pin Code-190 006

Shah Sejal
ITER-India
Institute for Plasma Research
Block A, Sangath Skyz
Bhat-Motera Road, Koteshwar
Ahmedabad-380 005

Sharma Ramphal
Department of Physics
Dr. Babasaheb Ambedkar Marathwada University
University Campus, Near Soneri Mahal
Jaisingpura, Aurangabad, Maharashtra-431 004

Singh Vaishali
BFR – 303
Univ. School of Basic & Applied Sciences
Guru Gobind Singh Indraprastha University
Sec-16 C, Dwarka, New Delhi-110 078

Shivakumara C.
Solid State and Structural Chemistry Unit
Indian Institute of Science, Bangalore
Pin Code-560 012

Shukla Rajni
Department of Physics
Deenbandhu Chhotu Ram Univ. of Sc. &Tech.
Murthal, Sonepat
Pin Code-131039

Siddiqui Azher Majid
Department of Physics
Jamia Millia Islamia University
Mohammad Ali Johar Marg
Jamia Nagar, Okhla
New Delhi-110 025

Singh Anupinder
Department of Physics
Guru Nanak Dev University
Amritsar, Punjab-143 005

Singh A.P.
Department of Physics
Dr. B.R. Ambedkar National Int. of Tech.
Jalandhar-144 011

Singh Davinder Paul
Department of Physics
Guru Nanak Dev University
Amritsar, Punjab-143 005

Singh Lakhwant
Department of Physics
Guru Nanak Dev University
Amritsar, Punjab-143 005

Singhal Rahul
Department of Physics
Malaviya National Inst. of Tech. Jaipur
Jawahar Lal Nehru Marg, Jaipur-302 017

Thakur Anup
Deptt. of Basic & Applied Sciences
Punjab University, Patiala
Punjab, Pin Code-147 002

Tiwari Archana
Department of Physics
Sikkim University
Samdur, P.O, Tadong
Gangtok, Sikkim-737102

Tripathi Balram
Department of Physics
S.S. Jain Subodh (PG) College
Rambagh Circle, Jaipur-302 004 (Raj)

Tripathi Neeti
School of Physical Sciences
Department of Physics
Doon University
Doon University Campus
Kedarpur, Dehradun
Uttrakhand, Pin Code-248 001

Want Basharat
Department of Physics
University of Kashmir
Hazratbal, Srinagar-190 006 (J&K)

ACCELERATOR MASS SPECTROMETRY

Achyuthan Hema
Department of Geology
Anna University
Chennai-600 025

Handique Sumi
Deptt. of Environmental Science
Tezpur University. Napaam
Tezpur. Assam, Pin Code-784 028

Jaiswal Manoj Kumar
Department of Earth Sciences
IISER Kolkata
Mohanpur Campus
Pin Code-741 246 Nadia (WB)

Mani Buddha Rashmi
National Museum, ASI
Janpath, New Delhi-110 011

Manjul Sanjay Kumar
Archaeological Survey of India
Institute of Archaeology
Red Fort Complex, Delhi-110 006

Meena Narendra K.
Wadia Institute of Himalayan Geology
33 GMS Road, Dehradun-248 001

Mishra Umakanta
Department of History
Ravenshaw University
Cuttack-753 003

Naik Satish S.
Palaeobotany Lab
Department of Archaeology
Deccan College Post-Graduate & Research Institute
Deemed University, Pune-411 006

Chakraborty Supriyo
Indian Institute of Tropical Meteorology
Dr. Homi Bhabha Road, Pashan
Pune-411 008, Maharashtra

Pati Pitambar
Department of Earth Sciences
Indian Institute of Technology Roorkee
Roorkee-247 667 (Uttarakhand)

Rajendran C.P.
Geodynamics Unit
Jawaharlal Nehru Centre for Advanced Scientific Research
Rachenahalli Lake Rd, Jakkur
Bengaluru, Karnataka-560 064

Sabale P.D.
Department of Ancient Indian History
Culture & Archaeology, Deccan College
P.G.R.I. (Deemed University)
Pune-411 006

Saraswat Rajeev
National Institute of Oceanography
Geological Oceanography Division
Dona Paula, Goa, Pin Code-403 004

Sarkar Neera Sen
Psychology Section
Department of Botany
University of Kalyani
Kalyani, Nadia
West Bengal-741 235

Selvakumar V.
Deptt. of Epigraphy and Archeology
Tamil University
Thanjavur-613 010

Srivastava Alok
Department of Chemistry
Panjab University
Sector-14, Chandigarh-160 014

Nayak G.N.
Department of Marine Sciences
Goa University
Taleigao Plateau, Goa-403 206

Syiemlieh Hiambok Jones
Department of Geography
School of Human and Environmental Studies
North-Eastern Hill University
Shillong, Meghalaya, Pin Code-793 022

N. Karunakara
CARER, Mangalore University
Mangalagangothri-574 199, Karnataka

Tripathi Jayant Kumar
Lab. No. 013/101
School of Environmental Sciences
Jawaharlal Nehru University
New Delhi-110 067

Ota S.B.
Archaeological Survey of India, Janpath
New Delhi-110 011

Vikrama Bhuvan
Archaeological Survey of India
22 the Mall, Agra
Uttar Pradesh-282 001

ATOMIC PHYSICS

Karn Ranjeet Kumar
Department of Physics
Kolhan University
Chaibasa, Jharkhand
Pin Code-833 202

Singh K.P.
Department of Physics
Panjab University
Sector-14, Chandigarh-160 014

Mitra Debasis
Department of Physics
University of Kalyani
Kalyani, Nadia, West Bengal
Pin Code-741 235

Verma Punita
Department of Physics
Kalindi College
East Patel Nagar
University of Delhi
Pin Code-110 008

LOW ENERGY ION BEAM FACILITY

Bala Manju
Deptt. of Physics and Astrophysics
University of Delhi
Delhi, Pin Code-110 007

Dubey Santosh
Department of Physics
Univ. of Petroleum & Energy Studies
Bidholi, Via Premnagar, Dehradun
Uttarakhand, Pin Code-248 007

Basak Durga
Deptt. of Solid State Physics
Indian Association for the Cultivation of Science
2A & 2B Raja SC Mullick Road
Jadavpur, Kolkata, Pin Code-700 032

Bhattacharya Jaydeep
Lab 001, School of Biotechnology
Jawaharlal Nehru University
New Delhi-110 067

Birajdar Balaji
Special Centre for Nanosciences
Jawaharlal Nehru University
New Delhi-110 067

Chatterjee Shyamal
Room No. 120
School of Basic Sciences
IIT Bhubaneswar, Jatni
Khordha, Odisha-752 050

Dubey Radhekrishna L.
Department of Physics
St. Xavier's College-Autonomous
University of Mumbai
5 Mahapalika Marg
Mumbai, Pin Code-400 001

Rajput Jyoti
Room No. 96 (New Block)
Deptt of Physics & Astrophysics
Univ.of Delhi (North Campus)
Delhi, Pin Code-110 007

Singh Dharmvir
Department of Physics
Chaudhary Devi Lal University Sirsa
Haryana, Pin Code-125 055

Srivastava A.P.
Mechanical Metallurgy Division
Bhabha Atomic Research Centre
Trombay, Mumbai-400 085

G.N. Kumaraswamy
Department of Physics
Amrita School of Engineering
Amrita Vishwa Vidyapeetham
Kasavanahalli, Bengaluru
Pin Code-560 035

Jana Debnarayan
Department of Physics
University of Calcutta
92, A.P.C. Road
Kolkata-700 009

Kanjilal Aloke
Department of Physics
Shiv Nadar University
Greater Noida, Tehsil Dadri
Gautam Buddha Nagar, U.P.
Pin Code-201 314

Maya P.N.
ITER-India
Institute for Plasma Research
Bhat, Gandhinagar-382 428, Gujarat

Puri Sanjiv
Deptt. of Basic & Applied Sciences
Punjabi University, Patiala
Punjab, Pin Code-147 002

Venkatesh P. Sundara
Department of Physics
Sri S. Ramasamy Naidu Memorial College
Sattur/Madurai Kamaraj University
Madurai, Pin Code-626 203 (Tamil Nadu)

Wadhwa Shikha
Amity Inst. of Nanotechnology
Amity University
Uttar Pradesh, Pin Code-201 313

अन्तर-विश्वविद्यालय त्वरक केन्द्र

Inter-University Accelerator Centre

(विश्वविद्यालय अनुदान आयोग का स्वायत्त केन्द्र)

(An Autonomous Inter-University Centre of UGC)

Post Box No. 10502, Aruna Asaf Ali Marg, New Delhi - 110 067 (India)

Tel: 011-24126018, 24126022, 24126024-26, 24126029

Fax: 011-24126036, 24126041 Website : www.iuac.res.in

Printed by : Neelkanth Printers, 9871210948, neelkanthprinters@gmail.com